frontiers | Research Topics

# Nanomaterials for biology and medicine

**Edited by**
Guannan Wang, Xiangzhao Ai and Pengfei Xu

**Published in**
Frontiers in Bioengineering and Biotechnology
Frontiers in Chemistry
Frontiers in Molecular Biosciences

ISSN 1664-8714
ISBN 978-2-8325-3390-1
DOI 10.3389/978-2-8325-3390-1

## About Frontiers

Frontiers is more than just an open access publisher of scholarly articles: it is a pioneering approach to the world of academia, radically improving the way scholarly research is managed. The grand vision of Frontiers is a world where all people have an equal opportunity to seek, share and generate knowledge. Frontiers provides immediate and permanent online open access to all its publications, but this alone is not enough to realize our grand goals.

## Frontiers journal series

The Frontiers journal series is a multi-tier and interdisciplinary set of open-access, online journals, promising a paradigm shift from the current review, selection and dissemination processes in academic publishing. All Frontiers journals are driven by researchers for researchers; therefore, they constitute a service to the scholarly community. At the same time, the *Frontiers journal series* operates on a revolutionary invention, the tiered publishing system, initially addressing specific communities of scholars, and gradually climbing up to broader public understanding, thus serving the interests of the lay society, too.

## Dedication to quality

Each Frontiers article is a landmark of the highest quality, thanks to genuinely collaborative interactions between authors and review editors, who include some of the world's best academicians. Research must be certified by peers before entering a stream of knowledge that may eventually reach the public - and shape society; therefore, Frontiers only applies the most rigorous and unbiased reviews. Frontiers revolutionizes research publishing by freely delivering the most outstanding research, evaluated with no bias from both the academic and social point of view. By applying the most advanced information technologies, Frontiers is catapulting scholarly publishing into a new generation.

## What are Frontiers Research Topics?

Frontiers Research Topics are very popular trademarks of the *Frontiers journals series*: they are collections of at least ten articles, all centered on a particular subject. With their unique mix of varied contributions from Original Research to Review Articles, Frontiers Research Topics unify the most influential researchers, the latest key findings and historical advances in a hot research area.

Find out more on how to host your own Frontiers Research Topic or contribute to one as an author by contacting the Frontiers editorial office: frontiersin.org/about/contact

# Nanomaterials for biology and medicine

**Topic editors**
Guannan Wang — Jining Medical University, China
Xiangzhao Ai — Shanghai Jiao Tong University, China
Pengfei Xu — National University of Singapore, Singapore

**Citation**
Wang, G., Ai, X., Xu, P., eds. (2023). *Nanomaterials for biology and medicine*. Lausanne: Frontiers Media SA. doi: 10.3389/978-2-8325-3390-1

# Table of contents

frontiers | Frontiers in Chemistry

TYPE Editorial
PUBLISHED 17 August 2023
DOI 10.3389/fchem.2023.1244175

# Editorial: Nanomaterials for biology and medicine

Guannan Wang*

College of Medical Engineering and the Key Laboratory for Medical Functional Nanomaterials, Jining Medical University, Jining, China

KEYWORDS

nanomaterial, nanoprobes, nanoenzyme, biology, medicine

OPEN ACCESS

EDITED AND REVIEWED BY
John D. Wade,
University of Melbourne, Australia

*CORRESPONDENCE
Guannan Wang,
✉ chemwangguannan@gmail.com

RECEIVED 22 June 2023
ACCEPTED 31 July 2023
PUBLISHED 17 August 2023

CITATION
Wang G (2023), Editorial: Nanomaterials for biology and medicine.
*Front. Chem.* 11:1244175.
doi: 10.3389/fchem.2023.1244175

Editorial on the Research Topic
Nanomaterials for biology and medicine

The desire for novel technology applications in biology, chemistry, engineering, physics, and medical science has fueled nanomaterials research. Nanomaterials have risen to prominence in technological breakthroughs due to their adjustable thermal, mechanical, electronic, and biological properties and superior performance over bulk equivalents (Baig et al., 2021; Mazari et al., 2021). Accordingly, numerous strategies have been projected to construct various functional structures by the integration of various types of nanomaterials, ranging from metals, metal oxides, alloys, and semiconductive materials to multifarious inorganic and organic polymers (Hao et al., 2010; Wagner et al., 2019). Specifically, nanomaterials offer the virtues as the therapeutic and diagnostic tools, which is owing to their small sizes, design flexibility, large specific surface area, and simple surface modification to enhance avidity for the targeting molecule (Yu et al., 2021; Qiao et al., 2022; Pourmadadi et al., 2023). There has been an explosive development in the use of nanomaterials for biomedical applications to probe biological processes, diagnose and treat medical conditions. The distinguishing characteristics of nanomaterials enable them to preferentially penetrate and be retained by cells and tissues of living organisms, thereby achieving developments in new approaches to target in biological cells and biological tissues. Additionally, the size scale of nanomaterials will provide the inspiration to build complexity into the nanoprobes that endow them versatility with both diagnostic, therapy, and drug delivery function. Moreover, diversified surface modification strategies have broadened the application of nanomaterials for biomedical applications, which adds the property of stability, biocompatibility, biodistribution, solubility, biological or therapeutic effects (Sztandera et al., 2019; Liu et al., 2021).

In this Research Topic, the authors were invited to contribute their research works, which enable the better explanation on the recent advances in diversified applications of nanomaterial in the biology and medicine. Yu et al. have contributed a literature review on the current progress on the nanomaterials' application in diagnosing and treating of glioblastoma (GBM). They discussed the nanomaterials-based nano-diagnosis or treatment mechanisms. Additionally, the advanced application progress of nanomaterial combination diagnostic and therapeutic tools for GBM was summarized. Nano-catalytic therapy, acting as an innovative strategy, has been extensively explored. Shi et al. group synthesized a multi-functional magneto-gold nano-enzyme AuNC@$Fe_3O_4$ and evaluated their anti-cancer ability in the hepatocellular carcinoma (HCC cells) *in vitro*. The preparative nano-enzyme AuNC@$Fe_3O_4$ with a small size was characterized using various techniques and demonstrated with high peroxidase (POD)-like activity, good photothermal conversion efficiency, and can inhibit cell proliferation and enhance cell apoptotic ability in cancer cells, providing a potential anti-cancer method for HCC. Responding to the oxidation state of the micro-environment of bacterial infection, Dorma Momo et al. explored a near-infrared (NIR) photothermal bacterial inactivation by reasonably designing a Metal organic Framework (MOF)-based nano-composite, offering a novel inspiration for constructing precise nano-therapeutic systems. They systematically studied the strong deactivation effect on the Gram-negative and -positive bacteria and intense therapeutic effectiveness on the mouse skin wound infection model of the designed nano-system.

Native and synthetic nanomaterials have drawn a lot of research interests and been projected as the key components for construction of drug delivery systems for healing patients in clinical. Ravelo-Nieto et al. constructed a cellular drug delivery system by using silanized fullerenol and silica nanoparticles (SN) as the nano-structured supports to conjugate potent cell-penetrating agents. The nano-bioconjugates showed distinct intracellular trafficking and endosomal escape behavior in the cell lines, which indicated the potentiality to address the challenge of cytoplasmic drug delivery and the development of therapeutic methods for lysosome storage disease. You et al. developed a monodispersed and biocompatible mesoporous SN (MSN) divergent porous channel for loading dapagliflozin (DAPA). They constructed a drug delivery system through the surface-modification of the cardiac-targeting peptides to release drug for the hypoxic and weak acid damaged cardiomyocytes. This MSN-based nanocarriers for the DAPA delivery system can achieve the efficacious cardiac repair and regeneration *in vivo*. Gui et al. research group exploit a pH responsive antibacterial delivery system (Imi@ZIF-8) for the antibiosis treatment of *A. baumannii*. They found that at an imipenem concentration of 10 mg/kg, the Imi@ZIF-8 nano-system manifested the outstanding therapeutic efficacy against *A. baumannii* in the mice with celiac disease.

Intended as a one-stop reference, this Research Topic provides the reader with the most-up-to-date and comprehensive exploration of a variety of the nanomaterial applications for biology and medicine. Briefly, these nanomaterials can be applied to perspective to advance in intrinsic nano-therapy across the biomedical area, from cancer therapeutics to microbial infection treatment and tissue regeneration. As such, this Research Topic provides the most comprehensive coverage of this intriguing field of study. Currently, this Research Topic has published 11 articles and received over 2,900 downloads and 14,000 readings worldwide.

## Author contributions

The author confirms being the sole contributor of this work and has approved it for publication.

## Conflict of interest

The author declares that the research was conducted in the absence of any commercial or financial relationships that could be construed as a potential conflict of interest.

## Publisher's note

All claims expressed in this article are solely those of the authors and do not necessarily represent those of their affiliated organizations, or those of the publisher, the editors and the reviewers. Any product that may be evaluated in this article, or claim that may be made by its manufacturer, is not guaranteed or endorsed by the publisher.

## References

Baig, N., Kammakakam, I., and Falath, W. (2021). Nanomaterials: A review of synthesis methods, properties, recent progress, and challenges. *Mater. Adv.* 2 (6), 1821–1871. doi:10.1039/D0MA00807A

Hao, R., Xing, R. J., Xu, Z. C., Hou, Y. L., Gao, S., and Sun, S. H. (2010). Synthesis, functionalization, and biomedical applications of multifunctional magnetic nanoparticles. *Adv. Mater.* 22 (25), 2729–2742. doi:10.1002/adma.201000260

Liu, M., Zhu, H., Wang, Y., Sevencan, C., and Li, B. L. (2021). Functionalized $MoS_2$-Based nanomaterials for cancer phototherapy and other biomedical applications. *ACS Mater. Lett.* 3 (5), 462–496. doi:10.1021/acsmaterialslett.1c00073

Mazari, S. A., Ali, E., Abro, R., Khan, F. S. A., Ahmed, I., Ahmed, M., et al. (2021). Nanomaterials: Applications, waste-handling, environmental toxicities, and future challenges – a review. *J. Environ. Chem. Eng.* 9 (2), 105028. doi:10.1016/j.jece.2021.105028

Pourmadadi, M., Mahdi Eshaghi, M., Ostovar, S., Mohammadi, Z., Sharma, R. K., Paiva-Santos, A. C., et al. (2023). Innovative nanomaterials for cancer diagnosis, imaging, and therapy: Drug delivery applications. *J. Drug Deliv. Sci. Technol.* 82, 104357. doi:10.1016/j.jddst.2023.104357

Qiao, K., Xu, L., Tang, J., Wang, Q., Lim, K. S., Hooper, G., et al. (2022). The advances in nanomedicine for bone and cartilage repair. *J. Nanobiotechnology* 20 (1), 141. doi:10.1186/s12951-022-01342-8

Sztandera, K., Gorzkiewicz, M., and Klajnert-Maculewicz, B. (2019). Gold nanoparticles in cancer treatment. *Mol. Pharm.* 16 (1), 1–23. doi:10.1021/acs.molpharmaceut.8b00810

Wagner, A. M., Knipe, J. M., Orive, G., and Peppas, N. A. (2019). Quantum dots in biomedical applications. *Acta Biomater.* 94, 44–63. doi:10.1016/j.actbio.2019.05.022

Yu, Z., Gao, L., Chen, K., Zhang, W., Zhang, Q., Li, Q., et al. (2021). Nanoparticles: A new approach to upgrade cancer diagnosis and treatment. *Nanoscale Res. Lett.* 16 (1), 88. doi:10.1186/s11671-021-03489-z

Frontiers in Chemistry

TYPE Review
PUBLISHED 16 August 2022
DOI 10.3389/fchem.2022.988051

OPEN ACCESS

EDITED BY
Xiangzhao Ai,
Shanghai Jiao Tong University, China

REVIEWED BY
Magali Cucchiarini,
Saarland University Medical Center, Germany
Tao Feng,
Northwestern Polytechnical University, China

*CORRESPONDENCE
Xiao-Ling Xu,
ziyao1988@zju.edu.cn
Dao-Fang Ding,
dingdaofang@shutcm.edu.cn

†These authors have contributed equally to this work

SPECIALTY SECTION
This article was submitted to Nanoscience,
a section of the journal
Frontiers in Chemistry

RECEIVED 06 July 2022
ACCEPTED 21 July 2022
PUBLISHED 16 August 2022

CITATION
Liu X-H, Ding J-Y, Zhu Z-H, Wu X-C, Song Y-J, Xu X-L and Ding D-F (2022), Recent advances in enzyme-related biomaterials for arthritis treatment.
*Front. Chem.* 10:988051.
doi: 10.3389/fchem.2022.988051

# Recent advances in enzyme-related biomaterials for arthritis treatment

Xin-Hao Liu[1,2†], Jia-Ying Ding[1,2†], Zhi-Heng Zhu[1,2], Xi-Chen Wu[1,2], Yong-Jia Song[1,2], Xiao-Ling Xu[3]* and Dao-Fang Ding[1,2]*

[1]Center of Rehabilitation Medicine, Yueyang Hospital, Shanghai University of Traditional Chinese Medicine, Shanghai, China, [2]School of Rehabilitation Science, Shanghai University of Traditional Chinese Medicine, Shanghai, China, [3]Shulan International Medical College, Zhejiang Shuren University, Hangzhou, China

Arthritis is a group of highly prevalent joint disorders, and osteoarthritis (OA) and rheumatoid arthritis are the two most common types. The high prevalence of arthritis causes severe burdens on individuals, society and the economy. Currently, the primary treatment of arthritis is to relieve symptoms, but the development of arthritis cannot be effectively prevented. Studies have revealed that the disrupted balance of enzymes determines the pathological changes in arthritis. In particular, the increased levels of matrix metalloproteinases and the decreased expression of endogenous antioxidant enzymes promote the progression of arthritis. New therapeutic strategies have been developed based on the expression characteristics of these enzymes. Biomaterials have been designed that are responsive when the destructive enzymes MMPs are increased or have the activities of the antioxidant enzymes that play a protective role in arthritis. Here, we summarize recent studies on biomaterials associated with MMPs and antioxidant enzymes involved in the pathological process of arthritis. These enzyme-related biomaterials have been shown to be beneficial for arthritis treatment, but there are still some problems that need to be solved to improve efficacy, especially penetrating the deeper layer of articular cartilage and targeting osteoclasts in subchondral bone. In conclusion, enzyme-related nano-therapy is challenging and promising for arthritis treatment.

KEYWORDS

**biomaterials, nano-therapy, arthritis, matrix metalloproteinases, endogenous antioxidant enzymes**

## Introduction

Arthritis, which is a group of musculoskeletal diseases, is one of the leading causes of disability in the elderly population (Woolf and Pfleger, 2003). Osteoarthritis (OA) and rheumatoid arthritis (RA) are the most prevalent types of arthritis and affected 344 million people and 13 million people, respectively, globally in 2019 (Cieza et al., 2021). OA is characterized by joint degeneration, especially in the knee, and involves multiple joints, such as the hand, hip, knee and foot. A large-scale survey in the

United Kingdom in 2017 showed that the prevalence of OA in adults was 10.7% (Swain et al., 2020-06). The increases in obesity and the ageing population contribute to the prevalence of OA (Briggs et al., 2020-10). RA is an immunization-induced systemic disease characterized by synovial inflammation and joint destruction, and the prevalence of RA is 0.5–1.0% in the US (Palmer et al., 2019).

OA and RA are both inflammatory joint diseases that involve joint and synovial destruction and immune cell infiltration (Zhang et al., 2019-03) and is associated with joint pain, swelling, and limited movement, resulting in a decline in physical function, increased dependence and reduced quality of life. Furthermore, the prevalence of OA and RA is expected to increase significantly as the global population ages. The treatment of arthritis is often a long and complex process due to irreversible damage and the risk of comorbidities, resulting in extremely high medical and economic burdens on society, and these burdens continue to increase globally (Briggs et al., 2020-10).

To date, there is no effective cure for OA or RA. The current interventions include medications, physical therapy, and surgical intervention, all of which are aimed at alleviating symptoms and reducing joint damage and disability. Medications for OA, including topical, oral and intra-articular (IA) injectable drugs, are palliative and limited to controlling symptoms of joint swelling, pain and stiffness (Tschon et al., 2020-06). A randomized clinical trial has even shown that IA corticosteroids may accelerate the destruction of articular cartilage (McAlindon et al., 2017-05). Currently, non-steroidal anti-inflammatory drugs (NSAIDs), glucocorticoids (GCs) and disease-modifying anti-rheumatic drugs (DMARDs) are mainly used in the clinical treatment of RA. The targets of traditional DMARDs are not clear, and approximately 30%–50% of patients respond poorly to these drugs (Sparks, 2019). As a result of the poor bioavailability and short half-lives of anti-rheumatic drugs, prolonged repeated use can cause serious adverse reactions such as vomiting, drug resistance and bone marrow suppression.

Physical therapy for OA and RA includes weight loss, moderate exercise and knee joint distraction. Knee joint distraction can improve symptoms and promote tissue repair in severe knee joint degeneration, but there is frequent infection during the follow-up (Jansen and Mastbergen, 2022-01; van der Woude et al., 2017-01). When conservative treatment is not feasible for end-stage arthritis, surgical intervention, such as total joint replacement, can be considered, but this treatment strategy is related to persistent postsurgical pain and infection (Wylde et al., 2011-03; Chung et al., 2021-11).

Currently, new therapeutic strategies and drugs primarily alleviate symptoms to treat arthritis, and critically unsolved problems, such as how to restore abnormal cellular function in arthritis, should be considered. Cellular activity depends on various proteins, and some of these proteins are important enzymes for physiological and pathological processes. Herein, we summarized the essential enzymes that are involved in pathological changes in arthritis.

## Arthritis-related enzymes

The pathological changes in OA and RA are mainly characterized by cartilage destruction and synovial inflammation (Trachana et al., 2019; Scherer et al., 2020). Cell metabolism is often regulated by different enzymes, and abnormal levels of enzymes are typically associated with the occurrence of various diseases. In cartilage, different matrix metalloproteinases (MMPs) are responsible for destroying chondrocytes by degrading collagen and proteoglycans.

### 1 matrix metalloproteinases linked with arthritis

There is increasing evidence that these inflammatory mediators are involved in the pathogenesis of both OA and RA (Malemud, 2017; van Dalen et al., 2017). Neutrophils, monocytes and macrophages infiltrate cartilage and synovial tissue after inflammation occurs, releasing various inflammatory factors and chemokines, which cause an increase in MMPs.

The destruction or degradation of articular cartilage is regulated by MMPs, which are a family of proteolytic enzymes that hydrolyse extracellular matrix (ECM). Different types of MMPs are involved in degrading proteoglycans and collagens, which are the main components of ECM in cartilage, especially MMP-1, MMP-2, MMP-3, MMP-9 and MMP-13 (Itoh, 2017; Mehana et al., 2019). MMPs can degrade collagen, elastin, and other substances in the ECM of articular cartilage that maintain the structure of cartilage and ultimately destroy the integrity of ECM structure and function.

Under pathological conditions, the expression level of MMP-1 was significantly increased in OA and RA, and this factor degraded ECM collagen and mediated cartilage destruction (Wang et al., 2020a). In cartilage and synovium, MMP-1 expression increased steadily during the progression of OA in a rabbit model of anterior cruciate ligament transection (ACLT) (Wu et al., 2008). MMP-1 could lead to the degeneration of primary collagen (type II collagen) in cartilage, and this effect was irreversible (Macdonald et al., 2018).

The development of OA and RA is associated with the increased secretion and activity of MMP-2 in synovial cells and the joints of RA patients, respectively (Kim et al., 2011; Galasso et al., 2012). Furthermore, MMP-2-sensitive peptide was shown to be specifically released in inflammatory joints *in vitro* and *in vivo*, which might be an important approach for drug-targeted treatment of RA (Yu et al., 2022).

Significantly increased levels of MMP-3 in the serum of OA patients were positively correlated with the severity of knee OA and RA in patients (Ma et al., 2014; Georgiev et al., 2018; Pengas et al., 2018). Furthermore, serum MMP-3 levels were closely correlated with disease activity scores, suggesting that serum MMP-3 levels could be used as an indicator of structural damage and monitor disease progression (Galil et al., 2016; Tuncer et al., 2019).

MMP-9 was also positively correlated with disease severity in OA patients (Lipari and Gerbino, 2013). A meta-analysis showed that MMP-2 and MMP-9 protein expression levels were significantly higher in the OA group than in the control group, indicating that MMP-2 and MMP-9 are involved in the pathogenesis of OA (Zeng et al., 2015). Multiple studies have shown that the expression of MMP-9 in synovial fluid and synovial cells of RA patients is increased (Silosi et al., 2015; Ma et al., 2019). The degree of inflammation in RA patients correlated with Toll-like receptor 2 (TLR2) expression in peripheral blood monocytes. The increased expression of TLR2 led to the increased expression of MMP-9 (Chen et al., 2015). MMP-9 could participate in the synovial cell-mediated inflammatory response and the degeneration of ECM, especially proteoglycans, which might directly cause joint destruction (Metzger et al., 2012).

MMP-13 is a crucial enzyme leading to the degradation of collagen types I, II and III and the cartilage proteoglycan aggrecans and is considered a significant factor in the pathogenesis of OA (Fosang et al., 1996). MMP-13 attracted much attention due to its obvious overexpression in the articular cartilage of OA patients, but it was almost undetectable in normal adult tissues (Kaneva, 2022). Interfering with the expression of MMP-13 in a surgically induced OA model could efficiently alleviate OA severity (Hoshi et al., 2017). Given its critical role in ECM degradation, MMP-13 has been a promising target in OA treatment (Hu and Ecker, 2021). K/BxN serum-induced arthritis increases MMP-13 expression in C57BL/6 mice, and MMP-13-deficient (MMP-13−/−) mice exhibit reduced inflammation and joint destruction (Singh et al., 2013). In addition, MMP-13 was also associated with the progression of RA, providing crucial predictive information about future structural damage and severity in early RA patients (Tatematsu et al., 2018).

## 2 Endogenous antioxidant enzymes linked with arthritis

Apart from the direct effect of MMPs on ECM degradation in cartilage and promoting the progression of arthritis, endogenous antioxidants such as superoxide dismutases (SODs), glutathione peroxidase (GPx), catalase (CAT), and glutathione reductase (GR) also affect the occurrence of arthritis by scavenging intracellular reactive oxygen species (ROS) and alleviating cellular oxidative stress.

ROS are key signalling molecules in the progression of inflammatory diseases (Mittal et al., 2014). Under inflammatory conditions, the oxidative stress induced by macrophages, monocytes, and neutrophils leads to the formation of interendothelial junctions, accelerating the crossing of the endothelial barrier and ultimately promoting inflammation (You et al., 2018).

The levels of intra-articular ROS (including $H_2O_2$, $O_2^-$, $OH^-$, and HOCl) are significantly increased in OA patients, while ROS are maintained at low levels in normal articular tissue (Lepetsos and Papavassiliou, 2016; Yao et al., 2019). The overproduction of ROS causes overoxidation, protein carbonylation, and DNA damage and is considered the primary mechanism of chondrocyte loss and tissue damage (Hosseinzadeh et al., 2016). The associated ROS, including nitric oxide (NO), superoxide anion ($O_2^-$) and hydrogen peroxide ($H_2O_2$), are present in the articular cavities of RA patients in large quantities (Datta et al., 2014). When the local inflammatory response in RA joints is accelerated and ROS levels exceed physiological tolerance, they not only damage proteins, lipids, and nucleic acids but also act as important endogenous signalling regulators that amplify the synovial inflammatory response (Bala et al., 2017; Phull et al., 2018). Li et al. found that ROS significantly promoted the proliferation of RA synovial fibroblasts and the production of inflammatory factors and that inhibiting ROS significantly downregulated the inflammatory factors secreted by RA synovial fibroblasts, ultimately improving RA conditions (Li et al., 2018). Therefore, a potent antioxidant compound that can reduce ROS in inflammatory cells may be a key factor in the treatment of chronic inflammatory diseases.

ROS clearance is regulated by SODs, GPx, CAT and GR (He et al., 2017). CAT and GPx are involved in the decomposition of intracellular hydrogen peroxide and maintain normal ROS levels to reduce toxic reactions. SOD can catalyse $O_2^-$ into $O_2$ and $H_2O_2$. GR catalyses the reduction of glutathione disulfide (GSSG) to the sulfhydryl form of glutathione (GSH), which plays an important role in the tissue oxidative stress response (Deponte, 2013). The levels of SOD, CAT and other antioxidant enzymes in OA chondrocytes were significantly lower than those in normal chondrocytes, indicating that insufficient antioxidant capacity might cause cartilage damage (Zhuang et al., 2018). Unlike the expression pattern of other antioxidant enzymes, the expression of GR was increased in arthritis (Meshkibaf et al., 2019; Idzik et al., 2022).

The proliferation and activation of osteoclasts (OCs) are key factors leading to bone damage and bone metabolism disorders in RA (Auréal et al., 2020). Recent studies have shown a close correlation between bone destruction and oxidative stress in the pathogenesis of RA. ROS promote osteoclast differentiation (Gamal et al., 2018). Decreased expression of SOD, CAT and GPx was found in the ankle joints of RA rats (Ren et al., 2019a). ROS-induced peroxidation is inhibited by antioxidant enzymes, among which superoxide dismutase 3 (SOD3) is the key enzyme that protects cells from oxidative stress (Nguyen et al., 2020). SOD3 reduced proinflammatory cytokines (IL-1β, IL-2, IL-4, and TNF-α) and the release of MMPs (MMP-2, MMP-3 and MMP-9), ultimately inhibiting inflammatory responses (Xie et al.,

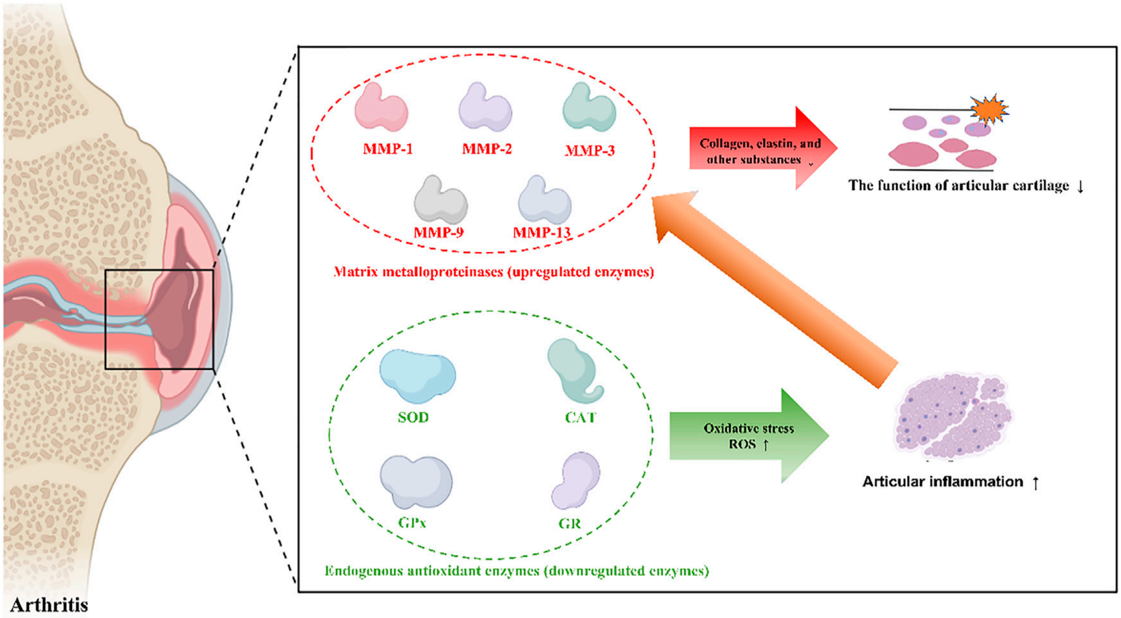

FIGURE 1
Upregulated enzymes (red) and downregulated enzymes (green) in arthritis pathology.

2021). Icariin protects synoviocytes induced by lipopolysaccharide (LPS) by inhibiting ferroptosis by activating the Xc/GPX4 axis (Luo and Zhang, 2021).

Considering the importance of MMPs and oxide reductase associated with ROS in the occurrence of arthritis, biomaterials that target endogenous enzymes have become a hot research topic in recent years. Next, we will introduce the application of biomaterials that are linked with these enzymes.

## Nanotherapies that target enzymes in arthritis

Enzymes that play critical roles in arthritis pathology are categorized into two groups according to their expression characteristics: upregulated enzymes and downregulated enzymes, which are listed in Figure 1. Enzyme homeostasis is critical for the human body. Both the upregulated and downregulated expression of these enzymes disrupt the balance of cell metabolism and can cause diseases. Therefore, therapeutic strategies have been designed according to the expression of these enzymes. If the expression of these enzymes is upregulated, nanomaterials can respond and release an effective drug to inhibit pathological changes, or nanomaterials can be fabricated to simulate the effects of downregulated enzymes. Next, we described two different functional enzymes in arthritis treatment.

### 1 Nanomaterials associated with upregulated enzymes in arthritis treatments

It is well known that MMPs are the main destructive enzymes in chondrocytes that degrade ECM components, such as proteoglycans and collagen networks. Degradation of the ECM leads to functional destruction of chondrocytes and cartilage erosion. Therefore, MMPs have become an important molecular target for studies on the treatment of OA. In particular, MMP-13, a critical protease in chondrocytes, is responsible for the degradation of type II collagen and proteoglycans.

OA is a chronic inflammatory disease. Growing evidence reveals that the changes in the OA microenvironment include excessive inflammation and MMP overexpression (Latourte et al., 2017; Li et al., 2017; Stocco et al., 2019). The microenvironment is an important factor in maintaining joint homeostasis. Long-term inhibition of MMP enzymatic activity may lead to adverse reactions. Therefore, it is necessary to design materials that are highly selective for MMPs and can adapt to the changes in MMP levels *in vivo*. When MMP expression is upregulated, MMP-responsive nanoparticles (NPs) work, and they are inactive when MMPs are at low levels.

The increased expression of MMPs in inflamed tissues may be a promising breakthrough for arthritis therapy. A commercially available, Food and Drug Administration (FDA)-approved molecule known as triglycerol monostearate (TGMS) has been shown to be responsive to MMPs (Wen et al., 2019).

MMP-responsive PEGylated lipid NPs (TGMS/DSPE-PEG2000 NPs) can be produced through the coassembly of TGMS and 1,2-distearoyl-sn-glycero-3-phosphoethanolamine-poly (ethylene glycol) (DSPE-PEG2000). Dexamethasone (Dex)-loaded MMP-responsive NPs were obtained by loading TGMS/DSPE-PEG2000 NPs with Dex, and Dex can be rapidly released from the lipid NPs after TGMS is cleaved by MMP-3 and MMP-9. Dex-loaded MMP-responsive NPs significantly reduced the degree of joint swelling and inhibited the production of TNF-α and IL-1β in the joint (He et al., 2020).

In another study, the nanozyme-like role of the hydrogel form of TGMS(TG-18) was further confirmed in RA treatment. A hydrogel platform that exhibits disassembly and drug release controlled by the concentration of enzymes during arthritis flares was constructed. In this study, a triglycerol monostearate hydrogel (TG-18) loaded with the corticosteroid triamcinolone acetonide (TA) exhibited drug release in response to the increased activities of arthritis-related enzymes *in vitro* (MMP-2, MMP-3, MMP-9) or synovial fluid from patients with RA (Joshi et al., 2018).

In addition to synovial inflammation and joint swelling, obvious cartilage damage and bone erosion are often observed in RA. Synovial macrophages mediate joint inflammation once activated, and OCs are responsible for arthritic bone erosion and resorption of the bone matrix. Both OCs and synovial macrophages express high levels of αvβ3 integrin, which plays an important role in activated macrophage-dependent inflammation and OC-dependent bone resorption. Macrophages and OCs fail to undergo apoptosis in the RA joint, leading to persistent inflammation and joint destruction. Therefore, inducing OC and macrophage apoptosis in RA joints represents a promising strategy for advanced RA treatment. According to the characteristics of OCs and synovial macrophages, novel CEL-loaded PRNPs (CEL-PRNPs) were synthesized that contained celastrol (CEL), which can induce apoptosis in OCs and macrophages, RGD, which is a ligand of αvβ3 that targets OCs and inflammatory macrophages, and polyethylene glycol (PEG), which is cleaved by MMP-9. In an adjuvant-induced arthritis rat model, CEL-PRNPs efficiently reduced the number of OCs and inflammatory macrophages and relieved various symptoms, including ankle and paw swelling and bone erosion, in the inflamed joints of AIA rats with advanced arthritis (Deng et al., 2021).

To determine the inflammatory condition and investigate the therapeutic effects of MMP-responsive biomaterials, fluorescence imaging was considered for diagnosis and therapy.

Inflamed cartilage is characterized by MMP-13 overexpression and an acidic microenvironment. Therefore, MMP-13/pH-responsive ferritin nanocages (CMFn) loaded with an anti-inflammatory drug (hydroxychloroquine, HCQ), termed CMFn@HCQ, were constructed for OA imaging and therapy. CMFn is a marker for imaging diagnosis that emits light in response to MMP-13 overexpression. The intensity of CMFn light increases with the severity of OA. However, in normal joints, this compound emits no light. The release of HCQ causes an anti-inflammatory effect in OA joints to reduce synovial inflammation, and the retention time lasts up to 14 days (Chen et al., 2019a).

Cartilage-targeting C-PPL was created by grafting collagen type II-targeting peptides with the sequence WRYGRL onto the polymer poly (2-ethyl-2-oxazoline)-poly (ε-caprolactone) (PPL). Additionally, PPL was conjugated with a specific peptide substrate of the MMP-13 enzyme (H2N–GPLGVRGC–SH) that was labelled with a fluorescent dye (Cy5.5) and was subsequently coupled with the black hole quencher-3 (BHQ-3) that can quench Cy5.5 fluorescence to obtain an MMP-13-responsive and pH-sensitive polymer (MR-Cy5.5-BHQ-3-PPL). A cartilage-targeting and OA-specific theragnostic nanoplatform (MRC-PPL) was obtained by the self-assembly of C-PPL and MR-PPL. Finally, MRC-PPL was loaded with the traditional Chinese medicine psoralidin (PSO) to form MRC-PPL@PSO nano-micelles, which specifically target and protect cartilage (Lan et al., 2020). The synthesis and mechanism of MRC-PPL@PSO nano-micelles to treat OA are shown in Figure 2.

In addition to MMP overexpression in arthritis tissue, the intrinsic properties of the OA microenvironment, especially synovial fluid, are also considered when designing novel nanomaterials. The increased activity of the GR enzyme was reported in the synovial fluid of RA and OA patients, and a selectively controlled drug release that is sensitive to the GR enzyme was designed for the treatment of arthritic diseases (Ostalowska et al., 2006; Sredzińska et al., 2009). Polymeric micelles were made of methoxypolyethylene glycol amine-glutathione-palmitic acid (mPEG-GSHn-PA) polymers. Dex was loaded into the cores of the polymeric micelles. The release of Dex was slow under physiological conditions, while the presence of the GR enzyme stimulated a burst release via a thiol–disulfide exchange between GSH and GSSG (Lima et al., 2021). The above biomaterials associated with MMPs are listed in Table 1.

## 2 Nanomaterials associated with downregulated enzymes in arthritis treatments

Apart from the destruction of cartilage tissue induced by the increased expression of MMPs, the decreased expression of oxide reductase associated with ROS showed a similar effect on cartilage. To reduce the expression of oxide reductase, the strategy was to supply these enzymes directly or mimic the activities with special biomaterials.

Supplementation with antioxidant enzymes such as SOD has been shown to be effective in treating arthritis. Chitosan was chemically conjugated with SOD to generate the nanoparticle-like conjugate 6-O-2′-hydroxylpropyltrimethyl ammonium chloride chitosan-SOD (O-HTCC-SOD), which was superior to unmodified SOD in bioavailability, prolonged half-life and

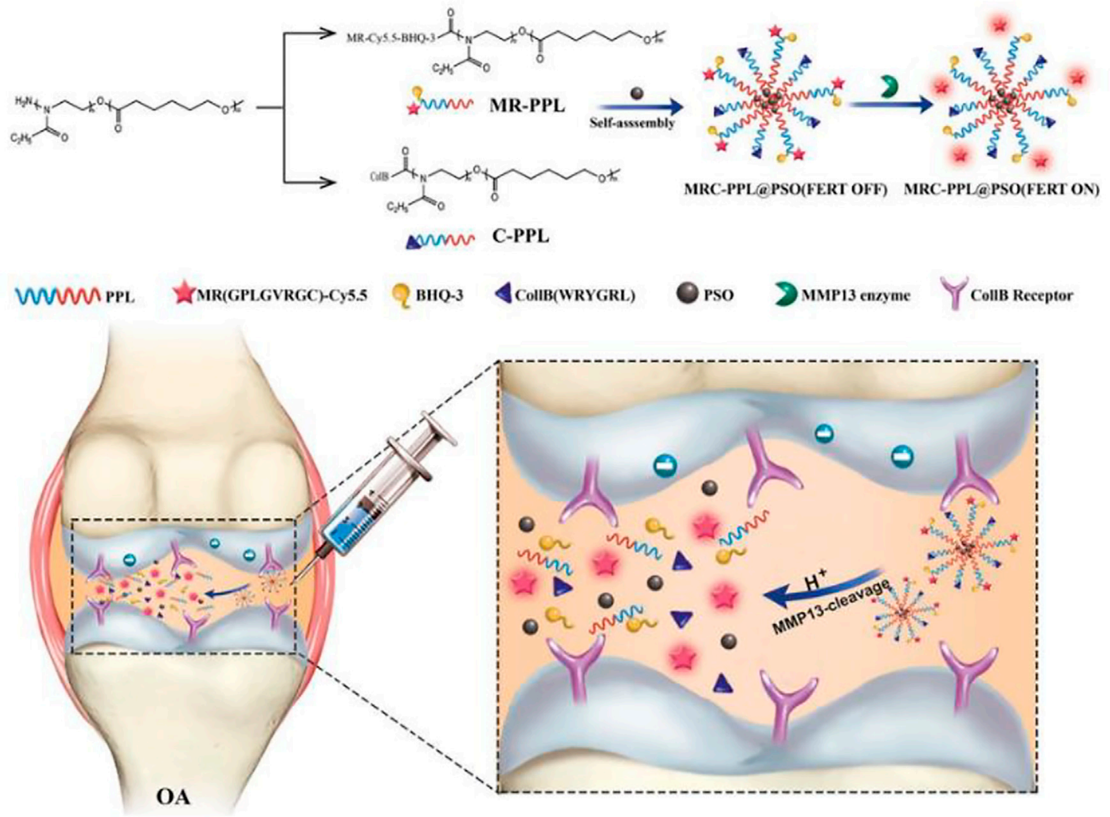

FIGURE 2
Schematic illustration of the synthesis and working mechanism of MMP-13 and pH responsive theranostic MRC-PPL@PSO nano-micelles for OA (Lan et al., 2020). Copyright, 2020, BMC.

residence in the rat joint cavity. After IA injection of O-HTCC-SOD into rats with MIA-induced OA, mechanical allodynia was greatly reduced, and changes in the gross morphological and histological lesions of articular cartilage were dramatically inhibited (Wang et al., 2020b).

Although the nanosized conjugate O-HTCC–SOD has exhibited higher enzyme activity and superior membrane permeability to native SOD, natural enzymes are unstable, expensive and difficult to store. Currently, biomaterials called nanozymes have been designed to mimic the effects of these oxide reductases. Nanozymes are a specific kind of nanomaterial that have the activities of intrinsic enzymes and possess unique advantages, such as high efficiency, increased compatibility with specific environments, such as high temperatures and pH variations, cyclic use, and a large surface area, and these materials can be conjugated to multiple ligands to achieve multifunctionality. These features give rise to their promising applications in a variety of fields (Pirmohamed et al., 2010).

Recently, numerous nanomaterials with enzyme-like properties have been discovered for OA treatment, including metals, metal oxides, and carbon-based materials.

As a representative metal oxide, cerium oxide has been evaluated in RA treatment. Engineered cerium oxide ($CeO_2$) nanoparticles (CeONPs), which are also known as nanoceria, have attracted much attention for exhibiting SOD$^-$, CAT$^-$, and oxidase-like activity (Heckert et al., 2008; Baldim et al., 2018; Kalashnikova et al., 2020). In reduction reactions, SOD catalyses $O_2^{\bullet -}$ into $H_2O_2$, which may undergo catalysis by CAT into $H_2O$.

Given that albumin is a natural protein and scavenging receptors are widely distributed in the inflamed joints of RA, albumin-nanoceria NPs (A-nanoceria) were synthesized by connecting albumin to nanoceria and further conjugated with near-infrared, indocyanine green (ICG) dye. Enzymatic properties and ROS scavenging activities against a monocyte cell line and systemic targeting potential were evaluated in a collagen-induced arthritis (CIA) mouse model. Such a design has the advantages of targeting inflammation, assessing severity, and controlling inflammation with imaging guidance in RA (Kratschmer et al., 1990).

Moreover, carbon-based materials have also exhibited the activities of nanozymes in scavenging ROS. Fullerene (C60) is a

TABLE 1 The biomaterials that target the upregulated enzymes in arthritis.

| Arthritis | Enzymes-responsive group | Nanomaterial | Platform | Components | Responsive enzymes | Drug | Ref |
|---|---|---|---|---|---|---|---|
| RA | TGMS | Dex-loaded TGMS/DSPE-PEG2000 | NPs | 1.TGMS<br>2.Dex<br>3.PEG2000<br>4.DSPE | MMP-3<br>MMP-9 | Dex | He et al. (2020) |
| RA | TGMS | TA-loaded TG-18 hydrogel | hydrogel | 1.TGMS<br>2.TA | MMP-2<br>MMP-3<br>MMP-9 | TA | Joshi et al. (2018) |
| RA | PEG | CEL-PRNPs | NPs | 1.celastrol (CEL)<br>2.RGD<br>3.PEG<br>4.PLGA | MMP-9 | | Deng et al. (2021) |
| OA | H2N–GPLGVRGC–SH | CMFn@HCQ | nanocages | 1.MMP-13 cleavble peptide<br>2.HCQ<br>3.collagen type II targeting peptides<br>4.BHQ3<br>5.Cy5.5<br>6.ferrritin | MMP-13 | HCQ | Chen et al. (2019a) |
| OA | H2N–GPLGVRGC–SH | MRC-PPL@PSO | micelles | 1.MMP-13 cleavble peptide<br>2.PSO<br>3.collagen type II targeting peptides<br>4.PPL<br>5.Cy5.5<br>6.BHQ-3 | MMP-13 | PSO | Lan et al. (2020) |
| OA | GSSG | Dex-loaded mPEG-GSHn-PA | micelles | 1.PEG<br>2.GSH<br>3.PA<br>4.Dex | GR enzyme | Dex | Lima et al. (2021) |

spherical carbon molecule with a unique cage structure that functions as a free-radical scavenger. Apart from inhibiting ROS-induced catabolism in cartilage, fullerene also decreases friction on the cartilage surface and subsequently prevents the further development of cartilage degeneration. With these advantages, fullerene has been used to synthesize biomaterials for the treatment of arthritis. For example, fullerene-like MoS$_2$ (F-MoS$_2$) NPs are efficient lubricants and antioxidants for artificial synovial fluid. These NPs possess intrinsic dual-enzyme-like activity, mimicking SOD and CAT under physiological conditions (pH 7.4, 25°C) and regulating the ROS level in artificial synovial fluid containing HA (Chen et al., 2019b).

Prussian blue (PB) has been approved by the U.S. FDA as a commonly used dye and medicine due to its excellent biocompatibility and biosafety. The peroxidase, CAT, and SOD activities of PBzymes mediate the scavenging of •OH, •OOH, and H$_2$O$_2$, exhibiting outstanding anti-inflammatory and antioxidative bioactivities (Long et al., 2016; Zhang et al., 2016; Dacarro et al., 2018; Qin et al., 2018).

A hollow PBzyme (HPBzyme) with a mesopore structure and a high specific surface area was produced that could remodel the OA microenvironment by mitigating the inflammatory response, protecting against chondrocyte ECM degradation, and exhibiting therapeutic efficacy *in vivo* (Hou et al., 2021).

PB has also been integrated into other therapeutic approaches, such as exosomes and ultrasound, for arthritis treatment. Low-density ultrasound is a noninvasive biophysical treatment that can reduce joint swelling and inflammation in OA models (Iwabuchi et al., 2014). The combined therapeutic effects of PB and low-density ultrasound on animal OA by scavenging oxygen free radicals

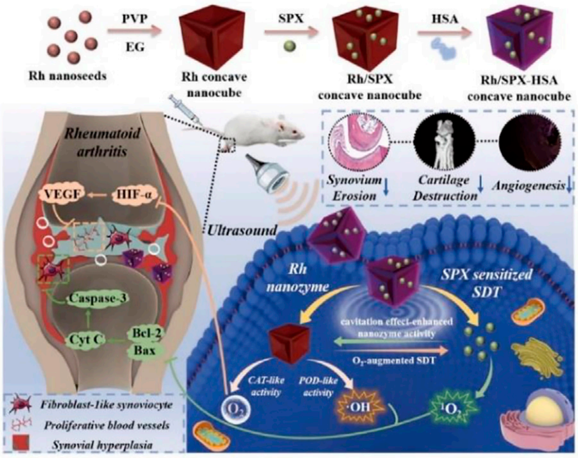

FIGURE 3
Schematic illustration of the synthesis and working mechanism of MMP-13 and pH responsive theranostic MRC-PPL@PSO nano-micelles for OA (Li et al., 2021). Copyright, 2021, Elsevier.

was investigated. It was found that this treatment could significantly remove ROS, alleviate ROS-induced apoptosis, and reduce the degeneration of articular cartilage (Zuo et al., 2021). Furthermore, neutrophil-derived exosomes engineered with ultrasmall PB nanoparticles (uPB-Exo) have been shown to be effective in treating RA. uPB-Exo selectively accumulated in activated fibroblast-like synoviocytes and acted as mimics of SOD2 and NOX2 in inflamed joints of RA *in vivo*, subsequently neutralizing proinflammatory factors, alleviating inflammatory synovitis and protecting against cartilage damage in an advanced RA mouse model (Zhang et al., 2022).

Selenium (Se) is an essential dietary nutrient and has been reported to have lower serum concentrations in RA patients than healthy individuals (Yu et al., 2016). Supplementation with Se is controversial in the treatment of arthritis is controversial due to its toxicity. Nanosized Se is known to have superior antioxidant effects and reduced toxicity (Malhotra et al., 2016). In a rat RA model, SeNPs exhibited potent anti-inflammatory effects and promoted the expression of CAT, SOD and GPX (Ren et al., 2019b).

Ultrasound, which is a noninvasive biophysical therapy and a common mode of sonodynamic therapy (SDT), can strongly penetrate inflammatory tissues and kill inflammatory cells, thus reducing synovial hyperplasia and minimizing oxidative damage to surrounding normal tissues. SDT is hampered by the hypoxic microenvironment of RA caused by fibroblast-like synoviocyte (FLS) proliferation. Rhodium NP (Rh) nanozymes with concave-cube shapes could compensate for the deficiency of ultrasound therapy by exhibiting the activities of POD and CAT, which generate $O_2$ and •OH to alleviate hypoxia. In addition to its remarkable sonosensitive properties, the antibacterial drug sparfloxacin (SPX) can reside for a long time in joint tissues after systemic administration, which makes it possible to target the abnormal proliferation of FLSs in synovial tissue in the joint and block the development of RA. A small glycoprotein rich in cysteine known as SPARC is overexpressed in the synovial fluid and synovium from RA patients and increased in mice with CIA (Liu et al., 2019). SPARC has high affinity for human serum albumin (HAS) (Park et al., 2019). Therefore, HSA-modified Rh/SPX nanozyme was fabricated for RA treatment by combining the advantages and characteristics of these components (Li et al., 2021). The preparation of Rh-SPX/HSA and its related mechanisms in the treatment of RA are shown in Figure 3.

In addition to the combination of ultrasound and nanozymes to treat arthritis, a promising technique that combines near-infrared (NIR) with nanozymes for the treatment of OA was proposed. Epigallocatechin gallate (EGCG)-coated Au-Ag nanojars (E@Au-Ag) were produced based on the POD-like activity of Au-Ag and the scavenging of oxygen free radicals by EGCG, which is sensitive to NIR. These multifunctional enzyme-like nanomaterials can repair mitochondrial damage, promote cartilage migration, and reduce chondrocyte apoptosis (Xu et al., 2022). Biomaterials associated with antioxidant enzymes for arthritis treatment are listed in Table 2.

## Discussion

OA and RA are both inflammatory diseases. RA is a systemic disease that affects joints all over the body, especially the overloaded knee joints, and affects normal movement (Radu and Bungau, 2021). OA is a local joint disease, which is common in patients with metabolic syndrome, trauma, and aging (Whittaker et al., 2021). In comparing OA and RA, a striking similarity in gene expression is found. For example, the increased levels of MMPs and the decreased expression of antioxidant enzymes occur in OA and RA, but the differences also exist. MMP-9 is the main enzyme that causes RA while MMP-13 is reported to be the most important enzyme for the development of OA. Meanwhile, in terms of pathological changes, the proliferation of synovial tissue and blood vessels in RA was more obvious than that in OA. Macrophages distributed in synovial tissue and osteoclasts from subchondral bone were the main sources of inflammation, ultimately leading to the destruction of cartilage. Therefore, chondrocytes, osteoclasts and macrophages have been the main targets for arthritis treatment with different biomaterials.

RA is a systemic inflammatory disease, and joint destruction is generally more intense than that in OA. Compared to IA injection, oral drug delivery for arthritis causes severe side effects. Recently, pain has been primarily controlled with corticosteroids and hyaluronic acid via IA injection. It is possible to deliver high drug concentrations directly to osteoarthritic joints through

TABLE 2 Biomaterials that mimic the downregulated enzymes in arthritis.

| Arthritis | Nanomaterial | Platform | Components | Enzyme mimics | Drug | Ref |
|---|---|---|---|---|---|---|
| RA | A-nanoceria-ICG | NPs | 1.Albumin<br>2.cerium oxide<br>3.ICG | SOD<br>CAT<br>POD | metal oxides | Kratschmer et al. (1990) |
| OA | F-$MoS_2$ | NPs | 1.Fullerene<br>2.MoS2 | SOD<br>CAT | carbon-based materials | Chen et al. (2019b) |
| OA | HPBzyme | NPs | Prussian blue | POD<br>CAT<br>SOD | Prussian blue | Hou et al. (2021) |
| OA | PBNPs | NPs | Prussian blue | POD<br>CAT<br>SOD | Prussian blue | Zuo et al. (2021) |
| RA | uPB-Exo | NPs | 1.neutrophil-derived exosomes<br>2.Prussian blue | SOD2<br>NOX2 | Prussian blue | Zhang et al. (2022) |
| RA | SeNPs | NPs | Selenium | SOD<br>CAT<br>GPx1 | metal | Ren et al. (2019b) |
| RA | HSA-modified Rh/SPX | nanocube | 1.human serum albumin (HSA)<br>2.Sparfloxacin (SPX)<br>3.Rhodium (Rh) | POD<br>CAT | noble metal | Li et al. (2021) |
| OA | E@Au-Ag | nano-jars | 1.EGCG<br>2.Au-Ag | POD | noble metal | Xu et al. (2022) |

direct IA delivery. The administration of IA corticosteroids efficiently reduces articular pain and synovitis, but high concentrations of corticosteroids can also damage chondrocyte metabolism, causing changes in ECM composition and articular cartilage structure. A novel treatment for arthritis is urgently needed.

Enzymes are involved in various physiological reactions and participate in the proteolytic degradation of proteins and complex regulatory signalling pathways. Aberrant expression of these enzymes in the human body plays a critical role in pathological processes, especially inflammatory reactions. Different types of MMPs were upregulated by inflammatory factors and subsequently degrade the ECM. In addition to MMPs, ROS also participate in the development of arthritis. The generation of ROS is inhibited by endogenous antioxidants such as SOD, CAT, GPX, and heme oxygenase (HO-1). Despite the complex pathological process of arthritis, different types of arthritis including OA and RA share the common features: the increased levels of MMPs and the decreased expression of antioxidant enzymes. Hence, it is extremely feasible to design nanomaterials based on these enzymes as molecular targets for arthritis therapy.

Although nanomaterials have the advantages of high biocompatibility and bioavailability due to their structural and functional characteristics, the biosafety of nanomaterials cannot be ignored (Chen et al., 2021-09). Nanomaterials enter the body through ingestion, injection, inhalation and skin contact and subsequently accumulate in organs through blood flow, affecting the structure and function of organs (Ai et al., 2011-01). For arthritis treatment, intra-articular injection of enzyme-related biomaterials can guarantee the controlled release and targeted therapy without affecting other tissues or organs through blood circulation. Natural polymers are more suitable and safer for clinical application due to their biodegradation. Especially, hyaluronic acid from cartilage tissue has been commonly used for biomaterial. It is a promising strategy for arthritis treatment through discovering more biologically active materials from the human body in the future and combining them with drugs to regulate the expression of the enzymes mentioned above.

Given that cartilage and the synovium are affected in arthritis, various NPs that target these upregulated or downregulated enzymes mainly act on these sites, especially macrophages from the synovium and OCs from the subchondral bone. Both macrophages and osteoclasts are inflammatory cells with the same receptor on the surface of the membrane and release inflammatory factors. Therefore, biomaterials that target these inflammatory cells or chondrocytes are the current options for arthritis treatment. For the treatment of inflammatory arthritis, nano-drug delivery technologies that respond to subchondral enzymes are rare. There are technical challenges, such as how to penetrate the cartilage and reach the deep layer to target OCs that destroy the subchondral bone. Second, aside from MMPs and endogenous reductase, many enzymes are also involved in the pathological processes of arthritis. The expression of cyclooxygenase-2 (COX-2) in joints has also been linked to synovial inflammation in arthritis, and COX-2 inhibitors (celecoxib) have been frequently used and have shown therapeutic benefits in arthritis. Synergistic treatments targeting several enzymes may obtain better results. Finally, avoiding rapid clearance after IA injection is critical for maintaining drug concentrations and guaranteeing efficacy.

It should be noted that the current studies regarding enzyme-related biomaterials in the field of arthritis are not numerous; nanotherapies are extremely challenging and are also promising based on the molecular mechanism underlying arthritis.

## Author contributions

Conceptualization, X-LX and D-FD; writing—original draft preparation, X-HL, J-YD; writing—review and editing, Z-HZ, -CW; visualization, Y-JS; All authors have read and agreed to publish the manuscript.

## Funding

This study was supported by National Natural Science Foundation of China (81902306, 82174406), the National Key R&D Program of China (Grant No. 2018YFC2001600) and Engineering Research Center of Traditional Chinese Medicine Intelligent Rehabilitation, Ministry of Education

## Conflict of interest

The authors declare that the research was conducted in the absence of any commercial or financial relationships that could be construed as a potential conflict of interest.

## Publisher's note

## References

Ai, J., Biazar, E., Jafarpour, M., Montazeri, M., Majdi, A., Aminifard, S., et al. (2011). Nanotoxicology and nanoparticle safety in biomedical designs. *Int. J. Nanomedicine* 6, 1117–1127. doi:10.2147/IJN.S16603

Auréal, M., Machuca-Gayet, I., and Coury, F. (2020). Rheumatoid arthritis in the view of osteoimmunology. *Biomolecules* 11 (1), 48. doi:10.3390/biom11010048

Bala, A., Mondal, C., Haldar, P. K., and Khandelwal, B. (2017). Oxidative stress in inflammatory cells of patient with rheumatoid arthritis: Clinical efficacy of dietary antioxidants. *Inflammopharmacology* 25 (6), 595–607. doi:10.1007/s10787-017-0397-1

Baldim, V., Bedioui, F., Mignet, N., Margaill, I., and Berret, J. F. (2018). The enzyme-like catalytic activity of cerium oxide nanoparticles and its dependency on Ce3+ surface area concentration. *Nanoscale* 10 (15), 6971–6980. doi:10.1039/c8nr00325d

Briggs, A. M., Shiffman, J., Shawar, Y. R., Åkesson, K., Ali, N., and Woolf, A. D. (2020). Global health policy in the 21st century: Challenges and opportunities to arrest the global disability burden from musculoskeletal health conditions. *Best. Pract. Res. Clin. Rheumatol.* 34 (5), 101549. doi:10.1016/j.berh.2020.101549

Chen, H., Qin, Z., Zhao, J., He, Y., Ren, E., Zhu, Y., et al. (2019). Cartilage-targeting and dual MMP-13/pH responsive theranostic nanoprobes for osteoarthritis imaging and precision therapy. *Biomaterials* 225, 119520. doi:10.1016/j.biomaterials.2019.119520

Chen, L., Huang, Q., Zhao, T., Sui, L., Wang, S., Xiao, Z., et al. (2021). Nanotherapies for sepsis by regulating inflammatory signals and reactive oxygen and nitrogen species: New insight for treating COVID-19. *Redox Biol.* 45, 102046. doi:10.1016/j.redox.2021.102046

Chen, T., Zou, H., Wu, X., Chen, Y., Situ, B., Zheng, L., et al. (2019). Fullerene-like $MoS_2$ nanoparticles as cascade catalysts improving lubricant and antioxidant abilities of artificial synovial fluid. *ACS Biomater. Sci. Eng.* 5 (6), 3079–3088. doi:10.1021/acsbiomaterials.9b00372

Chen, Z., Su, L., Xu, Q., Katz, J., Michalek, S. M., Fan, M., et al. (2015). IL-1R/TLR2 through MyD88 divergently modulates osteoclastogenesis through regulation of nuclear factor of activated T cells c1 (NFATc1) and B lymphocyte-induced maturation protein-1 (Blimp1). *J. Biol. Chem.* 290 (50), 30163–30174. doi:10.1074/jbc.M115.663518

Chung, H. K., Wen, S. H., Chang, W. C., and Liu, K. L. (2021). Acute surgical site infection after total knee arthroplasty in patients with rheumatoid arthritis versus osteoarthritis. *Sci. Rep.* 11 (1), 22704. doi:10.1038/s41598-021-02153-x

Cieza, A., Causey, K., Kamenov, K., Hanson, S. W., Chatterji, S., and Vos, T. (2021). Global estimates of the need for rehabilitation based on the global burden of disease study 2019: A systematic analysis for the global burden of disease study 2019. *Lancet* 396 (10267), 2006–2017. doi:10.1016/S0140-6736(20)32340-0

Dacarro, G., Taglietti, A., and Pallavicini, P. (2018). Prussian blue nanoparticles as a versatile photothermal tool. *Molecules* 23 (6), 1414. doi:10.3390/molecules23061414

Datta, S., Kundu, S., Ghosh, P., Ghosh, A., Chatterjee, M., and De, S. (2014). Correlation of oxidant status with oxidative tissue damage in patients with rheumatoid arthritis. *Clin. Rheumatol.* 33 (11), 1557–1564. doi:10.1007/s10067-014-2597-z

Deng, C., Zhang, Q., He, P., Zhou, B., He, K., Sun, X., et al. (2021). Targeted apoptosis of macrophages and osteoclasts in arthritic joints is effective against advanced inflammatory arthritis. *Nat. Commun.* 12 (1), 2174. doi:10.1038/s41467-021-22454-z

Deponte, M. (2013). Glutathione catalysis and the reaction mechanisms of glutathione-dependent enzymes. *Biochimica Biophysica Acta - General Subj.* 1830 (5), 3217–3266. doi:10.1016/j.bbagen.2012.09.018

Fosang, A. J., Last, K., Knäuper, V., Murphy, G., and Neame, P. J. (1996). Degradation of cartilage aggrecan by collagenase-3 (MMP-13). *FEBS Lett.* 380 (1-2), 17–20. doi:10.1016/0014-5793(95)01539-6

Galasso, O., Familiari, F., De Gori, M., and Gasparini, G. (2012). Recent findings on the role of gelatinases (matrix metalloproteinase-2 and -9) in osteoarthritis. *Adv. Orthop.* 2012, 1–7. doi:10.1155/2012/834208

Galil, S. M., El-Shafey, A. M., Hagrass, H. A., Fawzy, F., and Sammak, A. E. (2016). Baseline serum level of matrix metalloproteinase-3 as a biomarker of progressive joint damage in rheumatoid arthritis patients. *Int. J. Rheum. Dis.* 19 (4), 377–384. doi:10.1111/1756-185X.12434

Gamal, R. M., Hammam, N., Zakary, M. M., Abdelaziz, M. M., Razek, M. R. A., Mohamed, M. S. E., et al. (2018). Telomere dysfunction-related serological markers and oxidative stress markers in rheumatoid arthritis patients: Correlation with diseases activity. *Clin. Rheumatol.* 37 (12), 3239–3246. doi:10.1007/s10067-018-4318-5

Georgiev, T., Ivanova, M., Kopchev, A., Velikova, T., Miloshov, A., Kurteva, E., et al. (2018). Cartilage oligomeric protein, matrix metalloproteinase-3, and coll2-1 as serum biomarkers in knee osteoarthritis: A cross-sectional study. *Rheumatol. Int.* 38 (5), 821–830. doi:10.1007/s00296-017-3887-y

He, L., Fan, D., Liang, W., Wang, Q., and Fang, J. (2020). Matrix metalloproteinase-responsive PEGylated lipid nanoparticles for controlled drug delivery in the treatment of rheumatoid arthritis. *ACS Appl. Bio Mat.* 3 (5), 3276–3284. doi:10.1021/acsabm.0c00242

He, L., He, T., Farrar, S., Ji, L., Liu, T., and Ma, X. (2017). Antioxidants maintain cellular redox homeostasis by elimination of reactive oxygen species. *Cell. Physiol. biochem.* 44 (2), 532–553. doi:10.1159/000485089

Heckert, E. G., Karakoti, A. S., Seal, S., and Self, W. T. (2008). The role of cerium redox state in the SOD mimetic activity of nanoceria. *Biomaterials* 29 (18), 2705–2709. doi:10.1016/j.biomaterials.2008.03.014

Hoshi, H., Akagi, R., Yamaguchi, S., Muramatsu, Y., Akatsu, Y., Yamamoto, Y., et al. (2017). Effect of inhibiting MMP13 and ADAMTS5 by intra-articular injection of small interfering RNA in a surgically induced osteoarthritis model of mice. *Cell Tissue Res.* 368 (2), 379–387. doi:10.1007/s00441-016-2563-y

Hosseinzadeh, A., Kamrava, S. K., Joghataei, M. T., Darabi, R., Shakeri-Zadeh, A., Shahriari, M., et al. (2016). Apoptosis signaling pathways in osteoarthritis and possible protective role of melatonin. *J. Pineal Res.* 61 (4), 411–425. doi:10.1111/jpi.12362

Hou, W., Ye, C., Chen, M., Gao, W., Xie, X., Wu, J., et al. (2021). Excavating bioactivities of nanozyme to remodel microenvironment for protecting chondrocytes and delaying osteoarthritis. *Bioact. Mat.* 6 (8), 2439–2451. doi:10.1016/j.bioactmat.2021.01.016

Hu, Q., and Ecker, M. (2021). Overview of MMP-13 as a promising target for the treatment of osteoarthritis. *Int. J. Mol. Sci.* 22 (4), 1742. doi:10.3390/ijms22041742

Idzik, M., Poloczek, J., Skrzep-Poloczek, B., Chelmecka, E., Jochem, J., and Stygar, D. (2022). General rehabilitation Program after knee or hip replacement significantly influences erythrocytes oxidative stress markers and serum ST2 levels. *Oxid. Med. Cell. Longev.* 2022, 1358858. doi:10.1155/2022/1358858

Itoh, Y. (2017). Metalloproteinases in rheumatoid arthritis: Potential therapeutic targets to improve current therapies. *Prog. Mol. Biol. Transl. Sci.* 148, 327–338. doi:10.1016/bs.pmbts.2017.03.002

Iwabuchi, Y., Tanimoto, K., Tanne, Y., Inubushi, T., Kamiya, T., Kunimatsu, R., et al. (2014). Effects of low-intensity pulsed ultrasound on the expression of cyclooxygenase-2 in mandibular condylar chondrocytes. *J. Oral Facial Pain . Headache* 28 (3), 261–268. doi:10.11607/ofph.1156

Jansen, M. P., and Mastbergen, S. C. (2022). Joint distraction for osteoarthritis: Clinical evidence and molecular mechanisms. *Nat. Rev. Rheumatol.* 18 (1), 35–46. doi:10.1038/s41584-021-00695-y

Joshi, N., Yan, J., Levy, S., Bhagchandani, S., Slaughter, K. V., Sherman, N. E., et al. (2018). Towards an arthritis flare-responsive drug delivery system. *Nat. Commun.* 9 (1), 1275. doi:10.1038/s41467-018-03691-1

Kalashnikova, I., Chung, S. J., Nafiujjaman, M., Hill, M. L., Siziba, M. E., Contag, C. H., et al. (2020). Ceria-based nanotheranostic agent for rheumatoid arthritis. *Theranostics* 10 (26), 11863–11880. doi:10.7150/thno.49069

Kaneva, M. K. (2022). Neutrophil elastase and its inhibitors-overlooked players in osteoarthritis. *FEBS J.* 289 (1), 113–116. doi:10.1111/febs.16194

Kim, K. S., Choi, H. M., Lee, Y. A., Choi, I. A., Lee, S. H., Hong, S. J., et al. (2011). Expression levels and association of gelatinases MMP-2 and MMP-9 and collagenases MMP-1 and MMP-13 with VEGF in synovial fluid of patients with arthritis. *Rheumatol. Int.* 31 (4), 543–547. doi:10.1007/s00296-010-1592-1

Kratschmer, W., Lamb, L. D., Fostiropoulos, K., and Huffman, D. R. (1990). Solid C60: A new form of carbon. *Nature* 347, 354–358. doi:10.1038/347354a0

Lan, Q., Lu, R., Chen, H., Pang, Y., Xiong, F., Shen, C., et al. (2020). MMP-13 enzyme and pH responsive theranostic nanoplatform for osteoarthritis. *J. Nanobiotechnology* 18 (1), 117. doi:10.1186/s12951-020-00666-7

Latourte, A., Cherifi, C., Maillet, J., Ea, H. K., Bouaziz, W., Funck-Brentano, T., et al. (2017). Systemic inhibition of IL-6/Stat3 signalling protects against experimental osteoarthritis. *Ann. Rheum. Dis.* 76 (4), 748–755. doi:10.1136/annrheumdis-2016-209757

Lepetsos, P., and Papavassiliou, A. G. (2016). ROS/oxidative stress signaling in osteoarthritis. *Biochimica Biophysica Acta - Mol. Basis Dis.* 1862 (4), 576–591. doi:10.1016/j.bbadis.2016.01.003

Li, H., Wang, D., Yuan, Y., and Min, J. (2017). New insights on the MMP-13 regulatory network in the pathogenesis of early osteoarthritis. *Arthritis Res. Ther.* 19 (1), 248. doi:10.1186/s13075-017-1454-2

Li, W., Song, Y., Liang, X., Zhou, Y., Xu, M., Lu, Q., et al. (2021). Mutual-reinforcing sonodynamic therapy against Rheumatoid Arthritis based on sparfloxacin sonosensitizer doped concave-cubic rhodium nanozyme. *Biomaterials* 276, 121063. doi:10.1016/j.biomaterials.2021.121063

Li, Z., Chen, C., Zhu, X., Li, Y., Yu, R., and Xu, W. (2018). Glycyrrhizin suppresses RANKL-induced osteoclastogenesis and oxidative stress through inhibiting NF-κB and MAPK and activating AMPK/Nrf2. *Calcif. Tissue Int.* 103 (3), 324–337. doi:10.1007/s00223-018-0425-1

Lima, A. C., Reis, R. L., Ferreira, H., and Neves, N. M. (2021). Glutathione reductase-sensitive polymeric micelles for controlled drug delivery on arthritic diseases. *ACS Biomater. Sci. Eng.* 7 (7), 3229–3241. doi:10.1021/acsbiomaterials.1c00412

Lipari, L., and Gerbino, A. (2013). Expression of gelatinases (MMP-2, MMP-9) in human articular cartilage. *Int. J. Immunopathol. Pharmacol.* 26 (3), 817–823. doi:10.1177/039463201302600331

Liu, L., Hu, F., Wang, H., Wu, X., Eltahan, A. S., Stanford, S., et al. (2019). Secreted protein acidic and rich in cysteine mediated biomimetic delivery of methotrexate by albumin-based nanomedicines for rheumatoid arthritis therapy. *ACS Nano* 13 (5), 5036–5048. doi:10.1021/acsnano.9b01710

Long, J., Guari, Y., Guérin, C., and Larionova, J. (2016). Prussian blue type nanoparticles for biomedical applications. *Dalton Trans.* 45 (44), 17581–17587. doi:10.1039/c6dt01299j

Luo, H., and Zhang, R. (2021). Icariin enhances cell survival in lipopolysaccharide-induced synoviocytes by suppressing ferroptosis via the Xc-/GPX4 axis. *Exp. Ther. Med.* 21 (1), 72. doi:10.3892/etm.2020.9504

Ma, J. D., Jing, J., Wang, J. W., Yan, T., Li, Q. H., Mo, Y. Q., et al. (2019). A novel function of artesunate on inhibiting migration and invasion of fibroblast-like synoviocytes from rheumatoid arthritis patients. *Arthritis Res. Ther.* 21 (1), 153. doi:10.1186/s13075-019-1935-6

Ma, J. D., Zhou, J. J., Zheng, D. H., Chen, L. F., Mo, Y. Q., Wei, X. N., et al. (2014). Serum matrix metalloproteinase-3 as a noninvasive biomarker of histological synovitis for diagnosis of rheumatoid arthritis. *Mediat. Inflamm.* 2014, 1–10. doi:10.1155/2014/179284

Macdonald, C. D., Falconer, A. M. D., Chan, C. M., Wilkinson, D. J., Skelton, A., Reynard, L., et al. (2018). Cytokine-induced cysteine- serine-rich nuclear protein-1 (CSRNP1) selectively contributes to MMP1 expression in human chondrocytes. *PLoS One* 13 (11), e0207240. doi:10.1371/journal.pone.0207240

Malemud, C. J. (2017). Matrix metalloproteinases and synovial joint pathology. *Prog. Mol. Biol. Transl. Sci.* 148, 305–325. doi:10.1016/bs.pmbts.2017.03.003

Malhotra, S., Welling, M. N., Mantri, S. B., and Desai, K. (2016). *In vitro* and *in vivo* antioxidant, cytotoxic, and anti-chronic inflammatory arthritic effect of selenium nanoparticles. *J. Biomed. Mat. Res.* 104 (5), 993–1003. doi:10.1002/jbm.b.33448

McAlindon, T. E., LaValley, M. P., Harvey, W. F., Price, L. L., Driban, J. B., Zhang, M., et al. (2017). Effect of intra-articular triamcinolone vs saline on knee cartilage volume and pain in patients with knee osteoarthritis: A randomized clinical trial. *JAMA* 317 (19), 1967–1975. doi:10.1001/jama.2017.5283

Mehana, E. E., Khafaga, A. F., and El-Blehi, S. S. (2019). The role of matrix metalloproteinases in osteoarthritis pathogenesis: An updated review. *Life Sci.* 234, 116786. doi:10.1016/j.lfs.2019.116786

Meshkibaf, M. H., Maleknia, M., and Noroozi, S. (2019). Effect of curcumin on gene expression and protein level of methionine sulfoxide reductase A (MSRA), SOD, CAT and GPx in Freund's adjuvant inflammation-induced male rats. *J. Inflamm. Res.* 12, 241–249. doi:10.2147/JIR.S212577

Metzger, I. F., Sandrim, V. C., and Tanus-Santos, J. E. (2012). Endogenous nitric oxide formation correlates negatively with circulating matrix metalloproteinase (MMP)-2 and MMP-9 levels in black subjects. *Mol. Cell. Biochem.* 360 (1-2), 393–399. doi:10.1007/s11010-011-1079-8

Mittal, M., Siddiqui, M. R., Tran, K., Reddy, S. P., and Malik, A. B. (2014). Reactive oxygen species in inflammation and tissue injury. *Antioxid. Redox Signal.* 20 (7), 1126–1167. doi:10.1089/ars.2012.5149

Nguyen, N. H., Tran, G. B., and Nguyen, C. T. (2020). Anti-oxidative effects of superoxide dismutase 3 on inflammatory diseases. *J. Mol. Med.* 98 (1), 59–69. doi:10.1007/s00109-019-01845-2

Ostalowska, A., Birkner, E., Wiecha, M., Kasperczyk, S., Kasperczyk, A., Kapolka, D., et al. (2006). Lipid peroxidation and antioxidant enzymes in synovial fluid of patients with primary and secondary osteoarthritis of the knee joint. *Osteoarthr. Cartil.* 14 (2), 139–145. doi:10.1016/j.joca.2005.08.009

Palmer, J. S., Monk, A. P., Hopewell, S., Bayliss, L. E., Jackson, W., Beard, D. J., et al. (2019). Surgical interventions for symptomatic mild to moderate knee osteoarthritis. *Cochrane Database Syst. Rev.* 7, CD012128. doi:10.1002/14651858.CD012128.pub2

Park, C. R., Jo, J. H., Song, M. G., Park, J. Y., Kim, Y. H., Youn, H., et al. (2019). Secreted protein acidic and rich in cysteine mediates active targeting of human serum albumin in U87MG xenograft mouse models. *Theranostics* 9 (24), 7447–7457. doi:10.7150/thno.34883

Pengas, I., Eldridge, S., Assiotis, A., McNicholas, M., Mendes, J. E., and Laver, L. (2018). MMP-3 in the peripheral serum as a biomarker of knee osteoarthritis, 40 years after open total knee meniscectomy. *J. Exp. Orthop.* 5 (1), 21. doi:10.1186/s40634-018-0132-x

Phull, A. R., Nasir, B., Haq, I. U., and Kim, S. J. (2018). Oxidative stress, consequences and ROS mediated cellular signaling in rheumatoid arthritis. *Chem. Biol. Interact.* 281, 121–136. doi:10.1016/j.cbi.2017.12.024

Pirmohamed, T., Dowding, J. M., Singh, S., Wasserman, B., Heckert, E., Karakoti, A. S., et al. (2010). Nanoceria exhibit redox state-dependent catalase mimetic activity. *Chem. Commun.* 46 (16), 2736–2738. doi:10.1039/b922024k

Qin, Z., Li, Y., and Gu, N. (2018). Progress in applications of prussian blue nanoparticles in biomedicine. *Adv. Healthc. Mat.* 7 (20), e1800347. doi:10.1002/adhm.201800347

Radu, A. F., and Bungau, S. G. (2021). Management of rheumatoid arthritis: An overview. *Cells* 10 (11), 2857. doi:10.3390/cells10112857

Ren, S. X., Zhan, B., Lin, Y., Ma, D. S., and Yan, H. (2019). Selenium nanoparticles dispersed in phytochemical exert anti-inflammatory activity by modulating catalase, GPx1, and COX-2 gene expression in a rheumatoid arthritis rat model. *Med. Sci. Monit.* 25, 991–1000. doi:10.12659/MSM.912545

Ren, S. X., Zhan, B., Lin, Y., Ma, D. S., and Yan, H. (2019). Selenium nanoparticles dispersed in phytochemical exert anti-inflammatory activity by modulating catalase, GPx1, and COX-2 gene expression in a rheumatoid arthritis rat model. *Med. Sci. Monit.* 25, 991–1000. doi:10.12659/MSM.912545

Scherer, H. U., Häupl, T., and Burmester, G. R. (2020). The etiology of rheumatoid arthritis. *J. Autoimmun.* 110, 102400. doi:10.1016/j.jaut.2019.102400

Silosi, I., Cojocaru, M., Foia, L., Boldeanu, M. V., Petrescu, F., Surlin, P., et al. (2015). Significance of circulating and crevicular matrix metalloproteinase-9 in rheumatoid arthritis-chronic periodontitis association. *J. Immunol. Res.* 2015, 1–6. doi:10.1155/2015/218060

Singh, A., Rajasekaran, N., Hartenstein, B., Szabowski, S., Gajda, M., Angel, P., et al. (2013). Collagenase-3 (MMP-13) deficiency protects C57BL/6 mice from antibody-induced arthritis. *Arthritis Res. Ther.* 15 (6), R222. doi:10.1186/ar4423

Sparks, J. A. (2019). Rheumatoid arthritis. *Ann. Intern. Med.* 170 (1), ITC1–ITC16. doi:10.7326/AITC201901010

Sredzińska, K., Galicka, A., Porowska, H., Sredziński, Ł., Porowski, T., and Popko, J. (2009). Glutathione reductase activity correlates with concentration of extracellular matrix degradation products in synovial fluid from patients with joint diseases. *Acta Biochim. Pol.* 56 (4), 635–640. doi:10.18388/abp.2009_2496

Stocco, E., Barbon, S., Piccione, M., Belluzzi, E., Petrelli, L., Pozzuoli, A., et al. (2019). Infrapatellar fat pad stem cells responsiveness to microenvironment in osteoarthritis: From morphology to function. *Front. Cell Dev. Biol.* 7, 323. doi:10.3389/fcell.2019.00323

Swain, S., Sarmanova, A., Mallen, C., Kuo, C. F., Coupland, C., Doherty, M., et al. (2020). Trends in incidence and prevalence of osteoarthritis in the United Kingdom: Findings from the clinical practice research datalink (CPRD). *Osteoarthr. Cartil.* 28 (6), 792–801. doi:10.1016/j.joca.2020.03.004

Tatematsu, N., Waguri-Nagaya, Y., Kawaguchi, Y., Oguri, Y., Ikuta, K., Kobayashi, M., et al. (2018). Mithramycin has inhibitory effects on gliostatin and matrix metalloproteinase expression induced by gliostatin in rheumatoid fibroblast-like synoviocytes. *Mod. Rheumatol.* 28 (3), 495–505. doi:10.1080/14397595.2017.1350332

Trachana, V., Mourmoura, E., Papathanasiou, I., and Tsezou, A. (2019). Understanding the role of chondrocytes in osteoarthritis: Utilizing proteomics. *Expert Rev. Proteomics* 16 (3), 201–213. doi:10.1080/14789450.2019.1571918

Tschon, M., Salamanna, F., Martini, L., Giavaresi, G., Lorenzini, L., Calzà, L., et al. (2020). Boosting the intra-articular efficacy of low dose corticosteroid through a biopolymeric matrix: An *in vivo* model of osteoarthritis. *Cells* 9 (7), 1571. doi:10.3390/cells9071571

Tuncer, T., Kaya, A., Gulkesen, A., Kal, G. A., Kaman, D., and Akgol, G. (2019). Matrix metalloproteinase-3 levels in relation to disease activity and radiological progression in rheumatoid arthritis. *Adv. Clin. Exp. Med.* 28 (5), 665–670. doi:10.17219/acem/94065

van Dalen, S. C., Blom, A. B., Slöetjes, A. W., Helsen, M. M., Roth, J., Vogl, T., et al. (2017). Interleukin-1 is not involved in synovial inflammation and cartilage destruction in collagenase-induced osteoarthritis. *Osteoarthr. Cartil.* 25 (3), 385–396. doi:10.1016/j.joca.2016.09.009

van der Woude, J. A., Wiegant, K., van Heerwaarden, R. J., Spruijt, S., Emans, P. J., Mastbergen, S. C., et al. (2017). Knee joint distraction compared with total knee arthroplasty: A randomised controlled trial. *Bone Jt. J.* 99-B (1), 51–58. doi:10.1302/0301-620X.99B1.BJJ-2016-0099.R3

Wang, M., Zhou, Y., Huang, W., Zeng, Y., and Li, X. (2020). Association between matrix metalloproteinase-1 (MMP-1) protein level and the risk of rheumatoid arthritis and osteoarthritis: A meta-analysis. *Braz. J. Med. Biol. Res.* 54 (2), e10366. doi:10.1590/1414-431X202010366

Wang, Z., Zhang, R., Yan, X., and Fan, K. (2020). Structure and activity of nanozymes: Inspirations for de novo design of nanozymes. *Mat. TodayKidlingt.* 41, 81–119. doi:10.1016/j.mattod.2020.08.020

Wen, Y., Chen, X., Zhu, X., Gong, Y., Yuan, G., Qin, X., et al. (2019). Photothermal-chemotherapy integrated nanoparticles with tumor microenvironment response enhanced the induction of immunogenic cell death for colorectal cancer efficient treatment. *ACS Appl. Mat. Interfaces* 11 (46), 43393–43408. doi:10.1021/acsami.9b17137

Whittaker, J. L., Truong, L. K., Dhiman, K., and Beck, C. (2021). Osteoarthritis year in review 2020: Rehabilitation and outcomes. *Osteoarthr. Cartil.* 29 (2), 190–207. doi:10.1016/j.joca.2020.10.005

Woolf, A. D., and Pfleger, B. (2003). Burden of major musculoskeletal conditions. *Bull. World Health Organ.* 81 (9), 646–656. Epub 2003 Nov 14. doi:10.1590/S0042-96862003000900007

Wu, H., Du, J., and Zheng, Q. (2008). Expression of MMP-1 in cartilage and synovium of experimentally induced rabbit ACLT traumatic osteoarthritis: Immunohistochemical study. *Rheumatol. Int.* 29 (1), 31–36. doi:10.1007/s00296-008-0636-2

Wylde, V., Hewlett, S., Learmonth, I. D., and Dieppe, P. (2011). Persistent pain after joint replacement: Prevalence, sensory qualities, and postoperative determinants. *Pain* 152 (3), 566–572. doi:10.1016/j.pain.2010.11.023

Xie, Z., Hou, H., Luo, D., An, R., Zhao, Y., and Qiu, C. (2021). ROS-dependent lipid peroxidation and reliant antioxidant ferroptosis-suppressor-protein 1 in rheumatoid arthritis: A covert clue for potential therapy. *Inflammation* 44 (1), 35–47. doi:10.1007/s10753-020-01338-2

Xu, S., Chang, L., Zhao, X., Hu, Y., Lin, Y., Chen, Z., et al. (2022). Preparation of epigallocatechin gallate decorated Au-Ag nano-heterostructures as NIR-sensitive nano-enzymes for the treatment of osteoarthritis through mitochondrial repair and cartilage protection. *Acta Biomater.* 144, 168–182. doi:10.1016/j.actbio.2022.03.038

Yao, Y., Zhang, H., Wang, Z., Ding, J., Wang, S., Huang, B., et al. (2019). Reactive oxygen species (ROS)-responsive biomaterials mediate tissue microenvironments and tissue regeneration. *J. Mat. Chem. B* 7 (33), 5019–5037. doi:10.1039/c9tb00847k

You, Z., Sun, J., Xie, F., Chen, Z., Zhang, S., Chen, H., et al. (2018). Novel iron oxide–cerium oxide core–shell nanoparticles as a potential theranostic material for ROS related inflammatory diseases. *J. Mat. Chem. B* 6 (30), 4937–4951. doi:10.1039/c8tb00022k

Yu, C., Liu, H., Guo, C., Chen, Q., Su, Y., Guo, H., et al. (2022). Dextran sulfate-based MMP-2 enzyme-sensitive SR-A receptor targeting nanomicelles for the treatment of rheumatoid arthritis. *Drug Deliv. (Lond).* 29 (1), 454–465. doi:10.1080/10717544.2022.2032482

Yu, N., Han, F., Lin, X., Tang, C., Ye, J., and Cai, X. (2016). The association between serum selenium levels with rheumatoid arthritis. *Biol. Trace Elem. Res.* 172 (1), 46–52. doi:10.1007/s12011-015-0558-2

Zeng, G. Q., Chen, A. B., Li, W., Song, J. H., and Gao, C. Y. (2015). High MMP-1, MMP-2, and MMP-9 protein levels in osteoarthritis. *Genet. Mol. Res.* 14 (4), 14811–14822. doi:10.4238/2015.November.18.46

Zhang, L., Qin, Z., Sun, H., Chen, X., Dong, J., Shen, S., et al. (2022). Nanoenzyme engineered neutrophil-derived exosomes attenuate joint injury in advanced rheumatoid arthritis via regulating inflammatory environment. *Bioact. Mat.* 18, 1–14. doi:10.1016/j.bioactmat.2022.02.017

Zhang, S., Ren, Q., Qi, H., Liu, S., and Liu, Y. (2019). Adverse effects of fine-particle exposure on joints and their surrounding cells and microenvironment. *ACS Nano* 13 (3), 2729–2748. doi:10.1021/acsnano.8b08517

Zhang, W., Hu, S., Yin, J. J., He, W., Lu, W., Ma, M., et al. (2016). Prussian blue nanoparticles as multienzyme mimetics and reactive oxygen species scavengers. *J. Am. Chem. Soc.* 138 (18), 5860–5865. doi:10.1021/jacs.5b12070

Zhuang, C., Wang, Y., Zhang, Y., and Xu, N. (2018). Oxidative stress in osteoarthritis and antioxidant effect of polysaccharide from angelica sinensis. *Int. J. Biol. Macromol.* 115, 281–286. doi:10.1016/j.ijbiomac.2018.04.083

Zuo, D., Tan, B., Jia, G., Wu, D., Yu, L., and Jia, L. (2021). A treatment combined prussian blue nanoparticles with low-intensity pulsed ultrasound alleviates cartilage damage in knee osteoarthritis by initiating PI3K/Akt/mTOR pathway. *Am. J. Transl. Res.* 13 (5), 3987–4006. doi:10.21203/rs.3.rs-77010/v1

frontiers | Frontiers in Molecular Biosciences

TYPE Original Research
PUBLISHED 30 September 2022
DOI 10.3389/fmolb.2022.995853

OPEN ACCESS

EDITED BY
Pengfei Xu,
National University of Singapore,
Singapore

REVIEWED BY
Shereen A. Majeed,
Kuwait University, Kuwait
Lian Ying Zhang,
Qingdao University, China

*CORRESPONDENCE
Kamyar Shameli,
kamyarshameli@gmail.com
Hassan Moeini,
hassan.moeini@tum.de

SPECIALTY SECTION
This article was submitted
to Nanobiotechnology,
a section of the journal
Frontiers in Molecular Biosciences

RECEIVED 16 July 2022
ACCEPTED 09 September 2022
PUBLISHED 30 September 2022

CITATION
Ismail NA, Shameli K,
Mohamad Sukri SNA, Hara H, Teow S-Y
and Moeini H (2022), Sonochemical
synthesis of a copper reduced graphene
oxide nanocomposite using honey and
evaluation of its antibacterial and
cytotoxic activities.
*Front. Mol. Biosci.* 9:995853.
doi: 10.3389/fmolb.2022.995853

# Sonochemical synthesis of a copper reduced graphene oxide nanocomposite using honey and evaluation of its antibacterial and cytotoxic activities

Nur Afini Ismail[1], Kamyar Shameli[1]*,
Siti Nur Amalina Mohamad Sukri[1], Hirofumi Hara[2],
Sin-Yeang Teow[3] and Hassan Moeini[4]*

[1]Malaysia-Japan International Institute of Technology, Universiti Teknologi Malaysia Jalan Sultan Yahya Petra, Kuala Lumpur, Malaysia, [2]Department of Biotechnology, Graduate School of Agricultural and Life Sciences, University of Tokyo, Tokyo, Japan, [3]School of Medical and Life Sciences (SMLS), Sunway University, Kuala Lumpur, Malaysia, [4]School of Medicine, Institute of Virology, Technical University of Munich, Munich, Germany

The combination of graphene-based materials and inorganic nanoparticles for the enhancement of the nanomaterial properties is extensively explored nowadays. In the present work, we used a sonochemical method to synthesize a copper/reduced graphene oxide (Cu/RGO) nanocomposite using Australian honey and vitamin C as capping and reducing agents, respectively. The honey-mediated copper/reduced graphene oxide (H/Cu/RGO) nanocomposite was then characterized through UV-visible, XRD, HRTEM, and FTIR analysis. The copper nanoparticles (Cu-NPs) in the nanocomposite formed uniform spherical shapes with a size of 2.20 ± 0.70 nm, which attached to the reduced graphene oxide (RGO) layers. The nanocomposite could suppress bacterial growth in both types of bacteria strains. However, in this study, the nanocomposite exhibited good bactericidal activity toward the Gram-positive bacteria than the Gram-negative bacteria. It also showed a cytotoxic effect on the cancer colorectal cell line HCT11, even in low concentrations. These results suggested that the H/Cu/RGO nanocomposite can be a suitable component for biomedical applications.

KEYWORDS

**sonochemical method, copper/reduced graphene oxide nanocomposite, honey, antibacterial, cytotoxicity assay**

## Introduction

In the past 50 years, pathogenic bacteria have caused a plethora of diseases in the human population. Some of these major emerging bacteria include *Staphylococcus aureus* (*S. aureus*), *Escherichia coli* (*E. coli*), *Clostridium difficile*, *Campylobacter spp*., and *Helicobacter pylori* (Vouga and Greub, 2016). Although some commensal bacteria such as *Lactobacillus* and *Bifidobacterium* may exist as part of the human microbiota, which might play beneficial roles in maintaining homeostasis (Wang et al., 2017), many of these bacteria could also cause various illnesses such as liver diseases, infection, respiratory diseases, gastrointestinal malignancy, and metabolic disorders (Wang et al., 2017). The emergence of bacterial antimicrobial resistance (AMR) has even aggravated this issue and poses a major threat to global health. According to a recent systematic analysis, the six leading pathogens responsible for death associated with AMR are *E. coli*, *S. aureus*, *Klebsiella pneumoniae*, *Pseudomonas aeruginosa (P. aeruginosa)*, *Streptococcus pneumoniae*, and *Acinetobacter baumannii* which are the combination of both Gram-positive and Gram-negative strains (Murray et al., 2022).

The second main cause of death in the United States is cancer, and among different cancer types, lung cancer is the leading cause of cancer mortality (Siegel et al., 2022). For both sexes, the highest incidence of cancer is led by breast cancer, followed by prostate and lung/bronchus cancers (Siegel et al., 2022). Similarly, chemo- and/or radio-resistance presented by the patient's tumor remains the main barrier to effectively eradicating tumor from the body. On top of this, off-target side effects suffered by the patients due to cancer therapy are another obstacle (Miller et al., 2022). Hence, it is vital to look for a novel anticancer drug or therapeutic strategy to treat cancer more effectively.

Recently, nanomaterial has been widely explored for their special properties to mitigate these problems. There are various factors that may affect the biological activities of the nanomaterial, such as the shape, size, electronic structure, surface properties, and some additional factors related to the interaction conditions between the materials and the target cells (Sengupta et al., 2019). Copper nanoparticles (Cu-NPs) have been widely assessed for their properties. Aside from its low-cost production, copper also exhibits good thermal and electrical conductivity, and biological and antimicrobial activities (Zhou et al., 2019; Noman et al., 2020; Merugu et al., 2021). Recently, the United States Environmental Protection Agency recognized copper as the first solid antimicrobial material (Ouyang et al., 2013; Arendsen et al., 2019). However, researchers found that pure metallic Cu-NPs are difficult to obtain as copper tends to oxidize easily when exposed to the air, and it will also tend to agglomerate without proper protection (Rostami-Tapeh-Esmaeil et al., 2021). Hence, the usage of green material as a capping agent or stabilizer has gained researchers' attention since it is reported to produce monodispersed pure Cu-NPs by a fast and green method (Nagar and Devra, 2018).

Graphene is a unique structure that attracts great attention due to its interesting physical and chemical characteristics (Luo et al., 2020), including large surface area, good conductivity, and high thermal properties (Ouyang et al., 2013). Graphene and its derivatives are used in extensive applications such as electronic devices (Moozarm Nia et al., 2017), energy storage (Rawal et al., 2020), and biomedical applications (Kumar et al., 2017). The presence of oxygen functional groups such as epoxide, carboxyl, and hydroxyl in the structure of the graphene oxide (GO) and reduced graphene oxide (RGO) makes them suitable for the production of nanocomposites (Gan et al., 2019a). These groups act as bioactive molecules that could functionalize the graphene sheet with other materials such as metal and metal oxide nanoparticles (Gan et al., 2019b; Jang et al., 2020).

Graphene oxide can be decorated with some materials through chemical reduction (*in situ*), hydrothermal, and electrochemical processes, and through the attachment of the premade nanoparticles to the graphene surface (*ex situ*) to form graphene-based nanomaterials (Sarkar and Dolui, 2015; Yin et al., 2015; Iranshahi and Iranshahi, 2022; Thy et al., 2022). Luo et al. (2020) used refluxed process in synthesizing the reduced graphene oxide/copper nanocomposites (RGO/Cu-NCs) in an oil bath at 100°C for 24 h with hydrazine hydrate. This method involved a long processing time and hazardous material. In fact, nowadays, researchers are interested in using simple and green materials to synthesize the Cu/RGO nanocomposite since it is a much eco-friendlier method. Rios et al. (2019) used an *in situ* reduction method to produce reduced graphene oxide/copper nanoparticles (RGO/Cu-NPs) in the presence of ascorbic acid for 12 h at 80°C. Fahiminia et al. (2019) synthesized Cu/RGO nanocomposites using plant extract (*Euphorbia cheiradenia Boiss*) and applied it as a catalyst for dye removal. Yang et al. (2019) produced cuprous oxide/reduced graphene oxide ($Cu_2O$-RGO) nanocomposites through chemical reduction by using polyethylene glycol (PEG) and ascorbic acid with the addition of sodium hydroxide (NaOH), and used them for the antibacterial study.

Indeed, Tu et al. (2021) reported that the Cu/RGO nanocomposite exhibited better biological activity compared to the reduced graphene oxide (RGO) alone. Generally, the combination of RGO and copper ions happened by the cation-$\pi$ interaction between copper ions and $\pi$-electrons that coming from the aromatic rings of RGO (Xu et al., 2019; Yan et al., 2019; Ismail et al., 2021; Tu et al., 2021). This functionalized RGO could enhance the antibacterial activity where both participated in killing the bacteria cells through electrostatic interaction between the positive charge of copper ions from the nanocomposite and the negatively charged membranes of bacteria (Sanchez-Lopez et al., 2020). RGO could also kill bacteria through the sharp edge of its structure (Prasad et al., 2017). The aggregation of the RGO due to the $\pi$–$\pi$ stacking would have a hydrophobic structure which is known to give strong bacteria absorption that could help in better releasing copper ions and attacking the bacteria cell efficiently (Szunerits and Boukherroub, 2016). This will show excellent results in antibacterial activity compared to the copper ion and RGO alone. Up until now, few studies for anticancer using Cu/RGO nanocomposite were reported. Kodous et al. (2022) found that

Cu/RGO nanocomposites produced by using the ultrasonication method could inhibit human breast cancer cells (MCF-7 cancer cells).

Honey is considered a green material since it is a non-toxic substance that possesses rich sugar source carbohydrate components (Balasooriya et al., 2017). It is also a simple material that does not have to undergo any extraction process, unlike plants and microorganisms. Most importantly, it was also reported for its biological activity properties and its potential as a capping agent (Ismail et al., 2019). Eucalyptus flower species is usually one of the main sources of nectar for the Australian honeybees (*Apis mellifera*) to produce honey. The source of nectar, the combination of proteins secreted by the bee for the honey-ripening process, and protein from plant pollen will affect the honey's chemical composition. According to Beiranvand et al. (2021), the major component in pure Australian honey was carbohydrates, which could act as a capping and reducing agent. However, the chemical component such as carbohydrate in honey is considered a weak reducing agent so it needs another booster to enhance the reducing process of the nanoparticles, and for this, vitamin C (ascorbic acid) was chosen in this study since it is also a green material. Hence, in this work, we produced a honey-mediated copper reduced graphene oxide (H/Cu/RGO) nanocomposite using a sonochemical method, where Australian honey and ascorbic acid were served as capping and reducing agents, respectively, during the process. The sample was analyzed by using UV-visible, XRD, HRTEM, and FTIR, and it was then tested for antibacterial and cytotoxicity properties.

# Materials and methods

## Materials

The source of honey was from the Capilano Honey Limited (Australia). Standard graphene oxide (water dispersion, 4 mg/ml) was purchased from Graphene (U-Malaya). Copper II nitrate trihydrate ($Cu(NO_3)_2.3H_2O$, AR grade), ascorbic acid ($C_6H_8O_6$, AR grade), and sodium hydroxide (NaOH) were purchased from R&M Chemical, United Kingdom. All the chemicals were of analytical grade without further purification. Two Gram-positive bacteria, methicillin-resistant *Staphylococcus aureus* (MRSA, clinical isolate) and *Enterococcus faecalis* (*E. faecalis*, ATCC 33186), and two Gram-negative bacteria, *Escherichia coli* (*E. coli*, ATCC 11775) and *Pseudomonas aeruginosa* (*P. aeruginosa*, ATCC 10145), were used for antibacterial assessment. They were cultured and maintained in sterile Mueller–Hinton agar and broth media (Becton Dickinson, United States). The colorectal cancer cell line HCT116 (ATCC CCL-247) and human normal colon cell CCD112 (ATCC CRL-1541) were used for the cytotoxicity assay.

## Synthesis of reduced graphene oxide (RGO) and honey-mediated copper/reduced graphene oxide (H/Cu/RGO) nanocomposite

RGO was produced through the reduction of graphene oxide. For this, 2 ml of GO was added to 50 ml of deionized water. After vigorous stirring for around 30–40 min, 7.5 ml ascorbic acid (1 M) was slowly added to the solution using a dropper, while the sample was treated with ultrasonic irradiation for 10 min with a fixed setting parameter (amplitude 80%, pulse on 1s and pulse off 1 s). The mixture was then cooled down to room temperature (RT), centrifuged, washed with distilled water, and dried in the oven. The H/Cu/RGO nanocomposite was synthesized following the method by Zhang et al. (2016) with some modifications. In brief, Australian honey (15 w/v %) was dissolved in 50 ml of 0.025 M $Cu(NO_3)_2.3H_2O$, and the pH was adjusted between pH 7 to 8. Afterward, 1 ml of the RGO (1.5 mg/ml) was mixed with the combination of honey and copper salt solution under continuous stirring at RT for 30–40 min. The mixture solution was then treated with ultrasonic irradiation for 10 min by adding 7.5 ml of 1 M ascorbic acid dropwise simultaneously. The compound was finally cooled down to RT, centrifuged, washed with distilled water, and dried in the oven.

## Characterizations of the H/Cu/RGO nanocomposite

The synthesis H/Cu/RGO nanocomposite was determined using ultraviolet-visible (UV-vis) spectroscopy (UV-2600, SHIMADZU) in the range of 220–800 nm. X-ray diffraction (XRD, Philips, X'pert, Cu Ka) was used to analyze the structure of the H/Cu/RGO nanocomposite in the range of $5^\circ$–$80^\circ$ ($2\theta$). The size and the shape of the nanocomposite were evaluated by using high-resolution transmission electron microscopy (HRTEM, JEM-2100F). Fourier transform infrared (FTIR) spectra were obtained using an attenuated total reflectance (ATR) IRTracer-100 spectrophotometer (Shimadzu, Malaysia). The spectra were set within a range of 400–4,000 $cm^{-1}$.

## Antibacterial activity

To determine the minimum inhibitory concentration (MIC) values, the broth micro-dilution method was used for the H/Cu/RGO nanocomposite against Gram-positive (MRSA and *E. faecalis*) and Gram-negative (*E. coli* and *P. aeruginosa*) bacteria using the Clinical and Laboratory Standards Institute (CLSI) protocols. For this, a single colony of fresh bacterial culture (12–18 h) was isolated from the Mueller–Hinton agar

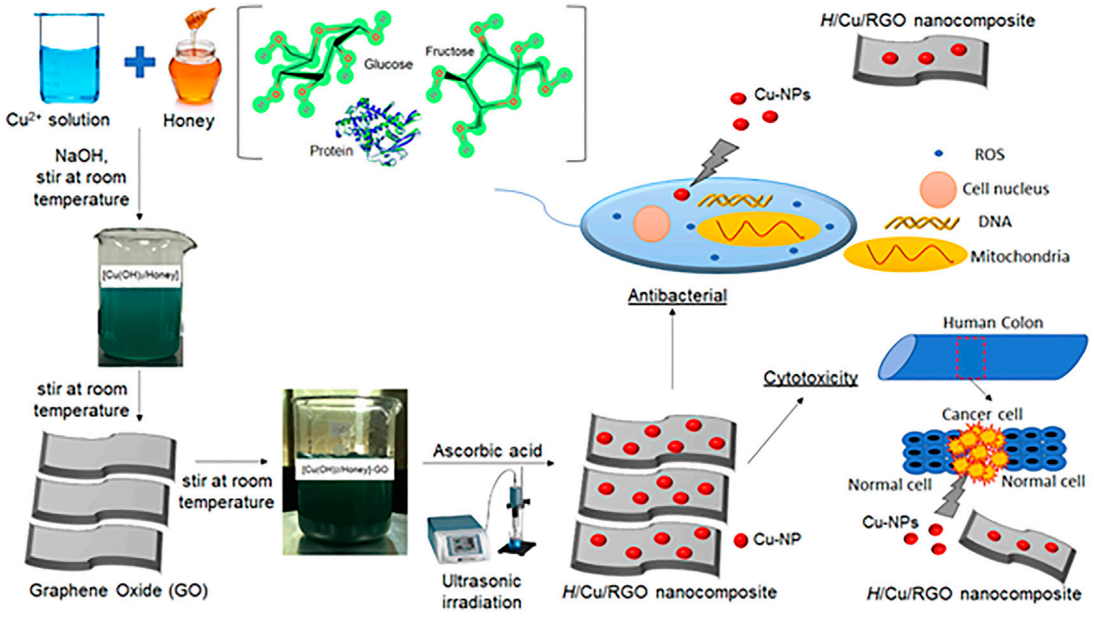

**SCHEME 1**
Schematic illustration of H/Cu/RGO nanocomposite synthesis and its applications.

(MHA) plates and inoculated into the Mueller–Hinton broth (MHB). The culture was grown overnight (16–18 h) prior to the experiments. The next day, the bacterial concentration was standardized to an optical density (OD) of 600 nm (approximately $1 \times 10^8$ CFU/ml) with MHB. Two-fold serial dilutions of the H/Cu/RGO nanocomposite were prepared in 96-well plates to get the final test concentrations of 0, 7.8, 15.6, 31.3, 62.5, 125, 250, 500, and 1,000 μg/ml per well. Thereafter, 10 μl of bacterial suspension equivalent to $10^6$ CFU/ml of exponentially growing bacterial cells were added to the wells followed by 18 h of incubation at 35 ± 2°C. The plate was then read for absorbance at 600 nm using a microplate reader (GloMax Discover Instrument, Promega). The percentage of cell viability was calculated using Equation (1), and the minimum inhibitory concentration which inhibits 50% bacterial growth ($MIC_{50}$) value was then determined.

$$\%\text{Viability} = \text{OD of sample well (mean)}/\text{OD of control well (mean)} \times 100. \quad (1)$$

## Cytotoxic effect of the H/Cu/RGO nanocomposite

Cell proliferation assay (Promega) was used to determine the cytotoxic properties of the H/Cu/RGO nanocomposite. Briefly, $5 \times 10^3$ human colorectal cancer cell line HCT116 and human normal colon cell CCD112 were seeded in a 96-well plate (100 μL/well) and incubated at 37°C overnight in a 5% $CO_2$ humidified incubator. The next day, 2-fold serially diluted nanocomposites (500, 250, 125, 62.5, 31.3, 15.6, 7.8, and 0 μg/ml) were added into the wells (100 μl/well). After 72 h incubation at 37°C in a 5% $CO_2$ humidified incubator, the wells were treated with 20 μl MTS (3-(4,5-dimethylthiazol-2-yl)-5-(3-carboxymethoxyphenyl)-2-(4-sulfophenyl)-2H-tetrazolium) reagent followed by an additional 3 h incubation at 37°C in the 5% $CO_2$ incubator. Optical density (OD) was then measured at 490 nm using a multimode microplate reader (Tecan). The dose–response graph was plotted by calculating the percent of cell viability using Eq. 1, and half maximal inhibitory concentration ($IC_{50}$) was then calculated.

# Results and discussion

## Synthesis of the H/Cu/RGO nanocomposite

As illustrated in Scheme 1, we used copper nitrate solution as a precursor for Cu-NPs synthesis. To accelerate the process, NaOH was added to form an intermediate which is copper hydroxide $Cu(OH)_2$. The pH of the solution was controlled between pH 7 to 8 since it is the preferred environment to produce smaller sizes of pure Cu-NPs. According to Amjad et al., when the pH increased (between pH 6 and pH 10), the size of nanoparticles decreased (Rajesh et al., 2016; Amjad et al., 2021). Since the aim of this study is to produce pure metallic Cu-NPs, the pH needs to be in a basic medium. The reduction process of

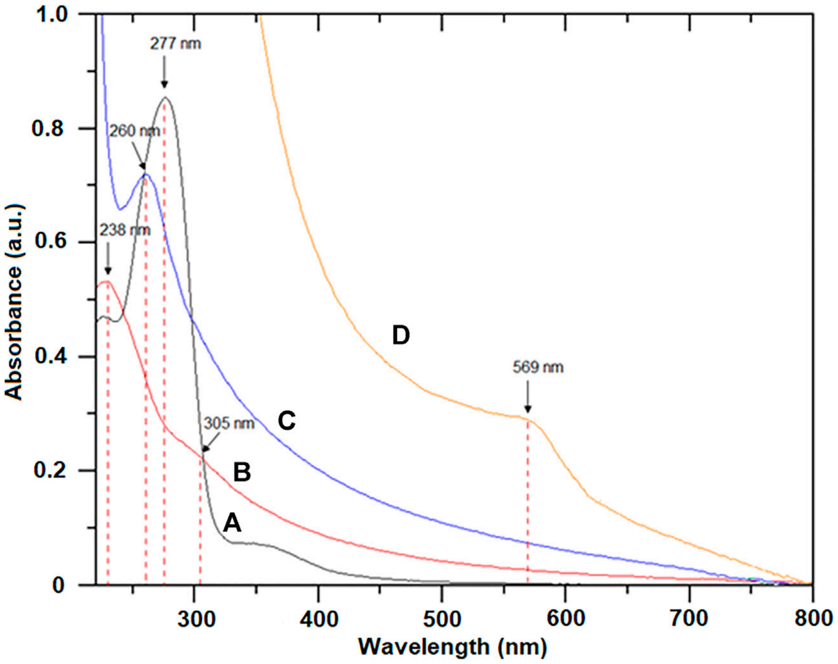

FIGURE 1
UV-visible spectra of **(A)** honey, **(B)** GO, **(C)** RGO, and **(D)** H/Cu/RGO nanocomposite.

the compound was furthered with the addition of the ascorbic acid as a reducing agent and assistance of ultrasonic irradiation to enhance the reaction process. Honey acts as a capping agent to control the size and shape of the nanoparticles in the solution. The nanocomposite was then tested against the bacteria and cancer cell line to observe its biological activities.

Meanwhile, Eqs 2–5 described the possible chemical formation of H/Cu/RGO nanocomposite.

$$Cu^{2+}\,(aq) + Honey\,(1) \xrightarrow[T=25\,\circ C]{Stirring} [Cu\,(Honey)]^{2+}\,(aq), \quad (2)$$

$$[Cu\,(Honey)]^{2+}\,(aq) + 2OH^{-}\,(aq) \xrightarrow[T=25\,\circ C]{Stirring} [Cu\,(OH)_2/Honey]\,(s), \quad (3)$$

$$[Cu\,(OH)_2/Honey]\,(aq) + GO\,(aq) \xrightarrow[T=25\,\circ C]{Stirring} [Cu\,(OH)_2/Honey] - GO\,(aq), \quad (4)$$

$$[Cu\,(OH)_2/Honey] - GO\,(aq) + 2H_2O\,(1) \xrightarrow[Ultrasonic\ Irradiation,\ t=10]{C_6H_8O_6} [H/Cu/RGO\ nanocomposite]\,(aq) + C_6H_6O_6\,(aq). \quad (5)$$

The formation of the reaction process of the $Cu(OH)_2$/honey complex (Eq. 2) resulted in a blue-colored solution as previously reported study (Ismail et al., 2019). $Cu(OH)_2$ was obtained by adding the sodium hydroxide (NaOH), and it acts as nuclei during the process. A mutarotation process occurs during this phase since $OH^-$ in the solution could change the α-glucose into β-glucose by opening the chain structure and forming the aldehyde group (-CHO) (Upadhyay and Kumar, 2017; Alejandro et al., 2017). This aldehyde group with the presence of the energy from the ultrasonic irradiation process was then oxidized by the complex copper ions to form the gluconic acid. This initiates the nucleation and growth of the Cu-NPs in the solution. In addition, the $Cu^{2+}$ ion growth could also occur at the nucleation site of the GO substrate as the reduction of $Cu^{2+}$ takes place through galvanic displacement and redox reaction (Eq. 4). The GO and copper ions were further reduced to H/Cu/RGO nanocomposites with the presence of ascorbic acid and the assistance of the ultrasonic irradiation process. It could be concluded that GO acts as a substrate and could also help as a reducing agent for the copper ions (Zhang et al., 2016). The GO sheets might bind with the copper ion by electrostatic interaction of the copper ion and through the cation-pi (cation-) interaction of the benzene ring with the cation ($Cu^{2+}$) (Alayande et al., 2020).

## Characterization of GO, RGO, and H/Cu/RGO nanocomposite

Figure 1 shows the UV-vis spectra of the honey, GO, RGO, and H/Cu/RGO nanocomposite samples. The absorption peak of the honey appeared around 277 nm due to the origin and age of the honey itself (Posudin, 2016; Zhang et al., 2016). The $\pi - \pi^*$

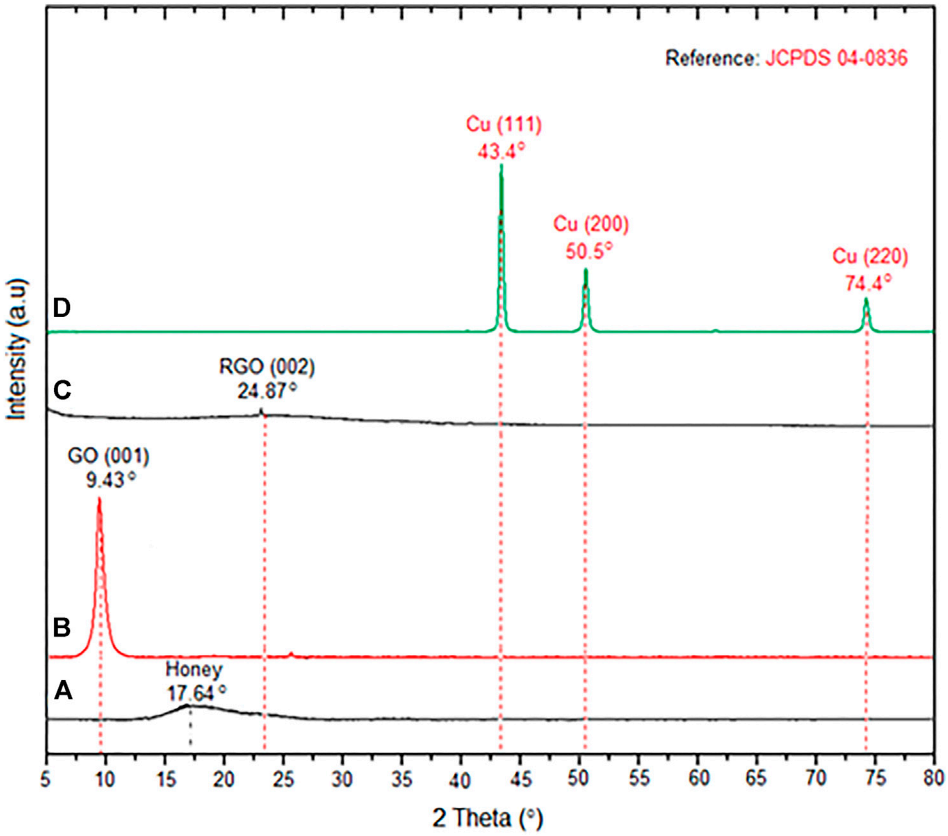

FIGURE 2
XRD patterns of **(A)** honey, **(B)** GO, **(C)** RGO, and **(D)** H/Cu/RGO nanocomposite.

transition of the C=C bond and n–$\pi^*$ transition of the C=O bond could be seen in Figure 1B for GO at 238 and 305 nm, respectively. The shifting peak at 260 nm to a higher wavelength and the peak around 305 nm disappeared for the RGO (Figure 1C) indicating the reduction of GO to RGO by the ascorbic acid. This phenomenon occurred because of the restoration of the aromatic system conjugation and the decrease of the carboxyl groups in the RGO layer (Navya Rani et al., 2019; Kang et al., 2020). The higher the conjugation degree, the lower the energy required in order to produce the electronic transition, and hence, the peak is shifted to a higher value associated with less energy involved (Rios et al., 2019). Figure 1D depicts the surface plasmon resonance of metallic phase copper nanoparticles (Cu-NPs) exhibited at 569 nm which proved the reduction of $Cu^{2+}$ to $Cu^0$ occurs during the synthesis process (Fahiminia et al., 2019).

XRD analysis was conducted for the honey, GO, RGO, and H/Cu/RGO nanocomposite. Figure 2A shows that the XRD diffraction pattern of honey at $2\theta = 17.64^\circ$ with a broad peak. The shifting of the diffraction peak in Figures 2B,C for GO and RGO from 9.43° to 24.87° indicated that the reduction of GO to RGO occurred under sonication treatment with the presence of the ascorbic acid. The interspacing distance between the layer of the GO and RGO was calculated by using Bragg's law equation as in Eq. 6

$$n\lambda = 2d \sin\theta, \tag{6}$$

where $n = 1$, $\lambda$ is the wavelength of the X-ray beam (0.154 nm), d is the distance between adjacent GO or RGO sheets, and $\theta$ is Bragg's angle. The values of interspacing distance were 0.937 and 0.357 nm, respectively, for GO and RGO. The decrement of the value shows that the formation of RGO occurs according to the previous study (Rana et al., 2018). The changes in the interspacing distance reveal the exfoliation of the RGO layer happened after the reduction process and the decrease of the oxygenated functional groups on the surface (Kumar et al., 2019). For the H/Cu/RGO nanocomposite (Figure 2D), three diffraction peaks at $2\theta = 43.4^\circ$, $50.5^\circ$, and $74.4^\circ$ could be assigned to the (111), (200), and (220) crystal planes corresponding to the cubic structure of Cu which signified the formation of metallic copper on the RGO. These diffraction peaks of Cu were matched with the standard reference of the metallic Cu for

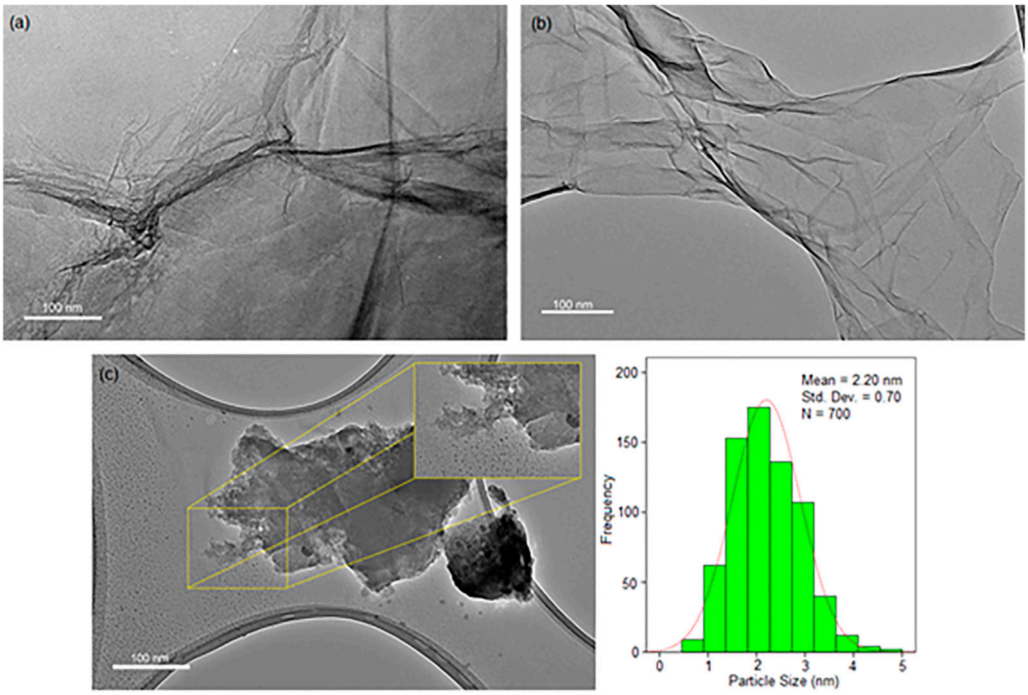

FIGURE 3
HRTEM images of **(A)** GO, **(B)** RGO, and **(C)** H/Cu/RGO nanocomposite.

the cubic structure which is JCPDS 04-0836. The peak for RGO could not be seen in the XRD pattern of the H/Cu/RGO nanocomposite, which could be related to the aggregation and restacking layer of the RGO with the insertion of the Cu-NPs in the nanocomposite (Guo et al., 2016; Kumar et al., 2019; Chen et al., 2020).

In the HRTEM images (Figure 3), GO showed a fine-layer structure like a sheet, while RGO revealed a wrinkled structure. This phenomenon is related to the reduction of the GO to RGO, where the GO layer was exfoliated and tended to be decreased in size as it was treated with the ultrasonic. The thermal treatment through the ultrasound irradiation process can lead to the wrinkling of the RGO due to the reduction of the amount of oxygen-containing functional groups during sheet exfoliation (Rana et al., 2018; Khan et al., 2020). The Cu-NPs in the nanocomposite formed uniform spherical particles with a size of 2.20 ± 0.70 nm on the RGO layers. The exfoliation of the RGO layers into smaller scale with a fine particle of Cu-NPs that either are decorated between or on the surface of RGO layers happened. It concludes that Cu-NPs can bind to the graphene-based materials to form Cu/RGO nanocomposite (Zhu et al., 2017; Menazea and Ahmed, 2020).

Through the FTIR spectra (Figure 4), the honey peak (Figure 4A) illustrated a strong and broad peak at 3,291 $cm^{-1}$ related to a hydroxyl group (-OH) stretching vibration which also might overlap with the -NH stretching vibration of primary amine protein (Boldeiu et al., 2019). Two weak peaks appeared at 2,924 $cm^{-1}$ and 2,883 $cm^{-1}$, matched to the C-H stretching bands of the aldehyde group of glucose. Carbonyl group (-C=O) stretching vibration of protein could be seen at 1,636 $cm^{-1}$, and the peak at 1,427 $cm^{-1}$ and 1,334 $cm^{-1}$ were related to C-H bending and C-O bending of glucose. While, at 1,017 $cm^{-1}$, the peak correlated to C-O-C stretching, C-O stretching, and C-N stretching amine of glucose, fructose, and protein in honey. The GO spectrum (Figure 4B) demonstrated O-H stretching vibration with a broad peak between 3,200 $cm^{-1}$ to 3,600 $cm^{-1}$. The peaks at 1734, 1,618, 1,394, 1,161, and 1,033 $cm^{-1}$ were correlated to the C=O stretching vibration of carbonyl groups presented in the GO sheet, C=C skeletal vibration, the $sp^3$ C-H stretching vibration of saturated carbon, the epoxy C-O stretching vibration, and the alkoxyl C-O stretching vibration, respectively (Nguyen et al., 2019; Sengupta et al., 2019). However, in RGO, the disappearance of the carboxyl group at 1,734 $cm^{-1}$ and $sp^3$ C-H stretching vibration of saturated carbon at 1,394 $cm^{-1}$ demonstrated the reduction of GO to RGO during the synthesis process. For the Cu/RGO nanocomposite (Figure 4D), the C=C vibration of the graphene skeleton peak could be observed at 1,539 $cm^{-1}$, indicating that the GO was reduced to form the Cu/RGO nanocomposite (Navya Rani et al., 2019). In addition, the

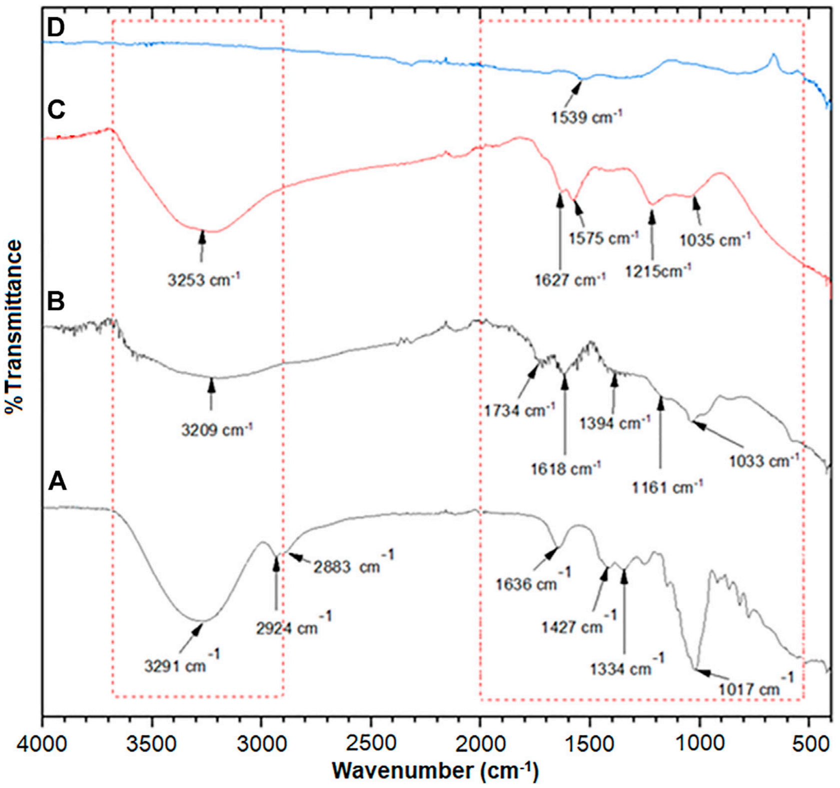

FIGURE 4
FTIR spectra of **(A)** honey, **(B)** GO, **(C)** RGO, and **(D)** H/Cu/RGO nanocomposite.

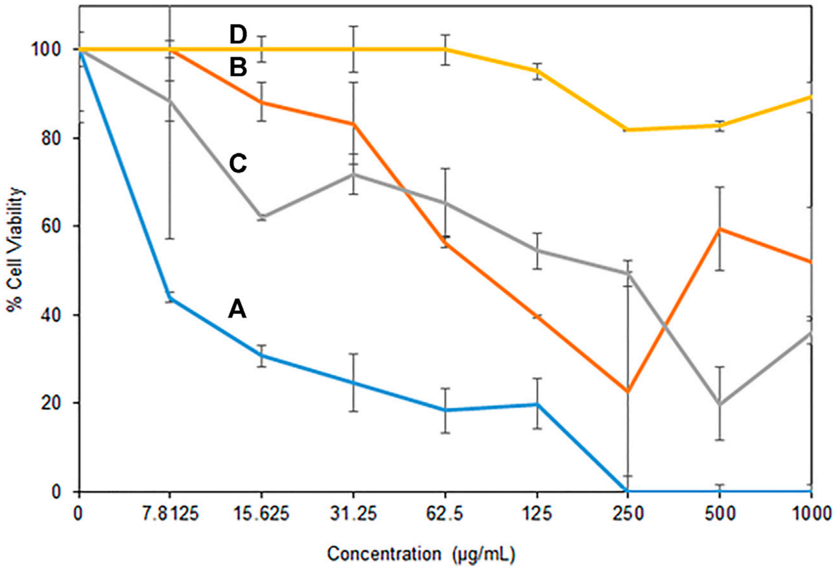

FIGURE 5
Antibacterial activity of H/Cu/RGO nanocomposite **(A)** *E. faecalis*, **(B)** MRSA, **(C)** *E. coli*, and **(D)** *P. aeruginosa*.

TABLE 1 $MIC_{50}$ values of H/Cu/RGO nanocomposite against four bacteria strains.

| **Sample** | **$MIC_{50}$ of sample (µg/ml)** | | | |
|---|---|---|---|---|
| | **Bacterial strains** | | | |
| H/Cu/RGO nanocomposite | *MRSA* | *E. faecalis* | *P. aeruginosa* | *E. coli* |
| | 67.96 | 6.12 | >1,000 | 134.16 |

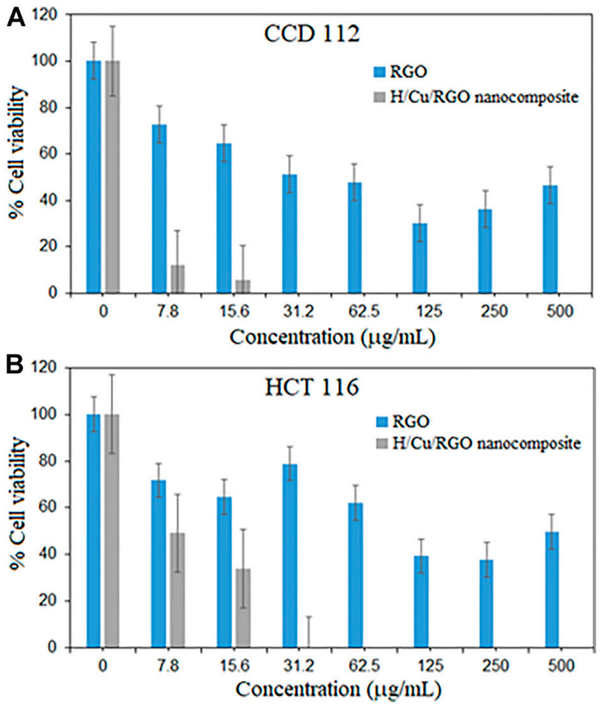

FIGURE 6
Cytotoxicity activity of *H*/Cu/RGO nanocomposite. **(A)** Normal colorectal cell line (CCD1 112). **(B)** Colorectal cancer cell line (HCT 116).

weak peak band area around 900 $cm^{-1}$ in Figure 4D could be due to the shifting of the C-O/C-N stretching of protein and carbohydrate of honey biomolecules presented in the H/Cu/RGO nanocomposite (Ismail et al., 2019).

## Antibacterial activity of the H/Cu/RGO nanocomposite

Antibacterial activity of the H/Cu/RGO nanocomposite toward bacterial strains was tested using the minimum inhibitory concentration (MIC) assay, where the selected Gram-positive (MRSA and *E. faecalis*) and Gram-negative (*P. aeruginosa* and *E. coli*) bacteria were found to be affected by the nanocomposite. Figure 5 illustrates that the inhibition activity of the nanocomposite was better toward Gram-positive bacteria compared to the Gram-negative strains. As shown in Table 1, the lowest $MIC_{50}$ value was detected toward *E. faecalis*, where the nanocomposite could inhibit the growth of less than a quarter of the bacteria at a low concentration of 6.12 µg/ml, while for MRSA, the $MIC_{50}$ was detected at the concentration of 67.96 µg/ml. For Gram-negative strains, the $MIC_{50}$ was at 134.16 µg/ml and greater than 1,000 µg/ml for *E. coli* and *P. aeruginosa*, respectively.

The value of Cu-NPs as antibacterial agents has been studied for a long time (Lv et al., 2020). However, the H/Cu/RGO nanocomposite gave better antibacterial activity performance compared to the Cu-NPs only. In a prior study where honey-mediated Cu-NPs was tested on *E. faecalis* and *E. coli*, the values of $MIC_{50}$ were 15.6 µg/ml and 250 µg/ml, respectively, which were higher than the value gained from the nanocomposite in current work. This is most possibly due to the toxic effects of Cu-NPs and the RGO that influenced the bacteria cells. It might be due to the Cu-NPs that affect bacteria by the generation of reactive oxygen species, lipid peroxidation, protein oxidation, and DNA degradation through liberating nascent Cu ions from the Cu-NP surface (Chatterjee et al., 2014). The cell membrane stress due to the graphene sheet layer structure itself is also possibly among the factors for the bactericidal activity to change (Prasad et al., 2017).

A possible explanation for the variation in antibacterial activity against different bacterial strains can be related to the difference in the bacteria cell envelope (Sriramulu et al., 2020). In contrast to Gram-positive strains which consist of the layers of peptidoglycan, Gram-negative bacteria, besides the inter thin peptidoglycan cell wall, are surrounded by an outer membrane containing lipopolysaccharide (LPS), which can act as an additional protection shield for the cell. It could be one of the possible reasons why *P. aeruginosa* could tolerate the H/Cu/RGO nanocomposite, even at high concentrations.

## Cytotoxic effect of the H/Cu/RGO nanocomposite

Cytotoxic activity of the nanocomposite was tested in both normal and cancer colorectal cell lines (Figure 6), where the H/Cu/RGO nanocomposite showed a higher cytotoxic effect compared to RGO, even at low concentrations. This could be due to the combination of Cu-NPs and RGO that enhanced the properties of the cytotoxic activity. This enhancement might also be attributed to the size of the Cu-NPs attached to the RGO, which is smaller in size with a spherical shape that makes them easier to interact with the cells and kill them. Similar to the

TABLE 2 $IC_{50}$ of the RGO and nanocomposite toward normal and cancer cell lines of the colorectal cell.

| Samples | $IC_{50}$ of sample (µg/ml) | |
|---|---|---|
| | CCD 112 (normal cell) | HCT 116 (cancer cell) |
| RGO | 33.70 | 141.50 |
| H/Cu/RGO nanocomposite | 2.14 | 7.7 |

antibacterial study, in comparison with our previous work, the H/Cu/RGO nanocomposite showed higher anticancer action ($IC_{50}$–7.7 µg/mL as shown in Table 2) than honey-mediated Cu-NPs without RGO ($IC_{50}$–46.11 µg/ml) in HCT116 cells (Ismail et al., 2019). A previous study reported that Cu-NPs killed SW480 human colon cancer cells at an $IC_{50}$ value of 68 µg/ml by inducing reactive oxygen species (ROS)-mediated apoptosis (Ghasemi et al., 2022). As this is the first study reporting potential anticancer action of the H/Cu/RGO nanocomposite, their exact mechanisms of cancer cell killing are not known and warrant further investigations.

In both graphs (Figures 6A,B), at a concentration of 31.2 µg/ml, the nanocomposite killed both cells at 100%, which indicates that this compound is not selective toward cancer cells. This could be seen in Table 2, where both RGO and H/Cu/RGO nanocomposite are non-selective toward cancer cells. Thus, further modifications are needed to enhance the selectivity of the nanocomposite toward cancer cells. For example, the nanocomposite can be conjugated to target-specific aptamers, peptides, antibodies, or other ligands to allow the nanocomposite to specifically bind to the surface molecules of cancer cells and enhance the drug localization, retention effect, and cellular uptake (Sutradhar and Amin, 2014; Martinelli et al., 2019).

## Conclusion

In conclusion, the green synthesized Cu/RGO nanocomposite using honey and ascorbic acid as capping and reducing agents, respectively, resulted in small-sized and spherical-shaped Cu-NPs attached to the RGO sheet. Our data proved that the agglomeration of copper could be prevented by combining the Cu-NPs with graphene-based materials in the presence of eco-friendly capping and reducing agents. The nanocomposite revealed good antibacterial and cytotoxicity activities, making them suitable for biomedical applications. However, the nanocomposite needs to be further studied to improve its specificity toward cancerous cells.

## Data availability statement

The original contributions presented in the study are included in the article/Supplementary Material; further inquiries can be directed to the corresponding authors.

## Author contributions

NI: writing—original draft, conceptualization, methodology, investigation, formal analysis, data curation, validation, resources, and data curation. KS: funding acquisition, methodology, conceptualization, investigation, resources, formal analysis, data curation, supervision, and writing—review and editing. SM: methodology, formal analysis, and validation. hirofumi hara: resources. S-YT: resources, funding acquisition, methodology, formal analysis, investigation, data curation, and writing—review and editing. HM: review and editing, supervision, and financial support of research publication.

## Funding

This research was funded by Takasago Thermal Engineering Co., Ltd. grant (R.K130000.7343.4B422) from the Research Management Center (RMC) of Universiti Teknologi Malaysia (UTM) and Malaysia–Japan International Institute of Technology (MJIIT). Special thanks to the School of Medical and Life Sciences, Sunway University for providing cell culture facilities for measuring anticancer assays.

## Conflict of interest

The authors declare that the research was conducted in the absence of any commercial or financial relationships that could be construed as a potential conflict of interest.

## Publisher's note

## References

Alayande, A. B., Obaida, M., and Kima, I. S. (2020). Antimicrobial mechanism of reduced graphene oxide-copper oxide (rGO-CuO) nanocomposite films: The case of *Pseudomonas aeruginosa* PAO1. *Mat. Sci. Eng. C Mat. Biol. Appl.* 109, 110596. doi:10.1016/j.msec.2019.110596

Alejandro, J., Gonzalez, F., Juan, A., and Di Nezio, M. S. (2017). Synthesis and characterization of silver nanoparticles prepared with honey: The role of carbohydrates. *Anal. Lett.* 50 (5), 877–888. doi:10.1080/00032719.2016.1199558

Amjad, R., Mubeen, B., Ali, S. S., Imam, S. S., Alshehri, S., Ghoneim, M. M., et al. (2021). Green synthesis and characterization of copper nanoparticles using Fortunella margarita leaves. *Polymers* 13 (24), 4364. doi:10.3390/polym13244364

Arendsen, L. P., Thakar, R., and Sultan, A. H. (2019). The use of copper as an antimicrobial agent in health care, including obstetrics and gynecology. *Clin. Microbiol. Rev.* 4 (32), e00125–e00128. doi:10.1128/CMR.00125-18

Balasooriya, E. R., Jayasinghe, C. D., Jayawardena, U. A., Ruwanthika, R. W. D., Mendis de Silva, R., and Udagama, P. V. (2017). Honey mediated green synthesis of nanoparticles: New era of safe nanotechnology. *J. Nanomater.* 2017, 1–10. doi:10.1155/2017/5919836

Beiranvand, S., Williams, A., Long, S., Brooks, P. R., and Russell, F. D. (2021). Use of kinetic data to model potential antioxidant activity: Radical scavenging capacity of Australian Eucalyptus honeys. *Food Chem.* 342, 128332. doi:10.1016/j.foodchem.2020.128332

Boldeiu, A., Simion, M., Mihalache, L., Radoi, A., Banu, M., Varasteanu, P., et al. (2019). Comparative analysis of honey and citrate stabilized gold nanoparticles: *In vitro* interaction with proteins and toxicity studies. *J. Photochem. Photobiol. B* 197, 111519–111610. doi:10.1016/j.jphotobiol.2019.111519

Chatterjee, A. K., Chakraborty, R., and Basu, T. (2014). Mechanism of antibacterial activity of copper nanoparticles. *Nanotechnology* 25 (13), 135101–135112. doi:10.1088/0957-4484/25/13/135101

Chen, M., Li, Z., and Chen, L. (2020). Highly antibacterial rGO/$Cu_2O$ nanocomposite from a biomass precursor: Synthesis, performance, and mechanism. *Nano Mater. Sci.* 2, 172–179. doi:10.1016/j.nanoms.2019.09.005

Fahiminia, M., Shamabadi, N. S., Nasrollahzadeh, M., and Sajadi, S. M. (2019). Phytosynthesis of Cu/RGO using Euphorbia cheiradenia Boiss extract and study of its ability in the reduction of organic dyes and 4 nitrophenol in aqueous medium. *IET Nanobiotechnol.* 13 (2), 202–213. doi:10.1049/iet-nbt.2018.5175

Gan, C., Liang, T., Li, W., Fan, X., and Zhu, M. (2019a). Amine-terminated ionic liquid modified graphene oxide/copper nanocomposite toward efficient lubrication. *Appl. Surf. Sci.* 491, 105–115. doi:10.1016/j.apsusc.2019.06.141

Gan, L., Li, B., Chen, Y., Yu, B., and Chen, Z. (2019b). Green synthesis of reduced graphene oxide using bagasse and its application in dye removal: A waste-to-resource supply chain. *Chemosphere* 219, 148–154. doi:10.1016/j.chemosphere.2018.11.181

Ghasemi, P., Shafiee, G., Ziamajidi, N., and Abbasalipourkabir, R. (2022). Copper nanoparticles induce apoptosis and oxidative stress in SW-480 human colon cancer cell line. *Biol. Trace. Elem. Res.* 63, 1–10. doi:10.21203/rs.3.rs-1885906/v1

Guo, M., Zhao, Y., Zhang, F., Xu, L., Yang, H., Song, X., et al. (2016). Reduced graphene oxide-stabilized copper nanocrystals with enhanced catalytic activity and SERS properties. *RSC Adv.* 6, 50587–50594. doi:10.1039/C6RA05186C

Iranshahi, S., and Iranshahi, S. (2022). Cobalt/graphene oxide nanocomposites: Electro-synthesis, structural, magnetic, and electrical properties. *Ceram. Int.* 9 (48), 12240–12254. doi:10.1016/j.ceramint.2022.01.086

Ismail, N. A., Shameli, K., Ali, R. R., Sukri, S. N. A., and Isa, E. D. M. (2021). Copper/graphene based materials nanocomposites and their antibacterial study: A mini review. *J. Res. Nanosci. Nanotech.* 1 (1), 44–52. doi:10.37934/jrnn.1.1.4452.1.1.4452

Ismail, N. A., Shameli, K., Wong, M. M., Teow, S. Y., Chew, J., and Sukri, S. N. A. (2019). Antibacterial and cytotoxic effect of honey mediated copper nanoparticles synthesized using ultrasonic assistance. *Mat. Sci. Eng. C Mat. Biol. Appl.* 104, 109899. doi:10.1016/j.msec.2019.109899

Jang, J., Choi, Y., Tanaka, M., and Choi, J. (2020). Development of silver/graphene oxide nanocomposites for antibacterial and antibiofilm applications. *J. Ind. Eng. Chem.* 83, 46–52. doi:10.1016/j.jiec.2019.11.011

Kang, X., Teng, D., Wu, S., Tian, Z., Liu, J., Li, P., et al. (2020). Ultrafine copper nanoparticles anchored on reduced graphene oxide present excellent catalytic performance toward 4-nitrophenol reduction. *J. Colloid Interface Sci.* 566, 265–270. doi:10.1016/j.jcis.2020.01.097

Khan, M. S., Yadav, R., Vyas, R., Sharma, A., Banerjee, M. K., and Sachdev, K. (2020). Synthesis and evaluation of reduced graphene oxide for supercapacitor application. *Mater. Today Proc.* 30, 153–156. doi:10.1016/j.matpr.2020.05.403

Kodous, A. S., Atta, M. M., Abdel-Hamid, G. R., and Ashry, H. A. (2022). Anti-metastatic cancer activity of ultrasonic synthesized reduced graphene oxide/copper composites. *Chem. Pap.* 76, 373–384. doi:10.1007/s11696-021-01866-7

Kumar, S. K., Mamatha, G., Muralidhara, H., Anantha, M., Yallappa, S., Hungund, B., et al. (2017). Highly efficient multipurpose graphene oxide embedded with copper oxide nanohybrid for electrochemical sensors and biomedical applications. *J. Sci. Adv. Mater. Devices* 2, 493–500. doi:10.1016/j.jsamd.2017.08.003

Kumar, S., Ojha, A. K., Bhorolua, D., Das, J., Kumar, A., and Hazarika, A. (2019). Facile synthesis of CuO nanowires and $Cu_2O$ nanospheres grown on rGO surface and exploiting its photocatalytic, antibacterial and supercapacitive properties. *Phys. B Condens. Matter* 558, 74–81. doi:10.1016/j.physb.2019.01.040

Luo, G., Zhu, L., Tan, B., Wang, T., Bi, X., Li, W., et al. (2020). A facile one-step chemical synthesis of copper@reduced graphene oxide composites as back contact for CdTe solar cells. *Sol. Energy* 211, 90–99. doi:10.1016/j.solener.2020.08.066

Lv, P., Zhu, L., Yu, Y., Wang, W., Liu, G., and Lu, H. (2020). Effect of NaOH concentration on antibacterial activities of Cu nanoparticles and the antibacterial mechanism. *Mat. Sci. Eng. C Mat. Biol. Appl.* 2020, 110669. doi:10.1016/j.msec.2020.110669

Martinelli, C., Pucci, C., and Ciofani, G. (2019). Nanostructured carriers as innovative tools for cancer diagnosis and therapy. *Apl. Bioeng.* 3 (1), 011502. doi:10.1063/1.5079943

Menazea, A. A., and Ahmed, M. K. (2020). Silver and copper oxide nanoparticles-decorated graphene oxide via pulsed laser ablation technique: Preparation, characterization, and photoactivated antibacterial activity. *Nano-Structures Nano-Objects* 22, 100464. doi:10.1016/j.nanoso.2020.100464

Merugu, R., Garimella, S., Velamakanni, R., Vuppugalla, P., Chitturi, K. L., and Jyothi, M. (2021). Synthesis, characterization and antimicrobial activity of bimetallic silver and copper nanoparticles using fruit pulp aqueous extracts of moringa oleifera. *Mater. Today Proc.* 44, 153–156. doi:10.1016/j.matpr.2020.08.549

Miller, K. S., Nogueira, L., Devasia, T., Mariotto, A. B., Yabroff, K. R., Jemal, A., et al. (2022). Cancer treatment and survivorship statistic, 2022. *CA Cancer J. Clin.* 2022, 1–28. doi:10.3322/caac.21731

Moozarm Nia, P., Woi, P. M., and Alias, Y. (2017). Facile one-step electrochemical deposition of copper nanoparticles and reduced graphene oxide as nonenzymatic hydrogen peroxide sensor. *Appl. Surf. Sci.* 413, 56–65. doi:10.1016/j.apsusc.2017.04.043

Murray, C. J. L., Ikuta, K. S., Sharara, F., Swetschinski, L., Aguilar, G. R., Gray, A., et al. (2022). Global burden of bacterial antimicrobial resistance in 2019: A systematic analysis. *Lancet* 399, 629–655. doi:10.1016/S0140-6736(21)02724-0

Nagar, N., and Devra, V. (2018). Green synthesis and characterization of copper nanoparticles using Azadirachta indica leaves. *Mat. Chem. Phys.* 213, 44–51. doi:10.1016/j.matchemphys.2018.04.007

Navya Rani, M., Murthy, M., Shyla Shree, N., Ananda, S., Yogesh, S., and Dinesh, R. (2019). Cuprous oxide anchored Reduced Graphene oxide ceramic nanocomposite using Tagetes Erecta flower extract and evaluation of its antibacterial activity and cytotoxicity. *Ceram. Int.* 45, 25020–25026. doi:10.1016/j.ceramint.2019.04.195

Nguyen, M. D., Phuong Linh, V. N., Huy, L. A., Huong, N. T., Tu, T. H., Lien Phuong, N. T., et al. (2019). Fabrication and antibacterial activity against *Pseudomonas aeruginosa* and *Staphylococcus aureus* of silver nanoparticle decorated reduced graphene oxide nanocomposites. *Mat. Technol. (N. Y. N. Y).* 34, 369–375. doi:10.1080/10667857.2019.1575555

Noman, M. S. M., Ahmed, T., Niazi, M. B. K., Hussain, S., Song, F., Manzoor, I., et al. (2020). Use of biogenic copper nanoparticles synthesized from a native Escherichia sp. as photocatalysts for azo dye degradation and treatment of textile effluents. *Environ. Pollut.* 257, 113514. doi:10.1016/j.envpol.2019.113514

Ouyang, Y., Cai, X., Shi, Q., Liu, L., Wan, D., Tan, S., et al. (2013). Poly-L-lysine-modified reduced graphene oxide stabilizes the copper nanoparticles with higher water-solubility and long-term additively antibacterial activity. *Colloids Surf. B Biointerfaces* 107, 107–114. doi:10.1016/j.colsurfb.2013.01.073

Posudin, Y. (2016). Spectroscopic analysis of honey. *Ukr. Food J.* 5 (3), 437–450. doi:10.24263/2304-974x-2016-5-3-3

Prasad, K., Lekshmi, G. S., Ostrikov, K., Lussini, V., Blinco, J., Mohandas, M., et al. (2017). Synergic bactericidal effects of reduced graphene oxide and silver nanoparticles against gram-positive and gram-negative bacteria. *Sci. Rep.* 7, 1591. doi:10.1038/s41598-017-01669-5

Rajesh, K. M., Ajitha, B., Reddy, Y. A. K., Suneetha, Y., and Sreedhara Reddy, P. (2016). Synthesis of copper nanoparticles and role of pH on particle size control. *Mater. Today Proc.* 3 (6), 1985–1991. doi:10.1016/j.matpr.2016.04.100

Rana, S., Sandhu, I. S., and Chitkara, M. (2018). “Exfoliation of graphene oxide via chemical reduction method,” in Proceeding of the 2018 6th edition of international conference on wireless networks & embedded systems (WECON), Rajpura, India, 2018 november 16-17, 54–57.

Rawal, N., Solanki, S., and Shah, D. (2020). Green synthesis of reduced graphene oxide with *in situ* decoration of metal nanoparticles for charge storage application. *Mater. Today Proc.* 21, 2066–2071. doi:10.1016/j.matpr.2020.01.325

Rios, P. L., Povea, P., Cerda-Cavieres, C., Arroyo, J. L., Morales-Verdejo, C., Abarca, G., et al. (2019). Novel *in situ* synthesis of copper nanoparticles supported on reduced graphene oxide and its application as a new catalyst for the decomposition of composite solid propellants. *RSC Adv.* 9, 8480–8489. doi:10.1039/C9RA00789J

Rostami-Tapeh-Esmaeil, E., Golshan, M., Salami-Kalajahu, M., and Roghani-Mamaqani, H. (2021). Synthesis of copper and copper oxide nanoparticles with different morphologies using aniline as reducing agent. *Solid State Commun.* 334, 114364. doi:10.1016/j.ssc.2021.114364

Sanchez-Lopez, E., Gomes, D., Esteruelas, G., Bonilla, L., Lopez-Machado, A. L., Galindo, R., et al. (2020). Metal-based nanoparticles as antimicrobial agents: An overview. *Nanomaterials* 10 (2), 2922–E339. doi:10.3390/nano10020292

Sarkar, C., and Dolui, S. K. (2015). Synthesis of copper oxide/reduced graphene oxide nanocomposite and its enhanced catalytic activity towards reduction of 4-nitrophenol. *RSC Adv.* 5, 60763–60769. doi:10.1039/C5RA10551J

Sengupta, I., Bhattacharya, P., Talukdar, M., Neogi, S., Pal, S. K., and Chakraborty, S. (2019). Bactericidal effect of graphene oxide and reduced graphene oxide: Influence of shape of bacteria. *Colloid Interface Sci. Commun.* 28, 60–68. doi:10.1016/j.colcom.2018.12.001

Siegel, R. L., Miller, K. D., Fuchs, H. E., and Jemal, A. (2022). Cancer statistics, 2022. *Ca. Cancer J. Clin.* 1 (72), 7–33. doi:10.3322/caac.21708

Sriramulu, M., Shanmugam, S., and Ponnusamy, V. K. (2020). Agaricus bisporus mediated biosynthesis of copper nanoparticles and its biological effects: An *in-vitro* study. *Colloid Interface Sci. Commun.* 35, 100254. doi:10.1016/j.colcom.2020.100254

Sutradhar, K. B., and Amin, M. L. (2014). Nanotechnology in cancer drug delivery and selective targeting. *ISRN Nanotechnol.* 2014, 1–12. doi:10.1155/2014/939378

Szunerits, S., and Boukherroub, R. (2016). Antibacterial activity of graphene-based materials. *J. Mat. Chem. B* 4 (43), 6892–6912. doi:10.1039/C6TB01647B

Thy, L. T. M., Tai, L. T., Hai, N. D., Cong, C. Q., Dat, N. M., Trinh, D. N., et al. (2022). Comparison of *in-situ* and *ex-situ* methods for synthesis of iron magnetic nanoparticles-doped graphene oxide: Characterization, adsorption capacity, and Fenton catalytic efficiency. *FlatChem* 33, 100365. doi:10.1016/j.flatc.2022.100365

Tu, Y., Li, P., Sun, J., Jiang, J., Dai, F., Wu, Y., et al. (2021). Remarkable antibacterial activity of reduced graphene oxide functionalized by copper ions. *Advance functional materials* 31, 1–16. doi:10.1002/adfm.202008018

Upadhyay, L. S. B., and Kumar, N. (2017). Green synthesis of copper nanoparticle using glucose and polyvinylpyrrolidone (PVP). *Inorg. Nano-Metal Chem.* 47 (10), 1436–1440. doi:10.1080/24701556.2017.1357576

Vouga, M., and Greub, G. (2016). Emerging bacterial pathogens: The past and beyond. *Clin. Microbiol. Infect.* 1 (22), 12–21. doi:10.1016/j.cmi.2015.10.010

Wang, B., Yao, M., Lv, L., Ling, Z., and Li, L. (2017). The human microbiota in health and disease. *Engineering* 1 (3), 71–82. doi:10.1016/J.ENG.2017.01.008

Xu, X., Shen, J., Qin, J., Duan, H., He, G., and Chen, H. (2019). Cytotoxicity of bacteriostatic reduced graphene oxide-based copper oxide nanocomposites. *JOM* 71 (1), 294–301. doi:10.1007/s11837-018-3197-1

Yan, Y., Li, C., Wu, H., Du, J., Feng, J., Zhang, J., et al. (2019). Montmorillonite-modified reduced graphene oxide stabilizes copper nanoparticles and enhances bacterial adsorption and antibacterial activity. *ACS Appl. Bio Mat.* 2 (5), 1842–1849. doi:10.1021/acsabm.8b00695

Yang, Z., Hao, X., Chen, S., Ma, Z., Wang, W., Wang, C., et al. (2019). Long-term antibacterial stable reduced graphene oxide nanocomposites loaded with cuprous oxide nanoparticles. *J. Colloid Interface Sci.* 533, 13–23. doi:10.1016/j.jcis.2018.08.053

Yin, P. T., Shah, S., Chhowalla, M., and Lee, K-B. (2015). Design, synthesis, and characterization of graphene–nanoparticle hybrid materials for bioapplications. *Chem. Rev.* 115, 2483–2531. doi:10.1021/cr500537t

Zhang, W., Chang, Q., Xu, L., Li, G., Yang, G., Ding, X., et al. (2016). Graphene oxide-copper nanocomposite-coated porous CaP scaffold for vascularized bone regeneration via activation of hif-1α. *Adv. Healthc. Mat.* 5, 1299–1309. doi:10.1002/adhm.201500824

Zhou, Y., Wu, S., and Liu, F. (2019). High-performance polyimide nanocomposites with polydopamine-coated copper nanoparticles and nanowires for electronic applications. *Mat. Lett.* 237, 19–21. doi:10.1016/j.matlet.2018.11.067

Zhu, J., Wang, J., Uliana, A. A., Tian, M., Zhang, Y., Zhang, Y., et al. (2017). Mussel-inspired architecture of high-flux loose nanofiltration membrane functionalized with antibacterial reduced graphene oxide-copper nanocomposites. *ACS Appl. Mat. Interfaces* 9, 28990–29001. doi:10.1021/acsami.7b05930

frontiers | Frontiers in Chemistry

TYPE Original Research
PUBLISHED 31 October 2022
DOI 10.3389/fchem.2022.1044931

# A metal–organic framework nanocomposite with oxidation and near-infrared light cascade response for bacterial photothermal inactivation

Christopher Dorma Momo Jr.[1†], Yuan Zhou[2,3†], Lanxin Li[1,4†], Weisheng Zhu[1], Luyao Wang[4], Xingping Liu[5], Wei Bing[4] and Zhijun Zhang[1*]

[1]Key Laboratory of Surface and Interface Science of Polymer Materials of Zhejiang Province, Department of Chemistry, Zhejiang Sci-Tech University, Hangzhou, China, [2]Department of Pharmacy, Taihe Hospital, Hubei University of Medicine, Shiyan, Hubei, China, [3]College of Pharmacy, Hubei University of Traditional Chinese Medicine, Wuhan, China, [4]School of Chemistry and Life Science, Changchun University of Technology, Changchun, China, [5]School of Pharmaceutical Science, University of South China, Hengyang, China

Photothermal treatment is an effective and precise bacterial disinfection method that can reduce the occurrence of bacterial drug resistance. However, most conventional photothermal treatment strategies have the problem that the photothermal response range does not match the infection area. Herein, a metal–organic framework (MOF) nanocomposite responding to the oxidation state of the bacterial infection microenvironment was constructed for near-infrared (NIR) photothermal bacterial inactivation. In this strategy, the MOF was used as a nanocarrier to load tetramethylbenzidine (TMB) and horseradish peroxidase (HPR). The high oxidation state of the bacterial infection microenvironment can trigger the enzyme-catalyzed reaction of the nanocomposite, thereby generating oxidation products with the NIR photothermal effect for bacterial disinfection. The synthesis and characterization of the nanocomposite, oxidation state ($H_2O_2$) response effect, photothermal properties, and antibacterial activities were systematically studied. This study provides a new idea for building a precision treatment system for bacterial infection.

KEYWORDS

**metal–organic framework, cascade response, antibacterial materials, photothermal therapy, nanodrug**

OPEN ACCESS

EDITED BY
Xiangzhao Ai,
Shanghai Jiao Tong University, China

REVIEWED BY
Haiwei Ji,
Nantong University, China
Haitao Li,
Yangzhou University, China

*CORRESPONDENCE
Zhijun Zhang,
zjzhang@zstu.edu.cn

†These authors have contributed equally to this work

SPECIALTY SECTION
This article was submitted to Nanoscience, a section of the journal Frontiers in Chemistry

RECEIVED 15 September 2022
ACCEPTED 11 October 2022
PUBLISHED 31 October 2022

CITATION
Dorma Momo C, Zhou Y, Li L, Zhu W, Wang L, Liu X, Bing W and Zhang Z (2022), A metal–organic framework nanocomposite with oxidation and near-infrared light cascade response for bacterial photothermal inactivation. *Front. Chem.* 10:1044931.
doi: 10.3389/fchem.2022.1044931

## Introduction

Bacterial infection seriously threatens human life and health. As a traditional medicine for treating bacterial infections, antibiotics have saved countless lives. However, the use of antibiotics will lead to the emergence of bacterial resistance, which greatly reduces the therapeutic effect of antibiotics and even makes antibiotics ineffective (Laxminarayan et al., 2013; Mamun et al., 2021). The abuse of antibiotics in recent years has accelerated the emergence of bacterial drug resistance. Unfortunately, the speed at which we develop new antibiotics is far lower than the speed at which bacterial drug resistance develops (Hutchings et al., 2019). According to the World Health Organization (WHO), around 7 00,000 people die of drug-resistant bacterial infections every year worldwide. If effective measures are not taken, it is estimated that 10 million people will die of drug-resistant bacterial infections every year by 2050. In the face of such a severe situation, on one hand, it is necessary to accelerate the development of antibiotics and meanwhile avoid the abuse of antibiotics; on the other hand, it is necessary to develop new antibacterial strategies.

Nanoparticle-mediated physical stimulation therapy is a promising bacterial therapy strategy that can partially replace antibiotics (Ji et al., 2022; Wang et al., 2022). In such a strategy, special nanoparticles are utilized as antennas to convert physical stimulation (e.g., light, magnetic, X-ray, and ultrasound) into heat energy or free radicals for bacterial inactivation (Jia and Zhao, 2021; Zhang et al., 2022b; Deng et al., 2022; Ji et al., 2022). For example, most of the noble metal nanoparticles, nano-carbon materials, magnetic nanomaterials, some nanopolymers, etc. can be heated under light, magnetic, ultrasonic, or other physical stimulations to generate high temperature for bacterial inactivation; photosensitizers and nanosemiconductor materials (such as titanium dioxide, bismuth vanadate, and quantum dots) can generate free radicals under light, X-ray, or even ultrasound irradiation for bacterial disinfection (Karami et al., 2021; Du et al., 2022; Fan et al., 2022). Among these strategies, the photothermal strategy has obvious advantages such as easy access to light sources, high bacterial inactivation efficiency, and low toxic side effects. In addition, photothermal treatment is not easy to induce bacterial resistance (Zhang et al., 2020; Mu et al., 2022). Therefore, in recent years, photothermal antibacterial therapy has attracted wide attention, and many progresses have been achieved in this field (Han et al., 2020). Achieving high antibacterial efficiency is no longer a major problem of photothermal methods. Improving the accuracy of treatment is currently a development trend in this field. Although modifying targeted molecules such as antibodies and antimicrobial peptides can improve the accuracy of nanophotothermal therapy to a certain extent, the modification also brings high cost problems. Using the special microenvironment of the lesion site to construct a responsive photothermal treatment strategy is an effective means to improve the accuracy of treatment. Such a strategy is expected to be a good solution to improve the accuracy of nanoparticle-mediated photothermal therapy.

In this study, a metal–organic framework (MOF) nanocomposite responding to the oxidation state of the bacterial infection microenvironment was constructed for near-infrared (NIR) photothermal bacterial inactivation. In this strategy, MOF (UiO-66) was used as a nanocarrier to load tetramethylbenzidine (TMB) and horseradish peroxidase (HPR) (Scheme 1). The high oxidation state of the bacterial infection microenvironment can trigger the enzyme-catalyzed reaction of the nanocomposite, thereby generating oxidation products with the NIR photothermal effect for bacterial disinfection.

## Materials and methods

### General information

1,4-Dicarboxybenzene, 70% zirconium propoxide [Zr(OnPr) 4] solution in 1-propanol, and tetramethylbenzidine (TMB) were purchased from Shanghai Aladdin Bio-Chem Technology Co., Ltd. Horseradish peroxidase (HPR) was purchased from Sigma-Aldrich. The transmission electron microscopy (TEM) image was captured with a 120-KV JEM-1400 microscope with a Gatan Rio16 digital camera. The sample for TEM was prepared by dropping the dilute UiO-66 solution onto carbon-coated copper grids. Powder X-ray diffraction (XRD) patterns were recorded with a Bruker D8 diffractometer (Bruker, Germany). UV-vis adsorption spectra were detected using a UV-1900 spectrometer (SHIMADZU, Japan). Fluorescence images were captured using a NIB900-FL fluorescent microscope with a Nexcan-T6CCD digital camera (Nexcope, China). A homemade 900-nm NIR light source was used for NIR light irradiation, and the power density was measured with a power density meter. A colony counter icount 11 (Xun Shu, China) was used to count colony-forming units.

### Synthesis of the metal–organic framework and the nanocomposite

MOF UiO-66 was synthesized according to the previous literature with some slight modifications (DeStefano et al., 2017). A measure of 3.5 ml of DMF, 2 ml of acetic acid (2.1 g, 35 mmol), and 30.5 μl of a 70% zirconium propoxide [Zr(OnPr)4] solution (in 1-propanol) (26 mg, 0.079 mmol) were mixed in a 10-ml scintillation vial. The solution was heated in an oil bath at 130°C for 2 h and then allowed to cool to room temperature. The color of the mixture changed from colorless to yellow during heating. To the solution, 37.5 mg of 1,4-dicarboxybenzene was added, and after sonication for 30 s, the solution was stirred at room temperature for 18 h. Then, the MOF was separated by centrifugation and washed several times with DMF and water and finally dispersed in water for further use. The nanocomposite (UiO-66@TMB-HRP, UTH) was synthesized by simple incubation of UiO-66 with TMB and HRP. Briefly, to a 5 ml solution of 5 mg/ml UiO-66, the TMB stock solution was added with a final concentration of 0.5 mM; after incubation for 3 h, 25 U HRP was added and stirred at 4°C for another 8 h. After then, the nanocomposite was separated by centrifugation, washed several times with water, and finally dispersed in water for further use.

## Photothermal measurement

The photothermal effect of UTH in different conditions under 900 nm light (0.5 w/cm$^2$) irradiation was measured by using a thermal imaging camera. The heating and cooling temperature changes were recorded, and the photothermal conversion efficiency ($\eta$) was calculated according to the following equations:

$$\eta = \frac{hs\left(T_{max} - T_{suur}\right) - Q_0}{I\left(1 - 10^{-A_{900}}\right)}, \tag{1}$$

$$\tau_s = \frac{m_d c_d}{hs}, \tag{2}$$

$$Q_{s0} = hs\left(T_{max.water} - T_{suur}\right), \tag{3}$$

where $\tau_s$ was observed by linearly fitting the plot of the cooling time versus $-\text{Ln}\theta$. $m_d$ is the mass of the UTH solution, and $C_d$ is the heat capacity of water (4.2 J g$^{-1}$ K$^{-1}$). $T_{\text{max}}$ is the equilibrium temperature; $T_{\text{surr}}$ is the surrounding ambient temperature; $T_{\text{max, water}}$ is the maximum temperature of the heated water.

## Antibacterial test

*Escherichia coli* (*E. coli*) and *Staphylococcus aureus* (*S. aureus*) were selected as Gram-positive and -negative model strains, respectively. Monocolonies of the bacteria on a solid agar plate were transferred to 2 ml LB medium and shaken under 150 rpm at 37°C for 12 h. In the photothermal antibacterial experiments, the bacterial solution (with an optical density at 600 nm of 0.5) was mixed with UTH and 1 mM $H_2O_2$ was added; after incubation for 5 min, the mixture was irradiated under 900-nm light for another 5 min. After then, the treated bacterial solution was diluted and transferred to the solid agar plate. After being placed in an incubator at 37°C for 12 h, the plates were photographed and colonies were counted.

## Therapeutic effect against mouse skin wound infection

Kunming mice were used for skin wound infection model fabrication, which has been approved by the Ethics Committee of Animal Experiments in Zhejiang Sci-Tech University, and all procedures followed the guidelines for animal experiments in Zhejiang Sci-Tech University. The hair of the mouse's quilt was removed with depilation cream. A small piece of the back skin was cut off to construct a wound model. A measure of 10 μl of the *S. aureus* solution with the OD600 of 1 was dropped to the wound for the infection. Then, 10 μl of UTH was dropped to the infected wound once a day for the first 3 days, followed by irradiation with 900-nm light for 5 min. Photographs of the wound were taken every day to record the changes.

# Results and discussion

## Synthesis and characteristics

Considering the porous characteristics and high stability, zr-mof (UiO-66) was chosen as the nanocarrier for TMB and HRP loading. The prepared UiO-66 is milky white and has good stability and dispersion in water. TEM characterization results show that UiO-66 has a size of about 100 nm and good dispersion (Figure 1A). The crystalline and phase information were investigated by powder X-ray diffraction (XRD), and the patterns are shown in Figure 1B. The appearance of sharp peaks in the XRD patterns indicates that UiO-66 has good crystallinity. The size and zeta potential of UiO-66 and UiO-66 loaded with TMB and HRP (UiO-66@TMB-HRP, UTH) were measured with a DLS machine. The main size was around 110 nm; after TMB and HRP loading, the obtained nanocomposite UTH showed a larger size of around 210 nm (Figure 1C). UiO-66 shows a positive zeta potential of 26.3 mV; after loading with TMB and HRP, the zeta potential increased to 46.1 mV (Figure 1D). The positive zeta potential of UiO-66 is ascribed to the positive charge of the $Zr^{4+}$ cation. Both TMB and HRP are positive structures; therefore, after the loading, the zeta potential of the nanoparticles increased to 46.1 mV. The pore structure and the intermolecular interactions of aromatic molecules are mostly responsible for the loading of TMB. The coordination between the $Zr^{4+}$ cation of UiO-66 and chelating groups (e.g., –COOH and –SH) of HRP would be the reasons for HRP loading. The changes in the size and zeta potential clearly indicated the successful preparation of the nanocomposite UTH. Moreover, the presence of the characteristic peaks of TMB and HRP in the absorption spectrum of the nanocomposite also indicated the successful loading of TMB and HRP by UiO-66 (Supplementary Figure S1).

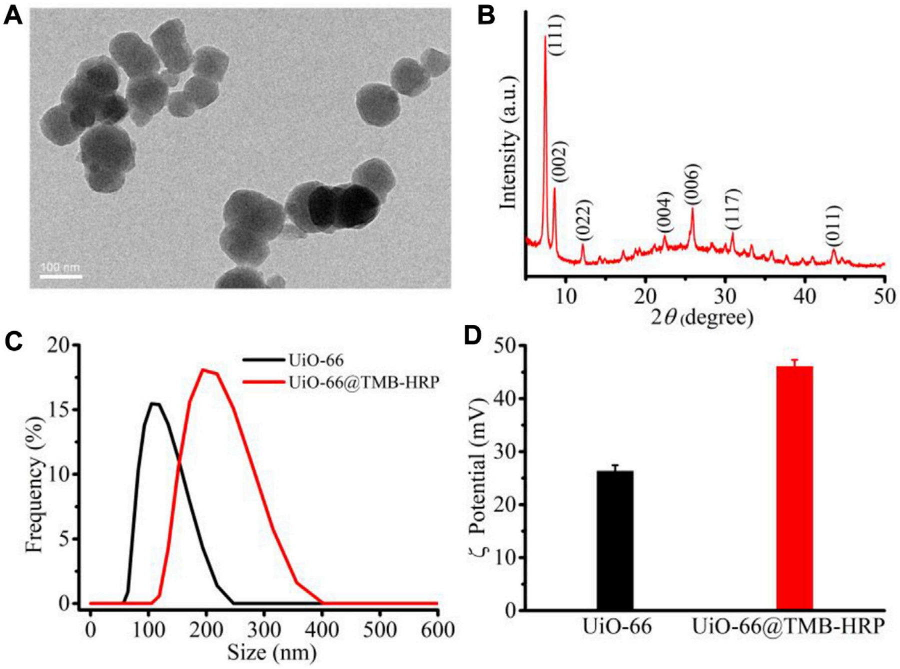

FIGURE 1
Characteristics of the nanocomposite preparation. TEM **(A)** image and XRD patterns **(B)** of the MOF (UiO-66), the size distribution **(C)**, and zeta potential **(D)** of the MOF and the obtained nanocomposite UiO-66@TMB-HRP (UTH).

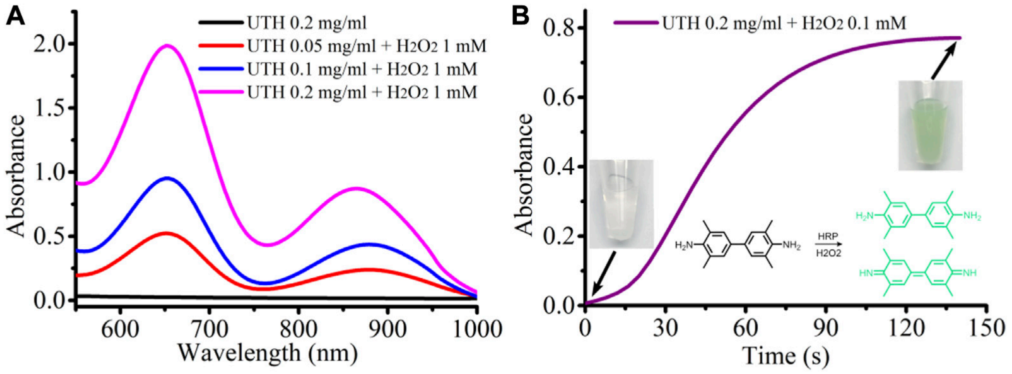

FIGURE 2
**(A)** Absorption spectra of the UTH before and after incubation with $H_2O_2$. **(B)** Change of the absorption value at 650 nm with time in the UTH–$H_2O_2$ system.

## Response characteristics to $H_2O_2$

Then, we studied the response characteristics of the nanocomposite to $H_2O_2$ (Figure 2). The nanocomposite UTH contains both the enzyme (HRP) and the substrate (TMB); in the presence of $H_2O_2$, the HRP will catalyze $H_2O_2$ to generate an intermediate that can oxidize TMB to a colored state. As expected, the color of the nanocomposite solution changes from light milky to dark turquoise, and the absorption spectra clearly indicate the generation of the oxidized product of TMB (Figure 2A). After being treated with $H_2O_2$, two strong absorption peaks around 650 nm and near 900 nm appeared. The intensity of the absorption peak increases with the increase in the concentration of the nanocomposite (Figure 2A). Even

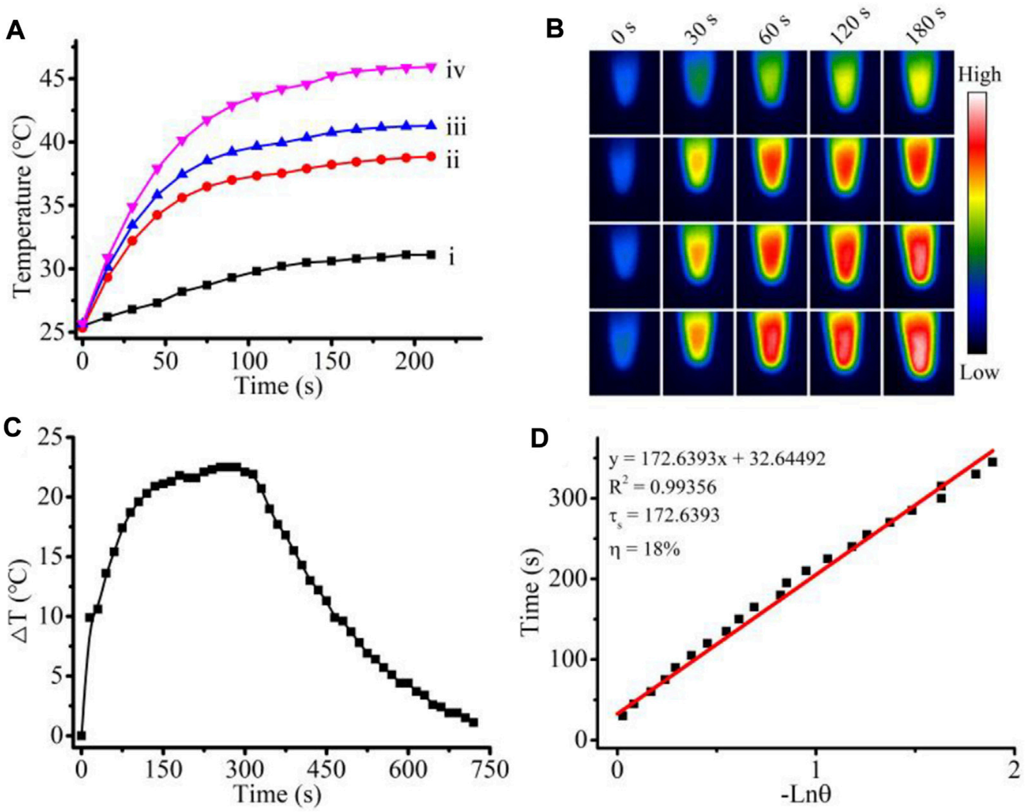

FIGURE 3
**(A)** Photo thermal effect of the UTH 0.2 mg/ml (i), UTH 0.05 mg/ml with 1 mM $H_2O_2$ (ii), UTH 0.1 mg/ml with 1 mM $H_2O_2$ (iii), and UTH 0.2 mg/ml with 1 mM $H_2O_2$ (iv) under 900-nm NIR light irradiation. **(B)** Corresponding thermal image in **(A)**. **(C)** "On-off" temperature change of UTH 0.2 mg/ml with 1 mM $H_2O_2$ under 900-nm light irradiation. **(D)** Liner cooling time data versus –Ln (θ) vs. negative natural logarithm of driving force temperature with τs = 172.63933 s.

when the concentration of $H_2O_2$ is as low as 0.1 mM, it can obviously cause discoloration of the nanocomposite in a short time, indicating that the nanocomposite has a high sensitivity to $H_2O_2$ (Figure 2B). It is worth mentioning that the photothermal effect of nanomaterials is often closely related to the intensity of their absorption peaks, which means that the oxidized nanocomposites will likely produce a strong photothermal effect under near-infrared light (900 nm) irradiation.

## Photothermal effect

As shown in Figures 3A,B, under 900-nm light irradiation, the solution of 0.2 mg/ml UTH showed a very slight temperature increase. However, in the presence of 1 mM $H_2O_2$, even a low concentration of UTH (0.05 mg/ml) could be sharply heated up by a 900-nm light irradiation. The heating rate and the maximum temperature increased with the increase in the concentration of nanocomposites. The temperature of the solution with 0.2 mg/ml UTH and 1 mM $H_2O_2$ can reach above 45°C within 3 min with 900 nm light irradiation, clearly indicating the excellent photothermal effect. It is worth mentioning that the concentration of $H_2O_2$ in the bacterial infection area is usually about 1 mM. In addition, during light irradiation, the local temperature of the nanoparticle surface is much higher than the solution temperature. These indicate that the nanoparticles provide the necessary basis for the sensitive response to $H_2O_2$ and efficient antibacterial activity in the infected area. Then, we calculated the photothermal efficiency by detecting the heating and cooling rates (Figures 3C,D), and the results showed that the photothermal efficiency of the nanocomposite UTH in the presence of $H_2O_2$ reached 18%. The photothermal conversion efficiency of most organic nanomaterials is between 20 and 50% (Li et al., 2020). Compared with these photothermal materials, the photothermal efficiency of 18% is slightly lower. Nevertheless, it is worth mentioning that indocyanine Green (ICG), as an organic molecule frequently used in photothermal therapy, has a photothermal efficiency of only 9% (Li et al., 2020). It indicates that 18% is enough for effective photothermal therapy.

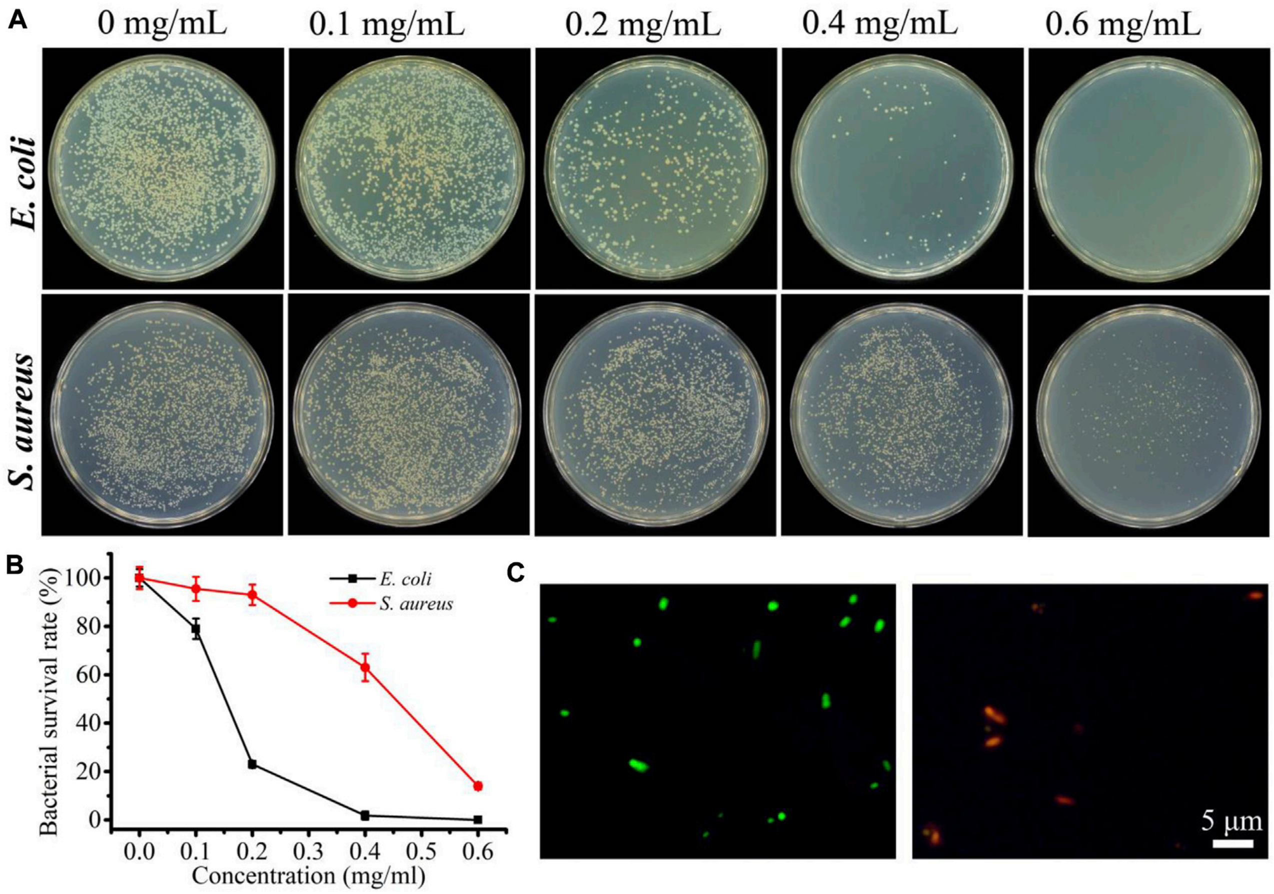

FIGURE 4
**(A)** Photograph of the colonies of *E. coli* and *S. aureus* treated with different concentrations of UTH in the presence of 1 mM $H_2O_2$ under 900-nm light irradiation. **(B)** Corresponding bacterial viabilities by counting **(A)**. **(C)** Fluorescence images (stained with SYTO 9 and PI) of *E. coli* before (left) and after (right) being treated with UTH in the presence of $H_2O_2$ under 900-nm light irradiation.

## Antibacterial effect

After verifying the sensitive response to $H_2O_2$ and the good photothermal effect of UTH, we then investigated the cascade antibacterial effect. We selected *E. coli* and *S. aureus* as Gram-negative and -positive bacterial models, respectively. The plate counting method was used to measure the antibacterial efficiency. The results showed that in the presence of only $H_2O_2$ (1 mM) or UTH (Supplementary Figure S2), NIR light irradiation could not cause significant antibacterial activity. However, in the presence of both $H_2O_2$ and UTH, NIR light irradiation can cause obvious antibacterial activity, and the antibacterial activity increases with the increase in the concentration of UTH. The $IC_{50}$ values of UTH on *E. coli* and *S. aureus* under NIR light irradiation with 1 mM $H_2O_2$ were around 150 and 450 μg/ml, respectively (Figures 4A,B). The significant antibacterial effect was observed in both Gram-positive and -negative bacteria, indicating such a cascade nanosystem has broad-spectrum antibacterial properties. Notably, the antibacterial effect of the photothermal system on the two stains is slightly different, and *E. coli* was more sensitive to the photothermal effect. The different antibacterial efficiencies may be related to the different structures of the two bacteria. *S. aureus* has a cell wall composed of peptidoglycan, which is relatively stable (Zhang et al., 2022a). However, the surface of *E. coli* is a cell membrane composed of phospholipid molecules, which is more fragile than the cell wall of *S. aureus*. Therefore, the photodynamic system has a stronger inactivation efficiency for *E. coli*. Subsequently, the antibacterial mechanism was primarily discussed by live/dead staining with a LIVE/DEAD bacterial viability kit. In such an assay, the green fluorescence (SYTO 9 dye) indicates the live bacteria and the red fluorescence (PI dye) indicates the cell wall-damaged dead bacteria. As shown in Figure 4C, most of the treated bacteria

FIGURE 5
Therapeutic effect against mouse wound infection (caused by *S. aureus*) under different conditions.

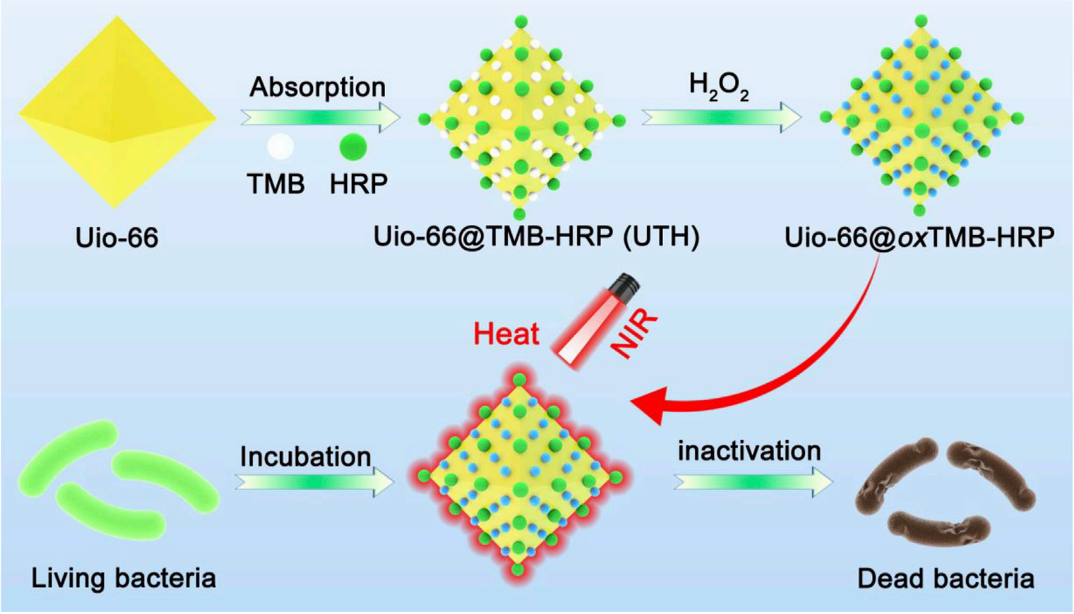

SCHEME 1
Schematic illustration of the preparation and antibacterial mechanism of the nanocomposite.

have strong red fluorescence, indicating that the cascade nano-system can cause cell wall damage to kill bacteria.

### Therapeutic effect against mouse wound infection

Finally, in order to verify the therapeutic effect on real wound infection, we constructed a mouse skin infection model. As shown in Figure 5, after being treated by NIR light irradiation or UTH, the mouse skin wounds infected by *S. aureus* showed obvious symptoms such as suppuration, and the wounds healed slowly. Even 10 days later, the wounds still had obvious dents. However, after being treated with UTH and NIR light irradiation, the wound purulent symptoms were less and the wound healing was faster. After 10 days, the wound basically healed. These results show that the cascade nano-system has a good therapeutic effect on skin wound infection.

## Conclusion

In this study, the MOF nanocomposite with the characteristics of $H_2O_2$ and NIR light cascade response was successfully constructed, and the photothermal antibacterial activities were verified. The nanocomposites can respond sensitively and quickly to $H_2O_2$. Due to the catalytic oxidation, the color of the nanocomposite changes to dark turquoise in the presence of $H_2O_2$; meanwhile, a strong absorption peak in the near-infrared region around 900 nm appeared. The oxidized nanocomposite can convert near-infrared photons into thermal energy with an efficiency of 18%. This nano-system showed a strong inactivation effect on both Gram-negative and -positive bacteria. Under the conditions of 1 mM hydrogen peroxide and 0.5 W/cm$^2$ NIR light intensity, the $IC_{50}$ values of the MOF nanocomposite on *E. coli* and *S. aureus* were 150 and 450 μg/ml, respectively. This cascade response nanomedicine also showed a strong therapeutic effect on the mouse skin wound infection model. This study not only provides an effective photothermal antibacterial strategy but also offers a new idea for building precise nano-therapeutic systems.

## Data availability statement

The original contributions presented in the study are included in the article/Supplementary material; further inquiries can be directed to the corresponding author.

## Ethics statement

The animal study was reviewed and approved by Zhejiang Sci-Tech University.

## Author contributions

ZZ: supervision, conceptualization, and writing—original draft preparation. CM, YZ, LL, and LW: methodology and investigation. CM, YZ, WZ, XL, and WB: writing—review and editing. ZZ and XL: funding acquisition.

## Funding

This research was financially supported by the National Natural Science Foundation of China (NSFC) (No. 22007083), the Zhejiang Provincial Natural Science Foundation of China (No. LQ20B010010), the Science Foundation of Zhejiang Sci-Tech University (ZSTU) under Grant No. 19062410-Y, the Anhui Provincial Natural Science Foundation (No. 2108085QB75), and the Zhejiang Provincial Innovation Center of Advanced Textile Technology and the Fundamental Research Funds of the Shaoxing Keqiao Research Institute of Zhejiang Sci-Tech University (No. KYY2022004C).

## Conflict of interest

The authors declare that the research was conducted in the absence of any commercial or financial relationships that could be construed as a potential conflict of interest.

## Publisher's note

## Supplementary material

The Supplementary Material for this article can be found online at: https://www.frontiersin.org/articles/10.3389/fchem.2022.1044931/full#supplementary-material

# References

Deng, Q., Zhang, L., Liu, X., You, Y., Ren, J., and Qu, X. (2022). Magnetoelectrically ignited nanozyme-eel for combating bacterial biofilms. *Chem. Commun.* 58, 7634–7637. doi:10.1039/d2cc02603a

DeStefano, M. R., Islamoglu, T., Garibay, S. J., Hupp, J. T., and Farha, O. K. (2017). Room-temperature synthesis of UiO-66 and thermal modulation of densities of defect sites. *Chem. Mat.* 29, 1357–1361. doi:10.1021/acs.chemmater.6b05115

Du, L., Ren, S., Qi, Y., Wen, R., Feng, Y., Tong, M., et al. (2022). Boron imidazolate framework-derived porous carbon nanospheres for dual-mode bioimaging-guided photothermal/sonodynamic synergistic cancer therapy. *Adv. Ther.* 5, 2200033. doi:10.1002/adtp.202200033

Fan, Y., Wang, Z., Ren, W., Liu, G., Xing, J., Xiao, T., et al. (2022). Space-confined synthesis of thin polypyrrole nanosheets in layered bismuth oxychloride for a photoresponse antibacterial within the near-infrared window and accelerated wound healing. *ACS Appl. Mat. Interfaces* 14, 36966–36979. doi:10.1021/acsami.2c11503

Han, Q., Lau, J. W., Do, T. C., Zhang, Z., and Xing, B. (2020). Near-infrared light brightens bacterial disinfection: Recent progress and perspectives. *ACS Appl. Bio Mater.* 4(5), doi:10.1021/acsabm.0c01341

Hutchings, M. I., Truman, A. W., and Wilkinson, B. (2019). Antibiotics: Past, present and future. *Curr. Opin. Microbiol.* 51, 72–80. doi:10.1016/j.mib.2019.10.008

Ji, H., Hu, H., Tang, Q., Kang, X., Liu, X., Zhao, L., et al. (2022). Precisely controlled and deeply penetrated micro-nano hybrid multifunctional motors with enhanced antibacterial activity against refractory biofilm infections. *J. Hazard. Mater.* 436, 129210. doi:10.1016/j.jhazmat.2022.129210

Jia, Y., and Zhao, L. (2021). The antibacterial activity of fluoroquinolone derivatives: An update (2018-2021). *Eur. J. Med. Chem.* 224, 113741. doi:10.1016/j.ejmech.2021.113741

Karami, A., Farivar, F., de Prinse, T. J., Rabiee, H., Kidd, S., Sumby, C. J., et al. (2021). Facile multistep synthesis of ZnO-coated β-NaYF4:Yb/Tm upconversion nanoparticles as an antimicrobial photodynamic therapy for persistent *Staphylococcus aureus* small colony variants. *ACS Appl. Bio Mat.* 4, 6125–6136. doi:10.1021/acsabm.1c00473

Laxminarayan, R., Duse, A., Wattal, C., Zaidi, A. K., Wertheim, H. F., Sumpradit, N., et al. (2013). Antibiotic resistance-the need for global solutions. *Lancet Infect. Dis.* 13, 1057–1098. doi:10.1016/s1473-3099(13)70318-9

Li, J., Liu, Y., Xu, Y., Li, L., Sun, Y., and Huang, W. (2020). Recent advances in the development of NIR-II organic emitters for biomedicine. *Coord. Chem. Rev.* 415, 213318. doi:10.1016/j.ccr.2020.213318

Mamun, M. M., Sorinolu, A. J., Munir, M., and Vejerano, E. P. (2021). Nanoantibiotics: Functions and properties at the nanoscale to combat antibiotic resistance. *Front. Chem.* 9, 687660. doi:10.3389/fchem.2021.687660

Mu, J., Xiao, M., Shi, Y., Geng, X., Li, H., Yin, Y., et al. (2022). The Chemistry of organic contrast agents in the NIR-II window. *Angew. Chem. Int. Ed. Engl.* 61, e202114722. doi:10.1002/anie.202114722

Wang, L., Zhu, W., Zhou, Y., Li, Q., Jiao, L., Qiu, H., et al. (2022). A biodegradable and near-infrared light-activatable photothermal nanoconvertor for bacterial inactivation. *J. Mater. Chem. B.* doi:10.1039/d1tb01781k

Zhang, Z., Han, Q., Lau, J. W., Wang, Z., Hu, M., Qiu, H., et al. (2022a). A metabolic labeling way to *in situ* fabricate bacterial FRET Platform for innate immune defence molecule. *Sensors Actuators B Chem.* 350, 130913. doi:10.1016/j.snb.2021.130913

Zhang, Z., Han, Q., Lau, J. W., and Xing, B. (2020). Lanthanide-doped upconversion nanoparticles meet the needs for cutting-edge bioapplications: Recent progress and perspectives. *ACS Mater. Lett.* 2, 1516–1531. doi:10.1021/acsmaterialslett.0c00377

Zhang, Z., Wang, J., Hu, Y., and Wang, L. (2022b). Microwaves, a potential treatment for bacteria: A review. *Front. Microbiol.* 13, 888266. doi:10.3389/fmicb.2022.888266

frontiers | Frontiers in Chemistry

TYPE Original Research
PUBLISHED 04 November 2022
DOI 10.3389/fchem.2022.1013910

OPEN ACCESS

EDITED BY
Guannan Wang,
Jining Medical University, China

REVIEWED BY
Hongxing Liu,
First Affiliated Hospital of Guangzhou Medical University, China
Qiong Huang,
Central South University, China

*CORRESPONDENCE
Lingli Xu,
xulingli0608@sina.com
Ming Lei,
leiming6891@163.com

[†]These authors have contributed equally to this work and share first authorship

SPECIALTY SECTION
This article was submitted to Nanoscience, a section of the journal Frontiers in Chemistry

RECEIVED 08 August 2022
ACCEPTED 21 October 2022
PUBLISHED 04 November 2022

CITATION
You L, Wang Q, Ma Y, Li Y, Ye H, Xu L and Lei M (2022), Precise dapagliflozin delivery by cardiac homing peptide functionalized mesoporous silica nanocarries for heart failure repair after myocardial infarction.
*Front. Chem.* 10:1013910.
doi: 10.3389/fchem.2022.1013910

# Precise dapagliflozin delivery by cardiac homing peptide functionalized mesoporous silica nanocarries for heart failure repair after myocardial infarction

Lijiao You[†], Qing Wang[†], Yuhui Ma[†], Yunfeng Li, Hui Ye, Lingli Xu* and Ming Lei*

Department of Critical Care Medicine, Seventh People's Hospital Affiliated to Shanghai University of TCM, Shanghai, China

Myocardial infarction (MI) may cause irreversible damage or destroy to part of the heart muscle, affecting the heart's ability and power to pump blood as efficiently as before, often resulting in heart failure (HF). Cardiomyocyte death and scar formation after MI may then trigger chronic neurohormonal activation and ventricular remodeling. We developed a biocompatible and mono-dispersed mesoporous silica nanoparticles (MSN) divergent porous channel for dapagliflozin (DAPA) loading. After surface modification of the cardiac-targeting peptides, the novel drug delivery system was successfully homed, and precisely released drugs for the hypoxic and weak acid damaged cardiomyocytes. Our biocompatible MSN- based nanocarriers for dapagliflozin delivery system could effective cardiac repair and regeneration *in vivo*, opening new opportunities for healing patients with ischemic heart disease in clinical.

KEYWORDS

**myocardial infarction, dapagliflozin, nano-targeted drugs delivery system, heart failure repair, hypoxia-inducible factor 1-α (HIF-1α)**

## 1 Introduction

Myocardial infarction (MI) contributes to more than 40% of sudden cardiac deaths and represents the leading cause of morbidity and mortality worldwide (Sathisha et al., 2011; Nigam 2007; Anwar et al., 2016). In myocardial ischemia area, broadscale myocardium tissue are impaired with apoptotic/necrotic cardiomyocytes. Due to the low proliferation capability of myocardial cells, the damaged myocardium tissue is always unable to be effective regeneration and restoration (Zhao, et al., 2022). Meanwhile, complications of heart failure (HF) after MI hospitalization may cause cardiomyocyte apoptosis and scar formation, subsequently triggering chronic neurohormonal activation and ventricular remodeling (Dudas et al., 2011; Roger 2013; Desta et al., 2015; Jenča D et al., 2021). The high prevalence of HF complications after hospital discharge greatly

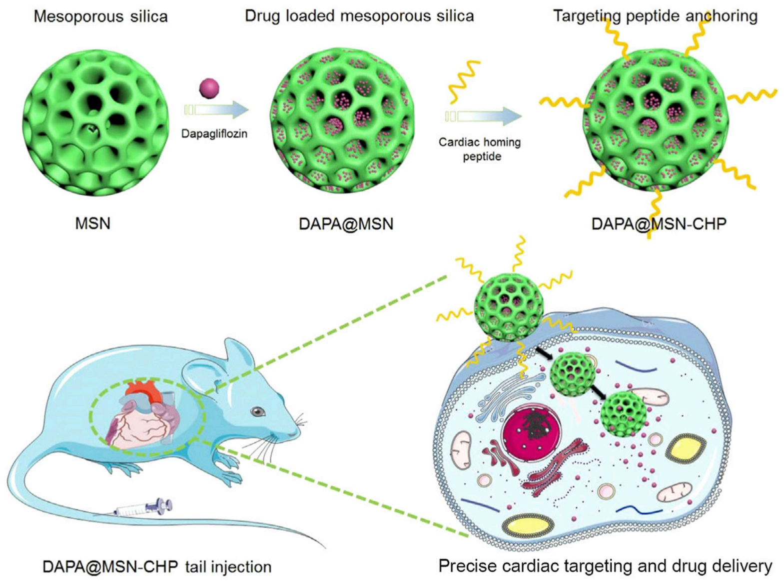

FIGURE 1
Dapagliflozin-loaded biocompatible mesoporous silica nanoparticles with surface functionalization of cardiac homing peptide fabrication for precise heart failure repair after myocardial infarction.

reduces the quality of life of MI patients. It is estimated that approximately 13% of patients will experience HF complications 30 days post-discharge, with this number increasing to 20–30% in the first year after discharge (Hung et al., 2013; Sulo et al., 2016). Thus, HF is associated with three alarmingly high rates: high incidence rate, high mortality rate, and high rehospitalization rate. Scientists recently reported that the sodium-glucose cotransporter two inhibitor, dapagliflozin (DAPA) is a promising new drug for the treatment of HF. DAPA is approved by the Food and Drug Administration (FDA)—could reduce the risk of cardiovascular death and hospitalization for cardiac deterioration, increase survival rate and improve symptoms of HF in patients with decreasing ejection fraction (McMurray et al., 2019b, a). DAPA can effectively improve cardiac structure and function, weaken cardiac fibrosis and myocardial apoptosis, as well as inhibit inflammatory cytokines (Wang K et al., 2021). While the low selectivity, poor biodistribution and high systematic toxicity of DAPA greatly restrict its further clinical application (Wilczewska ZA, et al., 2012). Furthermore, treatment for MI is expensive and extensive, the prognosis is poor. Frequent episodes of HF and repeated emergency treatment in MI patients further increase the cost of treatment (Cowper et al., 2019). This situation led to the urgent construction of a novel drug delivery system (DDS) for HF repair. The novel DDS can be loaded with DAPA, which improves HF symptoms and increases patient survival. In addition, the novel DDS should be targeted precisely to improve drug utilization.

Novel drug delivery systems have been rapidly developed over the past few decades. Both native and synthetic nanomaterials have been extensively explored and proposed as the main components of DDS (Rodrigues et al., 2016; Swamy and Sinniah 2016; Mohanty et al., 2017). Recently, synthesized nanomaterials, including carbon materials (Bao R et al., 2017; Sun X et al., 2017), dopamine nanoparticles (Chakroborty et al., 2011; Das and Jana 2015), inorganic silica (Yang et al., 2010; Zhu et al., 2011), and polymeric assembly nanohybrids (Syed et al., 2012; Kerr et al., 2022), have been employed as nanocarriers for DDS. Porous silica has been recommended as an ideal DDS based on the biocompatibility of silica's drug embedding ability in the mesoporous channel (Meng et al., 2010; Che et al., 2014; Chen K et al., 2020; Chen YJ et al., 2020). Furthermore, mesoporous silica nanospheres (MSNs) have been widely used for drug delivery because of their optimal surface area for drug loading, their facile synthesis and surface functionalization by anchoring targeting ligands, stimuli-responsive agents and sensing molecules (Sahoo et al., 2014; Sapino et al., 2015; Ugazio et al., 2016; Jafari et al., 2019). MSNs are considered biocompatible with the human body, as indicated by numerous investigations. The therapeutic dose of MSNs for DDS is well below the toxic level for humans, making MSN an excellent option for clinical applications.

Cardiac homing peptide (CHP) is a short peptide that preferentially binds to ischemic myocardium, and its sequence is CSTSMLKAC. CHP was first screened in a study of selective targeting of random peptides to ischemic tissue *in vivo* and was shown to be a safe peptide that did not cause any significant impairment of left ventricular systolic function. CHP has the potential to be used in the development of targeted therapy drugs for ischemic lesions of myocardial tissue (Kanki et al., 2011; Won et al., 2013; Vandergriff et al., 2018).

Here, we propose a conventional bi-phase approach for MSN synthesis for DAPA loading in heart failure repair. The hydrophobic and cation-π interaction properties of DAPA facilitate the efficient encapsulation of this drug in mesoporous channels (DAPA@MSN). Moreover, a CHP was functionalized on the surface of DAPA@MSN (DAPA@MSN-CHP). After intravenous injection of DAPA@MSN-CHP in a mouse model of HF after MI, this DDS efficiently and precisely accumulated in the HF site. DAPA-loaded MSNs have a slightly negative charge under normal physiological conditions but transform to a positive charge in the intracellular microenvironment of apoptotic cardiomyocytes because of the protonation effect under acidic conditions (Figure 1) (Wang et al., 2020). The results indicate that our DDS can effectively inhibit the apoptosis of cardiomyocytes, leading to viable myocardium preservation and cardiac function augmentation, laying a solid foundation for clinical HF repair.

## 2 Materials and characterization

Materials: Hexadecyltrimethylammonium bromide (CTAB), decahydronaphthalene, 1-octadecene (ODE) were purchased from Sigma-Aldrich. NaOH, cyclohexane and $NH_4NO_3$ were obtained from Shanghai Chemical Co., Ltd. Ammonia aqueous solution (28 wt%), tetraethyl orthosilicate (TEOS), (3-Aminopropyl) triethoxysilane (APTES), triethanolamine (TEA), decahydronaphthalene (98%) were purchased from Aladdin Industrial Inc. All chemicals were used as received without further purification.

Characterization: Transmission electron microscopy (TEM) measurements were carried out on a JEM 2100F microscope (Japan) operated at 200 kV. The samples were first dispersed in ethanol and then collected by using copper grids covered with carbon films for measurements. UV–vis–NIR absorption spectra were measured on a Shimadz spectrophotometer (UV-3150) (Japan) with wavelength range of 300 –1,200 nm, unless otherwise specified, all spectra were collected under identical experimental conditions. All animals underwent transthoracic echocardiography under anesthesia at 4 weeks after treatment using a VisualSonics Vevo 2,100 imaging system. The results were obtained by detecting Si content with inductively coupled plasma mass spectrometer in main organs.

### 2.1 Synthesis of mesoporous silica nanoparticles loading with DAPA and targeting peptides modification

#### 2.1.1 Mesoporous silica fabrication

The mesoporous silica nanoparticles were synthesized as the procedure reported previously. Briefly, 16 ml of (25 wt%) CTAB solution and 90 mg of triethanolamine were added to 20 ml of water and stirred gently at 60°C for 1 h in flask, then 1.5 ml of TEOS and 1 ml of cyclohexane was added to the solution and kept at 60°C with magnetic stirring for 24 h. The products were collected by centrifuging and washed by water and ethanol for several times, and then were dispersed in 30 ml of acetone and refluxed for 8 h to remove CTAB templates. The final products were washed with ethanol and dried in vacuum at 45°C for 8 h.

#### 2.1.2 Loading of dapagliflozin (DAPA)

DAPA was dissolved in DMSO (2.0 ml). Mesoporous silica nanoparticles (5.0 mg) were added to the solution and the suspension was stirred at room temperature for 48 h. The DAPA molecules could be adsorbed in the mesopore channels. The as-prepared DAPA-loaded mesoporous silica nanoparticles were collected by centrifugation. The amount of the adsorbed guests was determined from the difference between the initial amounts of DAPA by measuring the UV absorbance from the supernatant liquid and quantified from a standard curve.

#### 2.1.3 Cardiac homing peptides modification

To functionalization of DAPA@MSN, 3.0 g of silica was placed in a 100-ml round bottom flask with 50 ml of dry toluene and 2.4 g of 3-aminopropyltriethoxysilane (APTES). The mixture was stirred and refluxed at 110°C for 48 h under the protection of nitrogen. The white 3-aminopropyl functional silica washed with toluene, *n*-hexane and dichloromethane, respectively, and dried at 25°C for 12 h.

#### 2.1.4 DAPA@MSN-CHP fabrication

First, 20 mg CHP, 10 mg EDC and 8 mg NHS were dissolved in 20 ml anhydrous DMF, and incubated at room temperature overnight to activate the carboxyl groups of FA. Then, DAPA@ MSN with $NH_2$ modification (20 mg) was added. The mixed solution was allowed to react for 12 h, and the DAPA@MSN-CHP were obtained by centrifugation at 12,000 rpm for 20 min, and then washed with methanol three times.

### 2.2 *In vitro* cellular targeting and cell viability of DAPA@MSN-CHP

#### 2.2.1 Cell viability

All experiments were carried in 96-well plates. Cytotoxicity of MSN-CHP was tested *via* CCK-8 assay. Briefly, the primary cardiomyocytes isolated through enzymatic digestion were seeded into plate at $5\times10^3$/well in 100 μL of DMEM/Low glucose (10% FBS, 100 units/mL of penicillin and 100 μg/ml of streptomycin), and incubated for 24 h. Then, 10 μL CCK-8 solution was added followed by12 h incubation. After 12 h incubation, the absorbance of each well at wavelength of 450 nm was measured using a microplate reader. Data were presented as mean ± SD ($n = 3$).

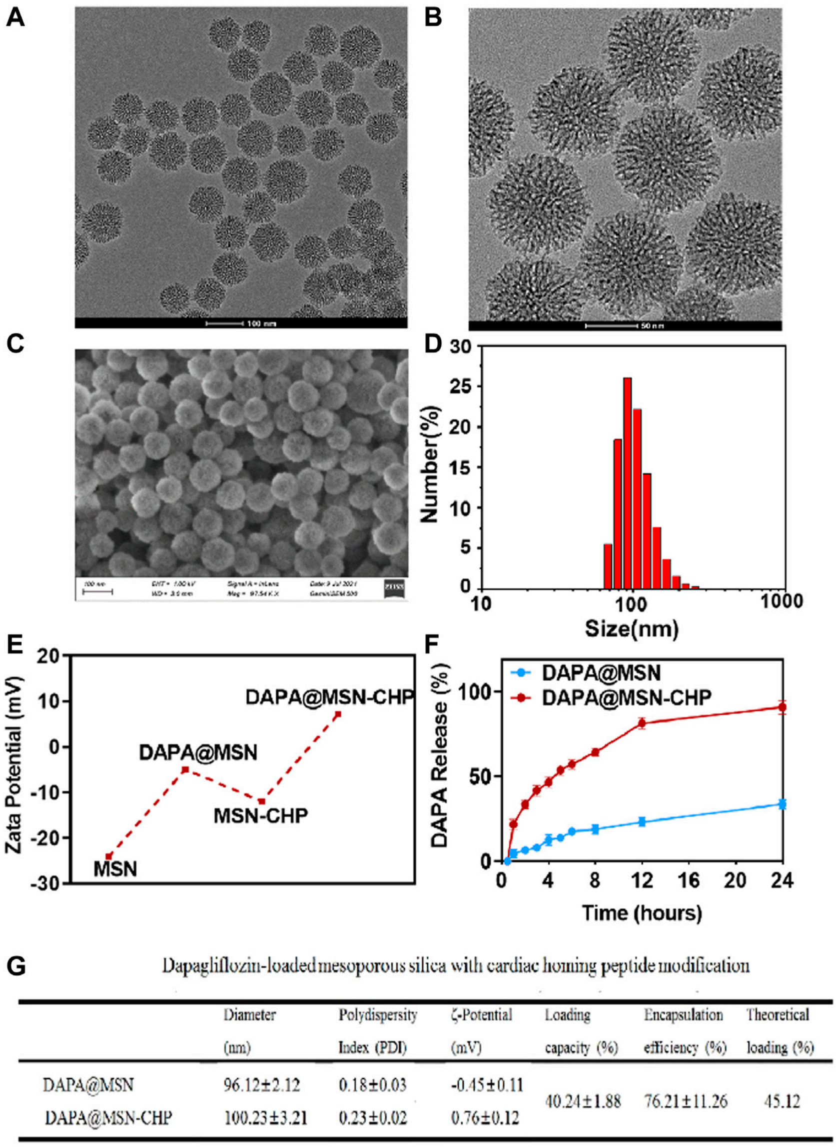

Dapagliflozin-loaded mesoporous silica with cardiac homing peptide modification

| | Diameter (nm) | Polydispersity Index (PDI) | ζ-Potential (mV) | Loading capacity (%) | Encapsulation efficiency (%) | Theoretical loading (%) |
|---|---|---|---|---|---|---|
| DAPA@MSN | 96.12±2.12 | 0.18±0.03 | -0.45±0.11 | 40.24±1.88 | 76.21±11.26 | 45.12 |
| DAPA@MSN-CHP | 100.23±3.21 | 0.23±0.02 | 0.76±0.12 | | | |

FIGURE 2
TEM image **(A)**, magnification TEM image **(B)** and SEM image of the bi-phase prepared MSN **(C)**. DLS result of size distribution of MSN **(D)**. Zeta-potential data of MSN, DAPA@MSN, MSN-CHP and DAPA@MSN-CHP **(E)**. DAPA release curve of DAPA@MSN-CHP under different pH values **(F)**. The corresponding physical and chemical parameters of the DDS **(G)**.

## 2.2.2 CLSM images of cellular uptake

The cellular uptake of DAPA@MSN-CHP was observed and imaged by confocal laser scanning microscopy (CLSM). Briefly, primary cardiomyocytes were seeded into 6-well plates at a density of 1×10$^5$/well with 1 ml of DMEM/Low glucose (10% FBS, 100 units/mL of penicillin and 100 μg/ml of streptomycin) media and incubated for 24 h. After the treatment with DAPA@MSN-CHP, DAPA@MSN at a final concentration of 100 μg/ml, the cardiomyocytes were incubated for 12 h. Then, the cardiomyocytes were washed with PBS for three times and DAPI (1 μg/ml in PBS) was used to stain nuclei for 30 min prior to being observed under CLSM.

## 2.2.3 Western-blot analysis

Cells were collected after 12 h incubation with PBS, DAPA, DAPA@MSN, and DAPA@MSN-CHP. Samples containing equal amounts of protein were electrophoresed using 10% SDS-PAGE, transferred onto polyvinylidene fluoride membranes and then incubated with specific primary antibodies. The blots were reacted with horseradish peroxidase-conjugated secondary antibodies and were detected using the enhanced chemiluminescence system (Santa Cruz Biotechnology, Inc.). The density of the band was quantified by densitometry and exposed to X-ray film (Eastman-Kodak, Rochester, NY, United States) using GAPDH levels as a control.

## 2.3 *In vivo* HF repair capability of DAPA@MSN-CHP

### 2.3.1 *In vivo* HF repair

Animal experiments were approved by the Animal Research Ethics Committee of Shanghai Seventh People's Hospital. Animal experiments were performed according to the animal use and care regulation and the animal management rules of the ministry of health of the People's Republic of China. C57BL/6 mice (8–10 weeks old) were bought from Shanghai Institute of Family Planning Science Laboratory Animal management Department. (Shanghai, China). All efforts were made to minimize animal suffering. The myocardial ischemia model was constructed based on previously reported works. A total of 70 male 8- to 10-week-old C57 mice were used for this work (Luo L et al., 2016; Snider JC et al., 2021). For the myocardial ischemia model construction, all mice were received permanent coronary artery ligation. Mice were anesthetized with 160 mg/kg barbital sodium *via* intraperitoneal injection. Typically, before preparing the surgical model, ventilation system after endotracheal intubation is recommend to use when coronary artery ligation can be successfully and routinely performing the within 3 min. Subsequently, a 1.2 cm of small skin cut was conducted over the left chest according previously reported. After the dissection, both pectoral major and minor muscle retracted, then the fourth intercostal space can be successfully observed. Simultaneously, in order to open both the pleural membrane and pericardium, a mosquito clamp was used to cut a small hole at this intercostal space. When the clamp was slightly opened, partial heart section was gently squeezed out through this hole. The coronary artery ligation was carefully located, sutured, and ligated (from its origin ≈3 mm) by a commonly used 6–0 silk suture. The surgical ligation was confirmed successfully when the anterior wall from left ventricular changed to pale. Immediately, the heart was put back to form the intrathoracic space followed by air manual evacuation and muscle and the skin closure through the previously used purse-string suture. During the recovery durations, the mice were allowed to breathe and carefully monitored, which was usually completed within 3–5 min. The artificial respiratory aid was not allowed during the recovery period. For the DAPA@MSN-CHP induced therapy, the C57BL/6 mice with myocardial ischemia were divided into four groups including the MI, DAPA, DAPA@MSN, and DAPA@MSN-CHP. Meanwhile, health mice were set as control group. Each group contained 4 mice. Each group contained 4 mice. The MI, MI + DAPA, MI + DAPA@MSN, and MI + DAPA@MSN-CHP groups were treated with 100 μL of PBS, DAPA, DAPA@MSN, and DAPA@MSN-CHP solutions *via* tail injection, respectively one time every day for 3 days. Meanwhile, the control groups were also received tail vein injection of PBS one time every day for 3 days.

### 2.3.2 Cardiac function assessment

All animals underwent transthoracic echocardiography under anesthesia at 4 weeks after treatment using a VisualSonics Vevo 2,100 imaging system. During ultrasound process, mice were anesthetized with 3% isofluorane *via* a R500-Comapct Small Animal Anesthesia Machine (Shenzhen, China). Hearts were imaged 2D in long-axis views at the level of the greatest left ventricular diameter. Estimation of the function and fractional shortening were determined by measurement from views taken from the infarcted area. All measurements were done in random order, with the surgeon and echocardiographer being blind to the treatment groups.

### 2.3.3 Histopathological evaluation

Hearts were harvested and cut into 10 μm-thick tissue sections. H&E and Masson's trichrome staining of normal, MI, DAPA, DAPA@MSN, and DAPA@MSN-CHP was performed. Image analysis related to viable myocardium and scar size was performed using NIH ImageJ software.

# 3 Results and discussion

## 3.1 DAPA@MSN-CHP fabrication and characterization

MSNs were fabricated using a novel biphase approach in a cyclohexane and water stratification system (Shen et al., 2014). The biphase stratification approach enables hydrolysis precursors in the interface. It conveniently regulates the nanoparticle assembly in the biphase interface by adding or changing other reactants in two different phases without affecting interfacial tension. The hydrophobic upper layer consisted of 25% tetraethyl orthosilicate (TEOS) solution in cyclohexane. The lower hydrophilic layer was a pure water solution mixed with cationic cetyl trimethylammonium cetyl bromide (CTAB) as the template and surfactant and 25% organic weak base triethanolamine (TEA) as a reducing agent. The dendritic hierarchical mesostructure with monodispersion was obtained *via* continuous interfacial growth in a facile one-pot strategy for 48 h (Figure 2A). A divergent mesoporous channel could be observed in the magnification transmission electron microscope (TEM) image (Figure 2B). The MSN pore size can be altered by changing the type of hydrophobic solvent in the upper layer.

The surface morphology of the MSN was also investigated using a scanning electron microscope (Figure 2C). The properties of the mesoporous channels and their uniform size were detected. The size distribution of our MSNs were also estimated by

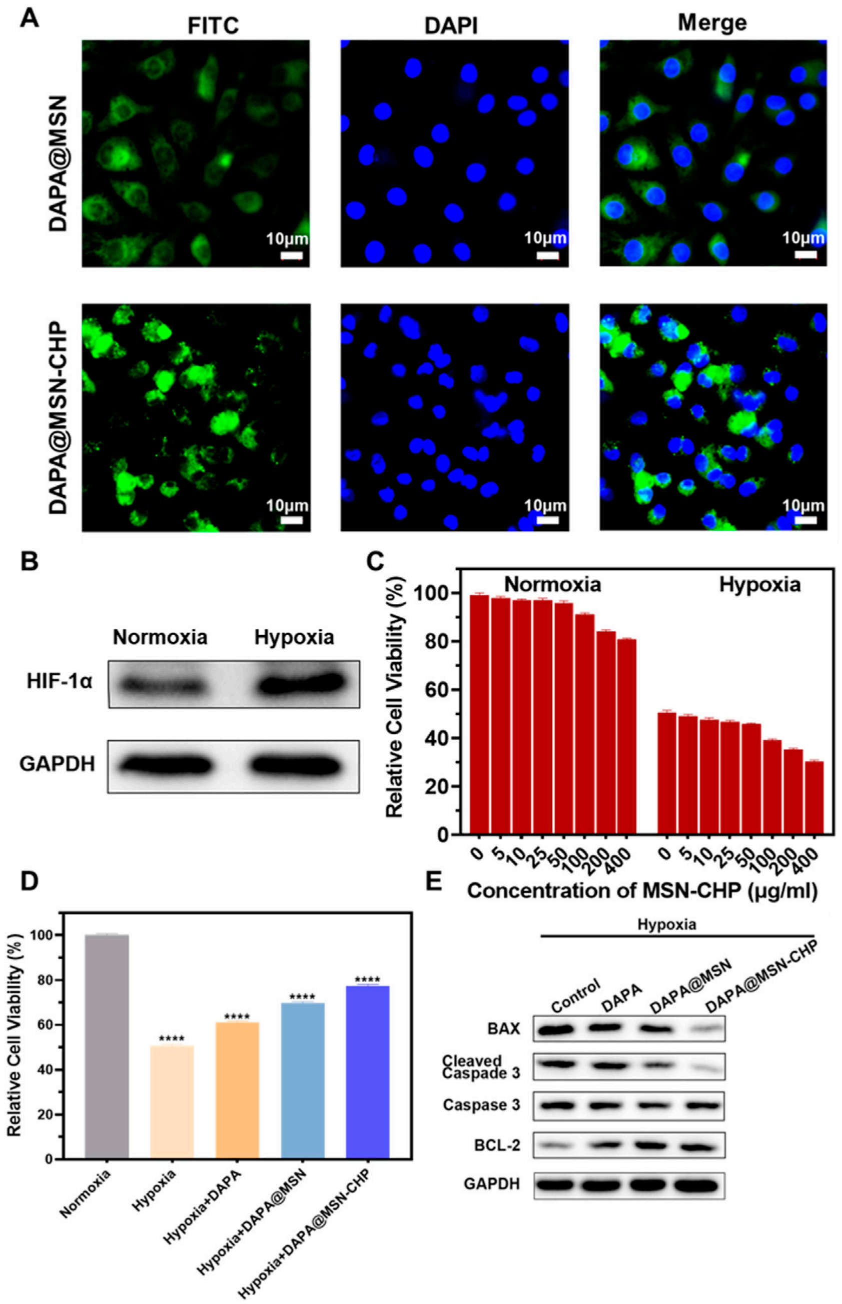

FIGURE 3
CLSM images of DAPA@MSN-CHP and DAPA@MSN with 12 h incubation **(A)**. Western blot result of HIF-1α expression in HF tissues and normal tissue **(B)**. Cell viabilities of cardiomyocytes toward MSN-CHP under hypoxia and normoxia conditions **(C)**. Cell viabilities of cardiomyocytes after different treatments in hypoxic conditions. Pure normoxia condition was set as the control group **(D)**. Bax, cleaved Caspase-3, Caspase-3 and BCL-2 expressions of cardiomyocytes after different treatments under hypoxia conditions **(E)**. All error bars represent mean ± SD ($n = 4$). Data analysis was performed using one-way ANOVA, **$p < 0\ 01$, ***$p < 0\ 001$.

dynamic light scattering (DLS). Results showed that the drug delivery carriers had a narrow unimodal size distribution with a ~96.2 nm peak, suggesting superior dispersity and uniform practical diameter (Figure 2D). Subsequently, the MSN surface was modified with the amino group in the ethanol solution through aminopropyltriethoxysilane hydrolysis. In the following step, DAPA was encapsulated in the mesoporous channels. Then, CHP could be anchored on the silica surface by EDC/NHS reaction between the MSN amino group and the carboxyl group of the targeting peptides.

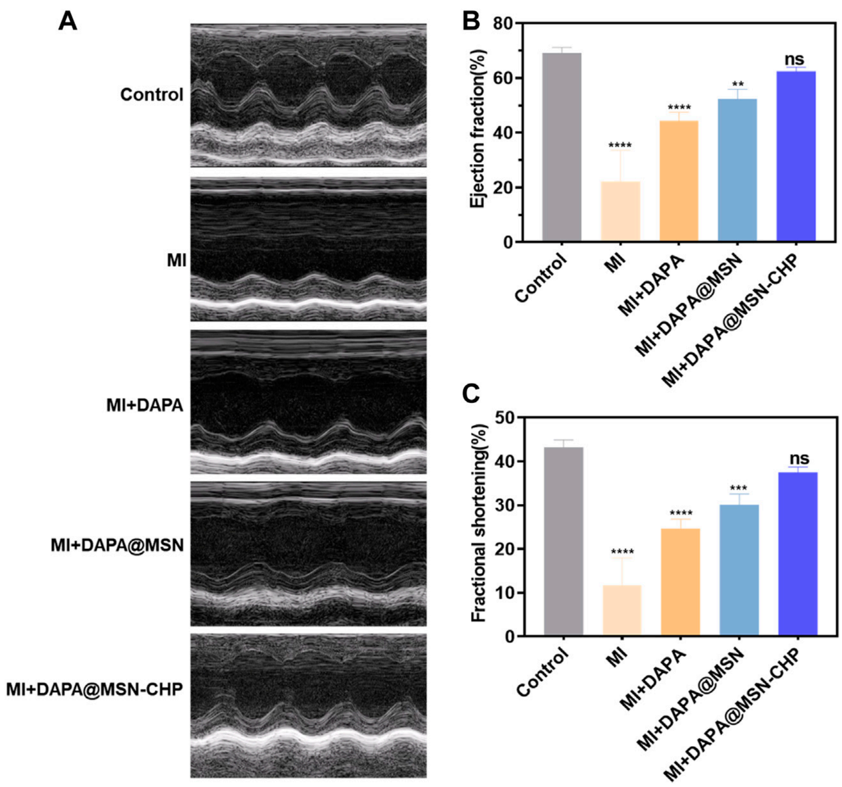

FIGURE 4
M-mode echocardiogram representative images of MI, MI + DAPA, MI + DAPA@MSN and MI + DAPA@MSN-CHP treatments. The healthy mice were set as controls **(A)**. Estimation of the function of MI hearts by ejection fraction **(B)** and fractional shortening **(C)** after MI, MI + DAPA, MI + DAPA@MSN and MI + DAPA@MSN-CHP treatments. The healthy mice were set as controls. All error bars represent mean ± SD ($n$ = 4). Data analysis was performed *via* one-way ANOVA, **$p$ < 01, ***$p$ < 001.

Zeta potential of MSN presents ~ -25 mV, contributing to the massive silicon hydroxyl group on the silica surface (Figure 2E). Interestingly, compared with free MSN, DAPA@MSN exhibits a weaker negative charge, mainly due to the positive charge of the amino group modification. DAPA@MSN-CHP has a positive charge in the aqueous solution, mainly because of the amino group consumption after the condensation reaction. The dominant positive charge of our DDS may originate from CHP, which facilitates the endocytosis of the DDS. The corresponding physical and chemical parameters of the DDS are listed in Figure 2G, showing all the sizes fluctuate minimally after drug loading or CHP modification. Loading efficiency meets theoretical efficiency estimations, further demonstrating that MSNs are the ideal nanocarriers for drug delivery. Li ZX et al. reported that small nanoparticles (< 200–300 nm) are normally taken up by cells *via* the endocytic pathway. Particle size, particle shape, and particle surface charge have a certain impact on the endocytic uptake of cells. Generally, particles with small particle size, rough surface and positively charged surface are more likely to be phagocytosed by cells (Li et al., 2012). The characterization results of the above materials suggest that DAPA@MSN-CHP may have good biocompatibility thanks to its small nanoparticle size, rough mesoporous surface, and positive charge characteristics.

MI leads to changes in the microenvironment at the site of cardiac injury. Constructing acidic pH-responsive DDS based on the weakly acidic microenvironmental characteristics of lesions can improve the value of drug utilization (Li et al., 2021). Finally, we investigated the drug release ability of DAPA@MSN-CHP under different pH conditions. Compared with the normal pH value of ~7.2, 92.1% of DAPA can be released after 24 h incubation in biological buffers with pH values of ~5.5 (Figure 2F). These results suggest that DAPA can continuously release under the weak acid in the HF site after MI which is beneficial to improve the utilization value of drugs.

## 3.2 *In vitro* investigation of DAPA@MSN-CHP

Following the excellent performance of DAPA@MSN-CHP, we then estimated the intracellular localization of DDS in cardiomyocytes. DAPA@MSN and DAPA@MSN-CHP were co-loaded with Fluorescein isothiocyanate (FITC) for intuitive

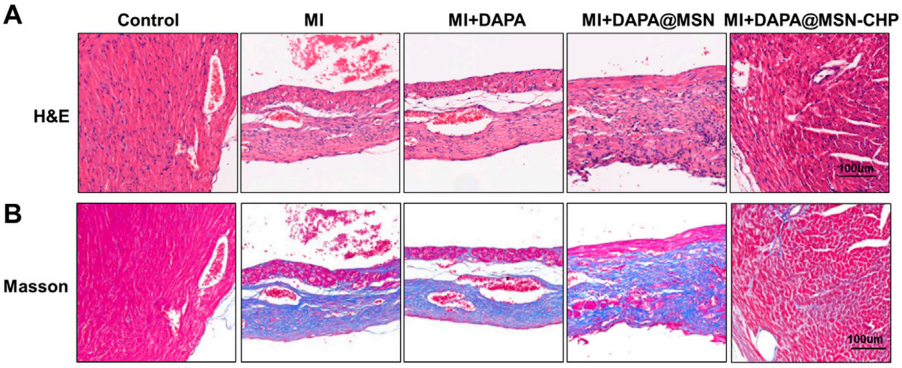

FIGURE 5
Representative H & E images **(A)** Masson's trichrome stain images **(B)** of cardiac sections after MI, MI + DAPA, MI + DAPA@MSN and MI + DAPA@MSN-CHP treatments. The healthy mice were set as controls.

observation under a Confocal Laser Scanning Microscope (CLSM). They were then added to two groups of cardiomyocytes for 12 h before CLSM observation. FITC signals at 550 nm were collected under 488 nm excitation. As shown in Figure 3A, DAPA@MSN-CHP presents stronger fluorescent spots than DAPA@MSN with no targeted protein modification. The fluorescent spots of DAPA@MSN-CHP were mainly localized in the cytoplasm. At present, the target receptor of CHP and the mechanism of its specific targeting to ischemic tissue are not yet clear, but CHP has been proved to have good targeting delivery ability in a number of studies on ischemic myocardial targeted substance delivery systems. In a gene delivery study, Young-Wook Won et al. used CHP as a guide to achieve increased gene expression in H9C2 cells under hypoxic conditions (Won et al., 2013). Another study reported CHP as a targeting peptide to increase the uptake of peptide-labeled exosomes by oxidatively damaged H9C2 cells (Vandergriff et al., 2018). Our findings also indicate the precise binding ability of CHP to the receptor on the membrane of cardiomyocytes.

Previous reports indicate that hypoxia also affects most sites of heart diseases such as HF, cardiac arrest and heart attack (Jianqiang et al., 2015; Amofa et al., 2017; Hesse et al., 2018). The hypoxic conditions may originate from inadequate blood oxygen concentration delivery following vessel impairment in the damaged tissues. Furthermore, Hypoxia-inducible factor 1-α (HIF-1α) promotes the adaptation to hypoxia-related stress through increasing oxygen delivery and decreasing oxygen consumption (Anand et al., 2007; Kumar et al., 2020; Nguyen et al., 2021). Accordingly, H9C2 cells were treated with hypoxia, and than the expression level of HIF-1α was significantly increased (Figure 3B), indicating the successful establishment of myocardial hypoxia model. Based on this, we used the cardiomyocyte hypoxia model to study the effect of DAPA@MSN-CHP *in vitro*.

We then explored cell viability of cardiomyocytes under conditions of both normoxia and hypoxia based on our MSN-CHP. Figure 3C shows negligible cytotoxicity with the DDS concentration as high as 400 μg/ml in both normoxia and hypoxia, compared with a control group. These findings further demonstrate the superior biocompatibility of the MSN. Cell viability of our DDS was also studied under various conditions. Our DDS promoted significantly higher cell activity in hypoxia (~77%). In contrast, only ~51%, 61%, 70% of hypoxic cells survived in the solvent, DAPA, and DAPA@MSN incubation conditions, respectively (Figure 3D). This result derives from the efficient and precise release of our DDS. DAPA successfully transported and gradually released the drug in the weak acid intracellular microenvironment of HF cells in DAPA@MSN-CHP. Simultaneously, western-blot results demonstrated that our DDS improved the expression of cell survival-promoting factor (BCL-2) while reducing the expression of apoptotic factors Caspase-3 and BAX (Figure 3E). DAPA has been found to be effective in reducing cardiotoxicity and inhibiting apoptosis *in vitro* (Chang et al. 2022). Our results suggesting that the precise targeted delivery of DDS enhanced the intervention effect of DAPA on hypoxia-induced cardiomyocyte apoptosis.

## 3.3 *In vivo* HF repair capability of DAPA@MSN-CHP

Since the targeting mechanism of CHP is not yet clear, the *in vitro* results are insufficient to demonstrate the targeting ability of DAPA@MSN-CHP. Therefore, we investigated HF repair efficiency using an MI mice model. The MI model was constructed with a temporary ligation of the left anterior descending coronary artery for 0.5 h. These mice were divided into four groups: pure MI, free DAPA, DAPA@MSN and DAPA@MSN-CHP groups, with normal mice as the control group (Figure 4A). Body distribution of DAPA@MSN-CHP results shows that the novel DDS had the highest cardiac-targeting efficiency compared with DAPA and DAPA@MSN (Supplementary Figure S1). Studies have reported changes in

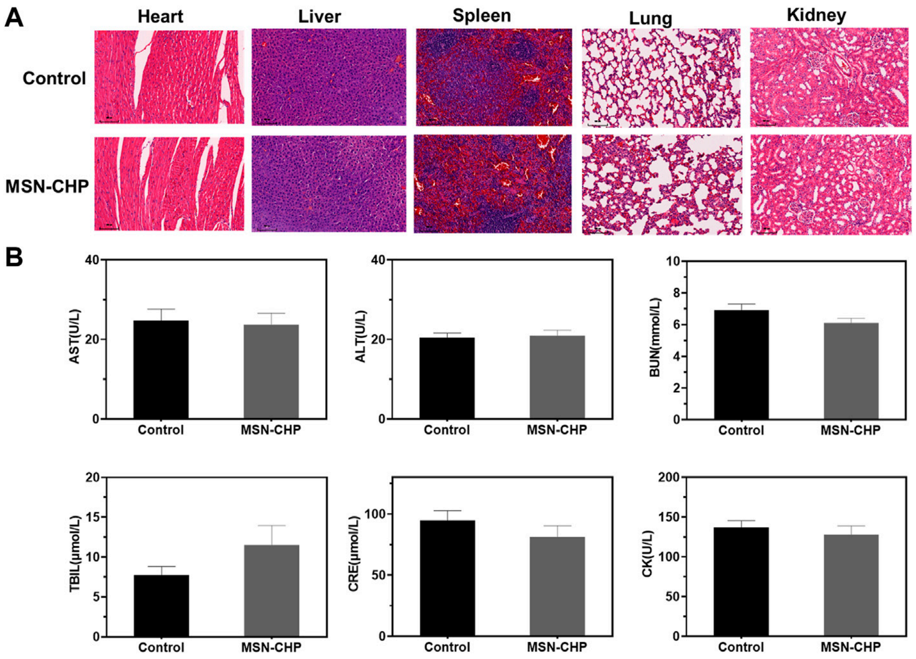

FIGURE 6
H&E-stained photographs of major organs after 3 days treatment of PBS and MSN-CHP **(A)**. Blood biochemistry results from PBS and MSN-CHP treated mice, respectively **(B)**.

protein expression and protein distribution in cardiomyocytes under ischemia and hypoxia conditions (Liu et al., 2014), suggesting that the unknown receptor protein of CHP may increase its binding to CHP through these changes to play a specific targeting role. In the study of Young-Wook Won et al. and Adam Vandergriff et al., CHP as a component of a drug delivery system was also reported to play an active role in targeting MI tissue *in vivo* (Won et al., 2013; Vandergriff et al., 2018).

Studies have shown that DAPA reduces heart failure exacerbations and improves symptoms in patients with heart failure and reduced ejection fraction (Kosiborod et al., 2020). After 1 month, the therapeutic efficiency of DDS was evaluated by detailed echocardiography analysis. The heart functions were carefully estimated by conventional M-mode echocardiography. Compared with the healthy group, the interventricular septum of the MI group without any administration became weak as septal amplitude decreased, proving the persistent and serious avascular necrosis in myocardium tissue. Compared with the no treatment condition, the morphology of the myocardial layer gradually improved in the echocardiogram image of the DAPA and DAPA@MSN groups. DAPA@MSN-CHP treatment significantly restored hearts, as shown by comparison with healthy hearts.

The conventional indicators of heart function were subsequently evaluated. The ejection fraction values of the left ventricle in normal, MI, DAPA, DAPA@MSN and DAPA@MSN-CHP groups were 69.2%, 22.3%, 44.6%, 50.8% and 63.1%, respectively (Figure 4B). Similar trend was also detected in the ultrasound photographs of whole heart that MI + DAPA@MSN-CHP displayed most effective MI repair capability with highest ejection fraction values (Supplementary Figure S2). The fractional shortening values of the left ventricle in healthy, MI, DAPA, DAPA@MSN and DAPA@MSN-CHP groups were 42.3%, 12.3%, 24.8%, 29.7% and 37.6%, respectively (Figure 4C). In contrast with the MI, DAPA, and DAPA@MSN groups, the DAPA@MSN-CHP treatment resulted in optimal performance in restoring both ejection fraction and fractional shortening. There was no significant difference between the normal group and the DAPA@MSN-CHP groups, demonstrating the superior repair capability of the DDS.

## 3.4 Histopathological evaluation of DAPA@MSN-CHP for HF repair

In the process of heart failure, pathological changes in cardiac tissue occur, mainly manifested as myocardial remodeling and inflammatory infiltration (de Boer et al., 2019). After various administrations, heart sections were stained with hematoxylin and eosin (H & E). The DAPA@MSN-CHP administration group was similar to the healthy mice and demonstrated a normal histoarchitecture with intact myocardial membranes, similar oval nuclei and regular cross striations (Figure 5A). In contrast, other groups showed histological alterations with myocardial separation and few scattered inflammatory cells. These atypical pathological phenomena were mainly caused by inflammatory leukocytes and wavy fibers. Masson's trichrome staining of heart tissue was also used to validate the associated collagen deposits and fibrotic transformation associated with MI. Pure MI, DAPA, and DAPA@MSN showed thick and dense interstitial collagen fibrils (blue) related to necrotic myocytes. DAPA@MSN-CHP and control groups exhibited normal heart histoarchitecture with slight interstitial collagen fibrils stained with blue (Figure 5B). All histopathological examination results demonstrated the superior therapeutic efficiency of MSN-based DDS to repair cardiac function following MI.

### 3.5 Biocompatibility evaluation *in vivo*

Finally, we herein evaluate the systematic toxicity of our MSN-based DDS *via* H&E tissue staining analysis and blood biochemistry assesement. The tissue of main orans including heart, liver, lung, spleen and kidney were dissected after the tail vein injection of MSN-CHP and then they were stained by H&E. As shown in Figure 6A, there was ignorable tissue damage in MI, DDS treated group, as compared with the control group (normal mice), testifying the superior biocompatibility of our MSN-based nanocarriers. For the blood biochemistry analysis, as displayed as liver functional makers including ALT (alanine aminotransferase), AST (asparatate aminotransferase), ALP (alkaline phosphatase), TBIL (total bilirubin), BUN (Blood urea nitrogen) and CRE (creatinine), no any variations of hepatic toxicity were found after MSN-CHP administration (Figure 6B). As indicator for heart muscle damage, CK (creatine kinase) value in the blood of MSN based DDS treated mice was also maintained at normal level (Figure 6B). The above results provide a validation that MSN-based nanocarriers bore no remarkable side effect *in vivo*.

## 4 Conclusion

We developed a straightforward approach to fabricate biocompatible and monodispersed MSNs of negligible toxicity. Their large surface area facilitated the DAPA encapsulation in the mesoporous channel, and the nanocarrier surface was then functionalized for cardiac-targeting peptides. The DDS was highly efficient in MI region in HF, and the DAPA could be precisely released in the hypoxic, apoptotic and weak acid intracellular environment. DAPA@MSN-CHP demonstrated optimal therapeutic efficiency toward MI model mice, restoring the MI hearts and making them comparable with those of the healthy group. MSN-based DDS provides a possible application of precise and effective repair of MI in clinical.

## Data availability statement

The original contributions presented in the study are included in the article/Supplementary Material, further inquiries can be directed to the corresponding authors.

## Ethics statement

The animal study was reviewed and approved by the Animal Research Ethics Committee of Shanghai Seventh People's Hospital.

## Author contributions

Conceptualization, LY, QW and YM; methodology, LY, QW and YM; software, YL and HY; validation, LY, QW and YM; formal analysis, YL; investigation, HY; resources, LY; data curation,QW; writing-original draft preparation, LY, QW and YM; writing-review and editing, LX and ML; visualization, YM; supervision, LY; project administration, LX; funding acquisition, ML. All authors have read and agreed to the published version of the manuscript.

## Funding

This research was financially supported by the National Natural Science Foundation of China (Nos. 81973649, 82174189), Key Laboratory of Emergency and Trauma (Hainan Medical University), Ministry of Education (Grant.KLET-202115), East China area and municipal-level TCM specialist disease alliance construction project of Shanghai Municipal Health Commission (ZY (2021-2023)-0302), General project of Pudong New Area Health Committee, Pudong New Area, Shanghai (PW2020A-18), Shanghai Seventh People's Hospital "Qumingxing" talent training plan (QMX2020-06) and Talents Training Program of the Seventh People's Hospital, Shanghai University of Traditional Chinese Medicine (Grant No. XX2022-12).

## Conflict of interest

The authors declare that the research was conducted in the absence of any commercial or financial relationships that could be construed as a potential conflict of interest.

## Publisher's note

All claims expressed in this article are solely those of the authors and do not necessarily represent those of their

## Supplementary material

The Supplementary Material for this article can be found online at: https://www.frontiersin.org/articles/10.3389/fchem.2022.1013910/full#supplementary-material

## References

Amofa, D., Hulin, A., Nakada, Y., Sadek, H. A., and Yutzey, K. E. (2017). Hypoxia promotes primitive glycosaminoglycan-rich extracellular matrix composition in developing heart valves. *Am. J. Physiol. Heart Circ. Physiol.* 313 (6), H1143–H1154. doi:10.1152/ajpheart.00209.2017

Anand, R. J., Gribar, S. C., Li, J., Kohler, J. W., Branca, M. F., Dubowski, T., et al. (2007). Hypoxia causes an increase in phagocytosis by macrophages in a HIF-1alpha-dependent manner. *J. Leukoc. Biol.* 82 (5), 1257–1265. doi:10.1189/jlb.0307195

Anwar, A., Khan, H. A., Hafeez, S., and Firdous, K. (2016). A comparative study of creatine Kinase-MB and troponin levels among diabetic and non diabetic patients with acute MI. *PJMHS* 10 (1), 296–297.

Bao, R., Tan, B., Liang, S., Zhang, N., Wang, W., and Liu, W. (2017). A π-π conjugation-containing soft and conductive injectable polymer hydrogel highly efficiently rebuilds cardiac function after myocardial infarction. *Biomaterials* 122, 63–71. doi:10.1016/j.biomaterials.2017.01.012

Chakroborty, D., Sarkar, C., Yu, H., Wang, J., Liu, Z., Dasgupta, P. S., et al. (2011). Dopamine stabilizes tumor blood vessels by up-regulating angiopoietin 1 expression in pericytes and Kruppel-like factor-2 expression in tumor endothelial cells. *Proc. Natl. Acad. Sci. U. S. A.* 108 (51), 20730–20735. doi:10.1073/pnas.1108696108

Chang, W. T., Shih, J. Y., Lin, Y. W., Chen, Z. C., Kan, W. C., Lin, T. H., et al. (2022). Dapagliflozin protects against doxorubicin-induced cardiotoxicity by restoring STAT3. *Arch. Toxicol.* 96 (7), 2021–2032. doi:10.1007/s00204-022-03298-y

Che, Y. W., Chen, P. J., Hu, S. H., Chen, I. W., and Chen, S. Y. (2014). NIR-triggered synergic photo-chemothermal therapy delivered by reduced graphene oxide/carbon/mesoporous silica nanocookies. *Adv. Funct. Mat.* 24, 451–459. doi:10.1002/adfm.201301763

Chen, K., Chang, C., Liu, Z., Zhou, Y., Xu, Q., Li, C., et al. (2020). Hyaluronic acid targeted and pH-responsive nanocarriers based on hollow mesoporous silica nanoparticles for chemo-photodynamic combination therapy. *Colloids Surfaces B Biointerfaces* 194, 111166. doi:10.1016/j.colsurfb.2020.111166

Cheng, Y. J., Hu, J. J., Qin, S. Y., Zhang, A. Q., and Zhang, X. Z. (2020). Recent advances in functional mesoporous silica-based nanoplatforms for combinational photo-chemotherapy of cancer. *Biomaterials* 232, 119738. doi:10.1016/j.biomaterials.2019.119738

Cowper, P. A., Knight, J. D., Davidson-Ray, L., Peterson, E. D., Wang, T. Y., Mark, D. B., et al. (2019). Acute and 1-year hospitalization costs for acute myocardial infarction treated with percutaneous coronary intervention: Results from the TRANSLATE-ACS registry. *J. Am. Heart Assoc.* 8 (8), e011322. doi:10.1161/JAHA.118.011322

Das, P., and Jana, N. R. (2015). Dopamine functionalized polymeric nanoparticle for targeted drug delivery. *RSC Adv.* 5 (42), 33586–33594. doi:10.1039/C5RA03302K

de Boer, R. A., De Keulenaer, G., Bauersachs, J., Brutsaert, D., Cleland, J. G., Diez, J., et al. (2019). Towards better definition, quantification and treatment of fibrosis in heart failure. A scientific roadmap by the Committee of Translational Research of the Heart Failure Association (HFA) of the European Society of Cardiology. *Eur. J. Heart Fail.* 21 (3), 272–285. doi:10.1002/ejhf.1406

Desta, L., Jernberg, T., Lofman, I., Hofman-Bang, C., Hagerman, I., Spaak, J., et al. (2015). Incidence, temporal trends, and prognostic impact of heart failure complicating acute myocardial infarction. The SWEDEHEART registry (Swedish web-system for enhancement and development of evidence-based care in heart disease evaluated according to recommended therapies): A study of 199, 851 patients admitted with index acute myocardial infarctions, 1996 to 2008. *JACC Heart Fail.* 3 (3), 234–242. doi:10.1016/j.jchf.2014.10.007

Dudas, K., Lappas, G., Stewart, S., and Rosengren, A. (2011). Trends in out-of-hospital deaths due to coronary heart disease in Sweden (1991 to 2006). *Circulation* 123 (1), 46–52. doi:10.1161/CIRCULATIONAHA.110.964999

Hesse, M., Welz, A., and Fleischmann, B. K. (2018). Heart regeneration and the cardiomyocyte cell cycle. *Pflugers Arch. - Eur. J. Physiol.* 470 (2), 241–248. doi:10.1007/s00424-017-2061-4

Hung, J., Teng, T. H., Finn, J., Knuiman, M., Briffa, T., Stewart, S., et al. (2013). Trends from 1996 to 2007 in incidence and mortality outcomes of heart failure after acute myocardial infarction: A population-based study of 20, 812 patients with first acute myocardial infarction in western Australia. *J. Am. Heart Assoc.* 2 (5), e000172. doi:10.1161/JAHA.113.000172

Jafari, S., Derakhshankhah, H., Alaei, L., Fattahi, A., Varnamkhasti, B. S., and Saboury, A. A. (2019). Mesoporous silica nanoparticles for therapeutic/diagnostic applications. *Biomed. Pharmacother.* 109, 1100–1111. doi:10.1016/j.biopha.2018.10.167

Jenča, D., Melenovský, V., Stehlik, J., Staněk, V., Kettner, J., Kautzner, J., et al. (2021). Heart failure after myocardial infarction: Incidence and predictors. *Esc. Heart Fail.* 8 (1), 222–237. doi:10.1002/ehf2.13144

Jianqiang, P., Ping, Z., Xinmin, F., Zhenhua, Y., Ming, Z., and Ying, G. (2015). Expression of hypoxia-inducible factor 1 alpha ameliorate myocardial ischemia in rat. *Biochem. Biophys. Res. Commun.* 465 (4), 691–695. doi:10.1016/j.bbrc.2015.08.046

Kanki, S., Jaalouk, D. E., Lee, S., Yu, A. Y., Gannon, J., and Lee, R. T. (2011). Identification of targeting peptides for ischemic myocardium by *in vivo* phage display. *J. Mol. Cell. Cardiol.* 50 (5), 841–848. doi:10.1016/j.yjmcc.2011.02.003

Kerr, A., Sagita, E., Mansfied, E. D. H., Nguyen, T. H., Feeney, O. M., Pouton, C. W., et al. (2022). Polymeric nanotubes as drug delivery Vectors─Comparison of covalently and supramolecularly assembled constructs. *Biomacromolecules* 23 (6), 2315–2328. doi:10.1021/acs.biomac.2c00063

Kosiborod, M. N., Jhund, P. S., Docherty, K. F., Diez, M., Petrie, M. C., Verma, S., et al. (2020). Effects of dapagliflozin on symptoms, function, and quality of life in patients with heart failure and reduced ejection fraction: Results from the DAPA-HF trial. *Circulation* 141 (2), 90–99. doi:10.1161/CIRCULATIONAHA.119.044138

Kumar, T., Pandey, R., and Chauhan, N. S. (2020). Hypoxia inducible factor-1α: The curator of gut homeostasis. *Front. Cell. Infect. Microbiol.* 10, 227. doi:10.3389/fcimb.2020.00227

Lee, C. H., Cheng, S. H., Huang, I. P., Souris, J. S., Yang, C. S., Mou, C. Y., et al. (2010). Intracellular pH-responsive mesoporous silica nanoparticles for the controlled release of anticancer chemotherapeutics. *Angew. Chem. Int. Ed.* 49 (44), 8214–8219. doi:10.1002/anie.201002639

Li, X., Zhang, Y., Ren, X., Wang, Y., Chen, D., Li, Q., et al. (2021). Ischemic microenvironment-responsive therapeutics for cardiovascular diseases. *Adv. Mat.* 33 (52), e2105348. doi:10.1002/adma.202105348

Li, Z., Barnes, J. C., Bosoy, A., Stoddart, J. F., and Zink, J. I. (2012). Mesoporous silica nanoparticles in biomedical applications. *Chem. Soc. Rev.* 41 (7), 2590–2605. doi:10.1039/c1cs15246g

Liu, M., Li, M., Sun, S., Li, B., Du, D., Sun, J., et al. (2014). The use of antibody modified liposomes loaded with AMO-1 to deliver oligonucleotides to ischemic myocardium for arrhythmia therapy. *Biomaterials* 35 (11), 3697–3707. doi:10.1016/j.biomaterials.2013.12.099

Luo, L., Tang, J., Nishi, K., Yan, C., Dinh, P. U., Core, J., et al. (2016). Fabrication of synthetic mesenchymal stem cells for the treatment of acute myocardial infarction in mice. *Circ. Res.* 120 (11), 1768–1775. doi:10.1161/circresaha.116.310374

McMurray, J. J. V., DeMets, D. L., Inzucchi, S. E., Kober, L., Kosiborod, M. N., Langkilde, A. M., et al. (2019b). A trial to evaluate the effect of the sodium-glucose co-transporter 2 inhibitor dapagliflozin on morbidity and mortality in patients with heart failure and reduced left ventricular ejection fraction (DAPA-HF). *Eur. J. Heart Fail.* 21 (5), 665–675. doi:10.1002/ejhf.1432

McMurray, J. J. V., DeMets, D. L., Inzucchi, S. E., Kober, L., Kosiborod, M. N., Langkilde, A. M., et al. (2019a). The dapagliflozin and prevention of adverse-outcomes in heart failure (DAPA-HF) trial: Baseline characteristics. *Eur. J. Heart Fail.* 21 (11), 1402–1411. doi:10.1002/ejhf.1548

Meng, H., Xue, M., Xia, T., Zhao, Y. L., Tamanoi, F., Stoddart, J. F., et al. (2010). Autonomous *in vitro* anticancer drug release from mesoporous silica nanoparticles by pH-sensitive nanovalves. *J. Am. Chem. Soc.* 132 (36), 12690–12697. doi:10.1021/ja104501a

Mohanty, S. K., Swamy, M. K., Sinniah, U. R., and Anuradha, M. (2017). Leptadenia reticulata (retz.) wight & arn. (Jivanti): Botanical, agronomical, phytochemical, pharmacological, and biotechnological aspects. *Molecules* 22 (6), 1019. doi:10.3390/molecules22061019

Nguyen, T. H., Conotte, S., Belayew, A., Decleves, A. E., Legrand, A., and Tassin, A. (2021). Hypoxia and hypoxia-inducible factor signaling in muscular dystrophies: Cause and consequences. *Int. J. Mol. Sci.* 22 (13), 7220. doi:10.3390/ijms22137220

Nigam, P. K. (2007). Biochemical markers of myocardial injury. *Indian J. Clin. biochem.* 22 (1), 10–17. doi:10.1007/BF02912874

Rodrigues, T., Reker, D., Schneider, P., and Schneider, G. (2016). Counting on natural products for drug design. *Nat. Chem.* 8 (6), 531–541. doi:10.1038/nchem.2479

Roger, V. L. (2013). Epidemiology of heart failure. *Circ. Res.* 113 (6), 646–659. doi:10.1161/CIRCRESAHA.113.300268

Sahoo, B., Devi, K. S., Dutta, S., Maiti, T. K., Pramanik, P., and Dhara, D. (2014). Biocompatible mesoporous silica-coated superparamagnetic manganese ferrite nanoparticles for targeted drug delivery and MR imaging applications. *J. Colloid Interface Sci.* 431, 31–41. doi:10.1016/j.jcis.2014.06.003

Sapino, S., Ugazio, E., Gastaldi, L., Miletto, I., Berlier, G., Zonari, D., et al. (2015). Mesoporous silica as topical nanocarriers for quercetin: Characterization and *in vitro* studies. *Eur. J. Pharm. Biopharm.* 89, 116–125. doi:10.1016/j.ejpb.2014.11.022

Sathisha, T. G., Manjunatha, G. B. K., Avinash, S. S., Shetty, J., and Devaki, R. N. (2011). Microalbuminuria in non-diabetic, non-hypertensive myocardial infarction in South Indian patients with relation to lipid profile and cardiac markers. *J. Clin. Diagnostic Res.* 5 (6), 1158–1160.

Shen, D., Yang, J., Li, X., Zhou, L., Zhang, R., Li, W., et al. (2014). Biphase stratification approach to three-dimensional dendritic biodegradable mesoporous silica nanospheres. *Nano Lett.* 14 (2), 923–932. doi:10.1021/nl404316v

Snider, J. C., Riley, L. A., Mallory, N. T., Bersi, M. R., Umbarkar, P., Gautam, R., et al. (2021). Targeting 5-HT$_{2B}$ receptor signaling prevents border zone expansion and improves microstructural remodeling after myocardial infarction. *Circulation* 143 (13), 1317–1330. doi:10.1161/circulationaha.120.051517

Sokolsky-Papkov, M., Agashi, K., Olaye, A., Shakesheff, K., and Domb, A. J. (2007). Polymer carriers for drug delivery in tissue engineering. *Adv. Drug Deliv. Rev.* 59 (4-5), 187–206. doi:10.1016/j.addr.2007.04.001

Steg, P. G., Dabbous, O. H., Feldman, L. J., Cohen-Solal, A., Aumont, M. C., Lopez-Sendon, J., et al. (2004). Determinants and prognostic impact of heart failure complicating acute coronary syndromes: Observations from the global registry of acute coronary events (GRACE). *Circulation* 109 (4), 494–499. doi:10.1161/01.CIR.0000109691.16944.DA

Sulo, G., Igland, J., Vollset, S. E., Nygard, O., Ebbing, M., Sulo, E., et al. (2016). Heart failure complicating acute myocardial infarction; burden and timing of occurrence: A nation-wide analysis including 86 771 patients from the cardiovascular disease in Norway (CVDNOR) project. *J. Am. Heart Assoc.* 5 (1), e002667. doi:10.1161/JAHA.115.002667

Sun, X., Shao, H., Xiang, K., Yan, Y., Yu, X., Li, D., et al. (2017). Poly(dopamine)-modified carbon nanotube multilayered film and its effects on macrophages. *Carbon* 113, 176–191. doi:10.1016/j.carbon.2016.11.040

Swamy, M. K., and Sinniah, U. R. (2016). Patchouli (Pogostemon cablin Benth.): Botany, agrotechnology and biotechnological aspects. *Industrial Crops Prod.* 87, 161. doi:10.1016/j.indcrop.2016.04.032

Syed, U., Ahmed, P., Sheikholeslami, P., Christopher, M., Colloid, E. J., and Science, P. (2012). Semi-batch control over functional group distributions in thermoresponsive microgels. *Colloid Polym. Sci.* 290, 1181. doi:10.1007/s00396-012-2642-x

Tao, Z., Morrow, M. P., Asefa, T., Sharma, K. K., Duncan, C., Anan, A., et al. (2008). Mesoporous silica nanoparticles inhibit cellular respiration. *Nano Lett.* 8 (5), 1517–1526. doi:10.1021/nl080250u

Ugazio, E., Gastaldi, L., Brunella, V., Scalarone, D., Jadhav, S. A., Oliaro-Bosso, S., et al. (2016). Thermoresponsive mesoporous silica nanoparticles as a carrier for skin delivery of quercetin. *Int. J. Pharm. X.* 511 (1), 446–454. doi:10.1016/j.ijpharm.2016.07.024

Vandergriff, A., Huang, K., Shen, D., Hu, S., Hensley, M. T., Caranasos, T. G., et al. (2018). Targeting regenerative exosomes to myocardial infarction using cardiac homing peptide. *Theranostics* 8 (7), 1869–1878. doi:10.7150/thno.20524

Wang, F., Wen, L., Liu, J., Peng, W., Meng, Z., Chen, Q., et al. (2020). Albumin nanocomposites with MnO2/Gd2O3 motifs for precise MR imaging of acute myocardial infarction in rabbit models. *Biomaterials* 230, 119614. doi:10.1016/j.biomaterials.2019.119614

Wang, K., Li, Z., Sun, Y., Liu, X., Ma, W., Ding, Y., et al. (2021). Dapagliflozin improves cardiac function, remodeling, myocardial apoptosis, and inflammatory cytokines in mice with myocardial infarction. *J. Cardiovasc. Transl. Res.* doi:10.1007/s12265-021-10192-y

Wilczewska, A. Z., Niemirowicz, K., Markiewicz, K. H., and Car, H. (2012). Nanoparticles as drug delivery systems. *Pharmacol. Rep.* 64 (5), 1020–1037. doi:10.1016/s1734-1140(12)70901-5

Won, Y. W., McGinn, A. N., Lee, M., Bull, D. A., and Kim, S. W. (2013). Targeted gene delivery to ischemic myocardium by homing peptide-guided polymeric carrier. *Mol. Pharm.* 10 (1), 378–385. doi:10.1021/mp300500y

Yakobson, B. I., and Avouris, P. J. (2001). "Mechanical properties of carbon nanotubes," in *Carbon nanotubes. Topics in applied physics*. Editors M. S. Dresselhaus, G. Dresselhaus, and P. Avouris (Berlin, Heidelberg: Springer), Vol. 80. doi:10.1007/3-540-39947-X_12

Yang, M., Li, H., Javadi, A., and Gong, S. (2010). Multifunctional mesoporous silica nanoparticles as labels for the preparation of ultrasensitive electrochemical immunosensors. *Biomaterials* 31 (12), 3281–3286. doi:10.1016/j.biomaterials.2010.01.033

Zhao, T., Wu, W., Sui, L., Huang, Q., Nan, Y., Liu, J., et al. (2022). Reactive oxygen species-based nanomaterials for the treatment of myocardial ischemia reperfusion injuries. *Bioact. Mat.* 7, 47–72. doi:10.1016/j.bioactmat.2021.06.006

Zhu, M., Wang, H., Liu, J., He, H., Hua, X., He, Q., et al. (2011). A mesoporous silica nanoparticulate/β-TCP/BG composite drug delivery system for osteoarticular tuberculosis therapy. *Biomaterials* 32 (7), 1986–1995. doi:10.1016/j.biomaterials.2010.11.025

Zhu, Y., Shi, J., Shen, W., Dong, X., Feng, J., Ruan, M., et al. (2005). Stimuli-responsive controlled drug release from a hollow mesoporous silica sphere/polyelectrolyte multilayer core-shell structure. *Angew. Chem. Int. Ed.* 44 (32), 5083–5087. doi:10.1002/anie.200501500

frontiers | Frontiers in Chemistry

TYPE Review
PUBLISHED 09 December 2022
DOI 10.3389/fchem.2022.1063152

OPEN ACCESS

EDITED BY
Pengfei Xu,
National University of Singapore,
Singapore

REVIEWED BY
Jun Cao,
Beijing University of Technology, China
Kai Han,
University of Michigan, United States

*CORRESPONDENCE
Xiang Li,
li.xiang@whu.edu.cn
Xing Niu,
xniu@cmu.edu.cn
Wei Wei,
wei.wei@whu.edu.cn

†These authors have contributed equally to this work and share first authorship

SPECIALTY SECTION
This article was submitted to
Nanoscience,
a section of the journal
Frontiers in Chemistry

RECEIVED 07 October 2022
ACCEPTED 28 November 2022
PUBLISHED 09 December 2022

CITATION
Yu S, Chen L, Xu H, Long S, Jiang J, Wei W, Niu X and Li X (2022), Application of nanomaterials in diagnosis and treatment of glioblastoma.
*Front. Chem.* 10:1063152.
doi: 10.3389/fchem.2022.1063152

# Application of nanomaterials in diagnosis and treatment of glioblastoma

Shuangqi Yu[1,2†], Lijie Chen[3†], Hongyu Xu[1,2†], Shengrong Long[1,2], Jiazhi Jiang[1,2], Wei Wei[1,2]*, Xing Niu[3]* and Xiang Li[1,2]*

[1]Department of Neurosurgery, Zhongnan Hospital, Wuhan University, Wuhan, Hubei, China, [2]Brain Research Center, Zhongnan Hospital, Wuhan University, Wuhan, Hubei, China, [3]China Medical University, Shenyang, Liaoning, China

Diagnosing and treating glioblastoma patients is currently hindered by several obstacles, such as tumor heterogeneity, the blood-brain barrier, tumor complexity, drug efflux pumps, and tumor immune escape mechanisms. Combining multiple methods can increase benefits against these challenges. For example, nanomaterials can improve the curative effect of glioblastoma treatments, and the synergistic combination of different drugs can markedly reduce their side effects. In this review, we discuss the progression and main issues regarding glioblastoma diagnosis and treatment, the classification of nanomaterials, and the delivery mechanisms of nanomedicines. We also examine tumor targeting and promising nano-diagnosis or treatment principles based on nanomedicine. We also summarize the progress made on the advanced application of combined nanomaterial-based diagnosis and treatment tools and discuss their clinical prospects. This review aims to provide a better understanding of nano-drug combinations, nano-diagnosis, and treatment options for glioblastoma, as well as insights for developing new tools.

KEYWORDS

**glioblastoma, glioma, tumor targeting, nanomaterial, blood-brain barrier**

## 1 Introduction

Glioblastoma (GBM) is a general term for tumors derived from glial cells and neuronal cells. It is the most common malignant tumor in the brain, accounting for 40%–50% of all intracranial tumors (Chen et al., 2017). The World Health Organization (WHO) classifies gliomas by cell type: astrocytoma, glioblastoma, and oligodendroglioma, and by malignancy grade (WHO I, II, III, IV). In 2021, the WHO CNS5 updated the molecular biomarkers for different tumor types, bringing more benefits and meaningful guidance to clinical practice. The WHO CNS5 has taken a new approach to classifying gliomas, glioneuronal tumors, and neuronal tumors, dividing them into six families: adult-type diffuse gliomas, pediatric-type diffuse low-grade gliomas, pediatric-type diffuse high-grade gliomas, circumscribed astrocytic gliomas, glioneuronal and neuronal tumors, and ependymomas (Louis et al., 2021). At present, temozolomide chemotherapy combined with radiotherapy after maximum feasible resection is the primary clinical treatment for adult primary GBM. With the emergence of many targeted therapies, bevacizumab and programmed death -1 (PD-1) have also been used in the standardized treatment of GBM (Khasraw et al., 2012; Cloughesy et al., 2019; Zhao M. et al., 2020; Detti et al., 2021). However, GBMs grow infiltratively and are not clearly demarcated from normal tissues. They are, therefore, difficult to completely remove surgically and have high recurrence rates. Meanwhile, the blood-brain barrier (BBB), a highly selective semipermeable structural and chemical barrier (Cai et al., 2018), hinders drug delivery to the brain. Thus, drugs rarely reach effective therapeutic concentrations at the tumor site, limiting the effect of radiotherapy and chemotherapy. Due to these obstacles, GBMs have high mortality rates. To overcome this, nanomaterials have been used as a new treatment modality. They have many interesting characteristics, such as small size and targetable transport, making them good delivery tools for drugs, genes, or proteins across cells or the BBB.

Nanomaterials are materials with at least one dimension in the three-dimensional space in the nanoscale or composed of such materials as basic units. Nanomaterials have small particle sizes, controllable texture, and strong plasticity. In GBM treatment, nanomaterials are mainly used as carriers for radiotherapy and chemotherapy drugs (Zhao M. et al., 2020), helping drugs cross the BBB and maintain the necessary blood drug concentration. Additionally, nanomaterials can cause tumor cell necrosis by affecting the tumor microenvironment (Zanganeh et al., 2019). For example, a nanocomposite drug consisting of a polyglycerol functionalized doxorubicin-containing nanodiamond was designed to re-adjust the inhibitory glioblastoma immune microenvironment. This nanocomposite provided GBM with immunosuppressive microenvironment by activating autophagy. This rebuilding promoted the anti-GBM immune response and strengthened the activation of dendritic cells (Li et al., 2019).

The primary purpose of nanomaterials is to improve the solubility, stability, and effective concentration of drugs and reduce their systemic toxicity (Zhao M. et al., 2020). The main nanomaterials used in current research are nanoparticles (NPs). They can be inorganic, polymeric, or bionic. Each type has its advantages. Inorganic NPs, for example, are highly stable, and their physical and chemical properties can be adjusted by using suitable materials and sizes (Bharti et al., 2019). In addition, polymeric nanoparticles can encapsulate drugs by electrostatic or covalent bonding, maintaining their blood concentration and thereby improving the bioavailability of drugs. Most importantly, modified polymeric NPs can aggregate at specific sites. Biomimetic nanocomposites have higher biological stability and can escape the immune system, allowing drugs to act on the target continuously without being cleared by the liver and kidney. Besides nanoparticles, other nanomaterials (e.g., liposomes, quantum dots, cellular and extracellular vesicles, or virus-like particles) are frequently used in GBM treatment research.

The emergence of nanomaterials has brought opportunities for the diagnosis and treatment of GBM, and their various characteristics can help overcome the current clinical challenges of GBM. Here, we review the current progress on the applications of nanomaterials in GBM treatment research to provide insights for developing new nano-drug combinations, nano-diagnosis, and GBM treatment schemes.

# 2 Blood brain barrier and delivery mechanism of nanomaterials

## 2.1 Blood brain barrier

The blood-brain barrier (BBB) is a specialized structure within the central nervous system that acts as a physical and metabolic barrier restricting transport between the blood and neural tissues. It consists of brain microvascular endothelial cells, pericytes, astrocytes, neurons, and a basement membrane. This physical barrier protects the brain and maintains the stability of the intracranial environment. The excellent barrier properties of the BBB protect the brain from harmful macromolecules and pathogens present in the blood (Xie et al., 2019). However, this barrier also hinders traditional drug delivery and affects drug efflux. Currently, most small-molecule drugs and almost all macromolecular drugs (e.g., recombinant proteins, therapeutic antibodies, and nucleic acids) cannot cross the BBB (Baratta, 2018). Thus, more and more researchers pay attention to nanomaterials, as shown in many clinical trials on the diagnosis and treatment of GBM (Dong, 2018). The delivery mechanisms of nanomaterials can be divided into passive targeting and active targeting (Zhao M. et al., 2020).

## 2.2 Passive targeting

In passive targeting, a drug of a specific size is injected through the BBB into the abnormal, porous vascular endothelium of the tumor. Since the tumor vascular endothelium lacks appropriate drainage, the drug remains in the tumor area for a long time. This phenomenon is also known as the enhanced permeability and retention (EPR) effect and was first proposed by Matsumura and Maeda in 1986 (Matsumura and Maeda, 1986). However, current studies have shown that the EPR effect is unstable and varies significantly among different tumors. Besides, the EPR effect achieved in rodent models cannot be reproduced clinically because human tumors have heterogeneity or lack fenestrations in the tumor endothelium, acidic and anoxic areas, low and heterogeneous pericyte coverage, and high interstitial fluid pressure induced by a dense extracellular matrix (Danhier, 2016).

## 2.3 Active targeting

Active targeting is a non-invasive approach that involves transporting drugs to target organs using site-specific ligands. In particular, drug-loaded nanocarriers that can target brain capillary endothelial cells and brain tumor cells show potential in oncology (Béduneau et al., 2007). In active targeting, nanocarriers enter cells by taking advantage of ligand-receptor interactions. So far, active targeting nanomaterials have been applied to the diagnosis and treatment of various malignant tumors, such as liver cancer, lung cancer, and lymphoma (Falgàs et al., 2020; Kaps and Schuppan, 2020). Developing active targeting nanomaterials able to cross the BBB requires understanding how to use the brain capillary endothelium. Nevertheless, the active targeting of the BBB represents a promising non-invasive strategy for improving anti-glioblastoma drug delivery (Miranda et al., 2017). Active targeting can be further subdivided into adsorptive-mediated, carrier-mediated, receptor-mediated, and cell-mediated delivery, which target cells in different ways.

### 2.3.1 Adsorptive-mediated delivery

Adsorptive-mediated endocytosis (AMT) can deliver drugs to the brain through the BBB by allowing cationic molecules to bind to and be adsorbed onto the surface of the endothelial cell lumen. Adsorption-mediated transcytosis is initiated by the electrostatic interaction between positively charged ligands and negatively charged cell membranes. Nanocarriers then enter cells through clathrin-dependent endocytosis (Patel and Patel, 2017). Cationic proteins combined with cell-penetrating peptides (CPPs) can improve transport. With their short amino acid sequence, CPPs can interact with cell membranes and pass through cell membranes by energy-dependent and energy-independent mechanisms. Studies have shown that cationic CPPs have significantly more flux to the brain parenchyma than amphiphilic CPPs *in vivo* (Komin et al., 2017). Due to electrostatic interactions, cationic CPPs are easily captured by intracellular organelles to some extent. The drug-CPP linkage type substantially affects their ability to cross the BBB. Liu et al. (2014) compared the effects of amide, maleimide, and disulfide linkers linking the endorphin 1 to the CPP synB3 on BBB crossing efficiency. The disulfide linkage was the most efficient, and it was able to release the free drug in the brain. The adsorption-mediated transcytosis combined with a targeting strategy can effectively improve the EPR effect and reduce nonspecific uptake. Srimanee et al. (2018) developed a non-covalent CPP-targeting peptide (CPP-TP) complex with the CPP PepFect 14 and a hexaglutamate-modified angiopep-2 (ANG), as a targeting peptide. This complex showed enhanced penetration ability and glioblastoma cell specificity as an siRNA carrier. During the last decades, nanoparticles with various compositions have been developed, such as polymeric nanoparticles (PPs), gold NPs, gadolinium NPs, selenium NPs, or protein-based NPs (Gupta and Sharma, 2019).

### 2.3.2 Carrier-mediated delivery

Carrier-mediated delivery is initiated by combining a designed nanocarrier and a specific transporter protein (Bourganis et al., 2018). This drug delivery system consists of nanocarriers (such as liposomes, NPs, polymeric micelles, dendrimers, or polymersomes) and ligands for various receptors, including transferrin receptor (TfR), lactoferrin receptor (LfR), low-density lipoprotein receptor (LDLR), and folate receptor (FR) (Chen et al., 2014; Wang et al., 2015). Ligand-modified drug carriers deliver drugs to the receptor-containing target cells like “guided missiles” (Liu et al., 2021).

Based on transport direction and substrate, transport modes can be divided into three categories: 1) The system pumping blood into the brain, which transports essential nutrients to the brain, including glucose, amino acids, and nucleotides. 2) The drug efflux pumps expelling exogenous substances out of the peripheral circulation to prevent them from entering the brain. 3) The efflux system from the brain to the blood, which mainly removes metabolic waste and neurotoxic substances in the interstitial fluid of the brain. Among them, the pumping system is the breakthrough point of carrier-mediated delivery. Nanocarriers going through the pumping system are generally designed as nutritional analogs with a high affinity for transporters, so their molecular weight is generally small. Cell-mediated delivery can be used in anticancer therapy (Naik et al., 2021). For example, Naik et al. (2021) developed doxorubicin-containing liposomes and confirmed that conjugating these liposomes with a ligand mimic increased their antiproliferative activity on cancer cells overexpressing the corresponding receptor.

### 2.3.3 Receptor-mediated delivery

Targeting receptors that mediate endocytosis allows more robust targeting than with adsorption-mediated and carrier-mediated delivery because of the high specificity of the ligand-receptor interaction. In one study, cationic liposomes loaded with temozolomide were encapsulated in a multilayer crown of plasma proteins with a natural affinity for the folic acid (FA) receptor, which is highly expressed in the BBB (Tang et al., 2021). In an *in vitro* BBB model, these cationic liposomes with multilayered biomolecular crowns exhibited high ingestion by endothelial cells of human umbilical vein, which promoted the anticancer effect of temozolomide in U-87 MG cells (Arcella et al., 2018). Mram Alho *et al.* (Ramalho et al., 2018) developed stable polylactic acid-co-glycolic acid nanoparticles functionalized with the OX26 monoclonal antibody for the transferrin receptor. These nanoparticles delivered temozolomide, an anti-glioma agent.

Up to now, researchers have used many ligands of receptors on the BBB or glioma cells as targeting moieties for BBB

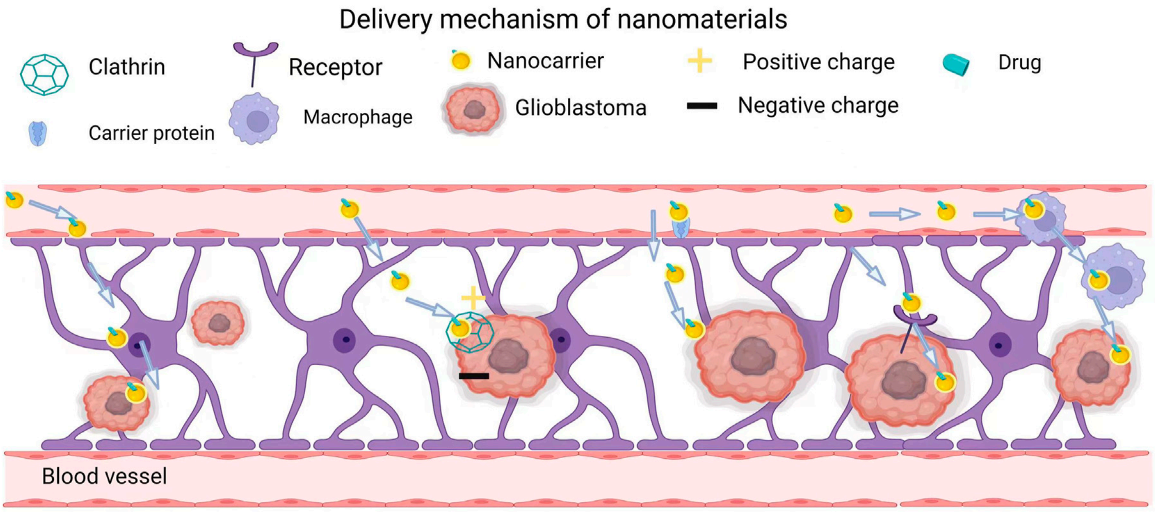

FIGURE 1
Delivery mechanism of nanomaterials.

crossover and/or glioma-targeted drug delivery, such as peptides (Wang et al., 2015). In addition, more and more studies have proved that BBB/glioma-specific targeting nanocarriers can help drugs selectively target glioma cells, increasing their therapeutic efficiency while reducing systemic toxicity (Wang et al., 2017; Ramalho et al., 2018). Receptor-mediated drug delivery may allow membrane-impermeable drugs to penetrate target cells and activate natural signaling cascades (McPherson et al., 2001).

Besides directly targeting tumor surface receptors, the receptor-mediated pathway includes three important steps, including the formation of ligand-receptor complexes, transport through the cytoplasm of endothelial cells, and extracellular secretion outside the base of the BBB (Azarmi et al., 2020). In the second step, the lysosomal system may threaten the integrity of the drug. This can be bypassed by using cationic molecules and pH-sensitive drug carriers (Shir et al., 2006). However, receptor-mediated transfer also faces some problems. The high affinity leads to strong interactions between multiligand receptors on the lumen side of the BBB, limiting the entry of therapeutic molecules into the brain parenchyma. By contrast, using ligands with lower affinities can lead to higher drug release into the brain, but this requires administering higher doses, which is usually not applicable (Clark and Davis, 2015).

### 2.3.4 Cell-mediated delivery

In recent years, cell-mediated transcytosis has received increasing attention because immunogenicity and instability can hinder the use of antibodies and peptides (Yu et al., 2016). Neural stem cells, mesenchymal stem cells, neutrophils, macrophages, and exosomes, among others, have an intrinsic tumor-homing ability, allowing them to target malignant GBMs for drug delivery (Cho et al., 2019). Neutrophils have been widely studied in the treatment of brain tumors, especially for the treatment of postoperative recurrent tumors. For example, inspired by the ability of macrophages to cross the BBB, Tingting *et al.* encapsulated catalase into silica nanoparticles to produce a nanoplatform called CAT@$SiO_2$-ICG (CSI). Next, they further encapsulated CSI into AS1411 aptamer-modified macrophage exosomes to form CSI@Ex-A (Wu et al., 2022) (Figure 1). Similarly, recent studies have confirmed that cell-mediated delivery systems can contribute to the clinical treatment of gliomas. Xue et al. (2017) have shown that neutrophils carrying liposomes that contain paclitaxel, can penetrate the brain and inhibit GBM recurrence in mice whose tumors have been surgically removed. Similarly, one study demonstrated that the dendritic cell-mediated delivery of doxorubicin-polyglycerol-nanodiamond composites stimulated GBM cells immunogenicity and elicited an anti-glioblastoma immune response (Li et al., 2018). These researches have revealed the feasibility of cell-mediated delivery for GBM treatments and laid the foundation for a translational study of this therapeutic paradigm to improve clinical outcomes in patients with malignant brain tumors.

## 2.4 Nano-assisted GBM diagnosis

Besides treating tumors, nanomaterials can be used in combination with imaging modalities, such as computed tomography (CT), functional magnetic resonance imaging (FMRI) (Richiardi et al., 2011), and positron emission tomography (PET) (Fink et al., 2015) to increase the sensitivity and accuracy of tumor detection. Moreover, ultrasound (Imbault et al., 2017) and fluorescence imaging (Li et al., 2017) have been widely used in the clinical diagnosis and treatment of GBM. First, under normal physiological conditions, the physical and chemical barriers of BBB can efficiently transport necessary particles to human brain and selectively discharge harmful or excessive materials (Wu et al., 2019). Under pathological situations, practically all kinds of macromolecular drugs (proteins, antibodies, peptides, developers, etc.,) and small molecular drugs can pass through the BBB (Umlauf and Shusta, 2019). Although multiple brain tumor diagnosis strategies exist, their various limitations have affected their efficacy in the diagnosis of GBM. Second, the perpetual drainage and circulation of blood-cerebrospinal fluid and interstitial fluid stop most macromolecules from entering the bloodstream and diagnostic drugs from entering the brain. Moreover, tumor-acquired characteristics of the brain prevent drug from penetrating into tumors. In particular, tumor-induced endothelial cell tight junction damage increases drug penetration, leading to a heterogeneous distribution (Groothuis, 2000; Roose et al., 2003; Arvanitis et al., 2020).

Magnevist, an extensively used clinical contrast agent, plays an important role in evaluating tumors and their recurrence in magnetic resonance imaging (MRI) (McDannold et al., 2012; Kim, 2020). However, due to its short half-life, maintaining a sufficient concentration in the tumor requires repeated high-dose injections. Vascular leakage (Zhao H. L. et al., 2020), pseudoprogression (Brandsma et al., 2008), and pseudoreaction (Batchelor et al., 2007; Dhermain et al., 2010) after radiotherapy or anti-angiogenesis therapy also affect MRI accuracy. Besides, magnetic resonance spectroscopy and PET are often used to quantify and describe the development of cerebral tumors. Integrated with tracers and positron radionuclides in existence, they will achieve evaluable and reliable tissue autoradiography (Kratochwil et al., 2019), providing important information needed in diagnosis on tumors. But it is the requirements for accurate diagnosis of cerebral tumors that still cannot meet. In response to these hurdles (substandard specificity and accuracy, ephemeral contrast agent half-life, large requirement for imaging, etc.,), and to improve imaging sensitivity in diagnosis, nanoparticles have been developed.

### 2.4.1 Nanomaterials for MRI

The properties of nanomaterials greatly help overcome the difficulties faced by traditional radiographic agents. For example, Self-assembled nanoparticles of amphiphilic gadolinium chelates show extremely high Gd3 + loading capacity for enhanced imaging (Othman et al., 2011). Coupling gadolinium to interleukin 13 (Li et al., 2015), an arginine-glycine-aspartate (RGD) peptide (Zhan et al., 2010; Sun et al., 2014; Richard et al., 2017), an epidermal growth factor receptor (EGFR) mutant antibody (EGFRvIII) (Hadjipanayis et al., 2010) or anti-gd2 antibody (Shah et al., 2013) can markedly enhance tumor targeting. Gadolinium metal fullerene nanoparticles have a cage surface charged by amino (-$NH^{3+}$), showing incredible 1H MR relaxation. These data suggest that composite nanoprobes can serve as alternatives to magnetic resonance contrast agents (Lajous et al., 2018). The clinical applications of nanodiagnostic agents consisting of other magnetic materials especially iron and manganese, have also been researched. Superparamagnetic iron oxide nanoparticles (SPIO) have been paid tremendous clinical attention due to their magnetic properties. For example, the tungsten-doped iron oxide crystal (WFe) contrast agent has a sterling T1-weighted effect. The WFe nanoparticles possessed high average T1, 22% shorter than that of ferritin at the injection site (Clavijo Jordan et al., 2014). In addition, the superparamagnetism of SPIO is beneficial to the aggregation of the magnetic target. For example, the synergistic release of SPIO by focused ultrasound and magnetic targeting notably increases its accumulation in the brain parenchyma (Lee et al., 2019). In addition, modifying SPIO with a brain tumor-targeting peptide cRGD (Richard et al., 2017), a targeting antibody EGFRvIII (Hadjipanayis et al., 2010), or the targeting toxin chlorotoxin (Stephen et al., 2014) can enhance its tumor-targeting specificity. Finally, manganese, chelated with albumin-binding molecules, has been evaluated as a new contrast agent in both subcutaneous and *in situ* brain tumor models (Zhou et al., 2019).

### 2.4.2 Nanomaterials for CT imaging and Surface Enhanced Resonance Raman Scattering

Gold nanoparticles have incredible biosafety properties and are readily synthesized. Thus, a series of gold NPs with Surface Enhanced Resonance Raman Scattering (SERRS) signals were developed to guide brain tumor resection (Saha et al., 2012; Karabeber et al., 2014). These nanoparticles show strong signal intensity in SERRS after 24 h of injection, yielding a clear tumor contour. Besides gold nanoparticles, a new PET/CT imaging reagent named $^{68}$galliumBNOTA-PRGD2 (68 Ga-PRGD2) showed some GBM diagnosis success (Li et al., 2014). Since GBM cells overexpress avb3, the target integrin of 68 Ga-PRGD2, the nanoparticle accumulates in GBM cells. The sensitivity and specificity of 68 Ga-PRGD2 for GBM grading were respectively 12% and 25% superior to those of the clinical PET/CT agent 18F-fluorodeoxyglucose (FDG). Moreover, Zhao et al. (2016) used the integrin a5b1 to enhance the specificity of 99mTc-HisoDGR SPECT/CT probes. 99mTcHisoDGR yielded precise contours in subcutaneous and *in situ* models 1.5 and 2 h after injection, respectively.

### 2.4.3 Nanomaterials for optical imaging

Currently, fluorescence imaging surgery guidance is widely used in clinical practice. Nanoparticles can be used as fluorescent dye carriers or fluorescent dyes to enhance optical imaging, dramatically reducing the failure rate of surgery (Wu et al., 2019). Several nanoparticles, including liposomes and polymer

NPs, can effectively deliver live imaging fluorescent dyes to brain tumor sites during the operation. Indocyanine green, a near-infrared fluorescent probe approved by the FDA, is widely used in tumor tracking and photothermal therapy. Liposome nanoparticles (LP-iDOPE) combined with VEGF-bevacizumab can enhance brain tumor imaging. One day after injection and before surgery, LP-iDOPE enhanced tumor localization (Suganami et al., 2015). Biodegradable polymers, such as polyalkylcyanoacrylate (Vauthier et al., 2003) and poly (lactic-co-glycolic acid) (Han et al., 2016; Guan et al., 2017; Orunoğlu et al., 2017), are widely used to prolong the retention period of nanoparticles *in vivo*. Besides, polymer nanoparticles can load cerebral tumor targeting particles like chlorotoxin or anti-PDGFRD antibody (Monaco et al., 2017). A novel optical contrast agent with good biocompatibility was developed by modifying a polymer nanomatrix with fluorescent dyes and silver nanosheet clusters. The contrast of these nanoparticles was 90% higher than that of the control (Ray et al., 2014).

Being activated by light at a particular wavelength, some nanoparticles can emit light at another (such as quantum dots (Liu M. X. et al., 2017; Tang et al., 2017) and upconversion luminescent materials (Wang et al., 2020)), making them ideal fluorescent dyes for cancer targeting and imaging. Quantum dots are widely used for biological imaging diagnosis due to their excellent water solubility, low fluorescence quenching rate, high fluorescence quantum yield, and stable chemical properties (Wu and Yan, 2013). Thus, quantum dots modified with tumor-targeting molecules can achieve specific biological imaging. Moreover, near-infrared technology can increase their fluorescence and Raman signals by several orders of magnitude (Gill and Le Ru, 2011), making them more sensitive for imaging in preclinical and clinical studies. Upconversion nanoparticles have considerable light stability, no fluorescence scintillation, deep tissue penetration, and low light damage effects (Gu et al., 2013; Liu et al., 2021; Mohan and Poddar, 2021), making them promising *in vivo* imaging probes (Idris et al., 2012; Yang et al., 2012). However, although these nanoparticles have strong tissue penetration ability, they cannot penetrate brain tissue like traditional fluorescent dyes (Li and Wang, 2018). To overcome this problem, research on second near-infrared transparent window (NIR-II, 1,000–1700 nm) fluorescent nanoprobes has gradually developed. NIR-II fluorescent nanoprobes have a stronger ability to penetrate tissues and achieve higher image fidelity. Ag2S quantum dots are one of the typical NIR-II fluorescent probes. Coupled to cyclic RGD peptides, the biocompatible NIR-II Ag2S fluorescent probe can achieve targeted labeling and imaging of U87 cells (Zhang et al., 2012). Considering the enhanced penetration depth of fluorescence signals, Qi et al. (2018) further analyzed the tissue penetration depth of NIR-II imaging probes. Near-infrared aggregation-induced emission under excitation with a 1,300 nm NIR-ii laser allowed the group to observe 5 mm blood vessels at a depth of 1,065 mm in the brain.

### 2.4.4 Nanomaterials for multimodal imaging

Since each diagnostic method has its own advantages and disadvantages, combining different diagnostic methods can optimize the outcomes. The development of dual-mode imaging nanoparticles has majorly impacted biomedical research. Angiopep-2 (ANG, TFFYGGSRGKRNNFKTEEY) coupled with upconversion dual-mode imaging nanoparticles (ANG/PEG-UCNPs) and Gd were constructed for targeting GBM. Compared with non-ANG and Gd-DTPA imaging, the nanoprobe yielded a significantly enhanced T1-weighted magnetic resonance contrast for glioblastoma. T2-weighted MRI also shows great potential for identifying clear glioblastoma borders (Ni et al., 2014). These results confirmed the advantage of MRI combined with fluorescent nanoprobes in GBM diagnosis. However, although dual-mode imaging improves the accuracy of high-resolution information, it still does not achieve overall tumor visualization. To improve the diagnosis accuracy and sensitivity, various imaging nanoparticles have been explored. For example, gold silicon-based SERS nanoparticles were used for three-mode imaging applications, where gold NPs were encapsulated by $Gd^{3+}$ ions. MRI, photoacoustic imaging, and SERS showed clear tumors. The three-dimensional rendering of the magnetic resonance and photoacoustic images showed good co-expression signals in the tumor (Kircher et al., 2012; Neuschmelting et al., 2018).

### 2.4.5 Summary

Traditional GBM diagnosis faces some tough obstacles, such as the BBB and tumor heterogeneity. Although nanotechnologies have solved these problems to a certain extent, single-dimension diagnosis remains extremely limited due to the complexity of GBM. Combining multiple diagnostic methods will become a critical research field. Therefore, it is essential to construct various nanomaterials meeting the requirements for multi-mode combinations. Table 1 lists existing diagnosis nanomaterials and their related mechanisms.

## 2.5 Nano-assisted GBM therapy

### 2.5.1 Ferroptosis

Ferroptosis is an iron-dependent programmed cell death distinct from apoptosis, necrosis, pyroptosis, and autophagy (Bogdan et al., 2016; Zheng et al., 2017; Shen et al., 2018; Zhang et al., 2020). Excessive iron reacts with hydrogen peroxide (H2O2), generating hydroxyl radicals and singlet oxygen in cells (this process is known as the Fenton reaction). High hydroxyl radical levels eventually lead to cytotoxic lipid peroxidation. Since ferroptosis and apoptosis are radically different in mechanism and phenotype, combination therapy targeting these two processes may be a strategy for treating GBM. Based on this idea, Yulin *et al.* proposed an innovative local chemotherapy approach. They constructed iron oxide

TABLE 1 Nanomaterialbased diagnostic for glioma.

| Application | Nanomaterial | Highlight |
|---|---|---|
| MR imaging | Self-assembling nanoparticles of amphiphilic gadolinium chelates | High loading capacity of Gd3+ ions, enhanced imaging effect |
| | conjunction of gadolinium with interleukin (IL)-13, the arginine– | Significantly enhanced tumor targeting ability |
| | Glycine–aspartic acid (RGD) peptide, the epidermal growth factor receptor (EGFR) deletion mutant (EGFRvIII) antibody or the anti-GD2 antibody | |
| | Gadolinium metallofullerene nanoparticles | Excellent 1H MR relaxivity |
| | Tungsten doped iron oxide crystal | Excellent T1-weighted effect |
| | Superparamagnetic iron oxide nanoparticles | Magnetically controlled target accumulation |
| | SPIO with brain tumor targeted peptides cRGD, targeted antibody EGFRvIII and targeted toxin chlorotoxin (CTX) | Specific targeting in tumors |
| Surface Enhanced Resonance Raman Scattering (SERRS) and CT imaging | Au NPs | A stronger SERRS signal intensity 24 h postinjection, and then an accurate outline of the tumor |
| | 68 Ga-PRGD2 | Enhanced sensitivity and specificity of glioma grading |
| | 99 mTc-HisoDGR SPECT/CT | Clear visualization in both subcutaneous and orthotopic models respectively 1.5 h and 2 h post injection |
| Optical imaging | Indocyanine green (ICG) loaded liposomal formulated nanoparticles (LP-iDOPE) | Enhanced imaging effect of brain tumors, excellent tumor-specific localization |
| | Poly-alkyl-cyano acrylates (PACA) and poly lacticcoglycolic acid (PLGA) | Extending the circulation time of nanoparticles in the body |
| | Polymer nano matrix loaded with silver nanoplate clusters and a fluorescent dye | Better biocompatibility and contrast |
| Multimodal imaging | Quantum dots (QDs) | Good solubility in water, high fluorescence quantum yield, low fluorescence quenching rate and stable chemical properties |
| | Quantum dots modified with tumor targeting molecules | Specific bioimaging |
| | Upconversion nanoparticles (UCNPs) | Good photostability, no fluorescence scintillation, deep tissue penetration and small photo damage |
| | $Ag_2S$ QDs | Deeper penetration potential through tissues, higher fidelity of images |
| | Angiopep-2 (ANG) dual-targeting simultaneously Gd-doped upconversion dual-mode imaging nanoparticles (ANG/PEG-UCNPs) | Enhanced T1-weighted MR contrast of glioblastoma, great potential in T2-weighted MRI, ability to show a clear glioblastoma boundary |
| | Gold–silica-based SERS nanoparticles | Ability to show clear tumor visualization by three modalities in triple-modality imaging |

nanoparticles (IONPs) based on gene therapy to treat patients with glioblastoma via ferroptosis and apoptosis after surgery. By modifying the porous structure of carboxyl-linked IONPs, they co-transferred small interfering RNA (siGPX4, targeting glutathione peroxidase 4) and cisplatin with a high drug loading efficiency. During intracellular degradation, IONPs markedly increased iron ($Fe^{2+}$ and $Fe^{3+}$) levels and activated reductive nicotinamide adenine dinucleotide phosphate (NADPH) oxidase (NOX), increasing $H_2O_2$ levels. The Fenton reaction between $Fe^{2+}$, $Fe^{3+}$, and intracellular $H_2O_2$ produced reactive oxygen species and initiated ferroptosis, while cisplatin destroyed nuclear and mitochondrial DNA, leading to apoptosis. Simultaneously, si-GPX4 was released, inhibiting GPX4 expression and produced a synergistic effect through mechanisms related to ferroptosis. Therefore, this system achieved an excellent therapeutic effect and low systemic toxicity both *in vitro* and *in vivo* (Zhang et al., 2020).

### 2.5.2 Gene therapy

Gene therapy is a potential method for the treatment of GBM. In this context, nanomaterials are mainly used as carriers for genes designed to treat tumors. The designed genes can be suicide genes (that convert nontoxic prodrugs into cytotoxic drugs), immunoregulatory genes (that stimulate the immune system), or tumor suppressor genes (Dixit and Kumthekar, 2017). In addition, Qiang *et al.* constructed lipid-polymer hybrid nanoparticles (LPHNs-cRGD) to efficiently and specifically deliver a CRISPR/Cas9 plasmid targeting the temozolomide resistance gene O-6-methylguanine-DNA methyltransferase (MGMT). To facilitate the entry of the genes into the GBM *in vivo*, they non-invasively and locally gained access into the BBB using focused ultrasound microbubbles. The nanocarrier successfully mediated the transfection of pCas9/MGMT, downregulating MGMT expression and increasing the sensitivity of GBM cells to temozolomide (Yang et al., 2021).

### 2.5.3 Radiotherapy

Radiotherapy is a common treatment method for malignant tumors. However, radiation damages normal tissues and tumor hypoxia can lead to radiation resistance. There are two solutions to overcome these problems: the first is to use more advanced radiotherapy technology, and the second is to develop a new generation of therapeutic agents able to sensitize tumor cells to ionizing radiations to improve their effect. Nanomaterials can be used as radiosensitizers or their carriers. They have achieved good results as radiosensitizers or carriers after photon and particle radiation (Caban-Toktas et al., 2020; Chung et al., 2020; Kazmi et al., 2020; Ruiz-Garcia et al., 2021). Some nanoparticles, such as gadolinium, gold, hafnium, bismuth, and platinum nanoparticles, can also achieve good results as sensitizers (Lux et al., 2019). The principle is that when photons and particles activate the nanoparticles, a photoelectric effect (Kazmi et al., 2020) amplifies the radiation effect (Lacombe et al., 2017; Kuncic and Lacombe, 2018). Gold nanoparticles became an important radiosensitizer due to their biocompatibility, tunable optical properties, and high stability. Kunoh et al. (2019) compared the radiosensitivity of gold nanoparticle-treated and untreated cells. Their experiments showed that pre-treating cells with gold NPs prevented radioresistance development in cancer cells. Interestingly, the gold NPs did not induce apoptosis but increased the number of abnormal nuclei, causing mitotic cell catastrophe.

### 2.5.4 Photothermal therapy

Photothermal therapy consists in injecting materials with high photothermal conversion efficiency into the body, making them accumulate around the tumor by targeted recognition technology, then irradiating them with an external light source (generally infrared light) to convert light into heat and kill cancer cells. Based on the above ferroptosis treatment, Yulin *et al.* blended gallic acid with $Fe^{2+}$ to form gallic acid/$Fe^{2+}$ nanoparticles with excellent photothermal conversion ability. Near-infrared light irradiation (808 nm) can drastically improve the $Fe^{2+}$ release efficiency of nanoparticles and induce ferroptosis in tumor cells while releasing a large amount of heat to kill tumor cells (Zhang et al., 2021).

### 2.5.5 Magnetothermal therapy

Magnetothermal therapy-mediated cancer therapy (MHCT) consists in exposing magnetic nanomaterials to an alternating magnetic field to heat tumor tissue and alter cellular mechanisms. A temperature rise from 37°C to 42°C–45°C can induce tumor cell death by activating specific intracellular and extracellular degradation mechanisms (Krawczyk et al., 2011; Zhang and Calderwood, 2011; Gupta and Sharma, 2019). At 42°C, tumor cells undergo irreversible damage leading to apoptosis, while achieving the same effect in normal cells requires at least 55°C.

However, magnetothermal therapy has not yet become one of the main GBM therapy because some challenges remain. First, the safety, efficacy, and appropriate dose range of MHCT are unclear, and this needs to be taken into account to determine the magnetic nanomaterial dose. Moreover, the choice of magnetic parameters and the appropriate magnetic field strength are also undetermined. Second, injecting effective drugs into targeted GBM cells through clinically feasible methods remains challenging. Most small-molecule drugs cannot penetrate the BBB, which dramatically hinders the delivery of drugs to tumor sites. In addition, some physical limitations affect hyperthermia performance. These include heat distribution, toxicity, magnetic nanosensors efficiency, and the reduction of hyperthermia performance of magnetic nanoparticles (MNPs) in the cellular environment, that is, once they are internalized by the cell (lysosomal aggregation phenomenon) (Di Corato et al., 2014; Soukup et al., 2015). Besides, the lack of methods to accurately measure local body temperature is another obstacle to MNP treatment evaluation (Dewhirst et al., 1997; Arthur et al., 2005). More importantly, achieving the precise targeting of tumor cells by MNPs is also one of the main challenges for GBM treatment.

According to a recent meta-analysis, less than 1% of injected particles accumulate at the tumor site. Thus, the use of targeted strategies to attach specific targeted moieties to the surface of nanomaterials has also become an important unsolved question. However, in some techniques, only 4% of the targeted portion of the used ligand is recognized by its targeted receptor, which may lead to heterogeneity and poor results (Herda et al., 2017). In addition, converting targeted strategies from basic research to clinical research is ineffective, especially MHCT. A study reported that in mouse xenograft models, the accumulation of antibodies usually varies between 0.5% and 50% of the injection dose per Gram of tumor tissue. Meanwhile, we observed that the accumulation of antibodies per Gram of tumor tissue in human tumors was less than 0.01% of the injection dose (Björnmalm et al., 2017). Gupta and Sharma. (2021) proposed magnetic dots coated with carboxymethyl-stevioside as a magnetic hyperthermia agent for GBM treatment. These magnetic dots showed significant water stability, and their specific absorption rate was 209.25 W/g under an alternating magnetic field of 359 kHz and 188 Oe. They also induced notable anti-migration and anti-invasive effects on GBM C6 cells by inhibiting the gene expression of matrix metalloproteinases 2 and 9. The key to solving these problems is controlling the amount of magnetic materials that can reach the tumor microenvironment. For this, doping in an appropriate proportion can improve the magnetism of MNPs (Li et al., 2021). Due to the high specific surface area volume ratio, van der Waals force, and strong dipole-dipole interaction, MNPs tend to agglomerate, resulting in increased particle size and reduced magnetism. The high polydispersity of nanoparticles can also reduce the magnetic heating capacity of MNP systems. Therefore, nanoparticle size crucially affects the magnetic and thermal efficiency of nanosystems. In biomedical applications, MNPs with a small diameter (10–100 nm) and narrow size distribution are preferred to prevent their rapid removal from the systemic circulation by the reticuloendothelial system (Cheng et al., 2021). In addition, surface coatings of nanoparticles [such as inorganic materials (alumina or silica), polymers (dextran, chitosan, polyethylene glycol, or stevioside), fatty acids (oleic acid), and liposomes] prevent aggregation and may contribute to colloidal stability through space and electrostatic repulsion (Karimi et al., 2013; Jamari et al., 2020).

Heat shocks can induce the expression of various heat shock proteins (HSPs), which act as molecular chaperones to protect proteins from thermal denaturation, assist protein folding, and induce heat tolerance in cells (Gong et al., 2012). HSP 27, 70, 73, and 90 are considered the key constitutively overexpressed HSPs in GBMs and play an essential role in cancer cell heat resistance against MHCT (Lee Titsworth et al., 2014). Thus, besides improving effective magnetism at the tumor microenvironment, methods targeting these heat shock proteins can also make tumor cells sensitive to magnetic hyperthermia therapy. Possible strategies include specifically inducing an immune response towards these tumor-specific overexpressed HSPs in GBM cells or using HSP gene inhibitors. The heat-induced antitumor immune response is also a new research direction.

### 2.5.6 Immunotherapy

To date, the standard high-grade GBMs therapy concerns multidisciplinary approaches, containing maximum surgical resection, radiotherapy, and chemotherapy. But the complete resection is nearly impossible because of the invasiveness of GBM, and the recurrence of tumor is practically inevitable even in patients undergoing multimodal therapy. Moreover, these recurrent tumors are often resistant to chemotherapy and radiotherapy (Leiva-Salinas et al., 2017). Thus, it is necessary to develop new therapeutic approaches against GBM. Immunotherapy consists in stimulating the patient's immune system to make it identify and attack malignant tumors through continuous anti-tumor immunity. However, many obstacles hinder the application of immunotherapy in the clinical practice. The first is the complexity of tumors. Tumors have various immune escape mechanisms. Second, the immune environment of brain is distinct from that in other organs, which is unable to produce an immune response against tumors (Zanganeh et al., 2019). Due to the BBB, the transport of immune effectors from the blood to the brain is limited. Moreover, although activated circulating T lymphocytes are present in the central nervous system, there are few naive T cells (Su et al., 2017).

Another challenge limiting immunotherapy against GBM is that various mechanisms promote immunosuppression inside and around the tumor. GBM is classified as a cold immune tumor, and its microenvironment represents an immune desert with little to no immune effector cell infiltration. Key factors of the glioblastoma-mediated immune cold microenvironment contain the abundance of $CD4^{+}CD25+FOXP3+$ regulatory T cells (Tregs) and myeloid cells, as well as immunosuppressive cytokines and secretory factors produced by tumor cells like transforming growth factor-β, interleukin 6 and interleukin 10 (Reardon et al., 2017). GBM grading is related to Treg infiltration into tumors. In malignant GBM, tumor-resident Tregs express high levels of PD-1 (Lowther et al., 2016), an essential inhibitory receptor expressed in activated T cells which is significant in the immune response (Sharpe and Pauken, 2018). Thus, although there is a small amount of immune cell infiltration, immune cells are often in a low response state due to immunosuppressive signals (Woroniecka et al., 2018).

A primary mediator of immunosuppression in GBM patients is tissue hypoxia, which activates signal transducers and activators of transcription 3 (STAT3) and an immunosuppressive signaling pathway which promotes the production of hypoxia-inducible factor-1-alpha (HIF1A). However, it then induces Treg activation and vascular endothelial growth factor (VEGF) synthesis (Almiron Bonnin et al., 2018).

In the face of the many challenges in immunotherapy, nanomaterials can be used as a breakthrough point. Nanomaterials can deliver drugs to tumors and induce cytotoxic anti-tumor T cell responses. Cancer vaccines with better efficacy can be designed by combining immunomodulators and antigens, direct targeting and T cell functionalization, nucleic acid delivery, adjuvants, immune checkpoint inhibitors, and inhibitory tumor microenvironment regulation (Riley et al., 2019). In a current research, poly (lactic-co-glycolic acid) nanoparticles modified by Angiopep-2 and IP10-EGFRvIIIscFv fusion proteins crossed the BBB and amassed in brain tissue. After binding to cytotoxic T lymphocytes, the nanoparticles notably increased the immune response and antitumor activity in a GBM model (Wang et al., 2018).

To re-adjust the inhibited GBM immune microenvironment, Tong Fei *et al.* designed a nanocomposite drug based on a polyglycerol functionalized doxorubicin-containing nanodiamond. The nanocomposite regulated the immunosuppressive microenvironment of GBM by activating autophagy, thereby stimulating the immune response. This rebuilding promoted the anti-glioblastoma immune response and strengthened the activation of dendritic cells (Li et al., 2019).

The tumor vascular laminin-411 (α4β1γ1) is associated with the high expression of tumor stem cell markers (Notch, CD133, Nestin, c-Myc) and a shorter survival time for GBM patients. Tao *et al.* designed a nano-bioconjugate which is able to cross the BBB to inhibit laminin-411. This nanobioconjugate targeting the tumor microenvironment prolonged animal survival and inhibited cancer stem cell markers in mice carrying intracranial GBM (Sun et al., 2019).

The low accumulation of antigens in antigen-presenting cells is another obstacle to effective immunotherapy against brain tumors. This is related to the low activation of antigen-presenting cells in GBM. Two approaches could solve this problem: enhancing the antigen-loading capacity of nanovaccines or

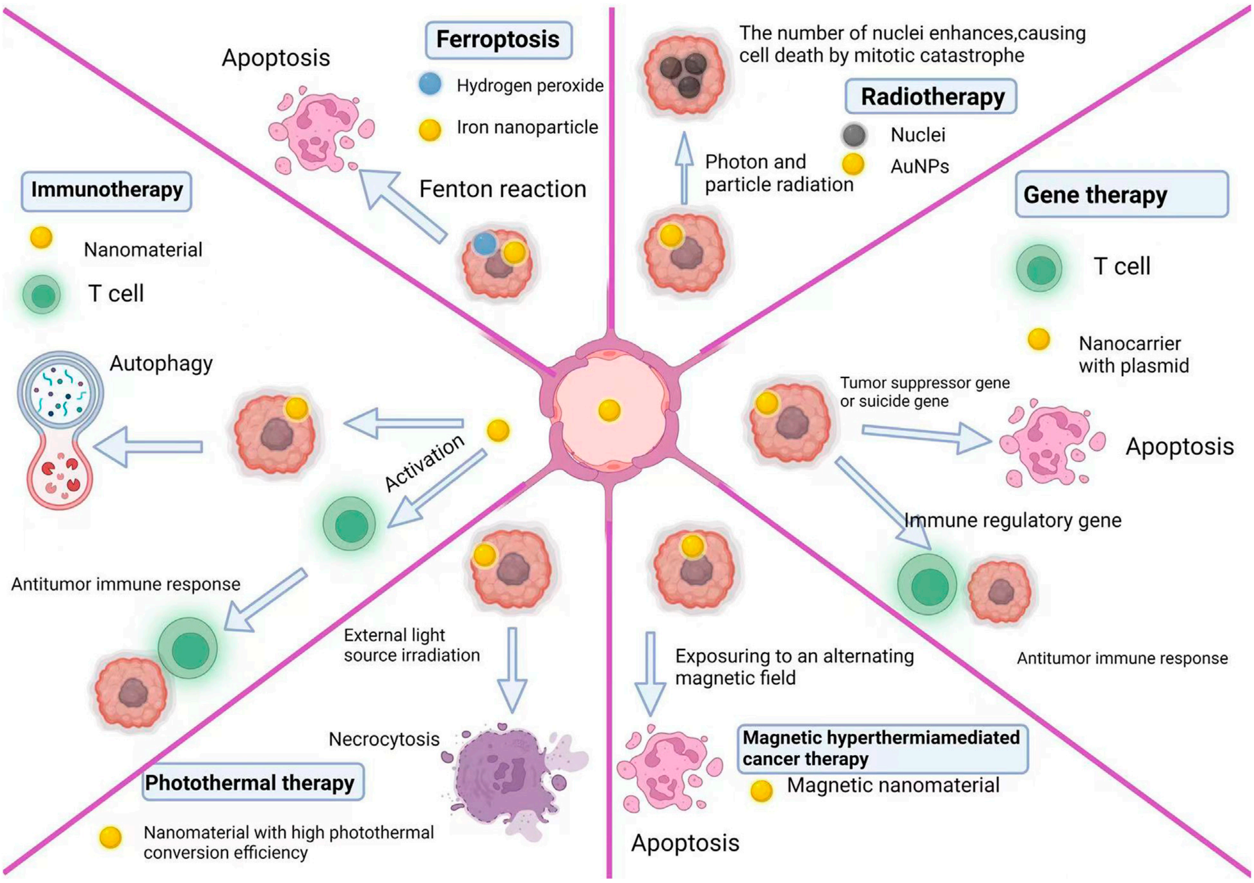

FIGURE 2
Glioblastoma therapy mechanism of nanomaterials.

adding substances that can sensitize antigen-presenting cells to nanomedicines. A hybrid “cluster bomb” nanovaccine, based on zinc oxide and triblock-copolymer nanoparticles, stimulated cellular and humoral immunity and increased the survival time of tumor-bearing mice (Shen et al., 2019). Another study combined exosomes derived from GBM with α-galactosylceramide (natural killer T-cell activator). Used subcutaneously in glioblastoma-bearing rats, it increased interferon γ and tumor necrosis factor α production and promoted the immune response (Liu H. et al., 2017).

### 2.5.7 Summary

Because of the heterogeneity, the complexity of the tumor microenvironment, the multiple immune escape mechanisms, and the weak sensitivity of the brain immune system, handling GBM from a single dimension is limited. GBM treatments need to be multimodal. However, combining different methods for killing glioma cells is insufficient. Comprehensive glioblastoma treatments should also target the tumor microenvironment, and stimulate immune cells of the brain (Figure 2).

## 3 Summary and outlook

This article reviews the definition, classification, diagnosis, and therapeutic applications of nanomaterial-based GBM treatments. Currently, the clinical application of nanoparticles and the complexity of GBM itself still face numerous challenges. Designing nanomaterials more suitable for clinical applications require optimizing nanomaterials by understanding the transport regulation mechanism of the BBB, the composition of the GBM tumor microenvironment and its influence on the BBB. Carefully studying the mechanisms of action of nanomaterials on the brain, discovering new properties of nanomaterials, improving their synthesis, and exploring new and promising drug delivery systems are crucial for developing clinical applications of nanomaterials in the diagnosis and treatment of glioblastoma. Most importantly, since single-dimension diagnostic and treatment methods are limited, future studies should focus on multi-dimensional nanomaterials. With further research, the clinical nano-diagnosis and treatment system for GBM is expected to improved.

## Author contributions

All authors contributed to the design and writing of the manuscript. XL, XN, and WW proposed the ideas and drafted the outlines. SY, LC, and HX performed the literature search and completed the manuscript. SL and JJ helped revise the manuscript and provided support in need.

## Funding

This work was supported by the National Natural Science Foundation of China (82001421).

## Conflict of interest

The authors declare that the research was conducted in the absence of any commercial or financial relationships that could be construed as a potential conflict of interest.

## Publisher's note

## References

Almiron Bonnin, D. A., Havrda, M. C., Lee, M. C., Liu, H., Zhang, Z., Nguyen, L. N., et al. (2018). Secretion-mediated STAT3 activation promotes self-renewal of glioma stem-like cells during hypoxia. *Oncogene* 37 (8), 1107–1118. doi:10.1038/onc.2017.404

Arcella, A., Palchetti, S., Digiacomo, L., Pozzi, D., Capriotti, A. L., Frati, L., et al. (2018). Brain targeting by liposome-biomolecular corona boosts anticancer efficacy of temozolomide in glioblastoma cells. *ACS Chem. Neurosci.* 9 (12), 3166–3174. doi:10.1021/acschemneuro.8b00339

Arthur, R. M., Straube, W. L., Trobaugh, J. W., and Moros, E. G. (2005). Non-invasive estimation of hyperthermia temperatures with ultrasound. *Int. J. Hyperth.* 21 (6), 589–600. doi:10.1080/02656730500159103

Arvanitis, C. D., Ferraro, G. B., and Jain, R. K. (2020). The blood-brain barrier and blood-tumour barrier in brain tumours and metastases. *Nat. Rev. Cancer* 20 (1), 26–41. doi:10.1038/s41568-019-0205-x

Azarmi, M., Maleki, H., Nikkam, N., and Malekinejad, H. (2020). Transcellular brain drug delivery: A review on recent advancements. *Int. J. Pharm.* 586, 119582. doi:10.1016/j.ijpharm.2020.119582

Baratta, M. G. (2018). Getting to the brain. *Nat. Nanotech.* 13 (7), 536. doi:10.1038/s41565-018-0182-3

Batchelor, T. T., Sorensen, A. G., di Tomaso, E., Zhang, W. T., Duda, D. G., Cohen, K. S., et al. (2007). AZD2171, a pan-VEGF receptor tyrosine kinase inhibitor, normalizes tumor vasculature and alleviates edema in glioblastoma patients. *Cancer Cell* 11 (1), 83–95. doi:10.1016/j.ccr.2006.11.021

Béduneau, A., Saulnier, P., and Benoit, J. P. (2007). Active targeting of brain tumors using nanocarriers. *Biomaterials* 28 (33), 4947–4967. doi:10.1016/j.biomaterials.2007.06.011

Bharti, S., Kaur, G., Jain, S., Gupta, S., and Tripathi, S. K. (2019). Characteristics and mechanism associated with drug conjugated inorganic nanoparticles. *J. Drug Target.* 27 (8), 813–829. doi:10.1080/1061186x.2018.1561888

Björnmalm, M., Thurecht, K. J., Michael, M., Scott, A. M., and Caruso, F. (2017). Bridging bio-nano science and cancer nanomedicine. *ACS Nano* 11 (10), 9594–9613. doi:10.1021/acsnano.7b04855

Bogdan, A. R., Miyazawa, M., Hashimoto, K., and Tsuji, Y. (2016). Regulators of iron homeostasis: New players in metabolism, cell death, and disease. *Trends Biochem. Sci.* 41 (3), 274–286. doi:10.1016/j.tibs.2015.11.012

Bourganis, V., Kammona, O., Alexopoulos, A., and Kiparissides, C. (2018). Recent advances in carrier mediated nose-to-brain delivery of pharmaceutics. *Eur. J. Pharm. Biopharm.* 128, 337–362. doi:10.1016/j.ejpb.2018.05.009

Brandsma, D., Stalpers, L., Taal, W., Sminia, P., and van den Bent, M. J. (2008). Clinical features, mechanisms, and management of pseudoprogression in malignant gliomas. *Lancet Oncol.* 9 (5), 453–461. doi:10.1016/s1470-2045(08)70125-6

Caban-Toktas, S., Sahin, A., Lule, S., Esendagli, G., Vural, I., Karlı Oguz, K., et al. (2020). Combination of Paclitaxel and R-flurbiprofen loaded PLGA nanoparticles suppresses glioblastoma growth on systemic administration. *Int. J. Pharm.* 578, 119076. doi:10.1016/j.ijpharm.2020.119076

Cai, Z., Qiao, P. F., Wan, C. Q., Cai, M., Zhou, N. K., and Li, Q. (2018). Role of blood-brain barrier in alzheimer's disease. *J. Alzheimers Dis.* 63 (4), 1223–1234. doi:10.3233/jad-180098

Chen, R., Smith-Cohn, M., Cohen, A. L., and Colman, H. (2017). Glioma subclassifications and their clinical significance. *Neurotherapeutics* 14 (2), 284–297. doi:10.1007/s13311-017-0519-x

Chen, Y. C., Chiang, C. F., Chen, L. F., Liang, P. C., Hsieh, W. Y., and Lin, W. L. (2014). Polymersomes conjugated with des-octanoyl ghrelin and folate as a BBB-penetrating cancer cell-targeting delivery system. *Biomaterials* 35 (13), 4066–4081. doi:10.1016/j.biomaterials.2014.01.042

Cheng, H. W., Tsao, H. Y., Chiang, C. S., and Chen, S. Y. (2021). Advances in magnetic nanoparticle-mediated cancer immune-theranostics. *Adv. Healthc. Mat.* 10 (1), e2001451. doi:10.1002/adhm.202001451

Cho, H. Y., Mavi, A., Chueng, S. D., Pongkulapa, T., Pasquale, N., Rabie, H., et al. (2019). Tumor homing reactive oxygen species nanoparticle for enhanced cancer therapy. *ACS Appl. Mat. Interfaces* 11 (27), 23909–23918. doi:10.1021/acsami.9b07483

Chung, K., Ullah, I., Kim, N., Lim, J., Shin, J., Lee, S. C., et al. (2020). Intranasal delivery of cancer-targeting doxorubicin-loaded PLGA nanoparticles arrests glioblastoma growth. *J. Drug Target.* 28 (6), 617–626. doi:10.1080/1061186x.2019.1706095

Clark, A. J., and Davis, M. E. (2015). Increased brain uptake of targeted nanoparticles by adding an acid-cleavable linkage between transferrin and the nanoparticle core. *Proc. Natl. Acad. Sci. U. S. A.* 112 (40), 12486–12491. doi:10.1073/pnas.1517048112

Clavijo Jordan, M. V., Beeman, S. C., Baldelomar, E. J., and Bennett, K. M. (2014). Disruptive chemical doping in a ferritin-based iron oxide nanoparticle to decrease r2 and enhance detection with T1-weighted MRI. *Contrast Media Mol. Imaging* 9 (5), 323–332. doi:10.1002/cmmi.1578

Cloughesy, T. F., Mochizuki, A. Y., Orpilla, J. R., Hugo, W., Lee, A. H., Davidson, T. B., et al. (2019). Neoadjuvant anti-PD-1 immunotherapy promotes a survival benefit with intratumoral and systemic immune responses in recurrent glioblastoma. *Nat. Med.* 25 (3), 477–486. doi:10.1038/s41591-018-0337-7

Danhier, F. (2016). To exploit the tumor microenvironment: Since the EPR effect fails in the clinic, what is the future of nanomedicine? *J. Control. Release* 244, 108–121. doi:10.1016/j.jconrel.2016.11.015

Detti, B., Scoccianti, S., Teriaca, M. A., Maragna, V., Lorenzetti, V., Lucidi, S., et al. (2021). Bevacizumab in recurrent high-grade glioma: A single institution retrospective analysis on 92 patients. *Radiol. Med.* 126 (9), 1249–1254. doi:10.1007/s11547-021-01381-5

Dewhirst, M. W., Prosnitz, L., Thrall, D., Prescott, D., Clegg, S., Charles, C., et al. (1997). Hyperthermic treatment of malignant diseases: Current status and a view toward the future. *Semin. Oncol.* 24 (6), 616–625.

Dhermain, F. G., Hau, P., Lanfermann, H., Jacobs, A. H., and van den Bent, M. J. (2010). Advanced MRI and PET imaging for assessment of treatment response in patients with gliomas. *Lancet Neurology* 9 (9), 906–920. doi:10.1016/s1474-4422(10)70181-2

Di Corato, R., Espinosa, A., Lartigue, L., Tharaud, M., Chat, S., Pellegrino, T., et al. (2014). Magnetic hyperthermia efficiency in the cellular environment for different nanoparticle designs. *Biomaterials* 35 (24), 6400–6411. doi:10.1016/j.biomaterials.2014.04.036

Dixit, K., and Kumthekar, P. (2017). Gene delivery in neuro-oncology. *Curr. Oncol. Rep.* 19 (11), 69. doi:10.1007/s11912-017-0628-z

Dong, X. (2018). Current strategies for brain drug delivery. *Theranostics* 8 (6), 1481–1493. doi:10.7150/thno.21254

Falgàs, A., Pallarès, V., Unzueta, U., Céspedes, M. V., Arroyo-Solera, I., Moreno, M. J., et al. (2020). A CXCR4-targeted nanocarrier achieves highly selective tumor uptake in diffuse large B-cell lymphoma mouse models. *Haematologica* 105 (3), 741–753. doi:10.3324/haematol.2018.211490

Fink, J. R., Muzi, M., Peck, M., and Krohn, K. A. (2015). Multimodality brain tumor imaging: MR imaging, PET, and PET/MR imaging. *J. Nucl. Med.* 56 (10), 1554–1561. doi:10.2967/jnumed.113.131516

Gill, R., and Le Ru, E. C. (2011). Fluorescence enhancement at hot-spots: The case of Ag nanoparticle aggregates. *Phys. Chem. Chem. Phys.* 13 (36), 16366–16372. doi:10.1039/c1cp21008d

Gong, T. W., Fairfield, D. A., Fullarton, L., Dolan, D. F., Altschuler, R. A., Kohrman, D. C., et al. (2012). Induction of heat shock proteins by hyperthermia and noise overstimulation in hsf1 -/- mice. *J. Assoc. Res. Otolaryngol.* 13 (1), 29–37. doi:10.1007/s10162-011-0289-9

Groothuis, D. R. (2000). The blood-brain and blood-tumor barriers: A review of strategies for increasing drug delivery. *Neuro Oncol.* 2 (1), 45–59. doi:10.1093/neuonc/2.1.45

Gu, Z., Yan, L., Tian, G., Li, S., Chai, Z., and Zhao, Y. (2013). Recent advances in design and fabrication of upconversion nanoparticles and their safe theranostic applications. *Adv. Mat.* 25 (28), 3758–3779. doi:10.1002/adma.201301197

Guan, J., Zhang, Z., Hu, X., Yang, Y., Chai, Z., Liu, X., et al. (2017). Cholera toxin subunit B enabled multifunctional glioma-targeted drug delivery. *Adv. Healthc. Mat.* 6 (23), 1700709. doi:10.1002/adhm.201700709

Gupta, R., and Sharma, D. (2021). (Carboxymethyl-stevioside)-coated magnetic dots for enhanced magnetic hyperthermia and improved glioblastoma treatment. *Colloids Surfaces B Biointerfaces* 205, 111870. doi:10.1016/j.colsurfb.2021.111870

Gupta, R., and Sharma, D. (2019). Evolution of magnetic hyperthermia for glioblastoma multiforme therapy. *ACS Chem. Neurosci.* 10 (3), 1157–1172. doi:10.1021/acschemneuro.8b00652

Hadjipanayis, C. G., Machaidze, R., Kaluzova, M., Wang, L., Schuette, A. J., Chen, H., et al. (2010). EGFRvIII antibody-conjugated iron oxide nanoparticles for magnetic resonance imaging-guided convection-enhanced delivery and targeted therapy of glioblastoma. *Cancer Res.* 70 (15), 6303–6312. doi:10.1158/0008-5472.Can-10-1022

Han, L., Kong, D. K., Zheng, M. Q., Murikinati, S., Ma, C., Yuan, P., et al. (2016). Increased nanoparticle delivery to brain tumors by autocatalytic priming for improved treatment and imaging. *ACS Nano* 10 (4), 4209–4218. doi:10.1021/acsnano.5b07573

Herda, L. M., Hristov, D. R., Lo Giudice, M. C., Polo, E., and Dawson, K. A. (2017). Mapping of molecular structure of the nanoscale surface in bionanoparticles. *J. Am. Chem. Soc.* 139 (1), 111–114. doi:10.1021/jacs.6b12297

Idris, N. M., Gnanasammandhan, M. K., Zhang, J., Ho, P. C., Mahendran, R., and Zhang, Y. (2012). *In vivo* photodynamic therapy using upconversion nanoparticles as remote-controlled nanotransducers. *Nat. Med.* 18 (10), 1580–1585. doi:10.1038/nm.2933

Imbault, M., Chauvet, D., Gennisson, J. L., Capelle, L., and Tanter, M. (2017). Intraoperative functional ultrasound imaging of human brain activity. *Sci. Rep.* 7 (1), 7304. doi:10.1038/s41598-017-06474-8

Jamari, S. K. M., Nordin, N. A., UbaidillahAziz, S. A. A., Nazmi, N., and Mazlan, S. A. (2020). Systematic review on the effects, roles and methods of magnetic particle coatings in magnetorheological materials. *Mater. (Basel)* 13 (23), 5317. doi:10.3390/ma13235317

Kaps, L., and Schuppan, D. (2020). Targeting cancer associated fibroblasts in liver fibrosis and liver cancer using nanocarriers. *Cells* 9 (9), 2027. doi:10.3390/cells9092027

Karabeber, H., Huang, R., Iacono, P., Samii, J. M., Pitter, K., Holland, E. C., et al. (2014). Guiding brain tumor resection using surface-enhanced Raman scattering nanoparticles and a hand-held Raman scanner. *ACS Nano* 8 (10), 9755–9766. doi:10.1021/nn503948b

Karimi, Z., Karimi, L., and Shokrollahi, H. (2013). Nano-magnetic particles used in biomedicine: Core and coating materials. *Mater. Sci. Eng. C* 33 (5), 2465–2475. doi:10.1016/j.msec.2013.01.045

Kazmi, F., Vallis, K. A., Vellayappan, B. A., Bandla, A., Yukun, D., and Carlisle, R. (2020). Megavoltage radiosensitization of gold nanoparticles on a glioblastoma cancer cell line using a clinical platform. *Int. J. Mol. Sci.* 21 (2), 429. doi:10.3390/ijms21020429

Khasraw, M., Simeonovic, M., and Grommes, C. (2012). Bevacizumab for the treatment of high-grade glioma. *Expert Opin. Biol. Ther.* 12 (8), 1101–1111. doi:10.1517/14712598.2012.694422

Kim, M. J. (2020). Improving survival with gadoxetic acid-enhanced MRI for hepatocellular carcinoma. *Radiology* 295 (1), 125–126. doi:10.1148/radiol.2020192713

Kircher, M. F., de la Zerda, A., Jokerst, J. V., Zavaleta, C. L., Kempen, P. J., Mittra, E., et al. (2012). A brain tumor molecular imaging strategy using a new triple-modality MRI-photoacoustic-Raman nanoparticle. *Nat. Med.* 18 (5), 829–834. doi:10.1038/nm.2721

Komin, A., Russell, L. M., Hristova, K. A., and Searson, P. C. (2017). Peptide-based strategies for enhanced cell uptake, transcellular transport, and circulation: Mechanisms and challenges. *Adv. Drug Deliv. Rev.* 110-111, 52–64. doi:10.1016/j.addr.2016.06.002

Kratochwil, C., Flechsig, P., Lindner, T., Abderrahim, L., Altmann, A., Mier, W., et al. (2019). (68)Ga-FAPI PET/CT: Tracer uptake in 28 different kinds of cancer. *J. Nucl. Med.* 60 (6), 801–805. doi:10.2967/jnumed.119.227967

Krawczyk, P. M., Eppink, B., Essers, J., Stap, J., Rodermond, H., Odijk, H., et al. (2011). Mild hyperthermia inhibits homologous recombination, induces BRCA2 degradation, and sensitizes cancer cells to poly (ADP-ribose) polymerase-1 inhibition. *Proc. Natl. Acad. Sci. U. S. A.* 108 (24), 9851–9856. doi:10.1073/pnas.1101053108

Kuncic, Z., and Lacombe, S. (2018). Nanoparticle radio-enhancement: Principles, progress and application to cancer treatment. *Phys. Med. Biol.* 63 (2), 02tr01. doi:10.1088/1361-6560/aa99ce

Kunoh, T., Shimura, T., Kasai, T., Matsumoto, S., Mahmud, H., Khayrani, A. C., et al. (2019). Use of DNA-generated gold nanoparticles to radiosensitize and eradicate radioresistant glioma stem cells. *Nanotechnology* 30 (5), 055101. doi:10.1088/1361-6528/aaedd5

Lacombe, S., Porcel, E., and Scifoni, E. (2017). Particle therapy and nanomedicine: State of art and research perspectives. *Cancer Nano.* 8 (1), 9. doi:10.1186/s12645-017-0029-x

Lajous, H., Riva, R., Lelièvre, B., Tétaud, C., Avril, S., Hindré, F., et al. (2018). Hybrid Gd(3+)/cisplatin cross-linked polymer nanoparticles enhance platinum accumulation and formation of DNA adducts in glioblastoma cell lines. *Biomater. Sci.* 6 (9), 2386–2409. doi:10.1039/c8bm00346g

Lee, M. J., Sayers, A. E., Drake, T. M., Singh, P., Bradburn, M., Wilson, T. R., et al. (2019). Malnutrition, nutritional interventions and clinical outcomes of patients with acute small bowel obstruction: Results from a national, multicentre, prospective audit. *BMJ Open* 9 (7), e029235. doi:10.1136/bmjopen-2019-029235

Lee Titsworth, W., Murad, G. J., Hoh, B. L., and Rahman, M. (2014). Fighting fire with fire: The revival of thermotherapy for gliomas. *Anticancer Res.* 34 (2), 565–574.

Leiva-Salinas, C., Schiff, D., Flors, L., Patrie, J. T., and Rehm, P. K. (2017). FDG PET/MR imaging coregistration helps predict survival in patients with glioblastoma and radiologic progression after standard of care treatment. *Radiology* 283 (2), 508–514. doi:10.1148/radiol.2016161172

Li, C., and Wang, Q. (2018). Challenges and opportunities for intravital near-infrared fluorescence imaging technology in the second transparency window. *ACS Nano* 12 (10), 9654–9659. doi:10.1021/acsnano.8b07536

Li, D., Zhao, X., Zhang, L., Li, F., Ji, N., Gao, Z., et al. (2014). (68)Ga-PRGD2 PET/CT in the evaluation of glioma: A prospective study. *Mol. Pharm.* 11 (11), 3923–3929. doi:10.1021/mp5003224

Li, S., Johnson, J., Peck, A., and Xie, Q. (2017). Near infrared fluorescent imaging of brain tumor with IR780 dye incorporated phospholipid nanoparticles. *J. Transl. Med.* 15 (1), 18. doi:10.1186/s12967-016-1115-2

Li, T. F., Li, K., Zhang, Q., Wang, C., Yue, Y., Chen, Z., et al. (2018). Dendritic cell-mediated delivery of doxorubicin-polyglycerol-nanodiamond composites elicits enhanced anti-cancer immune response in glioblastoma. *Biomaterials* 181, 35–52. doi:10.1016/j.biomaterials.2018.07.035

Li, T. F., Xu, Y. H., Li, K., Wang, C., Liu, X., Yue, Y., et al. (2019). Doxorubicin-polyglycerol-nanodiamond composites stimulate glioblastoma cell immunogenicity through activation of autophagy. *Acta Biomater.* 86, 381–394. doi:10.1016/j.actbio.2019.01.020

Li, T., Murphy, S., Kiselev, B., Bakshi, K. S., Zhang, J., Eltahir, A., et al. (2015). A new interleukin-13 amino-coated gadolinium metallofullerene nanoparticle for targeted MRI detection of glioblastoma tumor cells. *J. Am. Chem. Soc.* 137 (24), 7881–7888. doi:10.1021/jacs.5b03991

Li, X., Li, W., Wang, M., and Liao, Z. (2021). Magnetic nanoparticles for cancer theranostics: Advances and prospects. *J. Control. Release* 335, 437–448. doi:10.1016/j.jconrel.2021.05.042

Liu, H., Chen, L., Liu, J., Meng, H., Zhang, R., Ma, L., et al. (2017). Co-delivery of tumor-derived exosomes with alpha-galactosylceramide on dendritic cell-based immunotherapy for glioblastoma. *Cancer Lett.* 411, 182–190. doi:10.1016/j.canlet.2017.09.022

Liu, H., Zhang, W., Ma, L., Fan, L., Gao, F., Ni, J., et al. (2014). The improved blood-brain barrier permeability of endomorphin-1 using the cell-penetrating peptide synB3 with three different linkages. *Int. J. Pharm.* 476 (1-2), 1–8. doi:10.1016/j.ijpharm.2014.08.045

Liu, M. X., Zhong, J., Dou, N. N., Visocchi, M., and Gao, G. (2017). One-pot aqueous synthesization of near-infrared quantum dots for bioimaging and photodynamic therapy of gliomas. *Acta Neurochir. Suppl.* 124, 303–308. doi:10.1007/978-3-319-39546-3_44

Liu, P., Gao, C., Chen, H., Vong, C. T., Wu, X., Tang, X., et al. (2021). Receptor-mediated targeted drug delivery systems for treatment of inflammatory bowel disease: Opportunities and emerging strategies. *Acta Pharm. Sin. B* 11 (9), 2798–2818. doi:10.1016/j.apsb.2020.11.003

Louis, D. N., Perry, A., Wesseling, P., Brat, D. J., Cree, I. A., Figarella-Branger, D., et al. (2021). The 2021 WHO classification of tumors of the central nervous system: A summary. *Neuro Oncol.* 23 (8), 1231–1251. doi:10.1093/neuonc/noab106

Lowther, D. E., Goods, B. A., Lucca, L. E., Lerner, B. A., Raddassi, K., van Dijk, D., et al. (2016). PD-1 marks dysfunctional regulatory T cells in malignant gliomas. *JCI Insight* 1 (5), e85935. doi:10.1172/jci.insight.85935

Lux, F., Tran, V. L., Thomas, E., Dufort, S., Rossetti, F., Martini, M., et al. (2019). AGuIX($^{®}$) from bench to bedside-Transfer of an ultrasmall theranostic gadolinium-based nanoparticle to clinical medicine. *Br. J. Radiol.* 92 (1093), 20180365. doi:10.1259/bjr.20180365

Matsumura, Y., and Maeda, H. (1986). A new concept for macromolecular therapeutics in cancer chemotherapy: Mechanism of tumoritropic accumulation of proteins and the antitumor agent smancs. *Cancer Res.* 46 (12), 6387–6392.

McDannold, N., Arvanitis, C. D., Vykhodtseva, N., and Livingstone, M. S. (2012). Temporary disruption of the blood-brain barrier by use of ultrasound and microbubbles: Safety and efficacy evaluation in rhesus macaques. *Cancer Res.* 72 (14), 3652–3663. doi:10.1158/0008-5472.Can-12-0128

McPherson, P. S., Kay, B. K., and Hussain, N. K. (2001). Signaling on the endocytic pathway. *Traffic* 2 (6), 375–384. doi:10.1034/j.1600-0854.2001.002006375.x

Miranda, A., Blanco-Prieto, M. J., Sousa, J., Pais, A., and Vitorino, C. (2017). Breaching barriers in glioblastoma. Part II: Targeted drug delivery and lipid nanoparticles. *Int. J. Pharm.* 531 (1), 389–410. doi:10.1016/j.ijpharm.2017.07.049

Mohan, M., and Poddar, R. (2021). Polymerically engineered upconversion nanoparticles (UCNPs) as contrast agent for functionally modified optical coherence tomography (OCT). *Mater. Sci. Eng. C* 121, 111841. doi:10.1016/j.msec.2020.111841

Monaco, I., Camorani, S., Colecchia, D., Locatelli, E., Calandro, P., Oudin, A., et al. (2017). Aptamer functionalization of nanosystems for glioblastoma targeting through the blood-brain barrier. *J. Med. Chem.* 60 (10), 4510–4516. doi:10.1021/acs.jmedchem.7b00527

Naik, H., Sonju, J. J., Singh, S., Chatzistamou, I., Shrestha, L., Gauthier, T., et al. (2021). Lipidated peptidomimetic ligand-functionalized HER2 targeted liposome as nano-carrier designed for doxorubicin delivery in cancer therapy. *Pharm. (Basel)* 14 (3), 221. doi:10.3390/ph14030221

Neuschmelting, V., Harmsen, S., Beziere, N., Lockau, H., Hsu, H. T., Huang, R., et al. (2018). Dual-Modality Surface Enhanced Resonance Raman Scattering and multispectral optoacoustic tomography nanoparticle approach for brain tumor delineation. *Small* 14 (23), e1800740. doi:10.1002/smll.201800740

Ni, D., Zhang, J., Bu, W., Xing, H., Han, F., Xiao, Q., et al. (2014). Dual-targeting upconversion nanoprobes across the blood-brain barrier for magnetic resonance/fluorescence imaging of intracranial glioblastoma. *ACS Nano* 8 (2), 1231–1242. doi:10.1021/nn406197c

Orunoğlu, M., Kaffashi, A., Pehlivan, S. B., Şahin, S., Söylemezoğlu, F., Oğuz, K. K., et al. (2017). Effects of curcumin-loaded PLGA nanoparticles on the RG2 rat glioma model. *Mater. Sci. Eng. C* 78, 32–38. doi:10.1016/j.msec.2017.03.292

Othman, M., Desmaële, D., Couvreur, P., Vander Elst, L., Laurent, S., Muller, R. N., et al. (2011). Synthesis and physicochemical characterization of new squalenoyl amphiphilic gadolinium complexes as nanoparticle contrast agents. *Org. Biomol. Chem.* 9 (11), 4367–4386. doi:10.1039/c1ob00015b

Patel, M. M., and Patel, B. M. (2017). Crossing the blood-brain barrier: Recent advances in drug delivery to the brain. *CNS Drugs* 31 (2), 109–133. doi:10.1007/s40263-016-0405-9

Qi, J., Sun, C., Li, D., Zhang, H., Yu, W., Zebibula, A., et al. (2018). Aggregation-induced emission luminogen with near-infrared-II excitation and near-infrared-I emission for ultradeep intravital two-photon microscopy. *ACS Nano* 12 (8), 7936–7945. doi:10.1021/acsnano.8b02452

Ramalho, M. J., Sevin, E., Gosselet, F., Lima, J., Coelho, M. A. N., Loureiro, J. A., et al. (2018). Receptor-mediated PLGA nanoparticles for glioblastoma multiforme treatment. *Int. J. Pharm.* 545 (1-2), 84–92. doi:10.1016/j.ijpharm.2018.04.062

Ray, A., Mukundan, A., Xie, Z., Karamchand, L., Wang, X., and Kopelman, R. (2014). Highly stable polymer coated nano-clustered silver plates: A multimodal optical contrast agent for biomedical imaging. *Nanotechnology* 25 (44), 445104. doi:10.1088/0957-4484/25/44/445104

Reardon, D. A., Wucherpfennig, K., and Chiocca, E. A. (2017). Immunotherapy for glioblastoma: On the sidelines or in the game? *Discov. Med.* 24 (133), 201–208.

Richard, S., Boucher, M., Lalatonne, Y., Mériaux, S., and Motte, L. (2017). Iron oxide nanoparticle surface decorated with cRGD peptides for magnetic resonance imaging of brain tumors. *Biochimica Biophysica Acta - General Subj.* 1861 (6), 1515–1520. doi:10.1016/j.bbagen.2016.12.020

Richiardi, J., Eryilmaz, H., Schwartz, S., Vuilleumier, P., and Van De Ville, D. (2011). Decoding brain states from fMRI connectivity graphs. *Neuroimage* 56 (2), 616–626. doi:10.1016/j.neuroimage.2010.05.081

Riley, R. S., June, C. H., Langer, R., and Mitchell, M. J. (2019). Delivery technologies for cancer immunotherapy. *Nat. Rev. Drug Discov.* 18 (3), 175–196. doi:10.1038/s41573-018-0006-z

Roose, T., Netti, P. A., Munn, L. L., Boucher, Y., and Jain, R. K. (2003). Solid stress generated by spheroid growth estimated using a linear poroelasticity model. *Microvasc. Res.* 66 (3), 204–212. doi:10.1016/s0026-2862(03)00057-8

Ruiz-Garcia, H., Ramirez-Loera, C., Malouff, T. D., Seneviratne, D. S., Palmer, J. D., and Trifiletti, D. M. (2021). Novel strategies for nanoparticle-based radiosensitization in glioblastoma. *Int. J. Mol. Sci.* 22 (18), 9673. doi:10.3390/ijms22189673

Saha, K., Agasti, S. S., Kim, C., Li, X., and Rotello, V. M. (2012). Gold nanoparticles in chemical and biological sensing. *Chem. Rev.* 112 (5), 2739–2779. doi:10.1021/cr2001178

Shah, L., Yadav, S., and Amiji, M. (2013). Nanotechnology for CNS delivery of bio-therapeutic agents. *Drug Deliv. Transl. Res.* 3 (4), 336–351. doi:10.1007/s13346-013-0133-3

Sharpe, A. H., and Pauken, K. E. (2018). The diverse functions of the PD1 inhibitory pathway. *Nat. Rev. Immunol.* 18 (3), 153–167. doi:10.1038/nri.2017.108

Shen, C., Wang, X., Zheng, Z., Gao, C., Chen, X., Zhao, S., et al. (2019). Doxorubicin and indocyanine green loaded superparamagnetic iron oxide nanoparticles with PEGylated phospholipid coating for magnetic resonance with fluorescence imaging and chemotherapy of glioma. *Int. J. Nanomedicine* 14, 101–117. doi:10.2147/ijn.S173954

Shen, Z., Song, J., Yung, B. C., Zhou, Z., Wu, A., and Chen, X. (2018). Emerging strategies of cancer therapy based on ferroptosis. *Adv. Mat.* 30 (12), e1704007. doi:10.1002/adma.201704007

Shir, A., Ogris, M., Wagner, E., and Levitzki, A. (2006). EGF receptor-targeted synthetic double-stranded RNA eliminates glioblastoma, breast cancer, and adenocarcinoma tumors in mice. *PLoS Med.* 3 (1), e6. doi:10.1371/journal.pmed.0030006

Soukup, D., Moise, S., Céspedes, E., Dobson, J., and Telling, N. D. (2015). *In situ* measurement of magnetization relaxation of internalized nanoparticles in live cells. *ACS Nano* 9 (1), 231–240. doi:10.1021/nn503888j

Srimanee, A., Arvanitidou, M., Kim, K., Hällbrink, M., and Langel, Ü. (2018). Cell-penetrating peptides for siRNA delivery to glioblastomas. *Peptides* 104, 62–69. doi:10.1016/j.peptides.2018.04.015

Stephen, Z. R., Kievit, F. M., Veiseh, O., Chiarelli, P. A., Fang, C., Wang, K., et al. (2014). Redox-responsive magnetic nanoparticle for targeted convection-enhanced delivery of O6-benzylguanine to brain tumors. *ACS Nano* 8 (10), 10383–10395. doi:10.1021/nn503735w

Su, W., Gao, C., Wang, P., Huang, J., Qian, Y., Guo, L., et al. (2017). Correlation of circulating T lymphocytes and intracranial hypertension in intracerebral hemorrhage. *World Neurosurg.* 107, 389–395. doi:10.1016/j.wneu.2017.07.179

Suganami, A., Iwadate, Y., Shibata, S., Yamashita, M., Tanaka, T., Shinozaki, N., et al. (2015). Liposomally formulated phospholipid-conjugated indocyanine green for intra-operative brain tumor detection and resection. *Int. J. Pharm.* 496 (2), 401–406. doi:10.1016/j.ijpharm.2015.10.001

Sun, T., Patil, R., Galstyan, A., Klymyshyn, D., Ding, H., Chesnokova, A., et al. (2019). Blockade of a laminin-411-notch Axis with CRISPR/Cas9 or a nanobioconjugate inhibits glioblastoma growth through tumor-microenvironment cross-talk. *Cancer Res.* 79 (6), 1239–1251. doi:10.1158/0008-5472.Can-18-2725

Sun, X., Huang, X., Yan, X., Wang, Y., Guo, J., Jacobson, O., et al. (2014). Chelator-free (64)Cu-integrated gold nanomaterials for positron emission tomography imaging guided photothermal cancer therapy. *ACS Nano* 8 (8), 8438–8446. doi:10.1021/nn502950t

Tang, J., Huang, N., Zhang, X., Zhou, T., Tan, Y., Pi, J., et al. (2017). Aptamer-conjugated PEGylated quantum dots targeting epidermal growth factor receptor variant III for fluorescence imaging of glioma. *Int. J. Nanomedicine* 12, 3899–3911. doi:10.2147/ijn.S133166

Tang, P., Xing, M., Xing, X., Tao, Q., Cheng, W., Liu, S., et al. (2021). Receptor-mediated photothermal/photodynamic synergistic anticancer nanodrugs with SERS tracing function. *Colloids Surfaces B Biointerfaces* 199, 111550. doi:10.1016/j.colsurfb.2020.111550

Umlauf, B. J., and Shusta, E. V. (2019). Exploiting BBB disruption for the delivery of nanocarriers to the diseased CNS. *Curr. Opin. Biotechnol.* 60, 146–152. doi:10.1016/j.copbio.2019.01.013

Vauthier, C., Dubernet, C., Fattal, E., Pinto-Alphandary, H., and Couvreur, P. (2003). Poly(alkylcyanoacrylates) as biodegradable materials for biomedical applications. *Adv. Drug Deliv. Rev.* 55 (4), 519–548. doi:10.1016/s0169-409x(03)00041-3

Wang, K., Peña, J., and Xing, J. (2020). Upconversion nanoparticle-assisted photopolymerization. *Photochem. Photobiol.* 96 (4), 741–749. doi:10.1111/php.13249

Wang, S., Meng, Y., Li, C., Qian, M., and Huang, R. (2015). Receptor-mediated drug delivery systems targeting to glioma. *Nanomater. (Basel)* 6 (1), 3. doi:10.3390/nano6010003

Wang, S., Reinhard, S., Li, C., Qian, M., Jiang, H., Du, Y., et al. (2017). Antitumoral cascade-targeting ligand for IL-6 receptor-mediated gene delivery to glioma. *Mol. Ther.* 25 (7), 1556–1566. doi:10.1016/j.ymthe.2017.04.023

Wang, X., Xiong, Z., Liu, Z., Huang, X., and Jiang, X. (2018). Angiopep-2/IP10-EGFRvIIIscFv modified nanoparticles and CTL synergistically inhibit malignant glioblastoma. *Sci. Rep.* 8 (1), 12827. doi:10.1038/s41598-018-30072-x

Woroniecka, K., Chongsathidkiet, P., Rhodin, K., Kemeny, H., Dechant, C., Farber, S. H., et al. (2018). T-cell exhaustion signatures vary with tumor type and are severe in glioblastoma. *Clin. Cancer Res.* 24 (17), 4175–4186. doi:10.1158/1078-0432.Ccr-17-1846

Wu, P., and Yan, X. P. (2013). Doped quantum dots for chemo/biosensing and bioimaging. *Chem. Soc. Rev.* 42 (12), 5489–5521. doi:10.1039/c3cs60017c

Wu, T., Liu, Y., Cao, Y., and Liu, Z. (2022). Engineering macrophage exosome disguised biodegradable nanoplatform for enhanced sonodynamic therapy of glioblastoma. *Adv. Mater.* 34 (15), e2110364. doi:10.1002/adma.202110364

Wu, X., Yang, H., Yang, W., Chen, X., Gao, J., Gong, X., et al. (2019). Nanoparticle-based diagnostic and therapeutic systems for brain tumors. *J. Mat. Chem. B* 7 (31), 4734–4750. doi:10.1039/c9tb00860h

Xie, J., Shen, Z., Anraku, Y., Kataoka, K., and Chen, X. (2019). Nanomaterial-based blood-brain-barrier (BBB) crossing strategies. *Biomaterials* 224, 119491. doi:10.1016/j.biomaterials.2019.119491

Xue, J., Zhao, Z., Zhang, L., Xue, L., Shen, S., Wen, Y., et al. (2017). Neutrophil-mediated anticancer drug delivery for suppression of postoperative malignant glioma recurrence. *Nat. Nanotech.* 12 (7), 692–700. doi:10.1038/nnano.2017.54

Yang, Q., Zhou, Y., Chen, J., Huang, N., Wang, Z., and Cheng, Y. (2021). Gene therapy for drug-resistant glioblastoma via lipid-polymer hybrid nanoparticles combined with focused ultrasound. *Int. J. Nanomedicine* 16, 185–199. doi:10.2147/ijn.S286221

Yang, T., Sun, Y., Liu, Q., Feng, W., Yang, P., and Li, F. (2012). Cubic sub-20 nm NaLuF(4)-based upconversion nanophosphors for high-contrast bioimaging in different animal species. *Biomaterials* 33 (14), 3733–3742. doi:10.1016/j.biomaterials.2012.01.063

Yu, M., Yang, Y., Zhu, C., Guo, S., and Gan, Y. (2016). Advances in the transepithelial transport of nanoparticles. *Drug Discov. Today* 21 (7), 1155–1161. doi:10.1016/j.drudis.2016.05.007

Zanganeh, S., Georgala, P., Corbo, C., Arabi, L., Ho, J. Q., Javdani, N., et al. (2019). Immunoengineering in glioblastoma imaging and therapy. *Wiley Interdiscip. Rev. Nanomed. Nanobiotechnol.* 11 (6), e1575. doi:10.1002/wnan.1575

Zhan, C., Gu, B., Xie, C., Li, J., Liu, Y., and Lu, W. (2010). Cyclic RGD conjugated poly(ethylene glycol)-co-poly(lactic acid) micelle enhances paclitaxel anti-glioblastoma effect. *J. Control. Release* 143 (1), 136–142. doi:10.1016/j.jconrel.2009.12.020

Zhang, Y., and Calderwood, S. K. (2011). Autophagy, protein aggregation and hyperthermia: A mini-review. *Int. J. Hyperth.* 27 (5), 409–414. doi:10.3109/02656736.2011.552087

Zhang, Y., Fu, X., Jia, J., Wikerholmen, T., Xi, K., Kong, Y., et al. (2020). Glioblastoma therapy using codelivery of cisplatin and glutathione peroxidase targeting siRNA from iron oxide nanoparticles. *ACS Appl. Mat. Interfaces* 12 (39), 43408–43421. doi:10.1021/acsami.0c12042

Zhang, Y., Hong, G., Zhang, Y., Chen, G., Li, F., Dai, H., et al. (2012). Ag2S quantum dot: A bright and biocompatible fluorescent nanoprobe in the second near-infrared window. *ACS Nano* 6 (5), 3695–3702. doi:10.1021/nn301218z

Zhang, Y., Xi, K., Fu, X., Sun, H., Wang, H., Yu, D., et al. (2021). Versatile metal-phenolic network nanoparticles for multitargeted combination therapy and magnetic resonance tracing in glioblastoma. *Biomaterials* 278, 121163. doi:10.1016/j.biomaterials.2021.121163

Zhao, H., Gao, H., Zhai, L., Liu, X., Jia, B., Shi, J., et al. (2016). (99m Tc-HisoDGR as a potential SPECT probe for orthotopic glioma detection via targeting of integrin α5β1. *Bioconjugate Chem.* 27 (5), 1259–1266. doi:10.1021/acs.bioconjchem.6b00098

Zhao, H. L., Zhang, J., Zhu, Y., Wu, Y., Yan, Q. G., Peng, X. Y., et al. (2020). Protective effects of HBOC on pulmonary vascular leakage after haemorrhagic shock and the underlying mechanisms. *Artif. Cells Nanomedicine Biotechnol.* 48 (1), 1272–1281. doi:10.1080/21691401.2020.1835937

Zhao, M., van Straten, D., Broekman, M. L. D., Préat, V., and Schiffelers, R. M. (2020). Nanocarrier-based drug combination therapy for glioblastoma. *Theranostics* 10 (3), 1355–1372. doi:10.7150/thno.38147

Zheng, D. W., Lei, Q., Zhu, J. Y., Fan, J. X., Li, C. X., Li, C., et al. (2017). Switching apoptosis to ferroptosis: Metal-organic network for high-efficiency anticancer therapy. *Nano Lett.* 17 (1), 284–291. doi:10.1021/acs.nanolett.6b04060

Zhou, Z., Bai, R., Wang, Z., Bryant, H., Lang, L., Merkle, H., et al. (2019). An albumin-binding T(1)- T(2) dual-modal MRI contrast agents for improved sensitivity and accuracy in tumor imaging. *Bioconjugate Chem.* 30 (6), 1821–1829. doi:10.1021/acs.bioconjchem.9b00349

frontiers | Frontiers in Bioengineering and Biotechnology

TYPE Original Research
PUBLISHED 28 February 2023
DOI 10.3389/fbioe.2023.1109841

# Phytofabrication and characterization of *Alchornea cordifolia* silver nanoparticles and evaluation of antiplasmodial, hemocompatibility and larvicidal potential

Loick Pradel Kojom Foko [1,2], Joseph Hawadak [1,2], Vaishali Verma [3], Philippe Belle Ebanda Kedi [4,5,6], Carole Else Eboumbou Moukoko [7,8,9], Raghavendra Kamaraju [3], Veena Pande [2] and Vineeta Singh [1]*

[1]Parasite and Host Biology Group, ICMR-National Institute of Malaria Research, Dwarka, New Delhi, India, [2]Department of Biotechnology, Kumaun University, Nainital, Uttarakhand, India, [3]Vector Biology Group, ICMR-National Institute of Malaria Research, Dwarka, New Delhi, India, [4]Department of Animal Organisms, Faculty of Sciences, The University of Douala, Douala, Cameroon, [5]Nanosciences African Network, iThemba LABS-National Research Foundation, Cape Town, South Africa, [6]Laboratory of Innovative Nanostructured Material (NANO: C), Faculty of Medicine and Pharmaceutical Sciences, The University of Douala, Douala, Cameroon, [7]Department of Biological Sciences, Faculty of Medicine and Pharmaceutical Sciences, The University of Douala, Douala, Cameroon, [8]Malaria Research Unit, Centre Pasteur Cameroon, Yaoundé, Cameroon, [9]Laboratory of Parasitology, Mycology and Virology, Postgraduate Training Unit for Health Sciences, Postgraduate School for Pure and Applied Sciences, The University of Douala, Douala, Cameroon

Check for updates

OPEN ACCESS

EDITED BY
Guannan Wang,
Jining Medical University, China

REVIEWED BY
Hatem Fouad,
Zhejiang University, China
Shereen A. Majeed,
Kuwait University, Kuwait

*CORRESPONDENCE
Vineeta Singh,
✉ vineetas_2000@yahoo.com

SPECIALTY SECTION
This article was submitted to Nanobiotechnology, a section of the journal Frontiers in Bioengineering and Biotechnology

RECEIVED 28 November 2022
ACCEPTED 10 February 2023
PUBLISHED 28 February 2023

CITATION
Kojom Foko LP, Hawadak J, Verma V, Belle Ebanda Kedi P, Eboumbou Moukoko CE, Kamaraju R, Pande V and Singh V (2023), Phytofabrication and characterization of *Alchornea cordifolia* silver nanoparticles and evaluation of antiplasmodial, hemocompatibility and larvicidal potential. *Front. Bioeng. Biotechnol.* 11:1109841. doi: 10.3389/fbioe.2023.1109841

**Purpose:** The recent emergence of *Plasmodium falciparum* (*Pf*) parasites resistant to current artemisinin-based combination therapies in Africa justifies the need to develop new strategies for successful malaria control. We synthesized, characterized and evaluated medical applications of optimized silver nanoparticles using *Alchornea cordifolia* (AC-AgNPs), a plant largely used in African and Asian traditional medicine.

**Methods:** Fresh leaves of *A. cordifolia* were used to prepare aqueous crude extract, which was mixed with silver nitrate for AC-AgNPs synthesis and optimization. The optimized AC-AgNPs were characterized using several techniques including ultraviolet-visible spectrophotometry (UV-Vis), scanning/transmission electron microscopy (SEM/TEM), powder X-ray diffraction (PXRD), selected area electron diffraction (SAED), energy dispersive X-ray spectroscopy (EDX), Fourier transformed infrared spectroscopy (FTIR), dynamic light scattering (DLS) and Zeta potential. Thereafter, AC-AgNPs were evaluated for their hemocompatibility and antiplasmodial activity against *Pf* malaria strains 3D7 and RKL9. Finally, lethal activity of AC-AgNPs was assessed against mosquito larvae of *Anopheles stephensi*, *Culex quinquefasciatus* and *Aedes aegypti* which are vectors of neglected diseases such as dengue, filariasis and chikungunya.

**Results:** The AC-AgNPs were mostly spheroidal, polycrystalline (84.13%), stable and polydispersed with size of 11.77 ± 5.57 nm. FTIR revealed the presence of several peaks corresponding to functional chemical groups characteristics of alkanoids, terpenoids, flavonoids, phenols, steroids, anthraquonones and saponins. The AC-AgNPs had a high antiplasmodial activity, with $IC_{50}$ of 8.05 µg/mL and 10.31 µg/mL against 3D7 and RKL9 *Plasmodium falciparum* strains. Likewise, high larvicidal activity of AC-AgNPs was found after 24 h- and 48 h-exposure: $LC_{50}$ = 18.41 µg/mL and 8.97 µg/mL (*Culex quinquefasciatus*), $LC_{50}$ = 16.71 µg/mL and 7.52 µg/mL (*Aedes aegypti*) and $LC_{50}$ = 10.67 µg/mL and 5.85 µg/mL (*Anopheles stephensi*). The AC-AgNPs were highly hemocompatible ($HC_{50}$ > 500 µg/mL).

**Conclusion:** In worrying context of resistance of parasite and mosquitoes, green nanotechnologies using plants could be a cutting-edge alternative for drug/insecticide discovery and development.

KEYWORDS

***Alchornea cordifolia*, silver nanoparticles, green synthesis, characterization, hemocompatibility, biocidal activities, Plasmodium falciparum, culicidae mosquitoes**

## 1 Introduction

Nanotechnology has profoundly changed several aspects of human life through technological and health advances made in sectors such as new technologies, energy, cosmetics and health. This term encompasses a set of activities from development research to evaluation of materials sized 1–100 nm—also known as nanomaterials (Subedi, 2013; Bayda et al., 2020). In developed countries such as the United States of America, Japan and China, nanotechnologies are greatly funded, studied and evaluated for their ability to solve diverse problems (Dong et al., 2016; Qiu, 2016). In developing countries, studies are more focused on green nanotechnologies which rely on the development of nanomaterials using living organisms such as plants and microorganisms (Kojom Foko et al., 2019; Kojom Foko et al., 2021).

Green nanotechnologies are very attractive as these are cheaper to implement, safer and eco-friendly as compared to their chemical and physical counterparts (Tran et al., 2013; Gahlawat and Choudhury, 2019). Indeed, chemical and physical methods are time-consuming, costly and request reagents which are harmful to humans and environment (Shakeel et al., 2016). By blending living organisms (e.g., fungi, viruses, bacteria, alga, plants) or derived products with metal source, green metallic nanoparticles (MNPs) are synthesized and then can be tested for different biological and non-biological activities (Honary et al., 2013; Kojom Foko et al., 2019; Bayda et al., 2020; Chugh et al., 2021; Araújo et al., 2022). Also, the utilization of plants is more advantageous than with microorganisms due to increased risk of biohazard and cost to isolate, purify and maintain microbial cultures (Kalishwaralal et al., 2010; Shakeel et al., 2016).

Regarding biological activities, many studies reviewed biocidal potential of green MNPs against non-communicable diseases (e.g., diabetes, cancer), oxidative stress, diverse pathogens (e.g., bacteria, viruses), and disease vectors (e.g., mosquitoes, ticks) (Benelli et al., 2017; Patil and Chandrasekaran, 2020; Araújo et al., 2022). Roughly, plant-based MNPs show a high biocidal potential, and thus were proposed as new avenues for control of infectious diseases, especially mosquito-borne diseases (e.g., malaria, dengue and chikungunya) for which current control methods are jeopardized due to i) their toxicity to humans and environment, and ii) emergence and spread of drug-resistant parasites and insecticide-resistant mosquitoes (Kojom Foko et al., 2019; Kojom Foko et al., 2021). Thus, synthesis of plant-based MNPs could be interesting to develop new drugs and insecticides to control and eliminate mosquito-borne diseases. Malaria is the predominant vector-borne disease globally with an estimated 247 million cases and 619,000 deaths in 2021 (World Health Organization, 2022). Africa bears the bulk of this global malaria burden, with children under 5 years of age and pregnant women being most vulnerable groups (Dongang Nana et al., 2022; World Health Organization, 2022). Resistance of pathogens and mosquito vectors is a great threat to malaria control and elimination efforts (Arya et al., 2021). Recent studies pointed out independent emergence of malaria parasites resistant to current most effective antimalarial drugs (i.e., artemisinin-based combination therapies - ACTs) in two African countries (Rwanda and Uganda) (Uwimana et al., 2021, 2020; Balikagala et al., 2021).

There is paucity of data on biological activities of green MNPs in Cameroon where vector-borne diseases such as malaria are causes of concern (Lehman et al., 2018; Antonio-Nkondjio et al., 2019; Mbohou et al., 2019). In the present study, silver NPs were synthesized using leaves of *Alchornea cordifolia* (AC-AgNPs), optimized, characterized and evaluated for hemocompatibility and lethal activity against *Plasmodium falciparum—Pf* (the main and deadliest human malaria species) (Kojom Foko et al., 2021; Kojom Foko et al., 2022b; World Health Organization, 2022), and three mosquito species, i.e., *Anopheles stephensi*, *Culex quinquefasciatus* and *Aedes aegypti*, involved in human transmission of parasites and viruses (dengue, Zika, malaria and lymphatic filariasis) (Benelli et al., 2017; Wang et al., 2017; Patil and Chandrasekaran, 2020). *Alchornea cordifolia* Schumach. *and* Thonn.) Müll. Arg. (Euphorbiaceae) is largely distributed in sub-Saharan African countries (e.g., Cameroon, Ghana, Nigeria) where its leaves and root bark are traditionally used by populations for nutritional purposes and treating several infectious and inflammatory ailments such as rheumatism, pain and arthritis (Ngaha Njila et al., 2016; Cesar et al., 2017).

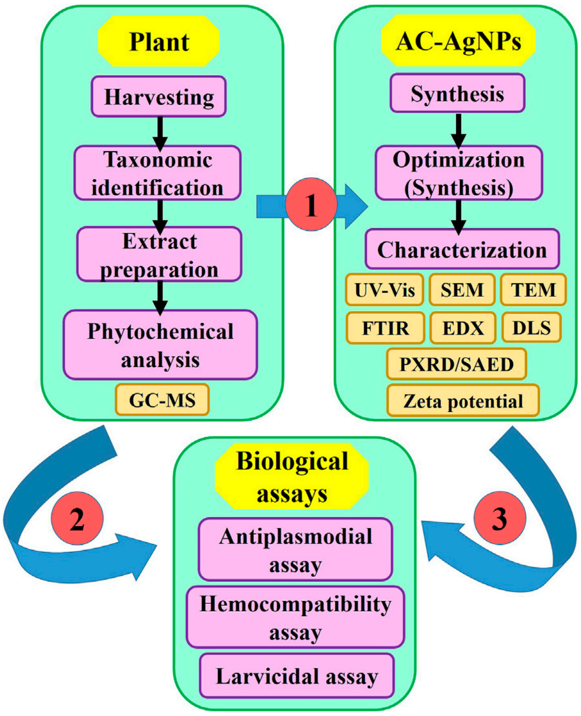

FIGURE 1
Flowchart depicting the study design. AC-AgNPs, *Alchornea cordifolia* silver nanoparticles; GC-MS, Gas chromatography—Mass spectrometry; DLS, Dynamic light scattering; EDX, Energy dispersive X-ray spectroscopy; FTIR, Fourier transformed infrared spectroscopy; PXRD, Powder X-ray diffraction; SAED, Selected area electron diffraction; SEM, Scanning electron microscopy; TEM, Transmission electron microscopy; UV-Vis, Ultraviolet—Visible spectrophotometry.

# 2 Materials and methods

## 2.1 Study design

This was an experimental study aimed at determining antiplasmodial, hemocompatibility and larvicidal potential of biosynthesized silver NPs using *A. cordifolia* leaves. The plant was harvested and authenticated taxonomically. Crude extract of *A. cordifolia* leaves (AC-CE) was screened for phytochemical composition and used for AgNPs synthesis. The optimization of AC-AgNPs was made, and the optimized AC-AgNPs were characterized and tested for antiplasmodial, hemocompatibility and larvicidal potential (Figure 1). The study was approved by ethical committee of the National Institute of Malaria Research (NIMR), India (N°PHB/NIMR/EC/2020/55).

## 2.2 Collection and authentication of plant material

Healthy and fresh leaves of *A. cordifolia* (AC) were collected at Faculty of Sciences (FS), main campus, University of Douala (UD), Littoral Region, Cameroon (Figure 2). Malaria is highly prevalent in Cameroon, and *P. falciparum* is the main malaria species. Other species including *Plasmodium vivax*, *Plasmodium ovale spp* have also been reported across the country (Kojom Foko et al., 2021; Kojom Foko et al., 2022a). The taxonomic authentication was done by Dr Tchiengue Barthelemy at Cameroon National Herbarium, Yaounde, in comparison with voucher specimen number 9657/SRF/Cam previously deposited.

## 2.3 Preparation of *A. cordifolia* aqueous extract

About 500 g of fresh *A. cordifolia* leaves were washed with running tap water and distilled water to remove dust and surface contaminant, and thereafter air-dried for 2 weeks at room temperature. The dried material was introduced in an electric grinder to obtain a fine powder. Ten grams of powder was taken in a conical flask containing 100 mL of distilled water, heated at 80°C for 10 min in a water bath under static conditions (Eya'ane Meva et al., 2016). The mixture was allowed to cool at room temperature, and then filtered using a Whatman paper n°1 to remove particulate matter. The filtrate obtained (crude extract, AC-CE) was used to perform phytochemical screening and AC-AgNPs biosynthesis. The AC-CE was not used more than a week following its preparation in order to avoid gradual loss of viability due to long storages (Eya'ane Meva et al., 2016). The AC-CE was lyophilized and stored for biological assays. The yield of extraction of AC-CE was 41% (w/v).

## 2.4 Phytochemical screening of *A. cordifolia* aqueous extract

The AC-CE was subjected to gas chromatography-mass spectrometry (GC-MS) analysis to identify the composition and percentage abundance of phytochemical constituents. The GC-MS was carried out on a Perkin Elmer Turbo Mass Spectrophotometer (Norwalk, CTO6859, NY, United States) which includes a Perkin Elmer Auto sampler XLGC. The column used was a Perkin Elmer Elite-5 capillary column measuring 30 m × 0.25 mm with a film thickness of 0.25 mm composed of 95% dimethyl polysiloxane. The carrier gas used was helium at a flow rate of 1.21 mL/min 1 µL sample injection volume was utilized. The inlet temperature was maintained at 260°C. Oven temperature was programmed initially at 100°C for 2 min, and then programmed to increase to 290°C at a flow rate of 10°C/min (Supplementary Figure S1). The total run time was 39.98 min. The Mass Spectrometry transfer line was maintained at a temperature of 200°C. The source temperature was maintained at 220°C. The GC-MS was analyzed using electron impact ionization at 70 eV. Full scan mode was used to detect analytes. Data were evaluated using total ion count for compound identification and quantification. Measurement of peak areas and data processing were carried out by Turbo-Mass-OCPTVS-Demo SPL software, and spectrums of the components were compared with database of spectrum of known components stored in the GC-MS library.

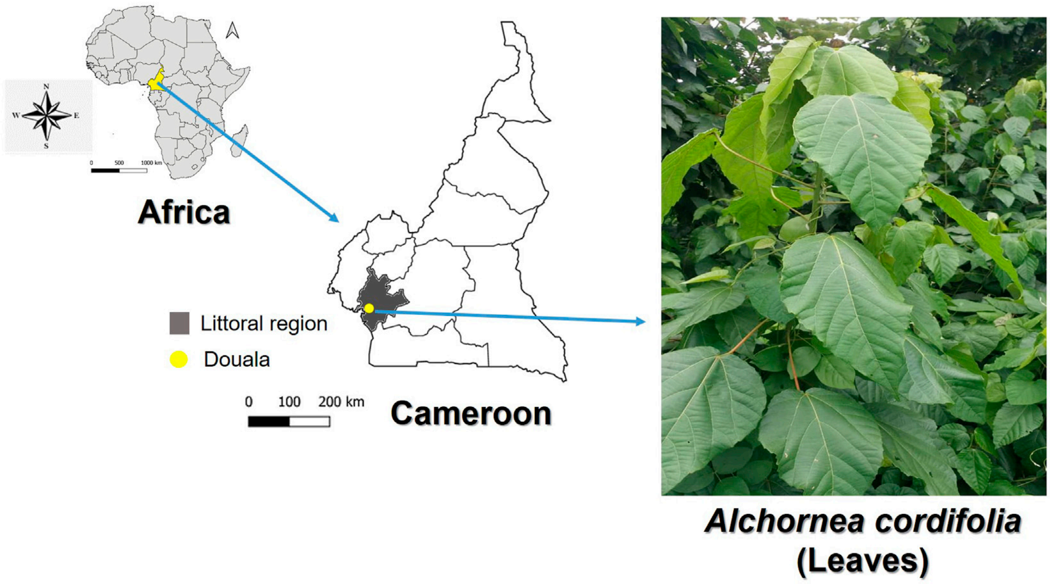

FIGURE 2
Maps of Africa, Cameroon and Douala (Littoral region) where fresh leaves of *Alchornea cordifolia* (Euphorbiaceae) were harvested. Maps were created using the QGIS software v3.10 (https://qgis.org/en/site/). Photograph of *A. cordifolia* is provided by author PBEK.

## 2.5 Phytofabrication and optimization studies of AC-AgNPs

AC-AgNPs were synthesized by blending $AgNO_3$ aqueous solution with freshly prepared AC-AE and incubated in dark until color change. The determination of optimal conditions for AC-AgNPs biosynthesis was performed by recording UV-Visible spectra of reaction mixtures after varying four parameters, namely, incubation temperature (35°C–85°C), incubation time (10 min–5 h), $AgNO_3$ concentration (0.5–5 mM), and $AgNO_3$/AC-CE volume ratio (10–100 µL) as described earlier (Hawadak et al., 2022). Thereafter, the optimized reaction mixture was centrifuged at 15,000 rpm for 10 min, the pellet was washed twice with distilled water and once with 95% ethanol, filtered using sterile syringe filter (MICRO-POR®, 0.22 µm), and then lyophilized for further AC-AgNPs characterization and biological assays.

## 2.6 Characterization of AC-AgNPs

The characteristics of green synthesized AC-AgNPs (i.e., surface plasmon resonance-SPR, size, shape, aggregation, functional chemical groups and crystallinity) were determined using several techniques (Figure 1). The formation of AC-AgNPs was monitored by visual inspection of the solution and then followed by UV–Vis spectrum measurement using a double beam spectrophotometer (Model n.o., BRI-2700, BR BIOCHEM Life Sciences Pvt., Ltd., India) operating at 1 nm resolution. Milli Q ultrapure water was used as blank. The selected area electron diffraction (SAED) and powder X-ray diffraction (XRD) were used to determine the physical nature of the AC-AgNPs. The PXRD was made at 45 kv voltage, 40 mA current, 2θ range of 10–80 and speed of 2°/minute (PANanalytical, Xpert Pro model). The PXRD patterns of optimized AC-AgNPs were compared to Joint Committee on Powder Diffraction Standards files (JCPDS 65-2871 and 31-1238). The size, shape and aggregation patterns of AC-AgNPs were determined using scanning electron microscopy—SEM coupled with EDX (Bruker AXS Microanalysis GmbH Berlin, Germany) and transmission electron microscopy—TEM coupled with SAED (TECNAI TF20, Fei, Electron Optics, Oregon, United States) operating at a potential of 20 kv and 200 kv, respectively. The size of NPs was calculated using the Scherrer equation: $D = \frac{K\lambda}{\beta \cos\theta}$, where D is diameter (nm) of the crystallite (i.e., NPs in this regard), K is the Scherrer constant (range values = 0.68–2.08) depending on shape of nanoparticles (e.g., K = 0.94 for spherical NPs); λ is the X-ray wavelength (in our study PXRD analysis was performed at wavelength for copper, $CuK_\alpha = 1.5406$ Å), β is the line broadening at full width at half maximum (FWHM) which is expressed in radians, and θ is the Bragg's angle of PXRD-related peaks which is expressed in degrees (Muniz et al., 2016). The atomic composition of the NPs was determined using energy dispersive X-ray (EDX). Fourier transformed infrared spectroscopy (FTIR) was used to determine functional chemical groups capped on the AC-AgNPs surface through potassium bromide method. Sample was grinded with KBr in an infrared path and the spectrum was recorded in the range 400–4000 $cm^{-1}$ using a FTIR spectrophotometer (Perkin Elmer, Frontier Model). Zeta potential and dynamic light scattering (DLS) were performed to evaluate NPs stability and size distribution using particle size analyzer (Zetasizer nano ZS, Malvern Instruments Ltd., U.K.). In practice, zeta potential of ±30 mV is considered as a good indicator of the stability of colloidal suspensions such as NPs while values outside the range indicate phenomena such as flocculation, aggregation and sedimentation (Kojom Foko et al., 2019).

**TABLE 1 Phytochemical screening of the AC-AE using GC-MS analysis.**

| Peak | Retention time | Area (%) | Name of the compounds |
|---|---|---|---|
| 1 | 6.76 | 2.58 | 4-Methylmannitol |
| 2 | 9.22 | 0.29 | Dodecanoic acid, methyl ester |
| 3 | 9.52 | 0.48 | 2(4H)-Benzofuranone, 5,6,7,7a-tetrahydro-4,4,7a-trimethyl-, (R)- |
| 4 | 10.04 | 0.57 | 1-Hexadecene |
| 5 | 10.99 | 0.41 | 8-Pentadecanone |
| 6 | 11.59 | 0.36 | 1,1,4,7-Tetramethyldecahydro-1H-cyclopropa[e]azulene-4,7-diol |
| 7 | 12.08 | 1.42 | 6-Hydroxy-4,4,7a-trimethyl-5,6,7,7a-tetrahydrobenzofuran-2(4H)-one |
| 8 | 12.31 | 0.58 | 1-Nonadecene |
| 9 | 12.37 | 0.51 | 2(4H)-Benzofuranone, 5,6,7,7a-Tetrahydro-6-hydroxy-4,4,7a-trimethyl- |
| 10 | 12.51 | 1.00 | (S,E)-4-Hydroxy-3,5,5-trimethyl-4-(3-oxobut-1-en-1-yl)cyclohex-2-enone |
| 11 | 12.77 | 1.28 | Neophytadiene |
| 12 | 12.84 | 1.08 | 2-Pentadecanone, 6,10,14-trimethyl- |
| 13 | 13.02 | 0.16 | 2-hexadecen-1-ol, 3,7,11,15-tetramethyl-, [R-[R*,R*-(E)]]- |
| 14 | 13.08 | 0.32 | 1,2-Benzenedicarboxylic acid, bis(2-methylpropyl) ester |
| 15 | 13.58 | 0.60 | 1,2-Benzenedicarboxylic acid, bis(2-methylpropyl) ester |
| 16 | 13.69 | 1.86 | Hexadecanoic acid, methyl ester |
| 17 | 14.22 | 2.36 | n-Hexadecanoic acid |
| 18 | 14.36 | 0.22 | 1-Octadecene |
| 19 | 14.84 | 1.99 | Hexadecanoic Acid, trimethylsilyl ester |
| 20 | 15.33 | 0.43 | 9,12-Octadecadienoic acid (Z,Z)-, methyl ester |
| 21 | 15.39 | 3.64 | 9,12,15-Octadecatrienoic acid, methyl ester, (Z,Z,Z)- |
| 22 | 15.51 | 25.17 | 2-Hexadecen-1-Ol, 3,7,11,15-Tetramethyl-, [R-[R*,R*-(E)]]- |
| 23 | 15.62 | 0.56 | Methyl stearate |
| 24 | 15.99 | 1.40 | Phytol, TMS derivative |
| 25 | 16.40 | 0.54 | Phytol, acetate |
| 26 | 17.63 | 0.21 | 4,8,12,16-Tetramethylheptadecan-4-olide |
| 27 | 19.09 | 1.41 | Bis(2-ethylhexyl) phthalate |
| 28 | 20.31 | 0.36 | Tetracontane |
| 29 | 21.14 | 1.70 | Squalene |
| 30 | 21.57 | 0.40 | .alpha.-Tocospiro B |
| 31 | 21.78 | 0.52 | Hexatriacontane |
| 32 | 22.52 | 1.11 | 9,12-Octadecadienoic Acid (Z,Z)-, 2,2-Dimethyl-1,3-Dioxolan-4-Ylmethyl Ester |
| 33 | 24.12 | 0.81 | Vitamin E |
| 34 | 24.84 | 3.32 | Ethanone, 1-(2,3,4,7,8,8a-hexahydro-3,6,8,8-tetramethyl-1H-3a,7-methanoazulen-5-yl)- |
| 35 | 25.93 | 3.65 | STIGMASTA-5,22-DIEN-3-OL |
| 36 | 26.87 | 4.69 | .gamma.-Sitosterol |
| 37 | 27.32 | 4.03 | 9,19-Cyclolanostane-3,7.beta.-diol, diacetate (20R,14.beta.) |
| 38 | 28.25 | 0.99 | 9,19-Cyclolanostan-3-ol, 24-methylene-, (3.beta.)- |

(Continued on following page)

**TABLE 1 (*Continued*) Phytochemical screening of the AC-AE using GC-MS analysis.**

| Peak | Retention time | Area (%) | Name of the compounds |
|---|---|---|---|
| 39 | 31.55 | 14.53 | Phytyl tetradecanoate |
| 40 | 35.11 | 3.40 | Methanesulfonic Acid 2-(3-Hydroxy-4,4,10,13,14-Pentamethyl-2,3,4,5,6,7,10,11,12,13,14,15,16,17-Tetradecahydro-1h-Cyclopenta[A]Phenan |
| 41 | 37.27 | 3.92 | 1-Eicosanol |
| 42 | 37.77 | 5.12 | 9,10,12,13-Tetrabromooctadecanoic acid |
| | Total | 100.00 | |

## 2.7 Assessment of antiplasmodial potential of AC-AgNPs

Chloroquine-sensitive 3D7 and chloroquine-resistant RKL9 of *Pf* strains were used for antiplasmodial assays for AC-AgNPs, AC-CE, and chloroquine (CQ). The *Pf* culture was maintained using standard protocols (Trager and Jensen, 1976; Schuster, 2002). Briefly, parasite cultures were maintained in fresh AB positive human erythrocytes suspended at 5% hematocrit in RPMI-1640 culture medium supplemented with L-glutamine and HEPES buffer (0.2% sodium bicarbonate, 0.4% albumax, 50 µg/L hypoxanthine, 200 U/mL penicillin and 200 µg/L streptomycin) and incubated at 37°C under a gas mixture of 1% $O_2$, 5% $CO_2$ and 94% $N_2$. Culture of infected erythrocytes were transferred daily into fresh complete culture medium and checked microscopically for parasite growth.

The *in vitro* evaluation of antiplasmodial activity was performed using culture-adapted *Pf* strains: i) 3D7, sensitive to CQ, artemisinin and its derivatives and ii) RKL9, resistant to CQ. Antimalarial drug screening was done based on SYBR green I-based fluorescence assay as described previously (Smilkstein et al., 2004). Parasite culture (0.5%–0.8%) was synchronized at ring stage with 5% sorbitol. A volume of 100 µL of complete medium were introduced into each well of 96-well microplate, then dilutions were performed for AC-AgNPs and AC-CE (4, 8, 16, 31.25, 62.5, 125, 250 and 500 µg/mL) and CQ (4, 6.25, 12.5, 25, 50, 100, and 200 µg/mL) were added. Ten microliters (10 µL) of synchronized blood were thereafter added in each well, mixed and kept in an incubator at 37°C for 48 h in 96-well flat bottom tissue culture-grade plates under reduced $O_2$ atmosphere. Each experiment was replicated thrice. CQ was used as standard drug, while complete medium was considered as negative control. After 48 h-incubation, 100 µL of SYBR Green I in lysis buffer (0.2 µL of the fluorochrome/mL of buffer) was added into each well, mixed gently twice, and the plate was then covered with foil and incubated in a dark chamber for 1 h at room temperature. The buffer lysis consisted of Triton X-100 (0.08% v/v), Tris (20 mM), EDTA (5 mM), and saponin (0.008% wt/v). The fluorescence counts were read using an ELISA reader (Synergy HTX 1708152, Agilent BioTek, Santa Clara, California, United States) with excitation and emission wavelength bands centered at 485 and 530 nm.

## 2.8 Validation of antiplasmodial assay

The SYBR Green based antiplasmodial assay was validated by inspecting microscopic slides of parasite cultures treated with negative control, standard drug, AC-CE and AC-AgNPs (Kaushik et al., 2015; Hawadak et al., 2022). After 48 h-incubation, thick and thin blood films were made, air-dried and stained with 10% Giemsa stain for 20 min. The number of schizonts with ≥2 nuclei out of 200 asexual parasites was noted. Also, fluorescence counts of untreated and treated *Pf* cultures were compared to detect any quenching effect-related measurement artefacts which may due to chemical compounds of AC-AgNPs and AC-CE (Kaushik et al., 2015).

## 2.9 Hemocompatibility investigation

The method described by Wang and others was used to evaluate hemocompatibility of biosynthesized AC-AgNPs (Wang et al., 2010). Human red blood cells (RBCs) were obtained from the ICMR-NIMR malaria parasite bank, washed with incomplete media, and diluted with phosphate-buffered saline (PBS) to obtain a suspension (Hematocrit = 1%). Different concentrations (2, 4, 8, 16, 30, 62.5, 125, 250 and 500 µg/mL) of AC-AgNPs and AC-CE were incubated with RBCs in Eppendorf tubes (20 µL of each concentration in 180 µL blood) at 37°C for 30 min and 24 h at pH of 7.40. The reaction was stopped by placing tubes at 4°C for 15 min. The mixtures were then centrifuged at 3,000 g for 4 min, and 100 µL of supernatant was loaded into a 96-well plate to measure the released hemoglobin at 540 nm (SPECTROstar$^{Nano}$, BMG LABTECH GmbH, Ortenberg Germany). Saponin was used as positive control, inducing 100% hemolysis, while PBS was considered as negative control. The experiment was performed in triplicate. RBCs hemolysis at each concentration after 30 min and 24 h was calculated as follows:

$$\%\,\text{hemolysis} = \frac{(\text{As} - \text{ANC})}{(\text{APC} - \text{ANC})} \times 100$$

where $A_S$, $A_{NC}$ and $A_{PC}$ are the absorbance of the sample, negative control (PBS) and positive control (saponin).

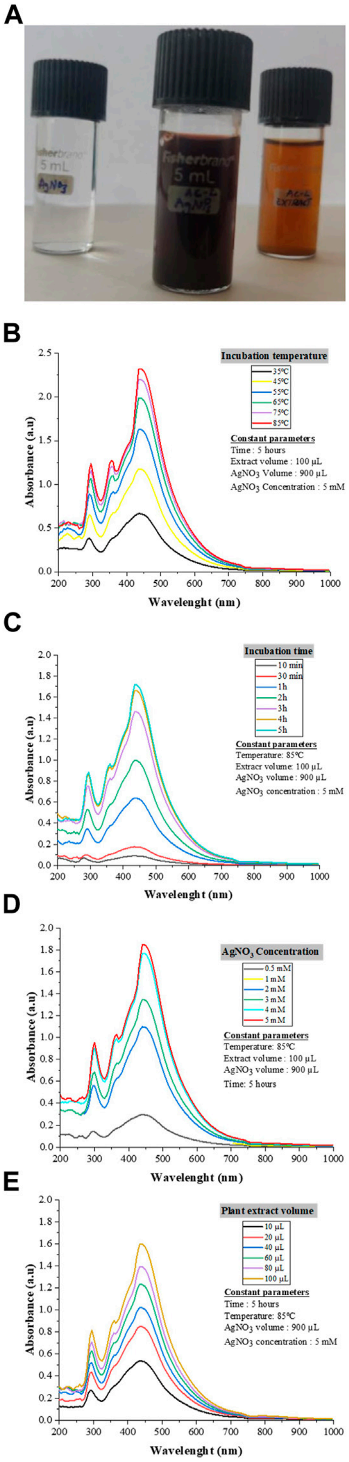

FIGURE 3
AC-AgNPs solution and UV-Vis findings. Color of $AgNO_3$, AC-AgNPs and AC-CE solutions **(A)**. The color change indicates $Ag^+$ reduction to elemental nanosilver. UV−visible spectrum of optimized AC-AgNPs for incubation temperature **(B)**, incubation time **(C)**, $AgNO_3$ concentration **(D)**, and volume of AC-CE **(E)**. AC-AgNPs, *Alchornea cordifolia* silver nanoparticles; AC-CE, *Alchornea cordifolia* crude extract; $AgNO_3$, Silver nitrate; UV-Vis, Ultraviolet−Visible spectrophotometry.

## 2.10 Mosquito rearing

The eggs of *An. stephensi*, *Cx. quinquefasciatus* and *Ae. aegypti* were obtained from NIMR Insectarium, New Delhi, India. The characteristics of mosquitoes used are as follows: *An. stephensi*—laboratory strain collected from Sonepat, Haryana, India (established in 1996; black and brown, malathion-deltamethrin-susceptible and DDT–resistant strain), *Cx. quinquefasciatus*—laboratory strain collected from Sonepat, Haryana, India (established in 1999; selected for permethrin resistance and is resistant to DDT, malathion and deltamethrin), and *Ae. aegypti*—laboratory strain collected from Delhi, India (established in 2006; DDT–malathion-deltamethrin strain). Adult *Ae. aegypti* were derived from batches of 100 eggs in 18 cm × 13 cm × 4 cm trays containing 500 mL of boiled and cooled water in a laboratory maintained at 25°C–29°C temperature and 65%–70% Relative humidity; 12:12 h Light/Dark photoperiod. Eggs were fed daily with TetraBits fish food (Tetra GmbH, Herrenteich, Germany), and late 3rd and 4th instar larvae were used for larval bioassays.

## 2.11 Larvicidal bioassays

The protocol described by the World health Organization (WHO) was used for this experiment (WHO, 2016). Late 3rd and 4th instar larvae were exposed to the AC-AgNPs with different concentrations (0–50 µg/mL). Each concentration was tested in triplicate comprising of 25 larvae placed into plastic bowls (8 cm diameter, 300 mL capacity) containing distilled water. The larval mortality was monitored after 24 h, 48 h and 72 h post-treatment periods, and the lethal concentrations to cause 50%/90% mortality in treated larvae ($LC_{50}/LC_{90}$) and percentage mortality after post-treatment periods were calculated as described previously in the WHO procedures (WHO, 2016). Distilled water was used as control. All experiments were performed under laboratory conditions as described above.

## 2.12 Statistical analysis

Data was keyed into an Excel spreadsheet (Microsoft Office, United States) and then exported to statistical package for social sciences v16 (SPSS, IBM, Inc., Chicago, United States), and GraphPad v5.03 (GraphPad PRISM, Inc., San Diego, California, United States) for statistical analysis. Using GraphPad software v8.03 (GraphPad PRISM, Inc., San Diego, CA, United States), fluorescence counts of antiplasmodial assay were used to plot graph of percent inhibition of *Pf* parasite growth against concentrations of AC-AgNPs, AC-CE, and CQ to determine 50% inhibition concentration ($IC_{50}$). The dose/time mortality response data of larvicidal assays was analyzed using log-probit regression model to determine $LC_{50}$ and $LC_{90}$ with their confidence interval at 95% (95% CI). The Abbott's formula was used to correct mortality rate if comprised between 5% and 20% in the negative control group (Sun and Shepard, 1947). Experiments were considered invalid when mortality rate in negative control group was >20%.

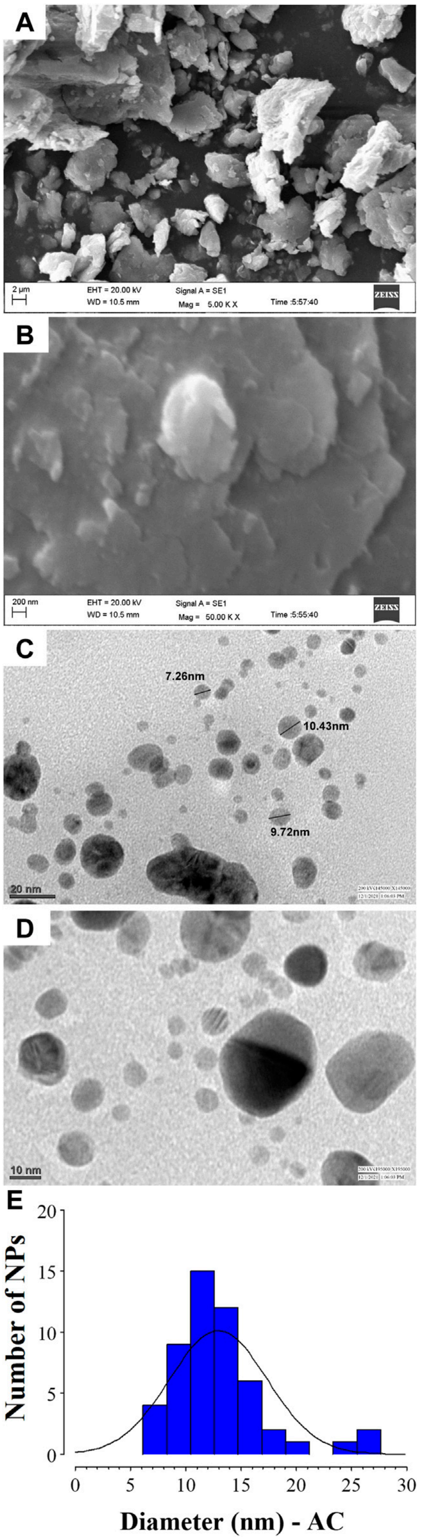

FIGURE 4
SEM and TEM analysis of AC-AgNPs. SEM images at 5.00 KX **(A)** and 50.00 KX **(B)** of AC-AgNPs. Micrographs of the AC-AgNPs using TEM at 20 nm **(C)** and 10 nm **(D)**, and size distribution of the nanocrystallites **(E)**. AC-AgNPs, *Alchornea cordifolia* silver nanoparticles; SEM, Scanning electron microscopy; TEM, Transmission electron microscopy.

Regarding hemocompatibility assay, the amount of NPs required to lyse 50% of RBCs (hemolysis concentration, $HC_{50}$) was determined. Quantitative and qualitative variables were presented as mean ± standard deviation (SD) and percentages, respectively. One-way analysis (ANOVA), McNemar's and Pearson's independence chi square tests were used to make comparisons. The level of statistical significance was set at $p$-value $<0.05$.

## 3 Results

### 3.1 GC-MS analysis

GC-MS chromatogram of AC-CE revealed several peaks which represent different compounds as shown in Supplementary Figure S1. A total of 42 compounds were identified in AC-CE after comparing the peaks with database of spectrum of known components stored in the GC-MS library (Table 1). Two compounds were predominantly represented, namely, 2-hexadecen-1-ol, 3,7,11,15-tetramethyl-, [R-[R*,R*-(E)]]- and phytyl tetradecanoate, with proportions of 25.14% and 14.53%, respectively (Supplementary Figure S2; Table 1).

### 3.2 UV-Vis spectroscopy and AC-AgNPs optimization

The synthesis of AC-AgNPs was noted after 2 minutes following the incubation of plant extract and $AgNO_3$ solution as a dark brown color was observed (Figure 3A). The UV-Vis spectrum analysis revealed a SPR at 445 nm wavelength (Figures 3B–E). The SPR did not change with the variation of four parameters used to optimize AC-AgNPs synthesis ($AgNO_3$ concentration, incubation time, incubation temperature and volume of plant extract). In contrast, the amplitude of UV-Vis curves gradually increased with increasing values of each parameter (Figures 3B–E). Thus, the optimization of AC-AgNPs was achieved for the following parameters: 100 µL of fresh plant extract was mixed with 900 µL of $AgNO_3$ (5 mM), and then incubated at 85°C for 5 h under static conditions.

### 3.3 Electron microscopy analysis of green AC-AgNPs

Analysis of SEM and TEM micrographs of AC-AgNPs is depicted in Figure 4. Based on SEM, agglomeration of AC-AgNPs was observed (Figures 4A, B). TEM images of silver colloidal solution exhibited that AC-AgNPs were polydispersed, predominantly spheroidal with various sizes (Figures 4C, D). The size distribution when a section of these NPs is considered is presented in Figure 4E. Following the digitization phase of various images, size distribution using ImageJ software was found to be within 5–25 nm range. The distribution of AC-AgNPs size was large, with mean size ±SD of 10.89 ± 5.67 nm.

## 3.4 PXRD analysis, SAED patterns, and composition of AC-AgNPs

The PXRD patterns outline that AC-AgNPs are face-centered cubic. The intense and narrow diffraction peaks revealed the formation of pure crystals of silver and silver chloride. The nanosilver crystal peaks obtained at 2θ values of 38.07°, 46.20°, 64.33° and 77.40° which correspond to the (111), (200), (220) and (311) planes of the face-centered cubic (fcc) structures, respectively (JCPDS file 65-2871). Additional peaks corresponding to silver chloride nanocrystallites were observed at 2θ values of 27.8°, 32.2°, 54.8°, 57.4° and 67.4° indexed to (111), (200), (311), (222) and (400) planes, respectively (JCPDS file 31-1238). SAED suggests that the NPs are polycrystalline with diffraction rings associated due to their stacking each other due to their magnetite phase (Figures 5A, B). The crystallinity percentage of AC-AgNPs was 84.13%. Using data from PXRD, the size of silver nanocrystals and silver chloride nanocrystals based on the Scherrer formula was 13.47 ± 5.81 nm and 10.42 ± 3.34 nm, respectively (Table 2). The overall mean size of AC-AgNPs was 11.77 ± 5.57 nm.

The EDX profile of AC-AgNPs showed a strong signal due to silver atom (Ag) which was involved in AC-AgNPs at a percentage of 58.31%. Other signals due to chlorine (Cl), cadmium (Cd), carbon (C) and oxygen (O) were also observed at 5.56%, 0.36%, 9.31% and 26.46%, respectively (Figure 5C). The identity of functional chemical groups at the interface of AC-AgNPs were determined using FTIR which revealed strong signals at 3,416 $cm^{-1}$, 1630 $cm^{-1}$, and 1023 $cm^{-1}$ which are characteristics of alcohols (O-H stretch), alkenes (C=O stretch) and alkyl and Aryl Halides (C-F stretch), respectively. Smaller signals corresponding to alkanes (C-H stretch) at 2927 $cm^{-1}$, alkanes/aldehydes/alkenes (C-H stretch, C-O stretch) at 2857/1739 $cm^{-1}$, nitriles (C≡N stretch) at 2373/2323 $cm^{-1}$, aromatic compounds (C=C stretch) at 1458 $cm^{-1}$, and nitro compounds ($NO_2$ stretch) at 1377 $cm^{-1}$ were also seen (Figure 5D; Table 3).

## 3.5 Zeta potential and DLS

The stability of AC-AgNPs was determined using zeta potential, and the analysis revealed a zeta potential value of −18.1 mV which outlines a good stability (Supplementary Figure S3). On analysis of DLS results, the AC-AgNPs had a mean size ±SD of 89.77 ± 16.50 nm, with polydispersity index of 0.242 (Supplementary Figure S4).

## 3.6 Antiplasmodial assays

High antiplasmodial activity was found for AC-AgNPs against 3D7 (CQ-sensitive) and RKL9 (CQ-resistant) *Pf* strains. Based on $IC_{50}$ values, AC-AgNPs exhibited higher antiplasmodial activity as compared to that of AC-CE irrespective of plasmodial strain, and differences were statistically significant ($p < 0.0001$): 8.05 μg/mL vs. 20.27 μg/mL for 3D7, and 10.31 μg/mL vs. 32.55 μg/mL for RKL9. The standard drug CQ exhibited $IC_{50}$ values of 0.04 μg/mL and 0.35 μg/mL against *Pf* strains 3D7 and RKL9 (Figures 6A, B). The SYBR green assay findings were supported by microscopic data. AC-AgNPs and AC-CE elicited no quenching effects as no statistically significant difference was found between fluorescence counts of NPs, standard drug and plant extract (Supplementary Figure S5).

## 3.7 Hemolysis induced by the green AC-AgNPs

We have noted that hemolysis rates were dependent on substance, dose and time (Figures 7A, B). After 30 min, hemolysis rates elicited by AC-AgNPs and AC-CE were significantly higher than that of CQ at doses ≥62.5 μg/mL. At these concentrations (125–500 μg/mL), hemolysis rates ranged from 6.25%–13.15% for CQ, 14.55%–48.14% for AC-AgNPs, and 5.50%–40.95% for AC-CE (Figure 7A). To be noted, $HC_{50}$ was not achieved after 30-min incubation as hemolysis rate was below 50% at 500 μg/mL. After 24 hour-incubation, hemolysis rates increased for all substances tested, with the highest values in AC-AgNPs-treated samples (maximum hemolysis of 98.14% at 500 μg/mL). Statistically significant difference between AC-AgNPs, AC-CE, and CQ were seen at doses ≥8 μg/mL (Figure 7B).

## 3.8 Toxic effect of the AC-AgNPs against mosquito species

Mortality of *Cx. quinquefasciatus*, *Ae. aegypti* and *An. stephensi* larval stages was followed 24h, 48h and 72 h after treatment with AC-AgNPs. Mortality rates of the three mosquito species increased as a function of time and concentration (Supplementary Figure S6). After 48 h incubation, larval mortality rates were 100% at doses 23.5 μg/mL for *Cx. quinquefasciatus*, 20 μg/mL for *Ae. aegypti*, and 15 μg/mL for *An. stephensi* (Supplementary Figure S6). AC-AgNPs were more lethal against *An. stephensi* regardless of exposure time, with $LC_{50}$ values of 10.67 μg/mL and 5.85 μg/mL at 24 h- and 48 h-exposure, respectively. These values were 16.71 μg/mL and 7.52 μg/mL for *Ae. aegypti*; 18.41 μg/mL and 8.97 μg/mL for *Cx. quinquefasciatus*, respectively. Regardless of exposure time, the larvicidal activity of AC-AgNPs was much higher than that of AC-CE for which $LC_{50}$ of 231.41 μg/mL, 110.33 μg/mL and 53.15 μg/mL against *Cx. quinquefasciatus*, *Ae. aegypti* and *An. stephensi* were found after 24 h exposure, respectively (Tables 4, 5). Interestingly, AC-CE did not cause any larval mortality at $LC_{50}$ and $LC_{90}$ concentrations found for AC-AgNPs.

## 3.9 Behavioral and morphological impact of the AC-AgNPs on the larvae

The stereomicroscopic observations of *Ae. aegypti*, *An. stephensi* and *Cx. quinquefasciatus* larval stages treated with AC-AgNPs are depicted in Figure 8, and revealed the induction of behavioral and morphological changes in mosquito larvae. It was observed that swimming behavior of larvae was reduced,

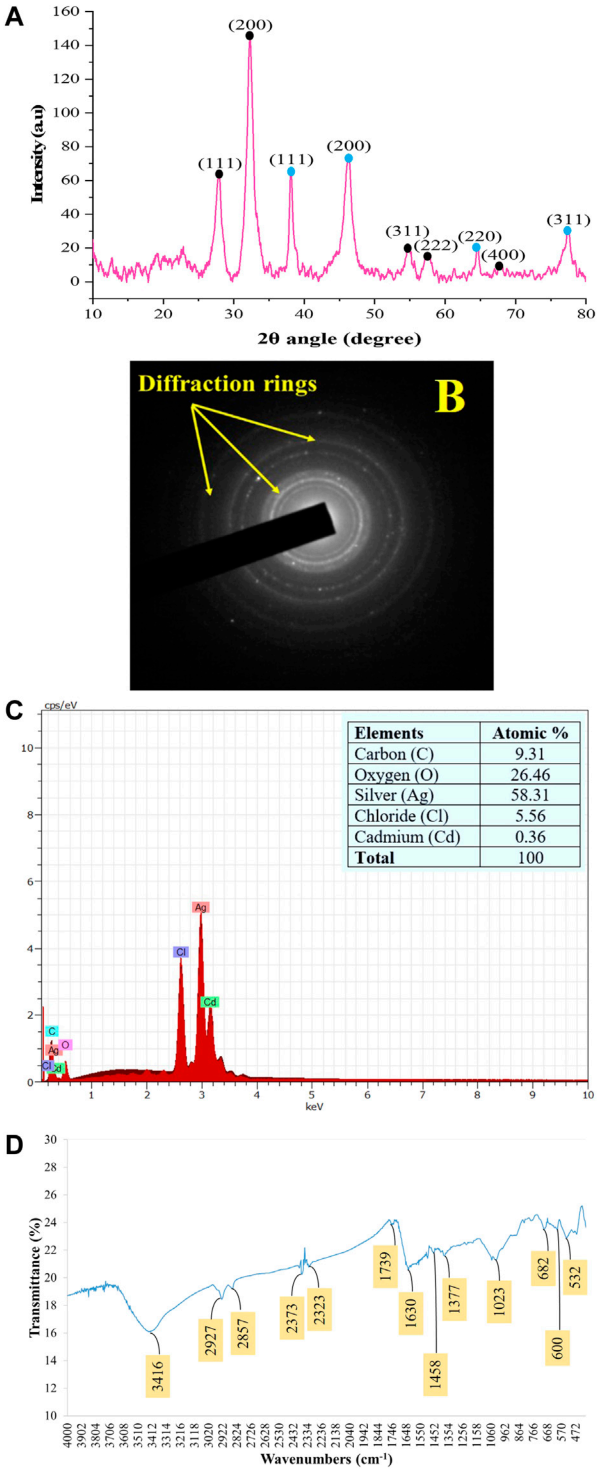

| Elements | Atomic % |
|---|---|
| Carbon (C) | 9.31 |
| Oxygen (O) | 26.46 |
| Silver (Ag) | 58.31 |
| Chloride (Cl) | 5.56 |
| Cadmium (Cd) | 0.36 |
| **Total** | 100 |

FIGURE 5
Patterns of the green synthesized AC-AgNPs using PXRD **(A)**, SAED **(B)**, EDX **(C)**, and FTIR **(D)**. In **(A)**, intensity of peaks is presented as arbitrary units (a.u). In **(A)**, peaks with blue and black round shape indicate silver nanocrystals and silver chloride nanocrystals, respectively. AC-AgNPs, *Alchornea cordifolia* silver nanoparticles; EDX, Energy dispersive X-ray spectroscopy; FTIR, Fourier transformed infrared spectroscopy; PXRD, Powder X-ray diffraction; SAED, Selected area electron diffraction.

with morbid larvae at the bottom of bowls and unable to swim to the surface. Several morphological changes were noted in AC-AgNPs-treated larvae and these included loss of external hairs/bristles, swelling of the apical cells, pigmentation of the body, shrinkage of the larvae, and necrosis and thickening of the epidermis (Figure 8).

**TABLE 2 Principal characteristic values of the powder X-ray diffractogram of AC-AgNPs.**

| S.No. | Position (2θ) | Peak amplitude (a.u) | FWHM (2θ) | Cos (θ) | Miller indices (HKL) | Nature | Size (nm) |
|---|---|---|---|---|---|---|---|
| 1 | 27.83 | 64.55 | 1.1219 | 0.97065 | (111) | AgCl | 7.62 |
| 2 | 32.31 | 146.69 | 1.2155 | 0.96051 | (200) | AgCl | 7.11 |
| 3 | 38.15 | 66.67 | 0.6446 | 0.94509 | (111) | Ag | 13.62 |
| 4 | 46.20 | 75.30 | 1.3896 | 0.91982 | (200) | Ag | 6.49 |
| 5 | 54.81 | 19.36 | 0.9351 | 0.88778 | (311) | AgCl | 10.00 |
| 6 | 57.41 | 16.20 | 0.7762 | 0.87710 | (222) | AgCl | 12.19 |
| 7 | 64.59 | 20.41 | 0.4035 | 0.84531 | (220) | Ag | 24.33 |
| 8 | 67.41 | 10.75 | 0.6573 | 0.83191 | (400) | AgCl | 15.17 |
| 9 | 77.40 | 31.95 | 1.1259 | 0.78043 | (311) | Ag | 9.44 |

a.u, Arbitrary units; FWHM, full width at half maximum; Cos, Cosinus.

**TABLE 3 Functional groups at a given wavenumber for the FTIR spectra of AC-AgNPs.**

| Absorption ($cm^{-1}$) | Appearance | Functional groups | Compound class |
|---|---|---|---|
| 3,416 | Medium | N-H stretching | Primary amine |
| 2,927 | Sharp | C-H stretching | Alkane |
| 2,857 | Medium | C-H stretching | Alkane |
| 2,373 | Sharp | O=C=O stretching | Carbon dioxide |
| | | C≡N stretching | Nitriles |
| 2,323 | Weak | O=C=O stretching | Carbon dioxide |
| | | C≡N stretching | Nitriles |
| 1,739 | Sharp | C=O stretching | Ester, Aldehyde, Saturated aliphatic, or δ-lactone |
| 1,630 | Medium | C=C stretching | Conjugated alkene |
| 1,458 | Medium | C-H bending | Alkane (methylene or methyl group) |
| 1,377 | Medium | C-H bending | Aldehyde or Alkane (gem dimethyl) |
| 1,023 | Sharp | C-O stretching | Alcohol, Ether, Carboxylic acids |
| 682 | sharp | C=C bending | Alkene or Aromatics |
| 600 | sharp | C-I stretching | Halo compound |
| 532 | Sharp | C-Br stretching | Alkyl halides |

# 4 Discussion

Vector-borne diseases such as malaria are an important public health problem throughout the world especially in Cameroon. This study demonstrated good hemocompatibility and high biocidal potential of green synthesized AgNPs using *A. cordifolia* leaves (Euphorbiaceae).

The synthesis of AC-AgNPs through green route was rapid as color change was noted a few minutes after mixing AC-CE and $AgNO_3$ aqueous solutions, thereby outlining the onset of AC-AgNPs synthesis through reduction of $Ag^+$ ions into $Ag^0$. This observation was further confirmed upon analysis of UV-Vis spectra with a peak at 445 nm wavelength. Karthik and others showed a close value (434 nm) for *Acalypha indica*, another Euphorbiaceae plant (Karthik et al., 2017). The UV-Vis peak corresponds to SPR phenomenon during which electron on NPs surface enter into resonance with the wavelength of incident light (Kojom Foko et al., 2021). The SPR band was increasing with parameters used for optimizing AC-AgNPs synthesis (i.e., $AgNO_3$ concentration, AC-CE volume, incubation time and incubation temperature), and such findings were seen previously with plants growing in Cameroon, especially *Megaphrynium macrostachyum* (Eya'ane Meva et al., 2016), and *Selaginella myosurus* (Belle Ebanda Kedi et al., 2018).

The biofabricated AC-AgNPs were small and mostly spherical which is consistent with earlier reports using

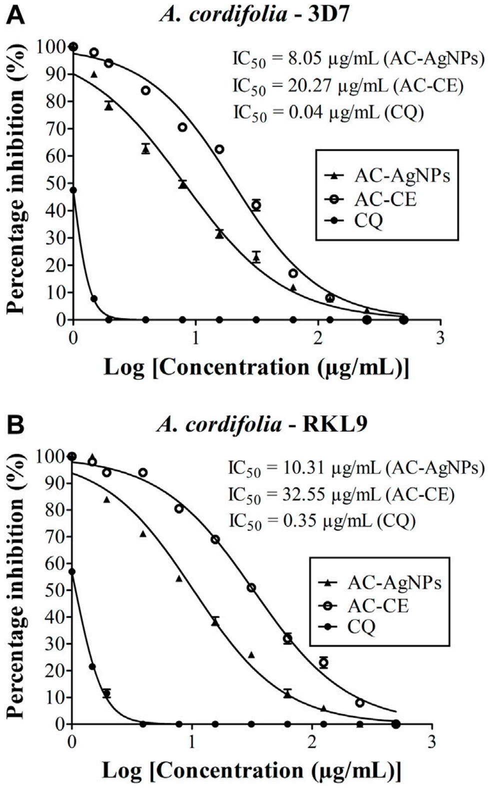

FIGURE 6
Antiplasmodial activity of AC-CE and AC-AgNPs against laboratory **(A)** *P. falciparum* 3D7 and **(B)** RKL9 strains. AC-AgNPs, *Alchornea cordifolia* silver nanoparticles; AC-CE, *Alchornea cordifolia* crude extract; CQ, Chloroquine; $IC_{50}$, 50% Inhibition concentration. CQ was used as standard drug. Reference *P. falciparum* strains 3D7 (CQ-sensitive) and RKL9 (CQ-resistant) were used. The experiments were triplicated.

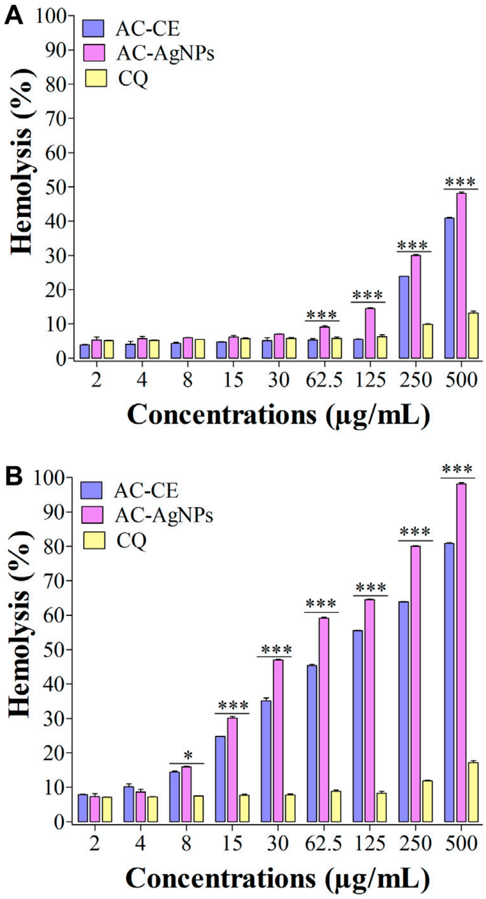

FIGURE 7
Hemolysis effect of AC-CE and AC-AgNPs after 30 min **(A)** and 24 h **(B)**. AC-AgNPs, *Alchornea cordifolia* silver nanoparticles; AC-CE, *Alchornea cordifolia* crude extract; CQ, Chloroquine; $IC_{50}$, 50% Inhibition concentration. The experiment was performed in triplicate. Saponin was used as positive control and PBS as negative control. Statistically significant at $^{*}p < 0.05$, $^{**}p < 0.01$ and $^{***}p < 0.0001$.

*Morinda citrifolia* and *Adiantum raddianum* (Suman et al., 2015; Govindarajan et al., 2017a). Using a systematic review, we previously reported that the bulk of NPs tested against *Plasmodium* parasites and mosquito vectors were spherical with a large range of size (Kojom Foko et al., 2019). Also, the nucleation theory of NPs synthesis suggests that slow rate of seed formation is expected to lead to broad size distribution of NPs (Liu et al., 2020). This result suggests that AC-AgNPs nucleation process was heterogeneous, and this can be influenced by several factors such as mixing time and solvation dynamics (Thanh et al., 2014; Deshpande et al., 2021). Size and shape of green NPs are modulated by complex interactions of plant- and experiment condition-related factors, and are crucial parameters that determine their physico-chemical and biological activities (Pal et al., 2007; Adams et al., 2014). Based on TEM analysis, AC-AgNPs were polydispersed with varied size. Such variation is commonly seen in AgNPs fabricated with plant extracts (Kojom Foko et al., 2019; Kojom Foko et al., 2021).

The analysis of PXRD and SAED patterns outlined that AC-AgNPs were polycrystalline with a crystallinity percentage of 84.13% and presence of additional peaks on diffractogram. This finding outlines that biosynthesized AC-AgNPs were not totally pure. At nanoscale level, a large number of metals present as face-centered cubic structures and tend to agglomerate due to high tension surface of ultrafine NPs (Belle Ebanda Kedi et al., 2018), thereby explaining the crystalline nature of AC-AgNPs. Also, with increasing nucleation and growing over time, NPs form twinned structures that then multiply with their surfaces bounded to cubic facets with the lowest binding energy (Annamalai and Nallamuthu, 2016). The SAED pattern clearly confirmed the crystalline nature of AC-AgNPs.

Silver atom was mainly involved in AC-AgNPs synthesis while other atoms such as oxygen and chlorine were also found, and these could be due to phytochemical compounds in AC-CE. FTIR spectrum revealed the presence of several peaks corresponding to functional chemical groups (e.g., O-H, C≡N, C=C) attributable to alkanoids, terpenoids, flavonoids, phenols, steroids, anthraquonones or saponins, and confirmed results from GC-MS-based phytochemical analysis done here and reported elsewhere (Osadebe et al., 2012). These compounds are likely involved in reducing silver ions during NPs synthesis along with their capping

**TABLE 4 Larval toxicity of AC-AE against larval stages of *Cx. quinquefasciatus, Ae. aegypti* and *An. stephensi* after 24h, 48h and 72 h exposure.**

| Time | $LC_{50}$ | 95% CI | $LC_{90}$ | 95% CI | Regression equation[a] | $\chi^2$ ($p$-value) |
|---|---|---|---|---|---|---|
| *Culex quinquefasciatus* | | | | | | |
| 24 h | 231.41 | 200.01–308.77 | 524.35 | 450.81–703.41 | $y = -1.16 + 0.004x$ | 3.31 (0.85) |
| 48 h | 188.71 | 161.69–214.03 | 431.49 | 362.87–539.18 | $y = -0.92 + 0.005x$ | 2.84 (0.78) |
| 72 h | 147.50 | 123.61–170.73 | 391.20 | 334.12–507.03 | $y = -0.76 + 0.005x$ | 3.91 (0.69) |
| *Aedes aegypti* | | | | | | |
| 24 h | 110.33 | 85.44–214.11 | 160.14 | 141.00–348.11 | $y = -3.25 + 0.036x$ | 8.44 (0.01) |
| 48 h | 90.30 | 71.80–109.37 | 141.42 | 123.02–241.88 | $y = -2.41 + 0.020x$ | 5.15 (0.97) |
| 72 h | 71.52 | 66.27–100.11 | 113.11 | 91.76–199.44 | $y = -2.30 + 0.044x$ | 4.01 (0.17) |
| *Anopheles stephensi* | | | | | | |
| 24 h | 53.15 | 47.33–60.01 | 121.88 | 87.14–199.01 | $y = -2.88 + 0.050x$ | 5.86 (0.001) |
| 48 h | 41.57 | 37.51–50.43 | 102.11 | 75.55–111.77 | $y = -3.36 + 0.081x$ | 8.30 (0.32) |
| 72 h | 37.23 | 28.83–52.68 | 57.01 | 41.15–63.52 | $y = -2.52 + 0.070x$ | 0.71 (0.15) |

*Control* no larval mortality recorded; *$LC_{50}$, $LC_{90}$* Lethal concentration of the substance that kills 50%, 90% of the exposed larvae, respectively; $LC_{50}$ and $LC_{90}$ are expressed in µg/mL; *95% CI*, Confidence interval at 95%; $\chi^2$ Chi square; Statistical significance was set at $p$-value <0.05.

[a]Determined using the probit model.

**TABLE 5 Larval toxicity of AC-AgNPs against larval stages of *Cx. quinquefasciatus, Ae. aegypti* and *An. stephensi* after 24h, 48h and 72h exposure.**

| Time | $LC_{50}$ | 95% CI | $LC_{90}$ | 95% CI | Regression equation[a] | $\chi^2$ ($p$-value) |
|---|---|---|---|---|---|---|
| *Culex quinquefasciatus* | | | | | | |
| 24 h | 18.41 | 11.75–21.02 | 24.35 | 19.11–38.96 | $y = -9.16 + 0.59x$ | 62.31 (<0.0001) |
| 48 h | 8.97 | 6.27–10.60 | 17.22 | 11.44–19.52 | $y = -7.32 + 0.52x$ | 57.14 (<0.0001) |
| 72 h[b] | — | — | — | — | — | — |
| *Aedes aegypti* | | | | | | |
| 24 h | 16.71 | 15.86–17.53 | 24.16 | 20.98–27.59 | $y = -2.27 + 1.36x$ | 7.15 (0.52) |
| 48 h | 7.52 | 5.81–9.42 | 16.63 | 15.54–17.97 | $y = -1.35 + 1.50x$ | 10.3 (0.24) |
| 72 h[b] | — | — | — | — | — | — |
| *Anopheles stephensi* | | | | | | |
| 24 h | 10.67 | 7.59–13.75 | 21.62 | 12.49–28.76 | $y = -3.58 + 1.48x$ | 5.35 (0.48) |
| 48 h | 5.85 | 3.75–8.94 | 12.06 | 10.55–19.80 | $y = -5.35 + 2.35x$ | 8.30 (0.32) |
| 72 h[b] | — | — | — | — | — | — |

*Control* no larval mortality recorded; *$LC_{50}$, $LC_{90}$* Lethal concentration of the substance that kills 50%, 90% of the exposed larvae, respectively; $LC_{50}$ and $LC_{90}$ are expressed in µg/mL; *95% CI*, Confidence interval at 95%; $\chi^2$ Chi square; Statistical significance was set at $p$-value <0.05.

[a]Determined using the probit model.

[b]No data were computed as all larvae were dead after 48 h

and stabilization (Hawadak et al., 2022). We found two predominant compounds in plant extract (2-hexadecen-1-ol, 3,7,11,15-tetramethyl-, [R-[R*,R*-(E)]]- (acyclic diterpene alcohol) and phytyl tetradecanoate (fatty acid phytyl ester) using GC-MS. Although mechanism of action of NPs reduction is uncertain, it is likely these compounds, alone or in combination with other compounds in plant extract, were involved in reduction, capping and stabilization of AC-AgNPs.

Zeta potential defines the stability of colloidal suspensions such NPs, and is a common parameter used to surface charge on a particle. In this study, zeta potential of AC-AgNPs was −18.1 mV. This value indicates a good stability of AC-AgNPs in dispersion medium. Indeed, negative surface charge is due to the binding affinity of AC-CE compounds with the NPs, conferring stability of AC-AgNPs and preventing several phenomena such as aggregation, sedimentation or flocculation which are known impair stability of particles (Faisal et al., 2021).

High lethal activity of green AC-AgNPs against *Pf* strains 3D7 and RKL9 was observed, with $IC_{50}$ < 10 µg/mL for 3D7 and $IC_{50}$ < 20 µg/mL for RKL9. This is consistent with value reported by Hawadak *et al.* and Rajkumar *et al.* using green NPs mediated by *Eclipta prostrata* and *Azadirachta indica*, respectively (Rajakumar et al., 2015; Hawadak et al., 2022). In contrast, our values are lower than those found previously with different

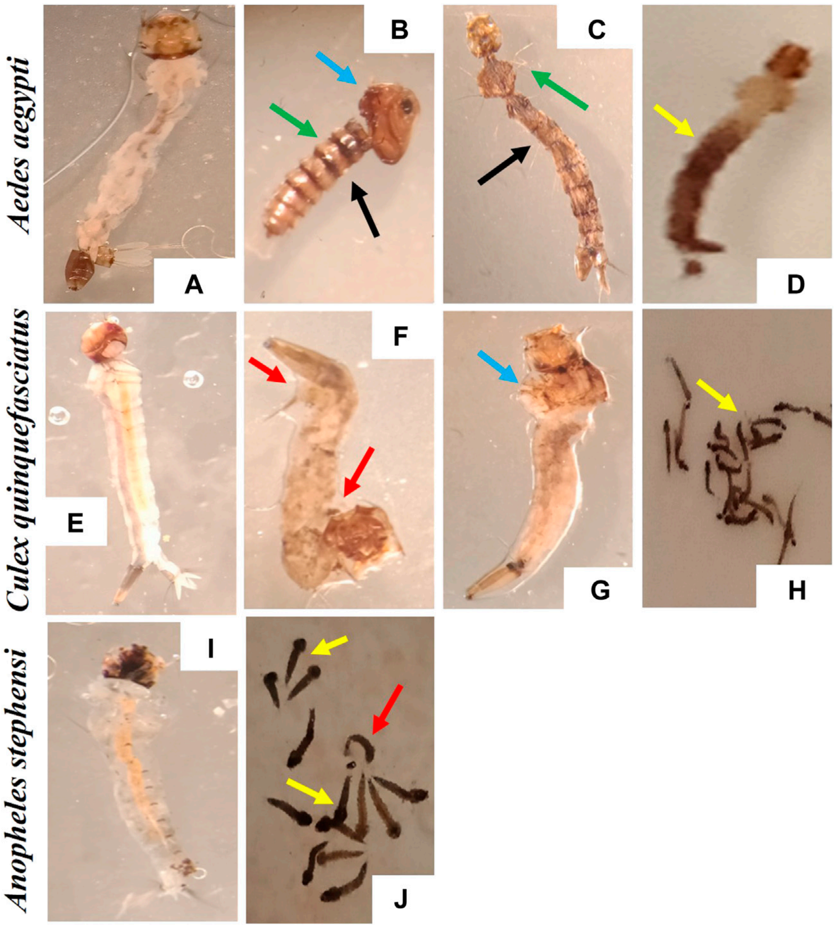

FIGURE 8
Morphological deformities induced by the exposure to AC-AgNPs ($LC_{50}$ dose) on larval stages of *Ae. aegypti*, *Cx. quinquefasciatus*, and *An. stephensi*. **(A)** *Ae. aegypti* larvae (Control), **(B–D)** *A. aegypti* larvae (AC-AgNPs-treated), **(E)** *Cx. quinquefasciatus* larvae (Control), **(F–H)** *Cx. quinquefasciatus* larvae (AC-AgNPs-treated), **(I)** *An. stephensi* larvae (Control), **(J)** *An. stephensi* larvae (AC-AgNPs-treated). Arrows indicate the difference morphological abnormalities seen in AC-AgNPs-treated larvae: swelling of the apical cells (blue arrows), pigmentation of body (yellow arrows), shrinkage of the larvae (red arrows), loss of external anal and head hairs/bristles (green arrows), necrosis and thickening of the epidermis (black arrows).

*Plasmodium* strains (Kojom Foko et al., 2019). This antiplasmodial activity exhibited by the AC-AgNPs is due to above mentioned phytochemical compounds which served as bioreactors for NPs reduction and capping. Several studies suggested potential mechanisms of action of NPs against *Plasmodium* parasites (Cox-georgian et al., 2019; Abubakar et al., 2020). The NPs could induce parasite death by acting on several targets including cell membrane, enzymes and internal organelles (Shakeel et al., 2016; Kamaraj et al., 2017; Varela-Aramburu et al., 2020). Using *in vivo* model, Karthik and others showed that antiplasmodial activity of marine actinobacterial-mediated gold NPs was associated with increased production of tumor growth factor but reduction in tumor necrosis factor, thereby emphasizing an immunomodulatory role of NPs (Karthik et al., 2013). *Pf* is highly prevalent in Cameroon (Kojom Foko et al., 2018; Antonio-Nkondjio et al., 2019; Kojom Foko et al., 2021), and our findings suggest that AgNPs could be interesting as antimalarial drug. A large number of NPs-related chemical and/or physical factors could explain discrepancies obtained between our findings and those from previous studies. These included mainly size distribution, shape, capping/reducing agents, aggregation and surface charge. Even though AC-AgNPs synthesized in this study showed broad size distribution (range 6–28 nm), these are still interesting for future antimalarial drug development. Optimal NPs size for integration into human drugs varies depending on the specific drug and its intended application (Mitchell et al., 2021). This size distribution found here is consistent with previous studies on potential of MNPs as either drug delivery agent (i.e., passive targeting to enhance the accumulation of drugs in tumors) or antimalarial drug (i.e., active targeting to specific cells/tissues) (Santos-Magalhães and Mosqueira, 2010; Rahman et al., 2019). It should be interesting to conduct more studies to define consistent NPs size cut-offs for antimalarial therapy purposes.

It is known that antimalarial drugs such as ACTs, the current medicines used for treating uncomplicated malaria in most of endemic countries, can induce hemolysis in patients (Rehman et al., 2014). Therefore, new antimalarial drug candidates should be screened for hemocompatibility profile. The hemolysis rate was below at 50% after 30 minute-incubation, thereby underlining a $HC_{50} > 500$ µg/mL for the AC-AgNPs. The biofabricated AC-AgNPs were therefore highly hemocompatible, consistent with findings of Hossain and coworkers, who reported $HC_{50}$ of 700 and 800 µg/mL for green aqueous and ethanolic NPs mediated by *Andrographis paniculata* stem (Hossain et al., 2019). Hemolysis increased as a function of time for AC-CE and AC-AgNPs which is in line with previous studies (Laloy et al., 2014; Avitabile et al., 2020). Hemolysis activity of NPs is strongly dependent on their size with higher hemolytic activity seen in smaller NPs (Chen et al., 2015). Thus, the small size of AC-AgNPs could likely explain their hemolytic activity (De La Harpe et al., 2019). Also, the anti-hemolytic activity of AC-AgNPs can be partially attributed to biomolecules coated on their surface. In fact, polyphenols are known to delay solubilization and inhibit oxidation of lipid frame; terpenes and flavonoids prevent interactions with hydrophobic parts of proteins and lipids, resulting in protecting and stabilizing cells membrane (Hoshyar et al., 2016; De La Harpe et al., 2019).

The phytofabricated AC-AgNPs exhibited a high toxicity against larval stages of *Ae. aegypti*, *Cx. quinquefasciatus* and *An. stephensi*, with $LC_{50}$ below 20 µg/mL. Consisting with previous reports on diverse families of plants such as *A. raddianum* (Pteridaceae), *Hugonia mystax* (Linaceae), *Psidium guajava* (Myrtaceae), *Holostemma ada-kodien* (Apocynaceae) and *Aganosma cymosa* (Apocynaceae) (Govindarajan et al., 2017a, 2017b; Benelli and Govindarajan, 2017; Alyahya et al., 2018; Ntoumba et al., 2020). In contrast, some authors reported $LC_{50} > 20$ µg/mL for AgNPs fabricated with *Ventilago maderaspatana* (Rhamnaceae), *Naregamia alata* (Meliaceae), *Hedychium coronarium* (Zingiberaceae) and *Sargassum wightii* (Sargassaceae) (Azarudeen et al., 2017a, 2017b; Kalimuthu et al., 2017; Murugan et al., 2017). The discrepancy observed between studies is likely due to a cocktail of factors including the phytochemical composition of plant used for NPs synthesis, size/shape of NPs and mosquito strains. The mechanisms through which NPs induce larval mortality are still elusive, but it is thought that nanosized materials such as NPs can easily pass through insect exoskeleton and cell membrane, bind to sulphur-containing proteins and/or DNA which then lead to interference with homeostatic and physiological processes essential for larvae (e.g., copper homeostasis, osmoregulatory and spiracle-related respiratory systems) (Armstrong et al., 2013; Kojom Foko et al., 2021; Araújo et al., 2022). Other authors reported NP-induced physical and molecular degradation of insect gut as additional death cause (Kalimuthu et al., 2017, 2016; Banumathi et al., 2017; Ishwarya et al., 2017; Suganya et al., 2019). Also, these putative mechanisms could also explain behavioral and morphological modifications in AC-AgNPs-treated larvae seen in this study and by several earlier studies on extracts and NPs (Banumathi et al., 2017; Ishwarya et al., 2017; Suganya et al., 2019).

## 5 Conclusion

In this study, we synthesized, optimized, characterized and evaluated some medical applications of green AC-AgNPs including antiplasmodial, hemocompatibility and larvicidal potential. The synthesis was rapid and the optimized AC-AgNPs were mostly spheroidal, small-sized, dispersed, stable and polycrystalline in nature. Several phytochemicals including alkanoids, terpenoids, flavonoids, phenols and steroids were responsible for reduction, capping and stabilization of AC-AgNPs. The AC-AgNPs exhibited higher antiplasmodial and mosquito larvicidal activities compared to plant extract. The AC-AgNPs induced several mortality-associated behavioral and morphological changes in larval stages of *Ae. aegypti*, *An. stephensi* and *Cx. quinquefasciatus*. Finally, the AC-AgNPs exhibited good hemocompatibility with $HC_{50} > 500$ µg/mL. In worrying context of resistance of malaria parasites to current drugs and mosquitoes to different classes of insecticides, green nanotechnology could be a valuable and cutting-edge alternative for advanced drug/insecticide development and research.

## Data availability statement

The original contributions presented in the study are included in the article/Supplementary Material, further inquiries can be directed to the corresponding author/s.

## Author contributions

LPKF and VS conceptualized the study. LPKF performed laboratory experiments and drafted the first version of the manuscript. JH helped in laboratory experiments. PBEK collected the plant and brought it to the National Herbarium for taxonomical authentication. JH, VV, PBEK, and CEEM helped in data interpretation. JH, VV, PBEK, CEEM, KR, VP, and VS revised the manuscript for important intellectual content. VV and KR supervised larvicidal assays and validated data. VS supervised the work at all stages. All authors read and approved the final version of the manuscript before submission.

## Acknowledgments

The authors are grateful to the India National Science Academy/Department of Biotechnology (INSA/DBT), New Delhi, India; The World Academy of Sciences (TWAS), Trieste, Italy; and ICMR-National Institute of Malaria Research, New Delhi, India, that granted a prestigious fellowship (INSA/DBT-TWAS Postgraduate Fellowship Programme—2017 and 2018, grants N° 3240300010 and N° 3240306345) awarded to authors LPKF and JH, respectively. PBEK acknowledges the International Foundation for Science (IFS) for the research grant N° I-1-F-6137-1. We are deeply grateful to Sangeeta Arora (Senior technical officer A/WHO-certified microscopist) from ICMR-NIMR for guidance in *Plasmodium falciparum* culture, antiplasmodial assays and microscopic examination. We acknowledge the help of ICMR-NIMR insectarium staff for mosquito rearing and Neha Loach for helping us for mosquito bioassays. Special thanks to Kapil Vashisht (Project scientist, ICMR-NIMR, New Delhi, India) and Kailash Chand Pandey (Scientist F and Principal investigator, ICMR-NIMR, New Delhi, India) for providing facilities to perform photographs of mosquitoes, AC-AgNPs purification/lyophilization and antiplasmodial assay-related spectrophotometric readings. We are also grateful to the Advanced Instrumentation Research Facility (AIRF), Jawaharlal Nehru University, India, and The Sophisticated Research Facility, The All India Institute for Medical Sciences (AIIMS), New Delhi, India, for physicochemical characterization of extract and nanoparticles. We thank reviewers who evaluated earlier version of this paper.

## Conflict of interest

The authors declare that the research was conducted in the absence of any commercial or financial relationships that could be construed as a potential conflict of interest.

## Publisher's note

## Supplementary material

The Supplementary Material for this article can be found online at: https://www.frontiersin.org/articles/10.3389/fbioe.2023.1109841/full#supplementary-material

## References

Abubakar, A., Ahmad, N. S., Akanya, H. O., and Abdulkadir, A. (2020). Antiplasmodial activity of total alkaloids and flavonoids of stem bark extracts of *Enantia chlorantha* in mice. *Compar Clin. Pathol.* 29, 873–881. doi:10.1007/s00580-020-03138-4

Adams, C. P., Walker, K. A., Obare, S. O., and Docherty, K. M. (2014). Size-dependent antimicrobial effects of novel palladium nanoparticles. *PLoS ONE* 9, e85981. doi:10.1371/journal.pone.0085981

Alyahya, S. A., Govindarajan, M., Alharbi, N. S., Kadaikunnan, S., Khaled, J. M., Mothana, R. A., et al. (2018). Swift fabrication of Ag nanostructures using a colloidal solution of *Holostemma ada-kodien* (Apocynaceae) – antibiofilm potential, insecticidal activity against mosquitoes and non-target impact on water bugs. *J. Photochem Photobiol. B Biol.* 181, 70–79. doi:10.1016/j.jphotobiol.2018.02.019

Annamalai, J., and Nallamuthu, T. (2016). Green synthesis of silver nanoparticles: Characterization and determination of antibacterial potency. *Appl. Nanosci.* 6, 259–265. doi:10.1007/s13204-015-0426-6

Antonio-Nkondjio, C., Ndo, C., Njiokou, F., Bigoga, J. D., Awono-Ambene, P., Etang, J., et al. (2019). Review of malaria situation in Cameroon: Technical viewpoint on challenges and prospects for disease elimination. *Parasit. Vectors* 12, 501. doi:10.1186/s13071-019-3753-8

Araújo, P. S., Caixeta, M. B., Canedo, A., da Silva Nunes, E., Monteiro, C., and Rocha, T. L. (2022). Toxicity of plant-based silver nanoparticles to vectors and intermediate hosts: Historical review and trends. *Sci. Total Environ.* 834, 155299. doi:10.1016/j.scitotenv.2022.155299

Armstrong, N., Ramamoorthy, M., Lyon, D., Jones, K., and Duttaroy, A. (2013). Mechanism of silver nanoparticles action on insect pigmentation reveals intervention of copper homeostasis. *PLoS ONE* 8, e53186. doi:10.1371/journal.pone.0053186

Arya, A., Kojom Foko, L. P., Chaudhry, S., Sharma, A., and Singh, V. (2021). Artemisinin-based combination therapy (ACT) and drug resistance molecular markers: A systematic review of clinical studies from two malaria endemic regions – India and sub-saharan Africa. *Int. J. Parasitol. Drugs Drug Resist* 15, 43–56. doi:10.1016/j.ijpddr.2020.11.006

Avitabile, E., Senes, N., D'Avino, C., Tsamesidis, I., Pinna, A., Medici, S., et al. (2020). The potential antimalarial efficacy of hemocompatible silver nanoparticles from Artemisia species against *P. falciparum* parasite. *PLoS ONE* 15, e0238532. doi:10.1371/journal.pone.0238532

Azarudeen, R. M. S. T., Govindarajan, M., AlShebly, M. M., AlQahtani, F. S., Amsath, A., and Benelli, G. (2017a). One pot green synthesis of colloidal silver nanocrystals using the *Ventilago maderaspatana* leaf extract: Acute toxicity on malaria, Zika virus and filariasis mosquito vectors. *J. Clust. Sci.* 28, 369–392. doi:10.1007/s10876-016-1103-y

Azarudeen, R. M. S. T., Govindarajan, M., Amsath, A., Muthukumaran, U., and Benelli, G. (2017b). Single-step biofabrication of silver nanocrystals using *Naregamia alata*: A cost effective and eco-friendly control tool in the fight against malaria, Zika virus and st. Louis encephalitis mosquito vectors. *J. Clust. Sci.* 28, 179–203. doi:10.1007/s10876-016-1067-y

Balikagala, B., Fukuda, N., Ikeda, M., Katuro, O. T., Tachibana, S.-I., Yamauchi, M., et al. (2021). Evidence of artemisinin-resistant malaria in Africa. *New Engl. J. Med.* 385, 1163–1171. doi:10.1056/NEJMoa2101746

Banumathi, B., Vaseeharan, B., Chinnasamy, T., Vijayakumar, S., Govindarajan, M., Alharbi, N. S., et al. (2017). *Euphorbia rothiana*-Fabricated Ag nanoparticles showed high toxicity on *Aedes aegypti* larvae and growth inhibition on microbial pathogens: A focus on morphological changes in mosquitoes and antibiofilm potential against bacteria. *J. Clust. Sci.* 28, 2857–2872. doi:10.1007/s10876-017-1263-4

Bayda, S., Adeel, M., Tuccinardi, T., Cordani, M., and Rizzolio, F. (2020). The history of nanoscience and nanotechnology: From chemical-physical applications to nanomedicine. *Molecules* 25, 112. doi:10.3390/molecules25010112

Belle Ebanda Kedi, P., Meva Eya'Ane, F., Kotsedi, L., Nguemfo, E. L., Bogning Zangueu, C., Ntoumba, A. A., et al. (2018). Eco-friendly synthesis, characterization, *in vitro* and *in vivo* anti-inflammatory activity of silver nanoparticle-mediated *Selaginella myosurus* aqueous extract. *Int. J. Nanomed* 13, 8537–8548. doi:10.2147/IJN.S174530

Benelli, G., and Govindarajan, M. (2017). Green-synthesized mosquito oviposition attractants and ovicides: Towards a nanoparticle-based "lure and kill" approach? *J. Clust. Sci.* 28, 287–308. doi:10.1007/s10876-016-1088-6

Benelli, G., Maggi, F., Romano, D., Stefanini, C., Vaseeharan, B., Kumar, S., et al. (2017). Nanoparticles as effective acaricides against ticks—a review. *Ticks Tick-borne Dis.* 8, 821–826. doi:10.1016/j.ttbdis.2017.08.004

Cesar, A. M., Oscar, M. M., and Jaine, N. (2017). Medicinal plants from the genus Alchornea (Euphorbiaceae): A review of their ethnopharmacology uses and phytochemistry. *Bol. Latinoam. Caribe Plantas Med. Aromáts* 16, 162–205.

Chen, L. Q., Fang, L., Ling, J., Ding, C. Z., Kang, B., and Huang, C. Z. (2015). Nanotoxicity of silver nanoparticles to red blood cells: Size-dependent adsorption, uptake and hemolytic activity. *Chem. Res. Toxicol.* 28, 501–509. doi:10.1021/tx500479m

Chugh, D., Viswamalya, V. S., and Das, B. (2021). Green synthesis of silver nanoparticles with algae and the importance of capping agents in the process. *J. Genet. Eng. Biotechnol.* 19, 126. doi:10.1186/s43141-021-00228-w

Cox-georgian, D., Ramadoss, N., Dona, C., and Basu, C. (2019). Therapeutic and medicinal uses of terpenes. *Med. Plants*, 333–359. doi:10.1007/978-3-030-31269-5_15

De La Harpe, K. M., Kondiah, P. P. D., Choonara, Y. E., Marimuthu, T., Du Toit, L. C., and Pillay, V. (2019). The hemocompatibility of nanoparticles: A review of cell-nanoparticle interactions and hemostasis. *Cells* 8, 1209. doi:10.3390/cells8101209

Deshpande, J. B., Chakrabarty, S., and Kulkarni, A. A. (2021). Heterogeneous nucleation in citrate synthesis of AgNPs: Effect of mixing and solvation dynamics. *Chem. Eng. J.* 421, 127753. doi:10.1016/j.cej.2020.127753

Dong, H., Gao, Y., Sinko, P. J., Wu, Z., Xu, J., and Jia, L. (2016). The nanotechnology race between China and the United States. *Nano Today* 11, 7–12. doi:10.1016/j.nantod.2016.02.001

Dongang Nana, R. R., Hawadak, J., Kojom Foko, L. P., Kumar, A., Chaudhry, S., Arya, A., et al. (2022). Intermittent preventive treatment with sulfadoxine pyrimethamine for malaria: A global overview and challenges affecting optimal drug uptake in pregnant women. *Pathog. Glob. Health* 00, 1–14. doi:10.1080/20477724.2022.2128563

Eya'ane Meva, F., Segnou, M. L., Ebongue, C. O., Ntoumba, A. A., Kedi, P. B. E., Deli, V., et al. (2016). Spectroscopic synthetic optimizations monitoring of silver nanoparticles formation from *Megaphrynium macrostachyum* leaf extract. *Rev. Bras. Farmacogn.* 26, 640–646. doi:10.1016/j.bjp.2016.06.002

Faisal, S., Jan, H., Shah, S. A., Shah, S., Khan, A., Akbar, M. T., et al. (2021). Green synthesis of zinc oxide (ZnO) nanoparticles using aqueous fruit extracts of *Myristica fragrans*: Their characterizations and biological and environmental Applications. *ACS Omega* 6, 9709–9722. doi:10.1021/acsomega.1c00310

Foko, Kojom, Loick, P., Eya'ane Meva, F., Eboumbou Moukoko, C. E., Ntoumba, A. A., Ekoko, W. E., et al. (2021). Green-synthesized metal nanoparticles for mosquito control: A systematic review about their toxicity on non-target organisms. *Acta Trop.* 214, 105792. doi:10.1016/j.actatropica.2020.105792

Foko, Kojom, Pradel, Loick, Arya, A., Sharma, A., and Singh, V. (2021). Epidemiology and clinical outcomes of severe *Plasmodium vivax* malaria in India. *J. Infect.* 82, 231–246. doi:10.1016/j.jinf.2021.03.028

Gahlawat, G., and Choudhury, A. R. (2019). A review on the biosynthesis of metal and metal salt nanoparticles by microbes. *RSC Adv.* 9, 12944–12967. doi:10.1039/c8ra10483b

Govindarajan, M., AlQahtani, F. S., AlShebly, M. M., and Benelli, G. (2017a). One-pot and eco-friendly synthesis of silver nanocrystals using *Adiantum raddianum*: Toxicity against mosquito vectors of medical and veterinary importance. *J. Appl. Biomed.* 15, 87–95. doi:10.1016/j.jab.2016.10.004

Govindarajan, M., Kadaikunnan, S., Alharbi, N. S., and Benelli, G. (2017b). Single-step biological fabrication of colloidal silver nanoparticles using *Hugonia mystax*: Larvicidal potential against Zika virus, dengue, and malaria vector mosquitoes. *Artif. Cells, Nanomed Biotechnol.* 45, 1317–1325. doi:10.1080/21691401.2016.1228664

Hawadak, J., Kojom Foko, L. P., Pande, V., and Singh, V. (2022). *In vitro* antiplasmodial activity, hemocompatibility and temporal stability of *Azadirachta indica* silver nanoparticles. *Artif. Cells, Nanomed Biotechnol.* 50, 286–300. doi:10.1080/21691401.2022.2126979

Honary, S., Gharaei-Fathabad, E., Barabadi, H., and Naghibi, F. (2013). Fungus-mediated synthesis of gold nanoparticles: A novel biological approach to nanoparticle synthesis. *J. Nanosci. Nanotechnol.* 13, 1427–1430. doi:10.1166/jnn.2013.5989

Hoshyar, N., Gray, S., Han, H., and Bao, G. (2016). The effect of nanoparticle size on *in vivo* pharmacokinetics and cellular interaction. *Nanomed* 11, 673–692. doi:10.2217/nnm.16.5

Hossain, M. M., Polash, S. A., Takikawa, M., Shubhra, R. D., Saha, T., Islam, Z., et al. (2019). Investigation of the antibacterial activity and *in vivo* cytotoxicity of biogenic silver nanoparticles as potent therapeutics. *Front. Bioeng. Biotechnol.* 7, 239. doi:10.3389/fbioe.2019.00239

Ishwarya, R., Vaseeharan, B., Anuradha, R., Rekha, R., Govindarajan, M., Alharbi, N. S., et al. (2017). Eco-friendly fabrication of Ag nanostructures using the seed extract of *Pedalium murex*, an ancient Indian medicinal plant: Histopathological effects on the Zika virus vector *Aedes aegypti* and inhibition of biofilm-forming pathogenic bacteria. *J. Photochem Photobiol. B Biol.* 174, 133–143. doi:10.1016/j.jphotobiol.2017.07.026

Kalimuthu, K., Panneerselvam, C., Chou, C., Lin, S. M., Tseng, L. C., Tsai, K. H., et al. (2016). Predatory efficiency of the copepod *Megacyclops formosanus* and toxic effect of the red alga *Gracilaria firma*-synthesized silver nanoparticles against the dengue vector *Aedes aegypti*. *Hydrobiol* 785, 359–372. doi:10.1007/s10750-016-2943-z

Kalimuthu, K., Panneerselvam, C., Chou, C., Tseng, L. C., Murugan, K., Tsai, K. H., et al. (2017). Control of dengue and Zika virus vector *Aedes aegypti* using the predatory copepod *Megacyclops formosanus*: Synergy with *Hedychium coronarium*-synthesized silver nanoparticles and related histological changes in targeted mosquitoes. *Process Saf. Environ.* 109, 82–96. doi:10.1016/j.psep.2017.03.027

Kalishwaralal, K., Deepak, V., Ram Kumar Pandian, S. B., Kottaisamy, M., BarathManiKanth, S., Kartikeyan, B., et al. (2010). Biosynthesis of silver and gold nanoparticles using *Brevibacterium casei*. *Colloid Surf. B* 77, 257–262. doi:10.1016/j.colsurfb.2010.02.007

Kamaraj, C., Balasubramani, G., Siva, C., Raja, M., Balasubramanian, V., Raja, R. K., et al. (2017). Ag nanoparticles synthesized using β-caryophyllene isolated from *Murraya koenigii*: Antimalarial (*Plasmodium falciparum* 3D7) and anticancer activity (A549 and HeLa cell lines). *J. Clust. Sci.* 28, 1667–1684. doi:10.1007/s10876-017-1180-6

Karthik, L., Kumar, G., Keswani, T., Bhattacharyya, A., Reddy, B. P., and Rao, K. V. B. (2013). Marine actinobacterial mediated gold nanoparticles synthesis and their antimalarial activity. *Nanomed Nanotechnol. Biol. Med.* 9, 951–960. doi:10.1016/j.nano.2013.02.002

Karthik, S., Suriyaprabha, R., Vinoth, M., Srither, S., Manivasakan, P., Rajendran, V., et al. (2017). Larvicidal, super hydrophobic and antibacterial properties of herbal nanoparticles from: *Acalypha indica* for biomedical applications. *RSC Adv.* 7, 41763–41770. doi:10.1039/C7RA05697D

Kaushik, N. K., Bagavan, A., Rahuman, A. A., Zahir, A. A., Kamaraj, C., Elango, G., et al. (2015). Evaluation of antiplasmodial activity of medicinal plants from north Indian buchpora and south Indian eastern ghats. *Malar. J.* 14, 65. doi:10.1186/s12936-015-0564-z

Kojom Foko, L., Kouemo Motse, F. D., Kamgain Mawabo, L., Pande, V., and Singh, V. (2021). First evidence of local circulation of *Plasmodium ovale curtisi* and reliability of a malaria rapid diagnostic test among febrile outpatients in Douala, Cameroon. *Infect. Genet. Evol.* 91, 104797. doi:10.1016/j.meegid.2021.104797

Kojom Foko, L., Ntoumba, A., Nyabeyeu Nyabeyeu, H., Wepnje, G. B., Tonga, C., and Lehman, L. G. (2018). Prevalence, patterns and predictors of self-medication with anti-malarial drugs among Cameroonian mothers during a recent illness episode. *J. Med. Biomed. Sci.* 7, 29–39. doi:10.4314/jmbs.v7i1.4

Kojom Foko, L. P., Eya'ane Meva, F., Eboumbou Moukoko, C. E., Ntoumba, A. A., Ngaha Njila, M. I., Ebanda Belle, K. P., et al. (2019). A systematic review on anti-malarial drug discovery and antiplasmodial potential of green synthesis mediated metal nanoparticles: Overview, challenges and future perspectives. *Malar. J.* 18, 337. doi:10.1186/s12936-019-2974-9

Kojom Foko, L. P., Hawadak, J., Kouemo Motse, F. D., Eboumbou Moukoko, E. C., Kamgain Mawabo, L., Pande, V., et al. (2022a). Non-falciparum species and submicroscopic infections in three epidemiological malaria facets in Cameroon. *BMC Infect. Dis.* 22, 900. doi:10.1186/s12879-022-07901-6

Kojom Foko, L. P., Narang, G., Tamang, S., Hawadak, J., Jakhan, J., Sharma, A., et al. 2022b. The spectrum of clinical biomarkers in severe malaria and new avenues for exploration. *Virulence* 13, 634–653. doi:10.1080/21505594.2022.2056966

Laloy, J., Minet, V., Alpan, L., Mullier, F., Beken, S., Toussaint, O., et al. (2014). Impact of silver nanoparticles on haemolysis, platelet function and coagulation. *Nanobiomed* 1, 4. doi:10.5772/59346

Lehman, L. G., Kojom Foko, L., Tonga, C., Nyabeyeu, H., Eboumbou, E. C., Kouodjip Nono, L., et al. (2018). Epidemiology of malaria using LED fluorescence microscopy among schoolchildren in Douala, Cameroon. *Int. J. Trop. Dis. Health* 29, 1–13. doi:10.9734/ijtdh/2018/38804

Liu, T., Baek, D. R., Kim, J. S., Joo, S. W., and Lim, J. K. (2020). Green synthesis of silver nanoparticles with size distribution depending on reducing species in glycerol at ambient pH and temperatures. *ACS Omega* 5, 16246–16254. doi:10.1021/acsomega.0c02066

Mbohou, N. C., Kojom Foko, L. P., Nyabeyeu Nyabeyeu, H., Tonga, C., Kouodjip Nono, L., Kangam, L., et al. (2019). Malaria screening at the workplace in Cameroon. *PLoS ONE* 14, e0225219. doi:10.1371/journal.pone.0225219

Mitchell, M. J., Billingsley, M. M., Haley, R. M., Wechsler, M. E., Peppas, N. A., and Langer, R. (2021). Engineering precision nanoparticles for drug delivery. *Nat. Rev. Drug Discov.* 20, 101–124. doi:10.1038/s41573-020-0090-8

Muniz, F. T. L., Miranda, M. A. R., Morilla Dos Santos, C., and Sasaki, J. M. (2016). The Scherrer equation and the dynamical theory of X-ray diffraction. *Acta Crystallogr. Sect. A Found. Adv.* A72, 385–390. doi:10.1107/S205327331600365X

Murugan, K., Roni, M., Panneerselvam, C., Aziz, A. T., Suresh, U., Rajaganesh, R., et al. (2017). *Sargassum wightii*-synthesized ZnO nanoparticles reduce the fitness and reproduction of the malaria vector *Anopheles stephensi* and cotton bollworm *Helicoverpa armigera*. *PMPP* 101, 202–213. doi:10.1016/j.pmpp.2017.02.004

Ngaha Njila, M. I., Dahlan, I., Massoma Lembe, D., Mandengue, S., and Yusuf, A. (2016). Comparative proximate analysis of leaves and bark of *Alchornea cordifolia* (Euphorbiaceae). *J. Agricul Environ. Sci.* 5, 200–206. doi:10.15640/jaes.v5n1a21

Ntoumba, A. A., Meva Eya'ane, F., Ekoko, W. E., Kojom Foko, L. P., Ngo Hondt, E., Schlüsener, C., et al. (2020). Biogenic synthesis of silver nanoparticles using Guava (*Psidium guajava*) leaf extract and its larvicidal action against *Anopheles gambiae*. *J. Biomater. Nanobiotechnol* 11, 49–66. doi:10.4236/jbnb.2020.111004

Osadebe, P. O., Okoye, F. B. C., Uzor, P. F., Nnamani, N. R., Adiele, I. E., and Obiano, N. C. (2012). Phytochemical analysis, hepatoprotective and antioxidant activity of *Alchornea cordifolia* methanol leaf extract on carbon tetrachloride-induced hepatic damage in rats. *Asian Pac J. Trop. Med.* 5, 289–293. doi:10.1016/S1995-7645(12)60041-8

Pal, S., Tak, Y. K., and Song, J. M. (2007). Does the antibacterial activity of silver nanoparticles depend on the shape of the nanoparticle? A study of the gram-negative bacterium *Escherichia coli*. *Appl. Environ. Microbiol.* 73, 1712–1720. doi:10.1128/AEM.02218-06

Patil, S., and Chandrasekaran, R. (2020). Biogenic nanoparticles: A comprehensive perspective in synthesis, characterization, application and its challenges. *J. Genet. Eng. Biotechnol.* 18, 67. doi:10.1186/s43141-020-00081-3

Qiu, J. (2016). Nanotechnology development in China: Challenges and opportunities. *Nat. Sci. Rev.* 3, 148–152. doi:10.1093/nsr/nww007

Rahman, K., Khan, S. U., Fahad, S., Chang, M. X., Abbas, A., Khan, W. U., et al. (2019). <p&gt;Nano-biotechnology: A new approach to treat and prevent malaria&lt;/p&gt;. *Int. J. Nanomed* 14, 1401–1410. doi:10.2147/IJN.S190692

Rajakumar, G., Rahuman, A. A., Chung, I. M., Kirthi, A. V., Marimuthu, S., and Anbarasan, K. (2015). Antiplasmodial activity of eco-friendly synthesized palladium nanoparticles using *Eclipta prostrata* extract against *Plasmodium berghei* in Swiss albino mice. *Parasitol. Res.* 114, 1397–1406. doi:10.1007/s00436-015-4318-1

Rehman, K., Lotsch, F., Kremsner, P. G., and Ramharter, M. (2014). Haemolysis associated with the treatment of malaria with artemisinin derivatives: A systematic review of current evidence. *Int. J. Infect. Dis.* 29, 268–273. doi:10.1016/j.ijid.2014.09.007

Santos-Magalhães, N. S., and Mosqueira, V. C. F. (2010). Nanotechnology applied to the treatment of malaria. *Adv. Drug Deliv. Rev.* 62, 560–575. doi:10.1016/j.addr.2009.11.024

Schuster, F. (2002). Cultivation of *Plasmodium spp. Clin. Microbiol. Rev.* 15, 355–364. doi:10.1128/cmr.15.3.355-364.2002

Shakeel, A., Mudasir, A., Babu Lal, S., and Saiqa, I. (2016). A review on plants extract mediated synthesis of silver nanoparticles for antimicrobial applications: A green expertise. *J. Adv. Res.* 7, 17–28. doi:10.1016/j.jare.2015.02.007

Smilkstein, M., Sriwilaijaroen, N., Kelly, J. X., Wilairat, P., and Riscoe, M. (2004). Simple and inexpensive fluorescence-based technique for high-throughput antimalarial drug screening. *Antimicrob. Agents Chemother.* 48, 1803–1806. doi:10.1128/AAC.48.5.1803-1806.2004

Subedi, S. K. (2013). An introduction to nanotechnology and its implications. *Himal. Phys.* 4, 78–81. doi:10.3126/hj.v5i0.12877

Suganya, S., Ishwarya, R., Jayakumar, R., Govindarajan, M., Alharbi, N. S., Kadaikunnan, S., et al. (2019). New insecticides and antimicrobials derived from *Sargassum wightii* and *Halimeda gracillis* seaweeds: Toxicity against mosquito vectors and antibiofilm activity against microbial pathogens. *South Afr. J. Bot.* 125, 466–480. doi:10.1016/j.sajb.2019.08.006

Suman, T. Y., Ravindranath, R. R. S., Elumalai, D., Kaleena, P. K., Ramkumar, R., Perumal, P., et al. (2015). Larvicidal activity of titanium dioxide nanoparticles synthesized using *Morinda citrifolia* root extract against *Anopheles stephensi, Aedes aegypti* and *Culex quinquefasciatus* and its other effect on non-target fish. *Asian Pac J. Trop. Dis.* 5, 224–230. doi:10.1016/S2222-1808(14)60658-7

Sun, Y., and Shepard, H. (1947). Methods of calculating and correcting the mortality of insects. *J. Econ. Entomol.* 40, 710–715. doi:10.1093/jee/40.5.710

Thanh, N. T. K., Maclean, N., and Mahiddine, S. (2014). Mechanisms of nucleation and growth of nanoparticles in solution. *Chem. Rev.* 114, 7610–7630. doi:10.1021/cr400544s

Trager, W., and Jensen, J. (1976). Human malaria parasites in continuous culture. *Science* 190, 673–675. doi:10.1126/science.781840

Tran, Q. H., Nguyen, V. Q., and Le, A. (2013). Silver nanoparticles: Synthesis, properties, toxicology, applications and perspectives. *Adv. Nat. Sci. Nanosci. Nanotechnol.* 4, 033001. doi:10.1088/2043-6262/4/3/033001

Uwimana, A., Legrand, E., Stokes, B. H., Ndikumana, J. L. M., Warsame, M., Umulisa, N., et al. (2020). Emergence and clonal expansion of *in vitro* artemisinin-resistant *Plasmodium falciparum kelch13* R561H mutant parasites in Rwanda. *Nat. Med.* 26, 1602–1608. doi:10.1038/s41591-020-1005-2

Uwimana, A., Umulisa, N., Venkatesan, M., Svigel, S. S., Zhou, Z., Munyaneza, T., et al. (2021). Association of *Plasmodium falciparum kelch13* R561H genotypes with delayed parasite clearance in Rwanda: An open-label, single-arm, multicentre, therapeutic efficacy study. *Lancet Infect. Dis.* 21, P1120–P1128. doi:10.1016/S1473-3099(21)00142-0

Varela-Aramburu, S., Ghosh, C., Goerdeler, F., Priegue, P., Moscovitz, O., and Seeberger, P. H. (2020). Targeting and inhibiting *Plasmodium falciparum* using ultra-small gold nanoparticles. *ACS Appl. Mater Interfaces* 12, 43380–43387. doi:10.1021/acsami.0c09075

Wang, C., Qin, X., Huang, B., He, F., and Zeng, C. (2010). Hemolysis of human erythrocytes induced by melamine-cyanurate complex. *Biochem. Biophy Res. Commun.* 402, 773–777. doi:10.1016/j.bbrc.2010.10.108

Wang, L., Hu, C., and Shao, L. (2017). The antimicrobial activity of nanoparticles: Present situation and prospects for the future. *Int. J. Nanomed* 12, 1227–1249. doi:10.2147/IJN.S121956

WHO (2016). *Interim guidance for entomologists*. Geneva, Switzerland: WHO Publications. Monitoring and managing insecticide resistance in *Aedes* mosquito populations.

World Health Organization, WHO (2022). *World malaria report 2022, world health organization*. World Health Organisation, Geneva. ISBN 978 92 4 1564403

## Glossary

**AC** Alchornea cordifolia

**ACT** Artemisinin based combination therapy

**AgNPs** Silver nanoparticles

**ANOVA** Analysis of variance

**a.u** Arbitrary units

**CE** Crude extract

**CI** Confidence interval

**Cos** Cosinus

**CQ** Chloroquine

**DDT** Dichlorodiphenyltrichloroethane

**DLS** Dynamic light scattering

**DNA** Deoxyribonucleic acid

**EDX** Energy dispersive X-ray

**ELISA** Enzyme-linked immunosorbent assay

**FCC** Face centered cubic

**FTIR** Fourier transformed infrared spectroscopy

**FWHM** Full width at half maximum

**GC-MS** Gas chromatography coupled with mass spectrometry

**HC50** 50% hemolysis concentration

**IC50** 50% inhibition concentration

**ICMR** Indian Council of Medical Research

**JCPDS** Joint Committee on Powder Diffraction Standards

**LC** Lethal concentration

**MNPs** Metallic nanoparticles

**NIMR** National Institute of Malaria Research

**PBS** Phosphate-buffered saline

**Pf** Plasmodium falciparum

**PI** Polydispersity index

**PXRD** Powder X-ray diffraction

**RBC** Red blood cell

**SAED** Selected area electron diffraction

**SD** Standard deviation

**SEM** Scanning electron microscopy

**SPR** Surface plasmon resonance

**TEM** Transmission electron microscopy

**UD** The University of Douala

**UV-Vis** Ultraviolet-Visible

**WHO** World Health Organization

Frontiers in Bioengineering and Biotechnology

TYPE Original Research
PUBLISHED 06 March 2023
DOI 10.3389/fbioe.2023.1140010

EDITED BY
Pengfei Xu,
National University of Singapore,
Singapore

REVIEWED BY
Md. Rizwanullah,
Jamia Hamdard University, India
Javier Alberto Garza Cervantes,
Autonomous University of Nuevo León,
Mexico

*CORRESPONDENCE
Fatemeh B. Rassouli,
behnam3260@um.ac.ir

SPECIALTY SECTION
This article was submitted to
Nanobiotechnology,
a section of the journal
Frontiers in Bioengineering and
Biotechnology

RECEIVED 08 January 2023
ACCEPTED 16 February 2023
PUBLISHED 06 March 2023

CITATION
Talebian S, Shahnavaz B, Nejabat M,
Abolhassani Y and Rassouli FB (2023),
Bacterial-mediated synthesis and
characterization of copper oxide
nanoparticles with antibacterial,
antioxidant, and anticancer potentials.
*Front. Bioeng. Biotechnol.* 11:1140010.
doi: 10.3389/fbioe.2023.1140010

# Bacterial-mediated synthesis and characterization of copper oxide nanoparticles with antibacterial, antioxidant, and anticancer potentials

Seyedehsaba Talebian[1], Bahar Shahnavaz[1], Masoud Nejabat[1], Yasaman Abolhassani[2] and Fatemeh B. Rassouli[3]*

[1]Department of Biology, Faculty of Science, Ferdowsi University of Mashhad, Mashhad, Iran, [2]Department of Medical Biotechnology and Nanotechnology, Faculty of Medicine, Mashhad University of Medical Science, Mashhad, Iran, [3]Novel Diagnostics and Therapeutics Research Group, Institute of Biotechnology, Ferdowsi University of Mashhad, Mashhad, Iran

The application of novel bacterial strains for effective biosynthesis of nanoparticles minimizes negative environmental impact and eliminates challenges of available approaches. In the present study, cell-free extract of *Stenotrophomonas* sp. BS95. was used for synthesis of copper oxide nanoparticles (CuONPs). Characterization of crude and calcined CuONPs was carried out by UV-vis spectroscopy, X-ray diffraction (XRD), fourier transform infrared (FTIR) spectroscopy, zeta potential, dynamic light scattering, field emission scanning electron microscopy, transmission electron microscopy, and atomic force microscopy. Afterward, biogenic CuONPs were evaluated for antibacterial, antioxidant, and cytotoxic effects using broth micro-dilution method, DPPH assay and alamarBlue assay, respectively. Finally, molecular mechanisms behind anticancer effects of CuONPs was ascertained by real time PCR. UV-vis absorbance spectra registered surface plasmon resonance peaks at 286 nm and 420 nm for crude and calcined CuONPs, respectively. FTIR spectra exhibited bands associated with organic functional groups of bacterial proteins, confirming capping and functionalization of CuONPs. The average crystallite size of crude and calcined CuONPs was determined as 18.24 and 21.3 nm by XRD, respectively. The average zeta potentials of crude and calcined CuONPs were as −28.57 ± 5.13 and −29.47 ± 4.78 mV, respectively, indicating their high stability. Electron microscopy revealed that crude and calcined CuONPs were roughly spherical particles with an average size of 35.24 ± 4.64 and 43.68 ± 2.31 nm, respectively. Biogenic CuONPs induced antibacterial effects with minimal inhibitory concentrations ranging from 62.5 to 1,000 μg/ml against Gram-negative and Gram-positive strains. The antioxidant activity of crude and calcined CuONPs was found to be 83% ± 2.64% and 78% ± 1.73%, respectively. More intriguingly, CuONPs exerted considerable cytotoxic effects on human colon and gastric adenocarcinoma cells, while induced low toxicity on normal cells. Anticancer effects of biogenic CuONPs were confirmed by significant changes induced in the expression of apoptosis-related genes, including *P53*, *BAX*, *BCL2* and *CCND1*. Hence, biosynthesized CuONPs could be considered as potential antimicrobial, antioxidant and anticancer agents.

KEYWORDS

***stenotrophomonas* sp. BS95, copper oxide nanoparticles, antimicrobial activity, antioxidant effects, anticancer properties**

## Introduction

Nanotechnology is as an evolving interdisciplinary research field that focuses on nanoparticles (NPs) with improved size-dependent features, such as robustness of the colloidal moiety, great surface area and high bioavailability to name a few (Pan et al., 2021). Conventionally, synthesis of NPs can be performed by physical, chemical and mechanical approaches, however, high cost and toxicity of these methods have shifted fabrication of NPs toward biological systems (Chandrasekaran et al., 2020; Lahiri et al., 2021). Among all microorganisms, bacteria are attractive candidates to synthesize NPs because of remarkable benefits like high stability, short generation time, mild experimental condition, easy culture, resistance to most toxic heavy metals and their ability to produce sustainable NPs at a large scale (Yusof et al., 2019; Waris et al., 2021).

Unique characteristics of metal oxide NPs made them suitable candidates for various commercial and domestic applications, such as energy harvesting, food processing and environmental protection (Tsuzuki, 2021). In addition, there is a growing interest to develop nano-scale pharmaceuticals for management of global health concerns. For instance, antibiotic resistance crisis, which has placed a substantial clinical and financial burden on healthcare systems, can be controlled by antibacterial potential of NPs. Furthermore, increasing incidence and mortality rate of cancer, which is due to poor diagnosis and low specificity of common chemotherapeutics, can be reversed by novel nano-based agents (Pearce et al., 2017; Fu et al., 2018; Zhang et al., 2018).

Copper oxide nanoparticles (CuONPs) have attracted much attention because of appropriate redox potential, high specific surface area, and excellent stability in different solutions (Nagajyothi et al., 2017; Verma and Kumar, 2019). The aim of present study was to synthesize CuONPs by a toxic-free, rapid, and eco-friendly approach and evaluate its biological activities. To do so, CuONPs were first synthesized by *Stenotrophomonas* sp. BS95, and then characterization was carried out by well-established techniques; Optical properties were defined by ultraviolet-visible (UV-vis) spectroscopy and fourier transform infrared (FTIR) defined functional groups. X-ray diffraction (XRD) was used to determin the crystallite size, while physical stability and surface charge were measured by zeta potential. Analysis of hydrodynamic particle size was carried out by dynamic light scattering (DLS) and electrone microscopy was used to study various surface phenomena such as morphology and roughness. Then after, crude and calcined CuONPs were assessed for antibacterial, antioxidant, and cytotoxic effects using broth micro-dilution method, DPPH assay and alamarBlue assay, respectively. Finally, molecular mechanisms behind anticancer effects of biogenic CuONPs was unraveled by real time polymerase chain reaction (PCR).

## Materials and methods

### Biosynthesis of CuONPs by hydrothermal cell lysate supernatant

Synthesis of CuONPs in the present study was carried out using bacterial cell lysate supernatant (CLS), as previously described (Nakhaeepour et al., 2019). A cold-tolerant bacterium, namely, *Stenotrophomonas* sp. BS95 was isolated from alpine soil samples collected in western Iran, and identified using 16s rRNA gene sequencing analysis. The data presented in this study are deposited in the GenBank repository, accession number OQ253458. To synthesize CuONPs, this strain was cultured in tryptic soy broth (TSB) medium (Merck) and incubated in a shaking incubator at 28°C and 150 rpm for 72 h. Afterward, the culture medium was centrifuged at 7,500 rpm for 15 min and the pellet was washed with 1 mM NaCl solution (Merck). Then, the cell pellet was resuspended in distilled $H_2O$ and after 24 h incubation, it was placed in an ultrasonic bath sonicator for 20 min to obtain the cell lysate. Upon centrifugation at 5,000 rpm for 20 min, the supernatant was added to 0.01 M copper (II) sulfate pentahydrate ($CuSO_4.5H_2O$) and heated at 121°C for 20 min. Followed by centrifugation at 10,000 rpm for 10 min, biogenic CuONPs were obtained and washed with distilled $H_2O$ and ethanol. Then, the purified NPs were dried in a vacuum oven at 80°C for 4 h to achieve crude CuONPs, and calcined CuONPs were obtained after incubation in a muffle furnace (470°C) for 4 h.

## Characterization of synthesized CuONPs

### UV-vis spectroscopy

To define optical properties of crude and calcined CuONPs, UV-vis spectroscopy was used (Ssekatawa et al., 2022). In this regard, 1 mg of each sample was dispersed in distilled $H_2O$ and dispensed into different cuvettes. Optical properties of samples were then obtained by UV-vis spectrophotometer (Shimadzu UV-1700, Japan), scanning at a resolution of 1 nm between 200 and 800 nm ranges.

### FTIR spectroscopy

The organic functional groups of crude and calcined CuONPs were identified by FTIR spectroscopy (Sarkar et al., 2020). In this regard, 2 mg of biogenic CuONPs and 2 g of potassium bromide (KBr) were mixed and compressed to obtain translucent circular pellets. Then, samples were scanned through 4,000 to 400 $cm^{-1}$ wavenumber range and a resolution of 4 $cm^{-1}$ for at least 32 scans per sample using Thermo Nicolet 6700 FTIR spectrometer (Nicolet Avatar, Madison, WI, United States of America). To note, KBr pellet was used as control.

### XRD analysis

To confirm crystallinity of crude and calcined CuONPs, XRD analysis was performed (Nakhaeepour et al., 2019). To do so, GNR Explorer X-ray diffractometer (Italy) fitted with Cu-Kα radiation ($\lambda$ = 1.5418 A°) and scanning from $2\theta = 20°–80°$, with a voltage of 40 kV, current of 30 mA and integration time of 0.2 s/step was used. Obtained data was visualized in OriginPro 2019b software, and validated by standard CuONPs 2θ values from the International Center for Diffraction Data (ICDD) database. The average crystallite size was calculated using the following formula:

$$d = 0.9\lambda / \beta \cos\theta$$

in which d is the average crystallite size, $\beta$ is full peak width at half maximum, $\lambda$ is the wavelength of X-ray (1.5418 Å) and θ is the 2θ angle in peak.

## DLS and zeta potential

The average size and stability of crude and calcined CuONPs were determined at neutral pH and room temperature as previously described (Sarkar et al., 2020). Briefly, to evaluate the average size distribution, 100 µg/ml of each sample was dispersed in ethanol and sonicated for 5 min. Afterward, samples were examined by DLS analyzer (vasco3. Cordouan, France) for three times, and zeta potential was determined by an electrophoretic light scattering instrument (Zeta Compact, CAD, France).

## FESEM, TEM and AFM analysis

To determine the particle size distribution and nanostructure of crude and calcined CuONPs, FESEM was used (Ali et al., 2020). In summary, each sample was spread onto an aluminum tape and coated with gold to become a conductor. Micrographs were taken at different magnifications using FESEM (Mira 3-FEG TESCAN, Czech Republic), operating at around 30 kV accelerating voltage. Morphological and topographical characteristics of biogenic CuONPs were also studied by TEM (Ssekatawa et al., 2022). In this regard, 1 mg/ml of each sample was dispersed in ethanol, sonicated and finally loaded on copper grid thin films. Micrographs were obtained by TEM (912AB, LEO, Germany) operating at around 100 kV accelerating voltage. The particle size distribution (PSD) plots were obtained by determining the size of 50 particles for each sample using ImageJ software.

The surface morphology of crude and calcined CuONPs was investigated by AFM (Barani et al., 2021). To do so, NSC15-type silicon probes with the radius of tip curvature less than 10 nm were used and samples were analyzed by AFM device (Brisk model, Ara Research, Iran). The height of each sample was finally estimated in scanning areas of 1 × 1 µm.

## Antibacterial activity

The antibacterial activity of biogenic CuONPs against pathogenic bacteria including *Bacillus subtilis* PTCC 1023, *Staphylococcus aureus* ATCC 25923, *Pseudomonas putida* KT2440 and *Escherichia coli* PTCC 1860 was evaluated using broth micro-dilution method (Binesh et al., 2021) The suspension of $1.5 \times 10^8$ CFU/mL bacteria (according to the 0.5 McFarland standard) was prepared in nutrient broth (NB, Merck). To assess minimum inhibitory concentration (MIC), 100 µl of CuONPs with serial dilutions (500–1.9 µg/ml) and 10 µl of pathogenic bacteria were transferred to each well of 96-well plates containing 100 µL Muller-Hinton broth medium (MHB, Merck) and incubated at 37°C in a shaker incubator for 18 h. The absorbance was then recorded at 630 nm using a spectrophotometer (Stat Fax 2100, England). To evaluate minimum bactericidal concentration (MBC), 5 µl from each dilution was spread on Muller-Hinton agar (MHA, Merck) plates and incubated at 37°C for another 24 h.

## Analysis of antioxidant activity

The antioxidant activity of crude and calcined CuONPs was assessed by measuring their capability to scavenge synthetic stable radicals of 2,2-diphenyl-1-picrylhydrazyl (DPPH), as previously reported (Barani et al., 2021). To do so, 0.14 mM DPPH in methanol was added to each well of 96-well plates containing different concentrations of CuONPs (31.2, 62.5, 125, 250, 500, and 1,000 µg/ml) and incubated at 37°C for 30 min, while ascorbic acid was used as a standard solution. Finally, the absorbance (A) was recorded at 517 nm using spectrophotometer (Awarness), and free radical scavenging activity of CuONPs was calculated using the following formula:

$$\text{DPPH radical scavenging activity } (\%) = \left(\frac{AS - (AT - AB)}{AS}\right) \times 100$$

in which AT is the absorbance of test wells, AB is the absorbance of blank wells, and AS is the absorbance of standard solution.

## Cell culture, treatment and viability assay

Human colon and gastric adenocarcinoma cells (LoVo and MKN-45 cell lines, respectively) along with human dermal fibroblasts (HDF cell line) were purchased from Pasteur Institute (Tehran, Iran). MKN-45 and HDF cells were cultured in Dulbecco's modified Eagle's medium (DMEM, Biowest), whereas LoVo cells were grown in Roswell Park Memorial Institute-1640 (RPMI-1640, Biowest). All media were supplemented with 10% fetal bovine serum (FBS) (Biowest) and 1% penicillin-streptomycin (Biowest). Cells were maintained at 37°C in normoxic (95% and 5% $CO_2$ in air) and hypoxic (93% $N_2$, 5% $CO_2$ and 2% $O_2$) conditions.

To evaluate cytotoxic effects of CuONPs and determine the half maximal inhibitory concentration ($IC_{50}$) values, alamarBlue assay was performed (Movaffagh et al., 2021). To do so, LoVo and MKN-45 cells were seeded at a density of 14,000 cell/well, in each well of 96-well plates, while HDF cells were seeded at a density of 10,000 cell/well. After 24 h incubation, cells were treated with 50, 100, and 200 µg/ml crude and calcined CuONPs, while untreated cells were considered as control. At the end of treatments (24 h), alamarBlue solution (Sigma-Aldrich) was added to each well (20 µl/well) followed by 2 h incubation at 37°C. Then, the absorbance (A) of each well was recorded at 600 nm using spectrophotometer (BioTek), and the viability of cells was calculated based on the following equation:

$$\text{Cell viability } (\%) = \left[100 - \left(\frac{AT - AU}{AB - AU}\right)\right] \times 100$$

in which AT is the absorbance of treated cells, AU is the absorbance of untreated cells, and AB is the absorbance of blank control.

**TABLE 1 List of primers, their sequence, and product length used in the present study.**

| Gene name | Forward (5′ to 3′) | Reverse (5′ to 3′) | Product size (bp) |
|---|---|---|---|
| *TBP* | ACAACAGCCTGCCACCTTA | GAATAGGCTGTGGGGTCAGT | 120 |
| *P53* | GTTCCGAGAGCTGAATGAGG | TTATGGCGGGAGGTAGACTG | 123 |
| *BAX* | GGACGAACTGGACAGTAACATGG | GCAAAGTAGAAAAGGGCGACAAC | 150 |
| *BCL2* | GATGACTGAGTACCTGAACCG | CAGAGACAGCCAGGAGAAATC | 124 |
| *CCND1* | TGAAGGAGACCATCCCCCTG | TGTTCAATGAAATCGTGCGG | 151 |

## Gene expression analysis

To assess the effects of biogenic CuONPs on the expression of apoptosis-related genes, real time PCR was applied (Mirzaei et al., 2022). In summary, total cellular RNA was extracted from LoVo cells treated with 100 µg/ml crude and calcined CuONPs, as well as untreated cells, using a total RNA isolation kit (DENAzist Asia). RNA purity was then evaluated by spectrophotometer at 260 and 280 nm (Nanodrop 2000 Thermo). For synthesis of cDNAs, M-MuLV reverse transcriptase (Parstous) was used according to the manufacturer's instruction. The validity of amplified cDNAs was then confirmed by PCR using *TBP* primers and final products were loaded on 1.5% agarose gel for electrophoresis. Real time PCR was conducted in an iQ5 real-time PCR detection system (Bio-Rad) using SYBR green master mix (BioFact) and specific primers listed in Table 1. To compare the level of gene expression, TBP transcripts were used as internal control and normalized values were plotted as relative fold change over untreated cells. PCR cycling conditions were as follows: 95°C for 5 min [95°C for 20 s, 58°C for 30 s, 72°C for 30 s] (35 cycles) for *P53*, *BAX*, *BCL2* and *CCND1* primers.

## Statistical analysis

The data were analyzed by one-way ANOVA and Dunnett's multiple comparison tests using GraphPad Prism version 8.4.3 software. Values were expressed as mean ± SD, and $p$ values less than 0.05, 0.01, 0.001 and 0.0001 were considered to be statistically significant.

# Results

## Biosynthesis of CuONPs

In the present study, synthesis of CuONPs was carried out using CLS of a psychrotolerant *Stenotrophomonas* species. In this approach, complicated downstream processes were not required and thus, the risk of microbial contamination was low. The biosynthesis of CuONPs was validated by monitoring four flasks containing *Stenotrophomonas* sp. BS95 after 48 h incubation, bacterial CLS, $CuSO_4$ solution and the reaction mixture of bacterial CLS with $CuSO_4$ (Figure 1). The instant precipitation of green aggregates, which did not change over 24 h incubation, indicated the formation of CuONPs.

## Optical properties of biogenic CuONPs

UV-vis spectroscopy was carried out to obtain optical properties of crude and calcined CuONPs. As presented in Figure 2A, surface plasmon resonance (SPR) peaks were recorded at 286 and 420 nm, which were assigned to efficient bio-reduction of $CuSO_4$ to CuONPs. Since the shift of UV-vis absorbance toward short wavelengths is mainly attributed to decrease in the NP size, the left shift observed in UV spectrum was associated with the small size of our biogenic crude CuONPs.

## FTIR analysis

The FTIR spectra of crude and calcined CuONPs revealed similar absorbance bands within the wavenumber range of 3,200–3,600, 1,652 and 1,235–1,360 $cm^{-1}$ (Figure 2B). As shown, three distinct bands were registered for crude CuONPs in the range of 2,958, 1,080 and 547 $cm^{-1}$, while two unique absorbance bands were recorded for calcined CuONPs in the range of 521 and 620 $cm^{-1}$.

## Analysis of XRD pattern

Completely similar to the standard pattern of CuO nanocrystals (JCPDS File No: 01-080-1917), analysis of XRD patterns revealed that all peaks representing CuONPs were present in our biogenic crude and calcined NPs (Figure 3). Bragg peaks positioned at 2θ values of 32.5°, 35.7°, 38.7°, 46.2°, 53.5°, 65.8°, 66.2°, 68.08° and 72.3° were registered for crude CuONPs, corresponded to the planes of (100), (002), (101), (102), (110), (103), (200), (112) and (004), respectively. However, diffraction peaks observed at 2θ values of 32.18°, 35.19°, 38.6°, 52.9°, 65.3°, 68.2° and 71.8° were registered for calcined CuONPs, assigned to crystal planes of (100), (002), (101), (110), (103), (112) and (004), respectively. The average crystallite size, measured using the Debye–Scherrer equation, was as 18.24 nm and 21.3 nm for crude and calcined CuONPs, respectively.

## Measurement of stability and particle size

The average zeta potentials of crude and calcined CuONPs were as −28.57 ± 5.13 mV and −29.47 ± 4.78 mV, respectively, indicating their high stability (Figures 4A, B). The size distribution histograms obtained from DLS analysis showed that the size of the crude

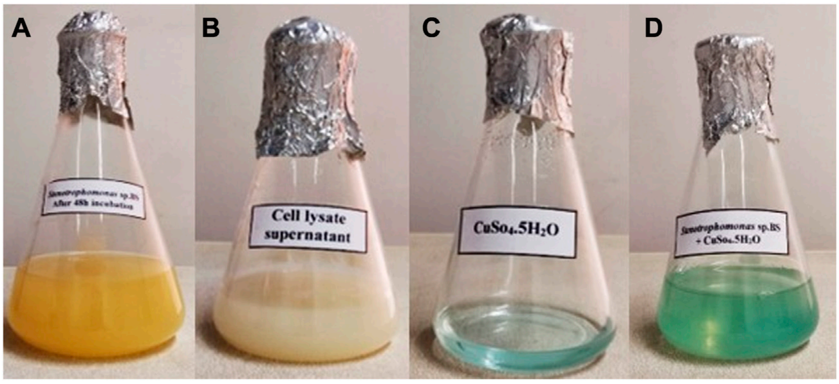

FIGURE 1
Visual detection of biosynthesized CuONPs. Four conical flasks containing *Stenotrophomonas* sp. BS95 after 48 h incubation **(A)**, bacterial CLS **(B)**, $CuSO_4$ solution **(C)**, and biogenic CuONPs **(D)**.

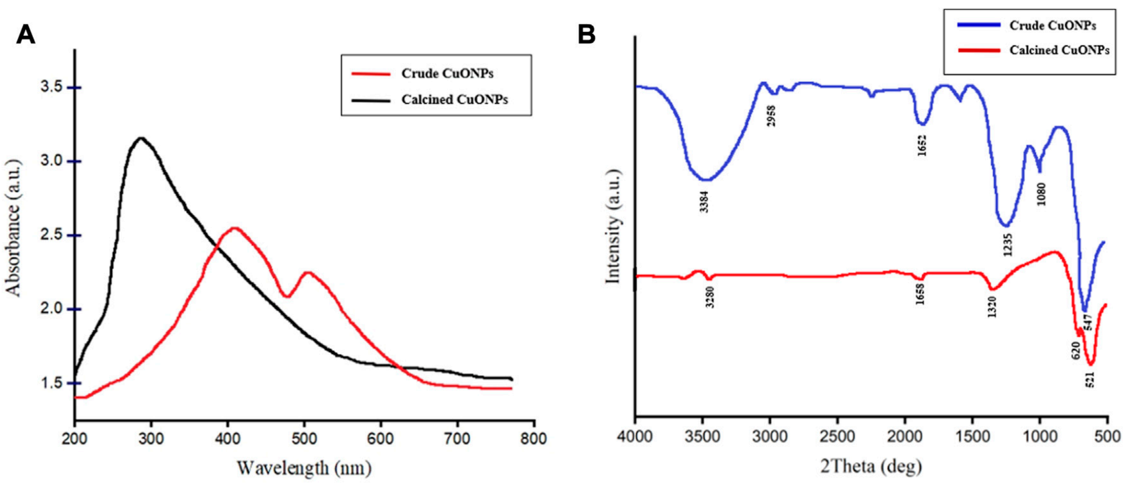

FIGURE 2
The UV-vis spectrum of crude and calcined CuONPs **(A)**; maximum absorbance bands were observed at 286 nm and 420 nm, respectively, FTIR spectrum of crude and calcined CuONPs **(B)**.

CuONPs ranged from 25 to 110 nm with a mean distribution diameter of 55.92 nm, and from 38 to 128 nm with an average of 68.35 nm for calcined CuONPs. In addition, the calculated polydispersity index (PDI) were as 0.26 nm and 0.13 nm for crude and calcined CuONPs, respectively (Figures 4C, D).

## Nanostructure analysis by FESEM, TEM and AFM

FESEM was used to determine morphology and size details of biogenic CuONPs. As presented in Figures 5A, B, crude and calcined CuONPs were spherical particles with the average PSD of 37.73 ± 3.27 and 48.37 ± 5.17 nm, respectively. Likewise, TEM micrographs revealed that crude and calcined CuONPs were roughly spherical particles with PSD values of 35.24 ± 4.64 and 43.68 ± 2.31 nm, respectively (Figures 5C, D).

To provide further insights into topological appearance and size of CuONPs, AFM images were prepared. As presented in Figure 6, crude and calcined CuONPs were detected as individual conical grains extending upwards with the average height as 5.155 and 6.547 nm, respectively.

## Antibacterial effects of biogenic CuONPs

The antibacterial activity of CuONPs was evaluated against Gram-negative and Gram-positive bacteria using the broth microdilution method (Table 2). Calculating MIC values revealed that crude CuONPs inhibited the growth of *B. subtilis*, *S. aureus*, *P. putida* and *E. coli* at 62.5, 125, 250, and 500 μg/ml, respectively. Furthermore, the MIC values of calcined CuONPs were found to be 250 μg/ml for *B. subtilis* and *S. aureus*, and 500 and 1,000 μg/ml for *P. putida* and *E. coli*, respectively. This observation demonstrated

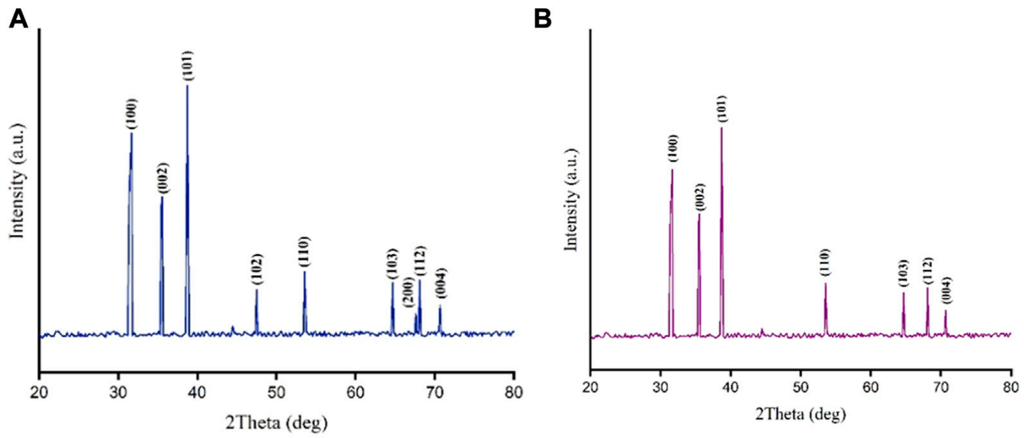

FIGURE 3
XRD patterns for crude **(A)** and calcined **(B)** CuONPs.

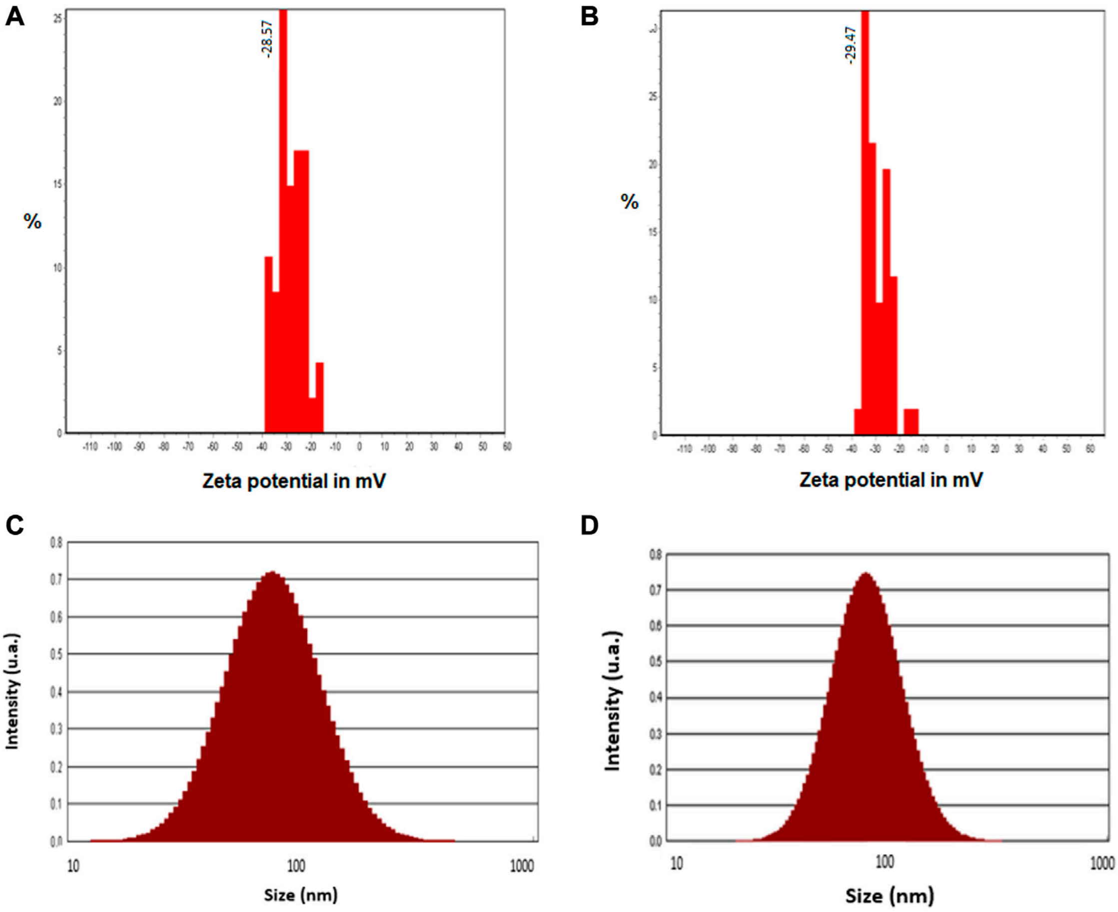

FIGURE 4
Zeta potential histograms **(A, B)** and particle size distribution pattern **(C, D)** of crude **(A, C)** and calcined **(B, D)** CuONPs.

that calcination reduced the bacterial inhibitory activity of CuONPs. As also indicated in Table 2, MBC values for crude CuONPs in the present study were 250 μg/ml for *B. subtilis, S. aureus* and *P. putida* and 500 μg/ml for *E. coli*. Likewise, the MBC values of calcined CuONPs were determined as 250 μg/ml for *B. subtilis* and *S. aureus*, and 500 μg/ml for *P. putida* and *E. coli*.

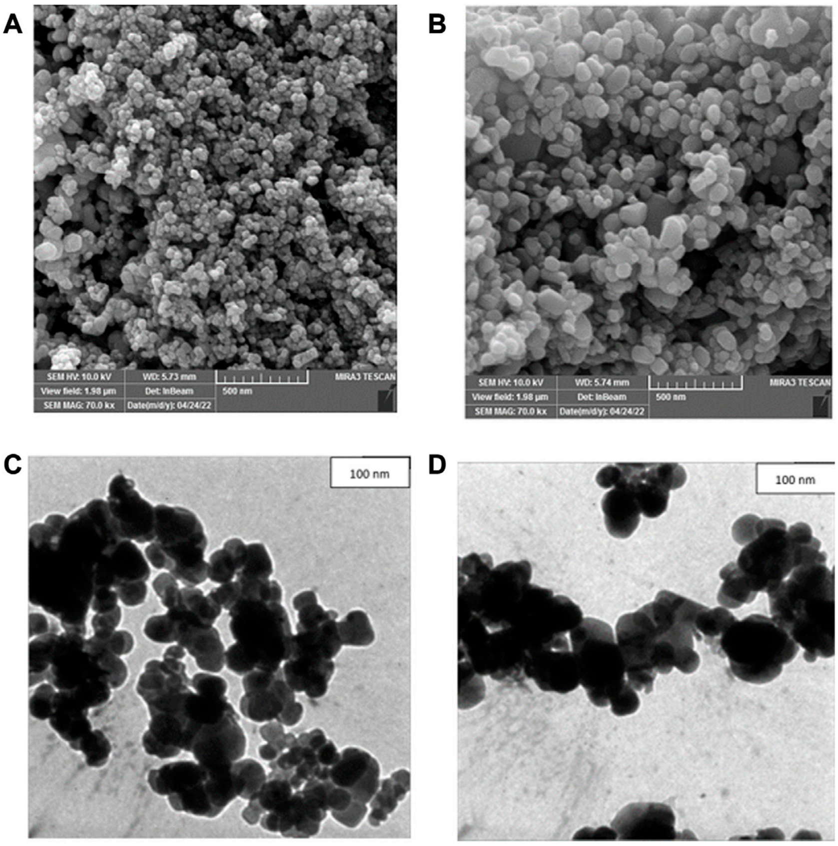

FIGURE 5
FESEM **(A, B)** and TEM **(C, D)** micrographs of crude **(A, C)** and calcined **(B, D)** CuONPs.

## Antioxidant activity of biogenic CuONPs

Evaluating the antioxidant activity of biogenic CuONPs in the present study indicated that they scavenged DPPH radicals in a dose-dependent manner. As presented in Figure 7, upon administration of 2000 μg/ml crude CuONPs, 83% ± 2.64% antioxidant activity was detected, while calcined CuONPs exhibited lower activity (78% ± 1.73%) in the same concentration. To note, in all concentrations, significant difference ($p < 0.0001$) was detected in the scavenging activity between ascorbic acid and biogenic CuONPs.

## Anticancer properties of biogenic CuONPs

Assessment of cell viability revealed that CuONPs induced cytotoxic effects in a dose-dependent manner. As shown in Figure 8, treatment of LoVo, MKN-45 and HDF cells with 50, 100 and 200 μg/ml crude and calcined CuONPs significantly reduced cell viability in comparison with untreated cells. To note, toxic effects of CuONPs were also cell type-dependent, as viability of LoVo cells reduced to lower amounts in comparison with MKN-45 cells, and more interestingly, our biogenic CuONPs induced lowest toxic effects on non-cancerous HDF cells. Similarly, morphological alterations, in the form of dispersed cells with cytoplasmic granulation, were apparent upon administration of crude and calcined CuONPs when compared with untreated cells (Figure 9). Calculated $IC_{50}$ values of crude and calcined CuONPs on LoVo, MKN-45 and HDF cells are presented in Table 3. Due to high toxicity of CuONPs in LoVo cells, we also assessed their anticancer potential in hypoxic condition. Our results demonstrated that in comparison with untreated cells, biogenic CuONPs induced considerable toxicity in hypoxic condition as well (Table 3; Figure 8).

To unravel mechanisms underlying anticancer effects of crude and calcined CuONPs, alterations induced in the expression of apoptosis-related genes was investigated by real time PCR. As shown in Figure 10, upon 24 h treatment of LoVo cells with 100 μg/ml biogenic CuONPs, significant ($p < 0.0001$) over expression of *P53* and *BAX* was detected in comparison with untreated cells. On the other hand, crude and calcined CuONPs significantly ($p < 0.001$) downregulated the expression of *BCL2* and *CCND1* when compared with untreated cells.

# Discussion

Biosynthesis of CuONPs was carried out in the present study by an efficient non-toxic approach using *Stenotrophomonas* sp. BS95 CLS. It has been shown that cellular biomolecules such as enzymes and proteins presented in the bacterial CLS could reduce copper ions into copper atoms leading to CuONPs formation (Nakhaeepour et al., 2019; Bandeira et al., 2020). This

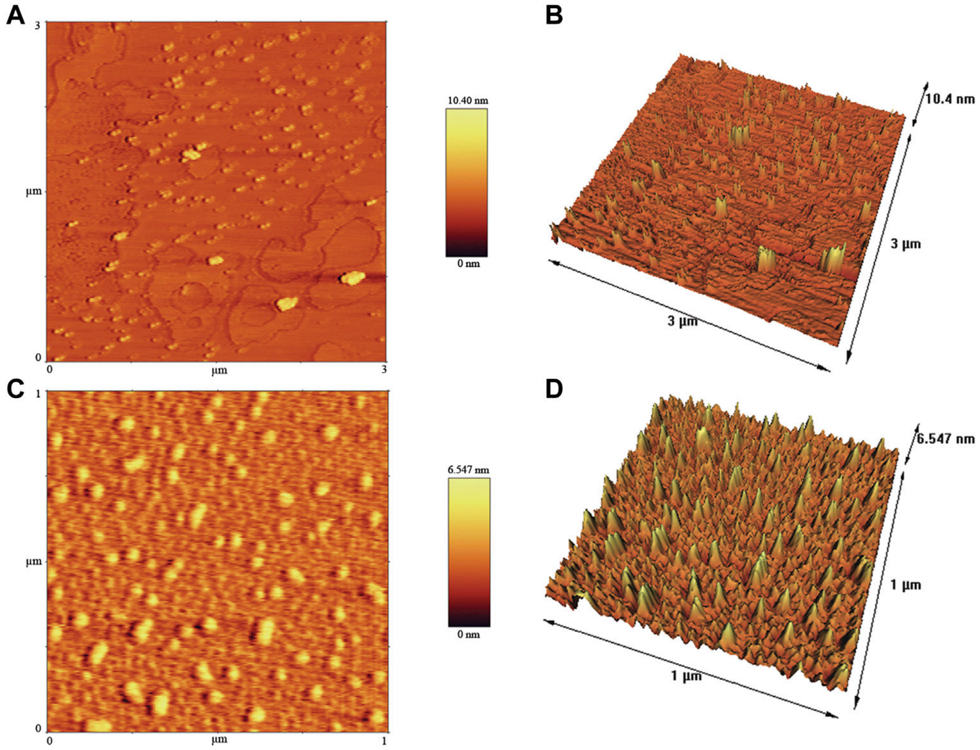

FIGURE 6
AFM images of crude **(A, B)** and calcined **(C, D)** CuONPs: 2D view **(A, C)** and 3D view **(B, D)**.

**TABLE 2 The MIC and MBC of biogenic CuONPs against different Gram-positive and Gram-negative bacteria.**

| | MIC (µg/ml) | | | | MBC (µg/ml) | | | |
|---|---|---|---|---|---|---|---|---|
| | *B. subtilis* | *S. aureus* | *P. putida* | *E. coli* | *B. subtilis* | *S. aureus* | *P. putida* | *E. coli* |
| Crude CuONPs | 62.5 | 125 | 250 | 500 | 250 | 250 | 250 | 500 |
| Calcined CuONPs | 250 | 250 | 500 | 1,000 | 250 | 250 | 500 | 500 |

mechanism might be involved in biosynthesis of CuONPs in our study as well. The reduction of $CuSO_4$ was subjected to spectral analysis by the UV-vis spectroscopy. SPR peaks of crude and calcined CuONPs were recorded between 286 and 420 nm, respectively. In line with these findings, it has been reported that UV-vis absorbance of biogenic CuONPs fall between 285 and 570 nm (Cheirmadurai et al., 2014; Duman et al., 2016). Furthermore, changes in the SPR peak position after calcination could be explained by elimination of capping agents, increased crystallite size and/or agglomeration of metal oxide NPs, as previously described (Tang et al., 2012; Kayani et al., 2015; Gharibshahi et al., 2017).

FTIR spectrophotometry was carried out to analyze bacterial biomolecules involved in reducing copper ions to CuONPs and subsequent capping. The organic functional groups entrapping CuONPs were determined as previously reported (Ali et al., 2020; Chandrasekaran et al., 2020; Kouhkan et al., 2020). Strong peaks at 3,200–3,600 cm$^{-1}$ demonstrated the N-H stretching vibrations of amine group or amide linkages in the protein contents of bacterial plasma membrane. The peak observed at 2,958 cm$^{-1}$ was associated with C-H stretching vibration of the aldehyde compound. The band at 1,652 cm$^{-1}$ was corresponded to the stretching vibration of C=O, usually found in proteins. The peaks seen at 1,080, 1,235 and 1,360 cm$^{-1}$ were further associated with the stretching vibration of C–N of aliphatic and aromatic amines. In this study, the bands at 547 and 521 cm$^{-1}$ for Cu–O confirmed the synthesis of CuONPs. To note, deletion of absorption peaks at 2,958 and 1,080 cm$^{-1}$ in calcined CuONPs might be due to the removal of peaks corresponding to functional groups, including aldehyde and amine.

The presence of sharp structural peaks in XRD patterns and crystallite size <100 nm revealed the nanocrystalline nature of crude and calcined CuONPs, which are in consistence with previous studies (Ahamed et al., 2014; Shankar and Rhim, 2014; Duman

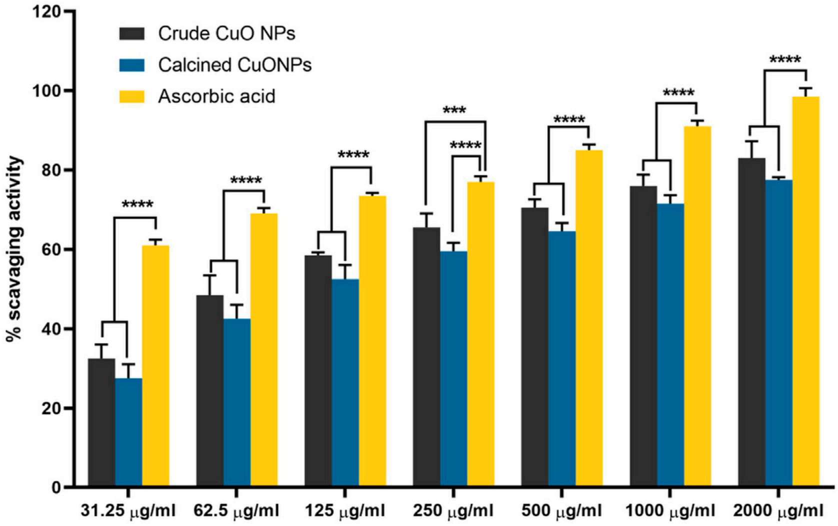

FIGURE 7
The antioxidant activity of biogenic CuONPs at different concentrations. Ascorbic acid was used as a standard. ****$p < 0.0001$ indicate significant difference with ascorbic acid.

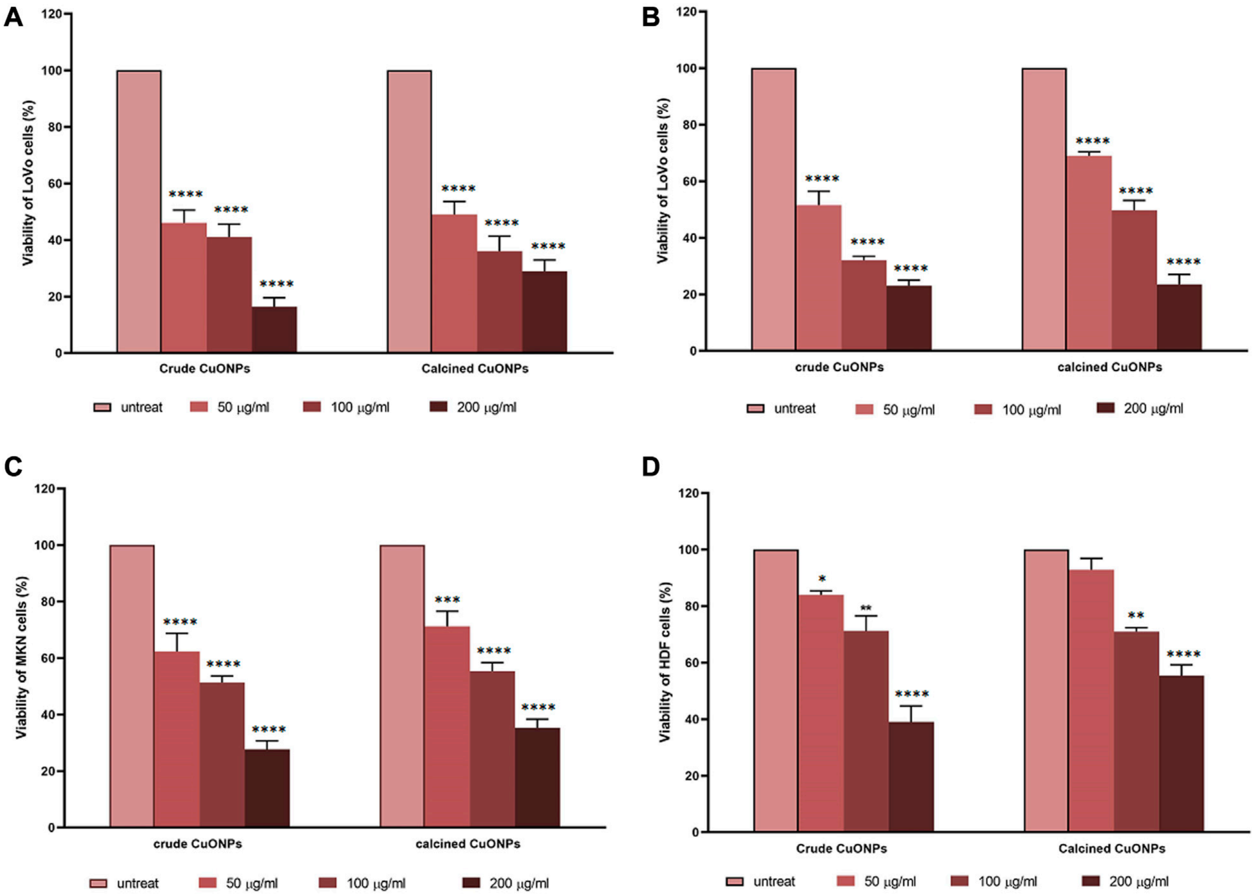

FIGURE 8
Dose-response curves representing the effects of crude and calcined CuONPs on viability of LoVo cells in normoxic **(A)** and hypoxic conditions **(B)**, MKN-45 cells **(C)**, and HDF cells **(D)**. Results are shown as mean ± SD. *$p < 0.05$, **$p < 0.01$***$p < 0.001$ and ****$p < 0.0001$ indicate significant difference with untreated cells.

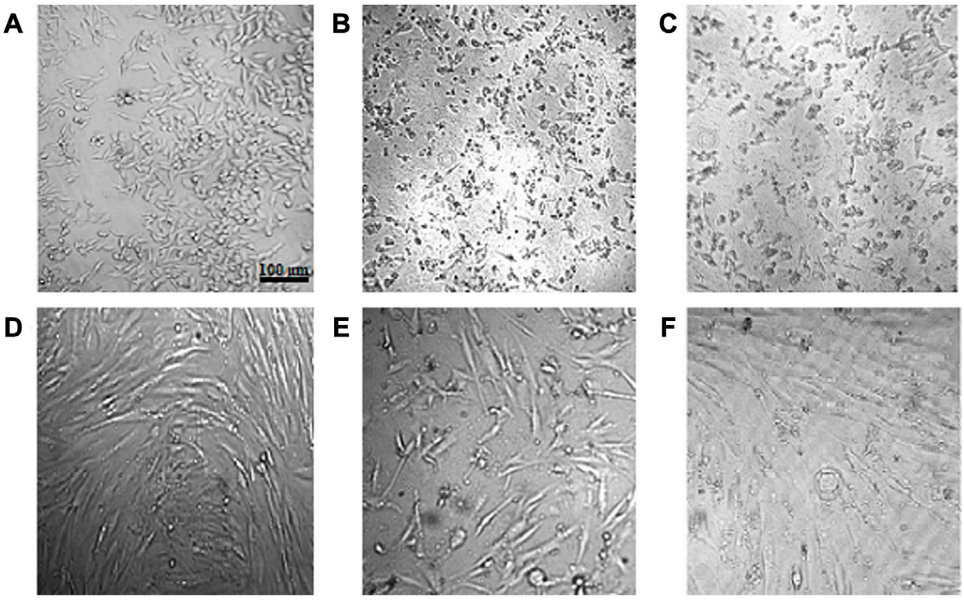

FIGURE 9
Morphological alterations of cells after administration of crude and calcined CuONPs. Phase contrast photomicrographs of LoVo **(A–C)** and HDF **(D–F)** cells; untreated **(A, D)**, treated with 200 µg/mL crude **(B, E)** and calcined **(C, F)** CuONPs.

**TABLE 3 Calculated $IC_{50}$ (µg/ml) values of crude and calcined CuONPs on different cell lines.**

| | LoVo | MKN | HDF | LoVo-hypoxia |
|---|---|---|---|---|
| Crude CuONPs | 48.36 | 90.23 | 158.2 | 50.84 |
| Calcined CuONPs | 44.96 | 117.5 | 222.8 | 92.43 |

et al., 2016). Metal oxide NPs with zeta potential values higher than +30 mV or lower than −30 mV typically have high degree of stability, which is of utmost importance to avoid their agglomeration in colloidal solution (Joseph and Singhvi, 2019). In the present study, zeta potential measurement indicated higher stability of crude and calcined CuONPs compared to previous reports (Tiwari et al., 2016; Chandrasekaran et al., 2020).

Defining the morphology and PSD of biogenic CuONPs by FESEM, TEM and AFM revealed their spherical shape, while crude CuONPs presented smaller size in comparison with calcined CuONPs. These observations confirmed results obtained from XRD and DLS analysis, and are in consistence with previous reports on biogenic CuONPs (Nasrollahzadeh et al., 2015; Gu et al., 2018; Kouhkan et al., 2020; Sarkar et al., 2020).

Evaluating antibacterial activity of CuONPs implied on their inhibitory effects on both Gram-negative and Gram-positive pathogens, although antibacterial potential of crude CuONPs was higher than calcined CuONPs. In consistence with current findings, previous reports indicated that metal oxide NPs such as CuONPs induced remarkable antimicrobial activity due to their small size and extremely large surface area that provide better contact with microorganisms (Azam et al., 2012; Laha et al., 2014). Various studies have also demonstrated bactericide effects of CuONPs against same pathogenic bacteria, for instance, MBC values of crude CuONPs on *E. coli* and *S. aureus* have been reported as 250 and 2,500 µg/ml, respectively (Ren et al., 2009). In addition, MBC of mechanochemically synthesized CuONPs against *E. coli* and *S. aureus* were as 750 and 5,000 µg/ml, respectively (Moniri et al., 2019). In another research, the MBC of phytofabricated CuONPs was reported as 10,000 µg/ml for both *E. coli* and *S. aureus* (Alavi et al., 2021). Based on our findings, biogenic CuONPs induced higher growth inhibitory and toxic effects on Gram-positive bacteria compared with Gram-negative ones. In this regard, it has been shown that lipopolysaccharide layer on the outer membrane of Gram-negative bacteria acts as an effective protection against NPs (Franco et al., 2022) that could explain, to some extent, observed effects in the present study. CuONPs induce antibacterial effects through binding to the bacterial cell membrane, production of reactive oxygen species and release of $Cu^{2+}$ ions that demolish DNA and cellular proteins, affect the membrane permeability, and finally induce cell death (Obeizi et al., 2020). Thus, considerable activity of biogenic CuONPs against *B. subtilis, S. aureus, P. putida, and E. coli* in our study might be mediated through the same mechanisms.

Current results also revealed high antioxidant activity of crude and calcined CuONPs, which has been attributed to the binding of transition metal ion catalysts to free radicals (Omran and Baek, 2021). Based on a recent report, the free radical scavenging activity of CuONPs may be enhanced by various bio-reductive groups (capping agents) of the bacterial proteins (Ssekatawa et al., 2022). As explained above, FTIR analysis confirmed the capping of crude CuONPs with aldehyde and amine groups, unlike calcined CuONPs. Therefore, higher antioxidant activity of crude CuONPs in our study was presumably due to bacterial-derived functional groups.

Malignancies of the gastrointestinal tract, including colorectal and gastric carcinomas, account for 36.2% of cancer mortality (Hong et al., 2022). Although use of chemical drugs is a systemic treatment for cancer patients, low specificity of common

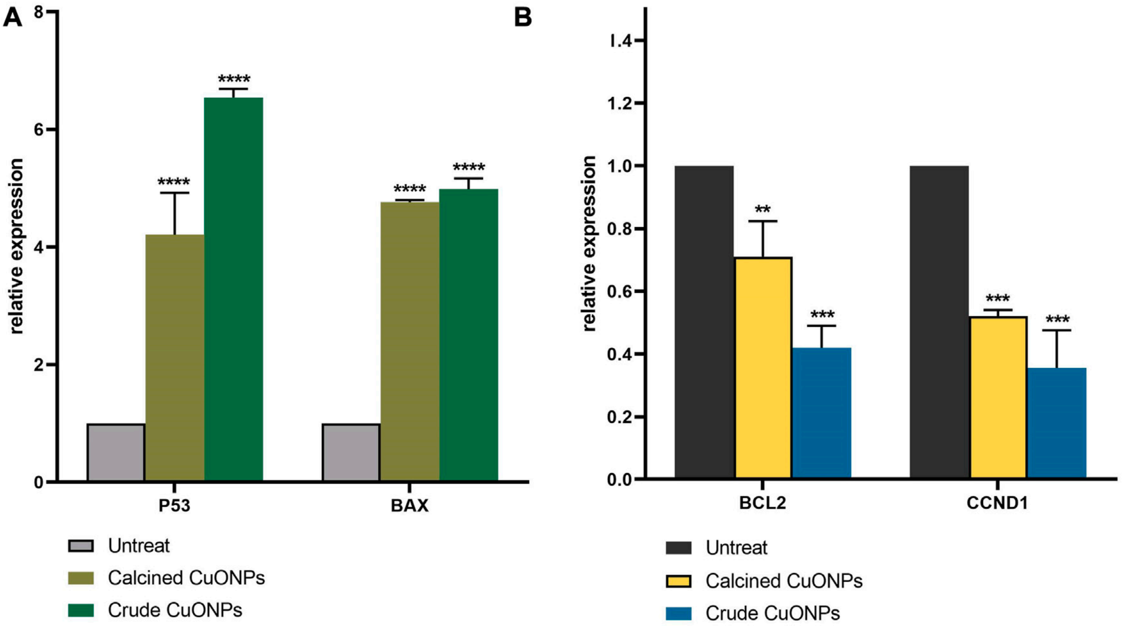

FIGURE 10
Analysis of gene expression by real-time PCR. The expression of *P53*, *BAX* **(A)**, *BCL2* and *CCND1* **(B)** were normalized and plotted as relative fold change compared with the untreated cells. Data are represented as mean ± SD. $^{**}p < 0.01$, $^{***}p < 0.001$, $^{****}p < 0.0001$ indicate significant difference with untreated cells.

chemotherapeutics causes many side effects that are mostly intolerable to patients and lead to reduced survival rates (Pearce et al., 2017; Fu et al., 2018; Zhang et al., 2018). To introduce novel and more effective therapeutics, we investigated anticancer potential of CuONPs, and obtained findings revealed that cytotoxicity of our biogenic CuONPs was dose- and cell type-dependent. Intriguingly, crude and calcined CuONPs induced more toxic effects on human colon and gastric adenocarcinoma cells than normal fibroblasts. Current results are in consistence with previous reports. For instance, it has been demonstrated that CuONPs synthesized by marine endophytic actinomycete and *Vibrio* sp. VLC. induced toxic effects on human lung and esophageal carcinoma cells in a dose-dependent manner, with $IC_{50}$ values of 500 and 37.52 μg/ml, respectively (Nakhaeepour et al., 2019; Zhao et al., 2022). In addition, low toxicity of CuONPs on normal HDF cells in the present study is in line with another research, which reported minimal toxic effects of CuONPs on human dermal fibroblasts (Sulaiman et al., 2018).

Hypoxia, a biological phenomenon in which oxygen level is below the tissue demand, is a feature of solid tumors, and an indicator of poor prognosis in many cancers including colon and gastric adenocarcinomas (Qi et al., 2020; Pei et al., 2021). Hypoxia causes a range of genetic, transcriptional, and metabolic adaptations in advanced tumors that ultimately promote survival and metastasis of cancer cells (Li et al., 2020). Thus, it has been recommended to assess anticancer effects of potent agents in hypoxic condition for accurate evaluation of their therapeutic potential (Nobre et al., 2018). Current findings that revealed considerable cytotoxicity of biogenic CuONPs in hypoxic condition suggest that these NPs have the potential to induce anticancer effects *in vivo*, although more research on animal models is required.

Carrying gene expression analysis indicated significant induction in *P53* expression after administration of biogenic CuONPs. *P53* is a tumor suppressor gene with critical roles in the cell cycle regulation and apoptosis (Vousden and Lu, 2002; Lacroix et al., 2006). Similar to our results, it has been reported that CuONPs induced apoptosis in human lung carcinoma cells through upregulation of *P53* (Kalaiarasi et al., 2018). In the present study, CuONPs effectively downregulated the expression of *BCL2,* while induced the expression of *BAX*. Current findings are in agreement with previous studies, which demonstrated that CuONPs inhibited cell growth and induced apoptosis in acute myeloid leukemia, breast, gastric, colon and lung cancer cells *via* significant induction of *BAX* and downregulation of *BCL2* (Shafagh et al., 2015; Gopinath et al., 2016; Khan et al., 2017; Kalaiarasi et al., 2018). Present results also revealed that CuONPs significantly decreased the expression of *CCND1*, a core cell cycle regulator that promotes cell proliferation and plays a major role in oncogenesis (Qie and Diehl, 2016). Similar to our findings, it has been shown that inhibited proliferation and induced apoptosis of oral carcinoma cells upon administration of metal oxide NPs were mediated by downregulation of *CCND1* (Li et al., 2020).

## Conclusion

Emergence of antibiotic-resistant strains is an intractable challenge to public health worldwide. In addition, acquired chemoresistance of cancer cells has vastly limited the clinical outcome of current pharmaceutical drugs. Although inorganic NPs could act as potent antibiotics and anticancer agents, disadvantages of conventional methods for NP synthesis have enforced to develop alternative approaches. In the present attempt, we successfully used *Stenotrophomonas* sp. BS95 to synthesize functional CuONPs. UV vis spectroscopy, XRD and DLS analyses and electron microscopy revealed small size, crystallin nature and spherical shape of CuONPs. In addition, good dispersion and high stability of biogenic CuONPs were confirmed by zeta potential analysis, and functional groups were determined by FTIR spectroscopy. Evaluating biological effects of CuONPs exhibited their antibacterial activity against *B. subtilis*, *S. aureus*, *P. putida*, and *E. coli*. Furthermore, biogenic CuONPs possessed remarkable antioxidant potential and induced considerable anticancer effects on human colon and gastric adenocarcinoma cells *via* modulation of apoptosis-related genes. Interestingly, biogenic CuONPs induced low toxicity on normal cells, and had the potential to exert cytotoxic effects in hypoxic condition. According to the current findings, our biogenic CuONPs could be considered as effective agents with potential medical applications. Nevertheless, complementary studies on other pathogenic bacteria, more cell lines and animal models are required to better evaluate the efficacy and safety of biogenic CuONPs. In addition, conjugation of biogenic CuONPs with antibiotics and anticancer drugs might improve the clinical outcome of current therapeutic modalities.

## Data availability statement

The original contributions presented in the study are included in the article/supplementary material, further inquiries can be directed to the corresponding author.

## Author contributions

All authors participated in the design, interpretation and analysis of the data and review of the manuscript; ST, MN, and YA carried out the experiments and analysis of the results, BS and FBR designed and supervised the project, supplied all reagents, and edited the manuscript.

## Funding

This work was supported with a grant from Ferdowsi University of Mashhad (No. 55887). The authors declare that they have no known competing financial interests or personal relationships that could have appeared to influence the work reported in this paper.

## Acknowledgments

The authors would like to thank Dr M. Taghavi for his help and technical advices.

## Conflict of interest

The authors declare that the research was conducted in the absence of any commercial or financial relationships that could be construed as a potential conflict of interest.

## Publisher's note

## References

Ahamed, M., Alhadlaq, H. A., Khan, M., Karuppiah, P., and Al-Dhabi, N. A. (2014). Synthesis, characterization, and antimicrobial activity of copper oxide nanoparticles. *J. Nanomater.* 2014, 1–4. doi:10.1155/2014/637858

Alavi, M., Dehestaniathar, S., Mohammadi, S., Maleki, A., and Karimi, N. (2021). Antibacterial activities of phytofabricated ZnO and CuO NPs by mentha pulegium leaf/flower mixture extract against antibiotic resistant bacteria. *Adv. Pharm. Bull.* 11 (3), 497–504. doi:10.34172/apb.2021.057

Ali, K., Saquib, Q., Ahmed, B., Siddiqui, M. A., Ahmad, J., Al-Shaeri, M., et al. (2020). Bio-functionalized CuO nanoparticles induced apoptotic activities in human breast carcinoma cells and toxicity against Aspergillus flavus: An *in vitro* approach. *Process Biochem.* 91, 387–397. doi:10.1016/j.procbio.2020.01.008

Azam, A., Ahmed, A. S., Oves, M., Khan, M., and Memic, A. (2012). Size-dependent antimicrobial properties of CuO nanoparticles against Gram-positive and-negative bacterial strains. *Int. J. Nanomedicine* 7, 3527–3535. doi:10.2147/IJN.S29020

Bandeira, M., Giovanela, M., Roesch-Ely, M., Devine, D. M., and da Silva Crespo, J. (2020). Green synthesis of zinc oxide nanoparticles: A review of the synthesis methodology and mechanism of formation. *Sustain. Chem. Pharm.* 15, 100223. doi:10.1016/j.scp.2020.100223

Barani, M., Masoudi, M., Mashreghi, M., Makhdoumi, A., and Eshghi, H. (2021). Cell-free extract assisted synthesis of ZnO nanoparticles using aquatic bacterial strains: Biological activities and toxicological evaluation. *Int. J. Pharm.* 606, 120878. doi:10.1016/j.ijpharm.2021.120878

Binesh, N., Farhadian, N., and Mohammadzadeh, A. (2021). Enhanced antibacterial activity of uniform and stable chitosan nanoparticles containing metronidazole against anaerobic bacterium of Bacteroides fragilis. *Colloids Surfaces B Biointerfaces.* 202, 111691. doi:10.1016/j.colsurfb.2021.111691

Chandrasekaran, R., Yadav, S. A., and Sivaperumal, S. (2020). Phytosynthesis and characterization of copper oxide nanoparticles using the aqueous extract of beta vulgaris L and evaluation of their antibacterial and anticancer activities. *J. Clust. Sci.* 31 (1), 221–230. doi:10.1007/s10876-019-01640-6

Cheirmadurai, K., Biswas, S., Murali, R., and Thanikaivelan, P. (2014). Green synthesis of copper nanoparticles and conducting nanobiocomposites using plant and animal sources. *RSC Adv.* 4 (37), 19507–19511. doi:10.1039/C4RA01414F

Duman, F., Ocsoy, I., and Kup, F. O. (2016). Chamomile flower extract-directed CuO nanoparticle formation for its antioxidant and DNA cleavage properties. *Mater. Sci. Eng. C* 60, 333–338. doi:10.1016/j.msec.2015.11.052

Franco, D., Calabrese, G., Guglielmino, S. P. P., and Conoci, S. (2022). Metal-based nanoparticles: Antibacterial mechanisms and biomedical application. *Microorganisms* 10 (9), 1778. doi:10.3390/microorganisms10091778

Fu, B., Wang, N., Tan, H.-Y., Li, S., Cheung, F., and Feng, Y. (2018). Multi-component herbal products in the prevention and treatment of chemotherapy-associated toxicity and side effects: A review on experimental and clinical evidences. *Front. Pharmacol.* 1394, 1394. doi:10.3389/fphar.2018.01394

Gharibshahi, L., Saion, E., Gharibshahi, E., Shaari, A. H., and Matori, K. A. (2017). Structural and optical properties of Ag nanoparticles synthesized by thermal treatment method. *Materials* 10 (4), 402. doi:10.3390/ma10040402

Gopinath, V., Priyadarshini, S., Al-Maleki, A., Alagiri, M., Yahya, R., Saravanan, S., et al. (2016). *In vitro* toxicity, apoptosis and antimicrobial effects of phyto-mediated copper oxide nanoparticles. *RSC Adv.* 6 (112), 110986–110995. doi:10.1039/C6RA13871C

Gu, H., Chen, X., Chen, F., Zhou, X., and Parsaee, Z. (2018). Ultrasound-assisted biosynthesis of CuO-NPs using Brown alga Cystoseira trinodis: Characterization, photocatalytic AOP, DPPH scavenging and antibacterial investigations. *Ultrason. Sonochemistry* 41, 109–119. doi:10.1016/j.ultsonch.2017.09.006

Hong, M.-Z., Li, J.-M., Chen, Z.-J., Lin, X.-Y., Pan, J.-S., and Gong, L.-L. (2022). Global burden of major gastrointestinal cancers and its association with socioeconomics, 1990–2019. *Front. Oncol.* 12, 942035. doi:10.3389/fonc.2022.942035

Joseph, E., and Singhvi, G. (2019). "Chapter 4 - multifunctional nanocrystals for cancer therapy: A potential nanocarrier," in *Nanomaterials for drug delivery and therapy*. Editor A. M. Grumezescu Berlin, Germany: Springer, 91–116. doi:10.1016/B978-0-12-816505-8.00007-2

Kalaiarasi, A., Sankar, R., Anusha, C., Saravanan, K., Aarthy, K., Karthic, S., et al. (2018). Copper oxide nanoparticles induce anticancer activity in A549 lung cancer cells by inhibition of histone deacetylase. *Biotechnol. Lett.* 40 (2), 249–256. doi:10.1007/s10529-017-2463-6

Kayani, Z. N., Saleemi, F., and Batool, I. (2015). Effect of calcination temperature on the properties of ZnO nanoparticles. *Appl. Phys. A* 119 (2), 713–720. doi:10.1007/s00339-015-9019-1

Khan, S., Ansari, A. A., Khan, A. A., Abdulla, M., Al-Obaid, O., and Ahmad, R. (2017). *In vitro* evaluation of cytotoxicity, possible alteration of apoptotic regulatory proteins, and antibacterial activity of synthesized copper oxide nanoparticles. *Colloids Surfaces B Biointerfaces.* 153, 320–326. doi:10.1016/j.colsurfb.2017.03.005

Kouhkan, M., Ahangar, P., Babaganjeh, L. A., and Allahyari-Devin, M. (2020). Biosynthesis of copper oxide nanoparticles using Lactobacillus casei subsp. casei and its anticancer and antibacterial activities. *Curr. Nanosci.* 16 (1), 101–111. doi:10.2174/1573413715666190318155801

Lacroix, M., Toillon, R.-A., and Leclercq, G. (2006). p53 and breast cancer, an update. *Endocrine-Related Cancer* 13 (2), 293–325. doi:10.1677/erc.1.01172

Laha, D., Pramanik, A., Laskar, A., Jana, M., Pramanik, P., and Karmakar, P. (2014). Shape-dependent bactericidal activity of copper oxide nanoparticle mediated by DNA and membrane damage. *Mater. Res. Bull.* 59, 185–191. doi:10.1016/j.materresbull.2014.06.024

Lahiri, D., Nag, M., Sheikh, H. I., Sarkar, T., Edinur, H. A., Pati, S., et al. (2021). Microbiologically-synthesized nanoparticles and their role in silencing the biofilm signaling cascade. *Front. Microbiol.* 12, 636588. doi:10.3389/fmicb.2021.636588

Li, H., Li, Q., Li, Y., Sang, X., Yuan, H., and Zheng, B. (2020). Stannic oxide nanoparticle regulates proliferation, invasion, apoptosis, and oxidative stress of oral cancer cells. *Front. Bioeng. Biotechnol.* 8, 768. doi:10.3389/fbioe.2020.00768

Mirzaei, S., Iranshahy, M., Gholamhosseinian, H., Matin, M. M., and Rassouli, F. B. (2022). Urolithins increased anticancer effects of chemical drugs, ionizing radiation and hyperthermia on human esophageal carcinoma cells *in vitro*. *Tissue Cell* 77, 101846. doi:10.1016/j.tice.2022.101846

Movaffagh, J., Salari, H., Merajifar, E., Gholamhosseinian, H., Shahroodi, A., Iranshahi, M., et al. (2021). 7-Geranyloxycoumarin enhanced radiotherapy effects on human gastric adenocarcinoma cells. *J. Cancer Res. Ther.* 2021, 1–10. doi:10.4103/jcrt.jcrt_701_21

Nagajyothi, P., Muthuraman, P., Sreekanth, T., Kim, D. H., and Shim, J. (2017). Green synthesis: *In-vitro* anticancer activity of copper oxide nanoparticles against human cervical carcinoma cells. *Arabian J. Chem.* 10 (2), 215–225. doi:10.1016/j.arabjc.2016.01.011

Nakhaeepour, Z., Mashreghi, M., Matin, M. M., NakhaeiPour, A., and Housaindokht, M. R. (2019). Multifunctional CuO nanoparticles with cytotoxic effects on KYSE30 esophageal cancer cells, antimicrobial and heavy metal sensing activities. *Life Sci.* 234, 116758. doi:10.1016/j.lfs.2019.116758

Nasrollahzadeh, M., Sajadi, S. M., Rostami-Vartooni, A., and Bagherzadeh, M. (2015). Green synthesis of Pd/CuO nanoparticles by Theobroma cacao L. seeds extract and their catalytic performance for the reduction of 4-nitrophenol and phosphine-free Heck coupling reaction under aerobic conditions. *J. Colloid Interface Sci.* 448, 106–113. doi:10.1016/j.jcis.2015.02.009

Nobre, A. R., Entenberg, D., Wang, Y., Condeelis, J., and Aguirre-Ghiso, J. A. (2018). The different routes to metastasis via hypoxia-regulated programs. *Trends Cell Biol.* 28 (11), 941–956. doi:10.1016/j.tcb.2018.06.008

Obeizi, Z., Benbouzid, H., Ouchenane, S., Yılmaz, D., Culha, M., and Bououdina, M. (2020). Biosynthesis of Zinc oxide nanoparticles from essential oil of Eucalyptus globulus with antimicrobial and anti-biofilm activities. *Mater. Today Commun.* 25, 101553. doi:10.1016/j.mtcomm.2020.101553

Omran, B., and Baek, K. H. (2021). Nanoantioxidants: Pioneer types, advantages, limitations, and future insights. *Molecules* 26 (22), 7031. doi:10.3390/molecules26227031

Pan, S., Goudoulas, T. B., Jeevanandam, J., Tan, K. X., Chowdhury, S., and Danquah, M. K. (2021). Therapeutic applications of metal and metal-oxide nanoparticles: Dermato-cosmetic perspectives. *Front. Bioeng. Biotechnol.* 9, 724499. doi:10.3389/fbioe.2021.724499

Pearce, A., Haas, M., Viney, R., Pearson, S.-A., Haywood, P., Brown, C., et al. (2017). Incidence and severity of self-reported chemotherapy side effects in routine care: A prospective cohort study. *Plos One* 12 (10), e0184360. doi:10.1371/journal.pone.0184360

Pei, J.-P., Zhang, C.-D., Yusupu, M., Zhang, C., and Dai, D.-Q. (2021). Screening and validation of the hypoxia-related signature of evaluating tumor immune microenvironment and predicting prognosis in gastric cancer. *Front. Immunol.* 12, 705511. doi:10.3389/fimmu.2021.705511

Qi, L., Chen, J., Yang, Y., and Hu, W. (2020). Hypoxia correlates with poor survival and M2 macrophage infiltration in colorectal cancer. *Front. Oncol.* 10, 566430. doi:10.3389/fonc.2020.566430

Qie, S., and Diehl, J. A. (2016). Cyclin D1, cancer progression, and opportunities in cancer treatment. *J. Mol. Med.* 94 (12), 1313–1326. doi:10.1007/s00109-016-1475-3

Ren, G., Hu, D., Cheng, E. W., Vargas-Reus, M. A., Reip, P., and Allaker, R. P. (2009). Characterisation of copper oxide nanoparticles for antimicrobial applications. *Int. J. Antimicrob. Agents* 33 (6), 587–590. doi:10.1016/j.ijantimicag.2008.12.004

Sarkar, J., Chakraborty, N., Chatterjee, A., Bhattacharjee, A., Dasgupta, D., and Acharya, K. (2020). Green synthesized copper oxide nanoparticles ameliorate defence and antioxidant enzymes in Lens culinaris. *Nanomaterials* 10 (2), 312. doi:10.3390/nano10020312

Shafagh, M., Rahmani, F., and Delirezh, N. (2015). CuO nanoparticles induce cytotoxicity and apoptosis in human K562 cancer cell line via mitochondrial pathway, through reactive oxygen species and P53. *Iran. J. Basic Med. Sci.* 18 (10), 993–1000.

Shankar, S., and Rhim, J.-W. (2014). Effect of copper salts and reducing agents on characteristics and antimicrobial activity of copper nanoparticles. *Mater. Lett.* 132, 307–311. doi:10.1016/j.matlet.2014.06.014

Ssekatawa, K., Byarugaba, D. K., Angwe, M. K., Wampande, E. M., Ejobi, F., Nxumalo, E., et al. (2022). Phyto-mediated copper oxide nanoparticles for antibacterial, antioxidant and photocatalytic performances. *Front. Bioeng. Biotechnol.* 10, 820218. doi:10.3389/fbioe.2022.820218

Sulaiman, G. M., Tawfeeq, A. T., and Jaaffer, M. D. (2018). Biogenic synthesis of copper oxide nanoparticles using olea europaea leaf extract and evaluation of their toxicity activities: An *in vivo* and *in vitro* study. *Biotechnol. Prog.* 34 (1), 218–230. doi:10.1002/btpr.2568

Tang, Z.-X., Fang, X.-J., Zhang, Z.-L., Zhou, T., Zhang, X.-Y., and Shi, L.-E. (2012). Nanosize MgO as antibacterial agent: Preparation and characteristics. *Braz. J. Chem. Eng.* 29, 775–781. doi:10.1590/S0104-66322012000400009

Tiwari, M., Jain, P., Chandrashekhar Hariharapura, R., Narayanan, K., Bhat, K. U., Udupa, N., et al. (2016). Biosynthesis of copper nanoparticles using copper-resistant Bacillus cereus, a soil isolate. *Process Biochem.* 51 (10), 1348–1356. doi:10.1016/j.procbio.2016.08.008

Tsuzuki, T. (2021). Mechanochemical synthesis of metal oxide nanoparticles. *Commun. Chem.* 4 (1), 143. doi:10.1038/s42004-021-00582-3

Verma, N., and Kumar, N. (2019). Synthesis and biomedical applications of copper oxide nanoparticles: An expanding horizon. *ACS Biomaterials Sci. Eng.* 5 (3), 1170–1188. doi:10.1021/acsbiomaterials.8b01092

Vousden, K. H., and Lu, X. (2002). Live or let die: The cell's response to p53. *Nat. Rev. Cancer* 2 (8), 594–604. doi:10.1038/nrc864

Waris, A., Din, M., Ali, A., Ali, M., Afridi, S., Baset, A., et al. (2021). A comprehensive review of green synthesis of copper oxide nanoparticles and their diverse biomedical applications. *Inorg. Chem. Commun.* 123, 108369. doi:10.1016/j.inoche.2020.108369

Yusof, H. M., Mohamad, R., Zaidan, U. H., and Abdul Rahman, N. A. (2019). Microbial synthesis of zinc oxide nanoparticles and their potential application as an antimicrobial agent and a feed supplement in animal industry: A review. *J. Animal Sci. Biotechnol.* 10 (1), 57–22. doi:10.1186/s40104-019-0368-z

Zhang, Y., Zhan, X., Xiong, J., Peng, S., Huang, W., Joshi, R., et al. (2018). Temperature-dependent cell death patterns induced by functionalized gold nanoparticle photothermal therapy in melanoma cells. *Sci. Rep.* 8 (1), 8720–8729. doi:10.1038/s41598-018-26978-1

Zhao, H., Maruthupandy, M., Al-mekhlafi, F. A., Chackaravarthi, G., Ramachandran, G., and Chelliah, C. K. (2022). Biological synthesis of copper oxide nanoparticles using marine endophytic actinomycetes and evaluation of biofilm producing bacteria and A549 lung cancer cells. *J. King Saud Univ. – Sci.* 34 (3), 101866. doi:10.1016/j.jksus.2022.101866

TYPE Original Research
PUBLISHED 23 March 2023
DOI 10.3389/fbioe.2023.1168750

OPEN ACCESS

EDITED BY
Xiangzhao Ai,
Shanghai Jiao Tong University, China

REVIEWED BY
Liu Ying Xiang,
Fourth Military Medical University, China
Zhuo Wang,
Fudan University, China

*CORRESPONDENCE
Guannan Wang,
✉ chemwangguannan@gmail.com

†These authors have contributed equally to this work

SPECIALTY SECTION
This article was submitted to Nanobiotechnology, a section of the journal Frontiers in Bioengineering and Biotechnology

RECEIVED 18 February 2023
ACCEPTED 14 March 2023
PUBLISHED 23 March 2023

CITATION
Shi X, Liu J and Wang G (2023), A peroxidase-like magneto-gold nanozyme AuNC@$Fe_3O_4$ with photothermal effect for induced cell apoptosis of hepatocellular carcinoma cells *in vitro*.
*Front. Bioeng. Biotechnol.* 11:1168750.
doi: 10.3389/fbioe.2023.1168750

# A peroxidase-like magneto-gold nanozyme AuNC@$Fe_3O_4$ with photothermal effect for induced cell apoptosis of hepatocellular carcinoma cells *in vitro*

Xinglong Shi[1†], Jifa Liu[1,2†] and Guannan Wang[1*]

[1]College of Medical Engineering & the Key Laboratory for Medical Functional Nanomaterials, Jining Medical University, Jining, China, [2]Cheeloo College of Medicine, Shandong University, Jinan, China

Hepatocellular carcinoma (HCC) is one of the most commonly diagnosed and malignant cancers worldwide. Conventional therapy strategies may not completely eradicate the tumor and may cause side effects during treatment. Nano-catalytic therapy, as a novel strategy, has attracted a great deal of attention. This study aimed to synthesize a multifunctional magneto-gold nanozyme AuNC@$Fe_3O_4$ and evaluate its anti-cancer potential in HepG2 cells *in vitro*. The characteristics of AuNC@$Fe_3O_4$ were assessed using a transmission electron microscope, dynamic light scattering, and energy-dispersive X-ray. The photothermal performance and peroxidase (POD)-like activity of AuNC@$Fe_3O_4$ were detected, using thermal camera and ultraviolet-visible spectrophotometer, respectively. The anti-cancer potential of AuNC@$Fe_3O_4$ was examined using cell counting kit-8, live/dead cell staining, and apoptosis analysis. Further research on HepG2 cells included the detection of intracellular reactive oxygen species (ROS) and lysosomal impairment. We observed that the AuNC@$Fe_3O_4$ had a small size, good photothermal conversion efficiency and high POD-like activity, and also inhibited cell proliferation and enhanced cell apoptotic ability in HepG2 cells. Furthermore, the AuNC@$Fe_3O_4$ enhanced ROS production and lysosomal impairment *via* the synergistic effect of photothermal and nano-catalytic therapies, which induced cell death or apoptosis. Thus, the magneto-gold nanozyme AuNC@$Fe_3O_4$ may offer a potential anti-cancer strategy for HCC.

KEYWORDS

**POD-like, magneto-gold, nanozyme, photothermal effect, cell apoptosis, hepatocellular carcinoma**

## 1 Introduction

Data from Global Cancer Incidence, Mortality and Prevalence 2020 revealed that liver cancer was the sixth commonly diagnosed and the third lethal cancer worldwide (Sung et al., 2021). China accounted for 23.7% and 30% of the global morbidity and mortality from liver cancer, respectively (Ferlay et al., 2021). It was predicted that between 2020 and 2040, there would be a 55% increase in the number of new cases of liver cancer per year, and the percentage of people who would die from the disease in 2040 would be more than 56.4% of those in 2020 (Rumgay et al., 2022). Primary liver cancer can be classified into three types: cholangiocarcinoma, hepatocellular carcinoma (HCC), and a combination of the two, with HCC accounting for approximately 90% of all cases (Llovet et al., 2016). HCC progression is influenced by several risk factors, such as alcohol abuse, smoking, toxic chemicals, and hepatitis virus (especially for HBV) infections (Yang et al., 2019). Owing to the absolute number of HBV-infected populations (Liu et al., 2016), the mortality rate of HBV-related liver cancer was consistently higher than the global level (Liu et al., 2019), which increased the burden of HCC in China.

In most cases, conventional treatments, such as surgery, radiation, and chemotherapy, do not completely eradicate the tumor and may cause side effects during treatment, such as cancer palindromia and drug resistance (Zhu et al., 2016; Xu et al., 2019; Raoul and Edeline, 2020; Liu and Song, 2021). For example, the surgery was initially considered to be used for patients with early-stage HCC; However, over 50% of patients experienced a recurrence within a year following surgery (Gil et al., 2015; Weber et al., 2015). Sorafenib was an option for patients with advanced-stage cancer, however, it was only effective in less than a third of them and caused drug tolerance or cytotoxicity (Llovet et al., 2008; Cheng et al., 2009; Bruix et al., 2012; Anwanwan et al., 2020). Besides surgery and chemotherapy, radiation therapy is a non-invasive and local ablative treatment approach to kill cancer cells. However, the efficiency of radiation therapy is easily limited by radioresistance, due to the DNA damage response and cell cycle checkpoints activation (Yoon and Seong, 2014; Wahl et al., 2016; Sun et al., 2020). Although the traditional strategies of HCC control the growth of HCC and prolong the survival time of patients, it still cannot satisfy their needs. Thus, it is necessary to discover a more efficient treatment approach to improve the quality of life for patients.

In recent years, nano-catalytic therapy, as a new tumor treatment strategy, has attracted the attention of an increasing number of researchers. Nanozymes are nanomaterials that catalyze chemical reactions of substrates under physiological states, obeying the patterns of enzyme kinetics (Wei et al., 2021). In 2007, Yan's team was the first to report that magnetic nanoparticles $Fe_3O_4$ possessed peroxidase (POD)-like activity, and proposed the concept of nano-catalysis (Gao et al., 2007). Furthermore, Shi *et al.* innovatively paved the way for further applications of nanoparticles in tumor nano-catalytic therapy, by disrupting the Fenton reaction that induced $H_2O_2$ disproportionation for •OH generation (Zhang et al., 2016). Currently, nano-catalytic therapy and photothermal therapy (PTT) are frequently employed in the treatment of tumors. The integration of PTT and nano-catalytic therapy has contributed to improving their cancer therapy efficiency. For instance, hyperthermia promoted the enzymatic activity of $Fe_3O_4$ nanozyme to generate more •OH, and simultaneously, •OH heightened the therapeutic impact of PTT (Wu et al., 2019; Zuo et al., 2022). It has also been reported that the $Fe_3O_4$@ZIF-8/GOx@$MnO_2$ hybrid nanozyme can enhance the efficiency of nanoparticles in anti-tumor therapy by combining multiple therapeutics (Zhang et al., 2021b).

$Fe_3O_4$ and Au nanoparticles, as is well known, demonstrated the unique characteristics of a high photothermal effect and POD-like activity (Zeng et al., 2013; Vallabani et al., 2017; Ghosh et al., 2022; Huang et al., 2022). Encouraged by the aforementioned description, we wonder if AuNC@$Fe_3O_4$ which has been employed as magnetic resonance imaging/com-puterized tomography multimodal imaging contrast agents of cancer owing to their high relaxivity value and excellent contrast enhancement (Wang et al., 2016b), also retains the photothermal and catalytic ability, or is beneficial to cancer therapy.

In this study, we synthesized multifunctional magneto-gold nanozyme AuNC@$Fe_3O_4$ and evaluated their anti-cancer ability in HCC cells *in vitro*. The AuNC@$Fe_3O_4$ exhibited high photothermal effect and POD-like activity. The results also reflected the influence of AuNC@$Fe_3O_4$ on engendering cell death and apoptosis. Furthermore, the synergistic effect of PTT and nano-catalytic therapy on reactive oxygen species (ROS) and lysosomal impairment in HepG2 cells were also studied.

# 2 Materials and methods

## 2.1 Materials and reagents

Ferric slat, gold (III) chloride (HAuCl4), other reagents related to AuNC@$Fe_3O_4$ synthesis and 3,3′,5,5′-Tetramethylbenzidine (TMB) were purchased from Sigma, Inc. (St. Louis, United States). $H_2O_2$ solution and different pH buffer solutions (pH = 2, 3, 4, 5, 6, 7, 8, and 9) were bought from Aladdin (Shanghai, China). Human umbilical vein endothelial cells (HUVEC), human HCC cell lines (HepG2 cells) and the specific culture mediums for the two cell lines were purchased from Procell (Wuhan, China). Cell Counting Kit-8 (CCK-8) was obtained from Sangon Biotech (Shanghai, China). 2′,7′-Dichlorodihydrofluorescein diacetate (DCFH-DA) was obtained from MedChemExpress (New Jersey, United States). Calcein-AM/propidium iodide (PI) kit, Annexin V-FITC apoptosis detection kit, Lyso-Tracker Red kit and Hoechst 33342 staining solution were purchased from Beyotime. Inc. (Shanghai, China).

## 2.2 AuNC@$Fe_3O_4$ synthesis

The AuNC@$Fe_3O_4$ was synthesized according to previous methods (Wang et al., 2016b). AuNC was initially synthesized and coated with poly (vinyl pyrrolidone) (PVP). Subsequently, PVP was replaced with 2-aminoethanethiol, and AuNC was transformed into AuNC-NH2 for interacting with carboxyl group functionalized $Fe_3O_4$ nanoparticles. The ultra-small $Fe_3O_4$ particles were prepared. To produce $Fe_3O_4$-COOH, ferric slats were vigorously stirred in pre-prepared polymer poly (acrylic acid) (PAA) solution. N-(3-Dimethylaminopropyl)-N-ethylcarbodiimide and N-hydroxysuccinimide activated the $Fe_3O_4$-COOH, which then reacted with AuNC-$NH_2$ to generate AuNC@$Fe_3O_4$. The AuNC@$Fe_3O_4$ was centrifugated, washed with ethanol and water, and then dispersed in dd$H_2O$ with different concentrations for further experiments.

## 2.3 AuNC@$Fe_3O_4$ characterization

The size of AuNC or AuNC@$Fe_3O_4$ nanoparticles was analyzed using a transmission electron microscope (TEM). Dynamic light scattering (DLS) was applied to detect hydrodynamic particle diameter and intensity of AuNC@$Fe_3O_4$ nanoparticles on a Malvern Zetasizer NANO ZS. Energy-dispersive X-ray (EDX) was utilized to analysis the element of AuNC@$Fe_3O_4$ nanoparticles on a FEI TECNAI G20 high-resolution TEM.

## 2.4 AuNC@$Fe_3O_4$ photothermal performance *in vitro*

To investigate the photothermal effect of the magneto-gold nanoparticles, First, 200 µl of AuNC@$Fe_3O_4$ solution with distinct concentrations (0, 50, 100, 200, 300, 400, and 500 µg/ml) was exposed to 808 nm laser at 1.0 W for 720 s; Second, 200 µl of AuNC@$Fe_3O_4$ solution with concentration of 50 µg/ml was exposed to 808 nm laser at different powers (1.0, 1.2, and 1.4 W) for 720 s. The thermal image and temperature change were recorded at different times by an infrared (IR) thermal camera (Fotric 220). As a control, dd$H_2O$ was irradiated under the same conditions.

To investigate the photothermal stability of the magneto-gold nanoparticles, AuNC@$Fe_3O_4$ aqueous solution (500 µg/ml) was irradiated under 808 nm laser at 1.0 W for 420 s, then the irradiation was turned off. After that, the temperature was further measured for another 360 s. The experiment was then repeated four more times. The thermal image and temperature change were recorded at different times by the IR thermal camera (Fotric 220). As a control, dd$H_2O$ was irradiated under the same operation.

To evaluate the photothermal conversion efficiency of AuNC@$Fe_3O_4$, the data from the cooling periods were calculated, according to previous report (Ren et al., 2015). Briefly, when the system reached energy balance, the equation was:

$$\sum_i m_i C_{p,i} \frac{dT}{dt} = Q_{AuNC@Fe_3O_4} + Q_s - Q_{loss} \tag{1}$$

where $Cp$ and m were the heat capacity and mass of AuNC@$Fe_3O_4$ solution, respectively. $T$ was the temperature of AuNC@$Fe_3O_4$ solution. $Q_{AuNC@Fe_3O_4}$ represented energy absorbed by AuNC@$Fe_3O_4$ nanoparticles. $Q_s$ represented the energy absorbed by dd$H_2O$. $Q_{loss}$ was the heat lost to the surroundings.

The equation for $Q_{AuNC@Fe_3O_4}$ was:

$$Q_{AuNC@Fe_3O_4} = I\left(1 - 10^{-A_\lambda}\right)\eta \tag{2}$$

where $I$ represented the laser power density, $A_\lambda$ denoted the absorbance of AuNC@$Fe_3O_4$ solution under 808 nm in a 96-well plate, and η represented its photothermal conversion efficiency.

The equation for $Q_{loss}$ was

$$Q_{loss} = hA\Delta T \tag{3}$$

where $A$ was the surface area of the container, $h$ denoted the heat transfer coefficient; $\Delta T$ represented the temperature changes, expressed as T-$T_{surr}$ (where T and $T_{surr}$ represent the solution and surrounding air temperature, respectively).

When heating dd$H_2O$, the heat input and output reached energy balance at the maximum steady-state temperature, therefore the equation for $Q_s$ was:

$$Q_s = Q_{loss} = hA\Delta T_{max,H_2O} \tag{4}$$

where $\Delta T_{max,H_2O}$ was the temperature changes of dd$H_2O$.

When the system reached its maximum balanced temperature, the energy input (the heat absorbed by AuNC@$Fe_3O_4$ and dd$H_2O$) was equal to the heat lost into the surrounding, and the equation could be:

$$Q_{AuNC@Fe_3O_4} + Q_s = Q_{loss} = hA\Delta T_{max,mix} \tag{5}$$

where $\Delta T_{max,mix}$ was the changed temperature of the AuNC@$Fe_3O_4$ solution.

According to Eqs 2, 4, 5, η was:

$$\eta = \frac{hA\Delta T_{max,mix} - hA\Delta T_{max,H_2O}}{I\left(1 - 10^{-A_\lambda}\right)} = \frac{hA\left(\Delta T_{max,mix} - \Delta T_{max,H_2O}\right)}{I\left(1 - 10^{-A_\lambda}\right)} \tag{6}$$

To calculate the unknown $hA$, θ was introduced, and could be expressed as following:

$$\theta = \frac{\Delta T}{\Delta T_{max}} \tag{7}$$

Adding Eq. 7 into Eq. 1, the new equation could be:

$$\frac{d\theta}{dt} = \frac{hA}{\sum_i m_i C_{p,i}} \left( \frac{Q_{AuNC@Fe_3O_4} + Q_s}{hA\Delta T_{max}} - \theta \right) \tag{8}$$

During the cooling period, the $Q_{AuNC@Fe_3O_4} + Q_s = 0$ in Eq. 8 was:

$$dt = -\frac{\sum_i m_i C_{p,i}}{hA} \frac{d\theta}{\theta} \tag{9}$$

which could be changed as following:

$$t = -\frac{\sum_i m_i C_{p,i}}{hA} \ln\theta \tag{10}$$

where $\frac{\sum_i m_i C_{p,i}}{hA}$ was calculated by time versus -ln(θ) plot. Since the mass of AuNC@$Fe_3O_4$ ($1 \times 10^{-7}$ kg) was relatively small when compared to that of dd$H_2O$ ($m = 2 \times 10^{-4}$ kg), its m and Cp were neglected. The value of $hA$ was then calculated using $m_{H_2O}$ of $2 \times 10^{-3}$ kg; $C_{p,H_2O}$ of $4.2 \times 10^3$ J/(Kg·°C). Furthermore, the η of AuNC@$Fe_3O_4$ was determined by substituting the value of $hA$ and other parameters into Eq. 6. The values of other parameters were as follows: $I = 2.3$ W/cm$^2$, $A_\lambda = 0.105$, $\Delta T_{max,mix} = 25.3$, and $\Delta T_{max,H_2O} = 0.1$.

## 2.5 POD-like activity assay

To evaluate the catalytic properties of AuNC@$Fe_3O_4$, AuNC@$Fe_3O_4$ (final concentration: 0, 5, 10, 20, 50, and 100 µg/ml), TMB (final concentration: 0.4 mM), and $H_2O_2$ (final concentration: 50 µM) was added into a final volume of 500 µl of phosphate-buffered saline (PBS) solution. The absorbance of the buffer was measured using an ultraviolet-visible (UV-vis) spectrophotometer at 500–800 nm. The POD-like activity assay of AuNC@$Fe_3O_4$ at varying pH levels (pH = 2, 3, 4, 5, 6, 7, 8, and 9) was performed in the presence of $H_2O_2$ and TMB in PBS solution, and the absorbance at 652 nm was detected by a microplate reader.

## 2.6 POD-like catalytic kinetic determination

When TMB was used as a substrate, the AuNC@$Fe_3O_4$ (final concentration: 50 µg/mL), TMB (final concentration: 0.0, 0.2, 0.4, 0.6, and 0.8 mM), and $H_2O_2$ (final concentration: 50 µM) was added into a final volume of 100 µl of PBS solution. The absorbance at 652 nm was detected by a microplate reader.

When $H_2O_2$ was used as a substrate, the AuNC@$Fe_3O_4$ (final concentration: 50 μg/ml), $H_2O_2$ (final concentration: 0, 10, 20, 30, 40, 50, 60, 70, and 80 μM) and TMB (final concentration: 0.4 mM) was added into a final volume of 100 μl of PBS solution. The absorbance at 652 nm was detected by a microplate reader.

Based on Michaelis-Menten Eq. 11 and saturation curve, the $V_{max}$ and Michaelis-Menten constant could be calculated,

$$\frac{1}{V} = \frac{K_m}{V_{max}} \frac{1}{[s]} + \frac{1}{V_{max}} \tag{11}$$

and the $V$ was calculated using Eq. 12:

$$V = \frac{A}{(b \times \varepsilon_{652\,nm} \times t)} \tag{12}$$

where $A$ was the absorbance of the reaction system at 652 nm. t = 600 s, which was the reaction time. b = 0.3125 cm, which was the light path in the reaction solution, and $\varepsilon_{652\,nm} = 39{,}000\ M^{-1}\ cm^{-1}$ (Dashtestani et al., 2019).

## 2.7 Cell viability assay

The HepG2 and the HUVEC cells were cultured to assess the cytotoxicity of AuNC@$Fe_3O_4$ through CCK-8 assay. 4000 of cells were cultured at 96-well plate well overnight at 37°C in a humidified incubator with 5% $CO_2$. Subsequently, 100 μl of fresh medium with distinct concentrations of AuNC@$Fe_3O_4$ (0, 10, 20, 30, 40, and 50 μg/ml) was changed and cultured for 24 h. The CCK-8 solution (final volume: 10 μl) was added into 100 μl of medium, and incubated for 2 h. Then, the absorbance of medium was detected at 450 nm.

## 2.8 Live/dead cell staining assay

HepG2 cells were cultured overnight in a 12-well plate with 500 μl of culture medium. The cells were then treated with PBS or AuNC@$Fe_3O_4$ (50 μg/ml) for 12 h. Then, the cells were cultured for an additional 12 h after either being irradiated by an 808 nm laser for 5 min at 1.4 W or not. The culture medium was then removed, and cells were washed once with PBS and incubated with 500 μl stain solution for 15 min. Finally, the cells were washed thrice with PBS and photographed by an inverted fluorescence microscope.

## 2.9 Apoptosis analysis

To investigate the ability of AuNC@$Fe_3O_4$ for inducing cell apoptosis, HepG2 cells were quantitatively detected by a flow cytometer. The cells were initially seeded into a 6-well plate and treated under different conditions for 24 h. They were collected with 0.25% trypsin and washed thrice with ice-cold PBS. Subsequently, these cells were resuspended in 195 μl of binding buffer. Ten microliters of PI and 5 μl of Annexin V-FITC were added, and the mixture was incubated for 20 min at room temperature, and cells were detected by flow cytometer.

## 2.10 Intracellular ROS detection

The intracellular POD-like catalytic ability of AuNC@$Fe_3O_4$ was detected using DCFH-DA. Except for an additional 4 h of culture, the method used for the laser-irradiated groups was similar to the treatment described above. Furthermore, 1 ml of PBS with DCFH-DA (5 μM) was added, and the mixture was incubated for another 30 min at 37°C in a humidified incubator with 5% $CO_2$. The wells were then washed thrice with PBS to remove the excess dye and photographed by an inverted fluorescence microscope.

## 2.11 Lysosomal impairment assay

After treatment, lysosomes and cell nuclei were stained with Lyso-Tracker Red and Hoechst 33342, respectively, according to the manufacturer's instructions. Subsequently, an inverted fluorescence microscope was used to capture images of cells.

## 2.12 Statistical analysis

Statistical analysis was achieved by GraphPad Prism version 8 (GraphPad Software, United States). Results were represented as mean ± standard deviation. The student t-test was used to compare the means of multiple groups. The statistical significances were as follows: * $0.01 < p < 0.05$, ** $0.001 < p < 0.01$, and ***$p < 0.001$.

# 3 Results and discussion

## 3.1 Synthesis and characterization of AuNC@$Fe_3O_4$

The structure and characteristics of AuNC and AuNC@$Fe_3O_4$ were determined by TEM. The results demonstrated that the diameter of AuNC and AuNC@$Fe_3O_4$ were 25–40 and 50–100 nm, respectively, with high uniformity and no agglomeration (Figures 1A, B). DLS was used to confirm the size of AuNC@$Fe_3O_4$, and the average hydrodynamic size distribution of these nanoparticles was approximately 55 nm (Figure 1C). The increase in the hydrodynamic size might be owing to the attachment of $Fe_3O_4$ to the surface of the AuNC. Elemental mapping analysis revealed the presence of the atoms Au, Fe and O, proving that AuNC@$Fe_3O_4$ was successfully formed (Figure 1D; Table 1). The "-CO-NH-", that came from the reaction of $Fe_3O_4$-COOH and AuNC-$NH_2$ and the carbon-coated brace used during sample preparation or analysis might have contributed to the existence of C element that was also present (Phongtongpasuk et al., 2016).

## 3.2 Photothermal performance of AuNC@$Fe_3O_4$

The thermal camera was used to investigate the photothermal conversion capabilities of AuNC@$Fe_3O_4$. The temperature changes of AuNC@$Fe_3O_4$ solution with different concentrations under

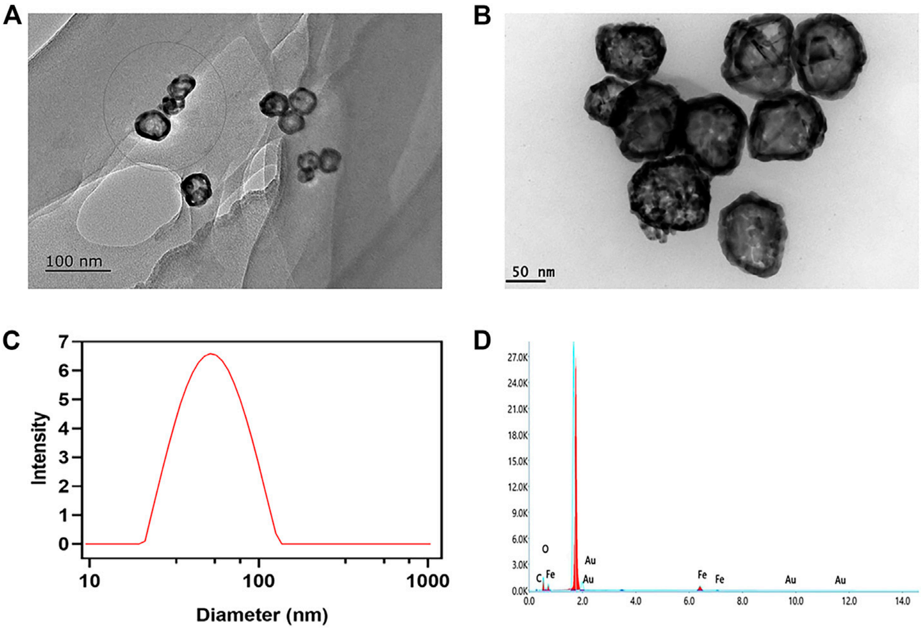

FIGURE 1
Characterization of AuNC@$Fe_3O_4$. **(A)** Transmission electron microscope (TEM) images of AuNC. Scale bar: 100 nm. **(B)** TEM images of AuNC@$Fe_3O_4$. Scale bar: 50 nm. **(C)** Dynamic light scattering (DLS) result of AuNC@$Fe_3O_4$. **(D)** Energy-dispersive X-ray (EDX) result of AuNC@$Fe_3O_4$.

**TABLE 1 The statistics of elements analysis for AuNC@$Fe_3O_4$ by energy-dispersive X-ray (EDX).**

| Compound | Element | Weight (%) |
|---|---|---|
| AuNC@$Fe_3O_4$ | Au | 23.1 |
| | Fe | 29.4 |
| | O | 42.4 |
| | C | 5.1 |

808 nm laser irradiation at 1.0 W for 360 s were recorded. As depicted in Figure 2A, the temperature of the solution increased in a concentration- and time-dependent pattern. For example, the temperature of different concentrations of AuNC@$Fe_3O_4$ solution reached steady statue at 8 min. The temperature of AuNC@$Fe_3O_4$ solution (500 μg/ml) was changed significantly from 25.9°C to 52.3°C compared with the neglected increase in that of dd$H_2O$ (from 26.0°C to 26.5°C), indicating the good photothermal response of AuNC@$Fe_3O_4$. For further investigation, the AuNC@$Fe_3O_4$ solution (50 μg/ml) was irradiation at different powers (1.0, 1.2, and 1.4 W). The laser power was increased from 1.0 to 1.4 W, which resulted in a significant increase in the temperature of the AuNC@$Fe_3O_4$ solution. A temperature of 45.3°C was achieved after 10 min of 808 nm laser irradiation at 1.4 W (Figure 2B). PTT, a promising cancer treatment strategy, converts light energy into heat to generate an area of hyperthermia, where tissues can be exposed to high temperatures (from 42°C to 45°C), which can damage or kill tumor cells (Tchouagué et al., 2019; Qu et al., 2022). The results of Figures 2A, B suggested a potential application of AuNC@$Fe_3O_4$ in anti-tumor.

Additionally, five cycles of the "On and Off" model were used to measure the temperature curve of the AuNC@$Fe_3O_4$ solution to assess its photothermal stability. The AuNC@$Fe_3O_4$ showed excellent photothermal stability since the temperature was raised to 52.9 °C and there was no reduction in the temperature rise following laser irradiation during the five cycles (Figure 2D).

Moreover, the average of the data from the five cooling periods was used to get the photothermal conversion efficiency (η) of AuNC@$Fe_3O_4$. The plot of the time value and −ln (θ) was displayed in Figure 2E, and its slope was 99.526. Using Eqs 6, 10, the η of AuNC@$Fe_3O_4$ was calculated to be 39.58%, which was similar with or higher than the PPT reagents previously reported, such as, EA-Fe@BSA NPs (31.2%) (Tian et al., 2020), $Fe_3O_4$@Carbon@Platinum-Chlorin e6 (28.28%) (Xu et al., 2022b), Au nanorods (22%) (Zeng et al., 2013), Au nanoshells (13%) (Hessel et al., 2011), PANi@Au (40.4%) and Au nanoparticles (21.7%) (Zhang et al., 2021a).

Collectively, these findings suggested that AuNC@$Fe_3O_4$ exhibited good photothermal conversion and photothermal stability, which implied a promising application in PTT for tumors.

## 3.3 POD-like activity of AuNC@$Fe_3O_4$

It was reported that Au and $Fe_3O_4$ nanoparticles demonstrated POD-like enzyme activity (Zandieh and Liu, 2021), therefore it was necessary to investigate whether the AuNC@$Fe_3O_4$ possessed similar characteristics. The peroxidase mimicking activity of AuNC@$Fe_3O_4$ was validated by TMB. TMB could be oxidized to blue oxTMB by •OH and detected at 652 nm, using UV-vis spectrophotometer (Zhu et al., 2022). As presented in Figure 3A,

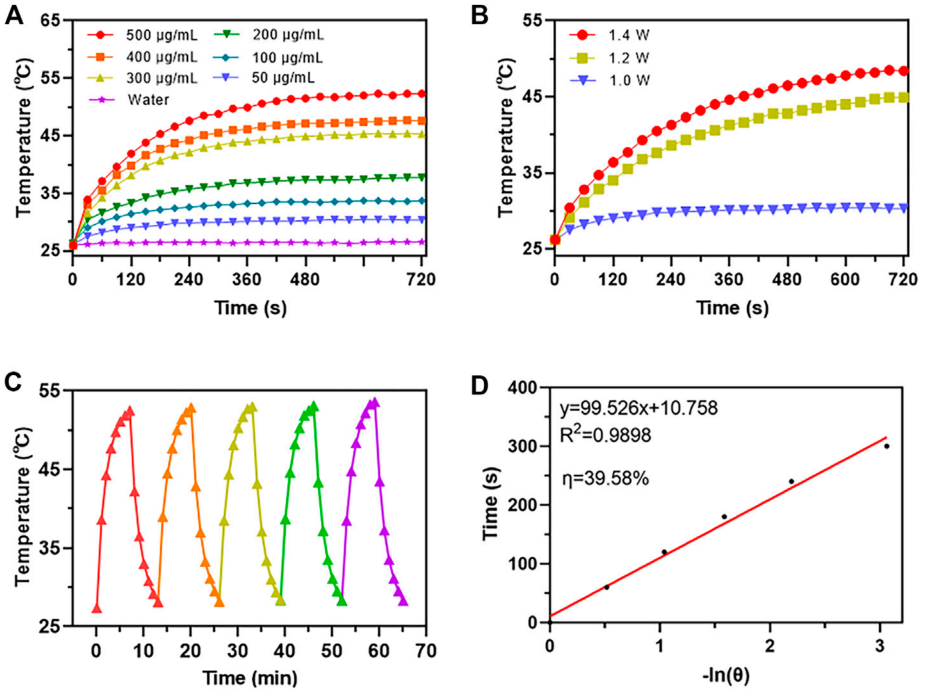

FIGURE 2
Photothermal performance analysis of AuNC@$Fe_3O_4$. **(A)** Temperature change curves of water and AuNC@$Fe_3O_4$ aqueous solution after different treatments **(B)** Temperature change curves of AuNC@$Fe_3O_4$ after different treatments **(C)** Photostability of AuNC@$Fe_3O_4$ solution under irradiation for five cycles. **(D)** Time versus -ln(θ) plot of the AuNC@$Fe_3O_4$ solution.

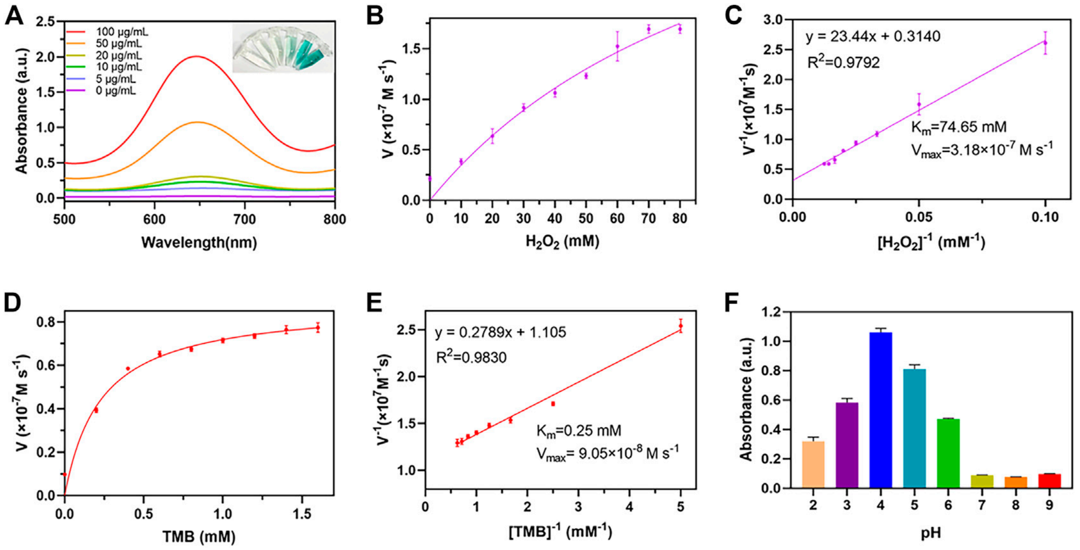

FIGURE 3
POD-like activity assay of AuNC@$Fe_3O_4$. **(A)** Ultraviolet-visible (UV-vis) absorption spectra of the reaction system with different concentrations. **(B)** Michaelis-Menten curve of AuNC@$Fe_3O_4$ for $H_2O_2$. **(C)** Lineweaver-Burk plotting of AuNC@$Fe_3O_4$ for $H_2O_2$. **(D)** Michaelis-Menten curve of AuNC@$Fe_3O_4$ for TMB. **(E)** Lineweaver-Burk plotting of AuNC@$Fe_3O_4$ for TMB. **(F)** The absorbance of the reaction system at 652 nm under different pH values.

the groups with different concentrations of AuNC@$Fe_3O_4$ had varying absorbance intensities at 652 nm. The group of AuNC@$Fe_3O_4$ with 100 μg/ml showed the strongest signal at 652 nm, followed by the group with 50 μg/ml. The intensity of absorbance tested with $H_2O$ displayed no peak at 652 nm. These findings, which indicated that the AuNC@$Fe_3O_4$ possessed POD-like enzyme activity, were further verified by the inset digital photos (Figure 3A). To further confirm the POD-like enzyme specificity of AuNC@$Fe_3O_4$, the UV-vis absorption spectra of the reaction system with varying conditions was collected. It was observed from Supplementary Figure S1 that absorbance peak of the AuNC@$Fe_3O_4$+TMB or AuNC@$Fe_3O_4$+$H_2O_2$ group was negligible. In the absence of AuNC@$Fe_3O_4$, the TMB + $H_2O_2$, TMB or $H_2O_2$ group showed no significant absorbance peak at 652 nm, which was consistent with the AuNC@$Fe_3O_4$ only group. The results suggested that, except AuNC@$Fe_3O_4$, other components in the reaction system could hardly catalyzed the conversion of $H_2O_2$ to •OH and oxidized TMB, which indicated AuNC@$Fe_3O_4$ exhibited a specific activity of POD-like enzyme.

Kinetic parameters were analyzed to quantitate the POD-like activity of AuNC@$Fe_3O_4$ using the initial rate method (Gao et al., 2017). First, the absorbance of the system was measured, while varying the concentrations of $H_2O_2$ concentrations from 0 to 80 mM and maintaining a TMB concentration of 0.4 mM (Supplementary Figure S2). Second, the velocity of reaction was calculated according Eq. 12 and the plot was consistent with traditional Michaelis-Menten curve (Figure 3B), which demonstrates that the catalytic reaction rate increased with the growth of substrate concentration and achieved steady state at high concentrations (Huang et al., 2022). Third, after Lineweaver-Burk fitting, the enzyme kinetic parameters, such as Michaelis-Menten constants ($K_m$) was calculated to be 47.65 mM and the maximum reaction velocity ($V_{max}$) was $3.18 \times 10^{-7}$ M $s^{-1}$ (Figure 3C). Forth, the absorbance of the solution was measured at 652 nm while varying TMB concentrations and maintaining $H_2O_2$ concentration as a constant (Supplementary Figure S3). Last, the $K_m$ and $V_{max}$ were 0.25 mM and $9.03 \times 10^{-8}$ M $s^{-1}$ respectively, and the results were presented in Figures 3D, E.

When the $H_2O_2$ was used as substrate, the velocity of AuNC@$Fe_3O_4$ was faster than that of $Fe_3O_4$ (Vallabani et al., 2017), and $K_m$ value that was lower than that of $Fe_3O_4$ (Vallabani et al., 2017). Similarly, when the TMB was used as substrate, AuNC@$Fe_3O_4$ had a velocity that was faster than that of Au NRT, Au NC, Au NS, and horseradish peroxidase (Ghosh et al., 2022), and its value of $K_m$ was also lower than those of them. In the catalytic reaction system, the $K_m$ represents the affinity between the enzyme and substrates, and the lower the $K_m$, the higher enzyme affinity (Jiang et al., 2018). Therefore, the results suggested that the catalytic ability and the affinity between AuNC@$Fe_3O_4$ nanozyme and substrates (such as TMB and $H_2O_2$) was stronger than that of $Fe_3O_4$ and Au nanoparticles. The following factors may contribute to the significant increase in POD-like activity of AuNC@$Fe_3O_4$ nanoparticles: the electronic structure of the interfaces between the $Fe_3O_4$ and Au, the synergistic effect, and polarization effects from Au to $Fe_3O_4$ (Lee et al., 2010; Sun et al., 2013; Wang et al., 2016a).

Considering the complex tumor microenvironment, such as hypoxia and weak acidity (Li et al., 2020; Zhao et al., 2021), it was unclear whether AuNC@$Fe_3O_4$ exhibits POD-like enzyme activity even at low pH. At low pH values ranging from 2 to 6, the AuNC@$Fe_3O_4$ exhibited higher POD-like enzyme activity, and the optional pH was 4. When the pH was higher than 7, the POD-like enzyme activity was reduced dramatically (Figure 3F). The results hinted that AuNC@$Fe_3O_4$ might have significantly varied POD-like enzyme activity between distinct parts of normal (pH = 7.4) and cancer tissues (pH = 6.5), especially for lysosomes (pH = 4.5–5.5) and endosomes (pH = 5.5–6.8) (Kuppusamy et al., 2002; Wojtkowiak et al., 2011).

Overall, these findings provided evidence for the high POD-like catalytic activity of AuNC@$Fe_3O_4$ nanozyme and implied potential catalytic ability in tumor.

## 3.4 *In vitro* anti-tumor effect of AuNC@$Fe_3O_4$

It is important to examine the biocompatibility of AuNC@$Fe_3O_4$ before performing further clinical applications. Therefore, HepG2 and HUVEC cells were incubated with AuNC@$Fe_3O_4$ at varying concentrations for 24 h to estimate the cytotoxicity using CCK-8 assay. Low concentrations of AuNC@$Fe_3O_4$ did not affect the survival rate of HepG2 cells; however, at 40 and 50 μg/ml, the viability of cells decreased to 77% and 60%, respectively (Figure 4A). In contrast, the viability of HUVEC cells was not drastically affected by AuNC@$Fe_3O_4$ after 24 h incubation at the varying treatments (Figure 4B). The findings indicated that AuNC@$Fe_3O_4$ was not toxic to normal cells at the concentration ranging from 0 μg/ml to 50 μg/ml and demonstrated good biocompatibility. The reason why AuNC@$Fe_3O_4$ showed more sensitive to HepG2 could be attributed to the fact that the pH of the tumor was lower than that of normal tissues (Kuppusamy et al., 2002; Wojtkowiak et al., 2011) and that the AuNC@$Fe_3O_4$ had higher POD-like enzyme activity in a lower pH reaction system, which meant it produced more •OH, which could be lethal to cells (Cui et al., 2018; Malfanti et al., 2022).

To explore the anti-tumor effect of AuNC@$Fe_3O_4$, the live/dead cell staining assay was utilized. There were nearly no dead cells in the PBS and PBS + NIR (near-infrared) groups; However, when the cells were treated with AuNC@$Fe_3O_4$ or AuNC@$Fe_3O_4$+NIR, the number of dead cells increased significantly, with the last group having the most cell death (Figure 4C). To further verify this result, the flow apoptosis assays of HepG2 cells with different conditions was conducted. As depicted in Figures 4D, E; Supplementary Table S1, the results indicated that approximately 51% apoptotic cells (Q2+Q3) were observed in the AuNC@$Fe_3O_4$+NIR group, which was greater than other groups.

The results revealed that AuNC@$Fe_3O_4$ displayed good biocompatibility, and the laser irradiation augmented the anti-tumor ability of AuNC@$Fe_3O_4$.

## 3.5 ROS and lysosomal impairment induced by AuNC@$Fe_3O_4$

To confirm the synergistic effect of PTT and POD-like enzyme catalytic activity of AuNC@$Fe_3O_4$, the production of the ROS in HepG2 cells was validated using the DCFH-DA probe. As reported, DCFH-DA crossed the cell membrane and was subsequently oxidized to DCF with green fluorescence (Afri et al., 2004). It was evident from Figure 5A that the HepG2 cells incubated with AuNC@$Fe_3O_4$ exhibited a higher green fluorescence signal than PBS and PBS + NIR, indicating the ability of AuNC@$Fe_3O_4$ to effectively

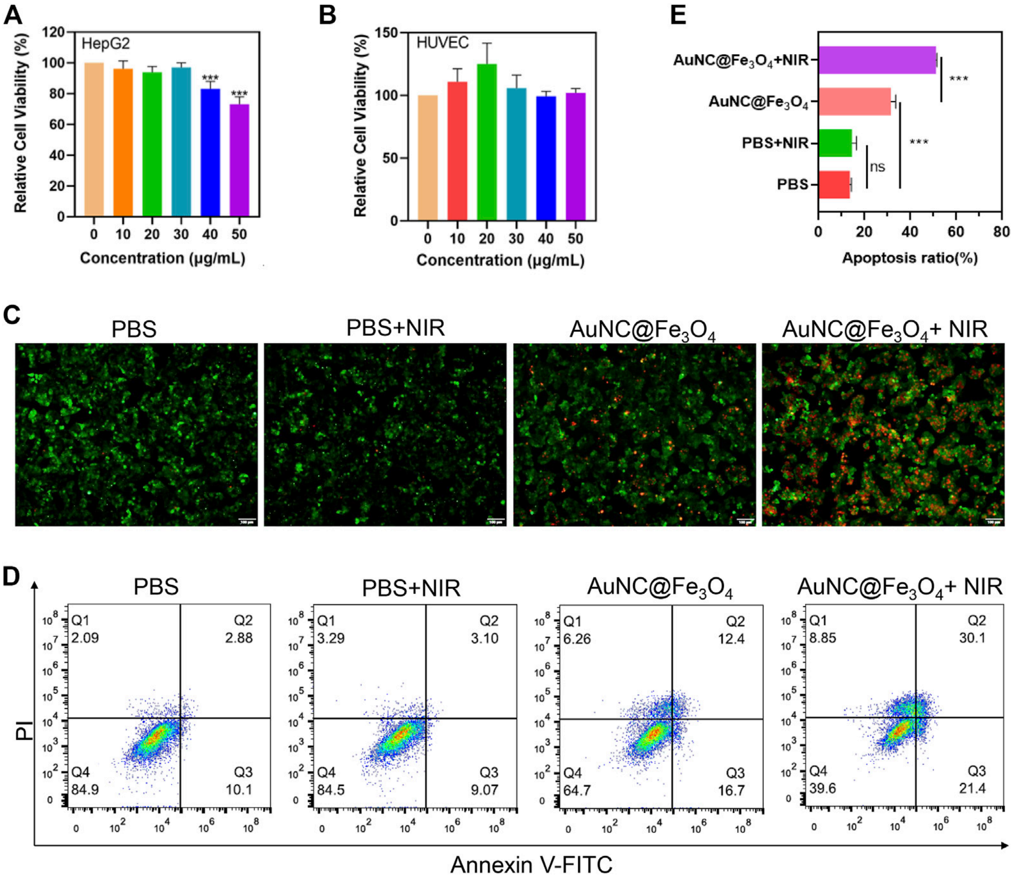

FIGURE 4
Evaluation for anti-tumor effect of AuNC@$Fe_3O_4$ *in vitro*. **(A)** Cell viability of HepG2 cells treated with AuNC@$Fe_3O_4$ for 24 h. **(B)** Cell viability of human umbilical vein endothelial cells (HUVEC) cells treated with AuNC@$Fe_3O_4$ for 24 h. **(C)** Calcein-Am/propidium iodide (PI) staining of HepG2 cells under different conditions. Scale bar: 100 μm. **(D)** Apoptosis analysis of HepG2 cells with different treatments. **(E)** The histogram results of apoptotic HepG2 cells derived from **(D)**. * $0.01 < p < 0.05$, ** $0.001 < p < 0.01$, and ***$p < 0.001$.

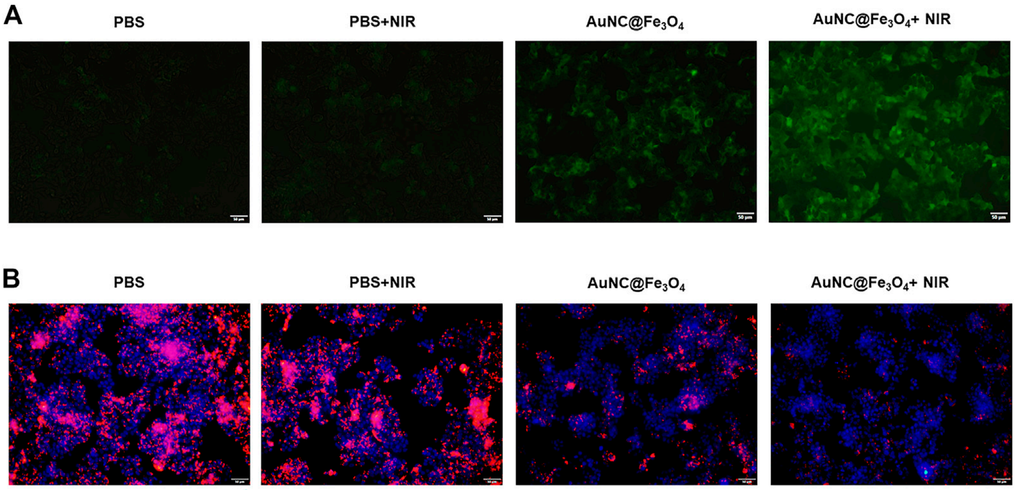

FIGURE 5
Analysis for synergistic effect of photothermal therapy (PTT) and catalytic activity of AuNC@$Fe_3O_4$. **(A)** Reactive oxygen species (ROS) detection of HepG2 cells with varying treatments. **(B)** Lysosomal impairment detection of HepG2 cells with varying treatments. Scale bar: 50 μm.

catalyze the conversion of intracellular $H_2O_2$ into •OH in cancer cells. Compared with the AuNC@$Fe_3O_4$ group, the signal of the AuNC@$Fe_3O_4$+NIR group was stronger. The similar result was collected by the detection of the absorbance intensities at 652 nm of the reaction system with or without NIR irradiation, using UV-vis spectrophotometer. We found the signal of reaction system with NIR irradiation was higher than that of group without irradiation (Supplementary Figure S4). The results confirmed that photothermal effect enhanced the POD-like enzyme catalytic activity of AuNC@$Fe_3O_4$.

The phenomenon could be attributed to the localized surface plasmon resonance (LSPR), which was the collective oscillation of surface free electrons in metal nanoparticles under light irradiation, leading to local heating (also called photothermal effect) and hot carriers (such as hot electrons and hot holes). One hand, energy of hot electrons may transfer to local heating by electron-phonon interactions, causing a rise in temperature (Brongersma et al., 2015). Similar with natural enzymes, the catalytic ability of nanozymes could be enhanced by elevated temperature (Wang et al., 2021; Zhu et al., 2022). Another hand, hot electrons could be transferred from AuNPs to empty orbits of $H_2O_2$, and activated the $H_2O_2$ to generate •OH under NIR light irradiation (Wang et al., 2017; Xu et al., 2022a).

It was reported that increased ROS could disrupt normal structure of the lysosomes (Shyam et al., 2021); however, whether the AuNC@$Fe_3O_4$ could induce lysosomal impairment remained unknown. The fluorescence images (Figure 5B) demonstrate that the PBS alone and PBS + NIR groups had negligible effects on the lysosomal impairment and that there were more HepG2 cells with lysosomal impairment following incubation with AuNC@$Fe_3O_4$. As expected, the lysosomal signal was the weakest in the AuNC@$Fe_3O_4$ under laser irradiation group. The results confirmed the synergistic effect of PTT and POD-like enzyme catalytic activity of AuNC@$Fe_3O_4$ on lysosomal impairment. Additionally, lysosomal impairment may contribute to an increase in lysosomal membrane permeability, a decrease in lysosomal quantity, a disruption in lysosomal enzyme activities, an increase in ROS levels, and most importantly, the induction of cell apoptosis (Abulikemu et al., 2022).

This at least partly, explained why AuNC@$Fe_3O_4$ with or without laser irradiation could cause cell death or apoptosis.

## 4 Conclusion

In summary, this study aimed to synthesize magneto-gold nanozyme AuNC@$Fe_3O_4$ and evaluate its anti-cancer effects for HCC *in vitro*. The AuNC@$Fe_3O_4$ showed the typical small size of about 55 nm. Additionally, it demonstrated a high photothermal conversion efficiency and POD-like activity. The CCK-8 results demonstrated that AuNC@$Fe_3O_4$ had good biocompatibility and HCC cell-killing ability. Moreover, AuNC@$Fe_3O_4$ could synergistically stimulate cell death or apoptosis. Finally, it was observed that magneto-gold nanocomposites could facilitate 808 nm laser irradiation to increase their catalytic ability to produce ROS. This might promote lysosomal impairment, causing cell death or apoptosis. These results suggested that the AuNC@$Fe_3O_4$ may offer a promising anti-cancer strategy for HCC *via* the synergistic effect of PTT and nano-catalytic therapy. Further research is required to investigate the therapeutic efficacy of AuNC@$Fe_3O_4$ for HCC *in vivo*.

## Data availability statement

The original contributions presented in the study are included in the article/Supplementary Material, further inquiries can be directed to the corresponding author.

## Author contributions

XS and GW proposed the conception and design of the study. XS and JL performed the experiments and interpretation of the data. XS and JL drafted the manuscript. GW reviewed and revised the manuscript. All authors read and approve the final manuscript.

## Funding

This research was funded by Scientific Research Foundation of Jining Medical University (No.600768001) and Research Fund for Academician Lin He New Medicine (JYHL2022MS14).

## Acknowledgments

We gratefully acknowledge support from Yangcui Qu, Haitao Han, Xueyan Wu and Huapeng Liu for technical support or donations in kind (e.g., equipments and reagents used for experiments).

## Conflict of interest

The authors declare that the research was conducted in the absence of any commercial or financial relationships that could be construed as a potential conflict of interest.

## Publisher's note

## Supplementary material

The Supplementary Material for this article can be found online at: https://www.frontiersin.org/articles/10.3389/fbioe.2023.1168750/full#supplementary-material

# References

Abulikemu, A., Zhao, X., Qi, Y., Liu, Y., Wang, J., Zhou, W., et al. (2022). Lysosomal impairment-mediated autophagy dysfunction responsible for the vascular endothelial apoptosis caused by silica nanoparticle via ROS/PARP1/AIF signaling pathway. *Environ. Pollut.* 304, 119202. doi:10.1016/j.envpol.2022.119202

Afri, M., Frimer, A. A., and Cohen, Y. (2004). Active oxygen chemistry within the liposomal bilayer. Part IV: Locating 2',7'-dichlorofluorescein (DCF), 2',7'-dichlorodihydrofluorescein (DCFH) and 2',7'-dichlorodihydrofluorescein diacetate (DCFH-DA) in the lipid bilayer. *Chem. Phys. Lipids* 131, 123–133. doi:10.1016/j.chemphyslip.2004.04.006

Anwanwan, D., Singh, S. K., Singh, S., Saikam, V., and Singh, R. (2020). Challenges in liver cancer and possible treatment approaches. *Biochim. Biophys. Acta Rev. Cancer* 1873, 188314. doi:10.1016/j.bbcan.2019.188314

Brongersma, M. L., Halas, N. J., and Nordlander, P. (2015). Plasmon-induced hot carrier science and technology. *Nat. Nanotechnol.* 10, 25–34. doi:10.1038/nnano.2014.311

Bruix, J., Raoul, J. L., Sherman, M., Mazzaferro, V., Bolondi, L., Craxi, A., et al. (2012). Efficacy and safety of sorafenib in patients with advanced hepatocellular carcinoma: Subanalyses of a phase III trial. *J. Hepatol.* 57, 821–829. doi:10.1016/j.jhep.2012.06.014

Cheng, A. L., Kang, Y. K., Chen, Z., Tsao, C. J., Qin, S., Kim, J. S., et al. (2009). Efficacy and safety of sorafenib in patients in the asia-pacific region with advanced hepatocellular carcinoma: A phase III randomised, double-blind, placebo-controlled trial. *Lancet Oncol.* 10, 25–34. doi:10.1016/s1470-2045(08)70285-7

Cui, Q., Wang, J. Q., Assaraf, Y. G., Ren, L., Gupta, P., Wei, L., et al. (2018). Modulating ROS to overcome multidrug resistance in cancer. *Drug Resist Updat* 41, 1–25. doi:10.1016/j.drup.2018.11.001

Dashtestani, F., Ghourchian, H., and Najafi, A. (2019). Silver-gold-apoferritin nanozyme for suppressing oxidative stress during cryopreservation. *Mater Sci. Eng. C Mater Biol. Appl.* 94, 831–840. doi:10.1016/j.msec.2018.10.008

Ferlay, J., Colombet, M., Soerjomataram, I., Parkin, D. M., PiñEROS, M., Znaor, A., et al. (2021). Cancer statistics for the year 2020: An overview. *Int. J. Cancer* 149, 778–789. doi:10.1002/ijc.33588

Gao, L., Zhuang, J., Nie, L., Zhang, J., Zhang, Y., Gu, N., et al. (2007). Intrinsic peroxidase-like activity of ferromagnetic nanoparticles. *Nat. Nanotechnol.* 2, 577–583. doi:10.1038/nnano.2007.260

Gao, L., Fan, K., and Yan, X. (2017). Iron oxide nanozyme: A multifunctional enzyme mimetic for biomedical applications. *Theranostics* 7, 3207–3227. doi:10.7150/thno.19738

Ghosh, S., Singh, P., Roy, S., Bhardwaj, K., and Jaiswal, A. (2022). Superior peroxidase-like activity of gold nanorattles in ultrasensitive H(2) O(2) sensing and antioxidant screening. *Chembiochem* 23, e202100691. doi:10.1002/cbic.202100691

Gil, E., Joh, J. W., Park, H. C., Yu, J. I., Jung, S. H., and Kim, J. M. (2015). Predictors and patterns of recurrence after curative liver resection in intrahepatic cholangiocarcinoma, for application of postoperative radiotherapy: A retrospective study. *World J. Surg. Oncol.* 13, 227. doi:10.1186/s12957-015-0637-z

Hessel, C. M., Pattani, V. P., Rasch, M., Panthani, M. G., Koo, B., Tunnell, J. W., et al. (2011). Copper selenide nanocrystals for photothermal therapy. *Nano Lett.* 11, 2560–2566. doi:10.1021/nl201400z

Huang, Y., Gu, Y., Liu, X., Deng, T., Dai, S., Qu, J., et al. (2022). Reusable ring-like Fe3O4/Au nanozymes with enhanced peroxidase-like activities for colorimetric-SERS dual-mode sensing of biomolecules in human blood. *Biosens. Bioelectron.* 209, 114253. doi:10.1016/j.bios.2022.114253

Jiang, B., Duan, D., Gao, L., Zhou, M., Fan, K., Tang, Y., et al. (2018). Standardized assays for determining the catalytic activity and kinetics of peroxidase-like nanozymes. *Nat. Protoc.* 13, 1506–1520. doi:10.1038/s41596-018-0001-1

Kuppusamy, P., Li, H., Ilangovan, G., Cardounel, A. J., Zweier, J. L., Yamada, K., et al. (2002). Noninvasive imaging of tumor redox status and its modification by tissue glutathione levels. *Cancer Res.* 62, 307–312.

Lee, Y., Garcia, M. A., Frey Huls, N. A., and Sun, S. (2010). Synthetic tuning of the catalytic properties of Au-Fe3O4 nanoparticles. *Angew. Chem. Int. Ed. Engl.* 49, 1271–1274. doi:10.1002/anie.200906130

Li, Y., Zhao, P., Gong, T., Wang, H., Jiang, X., Cheng, H., et al. (2020). Redox dyshomeostasis strategy for hypoxic tumor therapy based on DNAzyme-loaded electrophilic ZIFs. *Angew. Chem. Int. Ed. Engl.* 59, 22537–22543. doi:10.1002/anie.202003653

Liu, D., and Song, T. (2021). Changes in and challenges regarding the surgical treatment of hepatocellular carcinoma in China. *Biosci. Trends* 15, 142–147. doi:10.5582/bst.2021.01083

Liu, J., Zhang, S., Wang, Q., Shen, H., Zhang, M., Zhang, Y., et al. (2016). Seroepidemiology of Hepatitis B virus infection in 2 million men aged 21-49 years in rural China: A population-based, cross-sectional study. *Lancet Infect. Dis.* 16, 80–86. doi:10.1016/s1473-3099(15)00218-2

Liu, J., Liang, W., Jing, W., and Liu, M. (2019). Countdown to 2030: Eliminating Hepatitis B disease, China. *Bull. World Health Organ* 97, 230–238. doi:10.2471/blt.18.219469

Llovet, J. M., Ricci, S., Mazzaferro, V., Hilgard, P., Gane, E., Blanc, J. F., et al. (2008). Sorafenib in advanced hepatocellular carcinoma. *N. Engl. J. Med.* 359, 378–390. doi:10.1056/nejmoa0708857

Llovet, J. M., Zucman-Rossi, J., Pikarsky, E., Sangro, B., Schwartz, M., Sherman, M., et al. (2016). Hepatocellular carcinoma. *Nat. Rev. Dis. Prim.* 2, 16018. doi:10.1038/nrdp.2016.18

Malfanti, A., Catania, G., Degros, Q., Wang, M., Bausart, M., and Preat, V. (2022). Design of bio-responsive hyaluronic acid-doxorubicin conjugates for the local treatment of glioblastoma. *Pharmaceutics* 14, 124. doi:10.3390/pharmaceutics14010124

Phongtongpasuk, S., Poadang, S., and Yongvanich, N. (2016). Environmental-friendly method for synthesis of silver nanoparticles from dragon fruit peel extract and their antibacterial activities. *Energy Procedia* 89, 239–247. doi:10.1016/j.egypro.2016.05.031

Qu, Y., Lu, K., Zheng, Y., Huang, C., Wang, G., Zhang, Y., et al. (2022). Photothermal scaffolds/surfaces for regulation of cell behaviors. *Bioact. Mater* 8, 449–477. doi:10.1016/j.bioactmat.2021.05.052

Raoul, J. L., and Edeline, J. (2020). Systemic treatment of hepatocellular carcinoma: Standard of care in China and elsewhere. *Lancet Oncol.* 21, 479–481. doi:10.1016/s1470-2045(20)30082-6

Ren, W., Yan, Y., Zeng, L., Shi, Z., Gong, A., Schaaf, P., et al. (2015). A near infrared light triggered hydrogenated black TiO2 for cancer photothermal therapy. *Adv. Healthc. Mater* 4, 1526–1536. doi:10.1002/adhm.201500273

Rumgay, H., Arnold, M., Ferlay, J., Lesi, O., Cabasag, C. J., Vignat, J., et al. (2022). Global burden of primary liver cancer in 2020 and predictions to 2040. *J. Hepatol.* 77, 1598–1606. doi:10.1016/j.jhep.2022.08.021

Shyam, R., Ogando, D. G., Choi, M., Liton, P. B., and Bonanno, J. A. (2021). Mitochondrial ROS induced lysosomal dysfunction and autophagy impairment in an animal model of congenital hereditary endothelial dystrophy. *Invest. Ophthalmol. Vis. Sci.* 62, 15. doi:10.1167/iovs.62.12.15

Sun, H., Jiao, X., Han, Y., Jiang, Z., and Chen, D. (2013). Synthesis of Fe_3O_4-Au nanocomposites with enhanced peroxidase-like activity. *Eur. Chem. Soc. Publ.* 2013, 109. doi:10.1002/ejic.201201159

Sun, J., Zhu, Z., Li, W., Shen, M., Cao, C., Sun, Q., et al. (2020). UBE2T-regulated H2AX monoubiquitination induces hepatocellular carcinoma radioresistance by facilitating CHK1 activation. *J. Exp. Clin. Cancer Res.* 39, 222. doi:10.1186/s13046-020-01734-4

Sung, H., Ferlay, J., Siegel, R. L., Laversanne, M., Soerjomataram, I., Jemal, A., et al. (2021). Global cancer statistics 2020: GLOBOCAN estimates of incidence and mortality worldwide for 36 cancers in 185 countries. *CA Cancer J. Clin.* 71, 209–249. doi:10.3322/caac.21660

Tchouagué, M., Grondin, M., Glory, A., and Averill-Bates, D. (2019). Heat shock induces the cellular antioxidant defenses peroxiredoxin, glutathione and glucose 6-phosphate dehydrogenase through Nrf2. *Chem. Biol. Interact.* 310, 108717. doi:10.1016/j.cbi.2019.06.030

Tian, Q., An, L., Tian, Q., Lin, J., and Yang, S. (2020). Ellagic acid-Fe@BSA nanoparticles for endogenous H(2)S accelerated Fe(III)/Fe(II) conversion and photothermal synergistically enhanced chemodynamic therapy. *Theranostics* 10, 4101–4115. doi:10.7150/thno.41882

Vallabani, N. V. S., Karakoti, A. S., and Singh, S. (2017). ATP-mediated intrinsic peroxidase-like activity of Fe(3)O(4)-based nanozyme: One step detection of blood glucose at physiological pH. *Colloids Surf. B Biointerfaces* 153, 52–60. doi:10.1016/j.colsurfb.2017.02.004

Wahl, D. R., Stenmark, M. H., Tao, Y., Pollom, E. L., Caoili, E. M., Lawrence, T. S., et al. (2016). Outcomes after stereotactic body radiotherapy or radiofrequency ablation for hepatocellular carcinoma. *J. Clin. Oncol.* 34, 452–459. doi:10.1200/jco.2015.61.4925

Wang, C., Qian, J., Wang, K., Yang, X., Liu, Q., Hao, N., et al. (2016a). Colorimetric aptasensing of ochratoxin A using Au@Fe3O4 nanoparticles as signal indicator and magnetic separator. *Biosens. Bioelectron.* 77, 1183–1191. doi:10.1016/j.bios.2015.11.004

Wang, G., Gao, W., Zhang, X., and Mei, X. (2016b). Au nanocage functionalized with ultra-small Fe3O4 nanoparticles for targeting T1-T2Dual MRI and CT imaging of tumor. *Sci. Rep.* 6, 28258. doi:10.1038/srep28258

Wang, C., Shi, Y., Dan, Y. Y., Nie, X. G., Li, J., and Xia, X. H. (2017). Enhanced peroxidase-like performance of gold nanoparticles by hot electrons. *Chemistry* 23, 6717–6723. doi:10.1002/chem.201605380

Wang, X., Shi, Q., Zha, Z., Zhu, D., Zheng, L., Shi, L., et al. (2021). Copper single-atom catalysts with photothermal performance and enhanced nanozyme activity for bacteria-infected wound therapy. *Bioact. Mater* 6, 4389–4401. doi:10.1016/j.bioactmat.2021.04.024

Weber, S. M., Ribero, D., O'Reilly, E. M., Kokudo, N., Miyazaki, M., and Pawlik, T. M. (2015). Intrahepatic cholangiocarcinoma: Expert consensus statement. *HPB Oxf.* 17, 669–680. doi:10.1111/hpb.12441

Wei, H., Gao, L., Fan, K., Liu, J., He, J., Qu, X., et al. (2021). Nanozymes: A clear definition with fuzzy edges. *Nano Today* 40, 101269. doi:10.1016/j.nantod.2021.101269

Wojtkowiak, J. W., Verduzco, D., Schramm, K. J., and Gillies, R. J. (2011). Drug resistance and cellular adaptation to tumor acidic pH microenvironment. *Mol. Pharm.* 8, 2032–2038. doi:10.1021/mp200292c

Wu, H., Liu, L., Song, L., Ma, M., Gu, N., and Zhang, Y. (2019). Enhanced tumor synergistic therapy by injectable magnetic hydrogel mediated generation of hyperthermia and highly toxic reactive oxygen species. *ACS Nano* 13, 14013–14023. doi:10.1021/acsnano.9b06134

Xu, X. F., Xing, H., Han, J., Li, Z. L., Lau, W. Y., Zhou, Y. H., et al. (2019). Risk factors, patterns, and outcomes of late recurrence after liver resection for hepatocellular carcinoma: A multicenter study from China. *JAMA Surg.* 154, 209–217. doi:10.1001/jamasurg.2018.4334

Xu, G., Du, X., Wang, W., Qu, Y., Liu, X., Zhao, M., et al. (2022a). Plasmonic nanozymes: Leveraging localized surface plasmon resonance to boost the enzyme-mimicking activity of nanomaterials. *Small* 18, e2204131. doi:10.1002/smll.202204131

Xu, Z., Chen, J., Li, Y., Hu, T., Fan, L., XI, J., et al. (2022b). Yolk-shell Fe(3)O(4) @Carbon@Platinum-Chlorin e6 nanozyme for MRI-assisted synergistic catalytic-photodynamic-photothermal tumor therapy. *J. Colloid Interface Sci.* 628, 1033–1043. doi:10.1016/j.jcis.2022.08.006

Yang, J. D., Hainaut, P., Gores, G. J., Amadou, A., Plymoth, A., and Roberts, L. R. (2019). A global view of hepatocellular carcinoma: Trends, risk, prevention and management. *Nat. Rev. Gastroenterol. Hepatol.* 16, 589–604. doi:10.1038/s41575-019-0186-y

Yoon, H. I., and Seong, J. (2014). Multimodality treatment involving radiotherapy for advanced liver-confined hepatocellular carcinoma. *Oncology* 87 (1), 90–98. doi:10.1159/000368151

Zandieh, M., and Liu, J. (2021). Nanozyme catalytic turnover and self-limited reactions. *ACS Nano* 15, 15645–15655. doi:10.1021/acsnano.1c07520

Zeng, J., Goldfeld, D., and Xia, Y. (2013). A plasmon-assisted optofluidic (PAOF) system for measuring the photothermal conversion efficiencies of gold nanostructures and controlling an electrical switch. *Angew. Chem. Int. Ed. Engl.* 52, 4263–4267. doi:10.1002/ange.201210359

Zhang, C., Bu, W., Ni, D., Zhang, S., Li, Q., Yao, Z., et al. (2016). Synthesis of iron nanometallic glasses and their application in cancer therapy by a localized Fenton reaction. *Angew. Chem. Int. Ed. Engl.* 55, 2141–2146. doi:10.1002/ange.201510031

Zhang, B., Hu, X., Jia, Y., Li, J., and Zhao, Z. (2021a). Polyaniline@Au organic-inorganic nanohybrids with thermometer readout for photothermal immunoassay of tumor marker. *Mikrochim. Acta* 188, 63. doi:10.1007/s00604-021-04719-y

Zhang, Y., Yang, Y., Shi, J., and Wang, L. (2021b). A multimodal strategy of Fe(3)O(4) @ZIF-8/GOx@MnO(2) hybrid nanozyme via TME modulation for tumor therapy. *Nanoscale* 13, 16571–16588. doi:10.1039/d1nr04196g

Zhao, P., Jiang, Y., Tang, Z., Li, Y., Sun, B., Wu, Y., et al. (2021). Constructing electron levers in perovskite nanocrystals to regulate the local electron density for intensive chemodynamic therapy. *Angew. Chem. Int. Ed. Engl.* 60, 8987–8994. doi:10.1002/ange.202100864

Zhu, Z. X., Huang, J. W., Liao, M. H., and Zeng, Y. (2016). Treatment strategy for hepatocellular carcinoma in China: Radiofrequency ablation versus liver resection. *Jpn. J. Clin. Oncol.* 46, 1075–1080. doi:10.1093/jjco/hyw134

Zhu, Y., Wang, Z., Zhao, R., Zhou, Y., Feng, L., Gai, S., et al. (2022). Pt decorated $Ti_3C_2T_x$ MXene with NIR-II light amplified nanozyme catalytic activity for efficient phototheranostics. *ACS Nano* 16, 3105–3118. doi:10.1021/acsnano.1c10732

Zuo, W., Fan, Z., Chen, L., Liu, J., Wan, Z., Xiao, Z., et al. (2022). Copper-based theranostic nanocatalysts for synergetic photothermal-chemodynamic therapy. *Acta Biomater.* 147, 258–269. doi:10.1016/j.actbio.2022.05.030

Frontiers in Bioengineering and Biotechnology

TYPE Original Research
PUBLISHED 30 March 2023
DOI 10.3389/fbioe.2023.1171360

# Fullerenol inhibits tendinopathy by alleviating inflammation

Xin Jiao[1,2†], Zengguang Wang[1,2†], Yiming Li[1,2], Tianchang Wang[1,2], Chen Xu[1,2], Xianhao Zhou[1,2*] and Yaokai Gan[1,2*]

[1]Department of Orthopaedic Surgery, Shanghai Ninth People's Hospital, Shanghai Jiao Tong University School of Medicine, Shanghai, China, [2]Shanghai Key Laboratory of Orthopaedic Implants, Shanghai Ninth People's Hospital, Shanghai Jiao Tong University School of Medicine, Shanghai, China

OPEN ACCESS

EDITED BY
Pengfei Xu,
National University of Singapore,
Singapore

REVIEWED BY
Sin-Yeang Teow,
Kean University-Wenzhou, China
Cevat Erisken,
Nazarbayev University, Kazakhstan

*CORRESPONDENCE
Xianhao Zhou,
✉ zhouxianhaooier@163.com
Yaokai Gan,
✉ ganyk2004@126.com

†These authors have contributed equally to this work

SPECIALTY SECTION
This article was submitted to Nanobiotechnology, a section of the journal Frontiers in Bioengineering and Biotechnology

RECEIVED 22 February 2023
ACCEPTED 22 March 2023
PUBLISHED 30 March 2023

CITATION
Jiao X, Wang Z, Li Y, Wang T, Xu C, Zhou X and Gan Y (2023), Fullerenol inhibits tendinopathy by alleviating inflammation. *Front. Bioeng. Biotechnol.* 11:1171360. doi: 10.3389/fbioe.2023.1171360

Tendinopathy is a common disease in orthopaedics, seriously affecting tendon functions. However, the effects of non-surgical treatment on tendinopathy are not satisfactory and surgical treatments possibly impair the function of tendons. Biomaterial fullerenol has been proved to show good anti-inflammatory effects on various inflammatory diseases. For *in vitro* experiments, primary rat tendon cells (TCs) were treated by interleukin-1 beta (IL-1β) combined with aqueous fullerenol (5, 1, 0.3 μg/mL). Then inflammatory factors, tendon-related markers, migration and signaling pathways were detected. For *in vivo* experiments, rat tendinopathy model was constructed by local injection of collagenase into Achilles tendons of rats and fullerenol (0.5, 1 mg/mL) was locally injected 7 days after collagenase injection. Inflammatory factors and tendon-related markers were also investigated. Fullerenol with good water-solubility showed excellent biocompatibility with TCs. Fullerenol could increase expression of tendon-related factors (Collagen I and tenascin C) and decrease expression of inflammatory factors (matrix metalloproteinases-3, MMP-3, and MMP-13) and reactive oxygen species (ROS) level. Simultaneously, fullerenol slowed the migration of TCs and inhibited activation of Mitogen-activated protein kinase (MAPK) signaling pathway. Fullerenol also attenuated tendinopathy *in vivo*, including reduction of fiber disorders, decrease of inflammatory factors and increase of tendon markers. In summary, fullerenol is a promising biomaterial that can be used to treat tendinopathy.

KEYWORDS

**fullerenol, inflammation, ROS, MAPK, tendinopathy**

## 1 Introduction

Tendinopathy is chronic disorders of tendons usually caused by overuse, with an incidence of 0.2%–0.3% of adult patients (van der Vlist et al., 2020). Among them, athletes are the riskiest ones to suffer from tendinopathy with a morbidity of approximate 52% (Kujala et al., 2005) (Lagas et al., 2020). Tendinopathy causes pain, diffuse or localized swelling, loss of tissue integrity and impaired performance (Millar et al., 2021). The pathological mechanisms of tendinopathy are multiple, including apoptosis disorder, mechanical overload, imbalance of matrix metalloproteinases (MMPs) and tissue inhibitors of metalloproteinases (TIMPs), genetic factors, inflammation (Yuan et al., 2002) (Arnoczky et al., 2004) (Mokone et al., 2006). Current managements of tendinopathy consist of drug treatments, physical therapy, and surgery. However, curative effects of drug treatments and physical therapies are short-term. Surgeries possibly lead to secondary injury and tendon function postoperatively cannot recover to preoperative level. Thus, it is necessary to develop a new treatment method with minor injury.

Pathology of tendinopathy still remains controversial. Inflammation plays a key role in the appearance of tendinopathy, especially in the early phase (Legerlotz et al., 2012). From the perspective of risk factors, injuries, repetitive mechanical overloading and hypoxia all elevate inflammatory cytokines, such as tumor necrosis factor alpha (TNF-α), interleukin-1 beta (IL-1β), prostaglandin E2 (PGE2) (D'Addona et al., 2017). Moreover, hypoxic damage or increased oxygen demand of tendon cells caused by mechanical stresses also tends to raise oxygen free radicals like reactive oxygen species (ROS), leading to secondary damage of tendon tissues. Simultaneously, Dakin et al. found that both tendinopathic and ruptured Achilles tendons of human expressed many $CD14^+$ and $CD68^+$ cells and showed a complex inflammation signature, involving interferon, nuclear factor-kappa B (NF-κB) and signal transducer and activator of transcription 6 (STAT-6) activation pathways, which also proved that inflammation was a vital pathological process of tendinopathy (Dakin et al., 2018). Therefore, inhibiting inflammation is possibly an effective method to attenuate tendinopathy.

Fullerenol is a fullerene derivative with good water solubility, which expands its use in biological and medical fields. Structurally, there are numerous carbon-carbon double bonds in fullerenol, contributing to its antioxidative activity of scavenging reactive oxygen species (ROS) (Markelić et al., 2022). A lot of studies have reported good protective effects of fullerenol on cells under oxidative stress and DNA damage. It was found that fullerenol showed excellent curative or preventive effects on bleomycin-induced pulmonary fibrosis (Zhou et al., 2018), intervertebral disk degeneration (Yang et al., 2014a), myocardial ischemia-reperfusion injury (Ding and Li, 2020), osteoarthritis (Pei et al., 2019). In the meantime, fullerenol has the ability to rescue HaCaT human skin keratinocytes and corneal epithelial cells from ultraviolet B (wavelength between 280 and 320 nm) (Saitoh et al., 2011) (Chen et al., 2022). Apart from these, fullerenol presents promising results of osteogenic differentiation induction to repair bone defect. Despite of the favorable therapeutic benefits of fullerenol on multiple diseases, there is no study on the effects of fullerenol on tendinopathy.

Since inflammation was an important feature of tendinopathy, and fullerenol showed brilliant anti-inflammatory and antioxidant effects in various diseases, we hypothesized that fullerenol could mitigate tendinopathy by inhibiting inflammation. Therefore, this study aims to explore the effects of fullerenol on tendinopathy and investigate the potential mechanisms, in order to provide a new treatment method of tendinopathy.

# 2 Materials and methods

## 2.1 Characterization of fullerenol

Fullerenol powder was purchased from Chengdu Zhongke Times Nano Energy Tech Co., Ltd. The fullerenol powder was tested by Transmission Electron Microscope (TEM, TF20) for size and morphology and by Fourier transform infrared spectrometer (FTIR, Thermo Scientific Nicolet iS20, United States). At room temperature, fullerenol was suspended in distilled water to make aqueous fullerenol with the concentration of 50 mg/mL. Then, size distribution and zeta potential were investigated by Nano Sizer and Zeta potential Tester (Omni, United States). 50 mg/mL aqueous fullerenol was stored at room temperature shielded from light for further use. For cell treatment, aqueous fullerenol was diluted with Dulbecco's modified Eagle's medium (DMEM, Gibco, United States) to the concentration of 10, 5, 3, 1, 0.5, 0.3, 0.1 μg/mL and was sterilized with 0.22 μm filter membranes (Millipore, United States).

## 2.2 Tendon cells isolation and culture

Tendon cells (TCs) were isolated from the Achilles tendons of rats, as described previously (Jiao et al., 2022b). In brief, Achilles tendons of one-week-old rats were cut after disinfection. And tendons were immersed in 0.06% collagenase type I (Worthington, United States) solution at 37°C overnight. Then, the solution was centrifuged and the supernatant was discarded. The sediment was suspended and incubated in DMEM supplemented with 10% fetal bovine serum (FBS, Gibco, United States ) and 1% antibiotics (penicillin and streptomycin, Gibco, United States). Cells were subcultured when they reached 80%–90% confluence.

## 2.3 Cell Count Kit-8 assay

Cell Count Kit-8 (CCK-8) assay was performed using the kit (Dojindo, CK04-05, Japan) according to the instruction. TCs were seeded into 96-well plates with a density of $3 \times 10^3$ per well. Then, TCs were incubated using DMEM containing fullerenol with different concentrations (10, 5, 3, 1, 0.5, 0.3, 0.1 μg/mL). At 1 and 3 days, TCs were cultured in DMEM medium with 10% CCK-8 reagent at 37°C for 2 h. The absorbance of the supernatant at 450 nm was measured using a microplate reader (Infinite M200 Pro, Tecan, Switzerland).

## 2.4 Live/dead cell staining

Live/dead cell staining was performed using the kit (KeyGEN, Nanjing, China) according to the manufacturer's instruction. The samples were observed using a confocal microscope (Leica, Germany). Live (green) cells stained by Calcein AM were detected with excitation at 488 nm, and dead (red) cells stained by PI were observed with excitation at 555 nm.

## 2.5 RNA extraction and qRT-PCR

For inflammation induction and fullerenol treatment, TCs were treated by 50 ng/mL IL-1β combined with aqueous fullerenol. Then, total RNA was extracted using TRIzol reagent (Thermo Scientific, United States). A NanoDrop 1,000 spectrophotometer (Thermo Scientific, United States) was used to evaluate RNA purity and quantification. 1,000 ng of the extracted RNA was reverse transcribed to cDNA using

**TABLE 1 Sequences of primers for qRT-PCR.**

| Primer | Forward primer (5′ to 3′) | Reverse primer (5′ to 3′) |
|---|---|---|
| GAPDH | GGCAAGTTCAACGGCACAGT | GCCAGTAGACTCCACGACAT |
| COL1A1 | TGACTGGAAGAGCGGAGAGTA | GGGGTTTGGGCTGATGTACC |
| TNC | TGCCATAGCAACAACAGCCAT | AACTCTCCACCTGAGCAGTC |
| MMP-3 | TGCTCATGAACTTGGCCACT | GTGGGAGGTCCATAGAGGGAT |
| MMP-13 | GGGAACCACGTGTGGAGTTAT | GACAGCATCTACTTTGTCGCC |

**Abbreviations:** GAPDH, glyceraldehyde-3-phosphate dehydrogenase; COL1A1, collagen 1A1; TNC, tenascin C; MMP-3, matrix metalloproteinases-3; MMP-13, matrix metalloproteinases-13.

PrimeScript Master Mix (Takara, RR036A, Japan). The qRT-PCR reaction was performed with 2× SYBR Green qPCR Master Mix (Low ROX) (Bimake, B21703, China) and Applied Biosystems 7,500 Real-Time PCR System (Applied Biosystems, Foster City, CA, United States). The relative mRNA levels were calculated with $2^{-\Delta\Delta CT}$ method. Glyceraldehyde-3-phosphate dehydrogenase (GAPDH) was used as internal control. The primers used in this study are listed in Table 1.

## 2.6 Scratch assay

For scratch assay, TCs were seeded into 6-well plates and cultured to reach 80% confluence. Then, a straight scratch was scraped with a 200-μL pipette tip. And TCs were incubated with IL-1β and aqueous fullerenol. Cell migration was determined by measuring the distance at 0, 12 and 24 h.

## 2.7 Transwell assay

For the Transwell assay, Transwell chambers (BD Science, United States of America) were used. In 24-well plate, TCs ($5 \times 10^4$) in 150 μL of serum-free basal medium were seeded into the upper chamber, and 650 μL of DMEM supplemented with 10% FBS, IL-1β and aqueous fullerenol was added into the lower chamber. The Transwell system was placed in a 5% $CO_2$ incubator at 37 C for 24 h. Then, the cells were fixed and stained with crystal violet solution.

## 2.8 Protein extraction and Western blotting

For inflammation induction and fullerenol treatment, TCs were treated by 50 ng/mL IL-1β combined with aqueous fullerenol. For protein extraction, TCs were lysed using RIPA lysis buffer (Beyotime, China) supplemented with 1% protease and phosphatase inhibitor cocktail (100X) (Thermo Scientific, United States). Then, the mixture was centrifugated at a speed of 14,000 RCF for 15 min. The supernatant was separated and mixed with SDS-PAGE sample loading buffer (Beyotime, China) and boiled at 99°C for 5 min. Protein samples were electrophoresed on SDS gels and transferred onto polyvinylidene fluoride membranes (Millipore, United States). The membrane was then blocked in Tris-buffered saline Tween 20 (Solarbio, China) containing 5% non-fat milk (Sangon Biotech, China) or 5% bovine serum albumin (MPbio, United States) for 1 h at room temperature. After that, the membrane was incubated with primary antibodies at 4°C overnight and secondary antibodies for 1 h at room temperature. Protein immunoreactivity was detected with LI-COR Odyssey Fluorescence Imaging System (LI-COR Biosciences, United States), and ImageJ was used to measure the protein expression. The anti-bodies used were as follows: p44/42 MAPK (Erk1/2) (Cell Signaling Technology, United States), Phospho-p44/42 MAPK (Erk1/2) (Cell Signaling Technology, United States), SAPK/JNK (Cell Signaling Technology, United States), Phospho-SAPK/JNK (Cell Signaling Technology, United States), p38 MAPK (Cell Signaling Technology, United States), Phospho-p38 MAPK (Cell Signaling Technology, United States), Anti-rabbit IgG (H + L) (800 4X PEG Conjugate) (Cell Signaling Technology, United States), Anti-mouse IgG (H + L) (800 4X PEG Conjugate) (Cell Signaling Technology, United States).

## 2.9 Animal experiments

All animal experiments were approved by the Ethics Committee of Shanghai Ninth People's Hospital, Shanghai Jiaotong University School of Medicine (Approval number: SH9H-2021-A895-1). To establish tendinopathy models, Sprague-Dawley (SD) rats (male, 8 weeks old), purchased from Shanghai JieSiJie Laboratory Animals Co., LTD., were anesthetized. Then, 50 mg/mL collagenase type I (Worthington, United States) solution was injected into the Achilles tendons to trigger inflammation. At 7 days after injection, 50 μL aqueous fullerenol with the concentration of 0.5 mg/mL and 1 mg/mL were injected. At the 21st day after collagenase injection, tendons were collected and used for histological observation.

## 2.10 Histological observation

The histological observation methods were similar to those previously reported (Jiao et al., 2022a). Briefly, after fixation, embedding and section, Hematoxylin-eosin (HE) and Masson tri-chrome staining were performed. The method of evaluating fiber alignment was described in the previous studies (Adeoye et al.,

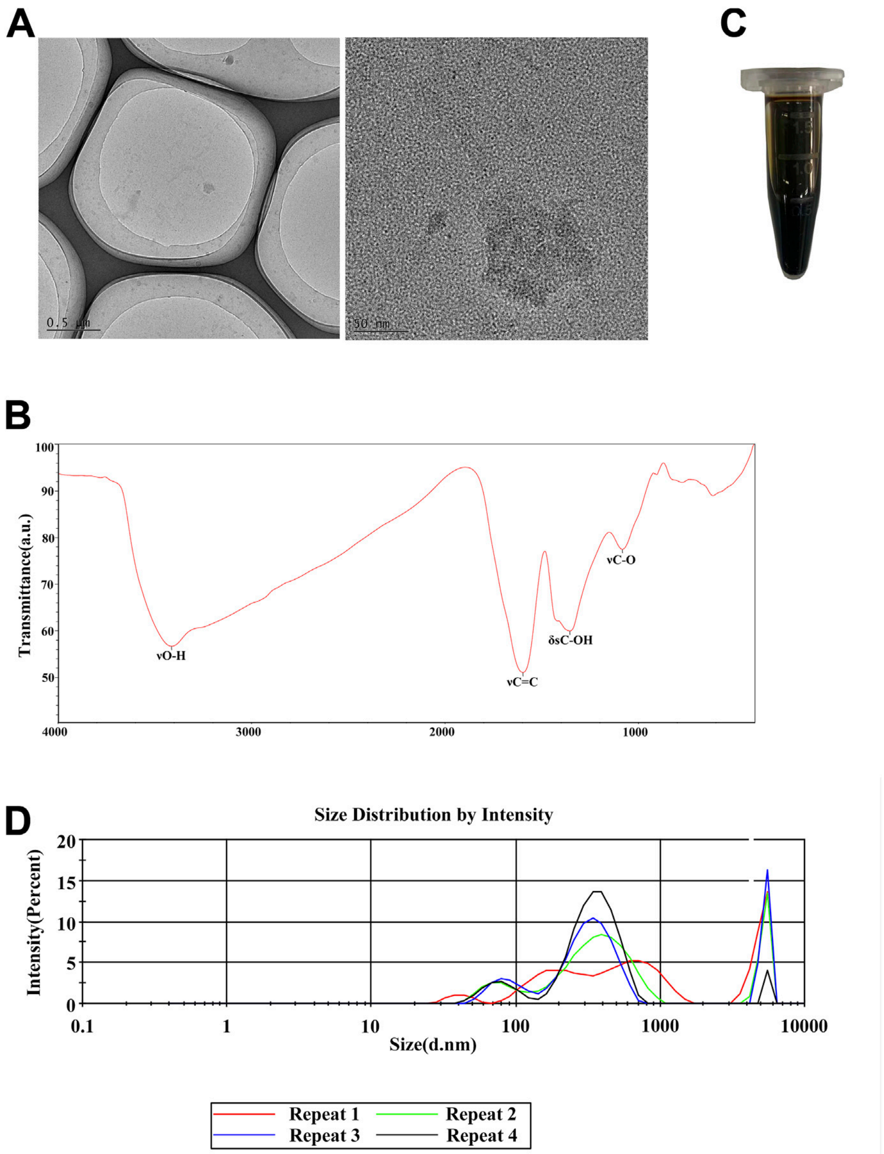

FIGURE 1
Characterization of fullerenol. **(A)** Transmission electron microscope (TEM) of fullerenol powder. Scale bar = 0.5 μm (left), 50 nm (right) **(B)** FTIR of fullerenol powder. **(C)** Image of aqueous fullerenol (50 mg/mL). **(D)** Hydrodynamic size of fullerenol in aqueous solution.

2022) (Ozlu et al., 2019) (Erisken et al., 2013). For immunohistochemical staining, we incubated sections overnight with different antibodies (COL I, COX-2, IL-6; Servicebio; China). On the next day, the sections were incubated with the secondary antibody (HRP-anti-rabbit IgG, Servicebio, China). After that, they were observed and captured.

## 2.11 Statistical analysis

All results are shown as the mean ± standard deviation. Student's t-test was used for comparisons between two groups, and one-way analysis of variance followed by Tukey's *post hoc* analysis was used for comparisons between three or more groups. Statistical significance was set at $p < 0.05$.

# 3 Results

## 3.1 Characterization of fullerenol

To detect the characterization of fullerenol, we investigated the size and morphology of fullerenol powder by TEM. Shown in Figure 1A, the diameter of fullerenol powder was over 1 μm. Furthermore, we detected characteristic absorption peaks of fullerenol powder by FTIR spectra. In Figure 1B, four characteristic absorption peaks existed. In detail, broad O–H

**TABLE 2** Zeta potential of aqueous fullerenol.

| Repeat | Zeta potential (mV) | Mobility (μ/s)/(V/cm) | Conductance (μS) | Count rate (kcps) |
|---|---|---|---|---|
| 1 | −16.61 | −1.30 | 25 | 586 |
| 2 | −13.21 | −1.03 | 26 | 601 |
| 3 | −16.51 | −1.29 | 26 | 601 |

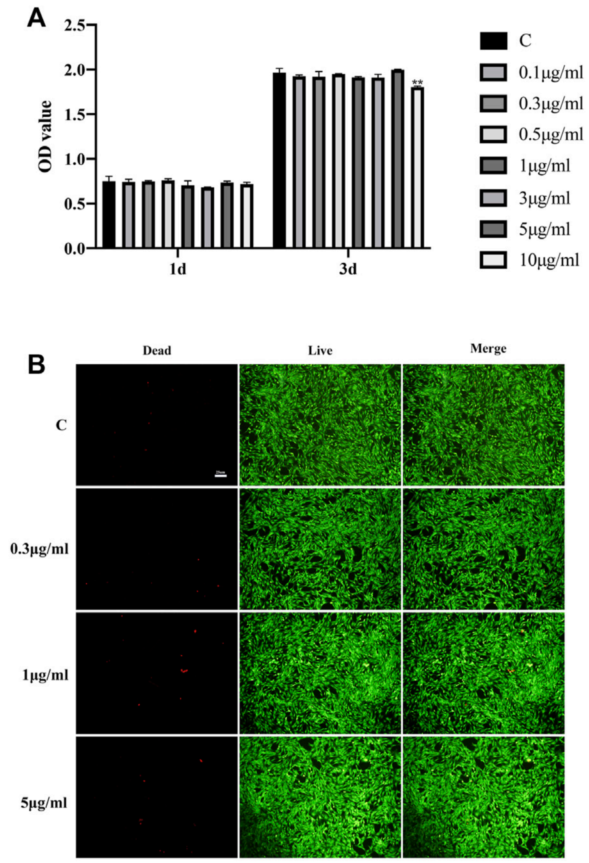

FIGURE 2
Biocompatibility of fullerenol with different concentrations. **(A)** Optical density (OD) value of TCs treated with different-concentration (0, 0.1, 0.3, 0.5, 1, 3, 5, 10 μg/mL) fullerenol at 1 and 3 days tested by CCK-8. **(B)** Live/dead cell staining of TCs treated with 0, 0.3, 1, 5 μg/mL fullerenol at 3 days. Scale bar = 25 μm. (Data are presented as the mean ± standard deviation. $^{*}p < 0.05$, $^{**}p < 0.01$).

stretching vibration (νO-H) presented at 3,412.80 $\text{cm}^{-1}$, C=C stretching vibration (νC = C) was shown at 1,596.71 $\text{cm}^{-1}$, O–H in-plane deformation vibration (δsC-OH) existed at 1,354.07 $\text{cm}^{-1}$, and C–O stretching vibration (νC-O) was at 1,082.82 $\text{cm}^{-1}$. Then, we dissolved fullerenol by water into the concentration of 50 mg/mL, which became brown to black liquid (Figure 1C). Although the diameter of fullerenol powder was over 1μm, according to size distribution, particles in aqueous fullerenol were mostly from 100 to 1000 nm (Figure 1D). Notably, there was another peak from 3,000 to 6000 nm, which was probably caused by agglomeration due to high concentration. At the same time, the surface zeta potential was −15.44 ± 1.93 mV (Table 2).

## 3.2 Fullerenol shows low cytotoxicity on rat TCs

To detect the cytotoxicity of fullerenol, we performed CCK-8 assay. Shown in Figure 2A, at 1 day after fullerenol (10, 5, 3, 1, 0.5, 0.3, 0.1 μg/mL) treatment, no significant difference existed between TCs treated with fullerenol and without fullerenol, indicating no cytotoxicity at 1 day. However, at 3 days, optical density (OD) value in the 10 μg/mL group was obviously lower than control group, suggesting that 10 μg/mL fullerenol influenced cell viability of TCs at 3 days. Based on this, we chose three concentrations (5, 1, 0.3 μg/mL) to conduct further experiments. Furthermore, we verified the cytotoxicity of fullerenol with the three concentrations at 3 days *via* live/dead cell staining (Figure 2B). It was found that almost no dead TCs existed at the three concentrations. All the results showed that low-concentration fullerenol had good cytocompatibility with TCs.

## 3.3 Fullerenol inhibits inflammation of TCs caused by IL-1β and rescues the impairments of TCs

Next, we investigated the effects of fullerenol on the inflammation of TCs and the expression of tendon-related markers. Collagen 1A1 (COL1A1) is the most important component of tendon tissues and expresses lower in tendinopathy (Cho et al., 2021; López De Padilla et al., 2021). Tenascin C (TNC) is a glycoprotein abundantly expressed in tendons subjected to high tensile and compressive stress (September et al., 2007). TNC has been proved in the regulation of cell-matrix interaction (September et al., 2007). Shown in Figure 3A, after adding IL-1β, expression of COL1A1 and TNC decreased, although there was no significant difference. Fullerenol enhanced the RNA level of COL1A1 and TNC remarkably, especially 5 μg/mL. Contrary to COL1A1 and TNC, IL-1β augmented matrix metalloproteinases-3 (MMP-3) and matrix metalloproteinases-13 (MMP-13) expression, which were closely related to inflammation. As an anti-inflammatory material, fullerenol lowered MMP-3 and MMP-13, suggesting that fullerenol alleviated inflammation. Consistent with RNA, the tendency of TNC, COL I and MMP-13 were increased by IL-1β and decreased by fullerenol (Figure 3B). In view of anti-oxidant effects of fullerenol, we also verified the anti-oxidant effect of fullerenol in tendinopathy. In Figure 3C, IL-1β induced ROS upregulation, showing that IL-1β exacerbated oxidant stress in TCs. However, after fullerenol treatment, ROS level of TCs diminished in a concentration-dependent manner and nearly disappeared in the concentration of 5 μg/mL. All the above

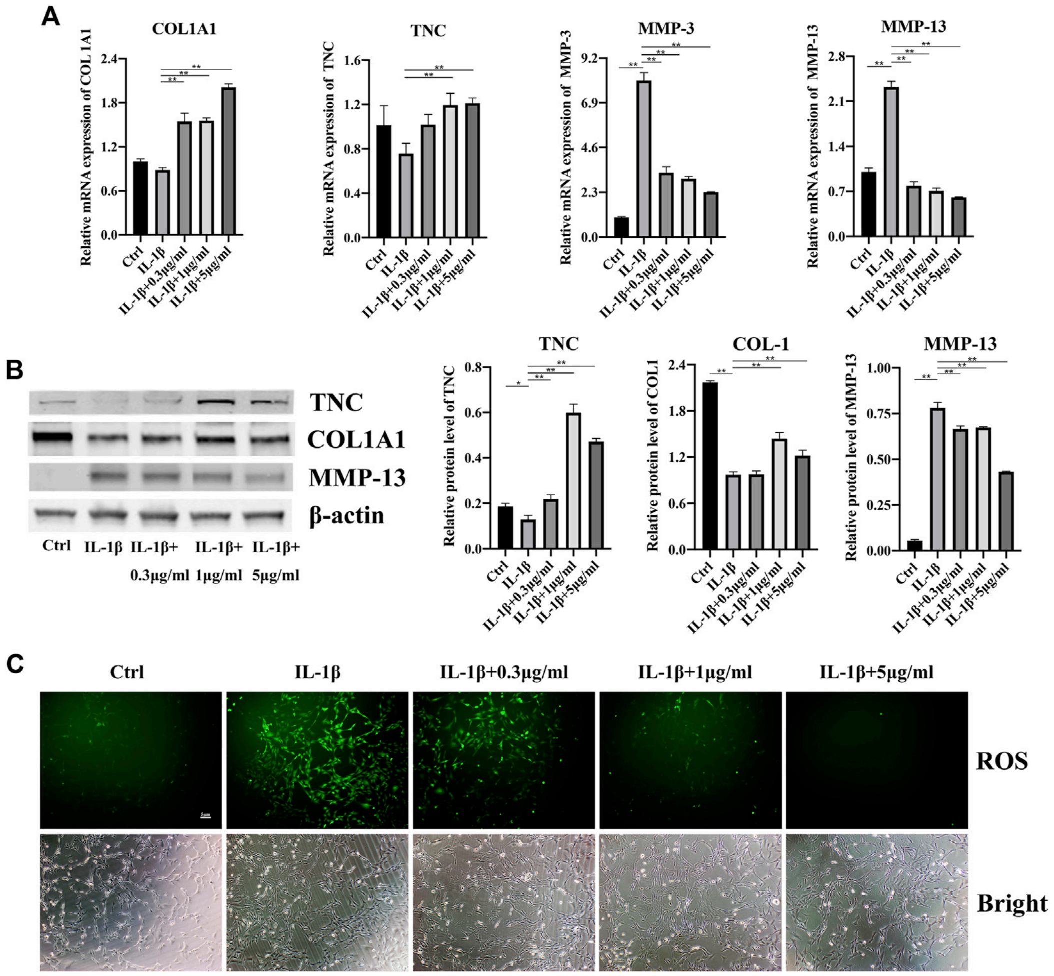

FIGURE 3
Effects of fullerenol on inflammation of TCs induced by IL-1β. **(A)** mRNA level of COL1A1, TNC, MMP-3 and MMP-13 of TCs after fullerenol and IL-1β treatment tested by qRT-PCR. **(B)** Protein level of TNC, COL1A1 and MMP-13 of TCs after fullerenol and IL-1β treatment tested by Western Blot (Left) and quantitative results (Right). **(C)** ROS level of TCs after fullerenol and IL-1β treatment tested by ROS assay kit.

results implied that fullerenol could attenuate inflammation and ROS level in TCs induced by IL-1β.

## 3.4 Fullerenol inhibits migration of TCs

It was reported that migration of TCs increased in an inflammatory environment (Jiao et al., 2022b) (Wang et al., 2019). Next, we investigated the influences of fullerenol on TCs migration through scratch assay and transwell assay. Shown in Figures 4A,C, TCs in all the five groups migrated gradually at 12 and 24 h. The addition of IL-1β accelerated migration of TCs to around 50% at 12 h and approximate 70% at 24 h. However, fullerenol was able to inhibit the migration of TCs effectively. Notably, the inhibitory effects were concentration dependent. Extremely low concentration like 0.3 μg/mL did not depress the migration of TCs, while 1 μg/mL and 5 μg/mL could suppress the migration. Similarly, in transwell assay, the number of TCs in IL-1β group increased obviously compared with control group (Ctrl). But the number declined after fullerenol treatment in a concentration-dependent manner (Figures 4B,D). The above results implied that fullerenol could effectively inhibit migration of TCs.

## 3.5 Fullerenol inhibits tendinopathy *via* MAPK pathway

Mitogen-activated protein kinase (MAPK) signaling pathway was reported to play a key role in inflammation (Jiao et al., 2022b) (Zhu et al., 2021). So, we explored the activation of MAPK signaling pathway. P38 MAPK pathway was strongly activated in stress, immune response and regulation of cell survival and differentiation (Cuadrado and Nebreda, 2010). Apparently, in our study, inflammation induced by IL-1β increased the phosphorylation level of p38. Nevertheless, addition of fullerenol availably hindered the activation of p38 (Figures 5A,B). Interestingly, phosphorylation level of p38 decreased in a concentration-dependent manner. Identically, Erk1/2 and JNK was activated by IL-1β and the activation was inhibited by fullerenol (Figures 5C–F). The results of Western blot suggested

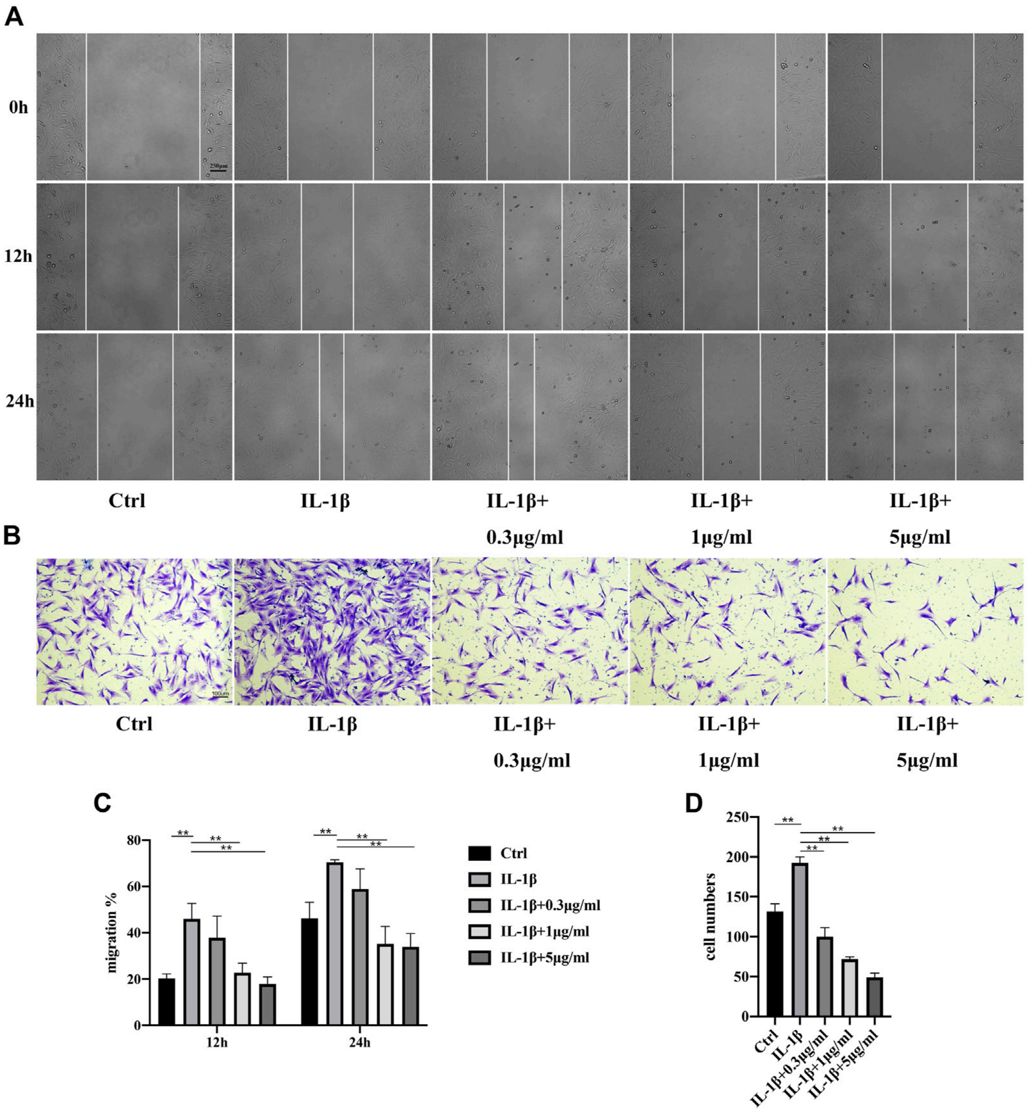

FIGURE 4
Migration of TCs after IL-1β (50 ng/mL) and fullerenol treatment. **(A)** Migration of TCs in control (Ctrl), IL-1β, IL-1β+0.3 μg/mL, IL-1β+1 μg/mL, IL-1β+5 μg/mL groups tested by scratch assay. Scale bar = 250 μm. **(B)** Migration of TCs in Ctrl, IL-1β, IL-1β+0.3 μg/mL, IL-1β+1 μg/mL, IL-1β+5 μg/mL groups tested by transwell assay. Scale bar = 100 μm. **(C)** Quantitative results of scratch assay. **(D)** Quantitative results of transwell assay. (Data are presented as the mean ± standard deviation. *$p < 0.05$, **$p < 0.01$).

that fullerenol could restrain the activation of MAPK pathway induced by IL-1β.

## 3.6 Fullerenol inhibits tendinopathy *in vivo*

Next, we furtherly tested anti-inflammatory effects of fullerenol on tendinopathy *in vivo*. Shown in Figure 6A, after collagenase I injection, tendinous fibers were fractured and arranged disorderly compared with Ctrl group in HE and Masson staining. But fullerenol alleviated impairment of tendinous fibers. Meanwhile, we detected expression of Collagen I (COL I), Cyclooxygenase 2 (COX-2) and IL-6 by immunohistochemical staining (Figure 6B). In Collagenase group, COL I decreased and inflammatory factors (COX-2 and IL-6) increased in comparison with Ctrl group, showing that collagenase induced inflammation of tendon tissues. Fullerenol could alleviate severity of inflammation and promote expression of COL I. All these data hinted that fullerenol reduced inflammation in tendinopathy *in vivo*.

## 4 Discussion

Tendinopathy is a common overload injury, with an incidence of two to three per 1,000 patients in general medicine practice (van der Vlist et al., 2021). It is challenging to manage tendinopathy. Current treatments have more or less limitations. For example, conservative treatments like eccentric exercises and shockwave therapy are not suitable for all kinds of tendinopathy (Figueroa et al., 2016). Pharmacological management, especially injection, is

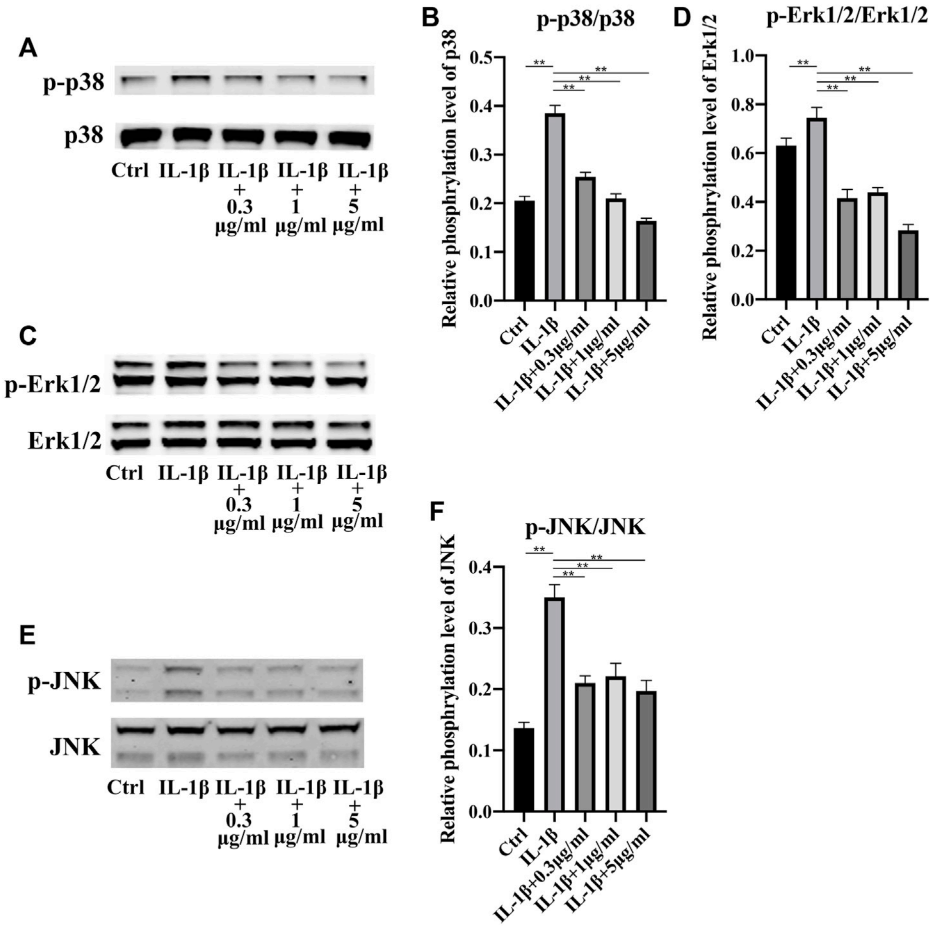

FIGURE 5
Expression of MAPK signaling pathway after IL-1β (50 ng/mL) and fullerenol (0.3, 1, 5 μg/mL) treatment. **(A)** The phosphorylation levels of p38 in TCs of Ctrl, IL-1β, IL-1β +0.3 μg/mL, IL-1β+1 μg/mL, IL-1β+5 μg/mL groups were examined by Western Blotting. **(B)** Quantitative results of phosphorylation levels of p38. **(C)** The phosphorylation levels of Erk1/2 in TCs of Ctrl, IL-1β, IL-1β +0.3 μg/mL, IL-1β+1 μg/mL, IL-1β+5 μg/mL groups were examined by Western Blotting. **(D)** Quantitative results of phosphorylation levels of Erk1/2. **(E)** The phosphorylation levels of JNK in TCs of Ctrl, IL-1β, IL-1β +0.3 μg/mL, IL-1β+1 μg/mL, IL-1β+5 μg/mL groups were examined by Western Blotting. **(F)** Quantitative results of phosphorylation levels of JNK. (Data are presented as the mean ± standard deviation. $^*p < 0.05$, $^{**}p < 0.01$)

another important way to treat tendinopathy. Unfortunately, no standard procedure of treat tendinopathy pharmacologically is established because there is a lack of comparative studies on effects of various drug injections (Aicale et al., 2020). Furthermore, surgical treatment impaired the function of tendons and there is a need of high-quality evidence on the effects of surgeries on different tendinopathy, such as chronic patellar tendinopathy (Khan and Smart, 2016). Therefore, it is necessary to develop a new method of tendinopathy management with low side effects.

Fullerenol is a hydroxylated derivative of fullerene. Identical to previous studies (Wang et al., 2016) (Zha et al., 2022), the diameter of our aqueous fullerenol ranged from 100 to 1,000 nm. Notably, fullerenol was also manufactured to be nanomaterial with diameter lower than 100 nm (Chen et al., 2022). In terms of biological function, fullerenol show good biocompatibility and low side effects in numerous studies (Yang et al., 2021) (Yang et al., 2014b) (Zhu et al., 2007). However, it was also reported that fullerenol was cytotoxic toward human retinal pigment epithelial (hRPE) cells at concentrations of 10–50 μM, and increased phototoxicity on hRPE cells in particular (Wielgus et al., 2010). So, in spite of good biocompatibility, fullerenol is not absolutely safe to all the normal tissue cells. In our study, we detected the cytotoxicity of fullerenol toward TCs. It was found that after short-term (1 day) treatment, fullerenol showed no cytotoxicity at concentrations of 0.1–10 μg/mL. Nonetheless, with extension of treatment time to 3 days, fullerenol at high concentration (10 μg/mL) became deleterious for cell viability of TCs. Overall, fullerenol, consisting of carbon, hydrogen and oxygen elements, exhibited good biocompatibility to TCs. But the extremely high concentration also caused impairment on TCs. All the results of cell viability are almost identical to previous studies.

Inflammation is one of the most features of tendinopathy and suppressing inflammation has been a vital treatment for tendinopathy. Mounting studies have employed anti-inflammatory drugs and biomaterials to treat tendinopathy. Chen et al. reported that ibuprofen-loaded hyaluronic acid nanofibrous membranes could reduce inflammation to prevent postoperative

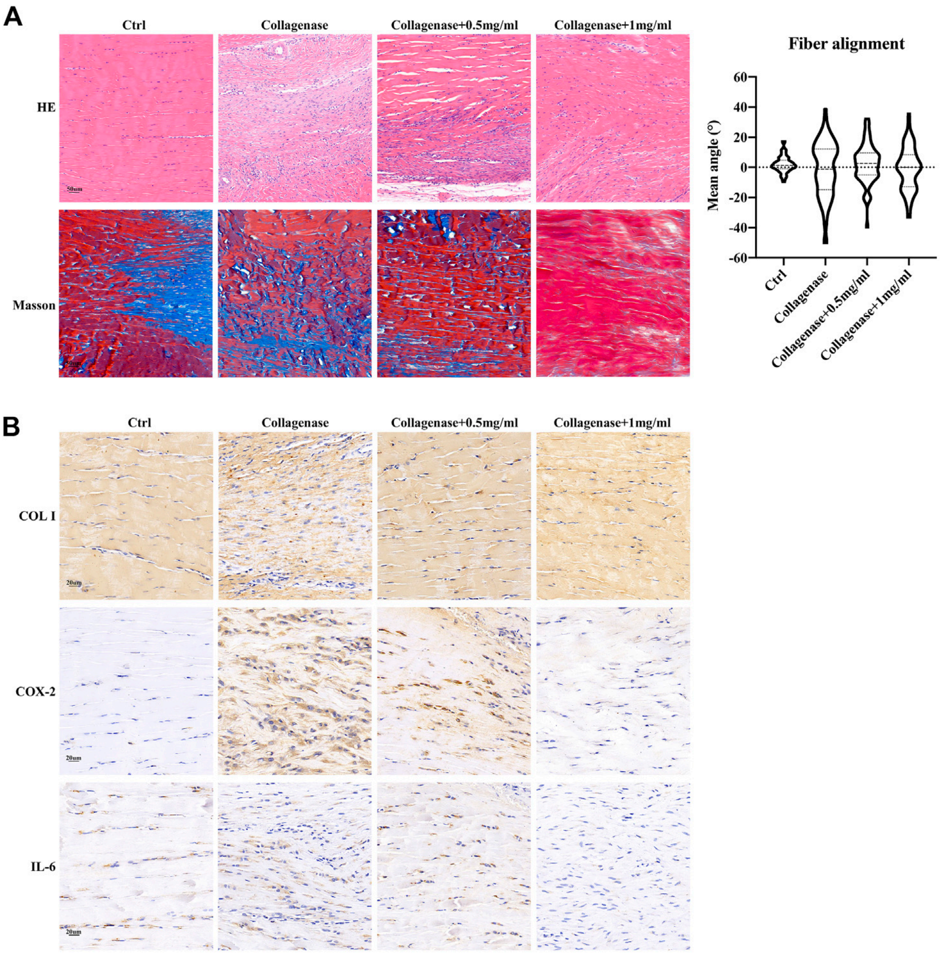

FIGURE 6
Inhibition of fullerenol (0.5, 1 mg/mL) on tendinopathy *in vivo*. **(A)** HE and Masson staining of tendons in Ctrl, Collagenase, Collagenase+0.5 mg/mL, Collagenase+1 mg/mL groups (Left). Statistical results of fiber alignment (Right). Scale bar = 50 μm. **(B)** Immunohistochemical staining (COL I, COX-2, IL-6) of tendons in Ctrl, Collagenase, Collagenase+0.5 mg/mL, Collagenase+1 mg/mL groups. Scale bar = 20 μm.

tendon adhesion (Chen et al., 2019). In the study of Choi et al., they synthesized lactoferrin-immobilized, heparin-anchored, poly (lactic-co-glycolic acid) nano-particles (LF/Hep-PLGA NPs) and also found that LF/Hep-PLGA NPs enhanced tendon restoration *via* inhibiting inflammation (Choi et al., 2020). In terms of drugs, plenty of drugs like aspirin were found to be conducive to tendinopathy treatment through many signaling pathways, such as JNK/STAT3 pathway (Wang et al., 2019). In our study, we investigated whether fullerenol helped mitigate tendinopathy. From RNA to protein level, under inflammatory environment, fullerenol increased expression of COL I and TNC and decreased expression of MMP-3 and MMP-13. It might imply that fullerenol played a key role in both reducing inflammation and protecting tendon tissues. Furthermore, production of ROS is another factor of damage to tendon. The results of our study showed that fullerenol also had the ability to remove ROS, which was possibly due to many carbon-carbon double bonds in fullerenol.

Stimulation of inflammation tends to change the behaviors of localized cells in different tissues. Cell migration is one of the most important behaviors affected by inflammation. In previous studies, it was found that the migration of human bronchial epithelial cells increased after being treated with TNF-α, which was also a way to induce inflammation (Ren et al., 2021). Similarly, migration of fibroblasts is also influenced by inflammation. Fibroblast-like synoviocytes (MH7A cell) in rheumatoid arthritis migrated faster than synoviocytes in control group (Cai et al., 2021) (Cai et al., 2022). Zhang et al. also reported that macrophage migration inhibitory factor, a proinflammatory cytokine, promoted migration of joint capsule fibroblasts (Zhang et al., 2021). Here, in our study, we investigated the influence of fullerenol on TCs migration under the inflammatory environment by scratch assay and transwell assay. Obviously, IL-1β treatment induced inflammation of TCs successfully and made migration of TCs faster, which was consistent with our previous study (Jiao et al., 2022b). In view of good anti-inflammatory and anti-oxidant effects of fullerenol on TCs from mRNA level to protein level, it could inhibit migration of TCs under inflammatory environment, unsurprisingly. After tendons are injured, migration of TCs may lead to formation of a fibrotic scar, causing loss of mechanical strength of the original tendon (Wang et al., 2019) (Nichols et al., 2019). Based on our results, fullerenol slowed the migration of TCs which was likely to reduce the impairment of tendon tissues.

A series of signaling pathways is of great importance in tendinopathy inhibition. Various inflammation-related pathways such as NF-κB, c-Jun N-terminal kinase (JNK)/STAT-3 signaling pathways (Wang et al., 2019) (Vinhas et al., 2020). Besides, MAPK signaling pathways play a part in tendinopathy (Wu et al., 2022) (Moqbel et al., 2020). MAPK cascade consists of three protein kinases, including a MAPK and two upstream components, MAPK kinase (MAPKK) and MAPKK kinase (MAPKKK). So far, three MAPK pathways are found in mammalian cells, namely, the extracellular signal-regulated kinases (ERKs) pathway, the c-Jun amino terminal kinase (JNK) pathway and the p38 MAPK pathway (Kumar et al., 2003). Considering the importance of MAPK signaling pathway in inflammation, we explored the activation of MAPK pathway after fullerenol treatment. Excitingly, fullerenol curbed the phosphorylation level of all p38, ERK, and JNK, suggesting fullerenol could effectively inhibit tendinopathy *via* MAPK pathway.

We furtherly detected the effects of fullerenol on tendinopathy *in vivo*. Collagenase injection has been a common method of constructing tendinopathy model (Liu et al., 2021) (Wu et al., 2019). Collagenase injection caused disorders and swelling of fibers in tendons. At the same time, collagenase leads to increase of inflammatory factors and decrease of Collagen I. Since fullerenol had good water-solubility, we decided to inject fullerenol locally into Achilles tendons, which had better effects for tendinopathy compared with intraperitoneal injection. In our study, identical to results of cell experiments, aqueous fullerenol alleviated disorders of tendon fibers and decreased expression of inflammatory factors like COX-2 and IL-6. The animal experiments showed fullerenol was an excellent and convenient therapeutic approach to tendinopathy.

Since tendinopathy is a localized inflammatory disease, traditional drug administration is the most common treatment. Here, we firstly injected aqueous fullerenol to treat tendinopathy. In view of good biocompatibility and anti-inflammatory effects, fullerenol shows good prospects in treating localized inflammatory diseases like tendinopathy in the future.

## 5 Conclusion

In conclusion, fullerenol is a promising biomaterial which has brilliant biocompatibility and anti-inflammatory effects and can be used to treat tendinopathy. Utilization of fullerenol helps reduce the side effects caused by drug administration and lower the economic burden.

## Data availability statement

The raw data supporting the conclusion of this article will be made available by the authors, without undue reservation.

## Ethics statement

The animal study was reviewed and approved by the Ethics Committee of Shanghai Ninth People's Hospital, Shanghai Jiaotong University School of Medicine.

## Author contributions

Conceptualization, XZ and YG; methodology, XJ and ZW; software, XJ; validation, ZW, YL, and TW; formal analysis, XJ and ZW; resources, CX; writing—original draft preparation, XJ, ZW, and YL; writing—review and editing, XJ, ZW, and XZ; supervision, YG; funding acquisition, YG. All authors have read and agreed to the published version of the manuscript.

## Funding

This research was funded by the National Natural Science Foundation of China (82172402), funds of the Clinical Research Plan of SHDC (16CR3099B), the Clinical Research Program of the 9th People's Hospital, Shanghai Jiao Tong University School of Medicine (JYLJ202101). Shanghai Key Laboratory of Orthopaedic Implants (KFKT202210).

## Conflict of interest

The authors declare that the research was conducted in the absence of any commercial or financial relationships that could be construed as a potential conflict of interest.

## Publisher's note

## References

Adeoye, A. O., Mukasheva, F., Smatov, S., Khumyrzakh, B., Kadyr, S., Shulgau, Z., et al. (2022). A biomimetic synthetic nanofiber-based model for anterior cruciate ligament regeneration. *Front. Bioeng. Biotechnol.* 10, 969282. doi:10.3389/fbioe.2022.969282

Aicale, R., Bisaccia, R. D., Oliviero, A., Oliva, F., and Maffulli, N. (2020). Current pharmacological approaches to the treatment of tendinopathy. *Expert Opin. Pharmacother.* 21, 1467–1477. doi:10.1080/14656566.2020.1763306

Arnoczky, S. P., Tian, T., Lavagnino, M., and Gardner, K. (2004). *Ex vivo* static tensile loading inhibits MMP-1 expression in rat tail tendon cells through a cytoskeletally based mechanotransduction mechanism. *J. Orthop. Res.* 22, 328–333. doi:10.1016/S0736-0266(03)00185-2

Cai, L., Mu, Y. R., Liu, M. M., Zhou, M. Y., Meng, B., Liu, F. Y., et al. (2021). Penta-acetyl geniposide suppresses migration, invasion, and inflammation of TNF-α-stimulated rheumatoid arthritis fibroblast-like synoviocytes involving wnt/β-catenin signaling pathway. *Inflammation* 44, 2232–2245. doi:10.1007/s10753-021-01495-y

Cai, L., Zhou, M. Y., Hu, S., Liu, F. Y., Wang, M. Q., Wang, X. H., et al. (2022). Umbelliferone inhibits migration, invasion and inflammation of rheumatoid arthritis fibroblast-like synoviocytes and relieves adjuvant-induced arthritis in rats by blockade of wnt/β-catenin signaling pathway. *Am. J. Chin. Med.* 50, 1945–1962. doi:10.1142/S0192415X22500835

Chen, C. T., Chen, C. H., Sheu, C., and Chen, J. P. (2019). Ibuprofen-loaded hyaluronic acid nanofibrous membranes for prevention of postoperative tendon adhesion through reduction of inflammation. *IJMS* 20, 5038. doi:10.3390/ijms20205038

Chen, X., Yang, J., Li, M., Zhu, S., Zhao, M., Yang, C., et al. (2022). Fullerenol protects cornea from ultraviolet B exposure. *Redox Biol.* 54, 102360. doi:10.1016/j.redox.2022.102360

Cho, Y., Hs, K., D, K., H, K., N, L., J, Y., et al. (2021). CTRP3 exacerbates tendinopathy by dysregulating tendon stem cell differentiation and altering extracellular matrix composition. *Sci. Adv.* 7, eabg6069. doi:10.1126/sciadv.abg6069

Choi, H. J., Choi, S., Kim, J. G., Song, M. H., Shim, K. S., Lim, Y. M., et al. (2020). Enhanced tendon restoration effects of anti-inflammatory, lactoferrin-immobilized, heparin-polymeric nanoparticles in an Achilles tendinitis rat model. *Carbohydr. Polym.* 241, 116284. doi:10.1016/j.carbpol.2020.116284

Cuadrado, A., and Nebreda, A. R. (2010). Mechanisms and functions of p38 MAPK signalling. *Biochem. J.* 429, 403–417. doi:10.1042/BJ20100323

D'Addona, A., Maffulli, N., Formisano, S., and Rosa, D. (2017). Inflammation in tendinopathy. *Surg.* 15, 297–302. doi:10.1016/j.surge.2017.04.004

Dakin, S. G., Newton, J., Martinez, F. O., Hedley, R., Gwilym, S., Jones, N., et al. (2018). Chronic inflammation is a feature of Achilles tendinopathy and rupture. *Br. J. Sports Med.* 52, 359–367. doi:10.1136/bjsports-2017-098161

Ding, M., Li, M., Zhang, E. M., and Yang, H. L. (2020). FULLEROL alleviates myocardial ischemia-reperfusion injury by reducing inflammation and oxidative stress in cardiomyocytes via activating the Nrf2/HO-1 signaling pathway. *Eur. Rev. Med. Pharmacol. Sci.* 24, 9665–9674. doi:10.26355/eurrev_202009_23056

Erisken, C., Zhang, X., Moffat, K. L., Levine, W. N., and Lu, H. H. (2013). Scaffold fiber diameter regulates human tendon fibroblast growth and differentiation. *Tissue Eng. Part A* 19, 519–528. doi:10.1089/ten.tea.2012.0072

Figueroa, D., Figueroa, F., and Calvo, R. (2016). Patellar tendinopathy: Diagnosis and treatment. *J. Am. Acad. Orthop. Surg.* 24, e184–e192. doi:10.5435/JAAOS-D-15-00703

Jiao, X., Sun, X., Li, W., Chu, W., Zhang, Y., Li, Y., et al. (2022a). 3D-Printed β-tricalcium phosphate scaffolds promote osteogenic differentiation of bone marrow-deprived mesenchymal stem cells in an N6-methyladenosine- dependent manner. *Int. J. Bioprint* 8, 544. doi:10.18063/ijb.v8i2.544

Jiao, X., Zhang, Y., Li, W., Zhou, X., Chu, W., Li, Y., et al. (2022b). HIF-1α inhibition attenuates severity of Achilles tendinopathy by blocking NF-κB and MAPK pathways. *Int. Immunopharmacol.* 106, 108543. doi:10.1016/j.intimp.2022.108543

Khan, W. S., and Smart, A. (2016). Outcome of surgery for chronic patellar tendinopathy: A systematic review. *Acta Orthop. Belg* 82, 610–326.

Kujala, U. M., Sarna, S., and Kaprio, J. (2005). Cumulative incidence of achilles tendon rupture and tendinopathy in male former elite athletes. *Clin. J. Sport Med.* 15, 133–135. doi:10.1097/01.jsm.0000165347.55638.23

Kumar, S., Boehm, J., and Lee, J. C. (2003). p38 MAP kinases: key signalling molecules as therapeutic targets for inflammatory diseases. *Nat. Rev. Drug Discov.* 2, 717–726. doi:10.1038/nrd1177

Lagas, I. F., Fokkema, T., Verhaar, J. A. N., Bierma-Zeinstra, S. M. A., Middelkoop, M. V., and Vos, R. J. D. (2020). Incidence of achilles tendinopathy and associated risk factors in recreational runners: A large prospective cohort study. *J. Sci. Med. Sport* 23, 448–452. doi:10.1016/j.jsams.2019.12.013

Legerlotz, K., Jones, E. R., Screen, H. R. C., and Riley, G. P. (2012). Increased expression of IL-6 family members in tendon pathology. *Rheumatology* 51, 1161–1165. doi:10.1093/rheumatology/kes002

Liu, A., Wang, Q., Zhao, Z., Wu, R., Wang, M., Li, J., et al. (2021). Nitric oxide nanomotor driving exosomes-loaded microneedles for achilles tendinopathy healing. *ACS Nano* 15, 13339–13350. doi:10.1021/acsnano.1c03177

López De Padilla, C. M., Coenen, M. J., Tovar, A., De la Vega, R. E., Evans, C. H., and Müller, S. A. (2021). Picrosirius red staining: Revisiting its application to the qualitative and quantitative assessment of collagen type I and type III in tendon. *J. Histochem Cytochem* 69, 633–643. doi:10.1369/00221554211046777

Markelić, M., Drača, D., Krajnović, T., Jović, Z., Vuksanović, M., Koruga, D., et al. (2022). Combined action of hyper-harmonized hydroxylated fullerene water complex and hyperpolarized light leads to melanoma cell reprogramming *in vitro*. *Nanomater. (Basel)* 12, 1331. doi:10.3390/nano12081331

Millar, N. L., Silbernagel, K. G., Thorborg, K., Kirwan, P. D., Galatz, L. M., Abrams, G. D., et al. (2021). *Tendinopathy. Nat. Rev. Dis. Prim.* 7, 1. doi:10.1038/s41572-020-00234-1

Mokone, G. G., Schwellnus, M. P., Noakes, T. D., and Collins, M. (2006). The COL5A1 gene and Achilles tendon pathology. *Scand. J. Med. Sci. Sports* 16, 19–26. doi:10.1111/j.1600-0838.2005.00439.x

Moqbel, S. A. A., Xu, K., Chen, Z., Xu, L., He, Y., Wu, Z., et al. (2020). Tectorigenin alleviates inflammation, apoptosis, and ossification in rat tendon-derived stem cells via modulating NF-kappa B and MAPK pathways. *Front. Cell. Dev. Biol.* 8, 568894. doi:10.3389/fcell.2020.568894

Nichols, A. E. C., Best, K. T., and Loiselle, A. E. (2019). The cellular basis of fibrotic tendon healing: Challenges and opportunities. *Transl. Res.* 209, 156–168. doi:10.1016/j.trsl.2019.02.002

Ozlu, B., Ergin, M., Budak, S., Tunali, S., Yildirim, N., and Erisken, C. (2019). A bioartificial rat heart tissue: Perfusion decellularization and characterization. *Int. J. Artif. Organs* 42, 757–764. doi:10.1177/0391398819863434

Pei, Y., Cui, F., Du, X., Shang, G., Xiao, W., Yang, X., et al. (2019). <p&gt; Antioxidative nanofullerol inhibits macrophage activation and development of osteoarthritis in rats&lt;/p&gt;. *IJN* 14, 4145–4155. doi:10.2147/IJN.S202466

Ren, X., Han, L., Li, Y., Zhao, H., Zhang, Z., Zhuang, Y., et al. (2021). Isorhamnetin attenuates TNF-α-induced inflammation, proliferation, and migration in human bronchial epithelial cells via MAPK and NF-κB pathways. *Anatomical Rec.* 304, 901–913. doi:10.1002/ar.24506

Saitoh, Y., Miyanishi, A., Mizuno, H., Kato, S., Aoshima, H., Kokubo, K., et al. (2011). Super-highly hydroxylated fullerene derivative protects human keratinocytes from UV-induced cell injuries together with the decreases in intracellular ROS generation and DNA damages. *J. Photochem. Photobiol. B Biol.* 102, 69–76. doi:10.1016/j.jphotobiol.2010.09.006

September, A. V., Schwellnus, M. P., Collins, M., and Gibson, W. (2007). Tendon and ligament injuries: The genetic component * COMMENTARY. *Br. J. Sports Med.* 41, 241–246. doi:10.1136/bjsm.2006.033035

van der Vlist, A. C., van Oosterom, R. F., van Veldhoven, P. L. J., Bierma-Zeinstra, S. M. A., Waarsing, J. H., Verhaar, J. A. N., et al. (2020). Effectiveness of a high volume injection as treatment for chronic achilles tendinopathy: Randomised controlled trial. *BMJ* 370, m3027. doi:10.1136/bmj.m3027

van der Vlist, A. C., Winters, M., Weir, A., Ardern, C. L., Welton, N. J., Caldwell, D. M., et al. (2021). Which treatment is most effective for patients with achilles tendinopathy? A living systematic review with network meta-analysis of 29 randomised controlled trials. *Br. J. Sports Med.* 55, 249–256. doi:10.1136/bjsports-2019-101872

Vinhas, A., Rodrigues, M. T., Gonçalves, A. I., Reis, R. L., and Gomes, M. E. (2020). Magnetic responsive materials modulate the inflammatory profile of IL-1β conditioned tendon cells. *Acta Biomater.* 117, 235–245. doi:10.1016/j.actbio.2020.09.028

Wang, X. X., Zha, Y. Y., Yang, B., Chen, L., and Wang, M. (2016). Suppression of synaptic plasticity by fullerenol in rat hippocampus *in vitro*. *Int. J. Nanomedicine* 11, 4947–4955. doi:10.2147/IJN.S104856

Wang, Y., He, G., Tang, H., Shi, Y., Kang, X., Lyu, J., et al. (2019). Aspirin inhibits inflammation and scar formation in the injury tendon healing through regulating JNK/STAT-3 signalling pathway. *Cell. Prolif.* 52, e12650. doi:10.1111/cpr.12650

Wielgus, A. R., Zhao, B., Chignell, C. F., Hu, D. N., and Roberts, J. E. (2010). Phototoxicity and cytotoxicity of fullerol in human retinal pigment epithelial cells. *Toxicol. Appl. Pharmacol.* 242, 79–90. doi:10.1016/j.taap.2009.09.021

Wu, P. T., Su, W. R., Li, C. L., Hsieh, J. L., Ma, C. H., Wu, C. L., et al. (2019). Inhibition of CD44 induces apoptosis, inflammation, and matrix metalloproteinase expression in tendinopathy. *J. Biol. Chem.* 294, 20177–20184. doi:10.1074/jbc.RA119.009675

Wu, T., Qi, W., Shan, H., Tu, B., Jiang, S., Lu, Y., et al. (2022). Ginsenoside Rg1 enhances the healing of injured tendon in achilles tendinitis through the activation of IGF1R signaling mediated by oestrogen receptor. *J. Ginseng Res.* 46, 526–535. doi:10.1016/j.jgr.2021.08.005

Yang, J., Liang, J., Zhu, Y., Hu, M., Deng, L., Cui, W., et al. (2021). Fullerol-hydrogel microfluidic spheres for *in situ* redox regulation of stem cell fate and refractory bone healing. *Bioact. Mater.* 6, 4801–4815. doi:10.1016/j.bioactmat.2021.05.024

Yang, X., Jin, L., Yao, L., Shen, F. H., Shimer, A., and Li, X. (2014a). Antioxidative nanofullerol prevents intervertebral disk degeneration. *IJN* 9, 2419–2430. doi:10.2147/IJN.S60853

Yang, X., Li, C. J., Wan, Y., Smith, P., Shang, G., and Cui, Q. (2014b). Antioxidative fullerol promotes osteogenesis of human adipose-derived stem cells. *Int. J. Nanomedicine* 9, 4023–4031. doi:10.2147/IJN.S66785

Yuan, J., Murrell, G. A. C., Wei, A., and Wang, M. (2002). Apoptosis in rotator cuff tendonopathy. *J. Orthop. Res.* 20, 1372–1379. doi:10.1016/s0736-0266(02)00075-x

Zha, Y., Jin, Y., Wang, X., Chen, L., Zhang, X., and Wang, M. (2022). Long-term maintenance of synaptic plasticity by Fullerenol Ameliorates lead-induced-impaired learning and memory *in vivo*. *J. Nanobiotechnology* 20, 348. doi:10.1186/s12951-022-01550-2

Zhang, Y., Lu, S., Fan, S., Xu, L., Jiang, X., Wang, K., et al. (2021). Macrophage migration inhibitory factor activates the inflammatory response in joint capsule fibroblasts following post-traumatic joint contracture. *Aging (Albany NY)* 13, 5804–5823. doi:10.18632/aging.202505

Zhou, Y., Zhen, M., Ma, H., Li, J., Shu, C., and Wang, C. (2018). Inhalable gadofullerenol/[70] fullerenol as high-efficiency ROS scavengers for pulmonary fibrosis therapy. *Nanomedicine Nanotechnol. Biol. Med.* 14, 1361–1369. doi:10.1016/j.nano.2018.03.008

Zhu, X., Zhu, L., Li, Y., Duan, Z., Chen, W., and Alvarez, P. J. J. (2007). Developmental toxicity in zebrafish (*Danio rerio*) embryos after exposure to manufactured nanomaterials: Buckminsterfullerene aggregates (nC60) and fullerol. *Environ. Toxicol. Chem.* 26, 976–979. doi:10.1897/06-583.1

Zhu, Y. X., Huang, J. Q., Ming, Y. Y., Zhuang, Z., and Xia, H. (2021). Screening of key biomarkers of tendinopathy based on bioinformatics and machine learning algorithms. *PLoS One* 16, e0259475. doi:10.1371/journal.pone.0259475

frontiers | Frontiers in Bioengineering and Biotechnology

TYPE Original Research
PUBLISHED 11 April 2023
DOI 10.3389/fbioe.2023.1166790

# A fresh pH-responsive imipenem-loaded nanocarrier against *Acinetobacter baumannii* with a synergetic effect

Shumin Gui[1], Xisheng Li[2], Mingming Feng[1], Hui Liu[3], Liwenhui Huang[3] and Xinqing Niu[1,3]*

[1]Department of Hematology, The Third Affiliated Hospital of Xinxiang Medical University, Xinxiang Medical University, Xinxiang, Henan, China, [2]Department of Laboratory Medicine, The Third Xiangya Hospital, Cental South University, Changsha, Hunan, China, [3]Henan Key Laboratory of Immunology and Targeted Drugs, School of Medical Technology, Xinxiang Medical University, Xinxiang, Henan, China

EDITED BY
Xiangzhao Ai,
Shanghai Jiao Tong University, China

REVIEWED BY
Md. Rizwanullah,
Jamia Hamdard University, India
Sin-Yeang Teow,
Kean University-Wenzhou, China

*CORRESPONDENCE
Xinqing Niu,
✉ 081045@xxmu.edu.cn

SPECIALTY SECTION
This article was submitted to Nanobiotechnology, a section of the journal Frontiers in Bioengineering and Biotechnology

RECEIVED 15 February 2023
ACCEPTED 31 March 2023
PUBLISHED 11 April 2023

CITATION
Gui S, Li X, Feng M, Liu H, Huang L and Niu X (2023), A fresh pH-responsive imipenem-loaded nanocarrier against *Acinetobacter baumannii* with a synergetic effect.
*Front. Bioeng. Biotechnol.* 11:1166790.
doi: 10.3389/fbioe.2023.1166790

In recent years, the treatment of *Acinetobacter baumannii* infections has become a pressing clinical challenge due to its increasing incidence and its serious pathogenic risk. The research and development of new antibacterial agents for *A. baumannii* have attracted the attention of the scientific community. Therefore, we have constructed a new pH-responsive antibacterial nano-delivery system (Imi@ZIF-8) for the antibacterial treatment of *A. baumannii*. Due to its pH-sensitive characteristics, the nano-delivery system offers an improved release of the loaded imipenem antibiotic at the acidic infection site. Based on the high loading capacity and positive charge of the modified ZIF-8 nanoparticles, they are excellent carriers and are suitable for imipenem loading. The Imi@ZIF-8 nanosystem features synergistic antibacterial effects, combining ZIF-8 and imipenem to eliminate *A. baumannii* through different antibacterial mechanisms. When the loaded imipenem concentration reaches 20 μg/mL, Imi@ZIF-8 is highly effective against *A. baumannii in vitro*. Imi@ZIF-8 not only inhibits the biofilm formation of *A. baumannii* but also has a potent killing effect. Furthermore, in mice with celiac disease, the Imi@ZIF-8 nanosystem demonstrates excellent therapeutic efficacy against *A. baumannii* at imipenem concentrations of 10 mg/kg, and it can inhibit inflammatory reaction and local leukocyte infiltration. Due to its biocompatibility and biosafety, this nano-delivery system is a promising therapeutic strategy in the clinical treatment of *A. baumannii* infections, providing a new direction for the treatment of antibacterial infections.

KEYWORDS

***Acinetobacter baumannii*, Imi@ZIF-8, antibacterial infection, synergistic effect, antibiofilm**

## Introduction

*Acinetobacter baumannii* is an aerobic, gram-negative coccobacillus and is a conditional pathogen that can cause community-acquired and hospital-acquired infection (Whiteway et al., 2022). In clinical settings, it is responsible for ventilator-associated pneumonia, catheter-associated blood and urinary tract infections, sepsis, endocarditis, skin and wound infections and meningitis (Chen, 2020). *A. baumannii* is ubiquitous in nature and persistent in the hospital environment, where it often infects immunocompromised patients, particularly those in intensive care units (Shan et al., 2022). According to worldwide data, the detection rate of *A. baumannii* in intensive care units rose from 4% to 7% between 1986 and 2003. Moreover, ICU mortality increased from 53.3% to 84.3% in patients with respiratory-associated pneumonia due to extensively drug-resistant *A. baumannii* (Saipriya et al., 2020). *A. baumannii* was regarded as ESKAPE pathogens. In order to study and develop effective antibacterial drugs against *A. baumannii* with acquired resistance to antibiotics, the WHO has placed it on priority list (Tacconelli et al., 2018). So, there is a need for research into combatting this pathogen.

Genomic and phenotypic identification analyses were performed, demonstrating the association between *A. baumannii* infection and multiple virulence factors, including outer membrane proteins, lipopolysaccharides, capsular polysaccharides, phospholipases, protein secretion systems, quantum sensing and biofilm production (Harding et al., 2018; Dehbanipour and Ghalavand, 2022). These virulence factors contribute to the colonization of pathogenic bacteria and exacerbate antibiotic resistance. At present, antibiotics for the treatment of *A. baumannii* infection are mainly selected based on the sensitivity of pathogens to antibiotics, the severity of the disease and the infection site. Based on its pathogenicity, the clinical treatments of *A. baumannii* include sulbactams, carbapenems, aminoglycosides, polymyxin, tegacycline and combined antibiotic therapy (Fishbain and Peleg, 2010; Isler et al., 2019). Carbapenems are highly effective broad-spectrum antibacterial drugs that exhibit strong antibacterial activity against gram-positive bacteria, gram-negative bacteria and anaerobes and are regarded as the "last line of defense" of antibiotics. Their antibacterial mechanism is similar to β-like lactam antibiotics, as they inhibit the formation of the bacterial cell wall by binding with penicillin-binding proteins (PBPs), leading to inactivation (Papp-Wallace et al., 2011; Skariyachan et al., 2019). Imipenem is the most widely-used carbapenem antibiotic in clinical practice and has high bactericidal activity, fast bactericidal rate and excellent bacterial inhibition against *A. baumannii*, especially for patients with moderate to severe infections and multi-drug resistant bacterial infections. Moreover, imipenem is a time-dependent antibacterial drug with a post-antibiotic effect on bacteria. Imipenem preferentially combines with PBP2, followed by PBP1a and PBP1b, and has a weak affinity for PBP3. This mechanism of action can reduce the release of lipopolysaccharide during bacteriolysis, providing good biological safety (Rodloff et al., 2006; Zhanel et al., 2007; Nowak and Paluchowska, 2016). However, with the wide application of carbapenem antibiotics in recent years, the drug resistance rate of *A. baumannii* to carbapenems has increased year by year (Jiang et al., 2022). Polymyxins are effective for treating *A. baumannii* infection, with low rates of resistance, but are associated with a higher risk of nephrotoxicity (Liu et al., 2021). The overall economic benefit of high-dose sulbactam or combination therapy is poor, and clinical data on the efficacy and resistance of the other antimicrobials mentioned are limited (Betrosian et al., 2008; Chu et al., 2013). Hence, finding new treatment schemes is an urgent problem.

The researcher has extensively studied and formulated treatment plans against bacterial infection and drug resistance, including the development of new antibiotic resistance inhibitors. However, the research of new antibiotics is time-consuming and costly, and the development of antibacterial resistance is significantly faster than the research and development of new antibiotics. Furthermore, drug-resistant inhibitors mainly inhibit the severe evolution of bacteria into drug-resistant bacteria, but the prevalence of drug resistance within a patient or in the population remains a challenge (Baym et al., 2016; Chang et al., 2022). In recent years, nanomaterials have attracted attention due to their physical and chemical properties, such as structural stability, large specific surface area, high porosity, easy surface modification, structural diversity and biocompatibility. They have been applied to biomedical engineering projects, such as biosensors (Singh et al., 2022), drug carriers (Vangijzegem et al., 2019; Huang et al., 2021; Liu et al., 2022), medical implants (Akgöl et al., 2021) and medical imaging (Kalva et al., 2022). The rise of nanomedicine has enabled advances in antimicrobial therapy.

Nanocarriers can selectively transport antibiotics to the site of infection due to their targeting properties, thus improving drug distribution, increasing the effectiveness of antibiotics, reducing drug side effects and overcoming bacterial resistance (Nazli et al., 2022). Many nanomaterials have been used in antimicrobial therapy, such as inorganic metal nanomaterials (gold, silver, copper, zinc, titanium), metal oxide nanoparticles (copper oxide, zinc oxide, titanium oxide, iron oxide), carbon-based nanomaterials (graphene and its derivatives, graphene quantum dots, carbon quantum dots), and organic nanostructures (chitosan, dendrimers, liposomes, micelles, vesicles), etc. (Modi et al., 2022). The antibacterial mechanisms of nanomaterials involve 1) the use of size, surface properties and other unique physicochemical properties to damage important intracellular components and interfere with the normal physiological metabolic processes of bacteria, ultimately leading to bacterial death (Cheng et al., 2022); 2) the use of the enzyme-like activity of nanomaterials, regulating the level of reactive oxygen species (ROS) to exert a strong bactericidal effect by disrupting bacterial biofilms (Godoy-Gallardo et al., 2021); 3) smart response platforms based on nanomaterials, such as pH, enzymes and temperature to enhance antimicrobial activity (Jiang et al., 2020); 4) the use of external stimulus-response properties of nanomaterials, such as light and microwaves, or synergistic antimicrobial drugs to achieve an antimicrobial activity in a single or combined treatment (Díez-Pascual, 2020; Nazli et al., 2022). Zeolite imidazole ester skeleton—8 (ZIF—8) is a porous crystalline material formed by the coordination self-assembly of zinc ion and 2-methylimidazole. ZIF-8 has not only high loading capacity but also has antibacterial activity, acid sensitivity, low cytotoxicity, and good biocompatibility, providing broad applications in biomedicine (Lian et al., 2022). The pH of the microenvironment of infected tissues is slightly lower than that of normal tissues due to acid production at the site of infection, so ZIF-8 can be used as an acid-responsive drug carrier for antimicrobial therapy with superior loading capacity, controlled drug release and enhanced targeting (Abdelhamid, 2021; Tan et al., 2022).

In summary, a novel antimicrobial nanodelivery system with pH acid response function was constructed by synthesizing positively-charged ZIF-8 (PEI@ZIF-8) and loading negatively-charged imipenem onto ZIF-8 nanoparticles (Imi@ZIF-8) using positive and negative charge adsorption forces under ultrasonic stirring. The loaded imipenem is effectively released at the site of bacterial infection due to the acidic microenvironment, displaying the antimicrobial synergy between imipenem and ZIF-8. In addition, subsequent research and experiments found that the Imi@ZIF-8 nanodrug system exerts a strong killing effect on *A. baumannii*. The development of an antibacterial nanosystem with good biocompatibility and biosafety provides a new strategy for the clinical treatment of *A. baumannii*.

# Materials and methods

## Materials

Imipenem was purchased from Aladdin Technology (China). Fetal bovine serum (FBS) and high glucose (Dulbecco’s modified Eagle’s medium DMEM) were obtained from Life Technologies. Dialysis membranes (2000 D), hematoxylin and eosin (HE), crystal violet (CV), and phenazine methosulfate were provided by Solarbio Technology (China). Mueller-Hinton (MH) broth was obtained from Solarbio. Polycarbonate porous membrane syringe filters (200 nm) were obtained from Whatman. The bacterial stock solution and reactive oxygen species (ROS) assay kits were purchased from Beyotime Technology (China). The LIVE/DEAD backlight bacterial viability kit was purchased from Yeasen Biotechnology (China). Anti-IL-6 and anti-Ly6G antibodies were manufactured by BOSTER Biological Technology (China). The HRP-conjugated goat anti-mouse IgG was purchased from BOSTER Biological Technology.

## Experimental cells and experimental animals

The mouse lung epithelial (MLE-12) cell line was provided by the Department of Laboratory Medicine, Xiangya Medicine School, Central South University. MLE-12 cells were cultured in a sterile environment at 37°C and 5% $CO_2$. We prepared 5 mL of 10% fetal bovine serum, 45 mL of DMEM (high sugar type) and 1 mL of penicillin-streptomycin (1%) to form the complete medium for the cells used. The 6-week-old female BALB/c mice used in our experiments were purchased from Shrek Laboratory Animals Ltd. in Hunan, China. All mice were kept in specific pathogen-free conditions at the Animal Resource Center of Xinxiang Medical University. All animal experiments were approved by the Xinxiang Medical University Experimental Animal Ethics Committee. The ethical approval code is XYLL-20230027.

## Bacterial strains and bacterial cultures

The *A. baumannii* strains were obtained from the Department of Laboratory Science, The Third Affiliated Hospital of Xinxiang Medical University (Xinxiang, Henan, China). The bacteria were stored in bacterial lyophilization solution at −80°C. A disposable sterile inoculating loop was used to collect the lyophilized solution, and the bacteria were allowed to grow on blood agar plates by triple zoning, followed by incubation at 5% $CO_2$ and 37°C for 24 h. Finally, individual colonies from the plates were lysed in a sterile LB broth liquid medium with a disposable sterile inoculating loop and incubated overnight at 200 rpm at 37°C to allow bacterial to growth to their logarithmic phase. The overnight culture was added to a fresh, sterilized LB broth medium, and the $OD_{600}$ value was measured using an enzyme marker at 0.6. All experiments were repeated three times, and the average of the three values was taken.

## Preparation of PEI@ZIF-8

2-methylimidazole was dissolved in methanol to form solution A, and zinc nitrate was dissolved in methanol to form solution B. Solutions A and B were mixed and allowed to react for a certain period of time, and ZIF-8 was obtained by centrifugation (Wang et al., 2020). The precipitate was washed then three times with water. ZIF-8 and PEI were mixed and stirred for a certain period of time, and the PEI-modified ZIF-8 was collected by centrifugation. Finally, the precipitate was washed three times with water.

## Determination of encapsulation and loading rates of imipenem in Imi@ZIF-8

1 mg of PEI@ZIF-8 was dissolved in 1 mL of deionized water ($ddH_2O$), and 1.2 mg of imipenem was added and stirred for 4–5 h at room temperature with a magnetic stirrer. The solution was left for 12 h in darkness, then the precipitate was centrifuged in darkness to obtain Imi@ZIF-8. The maximum absorbance of imipenem in the supernatant was determined by UV-visible spectrophotometry (Yu et al., 2014; Wang et al., 2016). The standard concentration gradient of imipenem was set, and the standard curve of concentration and absorbance was established. Then, the content of unbound imipenem in the supernatant was calculated.

The calculation formulas of encapsulation efficiency (EE) and loading efficiency (LE) are as follows:

$$EE = \left(\frac{imipenem\ added - imipenem\ remaining\ in\ supernatant}{imipenem\ added}\right) \times 100\%.$$

$$LE = \left(\frac{amount\ of\ imipenem\ added - amount\ of\ imipenem\ remaining\ in\ the\ supernatant}{total\ weight\ of\ Imi@ZIF - 8}\right) \times 100\%.$$

## Characterization of Imi@ZIF-8

Transmission electron microscopy (TEM) was performed to observe the particle size and morphology of ZIF-8, while the surface morphology of ZIF-8 was assessed using Scanning electron microscopy (SEM). A zeta potential-particle size analyzer was used to evaluate imipenem, ZIF-8, and Imi@ZIF-8, whereas dynamic light scattering instrument (DLS) was performed to analyze the hydrated particle size of ZIF-8 and Imi@ZIF-8. The characteristic absorption peak positions of ZIF-8, imipenem and Imi@ZIF-8 were detected by a ultraviolet-visible (UV-vis) spectrophotometer to further validate the successful construction of the nano-delivery system.

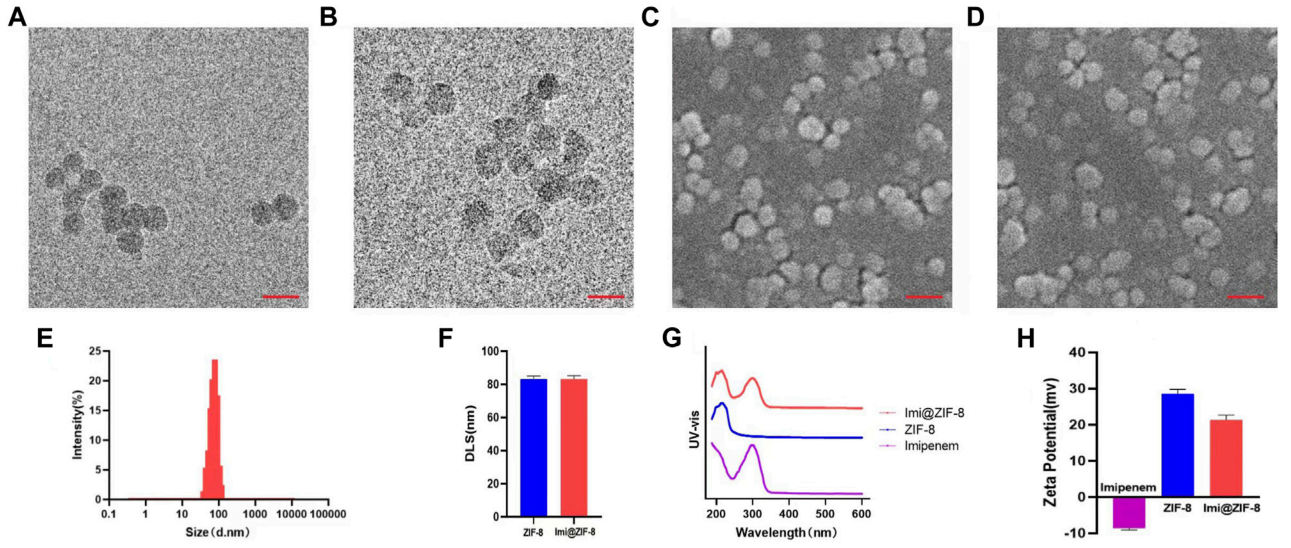

FIGURE 1
Characterization of ZIF-8 and Imi@ZIF-8. **(A)** TEM image of ZIF-8. **(B)** TEM image of Imi@ZIF-8. Scale bar is 150 nm. **(C)** SEM image of ZIF-8. **(D)** SEM image of Imi@ZIF-8. Scale bar is 200 nm. **(E)** Particle sizes of Imi@ZIF-8 detected by TEM. **(F)** Dynamic light scattering (DLS) analyze the hydrated particle size of ZIF-8 and Imi@ZIF-8. **(G)** UV-vis spectrometries of imipenem, ZIF-8 and Imi@ZIF-8. **(H)** Zeta Potential values of imipenem, ZIF-8 and Imi@ZIF-8. Data are presented as means ± SD ($n$ = 3).

## Release characteristics of Imi@ZIF-8

Imipenem release from Imi@ZIF-8 was monitored at pH = 7.4 and pH = 6.5 to investigate the acidic pH response properties of Imi@ZIF-8. Specifically, 5 mL of Imi@ZIF-8 was packed into dialysis bags, which were then immersed in 50 mL of PBS solution at pH = 7.4 and pH = 6.5, respectively (Zhou et al., 2022). The dialysate was collected at 6, 12, 18, and 24 h. The absorbance value of imipenem in the dialysate at 299 nm was measured using a UV-Vis spectrophotometer to determine the cumulative release of imipenem from the solution, and the percentage release—time curves at pH = 7.4 and pH = 6.5 were plotted. All experiments were repeated three times, and the average of the experimental values was taken.

## *In vitro* antibacterial and anti-biofilm effects of Imi@ZIF-8

### Minimum inhibitory concentration (MIC)

The minimum inhibitory concentration (MIC) of imipenem and ZIF-8 against *A. baumannii* was determined using the broth dilution method. A suspension of *A. baumannii* at a concentration of 1.5 × $10^6$ CFU/mL was added to a 96-well plate. First, the imipenem solution was prepared by serial 2-fold dilution to a final concentration of 0, 0.5, 1, 2, 4, and 8 μg/mL of imipenem in each well and a volume of 100 μL. A suspension of 1.5 × $10^6$ CFU/mL of *A. baumannii* was then prepared, and 100 μL of the suspension was added to each well using a pipette. The suspensions were incubated for 16–20 h at 37°C and 5% $CO_2$. Similarly, the minimum inhibitory concentration of ZIF-8 against *A. baumannii* was tested.

### Disc diffusion method

After obtaining individual colonies, the concentration of *A. baumannii* solution was adjusted to 0.5 MCF with physiological saline, and the solution was applied to MH agar with a sterile cotton swab in a flat layer. After placing a filter paper disc on the staining medium, different contents of the imipenem, ZIF-8 and Imi@ZIF-8 were injected into the paper. The MH agar plates were incubated at 5% $CO_2$, 37°C for 24 h, and the size of the inhibition circles was observed and measured.

### Live/dead backlight bacteria assay

*A. baumannii* was incubated with the corresponding treatment group materials for 24 h, then centrifuged and washed with sterile PBS 1–2 times, the precipitation was the treated *A. baumannii*. The DMAO/EthD—III mixed fluorescent dye was prepared according to the manufacturer's instructions, and the bacteria were resuspended with the prepared fluorescent dye mixture. The two mixtures were mixed and incubated at room temperature for 15–20 min in darkness. Subsequently, 15 μL of the stained bacterial suspension was dropped onto a sterile slide and covered with an 18 mm square sterile slide. The survival of bacteria was observed under a laser confocal microscope (CLSM).

### Crystal violet staining

100 μL of drug culture solution was added to each well of a 96-well cell culture plate, and 100 μL of an overnight culture of *A. baumannii* was inoculated at 37°C for 24 h to allow the cells to adhere to the wall. PBS was used to carefully wash three times to remove planktonic bacteria, and the bacterial biofilm was fixed with a formaldehyde solution. The samples were left to dry naturally, and 200 μL of 1% crystal violet dye was added to

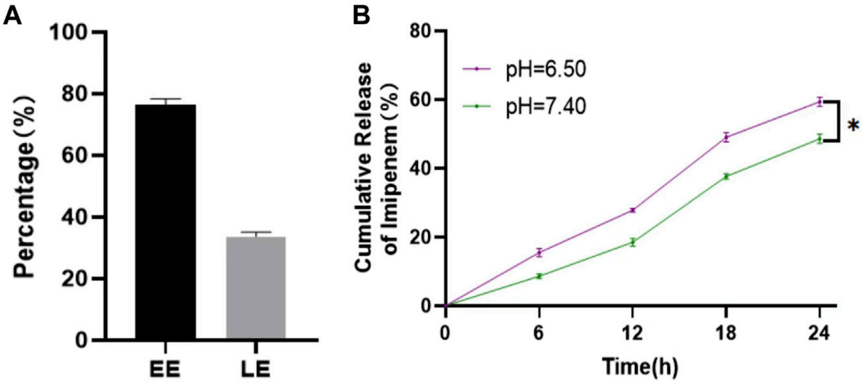

FIGURE 2
Drug loading and release rate of Imi@ZIF-8. **(A)** EE and LE of Imi@ZIF-8. **(B)** Cumulative release rates of imipenem from Imi@ZIF-8 at different pH values (6.5 and 7.4). Data are presented as means ± SD ($n$ = 3). Intergroup comparisons: $^*p < 0.05$.

each well and left for 15 min at room temperature. The stain was then washed off 2–3 times with PBS, left to dry, and lysed using 95% ethanol. Then, the solution was incubated in an incubator at 37°C for 25 min. The absorbance value of the lysate was measured using an enzyme marker (570 nm) to determine the biofilm biomass.

The percentage of biofilm eradication and inhibition was calculated as follows:

$$Biofilm\,eradication\Big/inhibition\,rate\ (\%) = \left(1 - \frac{OD\,experiment}{OD\,control}\right) \times 100\%.$$

## Confocal laser scanning microscope analysis

The biofilms of *A. baumannii* were formed in laser-scanning confocal Petri dishes, and the bacterial biofilms were fluorescently stained with a live/dead bacterial fluorescent dye kit to observe the survival of the biofilms under a CLSM.

# *In vitro* antibacterial mechanism of Imi@ZIF-8

## Reactive oxygen species (ROS) measurement

PBS, Imipenem, ZIF-8 and Imi@ZIF-8 solutions were added to the bacterial suspension ($1 \times 10^6$ CFU), co-cultured for 24 h and then resuspended in sterile saline. 1 μL of 2,7-dichlorodihydrofluorescein diacetate (DCFH-DA) fluorescent dye was added in the dark and incubated at 37°C for 1 h. The fluorescence value (excitation/emission wavelength 485/535 nm) was measured with a fluorescence enzyme marker, with the fluorescence intensity of 2,7-dichlorofluorescein (DCF) being proportional to the level of ROS (Scott et al., 1998; Hsieh et al., 2001).

## Determination of malondialdehyde (MDA)

*A. baumannii* was incubated with each group of drug culture solution for 24 h, centrifuged (12,000 rpm, 2 min), and the supernatant was discarded and resuspended in 1 mL of 2.5% (w/v) trichloroacetic acid. The solution was centrifuged (12,000 rpm, 20 min, 4°C) again to collect the supernatant, and 1 mL of 5% thiobarbituric acid (TBA) solution was added for dilution. An equal volume of 20% (w/v) TCA was added to the mixture; the reaction was carried out in a water bath at 100°C for 30 min, and the mixture was centrifuged (12,000 rpm, 20 min, 4°C). The final absorbance value was measured at 532 nm, and the MDA content (pg/mL) was calculated based on the molar extinction coefficient (1.56 $nM^{-1}cm^{-1}$).

## Construction of the mouse peritonitis model in *Acinetobacter baumannii*

The 6-week-old female BALB/c mice were randomly divided into four groups: the PBS group, imipenem group, ZIF-8 group, and Imi@ZIF-8 group. The mice were infected with an intraperitoneal injection of 150 μL containing $1 \times 10^6$ CFU/L *A. baumannii*. After 12–24 h, inflammation, necrosis and infiltration of inflammatory cells (neutrophils, lymphocytes and macrophages) were observed in the liver tissue of the mice, indicating the successful establishment of the abdominal infection mouse model. After the successful construction of the mouse model, the drug was administered once daily, and the injection continued for 3 days. The dosing concentration for each group was calculated based on the imipenem concentration, achieving a final dose of 10 mg/kg per group. After the seventh day of administration, whole blood was collected from the mice, and the liver tissues were stained with hematoxylin and eosin (HE) to observe the inflammatory infiltration and necrosis of liver tissues. Immunohistochemical staining was performed to detect the pro-inflammatory factors interleukin-6 (IL-6) and the neutrophil-specific marker Ly6G.

## Biocompatibility and biosafety of Imi@ZIF-8

The biocompatibility of Imi@ZIF-8 was assessed using the CCK-8 method. MLE-12 cells ($2 \times 10^3$/well) were inoculated in a 96-well plate and incubated for 24 h, washed 1–2 times with sterile PBS solution, and ZIF-8 was prepared at a concentration gradient of 10, 20, 40, 60, 80, 100, and 120 μg/mL (using DMEM medium as solvent). After incubation with MLE-12 cells for 24 h, CCK-8 solution (10 μL) was added to each well for 3 h, and

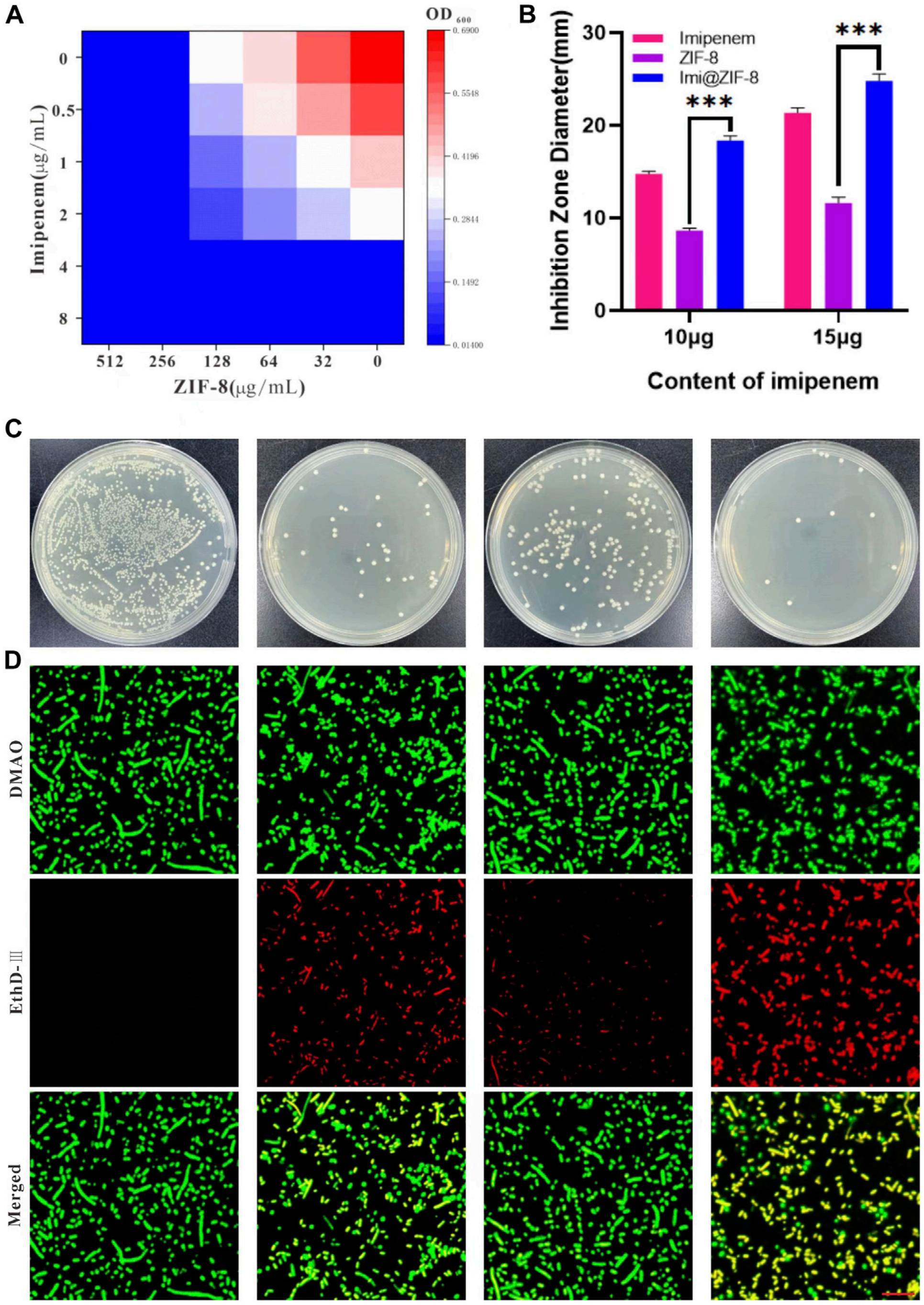

FIGURE 3
*In vitro* antibacterial effect of Imi@ZIF-8. **(A)** Different concentration of Imipenem and ZIF-8 inhibited on the growth of *A. baumannii*. **(B)** Corresponding inhibition zone diameters of imipenem, ZIF-8 and Imi@ZIF-8 against *A. baumannii*. **(C)** Photographs of agar plates showing the antibacterial activity for PBS, imipenem, ZIF-8 and Imi@ZIF-8 against *A. baumannii*. **(D)** CLSM imaging of death/live staining after *A. baumannii* exposure to various treatments (PBS, imipenem, ZIF-8 and Imi@ZIF-8) for 24 h. Scale bar is 20 μm. Data are presented as mean ± SD ($n = 3$). Compared to ZIF-8: $***p < 0.001$.

the absorbance value was measured at 450 nm. Healthy female BALB/c mice at 6 weeks of age were randomly divided into four groups and injected with PBS, Imipenem, ZIF-8 or Imi@ZIF-8 *via* the tail vein. After 1 week, whole blood was collected, and blood biochemical parameters (RBC, WBC, PLT, CRP, ALT, AST, BUN, and CREA) were measured. Mice were executed by cervical dislocation. The major organs (heart, liver, spleen, lungs and kidneys) were taken for hematoxylin and eosin (HE) staining, and the lesions were observed under the microscope.

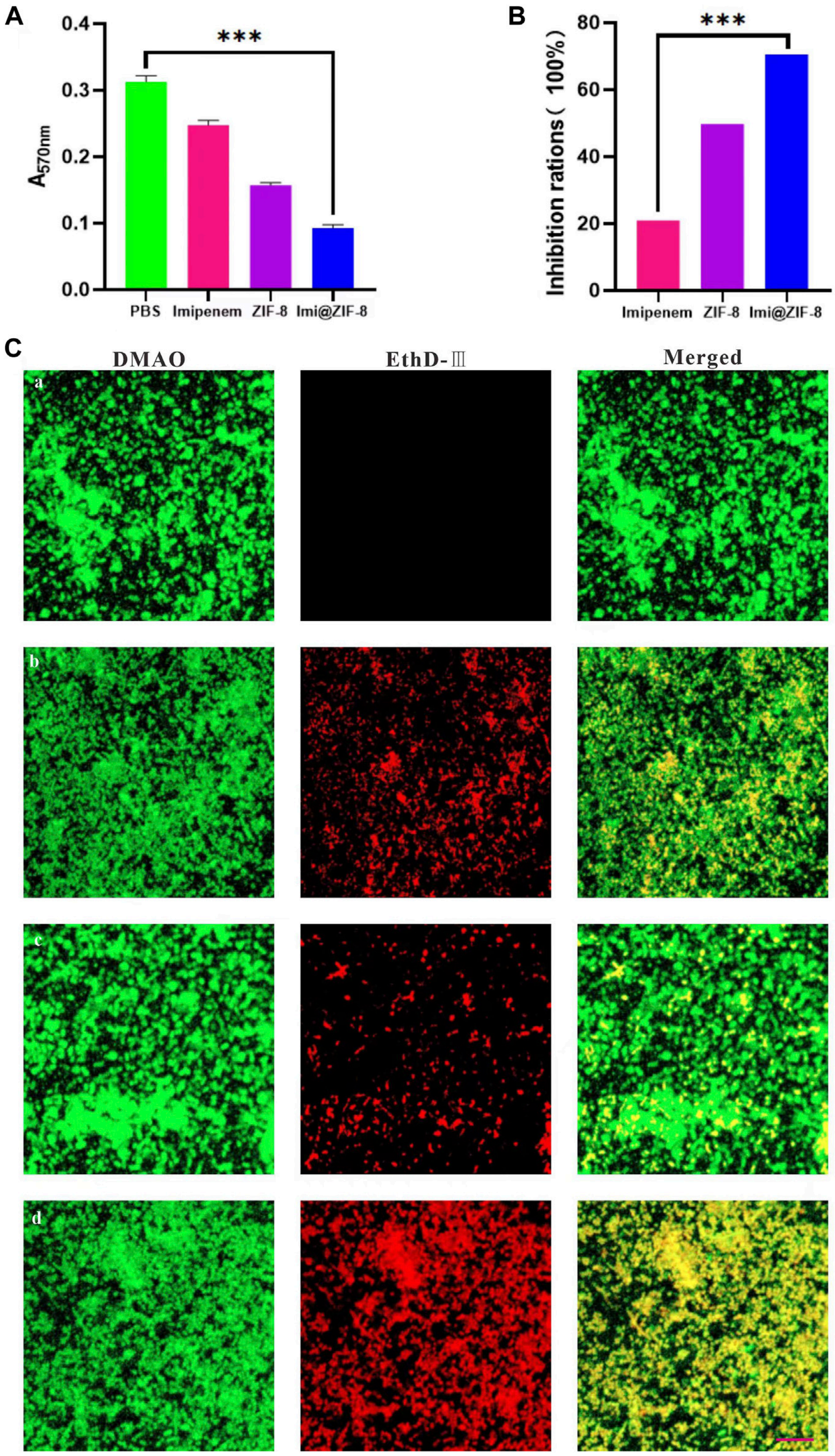

FIGURE 4
Influence of Imi@ZIF-8 on the biofilm formation and damage of *A. baumannii*. **(A)** CV staining analysis after receiving different treatments for 24 h. The absorbance value was detected using an enzyme marker (570 nm) to reflect biofilm formation. **(B)** CV staining analysis. Relative percentage of biofilm inhibition. **(C)** CLSM images of *A. baumannii* biofilms treated with various treatments (PBS, imipenem, ZIF-8, or Imi@ZIF-8) for 24 h. Scale bar is 20 μm. Data are indicated as mean ± SD ($n = 3$). Compared to the PBS group: ***$p < 0.001$; Compared to the imipenem group: ***$p < 0.001$.

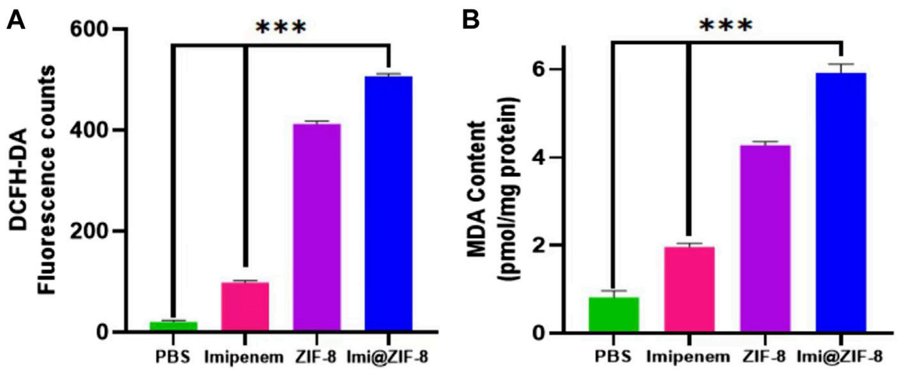

FIGURE 5
Antibacterial mechanism of Imi@ZIF-8. **(A)** The fluorescence intensity of *A. baumannii* was measured using a fluorometer to reflect ROS formation. **(B)** MDA contents of *A. baumannii* treated with respective materials (PBS, imipenem, ZIF-8 or Imi@ZIF-8) for 24 h represents the extent of membrane damage. Data are presented as mean ± SD ($n$ = 3). Compared to the PBS group and the imipenem group: ***$p < 0.001$.

## Statistical analysis

All data were expressed as mean ± standard deviation, and statistical analysis was performed using SPSS 20.0 software. Differences between groups were analyzed using oneway ANOVA, followed by further analysis using Tukey's post-test (*$p < 0.05$, **$p < 0.01$, ***$p < 0.001$).

# Results and discussion

## Construction and characterization of the Imi@ZIF-8 nano-drug delivery system

In this study, the new antibacterial nano drug delivery system Imi@ZIF-8 was designed and synthesized. The particle size, morphology and dispersion of the prepared nano-drug delivery system were studied by TEM. The positively-charged ZIF-8 synthesized in this experiment was spherical, with an average particle size of about 80 nm and uniform distribution (Figure 1A). The overall morphology of the imipenem-loaded Imi@ZIF-8 showed no significant change, with a spherical shape and a particle size of around 80 nm (Figures 1B, E). SEM confirmed the TEM results, showing both ZIF-8 and Imi@ZIF-8 with particle sizes of around 80 nm and good dispersion (Figures 1C, D). DLS allows analysis of the hydrated particle size of the nanoparticles, complementing the TEM results on nanoparticle size. As shown in Figure 1F, the average hydrated particle size of ZIF-8 and Imi@ZIF-8 was about 80 nm. Moreover, the ζ-potential analysis of imipenem, ZIF-8, and Imi@ZIF-8 was performed separately, as displayed in Figure 1H. The ζ-potential of ZIF-8 after PEI modification showed a positive charge of 28.59 ± 1.39 mV, while imipenem was negatively charged (−8.57 ± 0.59 mV). The zeta potential of Imi@ZIF-8 after loading imipenem was 21.35 ± 1.35 mV. This lower value indicated that ZIF-8 was successfully loaded with imipenem and that the Imi@ZIF-8 nano-delivery system had good stability and dispersibility. Subsequently, UV-vis spectroscopy was performed to verify the encapsulation of imipenem in the ZIF-8 nanoparticles. As illustrated in Figure 1G, ZIF-8 showed a characteristic absorption peak at 216.5 nm, while imipenem had a characteristic absorption peak at 299 nm. Imi@ZIF-8 exhibited both characteristic absorption peaks in UV-vis, corresponding to imipenem (299 nm) and ZIF-8 (216.5 nm), indicating that ZIF-8 was successfully loaded with imipenem. These results provide strong evidence for the successful preparation of the Imi@ZIF-8 nanodrug delivery system.

## *In vitro* release study of the Imi@ZIF-8 nano drug delivery system

ZIF-8 is an excellent nano-delivery vehicle due to its large specific surface area and porous structure, and the ZIF-8 nanoparticles were further modified to be positively charged, improving imipenem release. EE and LE of imipenem were determined using a UV-vis spectrophotometer at 299 nm. As shown in Figure 2A, the EE and LE of imipenem in the nano-delivery system were 76.38% ± 2.05% and 33.68% ± 1.53%, respectively. To investigate the pH response of the drug delivery system, the release of imipenem from Imi@ZIF-8 in neutral (pH = 7.4) and acidic environments (pH = 6.5) were evaluated at different time periods. Due to the anaerobic fermentation of bacteria at the site of infection, large amounts of organic acids are produced, creating an acidic microenvironment (Qiao et al., 2019). In this experiment, pH = 6.5 was used to simulate the acidic microenvironment of bacterial infection *in vivo*. The 24 h cumulative release efficiency of imipenem was 48.58% ± 1.49% at pH 7.4% and 59.36% ± 1.39% at pH 6.5 (Figure 2B), indicating that the acidic microenvironment resulted in a higher imipenem release rate. The facilitated release of imipenem from the nano-delivery system at the site of bacterial infection leads to superior antibacterial activity. This facilitated release is due to the protonation of the 2-methylimidazole ligand in ZIF-8 under acidic conditions, resulting in the breaking of the ligand bond between zinc and 2-methylimidazole, releasing imipenem from the nano-loaded system (Zheng et al., 2016; Soomro et al., 2019). The above experimental results indicated that ZIF-8 is a good drug delivery

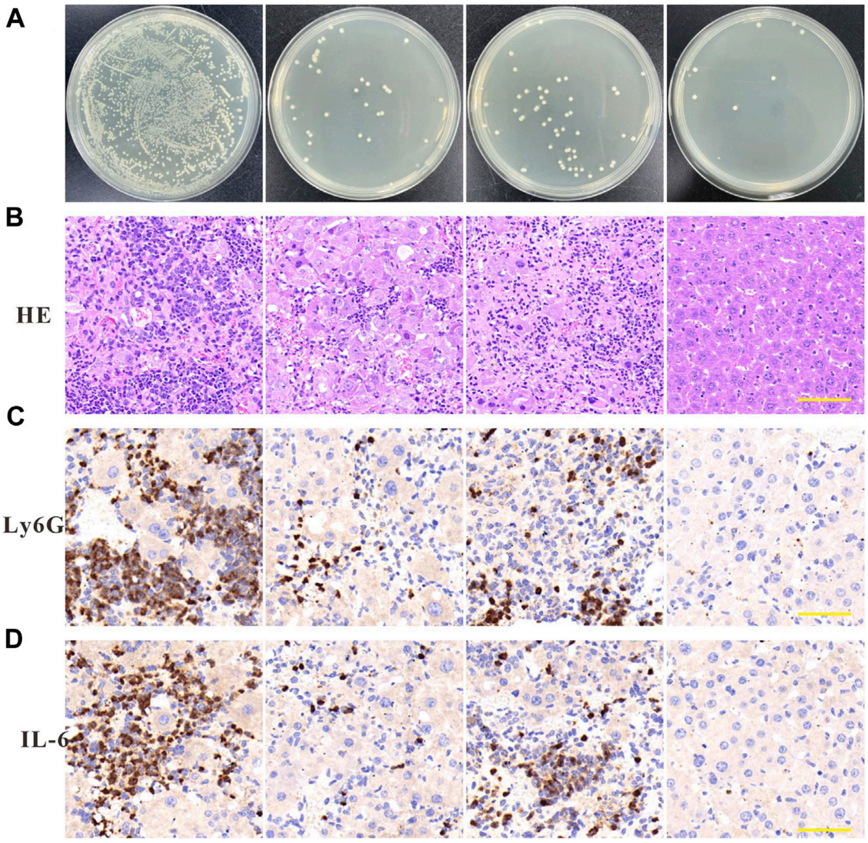

FIGURE 6
Anti-infection effects of Imi@ZIF-8 *in vivo*. After successful establishment of the mouse peritonitis model in *A. baumannii*, BALB/c mice were intraperitoneal injected with PBS, imipenem, ZIF-8, or Imi@ZIF-8 (10 mg imi/kg). **(A)** Bacterial counting of liver tissues after treated with the respective materials. Data are indicated as means ± SD ($n$ = 3). **(B)** Representative images of liver tissues after H&E staining at 7 days after intraperitoneal injection of different treatments. Scale bar is 100 μm. **(C)** Immunohistochemistry staining of Ly6G in liver tissues at 7 days after intraperitoneal injected with PBS, imipenem, ZIF-8, or Imi@ZIF-8, respectively. **(D)** Immunohistochemistry staining of IL-6 in liver tissues. Scale bar is 100 μm.

vehicle, and Imi@ZIF-8 is responsive to acidic microenvironments, providing superior antibacterial drug release at the site of bacterial infection.

## *In vitro* antibacterial and anti-biofilm effects of Imi@ZIF-8

MIC is a measure of the antimicrobial performance of an antimicrobial agent. A broth dilution method was used to determine the MIC value of the free drugs. As shown in Figure 3A, the MIC value of imipenem and ZIF-8 against *A. baumannii* was 4 μg/mL and 256 μg/mL, respectively. Based on the results, the fractional inhibitory concentration (FIC) index of imipenem and ZIF-8 against *A. baumannii* was calculated to be less than 0.5, which illustrates the synergistic antibacterial effect of imipenem and ZIF-8 against *A. baumannii*. Furthermore, the inhibition activity of free imipenem, ZIF-8 and Imi@ZIF-8 were compared using the disc diffusion method, showing that Imi@ZIF-8 had the largest inhibition circle diameter at similar levels. The diameters of the inhibition circles of 15 μg Imi@ZIF-8, Imipenem and ZIF-8 were 24.81 ± 0.73 mm, 21.39 ± 0.51 mm and 11.64 ± 0.63 mm, respectively (Figure 3B). Figure 3C shows the bacterial counts of *A. baumannii* after 24 h treatment with PBS, ZIF-8, imipenem, and Imi@ZIF-8. A lower number of colonies was observed in the ZIF-8 group compared to the PBS group, but the inhibition effect was not significant. In contrast, the bacterial growth in the free imipenem and Imi@ZIF-8 groups was significantly inhibited, with the Imi@ZIF-8 group showing the most obvious effect. The above results indicate that ZIF-8 can enhance the antibacterial ability of imipenem against *A. baumannii*. Subsequently, the DMAO/EthD-III live/dead bacterial staining kit was used to further observe the bacterial survival status of the free drug and Imi@ZIF-8 groups. Each treatment group underwent live-dead fluorescence staining and was observed under a CLSM. The DMAO fluorescent dye stains dead and alive bacteria green, whereas EthD-III only stains dead bacteria with a red fluorescent dye. The PBS group showed basically no red fluorescence signal, indicating that *A. baumannii* was alive (Figure 3D). However, the ZIF-8, Imipenem, and Imi@ZIF-8 treated groups demonstrated an increasing intensity of red fluorescence, indicating increasing *A. baumannii* death. After 24 h of Imi@ZIF-8 treatment, nearly all *A.*

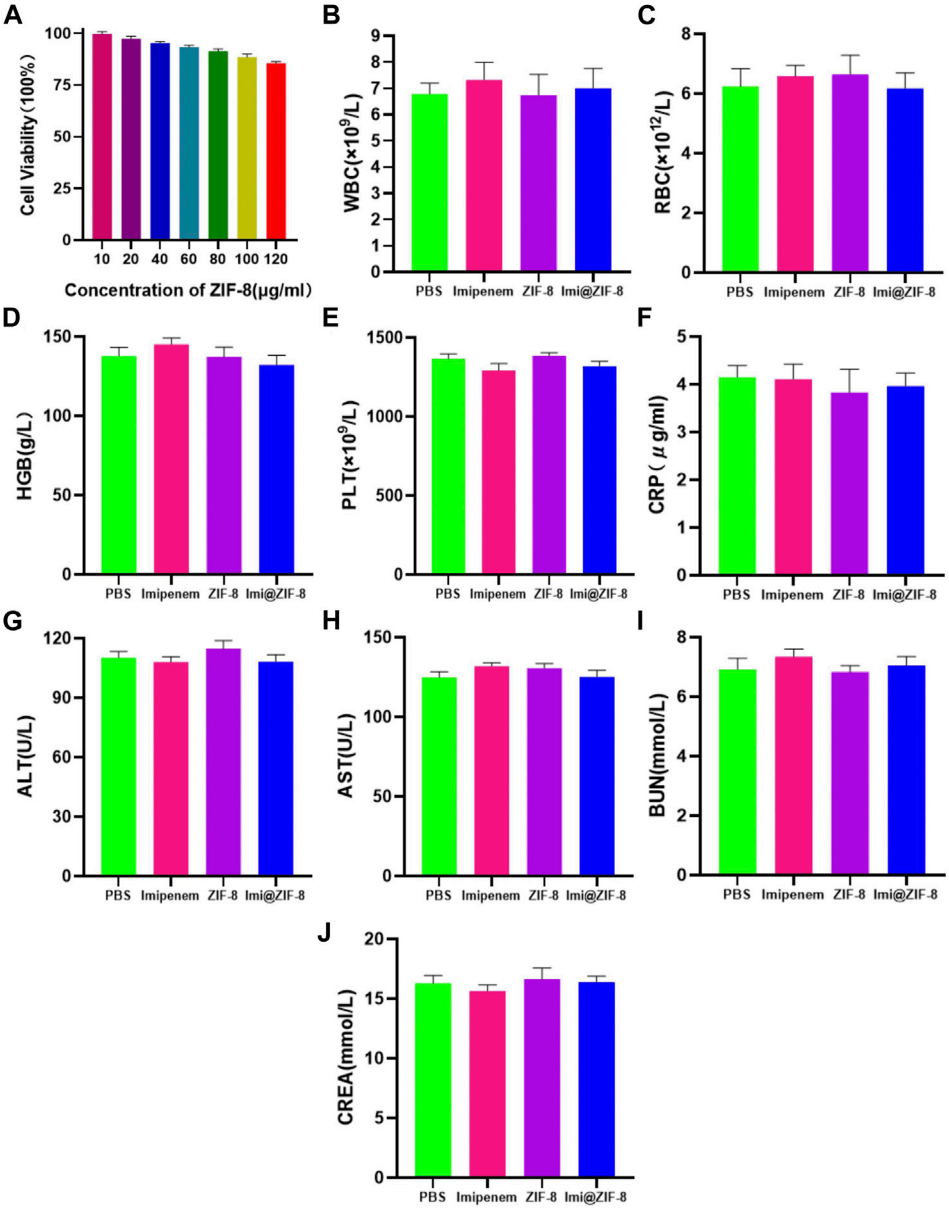

FIGURE 7
The toxicity assessment of Imi@ZIF-8. **(A)** MLE-12 cells was treated with various concentration of ZIF-8 for 24 h; the cell viability (%) was assayed by CCK-8. **(B–J)** Blood routine and blood biochemical indices of mice at 7 days after intraperitoneal injection of PBS, imipenem, ZIF-8 and Imi@ZIF-8. Data are indicated as means ± SD (*n* = 3).

*baumannii* were dead. In summary, ZIF-8 and imipenem exerted synergistic antibacterial effects against *A. baumannii*, with the Imi@ZIF-8 nano-delivery system being more effective than free imipenem and ZIF-8. Therefore, the nano-delivery system was effective against *A. baumannii* infection.

Bacterial biofilms are associated with bacterial drug resistance, and the ability to inhibit biofilm formation is an important indicator in determining the clinical application of antimicrobial agents (Sharahi et al., 2019). Crystalline violet staining (CV) is a commonly used assay for early and mid-stage biofilm formation, with higher absorbance values indicating higher amounts of biofilm production by bacteria. As shown in Figure 4A, the absorbance value of the PBS group at 570 nm after 24 h of treatment is 0.313 ± 0.0097, while the Imi@ZIF-8 group had an absorbance value of only 0.092 ± 0.006; Figure 4B shows the percentage of biofilm inhibition of *A. baumannii* by each treatment group after 24 h of treatment. The Imi@ZIF-8 group demonstrated a biofilm inhibition rate of about 71%, much higher than that of the imipenem group (20.93%) and the ZIF-8 group (49.74%), indicating that Imi@ZIF-8 exerted the strongest inhibitory effect on *A. baumannii* biofilm formation. To investigate the killing ability of the Imi@ZIF-8 nano-delivery system on *A. baumannii* biofilms, the “Live/Dead Bacterial Staining Kit” was used, and the survival of the biofilms was assessed under CLSM. The strongest red fluorescence was observed in the Imi@ZIF-8 group, indicating a basically all-dead biofilm, showing a

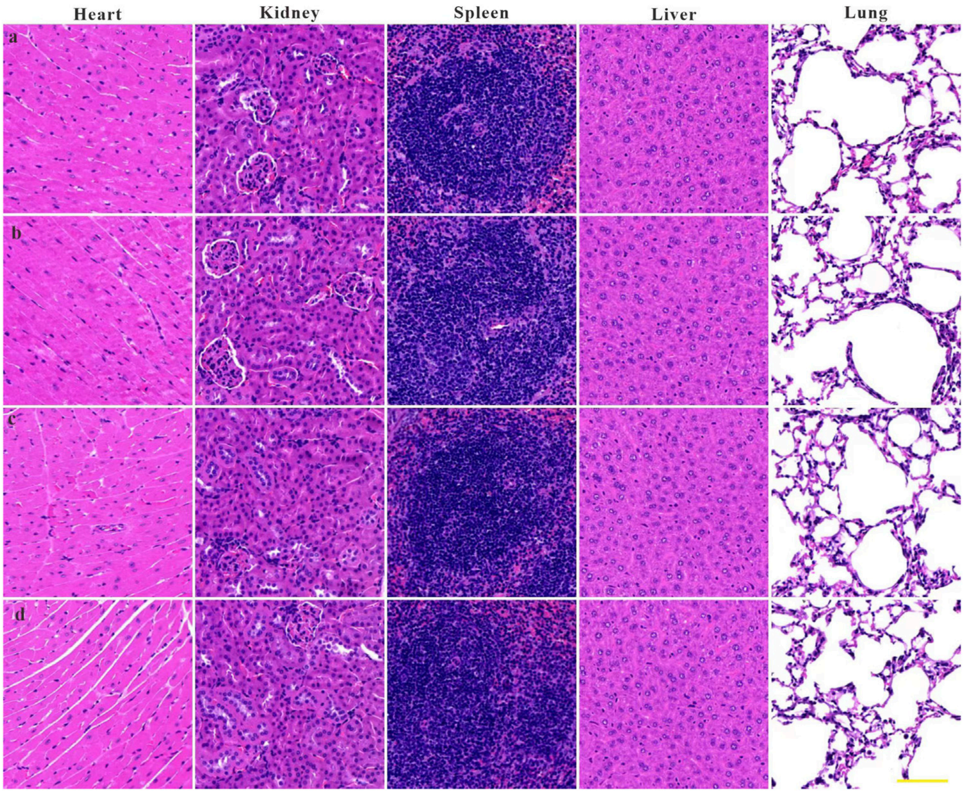

FIGURE 8
Histological evaluation of heart, liver, spleen, lung, and kidney samples from mice at 7 days upon administration of **(A)** PBS, **(B)** imipenem, **(C)** ZIF-8 and **(D)** Imi@ZIF-8. Scale bar is 100 μm.

significantly stronger killing effect on *A. baumannii* than the PBS, imipenem and ZIF-8 groups (Figure 4C).

## Antimicrobial mechanism of Imi@ZIF-8

Although small amounts of ROS are important for maintaining the life cycle of cells, excessive ROS can lead to oxidative stress, disrupting the integrity of bacterial cell membranes and interfering with a range of normal physiological activities, ultimately inducing bacterial death (Hui et al., 2020). Therefore, a DCFH-DA fluorescent probe was used to detect intracellular ROS production in *A. baumannii*. As shown in Figure 5A, the four groups, PBS, Imipenem, ZIF-8 and Imi@ZIF-8, showed increasing ROS production by *A. baumannii*, with the Imi@ZIF-8 group inducing a significantly higher amount of ROS production than the other treatment groups. In addition, nanomaterials may trigger lipid oxidation reactions in bacteria, and the MDA method was used to detect the lipid oxidation levels in *A. baumannii* to reflect the extent of bacterial damage. A significant difference in MDA content was observed between the different treatment groups (Figure 5B), with the highest MDA content produced by *A. baumannii* after Imi@ZIF-8 treatment. These findings suggested that Imi@ZIF-8 induced the most severe damage to *A. baumannii*.

The above results indicated that the Imi@ZIF-8 nano-delivery system effectively eliminated *A. baumannii* by interfering with the normal physiological activities of bacterial cells, catalyzing the production of ROS, inducing lipid oxidation and other antibacterial mechanisms.

## *In vivo* anti-infective effect of Imi@ZIF-8

To further investigate the *in vivo* anti-amastigotes effect of Imi@ZIF-8, a celiac disease mouse model was constructed by infection with *A. baumannii*. The mice with peritonitis were randomly divided into the PBS group, imipenem group, ZIF-8 group and Imi@ZIF-8 treatment groups. After 3 days of continuous tail vein administration, the mice were removed and executed, and the liver tissues were collected under aseptic conditions for bacterial counting. The different treatment groups showed significantly different results. Compared with the other treatment groups, the Imi@ZIF-8 group had the lowest number of *A. baumannii* in the liver tissues, followed by the imipenem group, the ZIF-8 group, and the PBS group (Figure 6A). The pathological hepatic changes in mice with peritonitis were observed by HE staining. Furthermore, the HE section results also provided good evidence of the *in vivo* antibacterial effect of Imi@ZIF-8. As shown in Figure 6B, severe inflammatory cell infiltration and congestion were visible in the liver tissue sections of the PBS group, demonstrating a significant inflammatory response. However, the liver tissue in the Imi@ZIF-8 group was significantly milder than the other treatment groups, with no significant inflammatory cell infiltration and mostly normal liver morphology. Among all the treatments, Imi@ZIF-8 was the most effective in combating *A. baumannii* infection. Subsequently, immunohistochemical staining was used to detect inflammation in the liver tissue following *A. baumannii* infection by determining the expression levels of IL-6 and Ly6G, which was positive when brownish-yellow particles were present. The immunohistochemical images revealed that the increased expression of IL-6 and Ly6G in the imipenem, ZIF-8 and PBS groups, in order, which were significantly higher than those in Imi@ZIF-8 group (Figures 6C, D). These results indicated that Imi@ZIF-8 effectively inhibited the infiltration and inflammatory response of leukocytes and had excellent therapeutic efficacy in mice with celiac disease caused by *A. baumannii*. Collectively, the above *in vivo* and *in vitro* results demonstrated that Imi@ZIF-8 could be an effective novel nano-delivery system against *A. baumannii*.

### Biocompatibility and biosafety of Imi@ZIF-8

To investigate the feasibility of ZIF-8 as a nanodrug carrier for antimicrobial therapy, the biocompatibility and biosafety of the Imi@ZIF-8 nanodrug delivery system were analyzed. MLE-12 cells were treated with different concentrations (10, 20, 40, 60, 80, 100, and 120 μg/mL) of ZIF-8 for 24 h, and the cell viability of the MLE-12 cells was assayed using the CCK-8 method. The results are shown in Figure 7A. MLE-12 cell activity decreased as the concentration of ZIF-8 was increased, but its cell survival rate remained higher than 80%, indicating the good biocompatibility of Imi@ZIF-8. These results have laid a foundation for clinical antibacterial treatment. To assess the *in vivo* safety and toxic effects of ZIF-8 and Imi@ZIF-8, female BALA/c mice were randomly divided into four groups and injected with PBS, Imipenem, ZIF-8, and Imi@ZIF-8, respectively. Hematological parameters were measured to detect the toxicity of the nanomaterials in mice 1 week after tail vein administration, including whole blood parameters such as white blood cells (WBC), red blood cells (RBC), hemoglobin (HGB), and platelets (PLT), C-reactive protein (CRP), liver function parameters alanine aminotransferase (ALT) and glutathione aminotransferase (AST), and renal function parameters such as blood urea nitrogen (BUN), and creatinine (CREA). As shown in Figures 7B–J, no significant difference was observed in all hematological indicators between the groups, indicating no significant toxic effect from ZIF-8 and Imi@ZIF-8. In addition, the pathological changes in the major organs (heart, liver, spleen, lung and kidney) were assessed by HE staining to further clarify the *in vivo* toxicity of ZIF-8 and Imi@ZIF-8, as shown in Figure 8, no inflammation, fibrosis, necrosis or histological abnormalities were observed. The results suggest that ZIF-8 and Imi@ZIF-8 induce no significant damage to the heart, liver, spleen, lungs and kidneys and that they have good biosafety and low toxic side effects. In conclusion, the Imi@ZIF-8 nano-delivery system has good biocompatibility and biosafety.

## Conclusion

The above experimental studies demonstrated the promising potential of our novel antimicrobial nano-delivery system (Imi@ZIF-8) in the treatment of *A. baumannii* infections, showing good biocompatibility, high biosafety, pH acid responsiveness and efficient antimicrobial action. Due to its response to acidic pH, the Imi@ZIF-8 nano-delivery system features an improved release of the loaded imipenem at the acidic bacterial infection sites. Therefore, a synergistic antibacterial effect is achieved between the ZIF-8 and imipenem in the nano-delivery system, further enhancing its antibacterial activity against *A. baumannii*. When the loaded imipenem concentration reaches 20 μg/mL, Imi@ZIF-8 is highly effective against *A. baumannii in vitro*. Moreover, Imi@ZIF-8 exerts excellent therapeutic efficacy against *A. baumannii* at imipenem concentrations of 10 mg/kg and facilitates the inhibition of inflammatory response and leukocyte infiltration in mice with peritonitis, which promotes tissue recovery after bacterial infection. Overall, the Imi@ZIF-8 nano-delivery system provides a new clinical treatment strategy for the antimicrobial treatment of *A. baumannii* and provides a strong foundation for nano-antimicrobial therapy. More studies on the preventive effect of this nanomaterial on bacterial infections can be conducted in the future.

## Data availability statement

The original contributions presented in the study are included in the article/Supplementary Material, further inquiries can be directed to the corresponding author.

## Ethics statement

The animal study was reviewed and approved by Ethics Committee of The Third Affiliated Hospital of Xinxiang Medical University.

## Author contributions

GSM and LXS conceived and designed the project. NXQ supervised this project. LXS conducted the experiments and analyzed experimental data. FMM and HLWH performed in vivo mice test. LH performed the statistical analysis. GSM wrote the manuscript, and all authors discussed the results and proofread this paper.

## Conflict of interest

The authors declare that the research was conducted in the absence of any commercial or financial relationships that could be construed as a potential conflict of interest.

## Publisher's note

# References

Abdelhamid, H. N. (2021). Zeolitic imidazolate frameworks (ZIF-8) for biomedical applications: A review. *Curr. Med. Chem.* 28 (34), 7023–7075. doi:10.2174/0929867328666210608143703

Akgöl, S., Ulucan-Karnak, F., Kuru, C., and Kuşat, K. (2021). The usage of composite nanomaterials in biomedical engineering applications. *Biotechnol. Bioeng.* 118 (8), 2906–2922. doi:10.1002/bit.27843

Baym, M., Stone, L. K., and Kishony, R. (2016). Multidrug evolutionary strategies to reverse antibiotic resistance. *Science* 351 (6268), aad3292. doi:10.1126/science.aad3292

Betrosian, A. P., Frantzeskaki, F., Xanthaki, A., and Douzinas, E. E. (2008). Efficacy and safety of high-dose ampicillin/sulbactam vs. colistin as monotherapy for the treatment of multidrug resistant Acinetobacter baumannii ventilator-associated pneumonia. *J. Infect.* 56 (6), 432–436. doi:10.1016/j.jinf.2008.04.002

Chang, R. Y. K., Nang, S. C., Chan, H. K., and Li, J. (2022). Novel antimicrobial agents for combating antibiotic-resistant bacteria. *Adv. Drug Deliv. Rev.* 187, 114378. doi:10.1016/j.addr.2022.114378

Chen, W. (2020). Host-pathogen interactions in acinetobacter baumannii infection: Recent advances and future challenges. *Future Microbiol.* 15, 841–845. doi:10.2217/fmb-2020-0032

Cheng, X., Pei, X., Xie, W., Chen, J., Li, Y., Wang, J., et al. (2022). pH-triggered size-tunable silver nanoparticles: Targeted aggregation for effective bacterial infection therapy. *Small* 18 (22), e2200915. doi:10.1002/smll.202200915

Chu, H., Zhao, L., Wang, M., Liu, Y., Gui, T., and Zhang, J. (2013). Sulbactam-based therapy for acinetobacter baumannii infection: A systematic review and meta-analysis. *Braz J. Infect. Dis.* 17 (4), 389–394. doi:10.1016/j.bjid.2012.10.029

Dehbanipour, R., and Ghalavand, Z. (2022). Acinetobacter baumannii: Pathogenesis, virulence factors, novel therapeutic options and mechanisms of resistance to antimicrobial agents with emphasis on tigecycline. *J. Clin. Pharm. Ther.* 47 (11), 1875–1884. doi:10.1111/jcpt.13787

Díez-Pascual, A. M. (2020). Antibacterial action of nanoparticle loaded nanocomposites based on graphene and its derivatives: A mini-review. *Int. J. Mol. Sci.* 21 (10), 3563. doi:10.3390/ijms21103563

Fishbain, J., and Peleg, A. Y. (2010). Treatment of acinetobacter infections. *Clin. Infect. Dis.* 51 (1), 79–84. doi:10.1086/653120

Godoy-Gallardo, M., Eckhard, U., Delgado, L. M., de Roo Puente, Y. J. D., Hoyos-Nogués, M., Gil, F. J., et al. (2021). Antibacterial approaches in tissue engineering using metal ions and nanoparticles: From mechanisms to applications. *Bioact. Mater* 6 (12), 4470–4490. doi:10.1016/j.bioactmat.2021.04.033

Harding, C. M., Hennon, S. W., and Feldman, M. F. (2018). Uncovering the mechanisms of Acinetobacter baumannii virulence. *Nat. Rev. Microbiol.* 16 (2), 91–102. doi:10.1038/nrmicro.2017.148

Hsieh, C. C., Yen, M. H., Yen, C. H., and Lau, Y. T. (2001). Oxidized low density lipoprotein induces apoptosis via generation of reactive oxygen species in vascular smooth muscle cells. *Cardiovasc Res.* 49 (1), 135–145. doi:10.1016/s0008-6363(00)00218-2

Huang, R., Zhang, C., Bu, Y., Li, Z., Zheng, X., Qiu, S., et al. (2021). A multifunctional nano-therapeutic platform based on octahedral yolk-shell Au NR@CuS: Photothermal/photodynamic and targeted drug delivery tri-combined therapy for rheumatoid arthritis. *Biomaterials* 277, 121088. doi:10.1016/j.biomaterials.2021.121088

Hui, S., Liu, Q., Huang, Z., Yang, J., Liu, Y., and Jiang, S. (2020). Gold nanoclusters-decorated zeolitic imidazolate frameworks with reactive oxygen species generation for photoenhanced antibacterial study. *Bioconjug Chem.* 31 (10), 2439–2445. doi:10.1021/acs.bioconjchem.0c00485

Isler, B., Doi, Y., Bonomo, R. A., and Paterson, D. L. (2019). New treatment options against carbapenem-resistant acinetobacter baumannii infections. *Antimicrob. Agents Chemother.* 63 (1), e01110–e01118. doi:10.1128/aac.01110-18

Jiang, S., Lin, K., and Cai, M. (2020). ZnO nanomaterials: Current advancements in antibacterial mechanisms and applications. *Front. Chem.* 8, 580. doi:10.3389/fchem.2020.00580

Jiang, Y., Ding, Y., Wei, Y., Jian, C., Liu, J., and Zeng, Z. (2022). Carbapenem-resistant acinetobacter baumannii: A challenge in the intensive care unit. *Front. Microbiol.* 13, 1045206. doi:10.3389/fmicb.2022.1045206

Kalva, S. K., Sánchez-Iglesias, A., Deán-Ben, X. L., Liz-Marzán, L. M., and Razansky, D. (2022). Rapid volumetric optoacoustic tracking of nanoparticle kinetics across murine organs. *ACS Appl. Mater Interfaces* 14 (1), 172–178. doi:10.1021/acsami.1c17661

Lian, Z., Lu, C., Zhu, J., Zhang, X., Wu, T., Xiong, Y., et al. (2022). Mo@ZIF-8 nanozyme preparation and its antibacterial property evaluation. *Front. Chem.* 10, 1093073. doi:10.3389/fchem.2022.1093073

Liu, J., Shu, Y., Zhu, F., Feng, B., Zhang, Z., Liu, L., et al. (2021). Comparative efficacy and safety of combination therapy with high-dose sulbactam or colistin with additional antibacterial agents for multiple drug-resistant and extensively drug-resistant acinetobacter baumannii infections: A systematic review and network meta-analysis. *J. Glob. Antimicrob. Resist* 24, 136–147. doi:10.1016/j.jgar.2020.08.021

Liu, Y., Xu, Z., Qiao, M., Cai, H., and Zhu, Z. (2022). Metal-based nano-delivery platform for treating bone disease and regeneration. *Front. Chem.* 10, 955993. doi:10.3389/fchem.2022.955993

Modi, S., Inwati, G. K., Gacem, A., Saquib Abullais, S., Prajapati, R., Yadav, V. K., et al. (2022). Nanostructured antibiotics and their emerging medicinal applications: An overview of nanoantibiotics. *Antibiot. (Basel)* 11 (6), 708. doi:10.3390/antibiotics11060708

Nazli, A., He, D. L., Liao, D., Khan, M. Z. I., Huang, C., and He, Y. (2022). Strategies and progresses for enhancing targeted antibiotic delivery. *Adv. Drug Deliv. Rev.* 189, 114502. doi:10.1016/j.addr.2022.114502

Nowak, P., and Paluchowska, P. (2016). Acinetobacter baumannii: Biology and drug resistance - role of carbapenemases. *Folia Histochem Cytobiol.* 54 (2), 61–74. doi:10.5603/FHC.a2016.0009

Papp-Wallace, K. M., Endimiani, A., Taracila, M. A., and Bonomo, R. A. (2011). Carbapenems: Past, present, and future. *Antimicrob. Agents Chemother.* 55 (11), 4943–4960. doi:10.1128/aac.00296-11

Qiao, Z., Yao, Y., Song, S., Yin, M., and Luo, J. (2019). Silver nanoparticles with pH induced surface charge switchable properties for antibacterial and antibiofilm applications. *J. Mater Chem. B* 7 (5), 830–840. doi:10.1039/c8tb02917b

Rodloff, A. C., Goldstein, E. J., and Torres, A. (2006). Two decades of imipenem therapy. *J. Antimicrob. Chemother.* 58 (5), 916–929. doi:10.1093/jac/dkl354

Saipriya, K., Swathi, C. H., Ratnakar, K. S., and Sritharan, V. (2020). Quorum-sensing system in acinetobacter baumannii: A potential target for new drug development. *J. Appl. Microbiol.* 128 (1), 15–27. doi:10.1111/jam.14330

Scott, J. A., Weir, M. L., Wilson, S. M., Xuan, J. W., Chambers, A. F., and McCormack, D. G. (1998). Osteopontin inhibits inducible nitric oxide synthase activity in rat vascular tissue. *Am. J. Physiol.* 275 (6), H2258–H2265. doi:10.1152/ajpheart.1998.275.6.H2258

Shan, W., Kan, J., Cai, X., and Yin, M. (2022). Insights into mucoid acinetobacter baumannii: A review of microbiological characteristics, virulence, and pathogenic mechanisms in a threatening nosocomial pathogen. *Microbiol. Res.* 261, 127057. doi:10.1016/j.micres.2022.127057

Sharahi, J. Y., Azimi, T., Shariati, A., Safari, H., Tehrani, M. K., and Hashemi, A. (2019). Advanced strategies for combating bacterial biofilms. *J. Cell Physiol.* 234, 14689–14708. doi:10.1002/jcp.28225

Singh, K. R. B., Rathee, S., Nagpure, G., Singh, J., and Singh, R. P. (2022). Smart and emerging nanomaterials-based biosensor for SARS-CoV-2 detection. *Mater Lett.* 307, 131092. doi:10.1016/j.matlet.2021.131092

Skariyachan, S., Taskeen, N., Ganta, M., and Venkata Krishna, B. (2019). Recent perspectives on the virulent factors and treatment options for multidrug-resistant Acinetobacter baumannii. *Crit. Rev. Microbiol.* 45 (3), 315–333. doi:10.1080/1040841x.2019.1600472

Soomro, N. A., Wu, Q., Amur, S. A., Liang, H., Ur Rahman, A., Yuan, Q., et al. (2019). Natural drug physcion encapsulated zeolitic imidazolate framework, and their application as antimicrobial agent. *Colloids Surf. B Biointerfaces* 182, 110364. doi:10.1016/j.colsurfb.2019.110364

Tacconelli, E., Carrara, E., Savoldi, A., Harbarth, S., Mendelson, M., Monnet, D. L., et al. (2018). Discovery, research, and development of new antibiotics: The WHO priority list of antibiotic-resistant bacteria and tuberculosis. *Lancet Infect. Dis.* 18 (3), 318–327. doi:10.1016/s1473-3099(17)30753-3

Tan, L., Yuan, G., Wang, P., Feng, S., Tong, Y., and Wang, C. (2022). pH-responsive Ag-Phy@ZIF-8 nanoparticles modified by hyaluronate for efficient synergistic bacteria disinfection. *Int. J. Biol. Macromol.* 206, 605–613. doi:10.1016/j.ijbiomac.2022.02.097

Vangijzegem, T., Stanicki, D., and Laurent, S. (2019). Magnetic iron oxide nanoparticles for drug delivery: Applications and characteristics. *Expert Opin. Drug Deliv.* 16 (1), 69–78. doi:10.1080/17425247.2019.1554647

Wang, Y., Ding, X., Chen, Y., Guo, M., Zhang, Y., Guo, X., et al. (2016). Antibiotic-loaded, silver core-embedded mesoporous silica nanovehicles as a synergistic antibacterial agent for the treatment of drug-resistant infections. *Biomaterials* 101, 207–216. doi:10.1016/j.biomaterials.2016.06.004

Wang, Q., Sun, Y., Li, S., Zhang, P., and Yao, Q. (2020). Synthesis and modification of ZIF-8 and its application in drug delivery and tumor therapy. *RSC Adv.* 10 (62), 37600–37620. doi:10.1039/d0ra07950b

Whiteway, C., Breine, A., Philippe, C., and Van der Henst, C. (2022). Acinetobacter baumannii. *Trends Microbiol.* 30 (2), 199–200. doi:10.1016/j.tim.2021.11.008

Yu, J., Chu, X., Cai, Y., Tong, P., and Yao, J. (2014). Preparation and characterization of antimicrobial nano-hydroxyapatite composites. *Mater Sci. Eng. C Mater Biol. Appl.* 37, 54–59. doi:10.1016/j.msec.2013.12.038

Zhanel, G. G., Wiebe, R., Dilay, L., Thomson, K., Rubinstein, E., Hoban, D. J., et al. (2007). Comparative review of the carbapenems. *Drugs* 67 (7), 1027–1052. doi:10.2165/00003495-200767070-00006

Zheng, H., Zhang, Y., Liu, L., Wan, W., Guo, P., Nyström, A. M., et al. (2016). One-pot synthesis of metal-organic frameworks with encapsulated target molecules and their applications for controlled drug delivery. *J. Am. Chem. Soc.* 138 (3), 962–968. doi:10.1021/jacs.5b11720

Zhou, Y., Wu, J., Zhou, J., Lin, S., and Cheng, D. (2022). pH-responsive release and washout resistance of chitosan-based nano-pesticides for sustainable control of plumeria rust. *Int. J. Biol. Macromol.* 222, 188–197. doi:10.1016/j.ijbiomac.2022.09.144

frontiers | Frontiers in Bioengineering and Biotechnology

TYPE Original Research
PUBLISHED 09 May 2023
DOI 10.3389/fbioe.2023.1184973

OPEN ACCESS

EDITED BY
Xiangzhao Ai,
Shanghai Jiao Tong University, China

REVIEWED BY
Sin-Yeang Teow,
Kean University-Wenzhou, China
Jing Mu,
Peking University, China

*CORRESPONDENCE
Juan C. Cruz,
✉ jc.cruz@uniandes.edu.co

RECEIVED 13 March 2023
ACCEPTED 25 April 2023
PUBLISHED 09 May 2023

CITATION
Ravelo-Nieto E, Cifuentes J, Ruiz Puentes P, Rueda-Gensini L, Quezada V, Ostos C, Muñoz-Camargo C, Reyes LH, Duarte-Ruiz A and Cruz JC (2023), Unlocking cellular barriers: silica nanoparticles and fullerenol conjugated cell-penetrating agents for enhanced intracellular drug delivery.
*Front. Bioeng. Biotechnol.* 11:1184973.
doi: 10.3389/fbioe.2023.1184973

# Unlocking cellular barriers: silica nanoparticles and fullerenol conjugated cell-penetrating agents for enhanced intracellular drug delivery

Eduardo Ravelo-Nieto[1,2], Javier Cifuentes[2], Paola Ruiz Puentes[2], Laura Rueda-Gensini[2], Valentina Quezada[2], Carlos Ostos[3], Carolina Muñoz-Camargo[2], Luis H. Reyes[4], Alvaro Duarte-Ruiz[1] and Juan C. Cruz[2]*

[1]Department of Chemistry, Universidad Nacional de Colombia, Bogotá, Colombia, [2]Department of Biomedical Engineering, Universidad de los Andes, Bogotá, Colombi, [3]Grupo CATALAD, Instituto de Química, Universidad de Antioquia, Medellín, Colombia, [4]Grupo de Diseño de Productos y Procesos (GDPP), Department of Chemical and Food Engineering, Universidad de los Andes, Bogotá, Colombia

The limited delivery of cargoes at the cellular level is a significant challenge for therapeutic strategies due to the presence of numerous biological barriers. By immobilizing the Buforin II (BUF-II) peptide and the OmpA protein on magnetite nanoparticles, a new family of cell-penetrating nanobioconjugates was developed in a previous study. We propose in this study to extend this strategy to silica nanoparticles (SNPs) and silanized fullerenol (F) as nanostructured supports for conjugating these potent cell-penetrating agents. The same molecule conjugated to distinct nanomaterials may interact with subcellular compartments differently. On the obtained nanobioconjugates (OmpA-SNPs, BUF-II-PEG$_{12}$-SNPs, OmpA-F, and BUF-II-PEG$_{12}$-F), physicochemical characterization was performed to evaluate their properties and confirm the conjugation of these translocating agents on the nanomaterials. The biocompatibility, toxicity, and internalization capacity of nanobioconjugates in Vero cells and THP-1 cells were evaluated *in vitro*. Nanobioconjugates had a high internalization capacity in these cells without affecting their viability, according to the findings. In addition, the nanobioconjugates exhibited negligible hemolytic activity and a low tendency to induce platelet aggregation. In addition, the nanobioconjugates exhibited distinct intracellular trafficking and endosomal escape behavior in these cell lines, indicating their potential for addressing the challenges of cytoplasmic drug delivery and the development of therapeutics for the treatment of lysosomal storage diseases. This study presents an innovative strategy for conjugating cell-penetrating agents using silica nanoparticles and silanized fullerenol as nanostructured supports, which has the potential to enhance the efficacy of cellular drug delivery.

KEYWORDS

**nanobioconjugate, Buforin II, OmpA, silica nanoparticles, fullerenol, cellular uptake, endosomal escape**

## 1 Introduction

One of the significant obstacles to the safe and efficient delivery of pharmacological agents to the desired tissues or cells is the development of carriers that can pass through different biological barriers, such as the cellular membrane, while avoiding the immune response, side-target effects, or degradative pathways, to ultimately reach the target site while maintaining high availability of the therapeutic cargo (McNeil, 2011; McNeil, 2018).

Carriers based on nanoparticles (NPs) have been evaluated due to their multifunctionality, which results from their easily modifiable particle shape and size, material composition, and structure, according to the requirements of both the different cargoes and the target sites, achieving not only high biocompatibility, bioavailability, and biodistribution, but also on-target effects (Hossen et al., 2018; Karabasz et al., 2020). For instance, Planque et al. (2011) reported that membrane permeability and integrity are highly dependent on the size and surface chemistry of the NPs. Silica nanoparticles (SNPs) are one of the preferred nanomaterials for drug delivery due to their many advantageous properties. This material is an excellent candidate for drug carriers due to its high thermal stability, chemical inertness, high hydrophilicity and biocompatibility, simple functionalization and high loading capacity, and inexpensive synthesis (Gonçalves, 2018; Esim et al., 2019). Recently, SNPs have been utilized for the diagnostic and therapeutic delivery of contrast agents and drugs, biosensors, DNA carriers, and enzyme immobilization (Kim et al., 2019). Fullerenes, on the other hand, are an emerging class of carbon-based nanomaterials for cellular-level cargo delivery (Bolskar, 2013). These materials exhibit a structure with unique physicochemical properties and a highly symmetric cage with different sizes. The $C_{60}$ fullerene has the most symmetrical structure. Fullerene-based systems have been used to investigate the release of chemotherapeutic agents to eliminate the side effects of drugs such as doxorubicin and paclitaxel, photosensitizers for the activation of reactive oxygen species for the treatment of cancer cells, nucleic acid release, drugs with anti-HIV-1 activity, transdermal release, fullerenols with antioxidant activity, cardiovascular drugs and release in the brain (Kazemzadeh and Mozafari, 2019).

In addition to the use of nanomaterials, known cell penetration agents, such as the protein OmpA (López-Barbosa et al., 2019) or the antimicrobial peptide BUF-II (Cuellar et al., 2018), are also used to increase the membrane permeability of drugs. These agents have the ability to translocate across biological barriers such as the cell membrane or even the blood–brain barrier (Komin et al., 2017). However, these molecules lack stability and have a short lifetime in biological systems, a problem that can be resolved by immobilizing them on nanomaterials (Alves and Olívia Pereira, 2014). Over the past few years, we have developed a dual strategy to engineer the surface of nanocarriers. This strategy involves functionalizing them with cell-penetrating agents and combining their attributes to create carriers that are more stable and have a higher loading capacity for therapeutic agents. By doing so, we aim to enhance the release of therapeutic agents from these carriers. The purpose of this study is to examine the effect of changing the nanostructured support on the translocation capacity and endosomal escape ability of cell-penetrating agents. To accomplish this, we intend to combine our knowledge of SNPs and fullerenol as potential nanostructured supports for conjugating these agents. Our goal is to determine if the resulting nanobioconjugates have the potential for efficient cell penetration and endosomal escape, which is essential for the success of many drug therapies.

Overall, the objective of our research is to determine the efficacy of various nanostructured supports in enhancing the performance of cell-penetrating agents. By investigating the translocation and endosomal escape ability of these agents, we hope to gain insights that will lead to the future development of more effective drug therapies.

## 2 Materials and methods

### 2.1 Materials

Tetraethylorthosilicate (TEOS) (98%), methanol, ammonia solution (30%–32%), tetramethylammonium hydroxide (TMAH) (25%), (3-Aminopropyl)triethoxysilane (APTES) (98%), glutaraldehyde (25%), amine-PEG$_{12}$-propionic acid, N-hydroxysuccinimide (NHS) (98%), N-[3-dimethylammino)-propyl]-N′-ethyl carbodiimide hydrochloride (EDC) (98%), dimethyl sulfoxide (DMSO), Fullerene $C_{60}$, Tetra-n-butylammonium hydroxide (TBAH) (40% in water), toluene, hydrogen peroxide ($H_2O_2$), glacial acetic acid, 2-propanol, diethyl ether, and hexane were purchased from Sigma-Aldrich (MO, United States). Buforin II (BUF-II-TRSSRAGLQFPVGRVHRLLRK) was purchased from GL Biochem Shanghai (Shanghai, China). Vero Cells (ATCC® CCL-81) and THP-1 Cells (ATCC® TIB-202) were used for delivery assays. MTT (3-[4,5-Dimethylthiazol-2-yl]-2,5-Diphenyltetrazolium Bromide), DAPI (4′,6-diamidino-2-phenylindole, dihydrochloride), and Lysotracker Green DND-26 was purchased from Thermo Scientific (MA, United States). Dulbecco's modification of Eagle medium (DMEM), Roswell Park Memorial Institute (RPMI) 1640 medium, and fetal bovine serum (FBS) were obtained from Biowest (MO, United States).

### 2.2 OmpA overexpression in *E. coli*

OmpA protein was obtained from overexpression in *Escherichia coli*, following the protocol developed by Aguilera-Segura et al. (2014). *E. coli* K-12 W3110/pCA24N OmpA+34 was grown in Luria-Bertani (LB) agar plates [yeast extract (5 g L$^{-1}$), bacto tryptone (10 g L$^{-1}$), NaCl (10 g L$^{-1}$)] supplemented with chloramphenicol (50 μg mL$^{-1}$), and incubated for 16 h at 37°C, 250 rpm. Fresh liquid LB medium (19.5 mL) was inoculated with 500 μL from the previous culture and incubated at 37°C, 250 rpm, until reaching an optical density of 0.7 at 600 nm (OD600 nm). OmpA was obtained by inducing with IPTG (isopropylthio-β-galactoside) (2 mM) and by culturing for 3 more hours.

### 2.3 OmpA purification and characterization

The culture was centrifugated to obtain a pellet of OmpA overexpressed *E. coli*. The pellet was resuspended in buffer lysis in a ratio of 4 mL g$^{-1}$, sonicated at 4°C for 40 min and 37% amplitude, and centrifuged at 13,000 rpm and 4°C for 15 min.

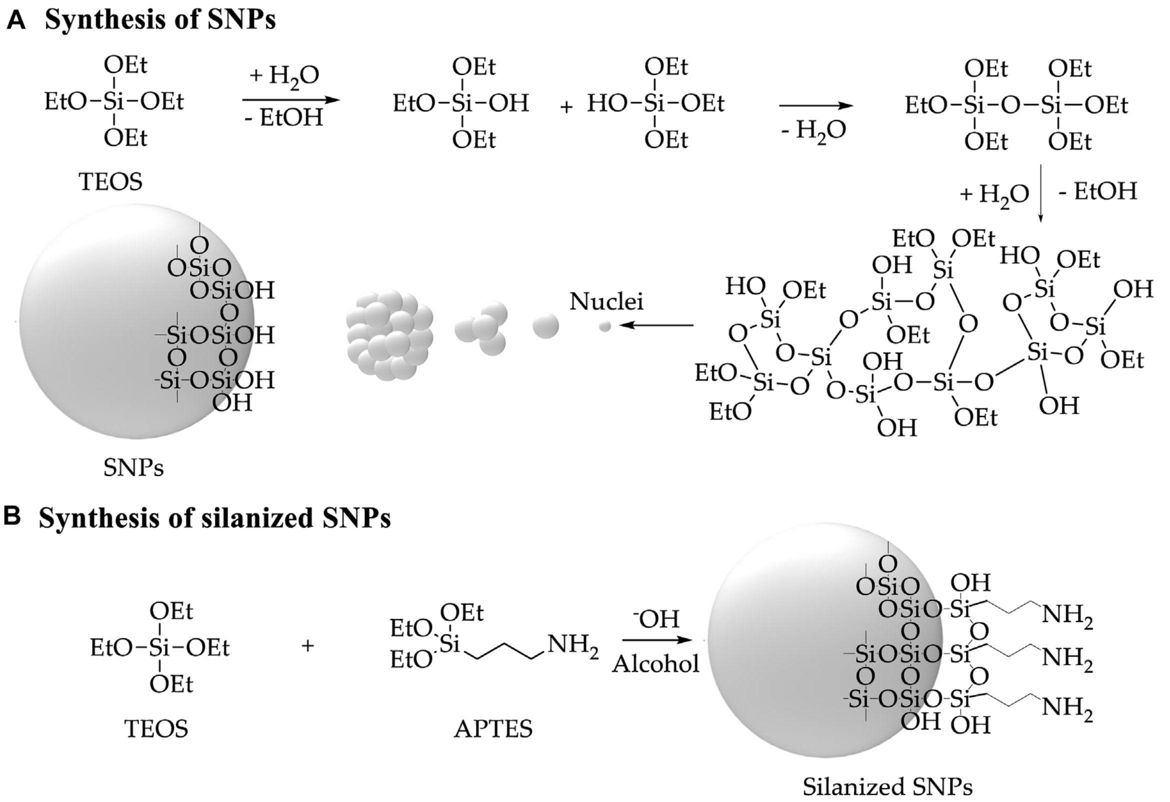

FIGURE 1
Schematic of the synthesis and silanization of SNPs **(A)** Synthesis of SNPs by TEOS hydrolysis in alcohol, water, and ammonia solution **(B)** Silanization of SNPs by TEOS hydrolysis in alcohol, water, and ammonia solution with the addition of APTES (Masalov et al., 2011; Shafqat et al., 2019).

Since OmpA protein was cloned with a His-tag, purification was attained by exposing the recovered supernatant to the Dynabeads® TALON® kit (Invitrogen). Purified OmpA protein was verified by SDS-PAGE, which showed a single 31 kDa band that agrees well with the molecular weight of OmpA. Concentration was measured via NanoDrop Spectrophotometer (Thermo Fisher Scientific) at 280 nm.

## 2.4 Synthesis and silanization of SNPs

SNPs were synthesized based on a Stober-like approach. The method involves hydrolysis and polycondensation of TEOS in an alcohol, water, and ammonia solution (Figure 1A) (Stober et al., 1968; Edrissi et al., 2011). Briefly, Ultrapure (type I) water (ultrapure water with a resistivity> 18 MΩ-cm and conductivity <0.056 $\mu S\ cm^{-1}$) (1.5 mL) and methanol (66.3 mL) were mixed. TEOS (0.9 mL) was then added and sonicated for 20 min using an ultrasonic bath (Elmasonic EASY 60H, 37 kHz, 150 W), then 30% ammonia in an aqueous solution (4.5 mL) was added, and the mixture was left in ultrasound for another 60 min in which a cloudy white suspension formed. The SNPs were centrifuged (Z-216, Hermle Labortechnik GmbH, German) and washed with Ultrapure (type I) water (3 × 20 min, 14,500 rpm). Silanized SNPs were synthesized using a ratio of TEOS 95% and APTES 5% (Figure 1B) (Shafqat et al., 2019). Silanization with APTES renders aminopropyl functionalities on the surface of the NPs, which can be used to conjugate further BUF-II and OmpA or crosslinkers to generate reactive groups for coupling them. The silanized SNPs were centrifuged (Z-216, Hermle Labortechnik GmbH, German) (4 × 20 min, 14,500 rpm) and washed with Ultrapure (type I) water. BUF-II and OmpA were conjugated according to the calculations presented in Supplementary Data S1 (Rangel-Muñoz et al., 2020).

## 2.5 Synthesis and silanization of fullerenol

Fullerenol was prepared from fullerene $C_{60}$ by hydroxylation with $H_2O_2$ and TBAH as a phase transfer catalyst under organic-aqueous bilayer conditions (Kokubo et al., 2011). Briefly, to a solution of fullerene $C_{60}$ (100 mg) in toluene (50 mL), an aqueous solution of 30% $H_2O_2$ (10 mL) and TBAH (40% in water, 500 µL) was added and stirred for 16 h at 60°C. Subsequently, to eliminate residual TBAH, the aqueous phase containing the fullerenol was separated, and fullerenol was precipitated with a mix of 2-propanol, diethyl ether, and hexane (7:5:5, 85 mL). Then, to complete the purification, we combined dialysis (cellulose membrane dialysis tubing) and freeze-drying (Conversion: 100%, yield after purification: 75%) (De Santiago et al., 2019). Next, fullerenol (50 mg) was dissolved in 15 mL of Ultrapure (type I) water. TMAH solution (500 µl, 25% (v/v)) and

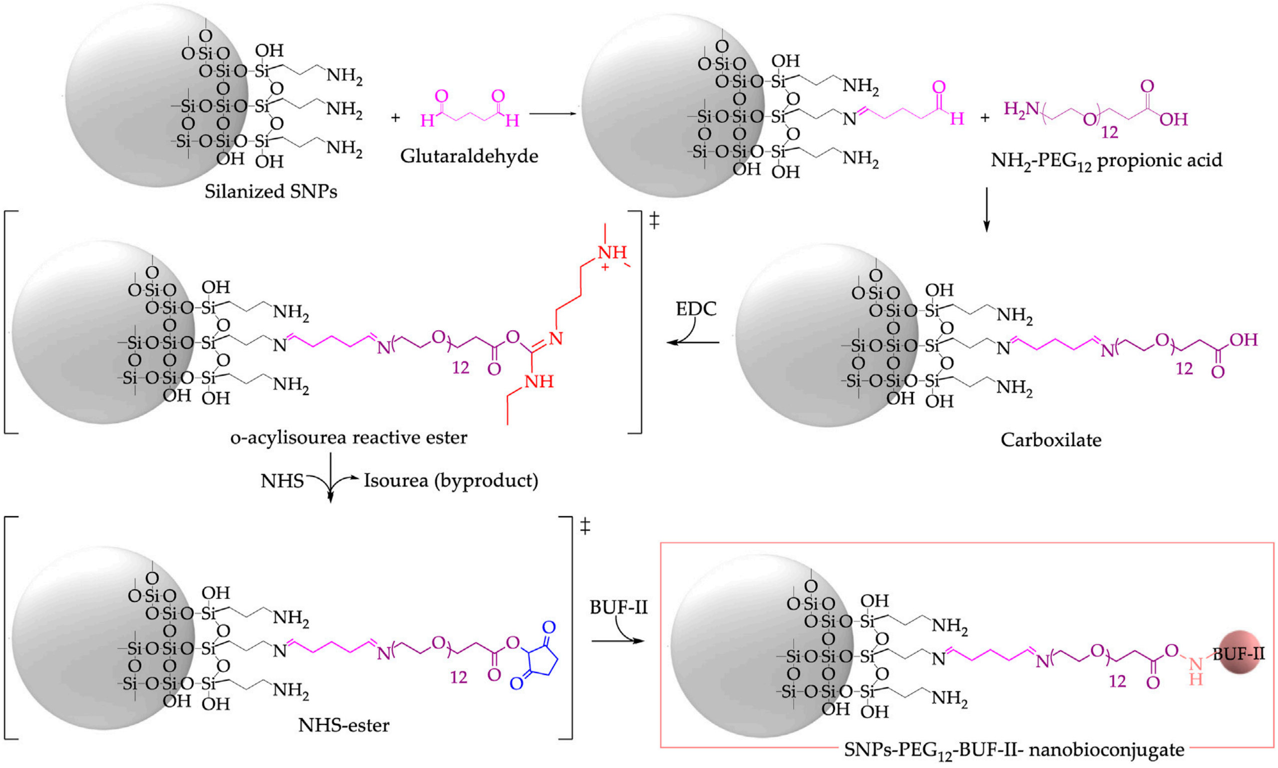

FIGURE 2
Synthesis of SNPs-PEG$_{12}$-BUF-II nanobioconjugates via a multi-step reaction involving glutaraldehyde, amine-PEG$_{12}$-propionic acid, and EDC/NHS to form an amide bond between a carboxylate and N-terminal of the peptide BUF-II.

glacial acetic acid (25 µL) were then added to the solution and sonicated for 10 min. APTES solution (500 µl, 20% (v/v)) was added to the fullerenol solution for silanization. The silanized fullerenol was washed with Ultrapure (type I) water to remove the APTES that was not covalently attached to the fullerenol.

## 2.6 BUF-II and OmpA bioconjugation

Briefly, 100 mg of silanized SNPs or fullerenol were suspended in 30 mL of Ultrapure (type I) water and sonicated for 10 min (Elmasonic EASY 60H, 37 kHz, 150 W). This was followed by adding 2 mL of glutaraldehyde 2% (v/v) and by letting the mixture left to react in an orbital shaker for 1 h at 220 rpm. The amine-PEG$_{12}$-propionic acid spacer was utilized to impart flexibility to BUF-II conjugated to SNPs or fullerenol, thereby increasing the probability of interaction with the target sites. After adding 10 mg of amine-PEG$_{12}$-propionic acid, the mixture was shaken for 24 h at 220 rpm. Finally, 100 mg of functionalized nanomaterial was resuspended in 30 mL of type I Ultrapure water. BUF-II was conjugated to the carboxyl groups of the spacer by its N-terminal using two equivalents of EDC and two equivalents of NHS (concerning the carboxyl groups) (Figure 2; Supplementary Figure S1). BUF-II (1 mg BUF-II per 100 mg of functionalized nanomaterial) was added and the mixture was shaken at 220 rpm for 24 h. The obtained nanobioconjugates were centrifuged (Z-216, Hermle Labortechnik GmbH, German) (4 × 20 min, 14,500 rpm) and washed with Ultrapure (type I) water (Cuellar et al., 2018; Perez et al., 2019; Ramírez-Acosta et al., 2020).

Crosslinking of amine-terminal groups in the protein with aminopropyl groups on the surface of silanized SNPs or fullerenol facilitated by the addition of glutaraldehyde as the crosslinking agent enabled immobilization of OmpA on SNPs or fullerenol (Figure 3; Supplementary Figure S2) (López-Barbosa et al., 2019; Rangel-Muñoz et al., 2020). Briefly, 100 mg of silanized SNPs or fullerenol were suspended in 30 mL of ultrapure (type I) water and sonicated for 10 min (Elmasonic EASY 60H, 37 kHz, 150 W). This was followed by adding 2 mL of glutaraldehyde 2% (v/v) and by letting the mixture left to react in an orbital shaker for 1 h at 220 rpm. Then, OmpA (30 mg OmpA/100 mg functionalized nanomaterial) was added and shaken for 24 h at 220 rpm. The obtained nanobioconjugates were centrifuged (Z-216, Hermle Labortechnik GmbH, German) (4 × 20 min, 14,500 rpm) and washed with ultrapure (type I) water.

## 2.7 Labeling of nanobioconjugates with rhodamine B

For confocal microscopy evaluation of cellular uptake and endosomal escape, the nanobioconjugates were labeled with the fluorescent probe rhodamine B. This was accomplished through the formation of amide bonds between the carboxylate group of rhodamine B and the free amine groups of nanobioconjugates.

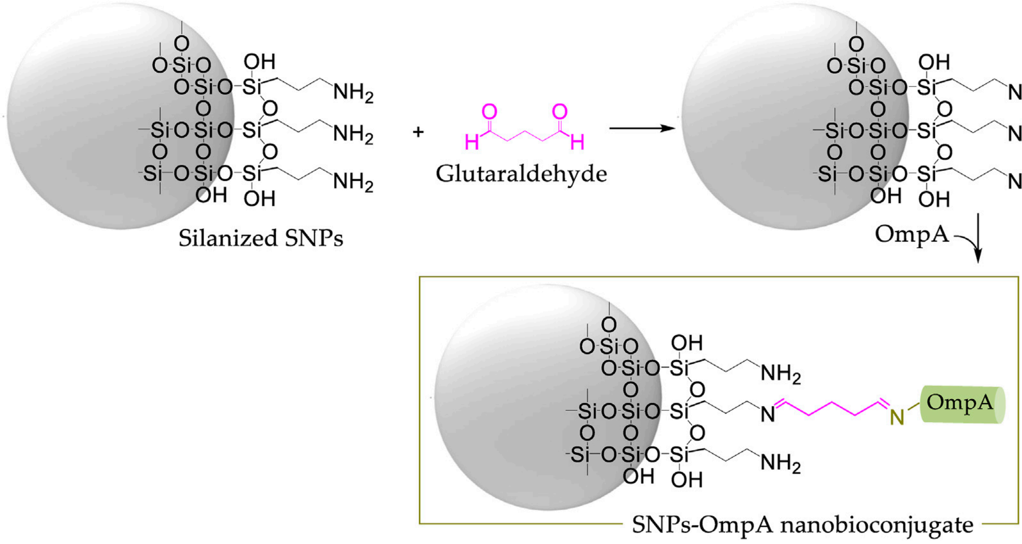

FIGURE 3
Synthesis of SNPs-OmpA nanobioconjugates using glutaraldehyde as the crosslinking agent.

Briefly, under dark conditions, 15 mg of EDC, 7.5 mg of NHS, and 1 mL of DMF were added to 5 mL of type I ultrapure water. Subsequently, 2 mg of rhodamine B was added, and the solution was heated to 40°C for 15 min with continuous magnetic stirring. This enables the activation of the carboxylate groups of rhodamine B to form amide bonds with the free amine groups of nanobioconjugates. The mixture was then allowed to cool to room temperature before being combined with 50 mg of nanobioconjugates. To prevent photobleaching, it was stirred for 24 h at 220 rpm using a shaker at room temperature and in complete darkness. The labeled nanobioconjugates were centrifuged (Z-216, Hermle Labortechnik GmbH, German) (20 min, 14,500 rpm) and washed several times with ultrapure (type I) water until no rhodamine B was detected in the supernatant (López-Barbosa et al., 2019).

## 2.8 Characterization of the nanobioconjugates

Infrared spectra were collected from 4,000–500 $cm^{-1}$ with a spectral resolution of 2 $cm^{-1}$ using a spectrometer ALPHA II FTIR Eco-ATR (Bruker Optik GmbH, Ettlingen, Germany) and an IRAffinity-1 spectrometer (Shimadzu Corporation). The hydrodynamic diameter and $\zeta$ potential of the nanobioconjugates were determined via Dynamic Light Scattering (DLS) and Electrophoretic Moobility (Zeta-Sizer Nano-ZS; Malvern Instruments, Malvern, UK). Thermogravimetric analysis (TGA, TA Instruments, New Castle, DE, United States) was used to estimate the amount of material conjugated to the SNPs and the fullerenol, implementing a linear temperature ramp at a rate of 10°C $min^{-1}$ from 25°C to 890°C under an inert atmosphere. Focused Ion Beam Scanning Electron Microscope (TESCAN LYRA3 FIB-SEM, Czech Republic) and Transmission Electron Microscope (TEM, FEI TECNAI G2 F20 Super Twin TMP, Hillsboro, OR, United States) were used to obtain information on the size, composition, and morphology of the nanomaterials. XPS spectra were obtained using a SPECS near-ambient pressure X-ray photoelectron spectrometer (NAP-XPS) with a PHOIBOS 150 1D-DLD analyzer, using a monochromatic source of Al-Kα (1,486.7 eV, 13 kV, 100 W) (SPECS GmbH, Berlin, Germany). The X-ray source and monochromator were aligned to get a 0.49 eV peak-resolution under a vacuum pressure of the chamber below $10^{-9}$ m bar. The samples were previously mounted on a non-conductive tape. The control of surface potential was achieved by an electron flood gun at 3 kV over a tantalum mesh with a nominal aperture of 0.43 mm. The spot size was 200 nm of diameter, the energy pass was fixed at 20 eV and the scan number for the high-resolution measurements was 20. The signals were calibrated to a binding energy of 284.6 eV for adventitious carbon and a Ta4f7/2 peak from the tantalum mesh was employed as reference. XPSPeak software was used for fitting the XPS spectra using a Shirley-type single-peaks background with a simultaneous GL peak-shape of 30% and full-width at half maximum (FWHM) data from literature.

Delivery of nanobioconjugates in mammalian cells was monitored using a confocal laser scanning microscope (Fluoview FV1000, Olympus, Tokyo, Japan). The images were obtained with a UPLSAPO 20x/0.75 NA objective and a PlanApo ×60/1.35 NA objective. Excitation/Emission wavelengths of 405/422, 488/520, and 559 nm/575 nm were used to detect DAPI (nuclei), LysoTracker green (acidic organelles: endosomes/lysosomes), and rhodamine B (nanobioconjugates), respectively. Colocalization within biologically relevant regions of interest (ROIs) was analyzed using the plugin Coloc 2 of the Fiji® software (https://imagej.net/Fiji/Downloads). At least 30 images were taken for each treatment (about 10 cells per image were analyzed).

## 2.9 *In vitro* analysis of the nanobioconjugates' hemolytic effect

Hemolysis is the rapid destruction of erythrocyte membranes, which results in the release of intra-erythrocyte contents into the blood plasma. The hemolytic activity of the nanobioconjugates was determined using the method described by previously Muñoz-Camargo et al. (2018). Briefly, blood from healthy donors was collected in BD Vacutainer® blood tubes using EDTA as an anticoagulant. The samples were obtained with the approval of the Ethical Committee at the Universidad de los Andes (minute number 928-2018). Blood was centrifuged at 1,800 rpm for 5 min (Micro Centrifuge Z 360, Hermle Laboratories GmbH) to collect red blood cells, and the hematocrit level (lower layer, red) and plasma (upper layer, yellow) were marked. The plasma was then removed, and the tube was refilled to the mark with 150 mM NaCl, inverting the tube gently to mix, and centrifuged again. Subsequently, the supernatant was removed and replaced with PBS (Phosphate Buffered Saline) (1X). A red blood cells stock was prepared by adding 1 mL of isolated red blood cells ($4.3 \times 10^6$ red blood cells $\mu L^{-1}$) in 9 mL of PBS (1X). Serial dilutions of nanobioconjugates (300, 150, 75, 37.5, and 18.75 $\mu g\ mL^{-1}$ in PBS) were prepared for the test in a 96-well microplate. 100 µL of each treatment and 100 µL of the diluted red blood cells were incubated for 1 h at 37°C and 5% $CO_2$. Finally, the microplate was centrifuged at 1,800 rpm for 5 min, and 100 µL of each supernatant was measured (oxyhemoglobin, 450 nm) in a microplate reader spectrophotometer (Multiskan™ FC, Thermo Fisher Scientific Inc., United States). PBS (1X) and Triton X-100 (1%) were used as negative and positive controls, respectively.

## 2.10 *In vitro* assessment of nanobioconjugates' blood coagulation effect

The effect of the nanobioconjugates on platelet aggregation was tested using platelet-rich plasma (PRP). Blood was obtained from healthy donors in BD Vacutainer® tubes, anticoagulated with sodium citrate. PRP was obtained by centrifugation of a human blood sample at 1,000 rpm for 15 min (Micro Centrifuge Z 360, Hermle Labortechnik GmbH), and the PRP was collected and transferred to a fresh tube. Serial dilutions of nanobioconjugates (300, 150, 75, 37.5, and 18.75 $\mu g\ mL^{-1}$ in PBS) were prepared for the test in a 96-well microplate. Subsequently, 100 µL of each treatment and 100 µL of PRP were incubated for 15 min at 37°C and 5% $CO_2$. Thrombin (6U) was used as a positive control, while PBS (1X) was a negative reference. Finally, the aggregation was measured by optical density (OD) at 620 nm in a microplate reader spectrophotometer (Multiskan™ FC, Thermo Fisher Scientific Inc., United States) (Lopez-Barbosa et al., 2020).

## 2.11 MTT cytotoxicity test

The MTT (3-[4,5-dimethylthiazol-2-yl]-2.5 diphenyl tetrazolium bromide) assay is based on the metabolic reduction of MTT into formazan crystals by viable cells (Meerloo et al., 2011). Briefly, Vero cells (ATCC® CCL-81) and THP1 cells (ATCC® TIB-202) were plated in 96-well culture plates in DMEM ($1.0 \times 10^6$ cells $100\ \mu L^{-1}$ per well) and incubated at 37°C and 5% $CO_2$ for 24 h. Culture media was removed from wells, and DMEM 1% penicillin/streptomycin (90 µL) (without FBS) was added to each well. Subsequently, 100 µL of each treatment (300, 150, 75, 37.5, and 18.75 $\mu g\ mL^{-1}$ in PBS) were added and incubated at 37°C, 5% $CO_2$ for 24 h, and 48 h. The medium was removed, and DMSO (500 µL) was used to dilute formazan crystals. Absorbance was read at 595 nm (reference 650 nm) in a microplate reader spectrophotometer (Multiskan™ FC, Thermo Fisher Scientific Inc., United States) and compared to the controls (Lopez-Barbosa et al., 2020).

## 2.12 Cell translocation and endosome escape

Vero Cells were seeded in a sterile glass slide previously placed in a 6-well microplate and incubated in DMEM medium supplemented with 10% (v/v) FBS at 37°C and 5% $CO_2$ for 24 h. Next, cells were exposed to fluorescently labeled nanobioconjugates (18.75 $\mu g\ mL^{-1}$), and the samples were incubated for 30 min and 4 h at 37°C and 5% $CO_2$. Supplemented culture medium was removed, and then, the cells were washed three times with DMEM medium and exposed for 10 min to DAPI (1 µL, 1:1,000) used to stain nuclei, and Lysotracker Green DND-26 (0.1 µL, 1:10,000) that labels acidic organelles (lysosomes/endosomes) before capturing confocal images (López-Barbosa et al., 2019). THP-1 Cells exposed to fluorescently labeled nanoconjugates (18.75 $\mu g\ mL^{-1}$) were incubated for 30 min and 4 h at 37°C and 5% $CO_2$. Then, the samples were exposed for 10 min to DAPI (1 µL, 1:1,000) and Lysotracker Green DND-26 (0.1 µL, 1: 10,000) before capturing confocal images (López-Barbosa et al., 2019).

## 2.13 Statistical analysis

Values (Hemolysis, platelet aggregation, cell viability) are expressed as the means ± SDs of triplicates. Significance tests were analyzed by nonparametric—the normality of data distributions was assessed using the Shapiro–Wilk test—one-way ANOVA (Kruskal–Wallis test) and Dunn's multiple comparison test, using the GraphPad Prism 8.0.1® software (GraphPad Software, La Jolla, CA, United States). $p$ values <0.05 were considered statistically significant.

# 3 Results and discussion

## 3.1 Physicochemical characterization of SNPs and nanobioconjugates based on SNPs

Figure 4A shows a schematic of the chemical structure of silanized SNPs and BUF-II-$PEG_{12}$-SNPs, and OmpA-SNPs nanobioconjugates. Figure 4B compares the FT-IR spectra of bare SNPs, silanized SNPs, free OmpA, free BUF-II, and nanobioconjugates. The bare SNPs exhibit distinctive absorptions at around 1,100 $cm^{-1}$ (Si-O *st as*, asymmetrical stretching), 970 $cm^{-1}$

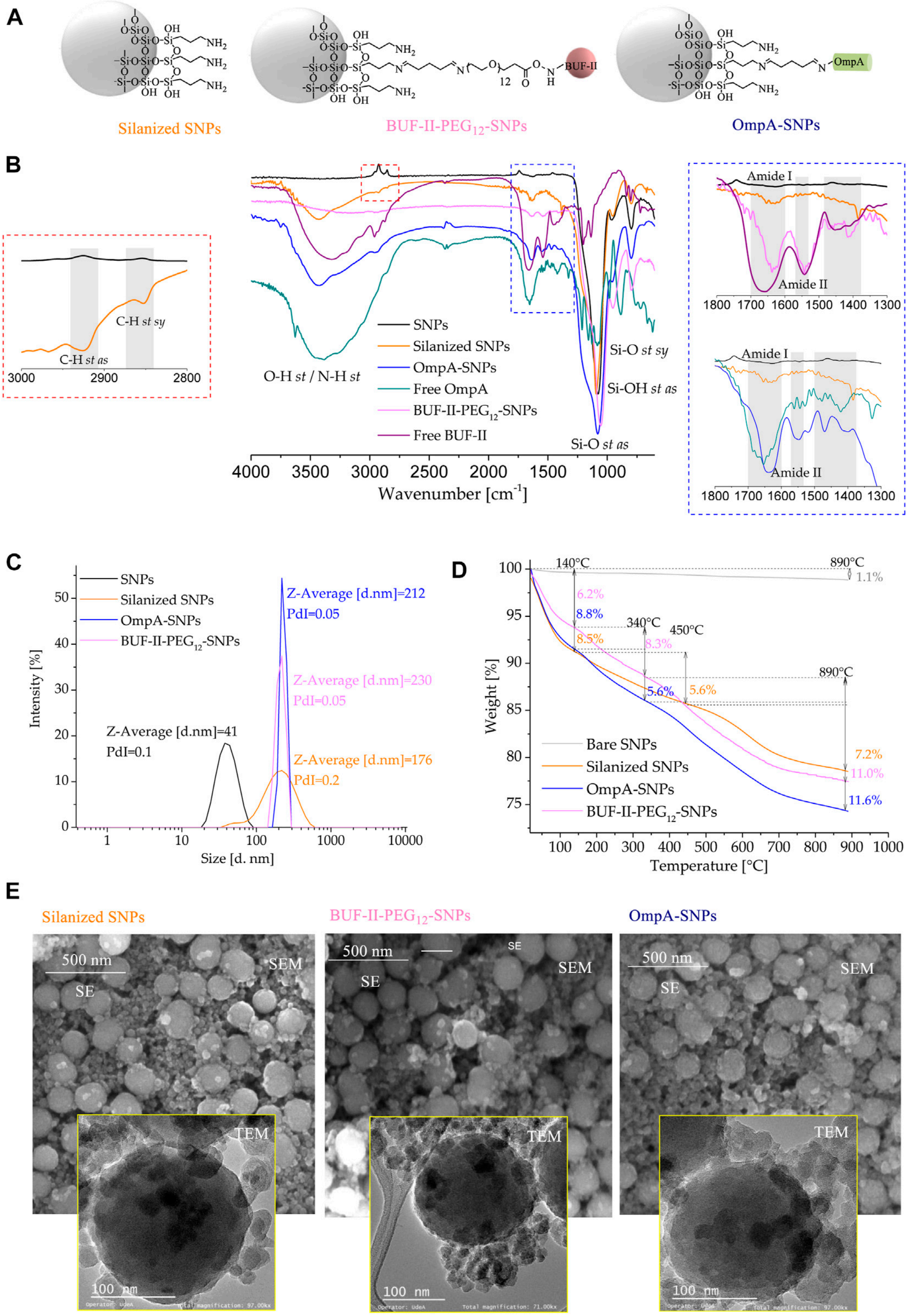

FIGURE 4
Spectroscopic and thermal analyses of silanized SNPs and the nanobioconjugates **(A)** Schematic of the chemical structure of silanized SNPs and the nanobioconjugates **(B)** FT-IR spectra of **(1)** bare SNPs, **(2)** silanized SNPs, **(3)** BUF-II-PEG$_{12}$-SNPs nanobioconjugates, **(4)** free BUF-II, **(5)** OmpA-SNPs, and **(6)** free OmpA **(C)** DLS histogram for the size intensity distribution **(D)** TGA thermogram of SNPs, silanized SNPs, and nanobioconjugates **(E)** SEM and TEM images of the silanized SNPs, and nanobioconjugates.

(Si-OH *st as*), and 801 cm$^{-1}$ (Si-O *st sy*, symmetrical) (Pretsch et al., 2009; Edrissi et al., 2011). New bands were observed at 2,925 cm$^{-1}$ (C-H *st as*), 2,852 cm$^{-1}$ (C-H *st sy*), and 1,639 cm$^{-1}$ (N-H *b*, bending vibration), evidencing the presence of propylamine groups on the surface of the silanized SNPs (Shafqat et al., 2019). On the free OmpA, OmpA-SNPs, free BUF-II, and BUF-II-PEG$_{12}$-SNPs spectra, the presence of amide vibrational modes known as amide I (1,700–1,600 cm$^{-1}$) and amide II (1,570–1,540 cm$^{-1}$) and other vibrations specific that are absent on bare SNPs suggests correct conjugation of protein or peptide (Pretsch et al., 2009; Tatulian, 2013; López-Barbosa et al., 2019). The amide I mode is generated mostly by contributions of the C=O *st*, CN *st*, CCN *ob* (out-of-plane bending), and by the NH *ib* (in-plane bending) modes (Tatulian, 2013). The amide II mode includes contributions of the NH *ib*, CN *st*, CO *ib*, CC *st*, and NC *st* (Tatulian, 2013). Other vibrational modes of the amide group of protein or peptide and crosslinking agents overlap with the vibrational modes of SNPs. Figure 4C shows particle size distribution by intensity determined by DLS. Bare SNPs exhibited a mean hydrodynamic diameter (Z-average size) of 41 nm with a Polydispersity Index (PdI) of 0.1. A ratio of 95% of TEOS and 5% of APTES produced two populations of silanized SNPs with mean hydrodynamic diameters around 40 and 220 nm (Z-average size: 176 nm, PdI: 0.2). Regarding this, Li et al. (2019) demonstrated that the total uptake of SNPs in Hela cells was higher in co-exposures of large and small SNPs — 50/100 and 80 nm/150 nm—than in single exposures of the same. It can also be observed that the Z-average size of the SNPs increased after peptide and protein conjugation for BUF-II-PEG$_{12}$-SNPs (Z-average size: 212 nm, PdI: 0.05) and OmpA-SNPs (Z-average size: 230 nm, PdI: 0.05). There is no consensus regarding the optimal size that maximizes cellular uptake and maintains cell viability. A number of experimental studies indicate that particle size reduction does not necessarily increase cellular uptake (Barisik et al., 2014). However, nanocarriers based on NPs in the size range of 10–200 nm are frequently used to facilitate the delivery of cargoes at the cellular level. These nanocarriers are not easily excreted by any of the physiological systems designed for this purpose and therefore reach target organs and tissues in sufficient concentrations (Selby et al., 2017; Chenthamara et al., 2019). Thermogravimetric analysis (TGA) was used to estimate the amount of material conjugated to the SNPs (Figure 4D). The bare SNPs exhibited excellent thermal stability, losing only about 1.1% of their weight when heated from room temperature to 890°C. In contrast, weight loss was observed for silanized SNPs and nanobioconjugates in three temperature ranges (silanized SNPs: room temperature to 140°C, 140°C–450°C, and >450°C; nanobioconjugates: room temperature to 140°C, 140°C–340°C, and >340°C). Silanized SNPs, BUF-II-PEG$_{12}$-SNPs, and OmpA-SNPs showed a first weight loss of 8.5%, 8.8%, and 6.2%, respectively, that can be attributed to water loss. A second weight loss of 5.6% was observed for the silanized SNPs and OmpA-SNPs, whereas for BUF-II-PEG$_{12}$-SNPs, it was 8.3%. These losses can be assigned to the presence of non-hydrolyzed ethoxy groups of APTES and residual alcohol within the silica nanostructure (Kunc et al., 2019). Finally, the weight loss at the highest temperatures can be assigned to the loss of aminopropyl groups (7.2%) for the silanized SNPs, and the detachment of BUF-II, OmpA, and crosslinking agents in the case of the BUF-II-PEG$_{12}$-SNPs (11.0%) and OmpA-SNPs (11.6%) nanobioconjugates (López-Barbosa et al., 2019; Perez et al., 2019). SEM and TEM images were consistent with the data obtained by DLS regarding the size and the presence of two size populations of particles. In addition, it can be observed that the nanoparticles have a predominantly spherical morphology. Apparently, after conjugation, the roughness of the nanoparticles changes; this could also affect their interaction with cells and their loading capacity (Niu et al., 2015; Alan et al., 2020) (Figure 4E). Additionally, $\zeta$ potential is indicative of the stability of the suspension; if all the particles in suspension have $\zeta$ potentials above +25 mV or below −25 mV, they repel each other, and therefore show no tendency for aggregation, coagulation, or flocculation (Shnoudeh et al., 2019). The $\zeta$ potential measurements of the SNPs indicate that in aqueous media—pH close to 7— it acquires a negative surface charge of −37.6 ± 4.91 mV; this value indicates good SNPs stability in water. The $\zeta$-potential reached values of 4.41 ± 3.27 mV, 7.34 ± 3.36 mV, and 18.1 ± 5.13 mV for the silanized SNPs, and BUF-II-PEG$_{12}$-SNPs, and OmpA-SNPs nanobioconjugates (in aqueous media—pH close to 7), respectively. At physiological pH, these nanobioconjugates tend to precipitate.

The chemical surface characterization of the nanobioconjugates was evaluated by XPS. The detailed experimental set-up carried out for the samples is shown in Section 2.8. Here, SNPs and fullerenol nanocarriers were considered. Figure 5 shows the high-resolution (HR) spectra for the SNPs and the corresponding nanobioconjugates under examination. The peak components from the decomposition analysis are denoted from high to low binding energy, and colored zones clearly distinguish them. The binding energy (BE) values for all components that are part of the overall fitting, marked as a red line over black dots related to the experimental recorded data, are shown in Table 1. Starting at the C1s core-level, four mean sub-peaks for functionalizing samples were fitted, which correspond to O-C-O/C=O (red); C-O/C-N (blue); C-C (green) and C-Si (magenta) bonds. For the silanized SNPs, there were no highly oxidized species, which clearly indicate the successful conjugation of OmpA and BUF-II on the NPs' surface. Since these biomolecules and their intermediate states are too complex due to their chemistry and molecular weight (MW), it is not possible to establish a stoichiometric ratio between the species; nevertheless, the counts (*Y*-axis) for each core-level were normalized prior to their placement on the plots. Conversely, a qualitative analysis can be done. As a result, it is possible to determine that the oxidizing species for C1s core-level in the OmpA-SNPs system are greater than those in the BUF-II-PEG12-SNPs nanobioconjugates. In contrast, the BUF-II-PEG12-SNPs exhibited a high (C-N/C-O)/C-C ratio due to their low molecular weight and high C-N/C-O terminal bonds. Consistent C-Si bonds were found in the studied systems, allowing us to conclude that the SNPs were properly silanized and that the biomolecules are bound to the inorganic nanoparticles via C-Si-O covalent bonds. The O1s core-level was deconvoluted into four mean sub-peak components associated with chemisorbed OH-molecules: O-C-O/Si-O, C-O, and O=C species. Slight shifts in binding energies and high similitudes of the integral intensity of every peak as calculated from the area under the curve were observed. Moreover, if we compare the overall peak intensity with that of C1s for each compound, the corresponding ratio for the nanobioconjugates is lower than for the SNPs. This is most likely due to the lower concentration of C/O species on the surface of

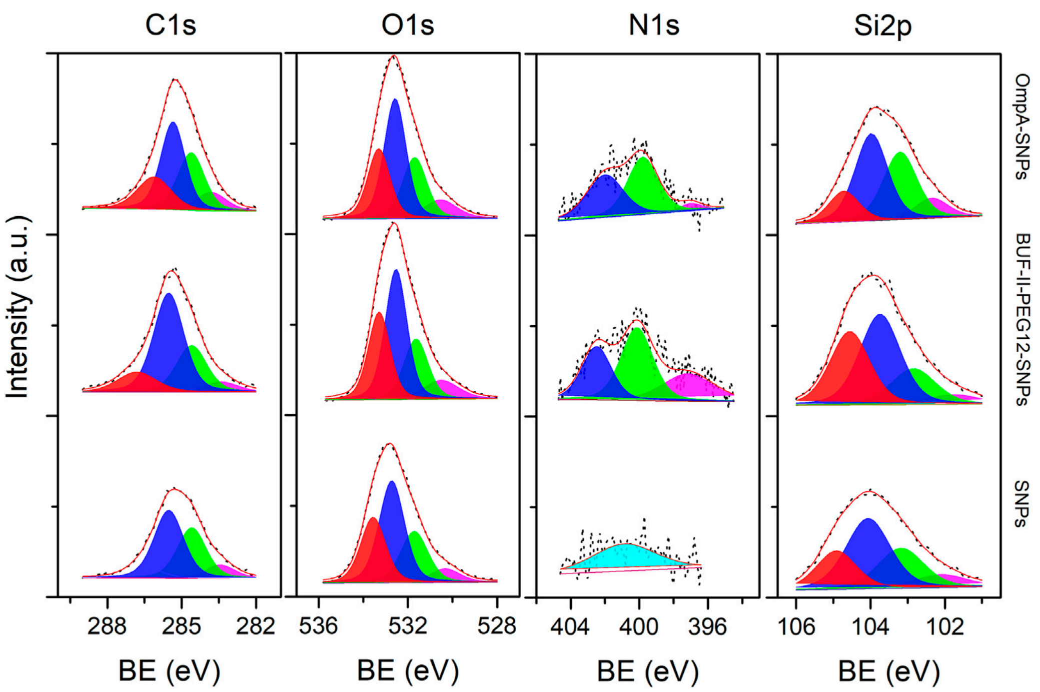

FIGURE 5
XPS spectra of the C1s, O1s, N1s, and Si2p (left to right) core-level regions of silanized SNPs, BUF-II-PEG12-SNPs nanobioconjugates, and OmpA-SNPs nanobioconjugates samples (bottom to top). Peak components for the XPS lines are differentiated by colors from high to low binding energy values (left to right).

**TABLE 1 Binding energy (BE) of the different XPS lines for C1s, O1s, N1s, and S2p peak components from silanized SNPs, BUF-II-PEG12-SNPs nanobioconjugates, and OmpA-SNPs nanobioconjugates samples.**

| Sample | C1s (BE- eV) | O1s (BE- eV) | N1s (BE- eV) | Si2p (BE- eV) |
|---|---|---|---|---|
| Silanized SNPs | 283.4 | 530.3 | 400.8 | 102.0 |
| | 284.6 | 531.7 | — | 103.2 |
| | 285.5 | 532.7 | — | 104.1 |
| | 286.5 | 533.6 | — | 104.9 |
| BUF-II-PEG$_{12}$-SNPs | 283.3 | 530.5 | 397.2 | 101.8 |
| | 284.6 | 531.6 | 400.1 | 102.8 |
| | 285.5 | 532.5 | 402.5 | 103.7 |
| | 286.8 | 533.3 | — | 104.6 |
| SNPs-OmpA | 283.8 | 530.5 | 396.9 | 102.3 |
| | 284.6 | 531.7 | 399.8 | 103.2 |
| | 285.4 | 532.6 | 401.9 | 104.0 |
| | 286.1 | 533.,3 | — | 104.7 |

SNPs, where only the APTES chain is present. As peptide and protein are conjugated, the proportion of atomic C species increases dramatically, as does the C/O ratio. Now passing through the N1s core-level, three mean sub-peak components for nanobioconjugates were fitted. In the case of silanized SNPs, a weak signal of nitrogen from the conjugated APTES can be assigned to a primary amine (Talavera-Pech et al., 2016). For the nanobioconjugates, protonated amines seem to be located at higher binding energies, followed by O-C-N and N=N-/N-H- bonds. The Si2p sub-peaks components corresponding to SiOx (red), Si-O- (blue), Si-O-C- (green) and Si-C- (magenta) bonds are shown from left to right for bare SNPs and nanobioconjugates (Talavera-Pech et al., 2016). Slight peak

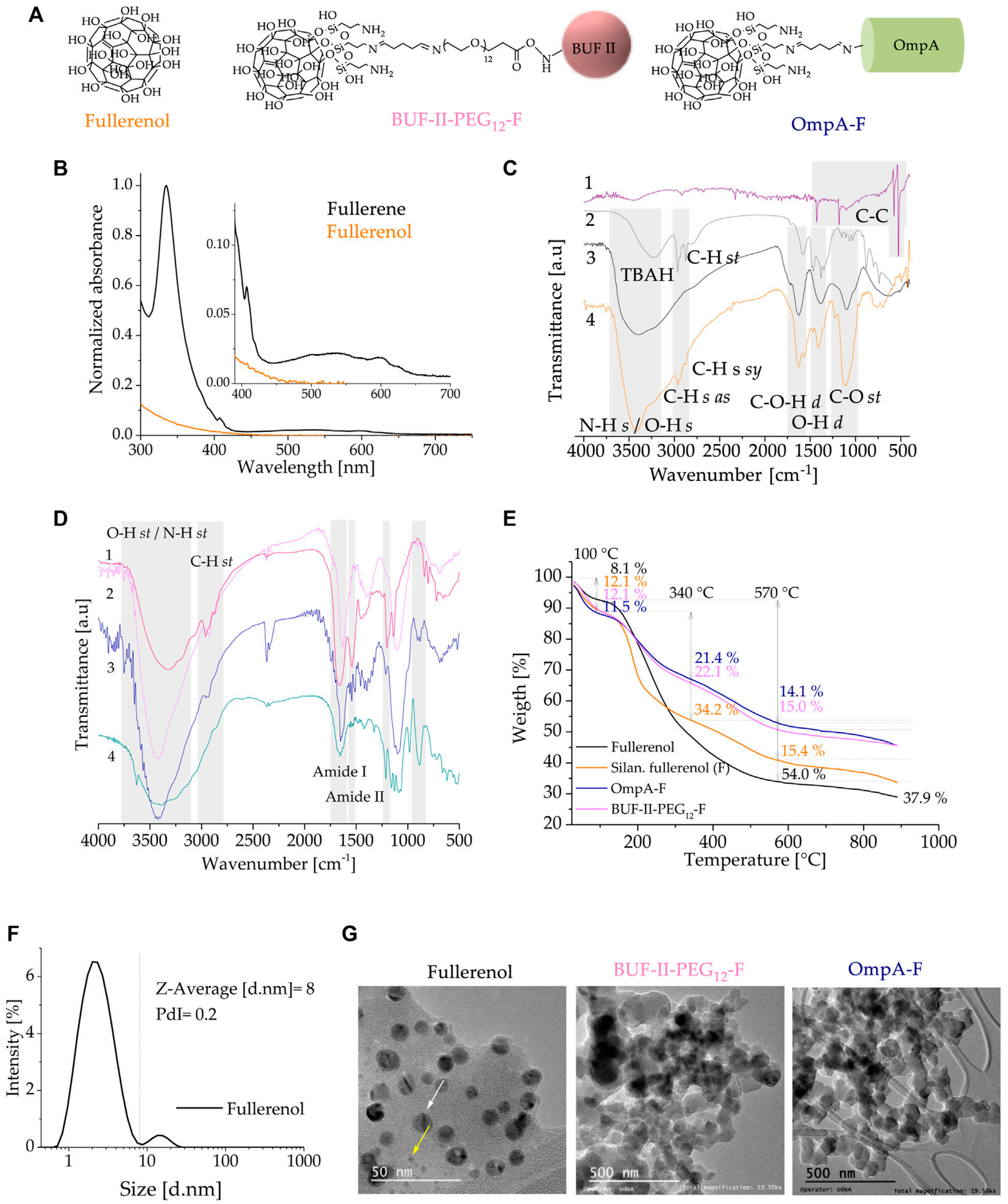

FIGURE 6
Spectroscopic and thermal analyses of fullerenol and the nanobioconjugates **(A)** UV–VIS spectra of $C_{60}$ in toluene and aqueous solution of fullerenol **(B)** Schematic of the chemical structure of fullerenol and the nanobioconjugates **(C)** FT-IR spectra of (1) fullerene, (2) fullerenol as produced (with TBAH residues), (3) purified fullerenol, and (4) silanized fullerenol **(D)** FT-IR spectra of (1) BUF-II-PEG12-F nanobioconjugates, (2) free fullerenol, silanized fullerenol, and nanobioconjugates **(E)** TGA thermogram of fullerenol, silanized fullerenol, and nanobioconjugates **(F)** DLS histogram for the size intensity distribution **(G)** TEM images of the fullerenol, and nanobioconjugates.

shifts and intensity changes can be attributed to conjugation of OmpA and BUF-II and are likely related to conformational changes upon conjugation.

## 3.2 Physicochemical characterization of fullerenol and fullerenol-based nanobioconjugates

Figure 6A shows a schematic of the chemical structure of silanized fullerenol, OmpA-F, and BUF-II-PEG$_{12}$-F nanobioconjugates. Figure 6B shows UV–visible absorption spectra of fullerene $C_{60}$ in toluene and fullerenol in water. $C_{60}$ fullerene dissolved in toluene has characteristic absorption bands with maxima at 283, 335, and 408 nm, followed by a broad absorption band in the range of 430–650 nm with reduced absorptions for the blue region and red; this combination gives the compound its distinctive purple color (Ajie et al., 1990). Fullerenol dissolved in water is yellow and almost transparent in the visible region due to its considerable perturbation of the π-conjugation upon hydroxylation (Kokubo et al., 2008). Figure 6C compares the FT-IR spectra of (1) fullerene, (2) fullerenol as synthesized (with TBAH residues), (3) purified fullerenol, and (4) silanized fullerenol. Fullerene $C_{60}$ has four active infrared modes at 1,429, 1,182, 573, and 525 cm$^{-1}$ due to C-C bonds (Krätschmer et al., 1990). In the as-synthesized fullerenol, the two peaks observed at 2,963 and 2,873 cm$^{-1}$ (C-H *st*) were attributed to residual TBAH (Kokubo et al., 2011). Purified fullerenol showed a broad band at around 3,424 cm$^{-1}$(O-H *st*) and four characteristic bands at 1,598 cm$^{-1}$ (C=C *st*), 1,410 cm$^{-1}$ (O-H *b*), 1,352 cm$^{-1}$ (C-O-H *b*), and 1,112 cm$^{-1}$ (C-O *st*), which agree well with previously reported data (Kokubo et al., 2011; Ravelo-Nieto et al., 2020). Silanization was confirmed by the presence of new bands at 2,964 cm$^{-1}$ (C-H *st as*), 2,934 cm$^{-1}$ (C-H *st sy*), 2,875 cm$^{-1}$ (H-C (-N) *st*), 1,564 cm$^{-1}$ (N-H *b*), and 1,344 cm$^{-1}$ (C-N *st*), which can be attributed to propylamine groups. Moreover, absorption bands at 1,653 cm$^{-1}$ (N-H *b*), 1,110 cm$^{-1}$ (Si-O *st*), 1,052 cm$^{-1}$ (Si-O-Si *st*), and 690 cm$^{-1}$ (Si-C *st*) overlap with the vibrational modes of fullerenol (Cuellar et al., 2018). Figure 6D compares the FT-IR spectra of (1) OmpA-F, (2) free OmpA, (3) BUF-II-PEG$_{12}$-F, and (4) free BUF-II (Shafqat et al., 2019). The free OmpA, OmpA-F, free BUF-II, and BUF-II-PEG$_{12}$-F spectra showed the amide I and amide II vibrational modes along with other specific vibrations that are absent in the non-functionalized fullerenol. However, these signals overlap with the vibrational modes of fullerenol. Thermal stability of fullerenol and nanobioconjugates was studied by TGA (Figure 6E). TGA results of purified fullerenol show three main a weight loss stages: room temperature to 100°C, 100°C–570°C, and >570°C. The initial weight loss (~8.1%) corresponds to dehydration of the samples (Kokubo et al., 2011). The second weight loss (~54.0%) corresponds to the dehydroxylation before the structural degradation of the fullerene nucleus that occurs at temperatures above 570°C (~37.9% residual weight) (Goswami et al., 2004). Then, using the method described by Goswami et al.( 2004), the number of −OH groups per fullerene could be estimated at 30, which is similar to results reported by others previously (Kokubo et al., 2011; Kovač et al., 2018; De Santiago et al., 2019). Four main weight loss steps are observed in silanized fullerenol, and BUF-II-PEG$_{12}$-F, OmpA-F nanobioconjugates: room temperature to 120°C, 120°C–340°C, 340°C–570°C and >570°C. Silanized fullerenol, BUF-II-PEG$_{12}$-F, and OmpA-F presented a first weight loss of ~12.1%, ~11.5%, and ~12.1%, respectively. These can be attributed to the dehydration of the samples. The second weight loss of ~34% was observed for the silanized fullerenol, whereas for BUF-II-PEG$_{12}$-F and OmpA-F were ~21% and ~22%, respectively. Silanized fullerenol, BUF-II-PEG$_{12}$-F, and OmpA-F presented a third weight loss of ~15.4%, ~14.1%, and ~15.0%, respectively. These losses in the temperature range of 150°C–570°C can be assigned to the decomposition of aminopropyl groups for the silanized fullerenol and the detachment of the aminopropyl groups, conjugating agents and the BUF-II and OmpA for the nanobioconjugates (Goswami et al., 2004; Cuellar et al., 2018; Perez et al., 2019). Figure 6F shows the particle size distribution by intensity determined by DLS. The fullerenols should have a diameter of ~1.0 nm but tend to form clusters in water easily (Brant et al., 2007; Kokubo et al., 2011). The synthesized fullerenol, re-dispersed by sonication, exhibited two populations of clusters with mean hydrodynamic diameters at around 2 nm and 14 nm (Z-average size: 8 nm, PdI: 0.2). After peptide and protein conjugation, the polydispersity of the samples increased and rendered them unsuitable for DLS measurements; consequently, we performed TEM analysis. (Figure 6G). Fullerenol TEM images were consistent with DLS data regarding cluster size and the presence of two cluster population sizes. Furthermore, a change in the morphology of the nanobioconjugates is evidenced after peptide and protein immobilization, as well as aggregate formation. The aggregation may be attributable to the use of glutaraldehyde, a bifunctional reagent with a propensity for uncontrolled polymerization during the conjugation process (Hermanson, 2013). The ζ potential measurements of the fullerenol indicate that in aqueous media—pH close to 7— it acquires a negative surface charge of −20.4 ± 7.47 mV. The ζ-potential varied to −12.9 ± 0.40 mV and −19.9 ± 0.65 mV for BUF-II-PEG$_{12}$-F and OmpA-F nanobioconjugates in aqueous media—pH close to 7 —, respectively. These nanobioconjugates tend to precipitate at physiological pH.

Figure 7 shows the high-resolution (HR) spectra of fullerenol and the corresponding nanobioconjugates under examination. The decomposed peak components are labeled from high to low binding energy and depicted by colored zones. The color code employed is similar to that utilized for SNPs. Table 2 presents the binding energy (BE) values for all components integrated in the overall fitting, represented as a red line over black dots related to the experimental recorded data. Starting with the C1s core-level, the deconvolution revealed a sub-peak at higher energies and the presence of the C-C cage at 284.6 eV (Nurzynska et al., 2022). Following silanization and conjugation of BUF-II or OmpA, the peak at the lowest energy became weak or null. This may be due to the photoelectrons' inability to escape the outermost surface layer. In contrast, the pristine fullerenol sample exhibited an energy shift, most likely due to the presence of highly oxidized species associated with the hydroxyl binding onto conjugated pi bonding systems. A modified fullerenol energy sub-peak was identified at 289 eV, which can be also attributed to highly oxidized bonds such as O-C-OO (marine blue) (Nurzynska et al., 2022). The presence of these bonds may result from the chemisorption of oxygen molecules onto C-O-

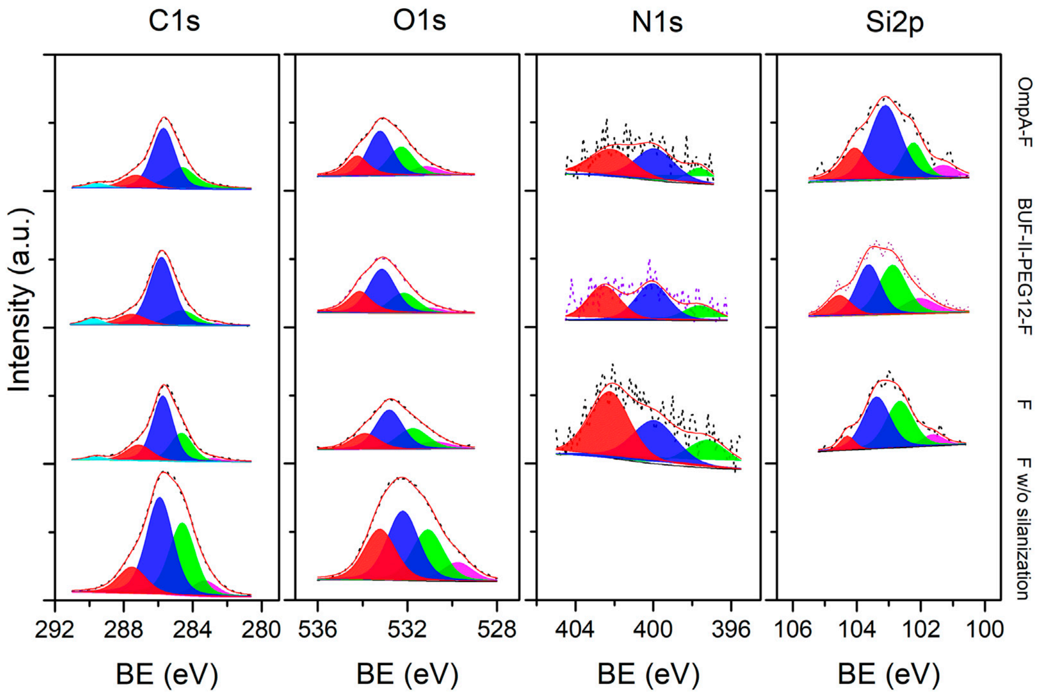

**FIGURE 7**
XPS spectra of the C1s, O1s, N1s and Si2p (left to right) core-level regions of Fullerenol, Silanized fullerenol (F), BUF-II-F and OmpA-F nanobioconjugates samples (bottom to top). Peak components for the XPS lines are differentiated by colors from high to low binding energy values (left to right).

**TABLE 2 Binding energy (BE) of the different XPS lines for C1s, O1s, N1s and S2p peak components from Fullerenol w/o silanization, F, BUF-II-F and OmpA-F nanobioconjugates samples.**

| Sample | C1s (BE- eV) | O1s (BE- eV) | N1s (BE- eV) | Si2p (BE- eV) |
|---|---|---|---|---|
| Fullerenol w/o silanization | 283.3 | 529.8 | — | — |
| | 284.6 | 531.1 | — | — |
| | 285.9 | 532.2 | — | — |
| | 287.5 | 533.2 | — | — |
| Silanized fullerenol (F) | 282.9 | 530.7 | 397.3 | 101.6 |
| | 284.6 | 531.7 | 400.0 | 102.6 |
| | 287.1 | 532.8 | 402.3 | 103.4 |
| | 289.6 | 533.9 | — | 104.3 |
| BUF-II-F | 282.6 | 531.0 | 397.6 | 102.0 |
| | 284.6 | 532.2 | 400.1 | 102.9 |
| | 285.8 | 533.1 | 402.5 | 103.6 |
| | 287.5 | 534.1 | — | 104.5 |
| | 289.8 | — | — | — |
| OmpA-F | 284.6 | 531.1 | 396.7 | 101.3 |
| | 285.7 | 532.3 | 400.0 | 102.2 |
| | 287.3 | 533.2 | 402.2 | 103.1 |
| | 289.5 | 534.,2 | — | 104.1 |

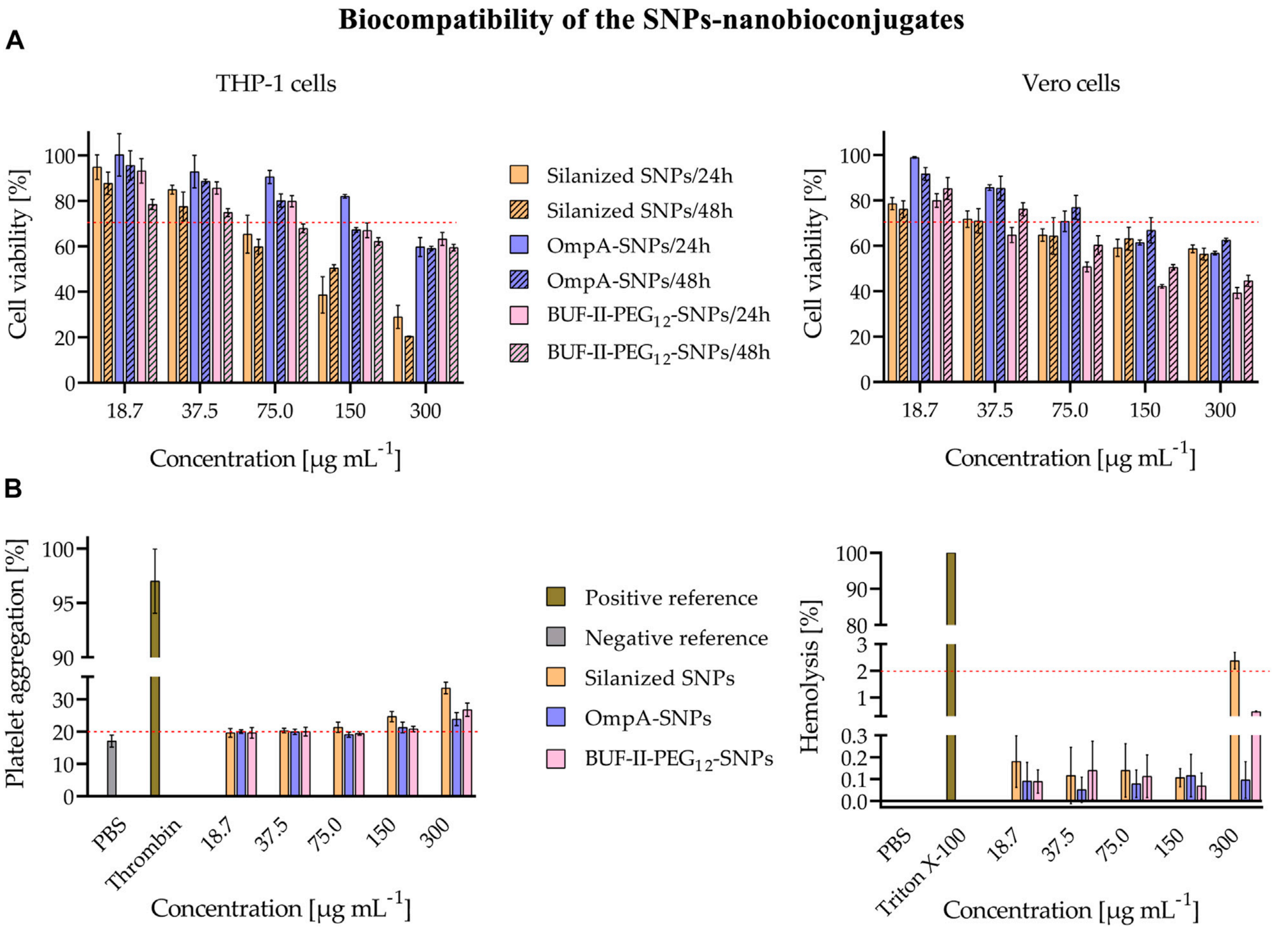

FIGURE 8
Evaluation of biocompatibility of the SNPs-nanobioconjugates **(A)** Evaluation of cytotoxicity of nanobioconjugates as tested by MTT assays after 24 and 48 h **(B)** *In vitro* evaluation of the hemocompatibility. Assessment of the hemolytic effect of nanobioconjugates (Positive control: Triton X-100, negative control: PBS. In all cases, hemolysis was below 3%; thus, the nanobioconjugates are not hemolytic; and Assessment of nanobioconjugates effects on blood coagulation (Positive control: Thrombin, negative control: PBS). There is no significant percent platelet aggregation induced by the nanobioconjugates.

radicals arising from the cleavage of C=C bonds and/or from C-O-bonds present in the activated hydroxyls before silanization. Crucially, BUF-II-PEG$_{12}$-F and OmpA-F nanobioconjugates exhibited a clearly differentiated C1s high-resolution spectra, confirming the successful conjugation of BUF-II and OmpA. The decreasing C-C/(C-O/C-N) ratio upon conjugation provided further evidence of the superior conjugation efficiency of BUF-II.

Concerning the O1s-core level, a sharper peak with a slight shift to higher energy was observed for silanized and nanobioconjugates samples compared to the reference. The larger full-width of half-maximum (FWHM) value of the pristine sample is likely associated with the overall electric field's spread on the outer C$_{60}$-cage surface due to defects that are absent on functionalized samples. This permits the favored ejection of O1s-photoelectron at lower kinetic energies. No evidence of work function alteration due to surface charge artifacts was found since the C1s-main peak of the cage was located at 284.6 eV. Nevertheless, the C1s-peak of the reference was also broader, without any evidence of a change in the peak asymmetry compared to the functionalized samples. In contrast, the main three N1s-subpeak components were detected for silanized and nanobioconjugates samples, with a higher intensity detected for the former due to the protonated amine species of the covalently attached APTES molecules. This contrasts with the observations for the SNPs discussed above. The area under the curve for the nitrogen binding energy was lower for the nanobioconjugates compared to the silanized samples due to the lower C/N ratio after conjugation of the peptide and protein molecules. Finally, the main Si2p-subpeak components provided further evidence of the successful silanization of fullerenol.

## 3.3 Biocompatibility

Biocompatibility is a crucial property in the development of nanocarriers for biomedical applications. A material is considered biocompatible if it does not elicit an undesired response from the organism. Therefore, the assessment of biocompatibility is a fundamental step in the design and

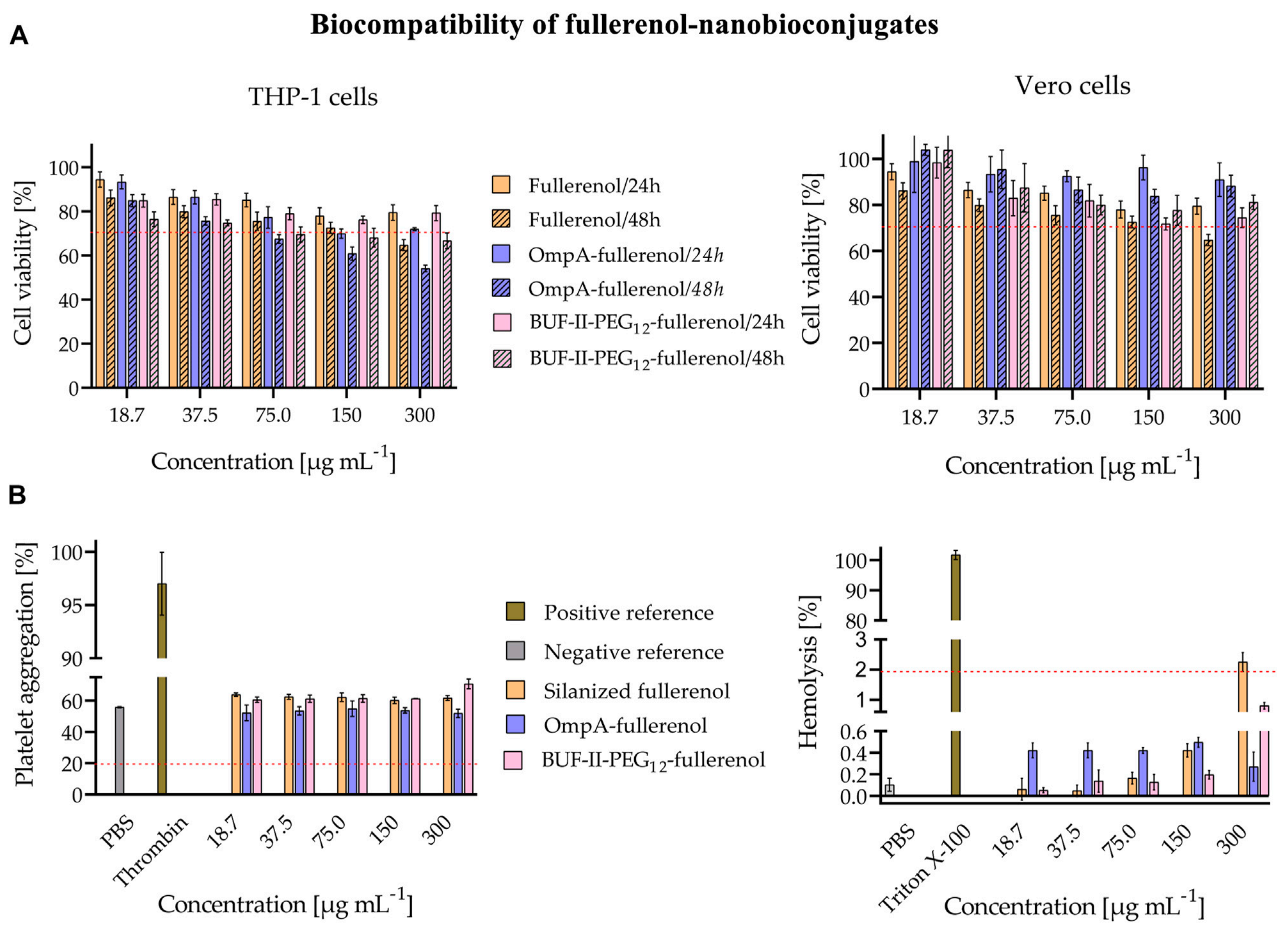

FIGURE 9
Evaluation of biocompatibility of the fullerenol-nanobioconjugates **(A)** Evaluation of cytotoxicity of nanobioconjugates as tested by MTT assays after 24 and 48 h **(B)** *In vitro* evaluation of the hemocompatibility. Assessment of the hemolytic effect of nanobioconjugates (Positive control: Triton X-100, negative control: PBS. In all cases, hemolysis was below 3%; thus, the nanobioconjugates are not hemolytic, and Assessment of nanobioconjugates effects on blood coagulation (Positive control: Thrombin, negative control: PBS). There is no significant platelet aggregation induced by the nanobioconjugates.

development of nanocarriers for drug delivery and diagnostic purposes. It is imperative to ensure that the nanocarriers are not toxic to the body and do not cause any adverse reactions (Soares et al., 2018). In order to ensure the biocompatibility of nanomaterials, multiple tests are required as per established standards such as the ISO 10993 series and ASTM F1903. Hemocompatibility and cytotoxicity tests are among the several necessary evaluations. The hemolytic properties, effects on blood coagulation, and cytotoxicity of the tested samples were assessed *in vitro*.

As shown in Figure 8A, cell viability was evaluated in THP-1 cells—a human leukemia monocytic cell line—and Vero cells—a monkey kidney epithelial line—after 24 and 48 h of exposure to the SNPs-based treatments. The outcomes demonstrated a concentration-dependent decrease in cell viability for all treatments and cell lines. Notably, at low doses of 18 and 37 μg/mL, no significant reduction in cell viability was observed for either cell type, implying the treatments' safety profile at lower concentrations. Moreover, it was observed that the cytotoxic potential of OmpA-SNPs was comparatively lower than that of BUF-II-PEG$_{12}$-SNPs. The viability of cells treated with OmpA-SNPs nanobioconjugates remained above 70% (dotted line) even at concentrations as high as 75 μg mL-1. Conversely, at the same concentration, the viability of THP-1 and Vero cell lines treated with BUF-II-PEG$_{12}$-SNPs nanobioconjugates was found to decrease. (International Organization for Standardization., 2009). In all cases, the covalent conjugation of BUF-II peptide and OmpA protein to these nanostructured materials involves the use of surface spacers (APTES, amine-PEG$_{12}$-propionic acid, glutaraldehyde, EDC, NHS), which has rendered the nanobioconjugates less cytotoxic than the bare SNPs. Surface functionalization modified the properties of the nanoparticles—e.g., the Z-average size, the ζ potential, the roughness—and thus the interactions between nanoparticles and biological components, such as proteins and cell membranes, ultimately reducing cytotoxicity (Kim et al., 2013). Figure 8B shows *in vitro* evaluation of the hemocompatibility. The treatments revealed platelet aggregation values between 2% and 16% above the negative reference—values higher than 20% are considered that induce platelet aggregation (dotted line) (Potter et al., 2018). The silanized SNPs or nanobioconjugates induced no

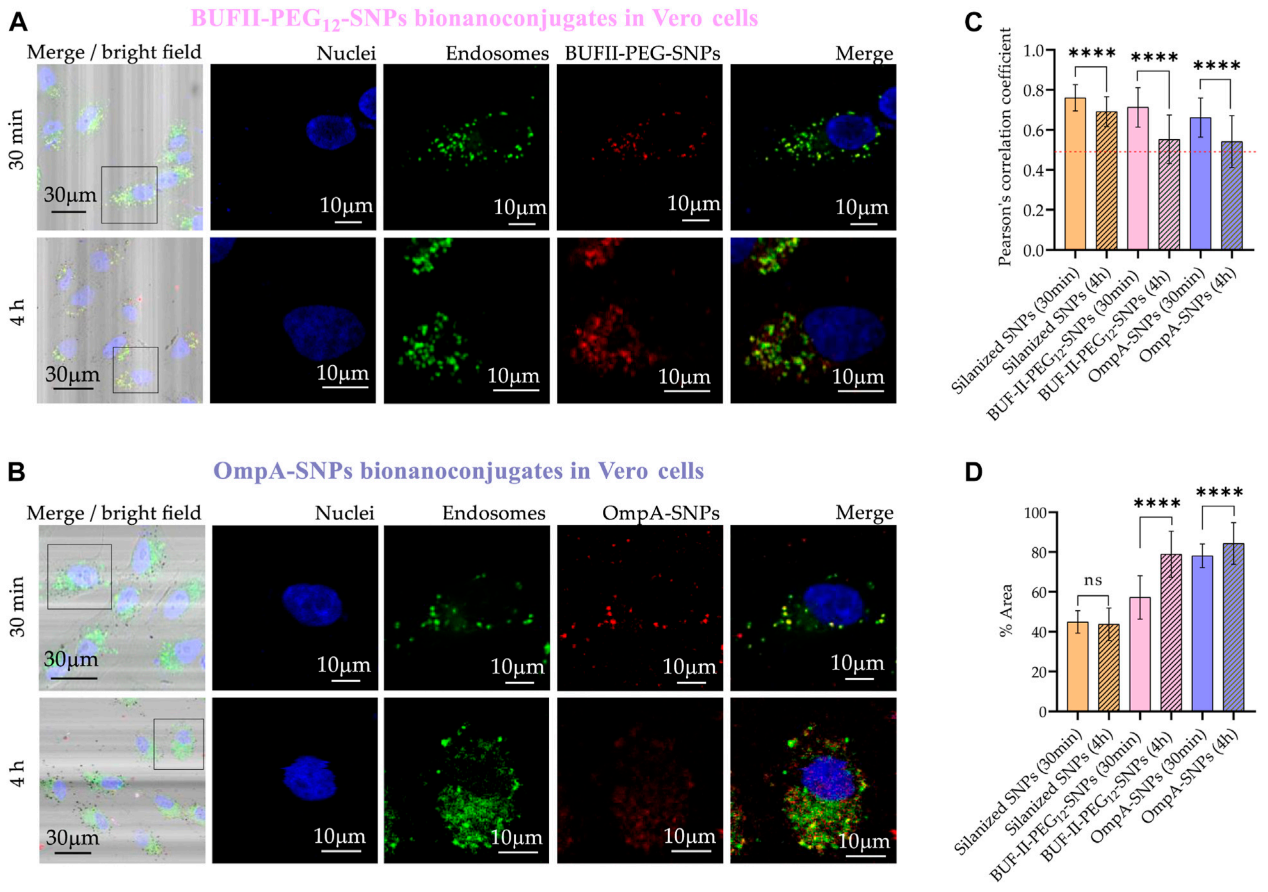

FIGURE 10
Cellular uptake and endosomal escape of the SNPs-nanobioconjugates in Vero cells **(A)** Confocal microscopy images of effective cellular uptake of BUF-II-PEG$_{12}$-SNPs nanobioconjugates in Vero cells. A zoomed view of the insets is shown on the right **(B)** Confocal microscopy images of effective cellular uptake of OmpA-SNPs nanobioconjugates in Vero cells. A zoomed view of the insets is shown on the right **(C)** Endosomal escape study via colocalization analysis **(D)** Intracellular area percentage coverage by silanized SNPs and the nanobioconjugates for Vero cells after the two exposure times (30 min and 4 h).

significant hemolytic effect, and the hemolysis values remained below 3% — Percent hemolysis less than 2 means the test sample is not hemolytic (dotted line); 2%–5% hemolysis means the test sample is slightly hemolytic; and >5% hemolysis means the test sample is hemolytic (Neun et al., 2018).

Similarly, in the case of nanobioconjugates that rely on fullerenol, cell viability remained uncompromised in both cell types, even at low doses of 18 and 37 µg mL-1 across all treatments. There was no significant reduction observed in the viability of the cells (Figure 9A). Figure 9B shows *in vitro* evaluation of the hemocompatibility. The results of the treatments showed platelet aggregation values that were 2%–15% higher than the negative reference in the fullerenol and BUF-II-PEG$_{12}$-F treatment. Conversely, there was no significant difference in platelet aggregation between the negative control and the OmpA-F nanobioconjugates treatment (Potter et al., 2018). The silanized fullerenol or nanobioconjugates did not induce a significant hemolytic effect, as evidenced by the hemolysis values remaining below 3% (Neun et al., 2018).

We recognize that the dosages used in our work may not exhibit toxicity towards target cells, such as cancer or infected cells, and that altering the dosage might change the mechanism of cellular uptake. As such, future studies should investigate the potential biological actions of these nanobioconjugates using a drug model to better understand their efficacy and safety in diverse cellular contexts. This will involve characterizing how the nanobioconjugates and their cargoes are trafficked inside cells and determining the appropriate cargo release concentrations for specific cell lines. Our current research serves as a foundation for developing conjugation strategies with known cell penetration agents and for exploring the potential of silica nanoparticles and fullerenol as nanostructured supports in targeted drug delivery applications.

## 3.4 Cellular uptake and endosomal escape

Figure 10 shows the cellular uptake of silanized SNPs, OmpA-SNPs, and BUF-II-PEG$_{12}$-SNPs nanobioconjugates by Vero cells. Rhodamine B-labeled nanobioconjugates (red) were observed to be homogeneously distributed within the cells, without significant penetration of the cell nucleus (blue). The colocalization of the nanobioconjugates with acidic organelles, such as endosomes/

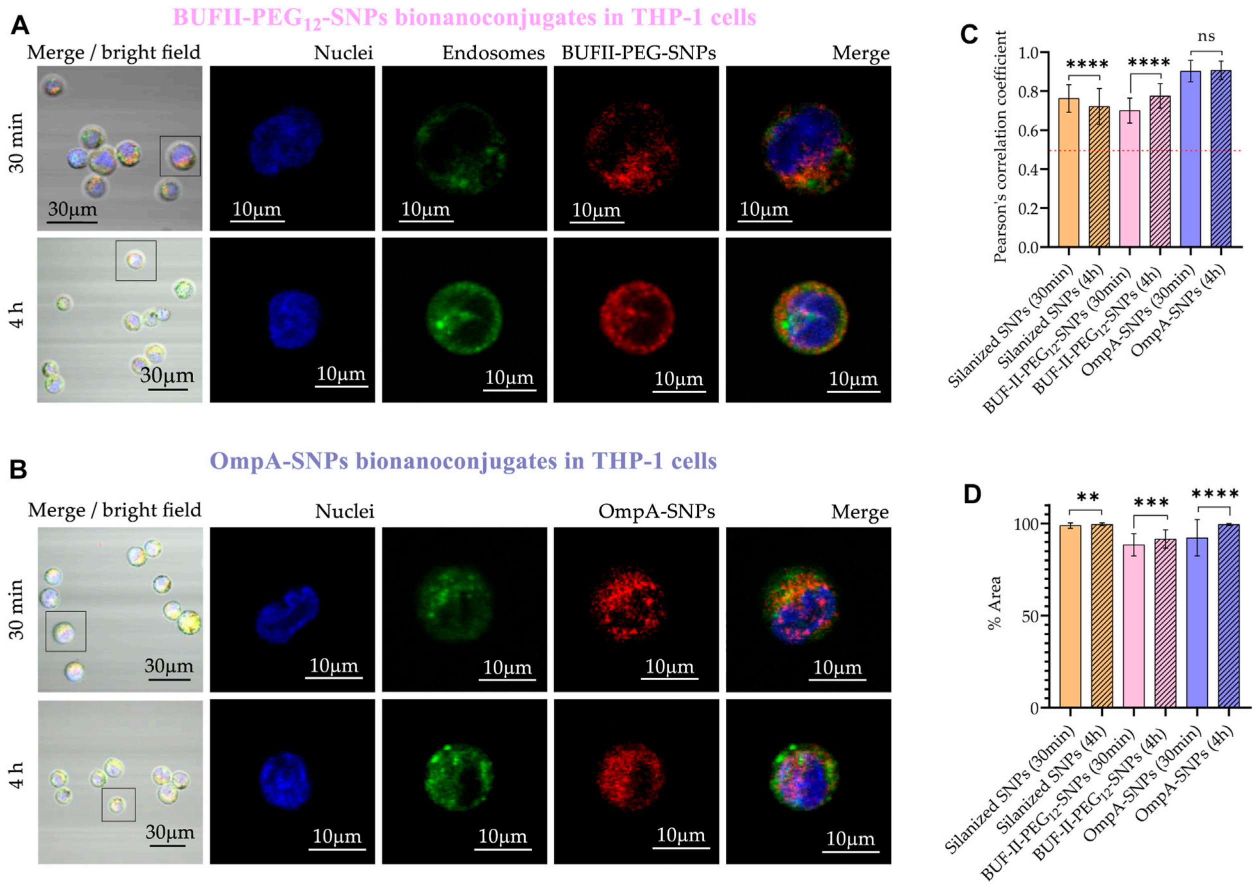

FIGURE 11
Cellular uptake and endosomal escape of the SNPs-nanobioconjugates in THP-1 cells **(A)** Confocal microscopy images of effective cellular uptake of silanized SNPs and BUF-II-PEG$_{12}$-SNPs nanobioconjugates in THP-1 cells. A zoomed view of individual cells is shown on the insets in the right panels **(B)** Confocal microscopy images of effective cellular uptake of silanized SNPs and OmpA-SNPs in THP-1 cells. A zoomed view of individual cells is shown on the insets in the right panels **(C)** Endosomal escape study via colocalization analysis **(D)** Intracellular area percentage coverage by silanized SNPs and the nanobioconjugates for THP-1 cells after the two exposure times (30 min and 4 h).

lysosomes, was determined quantitatively through correlation analysis, based on Pearson's coefficient (PC). The PC value ranges from 1 to −1, where 1 represents complete and positive correlation between the intensity of fluorescence signals, −1 denotes perfect but negative correlation, and 0 indicates no correlation (Adler and Parmryd, 2010; Dunn et al., 2011). Intracellular area percentage coverage by silanized SNPs and the nanobioconjugates was also determined.

CP values after 30 min in Vero cells were 0.76 ± 0.07; 0.71 ± 0.10; and 0.66 ± 0.10 for the silanized SNPs, BUF-II-PEG$_{12}$-SNPs, and OmpA-SNPs, respectively. These CP values decreased to 0.72 ± 0.09; 0.55 ± 0.12; and 0.54 ± 0.13; for the silanized SNPs, BUF-II-PEG$_{12}$-SNPs, and OmpA-SNPs, respectively, after 4 h of incubation. A reduced level of colocalization with the endosomal/lysosomal marker (green) is indicative of the propensity of nanobioconjugates to evade endosomes in Vero cells. While the precise mechanisms involved in endosomal escape are not fully understood, it is likely that this occurs either through the formation of temporary pores or via the proton sponge effect, as posited in prior studies (Cho et al., 2009; Cardoso et al., 2019; López-Barbosa et al., 2019; Lopez-Barbosa et al., 2020).

In the case of THP-1 cells (Figure 11), CP values after 30 min were 0.76 ± 0.07; 0.70 ± 0.06; and 0.90 ± 0.05 for silanized SNPs, BUF-II-PEG$_{12}$-SNPs, and OmpA-SNPs, respectively. After 4 h of incubation, the CP values approached 0.69 ± 0.77; 0.78 ± 0.06; and 0.91 ± 0.05; for the silanized SNPs, BUF-II-PEG$_{12}$-SNPs, and OmpA-SNPs, respectively, indicating a low tendency of nanobioconjugates to escape from endosomes in THP-1 cells. This behavior holds potential significance for the investigation of enzyme replacement therapies in the management of lysosomal storage diseases. Such diseases necessitate periodic intravenous infusions of human recombinant lysosomal enzymes, produced through recombinant DNA techniques. Following administration of the treatment, the recombinant enzymes disperse throughout the tissues, undergo internalization by cells, and are directed to the lysosomal compartment for the purpose of substituting the deficient protein in the patients (Parenti et al., 2013). Finally, the percentages of the area covered by the nanobioconjugates were higher in THP-1 cells than in Vero cells and increased with incubation time.

Figure 12 provides evidence of the cellular uptake of OmpA-F and BUF-II-PEG$_{12}$-F nanobioconjugates by Vero cells. The rhodamine B-labeled nanobioconjugates (red) were observed to

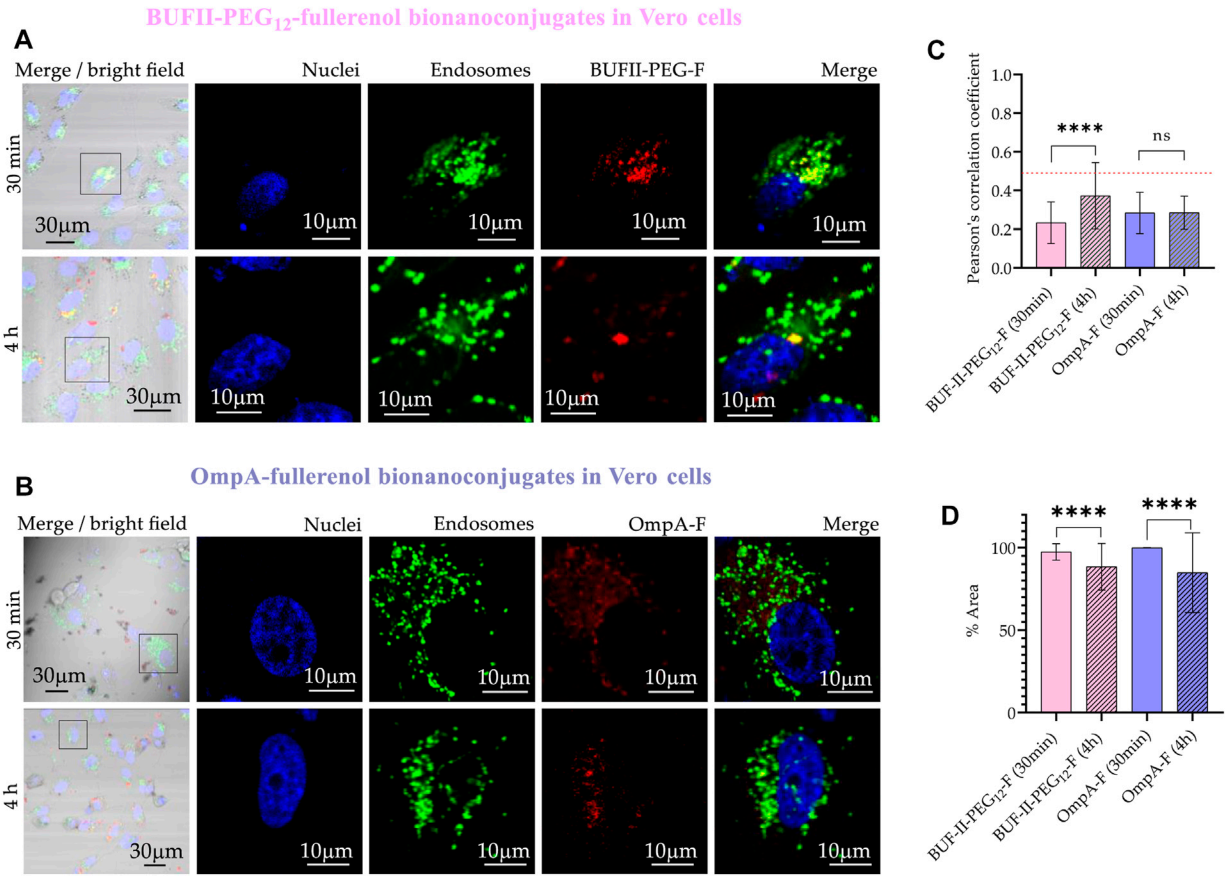

FIGURE 12
Cellular uptake and endosomal escape of the fullerenol-nanobioconjugates in Vero cells **(A)** Confocal microscopy images of effective cellular uptake of BUF-II-PEG$_{12}$-Fnanobioconjugates in Vero cells. A zoomed view of individual cells is shown on the insets in the right panels **(B)** Confocal microscopy images of effective cellular uptake of OmpA-F nanobioconjugates in Vero cells. A zoomed view of individual cells is shown on the insets in the right panels **(C)** Endosomal escape study via colocalization analysis **(D)** Intracellular area percentage coverage by the nanobioconjugates for Vero cells after the two exposure times (30 min and 4 h).

be homogeneously distributed within the cells but did not significantly reach the cell nucleus (blue). In contrast to SNP-based nanobioconjugates, fullerenol-based nanobioconjugates tend to aggregate and form clusters, which could have significant implications for their biological applications. CP values after 30 min were 0.23 ± 0.11; and 0.28 ± 0.11 for BUF-II-PEG$_{12}$-F and OmpA-F, respectively. After 4 h of incubation, the CP values approached 0.37 ± 0.17; and 0.29 ± 0.08; for BUF-II-PEG$_{12}$-F and OmpA-F, respectively. CP values less than 0.5 indicate a low degree of colocalization between the nanobioconjugates and the endosomes/lysosomes. The extensive coverage of the cytoplasmic area by the particles provides evidence for the internalization of the nanobioconjugates. These results suggest that the mechanism of entry of the nanobioconjugates into Vero cells is likely non-endocytic.

In the case of THP-1 cells (Figure 13), CP values after 30 min were 0.83 ± 0.07; and 0.77 ± 0.11 for BUF-II-PEG$_{12}$-F and OmpA-F, respectively. These CP values decreased to 0.74 ± 0.16; and 0.74 ± 0.12; for BUF-II-PEG$_{12}$-F and OmpA-fullerenol, respectively, after 4 h of incubation. This suggests a tendency of BUF-II-PEG$_{12}$-F nanobioconjugates to escape from endosomes in THP-1 cells, which is not observed for OmpA-F nanobioconjugates. The high coverage of the cytoplasmic area confirms the internalization of the nanobioconjugates.

In addition to the cell penetration and endosomal escape capabilities of our nanobioconjugates, it is essential to highlight their potential for targeted drug delivery to specific subcellular compartments. By functionalizing the nanobioconjugates with appropriate ligands, such as specific peptide sequences or small molecules, these drug delivery systems can be tailored to exhibit a high affinity for the desired organelle. This customization enables enhanced specificity in targeting organelles such as mitochondria or others of interest. Moreover, we acknowledge the potential benefits of non-endocytic mechanisms as a more straightforward route for targeting subcellular compartments. While endosomal escape is a crucial step in ensuring efficient delivery of cargo to the cytosol, non-endocytic routes might offer alternative advantages in achieving more targeted delivery to specific organelles. Further exploration of these strategies and the development of suitable ligands will be essential in optimizing the nanobioconjugates for specific therapeutic applications.

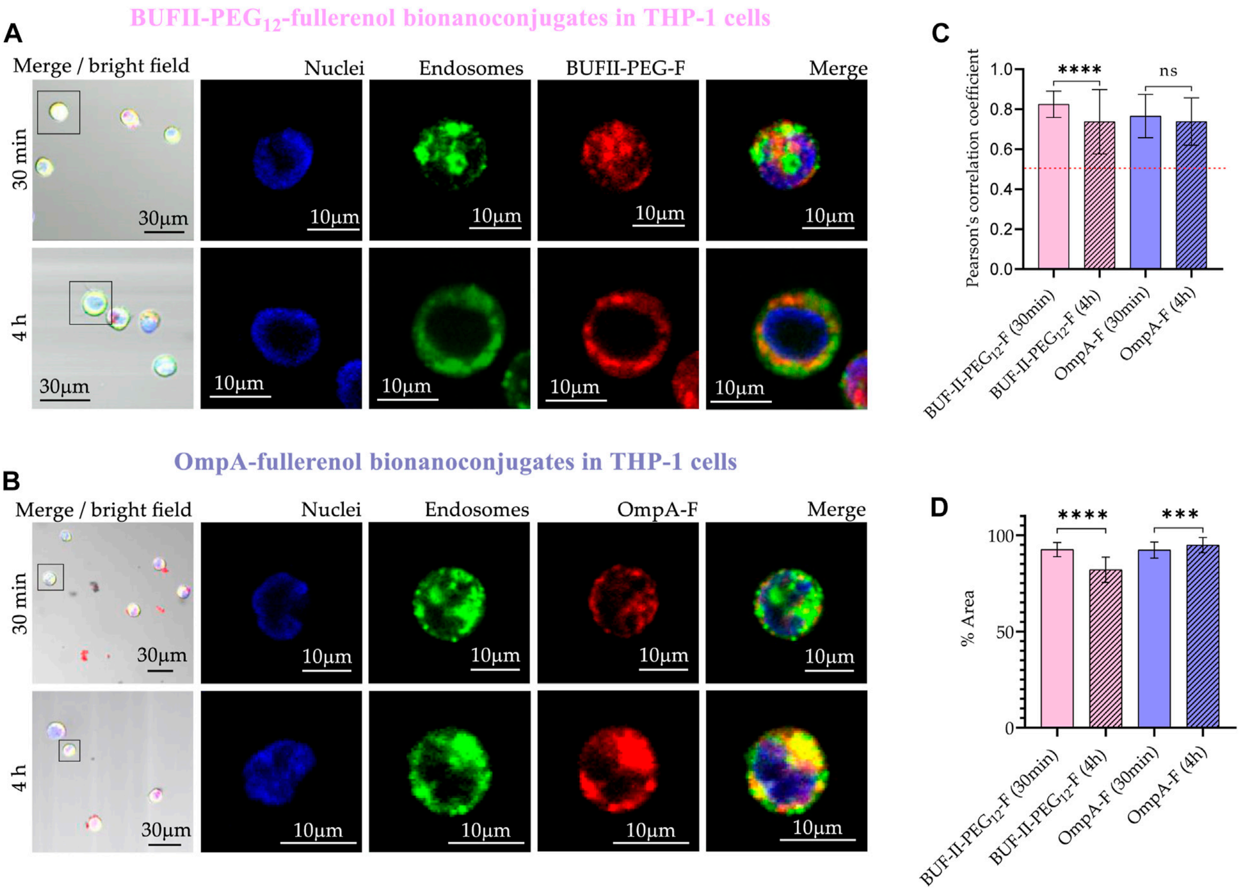

FIGURE 13
Cellular uptake and endosomal escape of the fullerenol-nanobioconjugates in THP-1 cells **(A)** Confocal microscopy images of effective cellular uptake of BUF-II-PEG$_{12}$-F nanobioconjugates in THP-1 cells. A zoomed view of individual cells is shown on the insets in the right panels **(B)** Confocal microscopy images of effective cellular uptake of OmpA-F nanobioconjugates in THP-1 cells. A zoomed view of individual cells is shown on the insets in the right panels **(C)** Endosomal escape study via colocalization analysis **(D)** Intracellular area percentage coverage by the nanobioconjugates for THP-1 cells after the two exposure times (30 min and 4 h).

# 4 Conclusion and outlook

In summary, our study demonstrates a comprehensive approach for immobilizing translocating biomolecules on SNPs and fullerenol. The success of this strategy was confirmed by a range of analytical techniques including FT-IR, TGA, DLS, Electrophoretic Mobility, SEM, TEM, and XPS. The resulting nanobioconjugates, including OmpA-SNPs, BUF-II-PEG$_{12}$-SNPs, OmpA-F, and BUF-II-PEG$_{12}$-F, exhibited high biocompatibility in both Vero and THP-1 cell lines. Moreover, our evaluations of hemolytic effects and platelet aggregation demonstrated their safety at the tested concentrations. Our confocal microscopy studies revealed efficient internalization of the different nanobioconjugates in both Vero and THP-1 cells, with notable differences in endosomal escape. In particular, OmpA-SNPs and BUF-II-PEG$_{12}$-SNPs showed a tendency to escape from endosomes in Vero cells, while remaining trapped in THP-1 cells. On the other hand, OmpA-F and BUF-II-PEG$_{12}$-F were effectively internalized by both cell lines, with a superior tendency to escape from endosomes in Vero cells. These findings are significant, as they provide evidence for the potential of our nanobioconjugates to enhance the stability and half-life of translocating biomolecules and cross biological membranes without affecting cell viability. The ability to develop highly tunable cargo delivery systems is crucial for meeting the needs of specific treatments and targeting cell or organelle types. Overall, our study highlights the promise of our nanobioconjugates as a platform for the development of innovative therapeutic approaches. In our forthcoming research, we aim to elucidate the intracellular trafficking mechanisms of these nanobioconjugates and their cargoes, as well as the targeted release of cargo within specific cell lines at precise concentrations.

# Data availability statement

The original contributions presented in the study are included in the article/Supplementary Material, further inquiries can be directed to the corresponding author.

## Ethics statement

Human blood samples were collected under the permission obtained from the ethics committee at Universidad de los Andes, minute number 928-2018 (17 September 2018). The patients/participants provided their written informed consent to participate in this study.

## Author contributions

Conceptualization, JCC, ER-N, and AD-R; Methodology, data curation, and data analysis ER-N, JC, CO, AD-R and JCC; Formal analysis and investigation, ER-N, JC, PR, LR-G, VQ; Validation, CM-C, LR, JCC, and AD-R; Writing—original draft preparation, ERN; Writing—review and editing, JCC, JC, and AD-R; Supervision, CM-C, LR, JCC, and AD-R. All authors have read and agreed to the published version of the manuscript.

## Funding

This work was supported by Minciencias grant 689-2018.

## Acknowledgments

The authors would like to thank the Department of Biomedical Engineering—Universidad de Los Andes —, the Department of Chemistry—Universidad Nacional de Colombia—for providing access to laboratory infrastructure, and the Universidad de Antioquia for their technical support with SEM, TEM imaging, and XPS. We thank Cristina Gonzalez Melo, Tatiana Carolina Beltran Gonzalez, Juan Camilo Orozco, Eliana P. Benincore Flórez, and Carlos A. Martínez Bonilla for technical support and additional insights into the characterization of our materials. The authors also would like to thank the Vice Presidency of Research and Creation's Publication Fund at Universidad de los Andes for its financial support.

## Conflict of interest

The authors declare that the research was conducted in the absence of any commercial or financial relationships that could be construed as a potential conflict of interest.

## Publisher's note

## Supplementary material

The Supplementary Material for this article can be found online at: https://www.frontiersin.org/articles/10.3389/fbioe.2023.1184973/full#supplementary-material

## References

Adler, J., and Parmryd, I. (2010). Quantifying colocalization by correlation: The pearson correlation coefficient is superior to the Mander's overlap coefficient. *Cytom. Part A* 77, 733–742. doi:10.1002/cyto.a.20896

Aguilera-Segura, S. M., Macías, A. P., Carrero-Pinto, D., Vargas, W. L., Vives-Florez, M. J., Castro-Barrera, H. E., et al. (2014). "Advances in computational biology proceedings of the 2nd Colombian congress on computational biology and bioinformatics (CCBCOL)," in Escherichia coli´s *OmpA as biosurfactant for cosmetic industry: Stability analysis and experimental validation based on molecular simulations*, 265–272. doi:10.1007/978-3-319-01568-2

Ajie, H., Alvarez, M. M., Anz, S. J., Beck, R. D., Diederich, F., Fostiropoulos, K., et al. (1990). Characterization of the soluble all-carbon molecules C60 and C70. *J. Phys. Chem.* 94, 8630–8633. doi:10.1021/j100387a004

Alan, B. O., Barisik, M., and Ozcelik, H. G. (2020). Roughness effects on the surface charge properties of silica nanoparticles. *J. Phys. Chem. C* 124, 7274–7286. doi:10.1021/acs.jpcc.0c00120

Alves, D., and Olívia Pereira, M. (2014). Mini-review: Antimicrobial peptides and enzymes as promising candidates to functionalize biomaterial surfaces. *Biofouling* 30, 483–499. doi:10.1080/08927014.2014.889120

Barisik, M., Atalay, S., Beskok, A., and Qian, S. (2014). Size dependent surface charge properties of silica nanoparticles. *J. Phys. Chem. C* 118, 1836–1842. doi:10.1021/jp410536n

Bolskar, R. D. (2013). "Nanomaterials for electrical energy storage devices," in *Encyclopedia of nanotechnology*. Editor B. Bhushan, 2473–2485. doi:10.1007/978-94-017-9780-1

Brant, J. A., Labille, J., Robichaud, C. O., and Wiesner, M. (2007). Fullerol cluster formation in aqueous solutions: Implications for environmental release. *J. Colloid Interface Sci.* 314, 281–288. doi:10.1016/j.jcis.2007.05.020

Cardoso, M. H., Meneguetti, B. T., Costa, B. O., Buccini, D. F., Oshiro, K. G. N., Preza, S. L. E., et al. (2019). Non-lytic antibacterial peptides that translocate through bacterial membranes to act on intracellular targets. *Int. J. Mol. Sci.* 20, 4877. doi:10.3390/ijms20194877

Chenthamara, D., Subramaniam, S., Ramakrishnan, S. G., Krishnaswamy, S., Essa, M. M., Lin, F., et al. (2019). Therapeutic efficacy of nanoparticles and routes of administration. *Biomater. Res.* 23, 20–29. doi:10.1186/s40824-019-0166-x

Cho, J. H., Sung, B. H., and Kim, S. C. (2009). Buforins: Histone H2A-derived antimicrobial peptides from toad stomach. *Biochim. Biophys. Acta - Biomembr.* 1788, 1564–1569. doi:10.1016/j.bbamem.2008.10.025

Cuellar, M., Cifuentes, J., Perez, J., Suarez-arnedo, A., Serna, J. A., Groot, H., et al. (2018). Novel BUF2-magnetite nanobioconjugates with cell-penetrating abilities. *Int. J. Nanomed.* 13, 8087–8094. doi:10.2147/IJN.S188074

De Santiago, H. A., Gupta, S. K., and Mao, Y. (2019). On high purity fullerenol obtained by combined dialysis and freeze-drying method with its morphostructural transition and photoluminescence. *Sep. Purif. Technol.* 210, 927–934. doi:10.1016/j.seppur.2018.08.033

Dunn, K. W., Kamocka, M. M., and McDonald, J. H. (2011). A practical guide to evaluating colocalization in biological microscopy. *Am. J. Physiol. - Cell Physiol.* 300, 723–742. doi:10.1152/ajpcell.00462.2010

Edrissi, M., Soleymani, M., and Adinehnia, M. (2011). Synthesis of silica nanoparticles by ultrasound-assisted sol-gel method: Optimized by Taguchi robust design. *Chem. Eng. Technol.* 34, 1813–1819. doi:10.1002/ceat.201100195

Esim, O., Kurbanoglu, S., Savaser, A., Ozkan, S. A., and Ozkan, Y. (2019). "Nanomaterials for drug delivery systems," in *New developments in nanosensors for pharmaceutical analysis* (London, UK: Academic Press), 237–301.

Gonçalves, M. C. (2018). Sol-gel silica nanoparticles in medicine: A natural choice. Design, synthesis and products. *Molecules* 23, 2021. doi:10.3390/molecules23082021

Goswami, T. H., Singh, R., Alam, S., and Mathur, G. N. (2004). Thermal analysis: A unique method to estimate the number of substituents in fullerene derivatives. *Thermochim. Acta* 419, 97–104. doi:10.1016/j.tca.2004.02.001

Hermanson, G. T. (2013). "Antibody modification and conjugation," in *Bioconjugate techniques* (San Diego, CA), 879.

Hossen, S., Hossain, K., Basher, M. K., Mia, M. N. H., Rahman, M. T., and Uddin, M. J. (2018). Smart nanocarrier-based drug delivery systems for cancer therapy and toxicity studies: A review. *J. Adv. Res.* 1, 1–18. doi:10.1016/j.jare.2018.06.005

International Organization for Standardization (2009). *ISO10993-5:2009(E) Biological evaluation of medical devices — Part 5: Tests for* in vitro *cytotoxicity*.

Karabasz, A., Bzowska, M., and Szczepanowicz, K. (2020). Biomedical applications of multifunctional polymeric nanocarriers: A review of current literature. *Int. J. Nanomed.* 15, 8673–8696. doi:10.2147/IJN.S231477

Kazemzadeh, H., and Mozafari, M. (2019). Fullerene-based delivery systems. *Drug Discov. Today* 24, 898–905. doi:10.1016/j.drudis.2019.01.013

Kim, S. T., Saha, K., Kim, C., and Rotello, V. M. (2013). The role of surface functionality in determining nanoparticle cytotoxicity. *Acc. Chem. Res.* 46, 681–691. doi:10.1021/ar3000647

Kim, W., Kim, W. K., Lee, K., Son, M. J., Kwak, M., Chang, W. S., et al. (2019). A reliable approach for assessing size-dependent effects of silica nanoparticles on cellular internalization behavior and cytotoxic mechanisms. *Int. J. Nanomed.* 14, 7375–7387. doi:10.2147/IJN.S224183

Kokubo, K., Matsubayashi, K., Tategaki, H., Takada, H., and Oshima, T. (2008). Facile synthesis of highly water-soluble fullerenes more than half-covered by hydroxyl groups. *ACS Nano* 2, 327–333. doi:10.1021/nn700151z

Kokubo, K., Shirakawa, S., Kobayashi, N., Aoshima, H., and Oshima, T. (2011). Facile and scalable synthesis of a highly hydroxylated water-soluble fullerenol as a single nanoparticle. *Nano Res.* 4, 204–215. doi:10.1007/s12274-010-0071-z

Komin, A., Russell, L. M., Hristova, K. A., and Searson, P. C. (2017). Peptide-based strategies for enhanced cell uptake, transcellular transport, and circulation: Mechanisms and challenges. *Adv. Drug Deliv. Rev.* 110–111, 52–64. doi:10.1016/j.addr.2016.06.002

Kovač, T., Borišev, I., Crevar, B., Kenjerić, F. Č., Ko, M., Strelec, I., et al. (2018). Fullerol C60(OH)24 nanoparticles modulate aflatoxin B 1 biosynthesis in Aspergillus flavus. *Sci. Rep.* 60, 12855–12858. doi:10.1038/s41598-018-31305-9

Krätschmer, W., Lamb, L. D., Fostiropoulos, K., and Huffman, D. R. (1990). Solid C60: A new form of carbon. *Nature* 347, 354–358. doi:10.1038/347354a0

Kunc, F., Balhara, V., Sun, Y., Daroszewska, M., Jakubek, Z. J., Hill, M., et al. (2019). Quantification of surface functional groups on silica nanoparticles: Comparison of thermogravimetric analysis and quantitative NMR. *Analyst* 144, 5589–5599. doi:10.1039/c9an01080g

Li, L., Xi, W., Su, Q., Li, Y., Yan, G., Liu, Y., et al. (2019). Unexpected size effect: The interplay between different- sized nanoparticles in their cellular uptake. *Small* 15, 1901687–1901688. doi:10.1002/smll.201901687

López-Barbosa, N., Suarez-Arnedo, A., Cifuentes, J., González-Barrios, A., Batista, C., Osma, J., et al. (2019). Magnetite-OmpA nanobioconjugates as cell-penetrating vehicles with endosomal escape abilities. *ACS Biomater. Sci. Eng.* 6, 415–424. doi:10.1021/acsbiomaterials.9b01214

Lopez-Barbosa, N., Garcia, J. G., Cifuentes, J., Castro, L. M., Vargas, F., Ostos, C., et al. (2020). Multifunctional magnetite nanoparticles to enable delivery of siRNA for the potential treatment of Alzheimer ' s. *Drug Deliv.* 27, 864–875. doi:10.1080/10717544.2020.1775724

Masalov, V. M., Sukhinina, N. S., Kudrenko, E. A., and Emelchenko, G. A. (2011). Mechanism of formation and nanostructure of Stöber silica particles. *Nanotechnology* 22, 275718. doi:10.1088/0957-4484/22/27/275718

McNeil, S. E. (2011). "Unique benefits of nanotechnology to drug delivery and diagnostics," in *Characterization of nanoparticles intended for drug delivery*. Editor S. E. McNeil (Frederick, MD, USA), 3–8. doi:10.1007/978-1-60327-198-1

McNeil, S. E. (2018). "Evaluating nanomedicines: Obstacles and advancements," in *Characterization of nanoparticles intended for drug delivery*. Editor S. E. McNeil (Frederick, MD, USA), 3–16. doi:10.1007/978-1-4939-7352-1

Meerloo, J. V., Kaspers, G. J. L., and Jacqueline, C. (2011). "Cell sensitivity assays: The MTT assay," in *Cancer cell culture: Methods and protocols*. Editor I. A. Cree (Portsmouth UK: Humana Press), 237–245. doi:10.1007/978-1-61779-080-5

Muñoz-Camargo, C., Salazar, V. A., Barrero-Guevara, L., Camargo, S., Mosquera, A., Groot, H., et al. (2018). Unveiling the multifaceted mechanisms of antibacterial activity of buforin II and frenatin 2.3S peptides from skin micro-organs of the orinoco lime treefrog (Sphaenorhynchus lacteus). *Int. J. Mol. Sci.* 19, 2170. doi:10.3390/ijms19082170

Neun, B. W., Ilinskaya, A. N., and Dobrovolskaia, M. A. (2018). "Updated method for *in vitro* analysis of nanoparticle hemolytic properties," in *Characterization of nanoparticles intended for drug delivery*. Editor S. E. McNeil (Frederick, MD, USA), 91–102. doi:10.1007/978-1-4939-7352

Niu, Y., Yu, M., Zhang, J., Yang, Y., Xu, C., Yeh, M., et al. (2015). Synthesis of silica nanoparticles with controllable surface roughness for therapeutic protein delivery. *J. Mater. Chem. B* 3, 8477–8485. doi:10.1039/C5TB01405K

Nurzynska, A., Piotrowski, P., Klimek, K., Król, J., Kaim, A., and Ginalska, G. (2022). Novel C60 fullerenol-gentamicin conjugate–physicochemical characterization and evaluation of antibacterial and cytotoxic properties. *Molecules* 27, 4366. doi:10.3390/molecules27144366

Parenti, G., Pignata, C., Vajro, P., and Salerno, M. (2013). New strategies for the treatment of lysosomal storage diseases (Review). *Int. J. Mol. Med.* 31, 11–20. doi:10.3892/ijmm.2012.1187

Perez, J., Cifuentes, J., Cuellar, M., Suarez-Arnedo, A., Cruz, J. C., and Muñoz-Camargo, C. (2019). Cell-penetrating and antibacterial BUF-II nanobioconjugates: Enhanced potency via immobilization on polyetheramine-modified magnetite nanoparticles. *Int. J. Nanomed.* 14, 8483–8497. doi:10.2147/IJN.S224286

Planque, M. R. R. D., Aghdaei, S., Roose, T., and Morgan, H. (2011). *Electrophysiological characterization of membrane disruption by nanoparticles*, 3599–3606.

Potter, T. M., Rodriguez, J. C., Neun, B. W., Ilinskaya, A. N., Cedrone, E., and Dobrovolskaia, M. A. (2018). "*In vitro* assessment of nanoparticle effects on blood coagulation," in *Characterization of nanoparticles intended for drug delivery*. Editor S. E. McNeil (Frederick, MD, USA), 103–124. doi:10.1007/978-1-4939-7352-1

Pretsch, E., Bühlmann, P., and Badertscher, M. (2009). Structure determination of organic compounds: Tables of spectral data. doi:10.1007/978-3-540-93810-1

Ramírez-Acosta, C. M., Cifuentes, J., Castellanos, M. C., Moreno, R. J., Muñoz-camargo, C., Cruz, J. C., et al. (2020). pH-responsive, cell-penetrating, core/shell magnetite/silver nanoparticles for the delivery of plasmids: Preparation, characterization, and preliminary *in vitro* evaluation. *Pharmaceutics* 12, 561–625. doi:10.3390/pharmaceutics12060561

Rangel-Muñoz, N., González-Barrios, A. F., Pradilla, D., Osma, J. F., and Cruz, J. C. (2020). Novel bionanocompounds: Outer membrane protein A and laccase Co-immobilized on magnetite nanoparticles for produced water treatment. *Nanomaterials* 10, 2278–2322. doi:10.3390/nano10112278

Ravelo-Nieto, E., Duarte-Ruiz, A., Reyes, L. H., and Cruz, J. C. (2020). Synthesis and characterization of a fullerenol derivative for potential biological applications. *Mater. Proc.* 4, 15. doi:10.3390/iocn2020-07793

Selby, L. I., Cortez-Jugo, C. M., Such, G. K., and Johnston, A. P. R. (2017). Nanoescapology: Progress toward understanding the endosomal escape of polymeric nanoparticles. *Wiley Interdiscip. Rev. Nanomed. Nanobiotechnol.* 9. doi:10.1002/wnan.1452

Shafqat, S. S., Khan, A. A., Zafar, M. N., Alhaji, M. H., Sanaullah, K., Shafqat, S. R., et al. (2019). Development of amino-functionalized silica nanoparticles for efficient and rapid removal of COD from pre-treated palm oil effluent. *J. Mater. Res. Technol.* 8, 385–395. doi:10.1016/j.jmrt.2018.03.002

Shnoudeh, A. J., Hamad, I., Abdo, R. W., Qadumii, L., Yousef Jaber, A., Salim Surchi, H., et al. (2019). "Synthesis, characterization, and applications of metal nanoparticles," in *Biomaterials and bionanotechnology* (E. Inc), 527–611. doi:10.1016/B978-0-12-814427-5.00015-9

Soares, S., Sousa, J., Pais, A., and Vitorino, C. (2018). Nanomedicine: Principles, properties, and regulatory issues. *Front. Chem.* 6, 360–415. doi:10.3389/fchem.2018.00360

Stober, W., Fink, A., and Bohn, E. (1968). Controlled growth of monodisperse silica spheres in the micron size range. *J. Collod interface Sci.* 26, 62–69. doi:10.1016/0021-9797(68)90272-5

Talavera-Pech, W. A., Esparza-Ruiz, A., Quintana-Owen, P., Vilchis-Nestor, A. R., Carrera-Figueiras, C., and Ávila-Ortega, A. (2016). Effects of different amounts of APTES on physicochemical and structural properties of amino-functionalized MCM-41-MSNs. *J. Sol-Gel Sci. Technol.* 80, 697–708. doi:10.1007/s10971-016-4163-4

Tatulian, S. A. (2013). "Structural characterization of membrane proteins and peptides by FTIR and ATR-FTIR spectroscopy," in *Lipid-protein interactions: Methods and protocols*, *Methods in Molecular Biology* (New York), 177–2018. doi:10.1007/978-1-62703-275-9_9

# Frontiers in
# Bioengineering and Biotechnology

**Accelerates the development of therapies, devices, and technologies to improve our lives**

A multidisciplinary journal that accelerates the development of biological therapies, devices, processes and technologies to improve our lives by bridging the gap between discoveries and their application.

---

## Discover the latest Research Topics

See more →

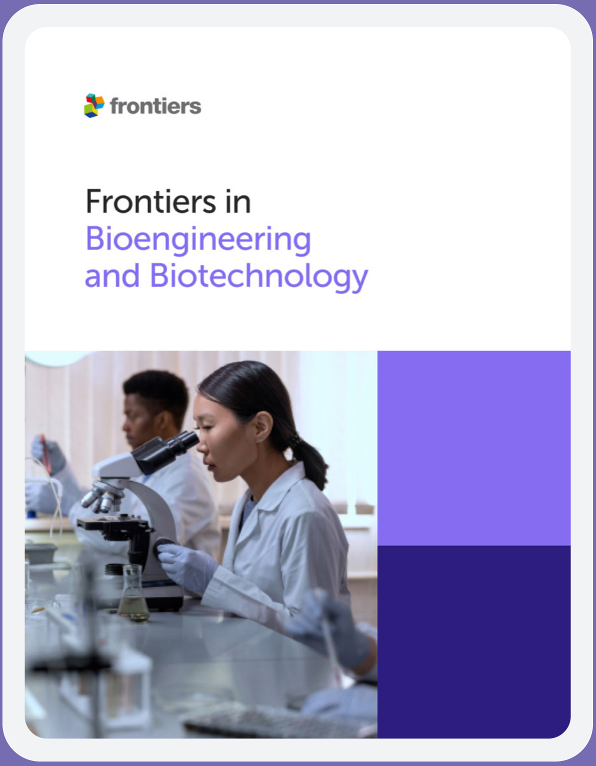
frontiers

Frontiers in
Bioengineering
and Biotechnology

**Frontiers**
Avenue du Tribunal-Fédéral 34
1005 Lausanne, Switzerland
frontiersin.org

**Contact us**
+41 (0)21 510 17 00
frontiersin.org/about/contact